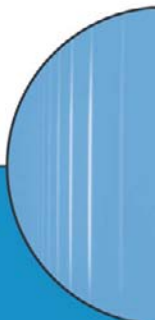


OXFORD MASTER SERIES IN ATOMIC, OPTICAL  
AND LASER PHYSICS

# Atomic Physics

Christopher J. Foot



oxford  
master  
series  
in atomic,  
optical,  
and laser  
physics

OXFORD MASTER SERIES IN PHYSICS

---

## OXFORD MASTER SERIES IN PHYSICS

---

The Oxford Master Series is designed for final year undergraduate and beginning graduate students in physics and related disciplines. It has been driven by a perceived gap in the literature today. While basic undergraduate physics texts often show little or no connection with the huge explosion of research over the last two decades, more advanced and specialized texts tend to be rather daunting for students. In this series, all topics and their consequences are treated at a simple level, while pointers to recent developments are provided at various stages. The emphasis is on clear physical principles like symmetry, quantum mechanics, and electromagnetism which underlie the whole of physics. At the same time, the subjects are related to real measurements and to the experimental techniques and devices currently used by physicists in academe and industry. Books in this series are written as course books, and include ample tutorial material, examples, illustrations, revision points, and problem sets. They can likewise be used as preparation for students starting a doctorate in physics and related fields, or for recent graduates starting research in one of these fields in industry.

### CONDENSED MATTER PHYSICS

1. M. T. Dove: *Structure and dynamics: an atomic view of materials*
2. J. Singleton: *Band theory and electronic properties of solids*
3. A. M. Fox: *Optical properties of solids*
4. S. J. Blundell: *Magnetism in condensed matter*
5. J. F. Annett: *Superconductivity*
6. R. A. L. Jones: *Soft condensed matter*

### ATOMIC, OPTICAL, AND LASER PHYSICS

7. C. J. Foot: *Atomic physics*
8. G. A. Brooker: *Modern classical optics*
9. S. M. Hooker, C. E. Webb: *Laser physics*

### PARTICLE PHYSICS, ASTROPHYSICS, AND COSMOLOGY

10. D. H. Perkins: *Particle astrophysics*
11. Ta-Pei Cheng: *Relativity, gravitation, and cosmology*

### STATISTICAL, COMPUTATIONAL, AND THEORETICAL PHYSICS

12. M. Maggiore: *A modern introduction to quantum field theory*
13. W. Krauth: *Statistical mechanics: algorithms and computations*
14. J. P. Sethna: *Entropy, order parameters, and complexity*

# Atomic Physics

---

C. J. FOOT

*Department of Physics  
University of Oxford*

**OXFORD**  
UNIVERSITY PRESS

**OXFORD**  
UNIVERSITY PRESS

Great Clarendon Street, Oxford OX2 6DP

Oxford University Press is a department of the University of Oxford.  
It furthers the University's objective of excellence in research, scholarship,  
and education by publishing worldwide in  
Oxford New York

Auckland Cape Town Dar es Salaam Hong Kong Karachi  
Kuala Lumpur Madrid Melbourne Mexico City Nairobi  
New Delhi Shanghai Taipei Toronto

With offices in

Argentina Austria Brazil Chile Czech Republic France Greece  
Guatemala Hungary Italy Japan South Korea Poland Portugal  
Singapore Switzerland Thailand Turkey Ukraine Vietnam

Oxford is a registered trade mark of Oxford University Press  
in the UK and in certain other countries

Published in the United States  
by Oxford University Press Inc., New York

© Oxford University Press 2005

The moral rights of the author have been asserted

Database right Oxford University Press (maker)

First published 2005

Reprinted 2005

All rights reserved. No part of this publication may be reproduced,  
stored in a retrieval system, or transmitted, in any form or by any means,  
without the prior permission in writing of Oxford University Press,  
or as expressly permitted by law, or under terms agreed with the appropriate  
reprographics rights organization. Enquiries concerning reproduction  
outside the scope of the above should be sent to the Rights Department,  
Oxford University Press, at the address above

You must not circulate this book in any other binding or cover  
and you must impose this same condition on any acquirer

A catalogue record for this title  
is available from the British Library

Library of Congress Cataloging in Publication Data  
(Data available)

ISBN-10: 0 19 850695 3 (Hbk) Ean code 978 0 19 850695 9  
ISBN-10: 0 19 850696 1 (Pbk) Ean code 978 0 19 850696 6  
10 9 8 7 6 5 4 3 2

Typeset by Julie M. Harris using L<sup>A</sup>T<sub>E</sub>X

Printed in Great Britain  
on acid-free paper by Antony Rowe, Chippenham

# Preface

This book is primarily intended to accompany an undergraduate course in atomic physics. It covers the core material and a selection of more advanced topics that illustrate current research in this field. The first six chapters describe the basic principles of atomic structure, starting in Chapter 1 with a review of the classical ideas. Inevitably the discussion of the structure of hydrogen and helium in these early chapters has considerable overlap with introductory quantum mechanics courses, but an understanding of these simple systems provides the basis for the treatment of more complex atoms in later chapters. Chapter 7 on the interaction of radiation with atoms marks the transition between the earlier chapters on structure and the second half of the book which covers laser spectroscopy, laser cooling, Bose–Einstein condensation of dilute atomic vapours, matter-wave interferometry and ion trapping. The exciting new developments in laser cooling and trapping of atoms and Bose–Einstein condensation led to Nobel prizes in 1997 and 2001, respectively. Some of the other selected topics show the incredible precision that has been achieved by measurements in atomic physics experiments. This theme is taken up in the final chapter that looks at quantum information processing from an atomic physics perspective; the techniques developed for precision measurements on atoms and ions give exquisite control over these quantum systems and enable elegant new ideas from quantum computation to be implemented.

The book assumes a knowledge of quantum mechanics equivalent to an introductory university course, e.g. the solution of the Schrödinger equation in three dimensions and perturbation theory. This initial knowledge will be reinforced by many examples in this book; topics generally regarded as difficult at the undergraduate level are explained in some detail, e.g. degenerate perturbation theory. The hierarchical structure of atoms is well described by perturbation theory since the different layers of structure within atoms have considerably different energies associated with them, and this is reflected in the names of the gross, fine and hyperfine structures. In the early chapters of this book, atomic physics may appear to be simply applied quantum mechanics, i.e. we write down the Hamiltonian for a given interaction and solve the Schrödinger equation with suitable approximations. I hope that the study of the more advanced material in the later chapters will lead to a more mature and deeper understanding of atomic physics. Throughout this book the experimental basis of atomic physics is emphasised and it is hoped that the reader will gain some factual knowledge of atomic spectra.

The selection of topics from the diversity of current atomic physics is necessarily subjective. I have concentrated on low-energy and high-precision experiments which, to some extent, reflects local research interests that are used as examples in undergraduate lectures at Oxford. One of the selection criteria was that the material is not readily available in other textbooks, at the time of writing, e.g. atomic collisions have not been treated in detail (only a brief summary of the scattering of ultracold atoms is included in Chapter 10). Other notable omissions include: X-ray spectra, which are discussed only briefly in connection with the historically important work of Moseley, although they form an important frontier of current research; atoms in strong laser fields and plasmas; Rydberg atoms and atoms in doubly- and multiply-excited states (e.g. excited by new synchrotron and free-electron laser sources); and the structure and spectra of molecules.

I would like to thank Geoffrey Brooker for invaluable advice on physics (in particular Appendix B) and on technical details of writing a textbook for the Oxford Master Series. Keith Burnett, Jonathan Jones and Andrew Steane have helped to clarify certain points, in my mind at least, and hopefully also in the text. The series of lectures on laser cooling given by William Phillips while he was a visiting professor in Oxford was extremely helpful in the writing of the chapter on that topic. The following people provided very useful comments on the draft manuscript: Rachel Godun, David Lucas, Mark Lee, Matthew McDonnell, Martin Shotter, Claes-Göran Wahlström (Lund University) and the (anonymous) reviewers. Without the encouragement of Sönke Adlung at OUP this project would not have been completed. Irmgard Smith drew some of the diagrams. I am very grateful for the diagrams and data supplied by colleagues, and reproduced with their permission, as acknowledged in the figure captions. Several of the exercises on atomic structure derive from Oxford University examination papers and it is not possible to identify the examiners individually—some of these exam questions may themselves have been adapted from some older sources of which I am not aware.

Finally, I would like to thank Professors Derek Stacey, Joshua Silver and Patrick Sandars who taught me atomic physics as an undergraduate and graduate student in Oxford. I also owe a considerable debt to the book on elementary atomic structure by Gordon Kemble Woodgate, who was my predecessor as physics tutor at St Peter’s College, Oxford. In writing this new text, I have tried to achieve the same high standards of clarity and conciseness of expression whilst introducing new examples and techniques from the laser era.

## Background reading

It is not surprising that our language should be incapable of describing the processes occurring with the atoms, for it was invented to describe the experiences of daily life, and these consist only of processes involving exceeding large numbers

of atoms. Furthermore, it is very difficult to modify our language so that it will be able to describe these atomic processes, for words can only describe things of which we can form mental pictures, and this ability, too, in the result of daily experience. Fortunately, mathematics is not subject to this limitation, and it has been possible to invent a mathematical scheme—the quantum theory—which seems entirely adequate for the treatment of atomic processes.

From *The physical principles of the quantum theory*, Werner Heisenberg (1930).

The point of the excerpt is that quantum mechanics is essential for a proper description of atomic physics and there are many quantum mechanics textbooks that would serve as useful background reading for this book. The following short list includes those that the author found particularly relevant: Mandl (1992), Rae (1992) and Griffiths (1995). The book *Atomic spectra* by Softley (1994) provides a concise introduction to this field. The books Cohen-Tannoudji *et al.* (1977), Atkins (1983) and Basdevant and Dalibard (2000) are very useful for reference and contain many detailed examples of atomic physics. Angular-momentum theory is very important for dealing with complicated atomic structures, but it is beyond the intended level of this book. The classic book by Dirac (1981) still provides a very readable account of the addition of angular momenta in quantum mechanics. A more advanced treatment of atomic structure can be found in Condon and Odabasi (1980), Cowan (1981) and Sobelman (1996).

*Oxford*

C. J. F.

Web site:

<http://www.physics.ox.ac.uk/users/foot>

This site has answers to some of the exercises, corrections and other supplementary information.

*This page intentionally left blank*

# Contents

|   |           |
|---|-----------|
| <b>1 Early atomic physics</b>                       | <b>1</b>  |
| 1.1 Introduction                                    | 1         |
| 1.2 Spectrum of atomic hydrogen                     | 1         |
| 1.3 Bohr's theory                                   | 3         |
| 1.4 Relativistic effects                            | 5         |
| 1.5 Moseley and the atomic number                   | 7         |
| 1.6 Radiative decay                                 | 11        |
| 1.7 Einstein $A$ and $B$ coefficients               | 11        |
| 1.8 The Zeeman effect                               | 13        |
| 1.8.1 Experimental observation of the Zeeman effect | 17        |
| 1.9 Summary of atomic units                         | 18        |
| Exercises   | 19        |
| <br>  |           |
| <b>2 The hydrogen atom</b>                          | <b>22</b> |
| 2.1 The Schrödinger equation                        | 22        |
| 2.1.1 Solution of the angular equation              | 23        |
| 2.1.2 Solution of the radial equation               | 26        |
| 2.2 Transitions                                     | 29        |
| 2.2.1 Selection rules                               | 30        |
| 2.2.2 Integration with respect to $\theta$          | 32        |
| 2.2.3 Parity  | 32        |
| 2.3 Fine structure                                  | 34        |
| 2.3.1 Spin of the electron                          | 35        |
| 2.3.2 The spin-orbit interaction                    | 36        |
| 2.3.3 The fine structure of hydrogen                | 38        |
| 2.3.4 The Lamb shift                                | 40        |
| 2.3.5 Transitions between fine-structure levels     | 41        |
| Further reading                                     | 42        |
| Exercises   | 42        |
| <br>  |           |
| <b>3 Helium</b>                                     | <b>45</b> |
| 3.1 The ground state of helium                      | 45        |
| 3.2 Excited states of helium                        | 46        |
| 3.2.1 Spin eigenstates                              | 51        |
| 3.2.2 Transitions in helium                         | 52        |
| 3.3 Evaluation of the integrals in helium           | 53        |
| 3.3.1 Ground state                                  | 53        |
| 3.3.2 Excited states: the direct integral           | 54        |
| 3.3.3 Excited states: the exchange integral         | 55        |

|  |            |
|--|------------|
| Further reading  | 56         |
| Exercises  | 58         |
| <b>4 The alkalis</b>   | <b>60</b>  |
| 4.1 Shell structure and the periodic table                         | 60         |
| 4.2 The quantum defect   | 61         |
| 4.3 The central-field approximation                                | 64         |
| 4.4 Numerical solution of the Schrödinger equation                 | 68         |
| 4.4.1 Self-consistent solutions                                    | 70         |
| 4.5 The spin-orbit interaction: a quantum mechanical approach      | 71         |
| 4.6 Fine structure in the alkalis                                  | 73         |
| 4.6.1 Relative intensities of fine-structure transitions           | 74         |
| Further reading  | 75         |
| Exercises  | 76         |
| <b>5 The <i>LS</i>-coupling scheme</b>                             | <b>80</b>  |
| 5.1 Fine structure in the <i>LS</i> -coupling scheme               | 83         |
| 5.2 The <i>jj</i> -coupling scheme                                 | 84         |
| 5.3 Intermediate coupling: the transition between coupling schemes | 86         |
| 5.4 Selection rules in the <i>LS</i> -coupling scheme              | 90         |
| 5.5 The Zeeman effect  | 90         |
| 5.6 Summary  | 93         |
| Further reading  | 94         |
| Exercises  | 94         |
| <b>6 Hyperfine structure and isotope shift</b>                     | <b>97</b>  |
| 6.1 Hyperfine structure  | 97         |
| 6.1.1 Hyperfine structure for s-electrons                          | 97         |
| 6.1.2 Hydrogen maser   | 100        |
| 6.1.3 Hyperfine structure for $l \neq 0$                           | 101        |
| 6.1.4 Comparison of hyperfine and fine structures                  | 102        |
| 6.2 Isotope shift  | 105        |
| 6.2.1 Mass effects   | 105        |
| 6.2.2 Volume shift   | 106        |
| 6.2.3 Nuclear information from atoms                               | 108        |
| 6.3 Zeeman effect and hyperfine structure                          | 108        |
| 6.3.1 Zeeman effect of a weak field, $\mu_B B < A$                 | 109        |
| 6.3.2 Zeeman effect of a strong field, $\mu_B B > A$               | 110        |
| 6.3.3 Intermediate field strength                                  | 111        |
| 6.4 Measurement of hyperfine structure                             | 112        |
| 6.4.1 The atomic-beam technique                                    | 114        |
| 6.4.2 Atomic clocks  | 118        |
| Further reading  | 119        |
| Exercises  | 120        |
| <b>7 The interaction of atoms with radiation</b>                   | <b>123</b> |
| 7.1 Setting up the equations                                       | 123        |

|          |   |            |
|----------|---|------------|
| 7.1.1    | Perturbation by an oscillating electric field     | 124        |
| 7.1.2    | The rotating-wave approximation                   | 125        |
| 7.2      | The Einstein $B$ coefficients                     | 126        |
| 7.3      | Interaction with monochromatic radiation          | 127        |
| 7.3.1    | The concepts of $\pi$ -pulses and $\pi/2$ -pulses | 128        |
| 7.3.2    | The Bloch vector and Bloch sphere                 | 128        |
| 7.4      | Ramsey fringes                                    | 132        |
| 7.5      | Radiative damping                                 | 134        |
| 7.5.1    | The damping of a classical dipole                 | 135        |
| 7.5.2    | The optical Bloch equations                       | 137        |
| 7.6      | The optical absorption cross-section              | 138        |
| 7.6.1    | Cross-section for pure radiative broadening       | 141        |
| 7.6.2    | The saturation intensity                          | 142        |
| 7.6.3    | Power broadening                                  | 143        |
| 7.7      | The a.c. Stark effect or light shift              | 144        |
| 7.8      | Comment on semiclassical theory                   | 145        |
| 7.9      | Conclusions                                       | 146        |
|          | Further reading                                   | 147        |
|          | Exercises   | 148        |
| <b>8</b> | <b>Doppler-free laser spectroscopy</b>            | <b>151</b> |
| 8.1      | Doppler broadening of spectral lines              | 151        |
| 8.2      | The crossed-beam method                           | 153        |
| 8.3      | Saturated absorption spectroscopy                 | 155        |
| 8.3.1    | Principle of saturated absorption spectroscopy    | 156        |
| 8.3.2    | Cross-over resonances in saturation spectroscopy  | 159        |
| 8.4      | Two-photon spectroscopy                           | 163        |
| 8.5      | Calibration in laser spectroscopy                 | 168        |
| 8.5.1    | Calibration of the relative frequency             | 168        |
| 8.5.2    | Absolute calibration                              | 169        |
| 8.5.3    | Optical frequency combs                           | 171        |
|          | Further reading                                   | 175        |
|          | Exercises   | 175        |
| <b>9</b> | <b>Laser cooling and trapping</b>                 | <b>178</b> |
| 9.1      | The scattering force                              | 179        |
| 9.2      | Slowing an atomic beam                            | 182        |
| 9.2.1    | Chirp cooling                                     | 184        |
| 9.3      | The optical molasses technique                    | 185        |
| 9.3.1    | The Doppler cooling limit                         | 188        |
| 9.4      | The magneto-optical trap                          | 190        |
| 9.5      | Introduction to the dipole force                  | 194        |
| 9.6      | Theory of the dipole force                        | 197        |
| 9.6.1    | Optical lattice                                   | 201        |
| 9.7      | The Sisyphus cooling technique                    | 203        |
| 9.7.1    | General remarks                                   | 203        |
| 9.7.2    | Detailed description of Sisyphus cooling          | 204        |
| 9.7.3    | Limit of the Sisyphus cooling mechanism           | 207        |

|           |  |            |
|-----------|--|------------|
| 9.8       | Raman transitions  | 208        |
| 9.8.1     | Velocity selection by Raman transitions  | 208        |
| 9.8.2     | Raman cooling  | 210        |
| 9.9       | An atomic fountain   | 211        |
| 9.10      | Conclusions  | 213        |
|           | Exercises  | 214        |
| <b>10</b> | <b>Magnetic trapping, evaporative cooling and<br/>Bose–Einstein condensation</b> | <b>218</b> |
| 10.1      | Principle of magnetic trapping   | 218        |
| 10.2      | Magnetic trapping  | 220        |
| 10.2.1    | Confinement in the radial direction  | 220        |
| 10.2.2    | Confinement in the axial direction   | 221        |
| 10.3      | Evaporative cooling  | 224        |
| 10.4      | Bose–Einstein condensation   | 226        |
| 10.5      | Bose–Einstein condensation in trapped atomic vapours                             | 228        |
| 10.5.1    | The scattering length  | 229        |
| 10.6      | A Bose–Einstein condensate   | 234        |
| 10.7      | Properties of Bose-condensed gases   | 239        |
| 10.7.1    | Speed of sound   | 239        |
| 10.7.2    | Healing length   | 240        |
| 10.7.3    | The coherence of a Bose–Einstein condensate                                      | 240        |
| 10.7.4    | The atom laser   | 242        |
| 10.8      | Conclusions  | 242        |
|           | Exercises  | 243        |
| <b>11</b> | <b>Atom interferometry</b>   | <b>246</b> |
| 11.1      | Young’s double-slit experiment   | 247        |
| 11.2      | A diffraction grating for atoms  | 249        |
| 11.3      | The three-grating interferometer   | 251        |
| 11.4      | Measurement of rotation  | 251        |
| 11.5      | The diffraction of atoms by light  | 253        |
| 11.5.1    | Interferometry with Raman transitions  | 255        |
| 11.6      | Conclusions  | 257        |
|           | Further reading  | 258        |
|           | Exercises  | 258        |
| <b>12</b> | <b>Ion traps</b>   | <b>259</b> |
| 12.1      | The force on ions in an electric field   | 259        |
| 12.2      | Earnshaw’s theorem   | 260        |
| 12.3      | The Paul trap  | 261        |
| 12.3.1    | Equilibrium of a ball on a rotating saddle                                       | 262        |
| 12.3.2    | The effective potential in an a.c. field   | 262        |
| 12.3.3    | The linear Paul trap   | 262        |
| 12.4      | Buffer gas cooling   | 266        |
| 12.5      | Laser cooling of trapped ions  | 267        |
| 12.6      | Quantum jumps  | 269        |
| 12.7      | The Penning trap and the Paul trap   | 271        |

|  |            |
|--|------------|
| 12.7.1 The Penning trap  | 272        |
| 12.7.2 Mass spectroscopy of ions   | 274        |
| 12.7.3 The anomalous magnetic moment of the electron                         | 274        |
| 12.8 Electron beam ion trap  | 275        |
| 12.9 Resolved sideband cooling   | 277        |
| 12.10 Summary of ion traps   | 279        |
| Further reading  | 279        |
| Exercises  | 280        |
| <b>13 Quantum computing</b>  | <b>282</b> |
| 13.1 Qubits and their properties   | 283        |
| 13.1.1 Entanglement  | 284        |
| 13.2 A quantum logic gate  | 287        |
| 13.2.1 Making a CNOT gate  | 287        |
| 13.3 Parallelism in quantum computing  | 289        |
| 13.4 Summary of quantum computers  | 291        |
| 13.5 Decoherence and quantum error correction                                | 291        |
| 13.6 Conclusion  | 293        |
| Further reading  | 294        |
| Exercises  | 294        |
| <b>A Appendix A: Perturbation theory</b>                                     | <b>298</b> |
| A.1 Mathematics of perturbation theory                                       | 298        |
| A.2 Interaction of classical oscillators of similar frequencies              | 299        |
| <b>B Appendix B: The calculation of electrostatic energies</b>               | <b>302</b> |
| <b>C Appendix C: Magnetic dipole transitions</b>                             | <b>305</b> |
| <b>D Appendix D: The line shape in saturated absorption spectroscopy</b>     | <b>307</b> |
| <b>E Appendix E: Raman and two-photon transitions</b>                        | <b>310</b> |
| E.1 Raman transitions  | 310        |
| E.2 Two-photon transitions   | 313        |
| <b>F Appendix F: The statistical mechanics of Bose–Einstein condensation</b> | <b>315</b> |
| F.1 The statistical mechanics of photons                                     | 315        |
| F.2 Bose–Einstein condensation   | 316        |
| F.2.1 Bose–Einstein condensation in a harmonic trap                          | 318        |
| <b>References</b>  | <b>319</b> |
| <b>Index</b>   | <b>326</b> |

*This page intentionally left blank*

# Early atomic physics

# 1

## 1.1 Introduction

The origins of atomic physics were entwined with the development of quantum mechanics itself ever since the first model of the hydrogen atom by Bohr. This introductory chapter surveys some of the early ideas, including Einstein's treatment of the interaction of atoms with radiation, and a classical treatment of the Zeeman effect. These methods, developed before the advent of the Schrödinger equation, remain useful as an intuitive way of thinking about atomic structure and transitions between the energy levels. The 'proper' description in terms of atomic wavefunctions is presented in subsequent chapters.

Before describing the theory of an atom with one electron, some experimental facts are presented. This ordering of experiment followed by explanation reflects the author's opinion that atomic physics should not be presented as applied quantum mechanics, but it should be motivated by the desire to understand experiments. This represents what really happens in research where most advances come about through the interplay of theory and experiment.

## 1.2 Spectrum of atomic hydrogen

It has long been known that the spectrum of light emitted by an element is characteristic of that element, e.g. sodium in a street lamp, or burning in a flame, produces a distinctive yellow light. This crude form of spectroscopy, in which the colour is seen by eye, formed the basis for a simple chemical analysis. A more sophisticated approach using a prism, or diffraction grating, to disperse the light inside a spectrograph shows that the characteristic spectrum for atoms is composed of discrete lines that are the 'fingerprint' of the element. As early as the 1880s, Fraunhofer used a spectrograph to measure the wavelength of lines, that had not been seen before, in light from the sun and he deduced the existence of a new element called helium. In contrast to atoms, the spectra of molecules (even the simplest diatomic ones) contain many closely-spaced lines that form characteristic molecular bands; large molecules, and solids, usually have nearly continuous spectra with few sharp features. In 1888, the Swedish professor J. Rydberg found that the spectral

|     |                                   |    |
|-----|-----------------------------------|----|
| 1.1 | Introduction                      | 1  |
| 1.2 | Spectrum of atomic hydrogen       | 1  |
| 1.3 | Bohr's theory                     | 3  |
| 1.4 | Relativistic effects              | 5  |
| 1.5 | Moseley and the atomic number     | 7  |
| 1.6 | Radiative decay                   | 11 |
| 1.7 | Einstein $A$ and $B$ coefficients | 11 |
| 1.8 | The Zeeman effect                 | 13 |
| 1.9 | Summary of atomic units           | 18 |
|     | Exercises                         | 19 |

lines in hydrogen obey the following mathematical formula:

$$\frac{1}{\lambda} = R \left( \frac{1}{n^2} - \frac{1}{n'^2} \right), \quad (1.1)$$

<sup>1</sup>The Swiss mathematician Johann Balmer wrote down an expression which was a particular case of eqn 1.1 with  $n = 2$ , a few years before Johannes (commonly called Janne) Rydberg found the general formula that predicted other series.

<sup>2</sup>A spectrum of the Balmer series of lines is on the cover of this book.

where  $n$  and  $n'$  are whole numbers;  $R$  is a constant that has become known as the Rydberg constant. The series of spectral lines for which  $n = 2$  and  $n' = 3, 4, \dots$  is now called the Balmer series and lies in the visible region of the spectrum.<sup>1</sup> The first line at 656 nm is called the Balmer- $\alpha$  (or  $H_\alpha$ ) line and it gives rise to the distinctive red colour of a hydrogen discharge—a healthy red glow indicates that most of the molecules of  $H_2$  have been dissociated into atoms by being bombarded by electrons in the discharge. The next line in the series is the Balmer- $\beta$  line at 486 nm in the blue and subsequent lines at shorter wavelengths tend to a limit in the violet region.<sup>2</sup> To describe such series of lines it is convenient to define the reciprocal of the transition wavelength as the wavenumber  $\tilde{\nu}$  that has units of  $m^{-1}$  (or often  $cm^{-1}$ ),

$$\tilde{\nu} = \frac{1}{\lambda}. \quad (1.2)$$

<sup>3</sup>In this book transitions are also specified in terms of their frequency (denoted by  $f$  so that  $f = c\tilde{\nu}$ ), or in electron volts (eV) where appropriate.

Wavenumbers may seem rather old-fashioned but they are very useful in atomic physics since they are easily evaluated from measured wavelengths without any conversion factor. In practice, the units used for a given quantity are related to the method used to measure it, e.g. spectrometers and spectrographs are calibrated in terms of wavelength.<sup>3</sup> A photon with wavenumber  $\tilde{\nu}$  has energy  $E = hc\tilde{\nu}$ . The Balmer formula implicitly contains a more general empirical law called the Ritz combination principle that states: the wavenumbers of certain lines in the spectrum can be expressed as sums (or differences) of other lines:  $\tilde{\nu}_3 = \tilde{\nu}_1 \pm \tilde{\nu}_2$ , e.g. the wavenumber of the Balmer- $\beta$  line ( $n = 2$  to  $n' = 4$ ) is the sum of that for Balmer- $\alpha$  ( $n = 2$  to  $n' = 3$ ) and the first line in the Paschen series ( $n = 3$  to  $n' = 4$ ). Nowadays this seems obvious since we know about the underlying energy-level structure of atoms but it is still a useful principle for analyzing spectra. Examination of the sums and differences of the wavenumbers of transitions gives clues that enable the underlying structure to be deduced, rather like a crossword puzzle—some examples of this are given in later chapters. The observed spectral lines in hydrogen can all be expressed as differences between energy levels, as shown in Fig. 1.1, where the energies are proportional to  $1/n^2$ . Other series predicted by eqn 1.1 were more difficult to observe experimentally than the Balmer series. The transitions to  $n = 1$  give the Lyman series in the vacuum ultraviolet region of the spectrum.<sup>4</sup> The series of lines with wavelengths longer than the Balmer series lie in the infra-red region (not visible to the human eye, nor readily detected by photographic film—the main methods available to the early spectroscopists). The following section looks at how these spectra can be explained theoretically.

<sup>4</sup>Air absorbs radiation at wavelengths shorter than about 200 nm and so spectrographs must be evacuated, as well as being made with special optics.

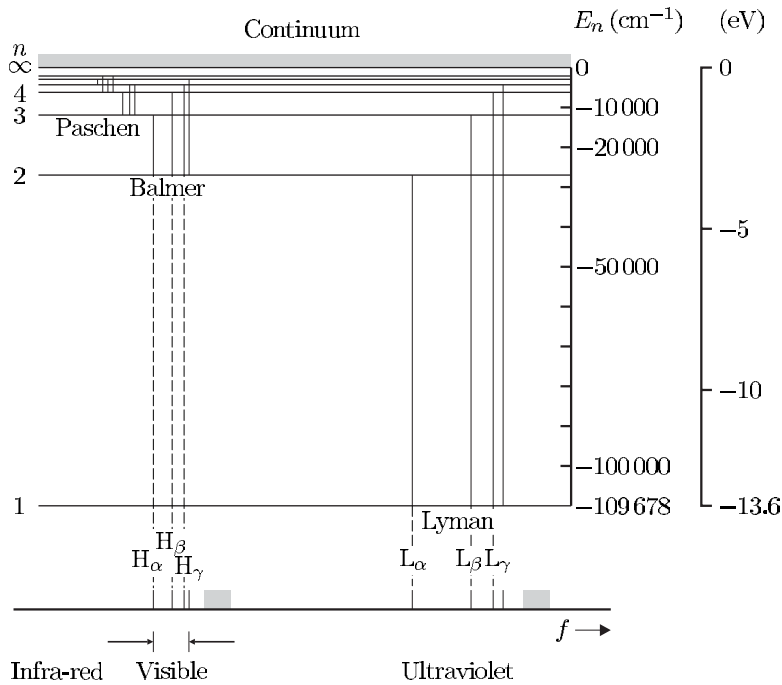


**Fig. 1.1** The energy levels of the hydrogen atom. The transitions from higher shells  $n' = 2, 3, 4, \dots$  down to the  $n = 1$  shell give the Lyman series of spectral lines. The series of lines formed by transitions to other shells are: Balmer ( $n = 2$ ), Paschen ( $n = 3$ ), Bragg ( $n = 4$ ) and Pfund ( $n = 5$ ) (the last two are not labelled in the figure). Within each series the lines are denoted by Greek letters, e.g.  $L_\alpha$  for  $n = 2$  to  $n = 1$  and  $H_\beta$  for  $n = 4$  to  $n = 2$ .

### 1.3 Bohr's theory

In 1913, Bohr put forward a radical new model of the hydrogen atom using quantum mechanics. It was known from Rutherford's experiments that inside atoms there is a very small, dense nucleus with a positive charge. In the case of hydrogen this is a single proton with a single electron bound to it by the Coulomb force. Since the force is proportional to  $1/r^2$ , as for gravity, the atom can be considered in classical terms as resembling a miniature solar system with the electron orbiting around the proton, just like a planet going around the sun. However, quantum mechanics is important in small systems and only certain electron orbits are allowed. This can be deduced from the observation that hydrogen atoms emit light only at particular wavelengths corresponding to transitions between discrete energies. Bohr was able to explain the observed spectrum by introducing the then novel idea of quantisation that goes beyond any previous classical theory. He took the orbits that occur in classical mechanics and imposed quantisation rules onto them.

Bohr assumed that each electron orbits the nucleus in a circle, whose radius  $r$  is determined by the balance between centripetal acceleration and the Coulomb attraction towards the proton. For electrons of mass  $m_e$  and speed  $v$  this gives

$$\frac{m_e v^2}{r} = \frac{e^2}{4\pi\epsilon_0 r^2}. \quad (1.3)$$

In SI units the strength of the electrostatic interaction between two

<sup>5</sup>Older systems of units give more succinct equations without  $4\pi\epsilon_0$ ; some of this neatness can be retained by keeping  $e^2/4\pi\epsilon_0$  grouped together.

charges of magnitude  $e$  is characterised by the combination of constants  $e^2/4\pi\epsilon_0$ .<sup>5</sup> This leads to the following relation between the angular frequency  $\omega = v/r$  and the radius:

$$\omega^2 = \frac{e^2/4\pi\epsilon_0}{m_e r^3}. \quad (1.4)$$

This is equivalent to Kepler's laws for planetary orbits relating the square of the period  $2\pi/\omega$  to the cube of the radius (as expected since all steps have been purely classical mechanics). The total energy of an electron in such an orbit is the sum of its kinetic and potential energies:

$$E = \frac{1}{2}m_e v^2 - \frac{e^2/4\pi\epsilon_0}{r}. \quad (1.5)$$

Using eqn 1.3 we find that the kinetic energy has a magnitude equal to half the potential energy (an example of the virial theorem). Taking into account the opposite signs of kinetic and potential energy, we find

$$E = -\frac{e^2/4\pi\epsilon_0}{2r}. \quad (1.6)$$

This total energy is negative because the electron is bound to the proton and energy must be supplied to remove it. To go further Bohr made the following assumption.

**Assumption I** There are certain allowed orbits for which the electron has a fixed energy. The electron loses energy only when it jumps between the allowed orbits and the atom emits this energy as light of a given wavelength.

That electrons in the allowed orbits do not radiate energy is contrary to classical electrodynamics—a charged particle in circular motion undergoes acceleration and hence radiates electromagnetic waves. Bohr's model does not explain why the electron does not radiate but simply takes this as an assumption that turns out to agree with the experimental data. We now need to determine which out of all the possible classical orbits are the allowed ones. There are various ways of doing this and we follow the standard method, used in many elementary texts, that assumes quantisation of the angular momentum in integral multiples of  $\hbar$  (Planck's constant over  $2\pi$ ):

$$m_e v r = n\hbar, \quad (1.7)$$

where  $n$  is an integer. Combining this with eqn 1.3 gives the radii of the allowed orbits as

$$r = a_0 n^2, \quad (1.8)$$

where the Bohr radius  $a_0$  is given by

$$a_0 = \frac{\hbar^2}{(e^2/4\pi\epsilon_0) m_e}. \quad (1.9)$$

This is the natural unit of length in atomic physics. Equations 1.6 and 1.8 combine to give the famous Bohr formula:

$$E = -\frac{e^2/4\pi\epsilon_0}{2a_0} \frac{1}{n^2}. \quad (1.10)$$

The positive integer  $n$  is called the **principal quantum number**.<sup>6</sup>

Bohr's formula predicts that in the transitions between these energy levels the atoms emit light with a wavenumber given by

$$\tilde{\nu} = R_{\infty} \left( \frac{1}{n^2} - \frac{1}{n'^2} \right). \quad (1.11)$$

This equation fits very closely to the observed spectrum of atomic hydrogen described by eqn 1.1. The Rydberg constant  $R_{\infty}$  in eqn 1.11 is defined by

$$hcR_{\infty} = \frac{(e^2/4\pi\epsilon_0)^2 m_e}{2\hbar^2}. \quad (1.12)$$

The factor of  $hc$  multiplying the Rydberg constant is the conversion factor between energy and wavenumbers since the value of  $R_{\infty}$  is given in units of  $\text{m}^{-1}$  (or  $\text{cm}^{-1}$  in commonly-used units). The measurement of the spectrum of atomic hydrogen using laser techniques has given an extremely accurate value for the Rydberg constant<sup>7</sup>  $R_{\infty} = 10\,973\,731.568\,525 \text{ m}^{-1}$ . However, there is a subtle difference between the Rydberg constant calculated for an electron orbiting a fixed nucleus  $R_{\infty}$  and the constant for real hydrogen atoms in eqn 1.1 (we originally wrote  $R$  without a subscript but more strictly we should specify that it is the constant for hydrogen  $R_H$ ). The theoretical treatment above has assumed an infinitely massive nucleus, hence the subscript  $\infty$ . In reality both the electron and proton move around the centre of mass of the system. For a nucleus of finite mass  $M$  the equations are modified by replacing the electron mass  $m_e$  by its reduced mass

$$m = \frac{m_e M}{m_e + M}. \quad (1.13)$$

For hydrogen

$$R_H = R_{\infty} \frac{M_p}{m_e + M_p} \simeq R_{\infty} \left( 1 - \frac{m_e}{M_p} \right), \quad (1.14)$$

where the electron-to-proton mass ratio is  $m_e/M_p \simeq 1/1836$ . This reduced-mass correction is not the same for different isotopes of an element, e.g. hydrogen and deuterium. This leads to a small but readily observable difference in the frequency of the light emitted by the atoms of different isotopes; this is called the **isotope shift** (see Exercises 1.1 and 1.2).

<sup>6</sup>The alert reader may wonder why this is true since we introduced  $n$  in connection with angular momentum in eqn 1.7, and (as shown later) electrons can have zero angular momentum. This arises from the simplification of Bohr's theory. Exercise 1.12 discusses a more satisfactory, but longer and subtler, derivation that is closer to Bohr's original papers. However, the important thing to remember from this introduction is not the formalism but the magnitude of the atomic energies and sizes.

<sup>7</sup>This is the 2002 CODATA recommended value. The currently accepted values of physical constants can be found on the web site of the National Institute of Science and Technology (NIST).

## 1.4 Relativistic effects

Bohr's theory was a great breakthrough. It was such a radical change that the fundamental idea about the quantisation of the orbits was at first difficult for people to appreciate—they worried about how the electrons could know which orbits they were going into before they jumped. It was soon realised, however, that the assumption of circular orbits is

too much of an over-simplification. Sommerfeld produced a quantum mechanical theory of electrons in elliptical orbits that was consistent with special relativity. He introduced quantisation through a general rule that stated ‘the integral of the momentum associated with a coordinate around one period of the motion associated with that coordinate is an integral multiple of Planck’s constant’. This general method can be applied to any physical system where the classical motion is periodic. Applying this quantisation rule to momentum around a circular orbit gives the equivalent of eqn 1.7:<sup>8</sup>

$$m_e v \times 2\pi r = nh. \quad (1.15)$$

<sup>8</sup>This has a simple interpretation in terms of the de Broglie wavelength associated with an electron  $\lambda_{dB} = h/m_e v$ . The allowed orbits are those that have an integer multiple of de Broglie wavelengths around the circumference:  $2\pi r = n\lambda_{dB}$ , i.e. they are standing matter waves. Curiously, this idea has some resonance with modern ideas in string theory.

In addition to quantising the motion in the coordinate  $\theta$ , Sommerfeld also considered quantisation of the radial degree of freedom  $r$ . He found that some of the elliptical orbits expected for a potential proportional to  $1/r$  are also stationary states (some of the allowed orbits have a high eccentricity, more like those of comets than planets). Much effort was put into complicated schemes based on classical orbits with quantisation, and by incorporating special relativity this ‘old quantum theory’ could explain accurately the fine structure of spectral lines. The exact details of this work are now mainly of historical interest but it is worthwhile to make a simple estimate of relativistic effects. In special relativity a particle of rest mass  $m$  moving at speed  $v$  has an energy

$$E(v) = \gamma mc^2, \quad (1.16)$$

where the gamma factor is  $\gamma = 1/\sqrt{1 - v^2/c^2}$ . The kinetic energy of the moving particle is  $\Delta E = E(v) - E(0) = (\gamma - 1)m_e c^2$ . Thus relativistic effects produce a fractional change in energy:<sup>9</sup>

$$\frac{\Delta E}{E} \simeq \frac{v^2}{c^2}. \quad (1.17)$$

This leads to energy differences between the various elliptical orbits of the same gross energy because the speed varies in different ways around the elliptical orbits, e.g. for a circular orbit and a highly elliptical orbit of the same gross energy. From eqns 1.3 and 1.7 we find that the ratio of the speed in the orbit to the speed of light is

$$\frac{v}{c} = \frac{\alpha}{n}, \quad (1.18)$$

where the fine-structure constant  $\alpha$  is given by

$$\alpha = \frac{e^2/4\pi\epsilon_0}{\hbar c}. \quad (1.19)$$

<sup>9</sup>We neglect a factor of  $\frac{1}{2}$  in the binomial expansion of the expression for  $\gamma$  at low speeds,  $v^2/c^2 \ll 1$ .

This fundamental constant plays an important role throughout atomic physics.<sup>10</sup> Numerically its value is approximately  $\alpha \simeq 1/137$  (see inside the back cover for a list of constants used in atomic physics). From eqn 1.17 we see that relativistic effects lead to energy differences of order  $\alpha^2$  times the gross energy. (This crude estimate neglects some

dependence on principal quantum number and Chapter 2 gives a more quantitative treatment of this fine structure.) It is not necessary to go into all the refinements of Sommerfeld's relativistic theory that gave the energy levels in hydrogen very precisely, by imposing quantisation rules on classical orbits, since ultimately a paradigm shift was necessary. Those ideas were superseded by the use of wavefunctions in the Schrödinger equation. The idea of elliptical orbits provides a connection with our intuition based on classical mechanics and we often retain some traces of this simple picture of electron orbits in our minds. However, for atoms with more than one electron, e.g. helium, classical models do not work and we must think in terms of wavefunctions.

## 1.5 Moseley and the atomic number

At the same time as Bohr was working on his model of the hydrogen atom, H. G. J. Moseley measured the X-ray spectra of many elements. Moseley established that the square root of the frequency of the emitted lines is proportional to the atomic number  $Z$  (that he defined as the position of the atom in the periodic table, starting counting at  $Z = 1$  for hydrogen), i.e.

$$\sqrt{f} \propto Z. \quad (1.20)$$

Moseley's original plot is shown in Fig. 1.2. As we shall see, this equation is a considerable simplification of the actual situation but it was remarkably powerful at the time. By ordering the elements using  $Z$  rather than relative atomic mass, as was done previously, several inconsistencies in the periodic table were resolved. There were still gaps that were later filled by the discovery of new elements. In particular, for the rare-earth elements that have similar chemical properties and are therefore difficult to distinguish, it was said 'in an afternoon, Moseley could solve the problem that had baffled chemists for many decades and establish the true number of possible rare earths' (Segrè 1980). Moseley's observations can be explained by a relatively simple model for atoms that extends Bohr's model for hydrogen.<sup>11</sup>

A natural way to extend Bohr's atomic model to heavier atoms is to suppose that the electrons fill up the allowed orbits starting from the bottom. Each energy level only has room for a certain number of electrons so they cannot all go into the lowest level and they arrange themselves in shells, labelled by the principal quantum number, around the nucleus. This shell structure arises because of the Pauli exclusion principle and the electron spin, but for now let us simply consider it as an empirical fact that the maximum number of electrons in the  $n = 1$  shell is 2, the  $n = 2$  shell has 8 and the  $n = 3$  shell has 18, etc. For historical reasons, X-ray spectroscopists do not use the principal quantum number but label the shells by letters: K for  $n = 1$ , L for  $n = 2$ , M for  $n = 3$  and so on alphabetically.<sup>12</sup> This concept of electronic shells explains the emission of X-rays from atoms in the following way. Moseley produced X-rays by bombarding samples of the given element with electrons that

<sup>11</sup>Tragically, Henry Gwyn Jeffreys Moseley was killed when he was only 28 while fighting in the First World War (see the biography by Heilbron (1974)).

<sup>12</sup>The chemical properties of the elements depend on this electronic structure, e.g. the inert gases have full shells of electrons and these stable configurations are not willing to form chemical bonds. The explanation of the atomic structure underlying the periodic table is discussed further in Section 4.1. See also Atkins (1994) and Grant and Phillips (2001).

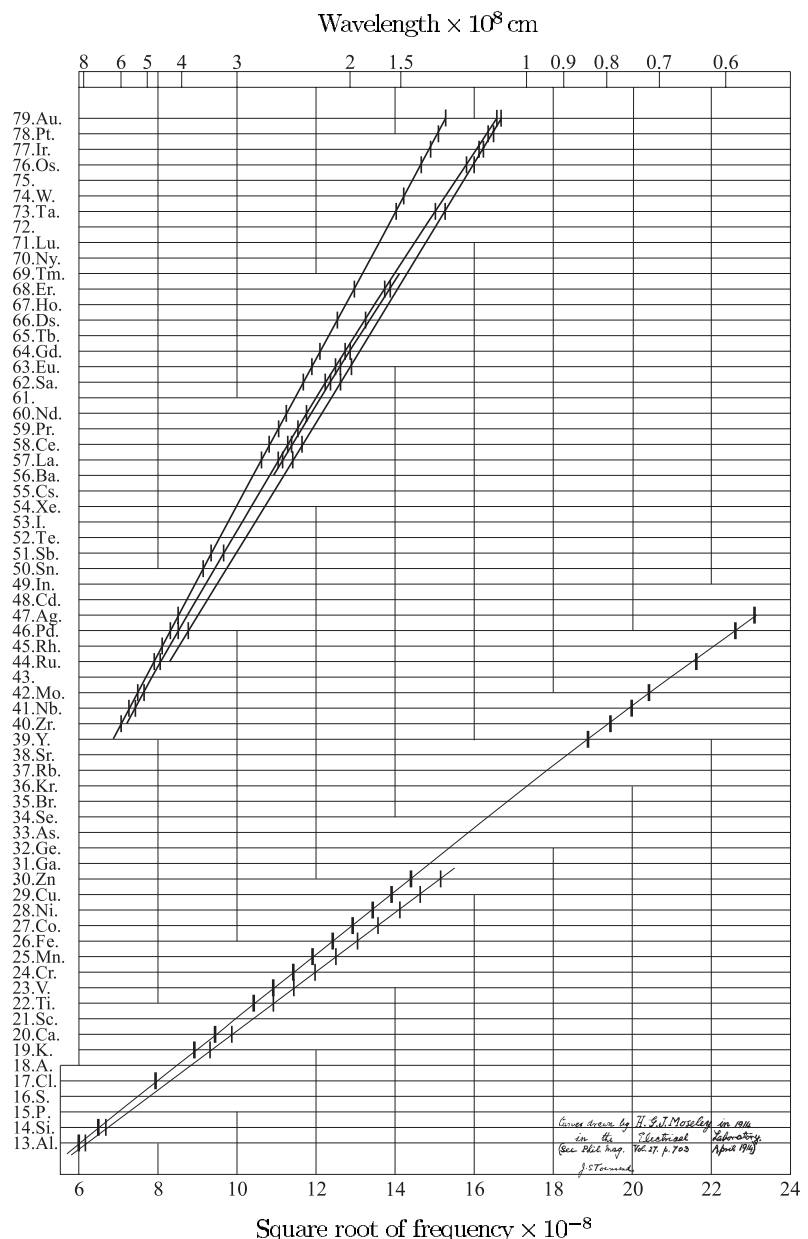


**Fig. 1.2** Moseley's plot of the square root of the frequency of X-ray lines of elements against their atomic number  $Z$ . Moseley's work established the atomic number  $Z$  as a more fundamental quantity than the 'atomic weight' (now called relative atomic mass). Following modern convention the units of the horizontal scales would be ( $10^8 \sqrt{\text{Hz}}$ ) at the bottom and ( $10^{-10} \text{ m}$ ) for the log scale at the top. (Archives of the Clarendon Laboratory, Oxford; also shown on the Oxford physics web site.)<sup>13</sup>

<sup>13</sup>The handwriting in the bottom right corner states that this diagram is the original for Moseley's famous paper in *Phil. Mag.*, **27**, 703 (1914).

had been accelerated to a high voltage in a vacuum tube. These fast electrons knock an electron out of an atom in the sample leaving a vacancy or hole in one of its shells. This allows an electron from a higher-lying shell to ‘fall down’ to fill this hole emitting radiation of a wavelength corresponding to the difference in energy between the shells.

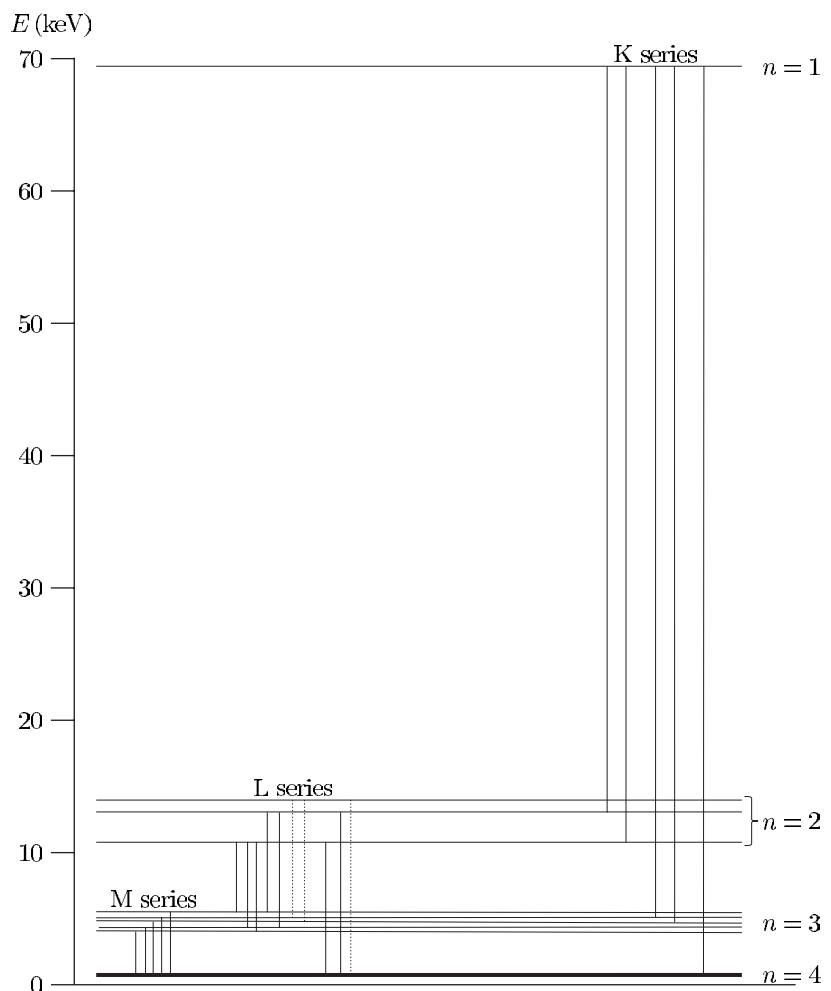
To explain Moseley’s observations quantitatively we need to modify the equations in Section 1.3, on Bohr’s theory, to account for the effect of a nucleus of charge greater than the  $+1e$  of the proton. For a nuclear charge  $Ze$  we replace  $e^2/4\pi\epsilon_0$  by  $Ze^2/4\pi\epsilon_0$  in all the equations, resulting in a formula for the energies like that of Balmer but multiplied by a factor of  $Z^2$ . This dependence on the square of the atomic number means that, for all but the lightest elements, transitions between low-lying shells lead to emission of radiation in the X-ray region of the spectrum. Scaling the Bohr theory result is accurate for hydrogenic ions, i.e. systems with one electron around a nucleus of charge  $Ze$ . In neutral atoms the other electrons (that do not jump) are not simply passive spectators but partly screen the nuclear charge; for a given X-ray line, say the K- to L-shell transition, a more accurate formula is

$$\frac{1}{\lambda} = R_\infty \left\{ \frac{(Z - \sigma_K)^2}{1^2} - \frac{(Z - \sigma_L)^2}{2^2} \right\}. \quad (1.21)$$

The screening factors  $\sigma_K$  and  $\sigma_L$  are not entirely independent of  $Z$  and the values of these screening factors for each shell vary slightly (see the exercises at the end of this chapter). For large atomic numbers this formula tends to eqn 1.20 (see Exercise 1.4). This simple approach does not explain why the screening factor for a shell can exceed the number of electrons inside that shell, e.g.  $\sigma_K = 2$  for  $Z = 74$  although only one electron remains in this shell when a hole is formed. This does not make sense in a classical model with electrons orbiting around a nucleus, but can be explained by atomic wavefunctions—an electron with a high principal quantum number (and little angular momentum) has a finite probability of being found at small radial distances.

The study of X-rays has developed into a whole field of its own within atomic physics, astrophysics and condensed matter, but there is only room to mention a few brief facts here. When an electron is removed from the K-shell the atom has an amount of energy equal to its binding energy, i.e. a positive amount of energy, and it is therefore usual to draw the diagram with the K-shell at the top, as in Fig. 1.3. These are the energy levels of the hole in the electron shells. This diagram shows why the creation of a hole in a low-lying shell leads to a succession of transitions as the hole works its way outwards through the shells. The hole (or equivalently the falling electron) can jump more than one shell at a time; each line in a series from a given shell is labelled using Greek letters (as in the series in hydrogen), e.g.  $K_\alpha, K_\beta, \dots$ . The levels drawn in Fig. 1.3 have some sub-structure and this leads to transitions with slightly different wavelengths, as shown in Moseley’s plot. This is fine structure caused by relativistic effects that we considered for Sommerfeld’s theory; the substitution  $e^2/4\pi\epsilon_0 \rightarrow Ze^2/4\pi\epsilon_0$ , as above, (or

**Fig. 1.3** The energy levels of the inner shells of the tungsten atom ( $Z = 74$ ) and the transitions between them that give rise to X-rays. The level scheme has several important differences from that for the hydrogen atom (Fig. 1.1). Firstly, the energies are tens of keV, as compared to eV for  $Z = 1$ , because they scale as  $Z^2$  (approximately). Secondly, the energy levels are plotted with  $n = 1$  at the top because when an electron is removed from the K-shell the system has more energy than the neutral atom; energies are shown for an atom with a vacancy (missing electron) in the K-, L-, M- and N-shells. The atom emits X-ray radiation when an electron drops down from a higher shell to fill a vacancy in a lower shell—this process is equivalent to the vacancy, or hole, working its way outwards. This way of plotting the energies of the system shows clearly that the removal of an electron from the K-shell leads to a cascade of X-ray transitions, e.g. a transition between the  $n = 1$  and 2 shells gives a line in the K-series which is followed by a line in another series (L-, M-, etc.). When the vacancy reaches the outermost shells of electrons that are only partially filled with valence electrons with binding energies of a few eV (the O- and P-shells in the case of tungsten), the transition energies become negligible compared to those between the inner shells. This level scheme is typical for electrons in a moderately heavy atom, i.e. one with filled K-, L-, M- and N-shells. (The lines of the L-series shown dotted are allowed X-ray transitions, but they do not occur following  $K_\alpha$  emission.)



equivalently  $\alpha \rightarrow Z\alpha$ ) shows that fine structure is of order  $(Z\alpha)^2$  times the gross structure, which itself is proportional to  $Z^2$ . Thus relativistic effects grow as  $Z^4$  and become very significant for the inner electrons of heavy atoms, leading to the fine structure of the L- and M-shells seen in Fig. 1.3. This relativistic splitting of the shells explains why in Moseley's plot (Fig. 1.2) there are two closely-spaced curves for the  $K_\alpha$ -line, and several curves for the L-series.

Nowadays much of the X-ray work in atomic physics is carried out using sources such as synchrotrons; these devices accelerate electrons by the techniques used in particle accelerators. A beam of high-energy electrons circulates in a ring and the circular motion causes the electrons to

radiate X-rays. Such a source can be used to obtain an X-ray absorption spectrum.<sup>14</sup> There are many other applications of X-ray emission, e.g. as a diagnostic tool for the processes that occur in plasmas in fusion research and in astrophysical objects. Many interesting processes occur at ‘high energies’ in atomic physics but the emphasis in this book is mainly on lower energies.

## 1.6 Radiative decay

An electric dipole moment  $-ex_0$  oscillating at angular frequency  $\omega$  radiates a power<sup>15</sup>

$$P = \frac{e^2 x_0^2 \omega^4}{12\pi\epsilon_0 c^3}. \quad (1.22)$$

An electron in harmonic motion has a total energy<sup>16</sup> of  $E = m_e \omega^2 x_0^2 / 2$ , where  $x_0$  is the amplitude of the motion. This energy decreases at a rate equal to the power radiated:

$$\frac{dE}{dt} = -\frac{e^2 \omega^2}{6\pi\epsilon_0 m_e c^3} E = -\frac{E}{\tau}, \quad (1.23)$$

where the classical radiative lifetime  $\tau$  is given by

$$\frac{1}{\tau} = \frac{e^2 \omega^2}{6\pi\epsilon_0 m_e c^3}. \quad (1.24)$$

For the transition in sodium at a wavelength of 589 nm (yellow light) this equation predicts a value of  $\tau = 16 \text{ ns} \simeq 10^{-8} \text{ s}$ . This is very close to the experimentally measured value and typical of allowed transitions that emit visible light. Atomic lifetimes, however, vary over a very wide range,<sup>17</sup> e.g. for the Lyman- $\alpha$  transition (shown in Fig. 1.1) the upper level has a lifetime of only a few nanoseconds.<sup>18,19</sup>

The classical value of the lifetime gives the fastest time in which the atom could decay on a given transition and this is often close to the observed lifetime for strong transitions. Atoms do not decay faster than a classical dipole radiating at the same wavelength, but they may decay more slowly (by many orders of magnitude in the case of forbidden transitions).<sup>20</sup>

## 1.7 Einstein A and B coefficients

The development of the ideas of atomic structure was linked to experiments on the emission, and absorption, of radiation from atoms, e.g. X-rays or light. The emission of radiation was considered as something that just has to happen in order to carry away the energy when an electron jumps from one allowed orbit to another, but the mechanism was not explained.<sup>21</sup> In one of his many strokes of genius Einstein devised a way of treating the phenomenon of spontaneous emission quantitatively,

<sup>14</sup>Absorption is easier to interpret than emission since only one of the terms in eqn 1.21 is important, e.g.  $E_K = hcR_\infty(Z - \sigma_K)^2$ .

<sup>15</sup>This total power equals the integral of the Poynting vector over a closed surface in the far-field of radiation from the dipole. This is calculated from the oscillating electric and magnetic fields in this region (see electromagnetism texts or Corney (2000)).

<sup>16</sup>The sum of the kinetic and potential energies.

<sup>17</sup>The classical lifetime scales as  $1/\omega^2$ . However, we will find that the quantum mechanical result is different (see Exercise 1.8).

<sup>18</sup>Higher-lying levels, e.g.  $n = 30$ , live for many microseconds (Gallagher 1994).

<sup>19</sup>Atoms can be excited up to configurations with high principal quantum numbers in laser experiments; such systems are called Rydberg atoms and have small intervals between their energy levels. As expected from the correspondence principle, these Rydberg atoms can be used in experiments that probe the interface between classical and quantum mechanics.

<sup>20</sup>The ion-trapping techniques described in Chapter 12 can probe transitions with spontaneous decay rates less than  $1 \text{ s}^{-1}$ , using single ions confined by electric and magnetic fields—something that was only a ‘thought experiment’ for Bohr and the other founders of quantum theory. In particular, the effect of individual quantum jumps between atomic energy levels is observed. Radiative decay resembles radioactive decay in that individual atoms spontaneously emit a photon at a given time but taking the average over an ensemble of atoms gives exponential decay.

<sup>21</sup>A complete explanation of spontaneous emission requires quantum electrodynamics.

<sup>22</sup>This treatment of the interaction of atoms with radiation forms the foundation for the theory of the laser, and is used whenever radiation interacts with matter (see Fox 2001). A historical account of Einstein's work and its profound implications can be found in Pais (1982).

<sup>23</sup>The frequency dependence of the interaction is considered in Chapter 7.

<sup>24</sup>The word **laser** is an acronym for light amplification by stimulated emission of radiation.

based on an intuitive understanding of the process.<sup>22</sup>

Einstein considered atoms with two levels of energies,  $E_1$  and  $E_2$ , as shown in Fig. 1.4; each level may have more than one state and the number of states with the same energy is the **degeneracy** of that level represented by  $g_1$  and  $g_2$ . Einstein considered what happens to an atom interacting with radiation of energy density  $\rho(\omega)$  per unit frequency interval. The radiation causes transitions from the lower to the upper level at a rate proportional to  $\rho(\omega_{12})$ , where the constant of proportionality is  $B_{12}$ . The atom interacts strongly only with that part of the distribution  $\rho(\omega)$  with a frequency close to  $\omega_{12} = (E_2 - E_1)/\hbar$ , the atom's resonant frequency.<sup>23</sup> By symmetry it is also expected that the radiation will cause transitions from the upper to lower levels at a rate dependent on the energy density but with a constant of proportionality  $B_{21}$  (the subscripts are in a different order for emission as compared to absorption). This is a process of stimulated emission in which the radiation at angular frequency  $\omega$  causes the atom to emit radiation of the same frequency. This increase in the amount of light at the incident frequency is fundamental to the operation of lasers.<sup>24</sup> The symmetry between up and down is broken by the process of spontaneous emission in which an atom falls down to the lower level, even when no external radiation is present. Einstein introduced the coefficient  $A_{21}$  to represent the rate of this process. Thus the **rate equations** for the populations of the levels,  $N_1$  and  $N_2$ , are

$$\frac{dN_2}{dt} = N_1 B_{12} \rho(\omega_{12}) - N_2 B_{21} \rho(\omega_{12}) - N_2 A_{21} \quad (1.25)$$

and

$$\frac{dN_1}{dt} = -\frac{dN_2}{dt}. \quad (1.26)$$

The first equation gives the rate of change of  $N_2$  in terms of the absorption, stimulated emission and spontaneous emission, respectively. The second equation is a consequence of having only two levels so that atoms leaving level 2 must go into level 1; this is equivalent to a condition that  $N_1 + N_2 = \text{constant}$ . When  $\rho(\omega) = 0$ , and some atoms are initially in the upper level ( $N_2(0) \neq 0$ ), the equations have a decaying exponential solution:

$$N_2(t) = N_2(0) \exp(-A_{21}t), \quad (1.27)$$

<sup>25</sup>This lifetime was estimated by a classical argument in the previous section.

where the mean lifetime<sup>25</sup> is

$$\frac{1}{\tau} = A_{21}. \quad (1.28)$$

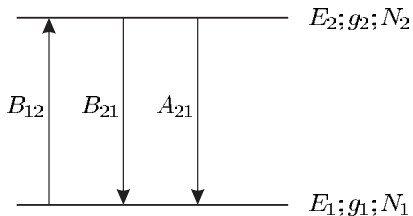


**Fig. 1.4** The interaction of a two-level atom with radiation leads to stimulated transitions, in addition to the spontaneous decay of the upper level.

Einstein devised a clever argument to find the relationship between the  $A_{21}$ - and  $B$ -coefficients and this allows a complete treatment of atoms interacting with radiation. Einstein imagined what would happen to such an atom in a region of black-body radiation, e.g. inside a box whose surface acts as a black body. The energy density of the radiation  $\rho(\omega) d\omega$  between angular frequency  $\omega$  and  $\omega + d\omega$  depends only on the temperature  $T$  of the emitting (and absorbing) surfaces of the box; this function is given by the Planck distribution law:<sup>26</sup>

$$\rho(\omega) = \frac{\hbar\omega^3}{\pi^2 c^3} \frac{1}{\exp(\hbar\omega/k_B T) - 1}. \quad (1.29)$$

Now we consider the level populations of an atom in this black-body radiation. At equilibrium the rates of change of  $N_1$  and  $N_2$  (in eqn 1.26) are both zero and from eqn 1.25 we find that

$$\rho(\omega_{12}) = \frac{A_{21}}{B_{21}} \frac{1}{(N_1/N_2)(B_{12}/B_{21}) - 1}. \quad (1.30)$$

At thermal equilibrium the population in each of the states within the levels are given by the Boltzmann factor (the population in each state equals that of the energy level divided by its degeneracy):

$$\frac{N_2}{g_2} = \frac{N_1}{g_1} \exp\left(-\frac{\hbar\omega}{k_B T}\right). \quad (1.31)$$

Combining the last three equations (1.29, 1.30 and 1.31) we find<sup>27</sup>

$$A_{21} = \frac{\hbar\omega^3}{\pi^2 c^3} B_{21} \quad (1.32)$$

and

$$B_{12} = \frac{g_2}{g_1} B_{21}. \quad (1.33)$$

The Einstein coefficients are properties of the atom.<sup>28</sup> Therefore these relationships between them hold for any type of radiation, from narrow-bandwidth radiation from a laser to broadband light. Importantly, eqn 1.32 shows that strong absorption is associated with strong emission. Like many of the topics covered in this chapter, Einstein's treatment captured the essential features of the physics long before all the details of the quantum mechanics were fully understood.<sup>29</sup>

<sup>26</sup>Planck was the first to consider radiation quantised into photons of energy  $\hbar\omega$ . See Pais (1986).

<sup>27</sup>These equations hold for all  $T$ , so we can equate the parts that contain  $\exp(\hbar\omega/k_B T)$  and the temperature-independent factors separately to obtain the two equations.

<sup>28</sup>This is shown explicitly in Chapter 7 by a time-dependent perturbation theory calculation of  $B_{12}$ .

<sup>29</sup>To excite a significant fraction of the population into the upper level of a visible transition would require black-body radiation with a temperature comparable to that of the sun, and this method is not generally used in practice—such transitions are easily excited in an electrical discharge where the electrons impart energy to the outermost electrons in an atom. (The voltage required to excite weakly-bound outer electrons is much less than for X-ray production.)

## 1.8 The Zeeman effect

This introductory survey of early atomic physics must include Zeeman's important work on the effect of a magnetic field on atoms. The observation of what we now call the Zeeman effect and three other crucial experiments were carried out just at the end of the nineteenth century, and together these discoveries mark the watershed between classical and quantum physics.<sup>30</sup> Before describing Zeeman's work in detail, I shall

<sup>30</sup>Pais (1986) and Segrè (1980) give historical accounts.

<sup>31</sup>This led to the measurement of the atomic X-ray spectra by Moseley described in Section 1.5.

<sup>32</sup>The field of nuclear physics was later developed by Rutherford, and others, to show that atoms have a very small dense nucleus that contains almost all the atomic mass. For much of atomic physics it is sufficient to think of the nucleus as a positive charge  $+Ze$  at the centre of the atoms. However, some understanding of the size, shape and magnetic moments of nuclei is necessary to explain the hyperfine structure and isotope shift (see Chapter 6).

<sup>33</sup>This is the same force that Thomson used to deflect free electrons in a curved trajectory to measure  $e/m_e$ . Nowadays such cathode ray tubes are commonly used in classroom demonstrations.

briefly mention the other three great breakthroughs and their significance for atomic physics. Röntgen discovered mysterious X-rays emitted from discharges, and sparks, that could pass through matter and blacken photographic film.<sup>31</sup> At about the same time, Bequerel's discovery of radioactivity opened up the whole field of nuclear physics.<sup>32</sup> Another great breakthrough was J. J. Thomson's demonstration that cathode rays in electrical discharge tubes are charged particles whose charge-to-mass ratio does not depend on the gas in the discharge tube. At almost the same time, the observation of the Zeeman effect of a magnetic field showed that there are particles with the same charge-to-mass ratio in atoms (that we now call electrons). The idea that atoms contain electrons is very obvious now but at that time it was a crucial piece in the jigsaw of atomic structure that Bohr put together in his model. In addition to its historical significance, the Zeeman effect provides a very useful tool for examining the structure of atoms, as we shall see at several places in this book. Somewhat surprisingly, it is possible to explain this effect by a classical-mechanics line of reasoning (in certain special cases). An atom in a magnetic field can be modelled as a simple harmonic oscillator. The restoring force on the electron is the same for displacements in all directions and the oscillator has the same resonant frequency  $\omega_0$  for motion along the  $x$ -,  $y$ - and  $z$ -directions (when there is no magnetic field). In a magnetic field  $\mathbf{B}$  the equation of motion for an electron with charge  $-e$ , position  $\mathbf{r}$  and velocity  $\mathbf{v} = \dot{\mathbf{r}}$  is

$$m_e \frac{d\mathbf{v}}{dt} = -m_e \omega_0^2 \mathbf{r} - e\mathbf{v} \times \mathbf{B}. \quad (1.34)$$

In addition to the restoring force (assumed to exist without further explanation), there is the Lorentz force that occurs for a charged particle moving through a magnetic field.<sup>33</sup> Taking the direction of the field to be the  $z$ -axis,  $\mathbf{B} = B\hat{\mathbf{e}}_z$  leads to

$$\ddot{\mathbf{r}} + 2\Omega_L \dot{\mathbf{r}} \times \hat{\mathbf{e}}_z + \omega_0^2 \mathbf{r} = 0. \quad (1.35)$$

This contains the Larmor frequency

$$\Omega_L = \frac{eB}{2m_e}. \quad (1.36)$$

We use a matrix method to solve the equation and look for a solution in the form of a vector oscillating at  $\omega$ :

$$\mathbf{r} = \text{Re} \left\{ \begin{pmatrix} x \\ y \\ z \end{pmatrix} \exp(-i\omega t) \right\}. \quad (1.37)$$

Written in matrix form, eqn 1.35 reads

$$\begin{pmatrix} \omega_0^2 & -2i\omega\Omega_L & 0 \\ 2i\omega\Omega_L & \omega_0^2 & 0 \\ 0 & 0 & \omega_0^2 \end{pmatrix} \begin{pmatrix} x \\ y \\ z \end{pmatrix} = \omega^2 \begin{pmatrix} x \\ y \\ z \end{pmatrix}. \quad (1.38)$$

The eigenvalues  $\omega^2$  are found from the following determinant:

$$\begin{vmatrix} \omega_0^2 - \omega^2 & -2i\omega\Omega_L & 0 \\ 2i\omega\Omega_L & \omega_0^2 - \omega^2 & 0 \\ 0 & 0 & \omega_0^2 - \omega^2 \end{vmatrix} = 0. \quad (1.39)$$

This gives  $\{\omega^4 - (2\omega_0^2 + 4\Omega_L^2)\omega^2 + \omega_0^4\}(\omega^2 - \omega_0^2) = 0$ . The solution  $\omega = \omega_0$  is obvious by inspection. The other two eigenvalues can be found exactly by solving the quadratic equation for  $\omega^2$  inside the curly brackets. For an optical transition we always have  $\Omega_L \ll \omega_0$  so the approximate eigenfrequencies are  $\omega \simeq \omega_0 \pm \Omega_L$ . Substituting these values back into eqn 1.38 gives the eigenvectors corresponding to  $\omega = \omega_0 - \Omega_L$ ,  $\omega_0$  and  $\omega_0 + \Omega_L$ , respectively, as

$$\mathbf{r} = \begin{pmatrix} \cos(\omega_0 - \Omega_L)t \\ -\sin(\omega_0 - \Omega_L)t \\ 0 \end{pmatrix}, \quad \begin{pmatrix} 0 \\ 0 \\ \cos\omega_0 t \end{pmatrix}$$

and  $\begin{pmatrix} \cos(\omega_0 + \Omega_L)t \\ \sin(\omega_0 + \Omega_L)t \\ 0 \end{pmatrix}$

The magnetic field does not affect motion along the  $z$ -axis and the angular frequency of the oscillation remains  $\omega_0$ . Interaction with the magnetic field causes the motions in the  $x$ - and  $y$ -directions to be coupled together (by the off-diagonal elements  $\pm 2i\omega\Omega_L$  of the matrix in eqn 1.38).<sup>34</sup> The result is two circular motions in opposite directions in the  $xy$ -plane, as illustrated in Fig. 1.5. These circular motions have frequencies shifted up, or down, from  $\omega_0$  by the Larmor frequency. Thus the action of the external field splits the original oscillation at a single frequency (actually three independent oscillations all with the same frequency,  $\omega_0$ ) into three separate frequencies. An oscillating electron acts as a classical dipole that radiates electromagnetic waves and Zeeman observed the frequency splitting  $\Omega_L$  in the light emitted by the atom.

This classical model of the Zeeman effect explains the polarization of the light, as well as the splitting of the lines into three components. The calculation of the polarization of the radiation at each of the three different frequencies for a general direction of observation is straightforward using vectors;<sup>35</sup> however, only the particular cases where the radiation propagates parallel and perpendicular to the magnetic field are considered here, i.e. the longitudinal and transverse directions of observation, respectively. An electron oscillating parallel to  $\mathbf{B}$  radiates an electromagnetic wave with linear polarization and angular frequency  $\omega_0$ . This  $\pi$ -component of the line is observed in all directions *except* along the magnetic field;<sup>36</sup> in the special case of transverse observation (i.e. in the  $xy$ -plane) the polarization of the  $\pi$ -component lies along  $\hat{\mathbf{e}}_z$ . The circular motion of the oscillating electron in the  $xy$ -plane at angular frequencies  $\omega_0 + \Omega_L$  and  $\omega_0 - \Omega_L$  produces radiation at these frequencies. Looking transversely, this circular motion is seen edge-on so that it looks like linear sinusoidal motion, e.g. for observation along

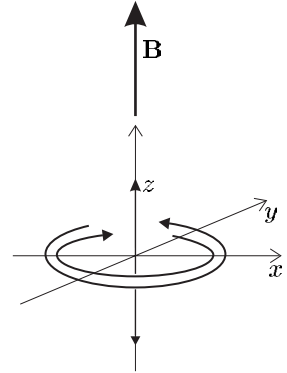


**Fig. 1.5** A simple model of an atom as an electron that undergoes simple harmonic motion explains the features of the normal Zeeman effect of a magnetic field (along the  $z$ -axis). The three eigenvectors of the motion are:  $\hat{\mathbf{e}}_z \cos \omega_0 t$  and  $\cos(\{\omega_0 \pm \Omega_L\}t) \hat{\mathbf{e}}_x \pm \sin(\{\omega_0 \pm \Omega_L\}t) \hat{\mathbf{e}}_y$ .

<sup>34</sup>The matrix does not have off-diagonal elements in the last column or bottom row, so the  $x$ - and  $y$ -components are not coupled to the  $z$ -component, and the problem effectively reduces to solving a  $2 \times 2$  matrix.

<sup>35</sup>Some further details are given in Section 2.2 and in Woodgate (1980).

<sup>36</sup>An oscillating electric dipole proportional to  $\hat{\mathbf{e}}_z \cos \omega_0 t$  does not radiate along the  $z$ -axis—observation along this direction gives a view along the axis of the dipole so that effectively the motion of the electron cannot be seen.

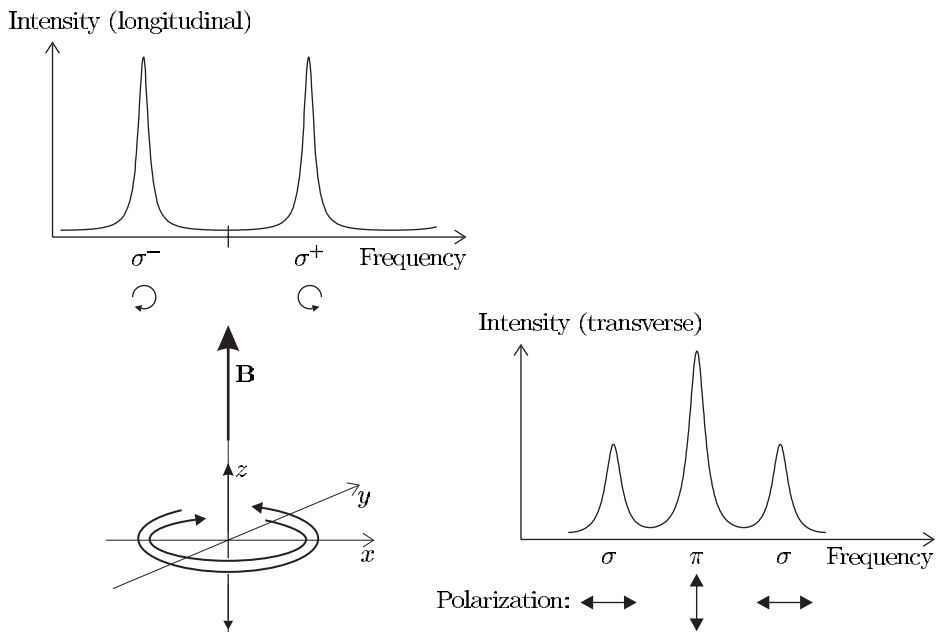


**Fig. 1.6** For the normal Zeeman effect a simple model of an atom (as in Fig. 1.5) explains the frequency of the light emitted and its polarization (indicated by the arrows for the cases of transverse and longitudinal observation).

the  $x$ -axis only the  $y$ -component is seen, and the radiation is linearly polarized perpendicular to the magnetic field—see Fig. 1.6. These are called the  $\sigma$ -components and, in contrast to the  $\pi$ -component, they are also seen in longitudinal observation—looking along the  $z$ -axis one sees the electron’s circular motion and hence light that has circular polarization. Looking in the opposite direction to the magnetic field (from the positive  $z$ -direction, or  $\theta = 0$  in polar coordinates) the circular motion in the anticlockwise direction is associated with the frequency  $\omega_0 + \Omega_L$ .<sup>37</sup> In addition to showing that atoms contain electrons by measuring the magnitude of the charge-to-mass ratio  $e/m_e$ , Zeeman also deduced the sign of the charge by considering the polarization of the emitted light. If the sign of the charge was not negative, as we assumed from the start, light at  $\omega_0 + \Omega_L$  would have the opposite handedness—from this Zeeman could deduce the sign of the electron’s charge.

For situations that only involve orbital angular momentum (and no spin) the predictions of this classical model correspond exactly to those of quantum mechanics (including the correct polarizations), and the intuition gained from this model gives useful guidance in more complicated cases. Another reason for studying the classical treatment of the Zeeman effect is that it furnishes an example of degenerate perturbation theory in classical mechanics. We shall encounter degenerate perturbation theory in quantum mechanics in several places in this book and an understanding of the analogous procedure in classical mechanics is very helpful.

<sup>37</sup>This is left-circularly-polarized light (Corney 2000).

### 1.8.1 Experimental observation of the Zeeman effect

Figure 1.7(a) shows an apparatus suitable for the experimental observation of the Zeeman effect and Fig. 1.7(b–e) shows some typical experimental traces. A low-pressure discharge lamp that contains the atom to be studied (e.g. helium or cadmium) is placed between the pole pieces of an electromagnet capable of producing fields of up to about 1 T. In the arrangement shown, a lens collects light emitted perpendicular to the field (transverse observation) and sends it through a Fabry–Perot étalon. The operation of such étalons is described in detail by Brooker (2003), and only a brief outline of the principle of operation is given here.

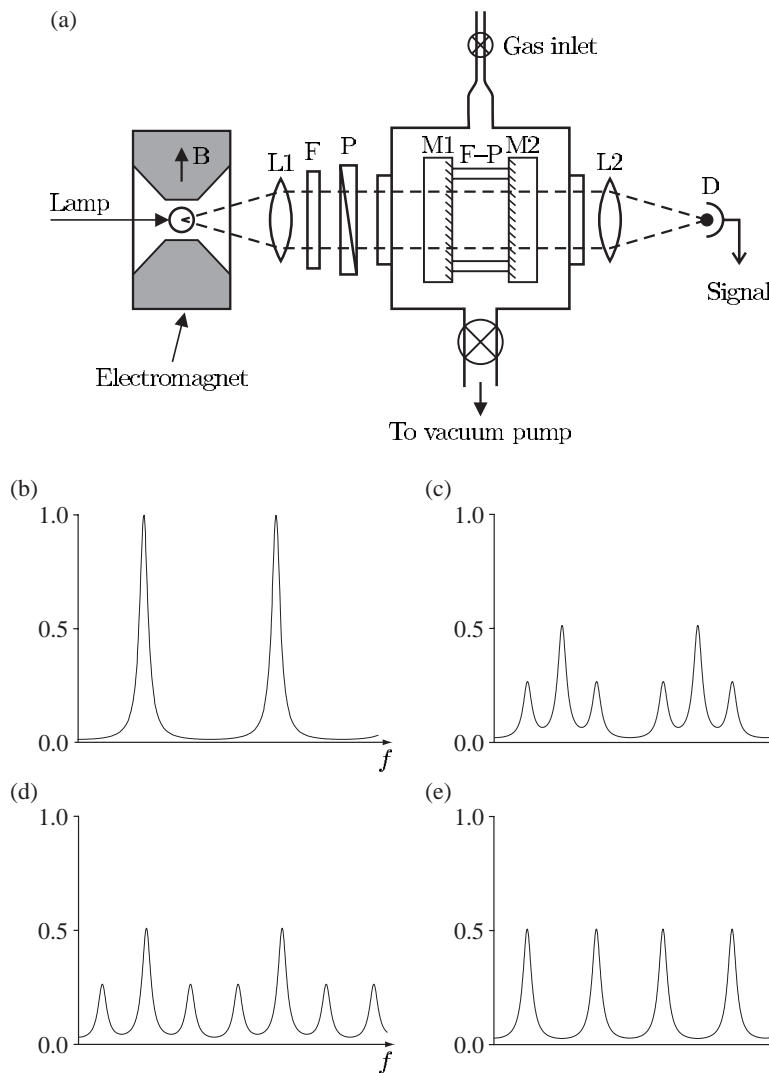


**Fig. 1.7** (a) An apparatus suitable for the observation of the Zeeman effect. The light emitted from a discharge lamp, between the pole pieces of the electromagnet, passes through a narrow-band filter and a Fabry–Perot étalon. Key: L1, L2 are lenses; F–filter; P–polarizer to discriminate between  $\pi$ - and  $\sigma$ -polarizations (optional); Fabry–Perot étalon made of a rigid spacer between two highly-reflecting mirrors (M1 and M2); D–detector. Other details can be found in Brooker (2003). A suitable procedure is to (partially) evacuate the étalon chamber and then allow air (or a gas with a higher refractive index such as carbon dioxide) to leak in through a constant-flow-rate valve to give a smooth linear scan. Plots (b) to (e) show the intensity  $I$  of light transmitted through the Fabry–Perot étalon. (b) A scan over two free-spectral ranges with no magnetic field. Both (c) and (d) show a Zeeman pattern observed perpendicular to the applied field; the spacing between the  $\pi$ - and  $\sigma$ -components in these scans is one-quarter and one-third of the free-spectral range, respectively—the magnetic field in scan (c) is weaker than in (d). (e) In longitudinal observation only the  $\sigma$ -components are observed—this scan is for the same field as in (c) and the  $\sigma$ -components have the same position in both traces.

- Light from the lamp is collected by a lens and directed on to an interference filter that transmits only a narrow band of wavelengths corresponding to a single spectral line.
- The étalon produces an interference pattern that has the form of concentric rings. These rings are observed on a screen in the focal plane of the lens placed after the étalon. A small hole in the screen is positioned at the centre of the pattern so that light in the region of the central fringe falls on a detector, e.g. a photodiode. (Alternatively, the lens and screen can be replaced by a camera that records the ring pattern on film.)
- The effective optical path length between the two flat highly-reflecting mirrors is altered by changing the pressure of the air in the chamber; this scans the étalon over several free-spectral ranges while the intensity of the interference fringes is recorded to give traces as in Fig. 1.7(b–e).

## 1.9 Summary of atomic units

<sup>38</sup>It equals the potential energy of the electron in the first Bohr orbit.

This chapter has used classical mechanics and elementary quantum ideas to introduce the important scales in atomic physics: the unit of length  $a_0$  and a unit of energy  $hcR_\infty$ . The natural unit of energy is  $e^2/4\pi\epsilon_0a_0$  and this unit is called a hartree.<sup>38</sup> This book, however, expresses energy in terms of the energy equivalent to the Rydberg constant, 13.6 eV; this equals the binding energy in the first Bohr orbit of hydrogen, or 1/2 a hartree. These quantities have the following values:

$$a_0 = \frac{\hbar^2}{(e^2/4\pi\epsilon_0)m_e} = 5.29 \times 10^{-11} \text{ m}, \quad (1.40)$$

$$hcR_\infty = \frac{m_e(e^2/4\pi\epsilon_0)^2}{2\hbar^2} = 13.6 \text{ eV}. \quad (1.41)$$

The use of these atomic units makes the calculation of other quantities simple, e.g. the electric field in a hydrogen atom at radius  $r = a_0$  equals  $e/(4\pi\epsilon_0a_0^2)$ . This corresponds to a potential difference of 27.2 V over a distance of  $a_0$ , or a field of  $5 \times 10^{11} \text{ V m}^{-1}$ .

Relativistic effects depend on the dimensionless fine-structure constant  $\alpha$ :

$$\alpha = \frac{(e^2/4\pi\epsilon_0)}{\hbar c} \simeq \frac{1}{137}. \quad (1.42)$$

The Zeeman effect of a magnetic field on atoms leads to a frequency shift of  $\Omega_L$  in eqn 1.36.<sup>39</sup> In practical units the size of this frequency shift is

$$\frac{\Omega_L}{2\pi B} = \frac{e}{4\pi m_e} = 14 \text{ GHz T}^{-1}. \quad (1.43)$$

Equating the magnetic energy  $\hbar\Omega_L$  with  $\mu_B B$ , the magnitude of the energy for a magnetic moment  $\mu_B$  in a magnetic flux density  $B$ , shows that the unit of atomic magnetic moment is the Bohr magneton

$$\mu_B = \frac{e\hbar}{2m_e} = 9.27 \times 10^{-24} \text{ J T}^{-1}. \quad (1.44)$$

<sup>39</sup>This Larmor frequency equals the splitting between the  $\pi$ - and  $\sigma$ -components in the normal Zeeman effect.

This magnetic moment depends on the properties of the unpaired electron (or electrons) in the atom, and has a similar magnitude for all atoms. In contrast, other atomic properties scale rapidly with the nuclear charge; hydrogenic systems have energies proportional to  $Z^2$ , and the same reasoning shows that their size is proportional to  $1/Z$  (see eqns 1.40 and 1.41). For example, hydrogenic uranium  $\text{U}^{+91}$  has been produced in accelerators by stripping 91 electrons off a uranium atom to leave a single electron that has a binding energy of  $92^2 \times 13.6 \text{ eV} = 115 \text{ keV}$  (for  $n = 1$ ) and an orbit of radius  $a_0/92 = 5.75 \times 10^{-13} \text{ m} \equiv 575 \text{ fm}$ . The transitions between the lowest energy levels of this system have short wavelengths in the X-ray region.<sup>40</sup>

The reader might think that it would be a good idea to use the same units across the whole of atomic physics. In practice, however, the units reflect the actual experimental techniques used in a particular region of the spectrum, e.g. radio-frequency, or microwave synthesisers, are calibrated in Hz (kHz, MHz and GHz); the equation for the angle of diffraction from a grating is expressed in terms of a wavelength; and for X-rays produced by tubes in which electrons are accelerated by high voltages it is natural to use keV.<sup>41</sup> A table of useful conversion factors is given inside the back cover.

The survey of classical ideas in this chapter gives a historical perspective on the origins of atomic physics but it is not necessary, or indeed in some cases downright confusing, to go through a detailed classical treatment—the physics at the scale of atomic systems can only properly be described by wave mechanics and this is the approach used in the following chapters.<sup>42</sup>

<sup>40</sup>Energies can be expressed in terms of the rest mass energy of the electron  $m_e c^2 = 0.511 \text{ MeV}$ . The gross energy is  $(Z\alpha)^2 \frac{1}{2} m_e c^2$  and the fine structure is of order  $(Z\alpha)^4 \frac{1}{2} m_e c^2$ .

<sup>41</sup>Laser techniques can measure transition frequencies of around  $10^{15} \text{ Hz}$  directly as a frequency to determine a precise value of the Rydberg constant, and there are no definite rules for whether a transition should be specified by its energy, wavelength or frequency.

<sup>42</sup>X-ray spectra are not discussed again in this book and further details can be found in Kuhn (1969) and other atomic physics texts.

## Exercises

### (1.1) Isotope shift

The deuteron has approximately twice the mass of the proton. Calculate the difference in the wavelength of the Balmer- $\alpha$  line in hydrogen and deuterium.

### (1.2) The energy levels of one-electron atoms

The table gives the wavelength<sup>43</sup> of lines observed in the spectrum of atomic hydrogen and singly-ionized helium. Explain as fully as possible the similarities and differences between the two spectra.

| H (nm) | $\text{He}^+$ (nm) |
|--------|--------------------|
| 656.28 | 656.01             |
| 486.13 | 541.16             |
| 434.05 | 485.93             |
| 410.17 | 454.16             |
|        | 433.87             |
|        | 419.99             |
|        | 410.00             |

<sup>43</sup>These are the wavelengths in air with a refractive index of 1.0003 in the visible region.

- (1.3) *Relativistic effects*  
 Evaluate the magnitude of relativistic effects in the  $n = 2$  level of hydrogen. What is the resolving power  $\lambda/(\Delta\lambda)_{\min}$  of an instrument that could observe these effects in the Balmer- $\alpha$  line?
- (1.4) *X-rays*  
 Show that eqn 1.21 approximates to eqn 1.20 when the atomic number  $Z$  is much greater than the screening factors.
- (1.5) *X-rays*  
 It is suspected that manganese ( $Z = 25$ ) is very poorly mixed with iron ( $Z = 26$ ) in a block of alloy. Predict the energies of the K-absorption edges of these elements and determine an X-ray photon energy that would give good contrast (between regions of different concentrations) in an X-ray of the block.
- (1.6) *X-ray experiments*  
 Sketch an apparatus suitable for X-ray spectroscopy of elements, e.g. Moseley's experiment. Describe the principle of its operation and the method of measuring the energy, or wavelength, of X-rays.
- (1.7) *Fine structure in X-ray transitions*  
 Estimate the magnitude of the relativistic effects in the L-shell of lead ( $Z = 82$ ) in keV. Also express your answer as a fraction of the  $K_\alpha$  transition.
- (1.8) *Radiative lifetime*  
 For an electron in a circular orbit of radius  $r$  the electric dipole moment has a magnitude of  $D = -er$  and radiates energy at a rate given by eqn 1.22. Find the time taken to lose an energy of  $\hbar\omega$ .  
 Use your expression to estimate the transition rate for the  $n = 3$  to  $n = 2$  transition in hydrogen that emits light of wavelength 656 nm.  
*Comment.* This method gives  $1/\tau \propto (er)^2 \omega^3$ , which corresponds closely to the quantum mechanical result in eqn 7.23.
- (1.9) *Black-body radiation*  
 Two-level atoms with a transition at wavelength  $\lambda = 600$  nm, between the levels with degeneracies  $g_1 = 1$  and  $g_2 = 3$ , are immersed in black-body radiation. The fraction in the excited state is 0.1. What is the temperature of the black body and the energy density per unit frequency interval  $\rho(\omega_{12})$  of the radiation at the transition frequency?
- (1.10) *Zeeman effect*  
 What is the magnitude of the Zeeman shift for an atom in (a) the Earth's magnetic field, and (b) a magnetic flux density of 1 T? Express your answers in both MHz, and as a fraction of the transition frequency  $\Delta f/f$  for a spectral line in the visible.
- (1.11) *Relative intensities in the Zeeman effect*  
 Without an external field, an atom has no preferred direction and the choice of quantisation axis is arbitrary. In these circumstances the light emitted cannot be polarized (since this would establish a preferred orientation). As a magnetic field is gradually turned on we do not expect the intensities of the different Zeeman components to change discontinuously because the field has little effect on transition rates. This physical argument implies that oppositely-polarized components emitted along the direction of the field must have equal intensities, i.e.  $I_{\sigma+} = I_{\sigma-}$  (notation defined in Fig. 1.6). What can you deduce about
  - the relative intensities of the components emitted perpendicularly to the field?
  - the ratio of the total intensities of light emitted along and perpendicular to the field?
- (1.12) *Bohr theory and the correspondence principle*  
 This exercise gives an alternative approach to the theory of the hydrogen atom presented in Section 1.3 that is close to the spirit of Bohr's original papers. It is somewhat more subtle than that usually given in elementary textbooks and illustrates Bohr's great intuition. Rather than the *ad hoc* assumption that angular momentum is an integral multiple of  $\hbar$  (in eqn 1.7), Bohr used the correspondence principle. This principle relates the behaviour of a system according to the known laws of classical mechanics and its quantum properties.
- Assumption II** The correspondence principle states that in the limit of large quantum numbers a quantum system tends to the same limit as the corresponding classical system.
- Bohr formulated this principle in the early days of quantum theory. To apply this principle to hydrogen we first calculate the energy gap between adjacent electron orbits of radii  $r$  and  $r'$ . For large radii, the change  $\Delta r = r' - r \ll r$ .
- (a) Show that the angular frequency  $\omega = \Delta E/\hbar$  of radiation emitted when an electron makes a quantum jump between these levels is
- $$\omega \simeq \frac{e^2/4\pi\epsilon_0}{2\hbar} \frac{\Delta r}{r^2}.$$
- (b) An electron moving in a circle of radius  $r$  acts as an electric dipole radiating energy at the

orbital frequency  $\omega$  given by eqn 1.4. Verify that this equation follows from eqn 1.3.

- (c) In the limit of large quantum numbers, the quantum mechanical and classical expressions give the same frequency  $\omega$ . Show that equating the expressions in the previous parts yields  $\Delta r = 2(a_0 r)^{1/2}$ .
- (d) The difference in the radii between two adjacent orbits can be expressed as a difference equation.<sup>44</sup> In this case  $\Delta n = 1$  and

$$\frac{\Delta r}{\Delta n} \propto r^{1/2}. \quad (1.45)$$

This equation can be solved by assuming that the radius varies as some power  $x$  of the quantum number  $n$ , e.g. if one orbit is labelled by an integer  $n$  and the next by  $n + 1$ , then  $r = an^x$  and  $r' = a(n + 1)^x$ . Show that  $\Delta r = axn^{x-1} \propto n^{x/2}$ . Determine the power  $x$  and the constant  $a$ .

Web site:

<http://www.physics.ox.ac.uk/users/foot>

This site has answers to some of the exercises, corrections and other supplementary information.

*Comment.* We have found eqn 1.8 from the correspondence principle without considering angular momentum. The allowed energy levels are easily found from this equation as in Section 1.3. The remarkable feature is that, although the form of the equation was derived for high values of the principal quantum number, the result works down to  $n = 1$ .

### (1.13) Rydberg atoms

- (a) Show that the energy of the transitions between two shells with principal quantum numbers  $n$  and  $n' = n + 1$  is proportional to  $1/n^3$  for large  $n$ .
- (b) Calculate the frequency of the transition between the  $n' = 51$  and  $n = 50$  shells of a neutral atom.
- (c) What is the size of an atom in these *Rydberg states*? Express your answer both in atomic units and in metres.

<sup>44</sup>A difference equation is akin to a differential equation but without letting the differences become infinitesimal.

# 2

# The hydrogen atom

|                              |    |
|------------------------------|----|
| 2.1 The Schrödinger equation | 22 |
| 2.2 Transitions              | 29 |
| 2.3 Fine structure           | 34 |
| Further reading              | 42 |
| Exercises                    | 42 |

The simple hydrogen atom has had a great influence on the development of quantum theory, particularly in the first half of the twentieth century when the foundations of quantum mechanics were laid. As measurement techniques improved, finer and finer details were resolved in the spectrum of hydrogen until eventually splittings of the lines were observed that cannot be explained even by the fully relativistic formulation of quantum mechanics, but require the more advanced theory of quantum electrodynamics. In the first chapter we looked at the Bohr–Sommerfeld theory of hydrogen that treated the electron orbits classically and imposed quantisation rules upon them. This theory accounted for many of the features of hydrogen but it fails to provide a realistic description of systems with more than one electron, e.g. the helium atom. Although the simple picture of electrons orbiting the nucleus, like planets round the sun, can explain some phenomena, it has been superseded by the Schrödinger equation and wavefunctions. This chapter outlines the application of this approach to solve Schrödinger’s equation for the hydrogen atom; this leads to the same energy levels as the Bohr model but the wavefunctions give much more information, e.g. they allow the rates of the transitions between levels to be calculated (see Chapter 7). This chapter also shows how the perturbations caused by relativistic effects lead to fine structure.

## 2.1 The Schrödinger equation

The solution of the Schrödinger equation for a Coulomb potential is in every quantum mechanics textbook and only a brief outline is given here.<sup>1</sup> The Schrödinger equation for an electron of mass  $m_e$  in a spherically-symmetric potential is

$$\left\{ \frac{-\hbar^2}{2m_e} \nabla^2 + V(r) \right\} \psi = E\psi. \quad (2.1)$$

<sup>1</sup>The emphasis is on the properties of the wavefunctions rather than how to solve differential equations.

<sup>2</sup>The operator for linear momentum is  $\mathbf{p} = -i\hbar\nabla$  and for angular momentum it is  $\hbar\mathbf{l} = \mathbf{r} \times \mathbf{p}$ . This notation differs in two ways from that commonly used in quantum texts. Firstly,  $\hbar$  is taken outside the angular momentum operators, and secondly, the operators are written without ‘hats’. This is convenient for atomic physics, e.g. in the vector model for the addition of angular momenta.

This is the quantum mechanical counterpart of the classical equation for the conservation of total energy expressed as the sum of kinetic and potential energies.<sup>2</sup> In spherical polar coordinates we have

$$\nabla^2 = \frac{1}{r^2} \frac{\partial}{\partial r} \left( r^2 \frac{\partial}{\partial r} \right) - \frac{1}{r^2} \mathbf{l}^2, \quad (2.2)$$

where the operator  $\mathbf{l}^2$  contains the terms that depend on  $\theta$  and  $\phi$ , namely

$$\mathbf{l}^2 = - \left\{ \frac{1}{\sin \theta} \frac{\partial}{\partial \theta} \left( \sin \theta \frac{\partial}{\partial \theta} \right) + \frac{1}{\sin^2 \theta} \frac{\partial^2}{\partial \phi^2} \right\}, \quad (2.3)$$

and  $\hbar^2 \mathbf{l}^2$  is the operator for the orbital angular momentum squared. Following the usual procedure for solving partial differential equations, we look for a solution in the form of a product of functions  $\psi = R(r)Y(\theta, \phi)$ . The equation separates into radial and angular parts as follows:

$$\frac{1}{R} \frac{\partial}{\partial r} \left( r^2 \frac{\partial R}{\partial r} \right) - \frac{2m_e r^2}{\hbar^2} \{V(r) - E\} = \frac{1}{Y} \mathbf{l}^2 Y. \quad (2.4)$$

Each side depends on different variables and so the equation is only satisfied if both sides equal a constant that we call  $b$ . Thus

$$\mathbf{l}^2 Y = b Y. \quad (2.5)$$

This is an eigenvalue equation and we shall use the quantum theory of angular momentum operators to determine the eigenfunctions  $Y(\theta, \phi)$ .

### 2.1.1 Solution of the angular equation

To continue the separation of variables we substitute  $Y = \Theta(\theta)\Phi(\phi)$  into eqn 2.5 to obtain

$$\frac{\sin \theta}{\Theta} \frac{\partial}{\partial \theta} \left( \sin \theta \frac{\partial \Theta}{\partial \theta} \right) + b \sin^2 \theta = - \frac{1}{\Phi} \frac{\partial^2 \Phi}{\partial \phi^2} = \text{const.} \quad (2.6)$$

The equation for  $\Phi(\phi)$  is the same as in simple harmonic motion, so<sup>3</sup>

$$\Phi = A e^{im\phi} + B e^{-im\phi}. \quad (2.7)$$

The constant on the right-hand side of eqn 2.6 has the value  $m^2$ . Physically realistic wavefunctions have a unique value at each point and this imposes the condition  $\Phi(\phi + 2\pi) = \Phi(\phi)$ , so  $m$  must be an integer. The function  $\Phi(\phi)$  is the sum of eigenfunctions of the operator for the  $z$ -component of orbital angular momentum

$$\hbar l_z = -i\hbar \frac{\partial}{\partial \phi}. \quad (2.8)$$

The function  $e^{im\phi}$  has magnetic quantum number  $m$  and its complex conjugate  $e^{-im\phi}$  has magnetic quantum number  $-m$ .<sup>4</sup>

A convenient way to find the function  $Y(\theta, \phi)$  and its eigenvalue  $b$  in eqn 2.5<sup>5</sup> is to use the **ladder operators**  $l_+ = l_x + i l_y$  and  $l_- = l_x - i l_y$ . These operators commute with  $\mathbf{l}^2$ , the operator for the total angular momentum squared (because  $l_x$  and  $l_y$  commute with  $\mathbf{l}^2$ ); therefore, the three functions  $Y$ ,  $l_+ Y$  and  $l_- Y$  are all eigenfunctions of  $\mathbf{l}^2$  with the same eigenvalue  $b$  (if they are non-zero, as discussed below). The ladder

<sup>3</sup>  $A$  and  $B$  are arbitrary constants. Alternatively, the solutions can be written in terms of real functions as  $A' \sin(m\phi) + B' \cos(m\phi)$ .

<sup>4</sup> The operator  $-\partial^2/\partial \phi^2 \equiv l_z^2$  and consequently  $\Phi(\phi)$  is an eigenfunction of  $l_z^2$  with eigenvalue  $m^2$ .

<sup>5</sup> The solution of equations involving the angular part of  $\nabla^2$  arises in many situations with spherical symmetry, e.g. in electrostatics, and the same mathematical tools could be used here to determine the properties of the spherical harmonic functions, but angular momentum methods give more physical insight for atoms.

operators can be expressed in polar coordinates as:

$$\begin{aligned} l_+ &= e^{i\phi} \left( \frac{\partial}{\partial\theta} + i \cot\theta \frac{\partial}{\partial\phi} \right), \\ l_- &= e^{-i\phi} \left( -\frac{\partial}{\partial\theta} + i \cot\theta \frac{\partial}{\partial\phi} \right). \end{aligned} \quad (2.9)$$

<sup>6</sup>The raising operator contains the factor  $e^{i\phi}$ , so that when it acts on an eigenfunction of the form  $Y \propto \Theta(\theta)e^{im\phi}$  the resulting function  $l_+Y$  contains  $e^{i(m+1)\phi}$ . The  $\theta$ -dependent part of this function is found below.

<sup>7</sup>These properties follow from the commutation relations for angular momentum operators, as shown in quantum mechanics texts.

<sup>8</sup>This statement can be proved rigorously using angular momentum operators, as shown in quantum mechanics texts.

<sup>9</sup>The dubious reader can easily check that  $l_+Y_{l,l} = 0$ . It is trivially obvious that  $l_z Y_{l,l} = l Y_{l,l}$ , where  $m = l$  for this function.

<sup>10</sup> $l_- Y_{1,-1} = 0$  and  $m = -1$  is the lowest eigenvalue of  $l_z$ . Proportional signs have been used to avoid worrying about normalisation; this leaves an ambiguity about the relative phases of the eigenfunctions but we shall choose them in accordance with usual convention.

<sup>11</sup>The relation  $Y_{l,-m} = Y_{l,m}^*$  shows that, if  $m_{\max} = l$ , then  $m_{\min} = -l$ . Between these two extremes there are  $2l + 1$  possible values of the magnetic quantum number  $m$  for each  $l$ . Note that the *orbital angular momentum quantum number*  $l$  is not the same as the length of the angular momentum vector (in units of  $\hbar$ ). Quantum mechanics tells us only that the expectation value of the square of the orbital angular momentum is  $l(l+1)$ , in units of  $\hbar^2$ . The length itself does not have a well-defined value in quantum mechanics and it does not make sense to refer to it. When people say that an atom has ‘orbital angular momentum of one, two, etc.’, strictly speaking they mean that the orbital angular momentum quantum number  $l$  is 1, 2, etc.

The operator  $l_+$  transforms a function with magnetic quantum number  $m$  into another angular momentum eigenfunction that has eigenvalue  $m + 1$ . Thus  $l_+$  is called the **raising operator**.<sup>6</sup> The lowering operator  $l_-$  changes the magnetic quantum number in the other direction,  $m \rightarrow m - 1$ . It is straightforward to prove these statements and other properties of these operators;<sup>7</sup> however, the purpose of this section is not to present the general theory of angular momentum but simply to outline how to find the eigenfunctions (of the angular part) of the Schrödinger equation.

Repeated application of the raising operator does not increase  $m$  indefinitely—for each eigenvalue  $b$  there is a maximum value of the magnetic quantum number<sup>8</sup> that we shall call  $l$ , i.e.  $m_{\max} = l$ . The raising operator acting on an eigenfunction with  $m_{\max}$  gives zero since by definition there are no eigenfunctions with  $m > m_{\max}$ . Thus solving the equation  $l_+Y = 0$  (Exercise 2.11) we find that the eigenfunctions with  $m_{\max} = l$  have the form

$$Y \propto \sin^l \theta e^{il\phi}. \quad (2.10)$$

Substitution back into eqn 2.5 shows that these are eigenfunctions  $\mathbf{l}^2$  with eigenvalue  $b = l(l+1)$ , and  $l$  is the **orbital angular momentum quantum number**. The functions  $Y_{l,m}(\theta, \phi)$  are labelled by their eigenvalues in the conventional way.<sup>9</sup> For  $l = 0$  only  $m = 0$  exists and  $Y_{0,0}$  is a constant with no angular dependence. For  $l = 1$  we can find the eigenfunctions by starting from the one with  $l = 1 = m$  (in eqn 2.10) and using the lowering operator to find the others:

$$\begin{aligned} Y_{1,1} &\propto \sin \theta e^{i\phi}, \\ Y_{1,0} &\propto l_- Y_{1,1} \propto \cos \theta, \\ Y_{1,-1} &\propto l_- Y_{1,0} \propto \sin \theta e^{-i\phi}. \end{aligned}$$

This gives all three eigenfunctions expected for  $l = 1$ .<sup>10</sup> For  $l = 2$  this procedure gives

$$Y_{2,2} \propto \sin^2 \theta e^{i2\phi},$$

⋮

$$Y_{2,-2} \propto \sin^2 \theta e^{-i2\phi}.$$

These are the five eigenfunctions with  $m = 2, 1, 0, -1, -2$ .<sup>11</sup> Normalised angular functions are given in Table 2.1.

Any angular momentum eigenstate can be found from eqn 2.10 by

**Table 2.1** Orbital angular momentum eigenfunctions.

|   |
|---|
| $Y_{0,0} = \sqrt{\frac{1}{4\pi}}$   |
| $Y_{1,0} = \sqrt{\frac{3}{4\pi}} \cos \theta$                                       |
| $Y_{1,\pm 1} = \mp \sqrt{\frac{3}{8\pi}} \sin \theta e^{\pm i\phi}$                 |
| $Y_{2,0} = \sqrt{\frac{5}{16\pi}} (3 \cos^2 \theta - 1)$                            |
| $Y_{2,\pm 1} = \mp \sqrt{\frac{15}{8\pi}} \sin \theta \cos \theta e^{\pm i\phi}$    |
| $Y_{2,\pm 2} = \sqrt{\frac{15}{32\pi}} \sin^2 \theta e^{\pm 2i\phi}$                |
| Normalisation: $\int_0^{2\pi} \int_0^\pi  Y_{l,m} ^2 \sin \theta d\theta d\phi = 1$ |

repeated application of the lowering operator.<sup>12</sup>

$$Y_{l,m} \propto (l_-)^{l-m} \sin^l \theta e^{il\phi}. \quad (2.11)$$

To understand the properties of atoms, it is important to know what the wavefunctions look like. The angular distribution needs to be multiplied by the radial distribution, calculated in the next section, to give the square of the wavefunction as

$$|\psi(r, \theta, \phi)|^2 = R_{n,l}^2(r) |Y_{l,m}(\theta, \phi)|^2. \quad (2.12)$$

This is the probability distribution of the electron, or  $-e|\psi|^2$  can be interpreted as the electronic charge distribution. Many atomic properties, however, depend mainly on the form of the angular distribution and Fig. 2.1 shows some plots of  $|Y_{l,m}|^2$ . The function  $|Y_{0,0}|^2$  is spherically symmetric. The function  $|Y_{1,0}|^2$  has two lobes along the  $z$ -axis. The squared modulus of the other two eigenfunctions of  $l = 1$  is proportional to  $\sin^2 \theta$ . As shown in Fig. 2.1(c), there is a correspondence between these distributions and the circular motion of the electron around the  $z$ -axis that we found as the normal modes in the classical theory of the Zeeman effect (in Chapter 1).<sup>13</sup> This can be seen in Cartesian coordinates where

$$\begin{aligned} Y_{1,0} &\propto \frac{z}{r}, \\ Y_{1,1} &\propto \frac{x + iy}{r}, \\ Y_{1,-1} &\propto \frac{x - iy}{r}. \end{aligned} \quad (2.13)$$

<sup>12</sup>This eigenfunction has magnetic quantum number  $l - (l - m) = m$ .

<sup>13</sup>Stationary states in quantum mechanics correspond to the time-averaged classical motion. In this case both directions of circular motion about the  $x$ -axis give the same distribution.

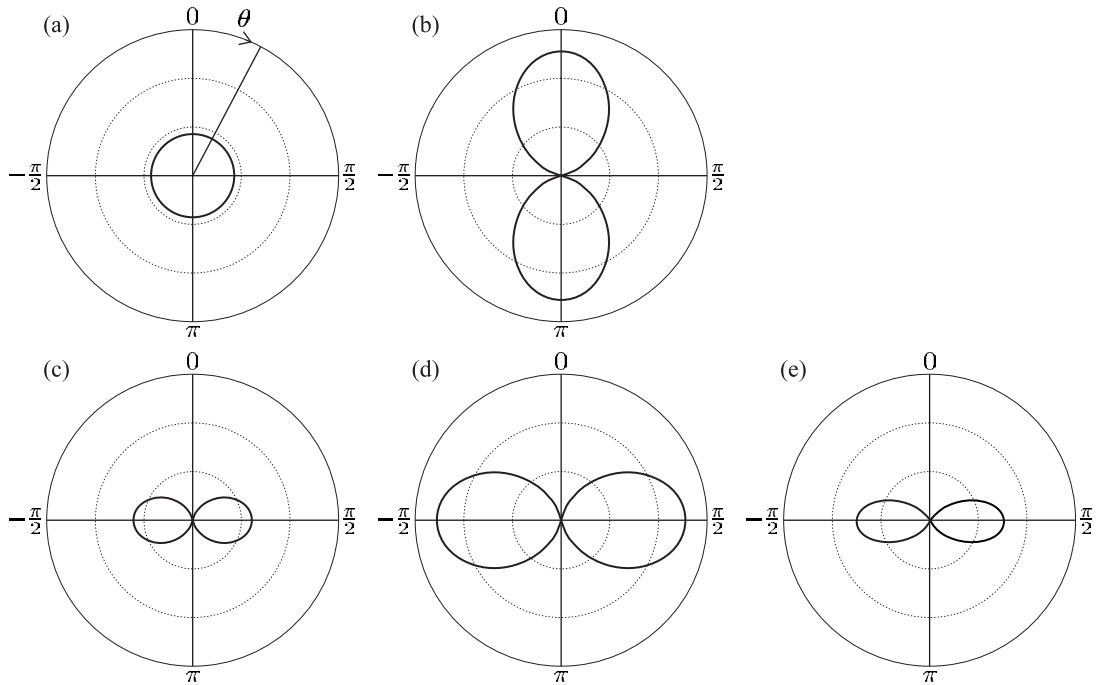


**Fig. 2.1** Polar plots of the squared modulus of the angular wavefunctions for the hydrogen atom with  $l = 0$  and  $1$ . For each value of the polar angle  $\theta$  a point is plotted at a distance proportional to  $|Y(\theta, \phi)|^2$  from the origin. Except for (d), the plots have rotational symmetry about the  $z$ -axis and look the same for any value of  $\phi$ . (a)  $|Y_{0,0}|^2$  is spherical. (b)  $|Y_{1,0}|^2 \propto \cos^2 \theta$  has two lobes along the  $z$ -axis. (c)  $|Y_{1,1}|^2 \propto \sin^2 \theta$  has an ‘almost’ toroidal shape—this function equals zero for  $\theta = 0$ . ( $|Y_{1,-1}|^2$  looks the same.) (d)  $|Y_{1,1} - Y_{1,-1}|^2 \propto |x/r|^2$  has rotational symmetry about the  $x$ -axis and this polar plot is drawn for  $\phi = 0$ ; it looks like (b) but rotated through an angle of  $\pi/2$ . (e)  $|Y_{2,2}|^2 \propto \sin^4 \theta$ .

Any linear combination of these is also an eigenfunction of  $\mathbf{l}^2$ , e.g.

$$Y_{1,-1} - Y_{1,1} \propto \frac{x}{r} = \sin \theta \cos \phi, \quad (2.14)$$

$$Y_{1,-1} + Y_{1,1} \propto \frac{y}{r} = \sin \theta \sin \phi. \quad (2.15)$$

<sup>14</sup>In the absence of an external field to break the spherical symmetry, all axes are equivalent, i.e. the atom does not have a preferred direction so there is symmetry between the  $x$ -,  $y$ - and  $z$ -directions. In an external magnetic field the states with different values of  $m$  (but the same  $l$ ) are not degenerate and so linear combinations of them are not eigenstates of the system.

These two real functions have the same shape as  $Y_{1,0} \propto z/r$  but are aligned along the  $x$ - and  $y$ -axes, respectively.<sup>14</sup> In chemistry these distributions for  $l = 1$  are referred to as p-orbitals. Computer programs can produce plots of such functions from any desired viewing angle (see Blundell 2001, Fig. 3.1) that are helpful in visualising the functions with  $l > 1$ . (For  $l = 0$  and  $1$  a cross-section of the functions in a plane that contains the symmetry axis suffices.)

## 2.1.2 Solution of the radial equation

An equation for  $R(r)$  is obtained by setting eqn 2.4 equal to the constant  $b = l(l+1)$  and putting in the Coulomb potential  $V(r) = -e^2/4\pi\epsilon_0 r$ . It

can be cast in a convenient form by the substitution  $P(r) = rR(r)$ :

$$-\frac{\hbar^2}{2m_e} \frac{d^2P}{dr^2} + \left\{ \frac{\hbar^2}{2m_e} \frac{l(l+1)}{r^2} - \frac{e^2/4\pi\epsilon_0}{r} - E \right\} P = 0. \quad (2.16)$$

The term proportional to  $l(l+1)/r^2$  is the kinetic energy associated with the angular degrees of freedom; it appears in this radial equation as an effective potential that tends to keep wavefunctions with  $l \neq 0$  away from the origin. Dividing through this equation by  $E = -|E|$  (a negative quantity since  $E \leq 0$  for a bound state) and making the substitution

$$\rho^2 = \frac{2m_e |E| r^2}{\hbar^2} \quad (2.17)$$

reduces the equation to the dimensionless form

$$\frac{d^2P}{d\rho^2} + \left\{ -\frac{l(l+1)}{\rho^2} + \frac{\lambda}{\rho} - 1 \right\} P = 0. \quad (2.18)$$

The constant that characterises the Coulomb interaction strength is

$$\lambda = \frac{e^2}{4\pi\epsilon_0} \sqrt{\frac{2m_e}{\hbar^2 |E|}}. \quad (2.19)$$

The standard method of solving such differential equations is to look for a solution in the form of a series. The series solutions have a finite number of terms and do not diverge when  $\lambda = 2n$ , where  $n$  is an integer.<sup>15</sup> Thus, from eqn 2.19, these wavefunctions have eigenenergies given by<sup>16</sup>

$$E = -\frac{2m_e (e^2/4\pi\epsilon_0)^2}{\hbar^2} \frac{1}{\lambda^2} = -hcR_\infty \frac{1}{n^2}. \quad (2.20)$$

This shows that the Schrödinger equation has stationary solutions at energies given by the Bohr formula. The energy does not depend on  $l$ ; this *accidental* degeneracy of wavefunctions with different  $l$  is a special feature of Coulomb potential. In contrast, degeneracy with respect to the magnetic quantum number  $m_l$  arises because of the system's symmetry, i.e. an atom's properties are independent of its orientation in space, in the absence of external fields.<sup>17</sup> The solution of the Schrödinger equation gives much more information than just the energies; from the wavefunctions we can calculate other atomic properties in ways that were not possible in the Bohr–Sommerfeld theory.

We have not gone through the gory details of the series solution, but we should examine a few examples of radial wavefunctions (see Table 2.2). Although the energy depends only on  $n$ , the shape of the wavefunctions depends on both  $n$  and  $l$  and these two quantum numbers are used to label the radial functions  $R_{n,l}(r)$ . For  $n = 1$  there is only the  $l = 0$  solution, namely  $R_{1,0} \propto e^{-\rho}$ . For  $n = 2$  the orbital angular momentum quantum number is  $l = 0$  or 1, giving

$$R_{2,0} \propto (1 - \rho) e^{-\rho}, \\ R_{2,1} \propto \rho e^{-\rho}.$$

<sup>15</sup>The solution has the general form  $P(\rho) = Ce^{-\rho}v(\rho)$ , where  $v(\rho)$  is another function of the radial coordinate, for which there is a polynomial solution (see Woodgate 1980 and Rae 1992).

<sup>16</sup>Using eqn 1.41.

<sup>17</sup>This is true for any spherically-symmetric potential  $V(r)$ .

**Table 2.2** Radial hydrogenic wavefunctions  $R_{n,l}$  in terms of the variable  $\rho = Zr/(na_0)$ , which gives a scaling that varies with  $n$ . The Bohr radius  $a_0$  is defined in eqn 1.40.

|   |
|---|
| $R_{1,0} = \left( \frac{Z}{a_0} \right)^{3/2} 2 e^{-\rho}$ $R_{2,0} = \left( \frac{Z}{2a_0} \right)^{3/2} 2 (1 - \rho) e^{-\rho}$ $R_{2,1} = \left( \frac{Z}{2a_0} \right)^{3/2} \frac{2}{\sqrt{3}} \rho e^{-\rho}$ $R_{3,0} = \left( \frac{Z}{3a_0} \right)^{3/2} 2 \left( 1 - 2\rho + \frac{2}{3}\rho^2 \right) e^{-\rho}$ $R_{3,1} = \left( \frac{Z}{3a_0} \right)^{3/2} \frac{4\sqrt{2}}{3} \rho \left( 1 - \frac{1}{2}\rho \right) e^{-\rho}$ $R_{3,2} = \left( \frac{Z}{3a_0} \right)^{3/2} \frac{2\sqrt{2}}{3\sqrt{5}} \rho^2 e^{-\rho}$ |
| Normalisation: $\int_0^\infty R_{n,l}^2 r^2 dr = 1$   |

These show a general feature of hydrogenic wavefunctions, namely that the radial functions for  $l = 0$  have a finite value at the origin, i.e. the power series in  $\rho$  starts at the zeroth power. Thus electrons with  $l = 0$  (called s-electrons) have a finite probability of being found at the position of the nucleus and this has important consequences in atomic physics.

Inserting  $|E|$  from eqn 2.20 into eqn 2.17 gives the scaled coordinate

$$\rho = \frac{Z}{n} \frac{r}{a_0}, \quad (2.21)$$

where the atomic number has been incorporated by the replacement  $e^2/4\pi\epsilon_0 \rightarrow Ze^2/4\pi\epsilon_0$  (as in Chapter 1). There are some important properties of the radial wavefunctions that require a general form of the solution and for future reference we state these results. The probability density of electrons with  $l = 0$  at the origin is

$$|\psi_{n,l=0}(0)|^2 = \frac{1}{\pi} \left( \frac{Z}{na_0} \right)^3. \quad (2.22)$$

For electrons with  $l \neq 0$  the expectation value of  $1/r^3$  is

$$\left\langle \frac{1}{r^3} \right\rangle = \int_0^\infty \frac{1}{r^3} R_{n,l}^2(r) r^2 dr = \frac{1}{l(l+\frac{1}{2})(l+1)} \left( \frac{Z}{na_0} \right)^3. \quad (2.23)$$

These results have been written in a form that is easy to remember; they must both depend on  $1/a_0^3$  in order to have the correct dimensions and the dependence on  $Z$  follows from the scaling of the Schrödinger

equation. The dependence on the principal quantum number  $n$  also seems to follow from eqn 2.21 but this is coincidental; a counterexample is<sup>18</sup>

$$\left\langle \frac{1}{r} \right\rangle = \frac{1}{n^2} \left( \frac{Z}{a_0} \right). \quad (2.24)$$

## 2.2 Transitions

The wavefunction solutions of the Schrödinger equation for particular energies are standing waves and give a distribution of electronic charge  $-e|\psi(r)|^2$  that is constant in time. We shall now consider how transitions between these stationary states occur when the atom interacts with electromagnetic radiation that produces an oscillating electric field<sup>19</sup>

$$\mathbf{E}(t) = |\mathbf{E}_0| \operatorname{Re}(\mathrm{e}^{-i\omega t} \hat{\mathbf{e}}_{\text{rad}}) \quad (2.25)$$

with constant amplitude  $|\mathbf{E}_0|$  and polarization vector  $\hat{\mathbf{e}}_{\text{rad}}$ .<sup>20</sup> If  $\omega$  lies close to the atomic resonance frequency then the perturbing electric field puts the atom into a superposition of different states and induces an oscillating electric dipole moment on the atom (see Exercise 2.10). The calculation of the stimulated transition rate requires time-dependent perturbation theory (TDPT), as described in Chapter 7. However, the treatment from first principles is lengthy and we shall anticipate some of the results so that we can see how spectra relate to the underlying structure of the atomic energy levels. This does not require an exact calculation of transition rates, but we only need to determine whether the transition rate has a finite value or whether it is zero (to first order), i.e. whether the transition is allowed and gives a strong spectral line, or is forbidden.

The result of time-dependent perturbation theory is encapsulated in the golden rule (or Fermi's golden rule);<sup>21</sup> this states that the rate of transitions is proportional to the square of the matrix element of the perturbation. The Hamiltonian that describes the time-dependent interaction with the field in eqn 2.25 is  $H' = -\mathbf{er} \cdot \mathbf{E}(t)$ , where the electric dipole operator is  $-\mathbf{er}$ .<sup>22</sup> This interaction with the radiation stimulates transitions from state 1 to state 2 at a rate<sup>23</sup>

$$\text{Rate} \propto |e\mathbf{E}_0|^2 \left| \int \psi_2^*(\mathbf{r} \cdot \hat{\mathbf{e}}_{\text{rad}}) \psi_1 \mathrm{d}^3\mathbf{r} \right|^2 \equiv |e\mathbf{E}_0|^2 \times |\langle 2 | \mathbf{r} \cdot \hat{\mathbf{e}}_{\text{rad}} | 1 \rangle|^2. \quad (2.26)$$

The concise expression in Dirac notation is convenient for later use. This treatment assumes that the amplitude of the electric field is uniform over the atom so that it can be taken outside the integral over the atomic wavefunctions, i.e. that  $\mathbf{E}_0$  does not depend on  $\mathbf{r}$ .<sup>24</sup> We write the dipole matrix element as the product

$$\langle 2 | \mathbf{r} \cdot \hat{\mathbf{e}}_{\text{rad}} | 1 \rangle = D_{12} \mathcal{I}_{\text{ang}}. \quad (2.27)$$

The radial integral is<sup>25</sup>

<sup>18</sup>This quantity is related to the quantum mechanical expectation value of the potential energy  $\langle \text{p.e.} \rangle$ ; as in the Bohr model the total energy is  $E = \langle \text{p.e.} \rangle / 2$ .

<sup>19</sup>The interaction of atoms with the oscillating magnetic field in such a wave is considerably weaker; see Appendix C.

<sup>20</sup>The unit vector  $\hat{\mathbf{e}}_{\text{rad}}$  gives the direction of the oscillating electric field. For example, for the simple case of linear polarization along the  $x$ -axis  $\hat{\mathbf{e}}_{\text{rad}} = \hat{\mathbf{e}}_x$  and the real part of  $\mathrm{e}^{-i\omega t}$  is  $\cos(\omega t)$ ; therefore  $\mathbf{E}(t) = |\mathbf{E}_0| \cos(\omega t) \hat{\mathbf{e}}_x$ .

<sup>21</sup>See quantum mechanics texts such as Mandl (1992).

<sup>22</sup>This is analogous to the interaction of a classical dipole with an electric field. Atoms do not have a permanent dipole moment, but one is induced by the oscillating electric field. For a more rigorous derivation, see Woodgate (1980) or Loudon (2000).

<sup>23</sup>The maximum transition rate occurs when  $\omega$ , the frequency of the radiation, matches the transition frequency  $\omega_{12}$ , as discussed in Chapter 7. Note, however, that we shall not discuss the so-called 'density of states' in the golden rule since this is not straightforward for monochromatic radiation.

<sup>24</sup>In eqn 2.25 the phase of the wave is actually  $(\omega t - \mathbf{k} \cdot \mathbf{r})$ , where  $\mathbf{r}$  is the coordinate relative to the atom's centre of mass (taken to be the origin) and  $\mathbf{k}$  is the wavevector. We assume that the variation of phase  $\mathbf{k} \cdot \mathbf{r}$  is small over the atom ( $ka_0 \ll 2\pi$ ). This is equivalent to  $\lambda \gg a_0$ , i.e. the radiation has a wavelength much greater than the size of the atom. This is called the dipole approximation.

<sup>25</sup>Note that  $D_{12} = D_{21}$ .

$$D_{12} = \int_0^\infty R_{n_2, l_2}(r) r R_{n_1, l_1}(r) r^2 dr. \quad (2.28)$$

The angular integral is

$$\mathcal{I}_{\text{ang}} = \int_0^{2\pi} \int_0^\pi Y_{l_2, m_2}^*(\theta, \phi) \hat{\mathbf{r}} \cdot \hat{\mathbf{e}}_{\text{rad}} Y_{l_1, m_1}(\theta, \phi) \sin \theta d\theta d\phi, \quad (2.29)$$

where  $\hat{\mathbf{r}} = \mathbf{r}/r$ . The radial integral is not normally zero although it can be small for transitions between states whose radial wavefunctions have a small overlap, e.g. when  $n_1$  is small and  $n_2$  is large (or the other way round). In contrast, the  $\mathcal{I}_{\text{ang}} = 0$  unless strict criteria are satisfied—these are the selection rules.

### 2.2.1 Selection rules

The selection rules that govern allowed transitions arise from the angular integral in eqn 2.29 which contains the angular dependence of the interaction  $\hat{\mathbf{r}} \cdot \hat{\mathbf{e}}_{\text{rad}}$  for a given polarization of the radiation. The mathematics requires that we calculate  $\mathcal{I}_{\text{ang}}$  for an atom with a well-defined quantisation axis (invariably chosen to be the  $z$ -axis) and radiation that has a well-defined polarization and direction of propagation. This corresponds to the physical situation of an atom experiencing the Zeeman effect of an external magnetic field, as described in Section 1.8; that treatment of the electron as a classical oscillator showed that the components of different frequencies within the Zeeman pattern have different polarizations. We use the same nomenclature of  $\pi$ - and  $\sigma$ -transitions here; transverse observation refers to radiation emitted perpendicular to the magnetic field, and longitudinal observation is along the  $z$ -axis.<sup>26</sup>

<sup>26</sup>If either the atoms have random orientations (e.g. because there is no external field) or the radiation is unpolarized (or both), then an average over all angles must be made at the end of the calculation.

To calculate  $\mathcal{I}_{\text{ang}}$  we write the unit vector  $\hat{\mathbf{r}}$  in the direction of the induced dipole as:

$$\begin{aligned} \hat{\mathbf{r}} &= \frac{1}{r} (x \hat{\mathbf{e}}_x + y \hat{\mathbf{e}}_y + z \hat{\mathbf{e}}_z) \\ &= \sin \theta \cos \phi \hat{\mathbf{e}}_x + \sin \theta \sin \phi \hat{\mathbf{e}}_y + \cos \theta \hat{\mathbf{e}}_z. \end{aligned} \quad (2.30)$$

Expressing the functions of  $\theta$  and  $\phi$  in terms of spherical harmonic functions as

$$\begin{aligned} \sin \theta \cos \phi &= \sqrt{\frac{2\pi}{3}} (Y_{1,-1} - Y_{1,1}), \\ \sin \theta \sin \phi &= i \sqrt{\frac{2\pi}{3}} (Y_{1,-1} + Y_{1,1}), \\ \cos \theta &= \sqrt{\frac{4\pi}{3}} Y_{1,0}, \end{aligned} \quad (2.31)$$

leads to

$$\hat{\mathbf{r}} \propto Y_{1,-1} \frac{\hat{\mathbf{e}}_x + i \hat{\mathbf{e}}_y}{\sqrt{2}} + Y_{1,0} \hat{\mathbf{e}}_z + Y_{1,1} \frac{-\hat{\mathbf{e}}_x + i \hat{\mathbf{e}}_y}{\sqrt{2}}. \quad (2.32)$$

We write the general polarization vector as

$$\hat{\mathbf{e}}_{\text{rad}} = A_{\sigma^-} \frac{\hat{\mathbf{e}}_x - i \hat{\mathbf{e}}_y}{\sqrt{2}} + A_\pi \hat{\mathbf{e}}_z + A_{\sigma^+} \left( -\frac{\hat{\mathbf{e}}_x + i \hat{\mathbf{e}}_y}{\sqrt{2}} \right), \quad (2.33)$$

where  $A_\pi$  depends on the component of the electric field along the  $z$ -axis and the component in the  $xy$ -plane is written as a superposition of two circular polarizations with amplitudes  $A_{\sigma+}$  and  $A_{\sigma-}$  (rather than in terms of linear polarization in a Cartesian basis).<sup>27</sup> Similarly, the classical motion of the electron was written in terms of three eigenvectors in Section 1.8: an oscillation along the  $z$ -axis and circular motion in the  $xy$ -plane, both clockwise and anticlockwise.

From the expression for  $\hat{\mathbf{r}}$  in terms of the angular functions  $Y_{l,m}(\theta, \phi)$  with  $l = 1$  we find that the dipole induced on the atom is proportional to<sup>28</sup>

$$\hat{\mathbf{r}} \cdot \hat{\mathbf{e}}_{\text{rad}} \propto A_{\sigma-} Y_{1,-1} + A_z Y_{1,0} + A_{\sigma+} Y_{1,+1}. \quad (2.34)$$

The following sections consider the transitions that arise from these three terms.<sup>29</sup>

### $\pi$ -transitions

The component of the electric field along the  $z$ -axis  $A_z$  induces a dipole moment on the atom proportional to  $\hat{\mathbf{e}}_{\text{rad}} \cdot \hat{\mathbf{e}}_z = \cos \theta$  and the integral over the angular parts of the wavefunctions is

$$\mathcal{I}_{\text{ang}}^\pi = \int_0^{2\pi} \int_0^\pi Y_{l_2, m_2}^*(\theta, \phi) \cos \theta Y_{l_1, m_1}(\theta, \phi) \sin \theta d\theta d\phi. \quad (2.35)$$

To determine this integral we exploit the symmetry with respect to rotations about the  $z$ -axis.<sup>30</sup> The system has cylindrical symmetry, so the value of this integral is unchanged by a rotation about the  $z$ -axis through an angle  $\phi_0$ :

$$\mathcal{I}_{\text{ang}}^\pi = e^{i(m_1 - m_2)\phi_0} \mathcal{I}_{\text{ang}}^\pi. \quad (2.36)$$

This equation is satisfied if either  $\mathcal{I}_{\text{ang}}^\pi = 0$  or  $m_{l_1} = m_{l_2}$ . For this polarization the magnetic quantum number does not change,  $\Delta m_l = 0$ .<sup>31</sup>

### $\sigma$ -transitions

The component of the oscillating electric field in the  $xy$ -plane excites  $\sigma$ -transitions. Equation 2.34 shows that the circularly-polarized radiation with amplitude  $A_{\sigma+}$  excites an oscillating dipole moment on the atom proportional  $Y_{1,1} \propto \sin \theta e^{i\phi}$ , for which the angular integral is

$$\mathcal{I}_{\text{ang}}^{\sigma+} = \int_0^{2\pi} \int_0^\pi Y_{l_2, m_2}^*(\theta, \phi) \sin \theta e^{i\phi} Y_{l_1, m_1}(\theta, \phi) \sin \theta d\theta d\phi. \quad (2.37)$$

Again, consideration of symmetry with respect to rotation about the  $z$ -axis through an arbitrary angle shows that  $\mathcal{I}_{\text{ang}}^{\sigma+} = 0$  unless  $m_{l_1} - m_{l_2} + 1 = 0$ . The interaction of an atom with circularly-polarized radiation of the opposite handedness leads to a similar integral but with  $e^{i\phi} \rightarrow e^{-i\phi}$ ; this integral  $\mathcal{I}_{\text{ang}}^{\sigma-} = 0$  unless  $m_{l_1} - m_{l_2} - 1 = 0$ . Thus the selection rule for the  $\sigma$ -transitions is  $\Delta m_l = \pm 1$ .

We have found the selection rules that govern  $\Delta m_l$  for each of the three possible polarizations of the radiation separately. These apply

<sup>27</sup>We will see that the labels  $\pi$ ,  $\sigma^+$  and  $\sigma^-$  refer to the transition that the radiation excites; for this it is only important to know how the electric field behaves at the position of the atom. The polarization state associated with this electric field, e.g. whether it is right- or left-handed circularly-polarized radiation, also depends on the direction of propagation (wavevector), but we shall try to avoid a detailed treatment of the polarization conventions in this discussion of the principles. Clearly, however, it is important to have the correct polarization when setting up actual experiments.

<sup>28</sup>The eigenvectors have the following properties:

$$\frac{\hat{\mathbf{e}}_x + i\hat{\mathbf{e}}_y}{\sqrt{2}} \cdot \frac{\hat{\mathbf{e}}_x - i\hat{\mathbf{e}}_y}{\sqrt{2}} = 1$$

and

$$\frac{\hat{\mathbf{e}}_x \pm i\hat{\mathbf{e}}_y}{\sqrt{2}} \cdot \frac{\hat{\mathbf{e}}_x \pm i\hat{\mathbf{e}}_y}{\sqrt{2}} = 0.$$

<sup>29</sup>In spherical tensor notation (Woodgate 1980) the three vector components are written  $A_{-1}$ ,  $A_0$  and  $A_{+1}$ , which is convenient for more general use; but writing eqn 2.34 as given emphasises that the amplitudes  $A$  represent the different polarizations of the radiation and the spherical harmonics come from the atomic response (induced dipole moment).

<sup>30</sup>Alternative methods are given below and in Exercise 2.9.

<sup>31</sup>We use  $m_l$  to distinguish this quantum number from  $m_s$ , the magnetic quantum number for spin angular momentum that is introduced later. Specific functions of the spatial variables such as  $Y_{l,m}$  and  $e^{-im\phi}$  do not need this additional subscript.

when the polarized light interacts with an atom that has a well-defined orientation, e.g. an atom in an external magnetic field. If the light is unpolarized or there is no defined quantisation axis, or both, then  $\Delta m_l = 0, \pm 1$ .

### Example 2.1 *Longitudinal observation*

<sup>32</sup>Similar behaviour arises in the classical model of the normal Zeeman effect in Section 1.8, but the quantum treatment in this section shows that it is a general feature of longitudinal observation—not just for the normal Zeeman effect.

## 2.2.2 Integration with respect to $\theta$

In the angular integral the spherical harmonic functions with  $l = 1$  (from eqn 2.34) are sandwiched between the angular momentum wavefunctions of the initial and final states so that

$$\mathcal{I}_{\text{ang}} \propto \int_0^{2\pi} \int_0^\pi Y_{l_2, m_2}^* Y_{l_1, m_1} Y_{l_1, m_1} \sin \theta d\theta d\phi. \quad (2.38)$$

<sup>33</sup>See the references on angular momentum in quantum mechanics; the reason why the magnetic quantum numbers add is obvious from  $\Phi(\phi)$ .

<sup>34</sup>We have  $\int_0^{2\pi} \int_0^\pi Y_{l', m'} Y_{l, m} \sin \theta d\theta d\phi = \delta_{l', l} \delta_{m', m}$ . This reduces to the normalization in Table 2.1 when  $l' = l$  and  $m' = m$ .

<sup>35</sup>This argument applies only for electric dipole radiation. Higher-order terms, e.g. quadrupole radiation, can give  $\Delta l > 1$ .

To calculate this angular integral we use the following formula:<sup>33</sup>

$$Y_{l_1, m} Y_{l_1, m_1} = A Y_{l_1+1, m_1+m} + B Y_{l_1-1, m_1+m}, \quad (2.39)$$

where  $A$  and  $B$  are constants whose exact values need not concern us. Thus from the orthogonality of the spherical harmonics<sup>34</sup> we find

$$\mathcal{I}_{\text{ang}} \propto A \delta_{l_2, l_1+1} \delta_{m_2, m_1+m} + B \delta_{l_2, l_1-1} \delta_{m_2, m_1+m}.$$

The delta functions give the selection rule found previously, namely  $\Delta m_l = m$ , where  $m = 0, \pm 1$  depending on the polarization, and also  $\Delta l = \pm 1$ . In the mathematics the functions with  $l = 1$  that represent the interaction with the radiation are sandwiched between the orbital angular momentum eigenfunctions of the initial and final states. Thus the rule  $\Delta l = \pm 1$  can be interpreted as conservation of angular momentum for a photon carrying one unit of angular momentum,  $\hbar$  (Fig. 2.8 illustrates this reasoning for the case of total angular momentum).<sup>35</sup> The changes in the magnetic quantum number are also consistent with this picture—the component of the photon's angular momentum along the  $z$ -axis being  $\Delta m_l = 0, \pm 1$ . Conservation of angular momentum does not explain why  $\Delta l \neq 0$ —this comes about because of parity, as explained below.

## 2.2.3 Parity

Parity is an important symmetry property throughout atomic and molecular physics and its general use will be explained before applying it to

selection rules. The parity transformation is an inversion through the origin given by  $\mathbf{r} \rightarrow -\mathbf{r}$ . This is equivalent to the following transformation of the polar coordinates:

$$\begin{aligned}\theta &\longrightarrow \pi - \theta : \text{ a reflection,} \\ \phi &\longrightarrow \phi + \pi : \text{ a rotation.}\end{aligned}$$

The reflection produces a mirror image of the original system and parity is also referred to as mirror symmetry. The mirror image of a hydrogen atom has the same energy levels as those in the original atom since the Coulomb potential is the same after reflection. It turns out that all the electric and magnetic interactions ‘look the same’ after reflection and all atoms have parity symmetry.<sup>36</sup> To find the eigenvalues for parity we use the full quantum mechanical notation, with hats to distinguish the operator  $\hat{P}$  from its eigenvalue  $P$  in the equation

$$\hat{P}\psi = P\psi, \quad (2.40)$$

from which it follows that  $\hat{P}^2\psi = P^2\psi$ . Two successive parity operations correspond to there being no change (the identity operator), i.e.  $\mathbf{r} \rightarrow -\mathbf{r} \rightarrow \mathbf{r}$ . Thus  $P^2 = 1$ . Therefore the parity operator has eigenvalues  $P = 1$  and  $-1$  that correspond to even and odd parity wavefunctions, respectively:

$$\hat{P}\psi = \psi \quad \text{or} \quad \hat{P}\psi = -\psi.$$

Both eigenvalues occur for the spherical harmonic functions,

$$\hat{P}Y_{l,m} = (-1)^l Y_{l,m}. \quad (2.41)$$

The value of the angular integral does not change in a parity transformation<sup>37</sup> so

$$\mathcal{I}_{\text{ang}} = (-1)^{l_2+l_1+1} \mathcal{I}_{\text{ang}}. \quad (2.42)$$

Thus the integral is zero unless the initial and final states have opposite parity (see Exercise 2.12). In particular, electric dipole transitions require an odd change in the orbital angular momentum quantum number ( $\Delta l \neq 0$ ).<sup>38</sup>

The treatment above of the parity operator acting on a wavefunction is quite general and even in complex atoms the wavefunctions have a definite parity. The selection rules we have discussed in this section and others are tabulated in Appendix C. If the electric dipole matrix element is zero between two states then other types of transition may occur but at a rate many orders of magnitude slower than allowed transitions.

The allowed transitions between the  $n = 1, 2$  and  $3$  shells of atomic hydrogen are shown in Fig. 2.2, as an example of the selection rules. The 2s configuration has no allowed transitions downwards; this makes it metastable, i.e. it has a very long lifetime of about  $0.125\text{ s}$ .<sup>39</sup>

Finally, a comment on the spectroscopic notation. It can be seen in Fig. 2.2 that the allowed transitions give rise to several series of

<sup>36</sup>This can be proved formally in quantum mechanics by showing that the Hamiltonians for these interactions commute with the parity operator. The weak interaction in nuclear physics does not have mirror symmetry and violates parity conservation. The extremely small effect of the weak interaction on atoms has been measured in exceedingly careful and precise experiments.

<sup>37</sup>See, for example, Mandl (1992).

<sup>38</sup>The radial integral is not changed by the parity transformation.

<sup>39</sup>This special feature is used in the experiment described in Section 2.3.4.

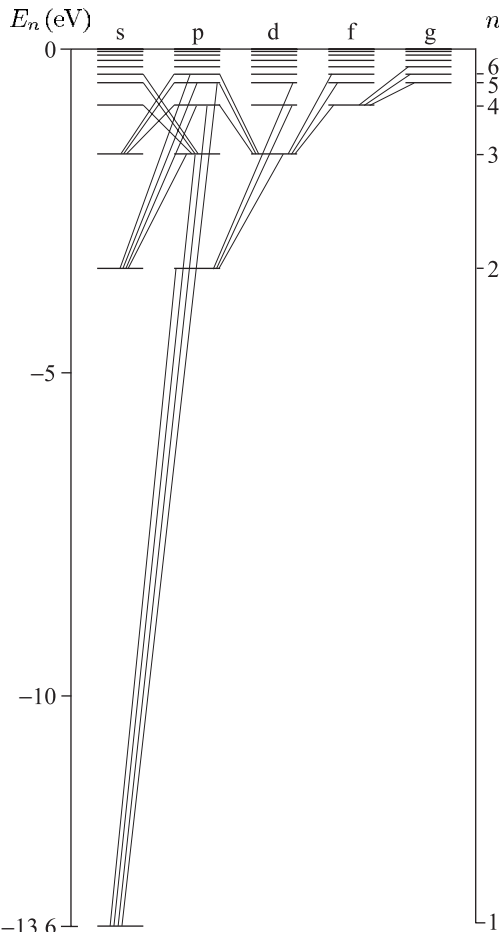


**Fig. 2.2** Allowed transitions between the configurations of hydrogen obey the selection rule  $\Delta l = \pm 1$ . The configurations with  $l = 0, 1, 2, 3, 4, \dots$  are labelled s, p, d, f, g, and so on alphabetically (the usual convention). In the special case of hydrogen the energy does not depend on the quantum number  $l$ .

<sup>40</sup>For hydrogen this is the Lyman series, as marked on Fig. 1.1; however, p-series is a general name.

<sup>41</sup>These names reflect the appearance of the lines in the first experimental observations.

lines. The series of lines to the ground configuration is called the p-series, where p stands for principal—this is the only series observed in absorption<sup>40</sup>—hence p labels configurations with  $l = 1$ . The s-series of lines goes from  $l = 0$  configurations (to a level with  $l = 1$ ), and similarly the d-series goes from  $l = 2$  configurations; s and d stand for sharp and diffuse, respectively.<sup>41</sup>

## 2.3 Fine structure

<sup>42</sup>By considering elliptical orbits, rather than just circular ones, Sommerfeld refined Bohr's theory to obtain a relativistic expression for the energy levels in hydrogen that gave very accurate predictions of the fine structure; however, details of that approach are not given here.

Relativistic effects lead to small splittings of the atomic energy levels called fine structure. We estimated the size of this structure in Section 1.4 by comparing the speed of electrons in classical orbits with the speed of light.<sup>42</sup> In this section we look at how to calculate fine structure by treating relativistic effects as a perturbation to the solutions of the Schrödinger equation. This approach requires the concept that electrons have spin.

### 2.3.1 Spin of the electron

In addition to the evidence provided by observations of the fine structure itself, that is described in this section, two other experiments showed that the electron has spin angular momentum, not just orbital angular momentum. One of these pieces of experimental evidence for spin was the observation of the so-called anomalous Zeeman effect. For many atoms, e.g. hydrogen and sodium, the splitting of their spectral lines in a magnetic field does not have the pattern predicted by the normal Zeeman effect (that we found classically in Section 1.8). This anomalous Zeeman effect has a straightforward explanation in terms of electron spin (as shown in Section 5.5). The second experiment was the famous Stern–Gerlach experiment that will be described in Section 6.4.1.<sup>43</sup>

Unlike orbital angular momentum, spin does not have eigenstates that are functions of the angular coordinates. Spin is a more abstract concept and it is convenient to write its eigenstates in Dirac's ket notation as  $|s m_s\rangle$ . The full wavefunction for a one-electron atom is the product of the radial, angular and spin wavefunctions:  $\Psi = R_{n,l}(r) Y_{l,m}(\theta, \phi) |s m_s\rangle$ . Or, using ket notation for all of the angular momentum, not just the spin,

$$\Psi = R_{n,l}(r) |l m_l s m_s\rangle. \quad (2.43)$$

These atomic wavefunctions provide a basis in which to calculate the effect of perturbations on the atom. However, some problems do not require the full machinery of (degenerate) perturbation theory and for the time being we shall treat the orbital and spin angular momenta by analogy with classical vectors. To a large extent this vector model is intuitively obvious and we start to use it without formal derivations. But note the following points. An often-used shorthand for the spin eigenfunctions is spin-up:

$$|s = \frac{1}{2}, m_s = \frac{1}{2}\rangle \equiv |\uparrow\rangle, \quad (2.44)$$

and similarly  $|\downarrow\rangle$  for the  $m_s = -\frac{1}{2}$  state (spin-down). However, in quantum mechanics the angular momentum cannot be completely aligned ‘up’ or ‘down’ with respect to the  $z$ -axis, otherwise the  $x$ - and  $y$ -components would be zero and we would know all three components simultaneously.<sup>44</sup> The vector model mimics this feature with classical vectors drawn with length  $|\mathbf{s}| = \sqrt{s(s+1)} = \sqrt{3}/2$ . (Only the expectation value of the square of the angular momentum has meaning in quantum mechanics.) The spin-up and spin-down states are as illustrated in Fig. 2.3 with components along the  $z$ -axis of  $\pm\frac{1}{2}$ . We can think of the vector as rotating around the  $z$ -axis, or just having an undefined direction in the  $xy$ -plane corresponding to a lack of knowledge of the  $x$ - and  $y$ -components (see also Grant and Phillips 2001).

The name ‘spin’ invokes an analogy with a classical system spinning on its axis, e.g. a sphere rotating about an axis through its centre of mass, but this mental picture has to be treated with caution; spin cannot be equal to the sum of the orbital angular momenta of the constituents since that will always be an integer multiple of  $\hbar$ . In any case, the electron is

<sup>43</sup>The fine structure, anomalous Zeeman effect and Stern–Gerlach experiment all involve the interaction of the electron's magnetic moment with a magnetic field—the internal field of the atom in the case of fine structure. Stern and Gerlach detected the magnetic interaction by its influence on the atom's motion, whereas the Zeeman effect and fine structure are observed by spectroscopy.

<sup>44</sup>This is not possible since the operators for the  $x$ -,  $y$ - and  $z$ -components of angular momentum do not commute (save in a few special cases; we can know that  $s_x = s_y = s_z = 0$  if  $s = 0$ ).

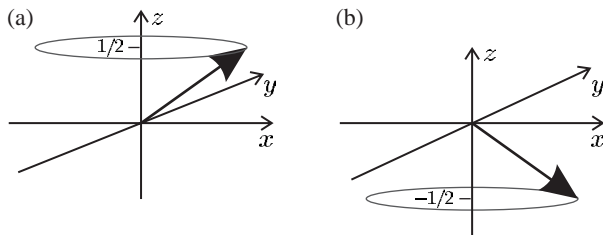


**Fig. 2.3** The representation of (a) spin-up and (b) spin-down states as vectors precessing around the  $z$ -axis.

a structureless elementary particle with no measurable size. So we are left with the experimental fact that the electron has an intrinsic spin angular momentum of  $\hbar/2$  and these half-integer values are perfectly acceptable within the general theory of angular momentum in quantum mechanics.

### 2.3.2 The spin-orbit interaction

The Schrödinger equation is non-relativistic, as can readily be seen by looking at the kinetic-energy operator that is equivalent to the non-relativistic expression  $p^2/2m_e$ . Some of the relativistic effects can be taken into account as follows. An electron moving through an electric field  $\mathbf{E}$  experiences an effective magnetic field  $\mathbf{B}$  given by

$$\mathbf{B} = -\frac{1}{c^2}\mathbf{v} \times \mathbf{E}. \quad (2.45)$$

This is a consequence of the way an electric field behaves under a Lorentz transformation from a stationary to a moving frame in special relativity. Although a derivation of this equation is not given here, it is certainly plausible since special relativity and electromagnetism are intimately linked through the speed of light  $c = 1/\sqrt{\epsilon_0\mu_0}$ . This equation for the speed of electromagnetic waves in a vacuum comes from Maxwell's equations;  $\epsilon_0$  being associated with the electric field and  $\mu_0$  with the magnetic field. Rearrangement to give  $\mu_0 = 1/(\epsilon_0 c^2)$  suggests that magnetic fields arise from electrodynamics and relativity.<sup>45</sup>

We now manipulate eqn 2.45 into a convenient form, by substituting for the electric field in terms of the gradient of the potential energy  $V$  and unit vector in the radial direction:

$$\mathbf{E} = \frac{1}{e} \frac{\partial V}{\partial r} \frac{\mathbf{r}}{r}. \quad (2.46)$$

The factor of  $e$  comes in because the electron's potential energy  $V$  equals its charge  $-e$  times the electrostatic potential. From eqn 2.45 we have

$$\mathbf{B} = \frac{1}{m_e c^2} \left( \frac{1}{er} \frac{\partial V}{\partial r} \right) \mathbf{r} \times m_e \mathbf{v} = \frac{\hbar}{m_e c^2} \left( \frac{1}{er} \frac{\partial V}{\partial r} \right) \mathbf{l}, \quad (2.47)$$

where the orbital angular momentum is  $\hbar \mathbf{l} = \mathbf{r} \times m_e \mathbf{v}$ . The electron has an intrinsic magnetic moment  $\boldsymbol{\mu} = -g_s \mu_B \mathbf{s}$ , where the spin has a magnitude of  $|\mathbf{s}| = s = 1/2$  (in units of  $\hbar$ ) and  $g_s \simeq 2$ , so the moment

<sup>45</sup>The Biot-Savart law for the magnetic field from a current flowing along a straight wire can be recovered from the Lorentz transformation and Coulomb's law (Griffiths 1999). However, this link can only be made in this direction for simple cases and generally the phenomenon of magnetism cannot be 'derived' in this way.

has a magnitude close to one Bohr magneton ( $\mu_B = e\hbar/2m_e$ ). The interaction of the electron's magnetic moment with the orbital field gives the Hamiltonian

$$\begin{aligned} H &= -\boldsymbol{\mu} \cdot \mathbf{B} \\ &= g_s \mu_B \mathbf{s} \cdot \frac{\hbar}{m_e c^2} \left( \frac{1}{er} \frac{\partial V}{\partial r} \right) \mathbf{l}. \end{aligned} \quad (2.48)$$

However, this expression gives energy splittings about twice as large as observed. The discrepancy comes from the Thomas precession—a relativistic effect that arises because we are calculating the magnetic field in a frame of reference that is not stationary but rotates as the electron moves about the nucleus. The effect is taken into account by replacing  $g_s$  with  $g_s - 1 \simeq 1$ .<sup>46</sup> Finally, we find the spin-orbit interaction, including the Thomas precession factor, is<sup>47</sup>

$$H_{s-o} = (g_s - 1) \frac{\hbar^2}{2m_e^2 c^2} \left( \frac{1}{r} \frac{\partial V}{\partial r} \right) \mathbf{s} \cdot \mathbf{l}. \quad (2.49)$$

For the Coulomb potential in hydrogen we have

$$\frac{1}{r} \frac{\partial V}{\partial r} = \frac{e^2 / 4\pi\epsilon_0}{r^3}. \quad (2.50)$$

The expectation value of this Hamiltonian gives an energy change of<sup>48</sup>

$$E_{s-o} = \frac{\hbar^2}{2m_e^2 c^2} \frac{e^2}{4\pi\epsilon_0} \left\langle \frac{1}{r^3} \right\rangle \langle \mathbf{s} \cdot \mathbf{l} \rangle. \quad (2.51)$$

The separation into a product of radial and angular expectation values follows from the separability of the wavefunction. The integral  $\langle 1/r^3 \rangle$  is given in eqn 2.23. However, we have not yet discussed how to deal with interactions that have the form of dot products of two angular momenta; let us start by defining the total angular momentum of the atom as the sum of its orbital and spin angular momenta,

$$\mathbf{j} = \mathbf{l} + \mathbf{s}. \quad (2.52)$$

This is a conserved quantity for a system without any external torque acting on it, e.g. an atom in a field-free region of space. This is true both in classical and quantum mechanics, but we concentrate on the classical explanation in this section. The spin-orbit interaction between  $\mathbf{l}$  and  $\mathbf{s}$  causes these vectors to change direction, and because their sum is constrained to be equal to  $\mathbf{j}$  they move around as shown in Fig. 2.4.<sup>49</sup> Squaring and rearranging eqn 2.52, we find that  $2\mathbf{s} \cdot \mathbf{l} = \mathbf{j}^2 - \mathbf{l}^2 - \mathbf{s}^2$ . Hence we can find the expectation value in terms of the known values for  $\langle \mathbf{j}^2 \rangle$ ,  $\langle \mathbf{l}^2 \rangle$  and  $\langle \mathbf{s}^2 \rangle$  as

$$\langle \mathbf{s} \cdot \mathbf{l} \rangle = \frac{1}{2} \{ j(j+1) - l(l+1) - s(s+1) \}. \quad (2.53)$$

Thus the spin-orbit interaction produces a shift in energy of

$$E_{s-o} = \frac{\beta}{2} \{ j(j+1) - l(l+1) - s(s+1) \}, \quad (2.54)$$

<sup>46</sup>This is almost equivalent to using  $g_s/2 \simeq 1$ , but  $g_s - 1$  is more accurate at the level of precision where the small deviation of  $g_s$  from 2 is important (Haar and Curtis 1987). For further discussion of Thomas precession see Cowan (1981), Eisberg and Resnick (1985) and Munoz (2001).

<sup>47</sup>We have derived this classically, e.g. by using  $\hbar\mathbf{l} = \mathbf{r} \times m_e \mathbf{v}$ . However, the same expression can be obtained from the fully relativistic Dirac equation for an electron in a Coulomb potential by making a low-velocity approximation, see Sakurai (1967). That quantum mechanical approach justifies treating  $\mathbf{l}$  and  $\mathbf{s}$  as operators.

<sup>48</sup>Using the approximation  $g_s - 1 \simeq 1$ .

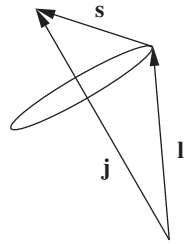


**Fig. 2.4** The orbital and spin angular momenta add to give a total atomic angular momentum of  $\mathbf{j}$ .

<sup>49</sup>In this precession about  $\mathbf{j}$  the magnitudes of  $\mathbf{l}$  and  $\mathbf{s}$  remain constant. The magnetic moment (proportional to  $\mathbf{s}$ ) is not altered in an interaction with a magnetic field, and because of the symmetrical form of the interaction in eqn 2.49, we do not expect  $\mathbf{l}$  to behave any differently. See also Blundell (2001) and Section 5.1.

where the spin-orbit constant  $\beta$  is (from eqns 2.51 and 2.23)

$$\beta = \frac{\hbar^2}{2m_e^2 c^2} \frac{e^2}{4\pi\epsilon_0} \frac{1}{(na_0)^3 l(l + \frac{1}{2})(l + 1)}. \quad (2.55)$$

A single electron has  $s = \frac{1}{2}$  so, for each  $l$ , its total angular momentum quantum number  $j$  has two possible values:

$$j = l + \frac{1}{2} \quad \text{or} \quad l - \frac{1}{2}.$$

From eqn 2.54 we find that the energy interval between these levels,  $\Delta E_{s-o} = E_{j=l+\frac{1}{2}} - E_{j=l-\frac{1}{2}}$ , is

$$\Delta E_{s-o} = \beta(l + \frac{1}{2}) = \frac{\alpha^2 hcR_\infty}{n^3 l(l + 1)}. \quad (2.56)$$

<sup>50</sup> As shown in Section 1.9,  $m_e \alpha c a_0 = \hbar$  and  $hcR_\infty = (e^2/4\pi\epsilon_0)/(2a_0)$ .

Or, expressed in terms of the gross energy  $E(n)$  in eqn 1.10,<sup>50</sup>

$$\Delta E_{s-o} = \frac{\alpha^2}{n l(l + 1)} E(n). \quad (2.57)$$

This agrees with the qualitative discussion in Section 1.4, where we showed that relativistic effects cause energy changes of order  $\alpha^2$  times the gross structure. The more complete expression above shows that the energy intervals between levels decrease as  $n$  and  $l$  increase. The largest interval in hydrogen occurs for  $n = 2$  and  $l = 1$ ; for this configuration the spin-orbit interaction leads to levels with  $j = 1/2$  and  $j = 3/2$ . The full designation of these levels is  $2p^2P_{1/2}$  and  $2p^2P_{3/2}$ , in the notation that will be introduced for the *LS*-coupling scheme. But some of the quantum numbers (defined in Chapter 5) are superfluous for atoms with a single valence electron and a convenient short form is to denote these two levels by  $2P_{1/2}$  and  $2P_{3/2}$ ; these correspond to  $nP_j$ , where P represents the (total) orbital angular momentum for this case. (The capital letters are consistent with later usage.) Similarly, we may write  $2S_{1/2}$  for the  $2s^2S_{1/2}$  level;  $3D_{3/2}$  and  $3D_{5/2}$  for the  $j = 3/2$  and  $5/2$  levels, respectively, that arise from the  $3d$  configuration.<sup>51</sup> But the full notation must be used whenever ambiguity might arise.

### 2.3.3 The fine structure of hydrogen

As an example of fine structure, we look in detail at the levels that arise from the  $n = 2$  and  $n = 3$  shells of hydrogen. Equation 2.54 predicts that, for the  $2p$  configuration, the fine-structure levels have energies of

$$\begin{aligned} E_{s-o}(2P_{1/2}) &= -\beta_{2p}, \\ E_{s-o}(2P_{3/2}) &= \frac{1}{2}\beta_{2p}, \end{aligned}$$

as shown in Fig. 2.5(a). For the  $3d$  configuration

$$\begin{aligned} E_{s-o}(3D_{3/2}) &= -\frac{3}{2}\beta_{3d}, \\ E_{s-o}(3D_{5/2}) &= \beta_{3d}, \end{aligned}$$

<sup>51</sup> Another short form found in the literature is  $2^2P_{1/2}$  and  $2^2P_{3/2}$ .

as shown in Fig. 2.5(b). For both configurations, it is easy to see that the spin-orbit interaction does not shift the mean energy

$$\bar{E} = (2j + 1) E_j(n, l) + (2j' + 1) E_{j'}(n, l), \quad (2.58)$$

where  $j' = l - 1/2$  and  $j = l + 1/2$  for the two levels. This calculation of the ‘centre of gravity’ for all the states takes into account the degeneracy of each level.

The spin-orbit interaction does not affect the  $2S_{1/2}$  or  $3S_{1/2}$  so we might expect these levels to lie close to the centre of gravity of the configurations with  $l > 0$ . This is not the case. Fig. 2.6 shows the energies of the levels for the  $n = 3$  shell given by a fully relativistic calculation. We can see that there are other effects of similar magnitude to the spin-orbit interaction that affect these levels in hydrogen. Quite remarkably, these additional relativistic effects shift the levels by just the right amount to make  $nP_{1/2}$  levels degenerate with the  $nS_{1/2}$  levels, and  $nP_{3/2}$  degenerate with  $nD_{3/2}$ . This structure does not occur by chance, but points to a deeper underlying cause. The full explanation of these observations requires relativistic quantum mechanics and the technical details of such calculations lie beyond the scope of this book.<sup>52</sup> We shall simply quote the solution of the Dirac equation for an electron in a Coulomb potential; this gives a formula for the energy  $E_{\text{Dirac}}(n, j)$  that depends only on  $n$  and  $j$ , i.e. it gives the same energy for levels of the same  $n$  and  $j$  but different  $l$ , as in the cases above. In a comparison of the

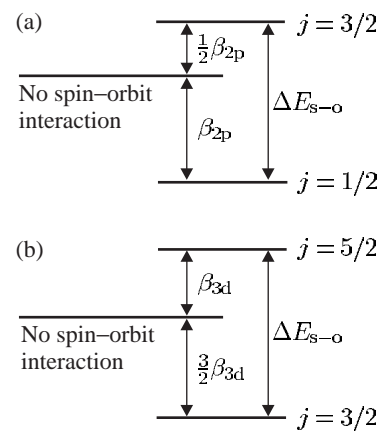


**Fig. 2.5** The fine structure of hydrogen. The fine structure of (a) the 2p and (b) the 3d configurations are drawn on different scales:  $\beta_{2p}$  is considerably greater than  $\beta_{3d}$ . All p- and d-configurations look similar apart from an overall scaling factor.

<sup>52</sup>See graduate-level quantum mechanics texts, e.g. Sakurai (1967) and Series (1988).

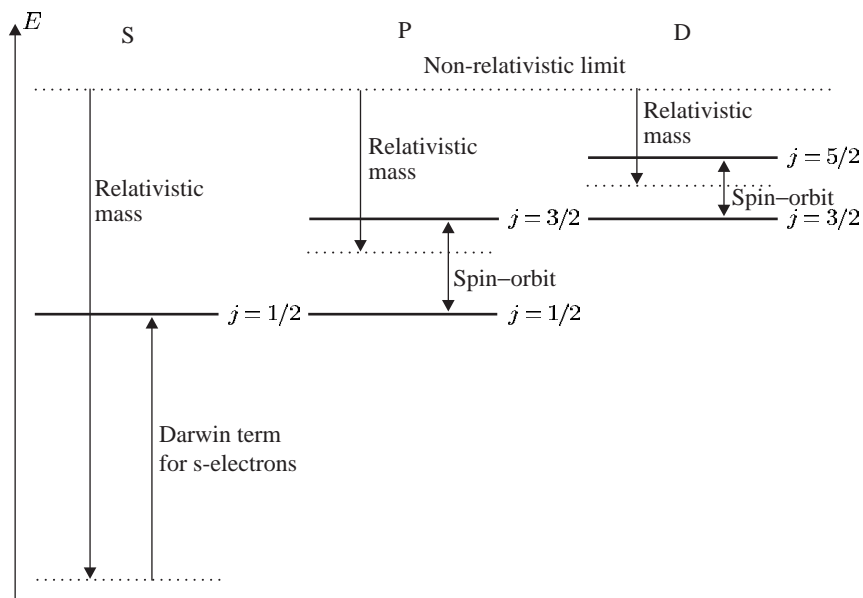


**Fig. 2.6** The theoretical positions of the energy levels of hydrogen calculated by the fully relativistic theory of Dirac depend on  $n$  and  $j$  only (not  $l$ ), as shown in this figure for the  $n = 3$  shell. In addition to the spin-orbit interaction, the effects that determine the energies of these levels are: the relativistic mass correction and, for s-electrons only, the Darwin term (that accounts for relativistic effects that occur at small  $r$ , where the electron’s momentum becomes comparable to  $m_ec$ ).

exact relativistic solution of the Dirac equation and the non-relativistic energy levels, three relativistic effects can be distinguished.

- (a) There is a straightforward relativistic shift of the energy (or equivalently mass), related to the binomial expansion of  $\gamma = (1 - v^2/c^2)^{-1/2}$ , in eqn 1.16. The term of order  $v^2/c^2$  gives the non-relativistic kinetic energy  $p^2/2m_e$ . The next term in the expansion is proportional to  $v^4/c^4$  and gives an energy shift of order  $v^2/c^2$  times the gross structure—this is the effect that we estimated in Section 1.4.
- (b) For electrons with  $l \neq 0$ , the comparison of the Dirac and Schrödinger equations shows that there is a spin-orbit interaction of the form given above, with the Thomas precession factor naturally included.<sup>53</sup>
- (c) For electrons with  $l = 0$  there is a Darwin term proportional to  $|\psi(r=0)|^2$  that has no classical analogue (see Woodgate (1980) for further details).

That these different contributions conspire together to perturb the wavefunctions such that levels of the same  $n$  and  $j$  are degenerate seems improbable from a non-relativistic point of view. It is worth reiterating the statement above that this structure arises from the relativistic Dirac equation; making an approximation for small  $v^2/c^2$  shows that these three corrections, and no others, need to be applied to the (non-relativistic) energies found from the Schrödinger equation.

### 2.3.4 The Lamb shift

<sup>54</sup>Lamb and Rutherford used a radiofrequency to drive the  $2S_{1/2}-2P_{1/2}$  transition directly. This small energy interval, now known as the Lamb shift, cannot be resolved in conventional spectroscopy because of Doppler broadening, but it can be seen using Doppler-free methods as shown in Fig. 8.7.

<sup>55</sup>The QED calculation of the Lamb shift is described in Sakurai (1967).

<sup>56</sup>Broadly speaking, in a mathematical treatment these vacuum fluctuations correspond to the zero-point energy of quantum harmonic oscillators, i.e. the lowest energy of the modes of the system is not zero but  $\hbar\omega/2$ .

<sup>57</sup>QED also explains why the  $g$ -factor of the electron is not exactly 2. Precise measurements show that  $g_s = 2.002\,319\,304\,371\,8$  (current values for the fundamental constants can be found on the NIST web site, and those of other national standards laboratories). See also Chapter 12.

Figure 2.7 shows the actual energy levels of the  $n = 2$  and  $n = 3$  shells. According to relativistic quantum theory the  $2S_{1/2}$  level should be exactly degenerate with  $2P_{1/2}$  because they both have  $n = 2$  and  $j = 1/2$ , but in reality there is an energy interval between them,  $E(2S_{1/2}) - E(2P_{1/2}) \simeq 1\text{ GHz}$ . The shift of the  $2S_{1/2}$  level to a higher energy (lower binding energy) than the  $E_{\text{Dirac}}(n = 2, j = 1/2)$  is about one-tenth of the interval between the two fine-structure levels,  $E(2P_{3/2}) - E(2P_{1/2}) \simeq 11\text{ GHz}$ . Although small, this discrepancy in hydrogen was of great historical importance in physics. For this simple one-electron atom the predictions of the Dirac equation are very precise and that theory cannot account for Lamb and Rutherford's experimental measurement that the  $2S_{1/2}$  level is indeed higher than the  $2P_{1/2}$  level.<sup>54</sup> The explanation of this Lamb shift goes beyond relativistic quantum mechanics and requires quantum electrodynamics (QED)—the quantum field theory that describes electromagnetic interactions. Indeed, the observation of the Lamb shift experiment was a stimulus for the development of this theory.<sup>55</sup> An intriguing feature of QED is so-called vacuum fluctuations—regions of free space are not regarded as being completely empty but are permeated by fluctuating electromagnetic fields.<sup>56</sup> The QED effects lead to a significant energy shift for electrons with  $l = 0$  and hence break the degeneracy of  $2S_{1/2}$  and  $2P_{1/2}$ .<sup>57</sup> The largest QED shift occurs for the  $1S_{1/2}$  ground level of hydrogen but there is no other level nearby and so a determination of its energy requires a precise mea-

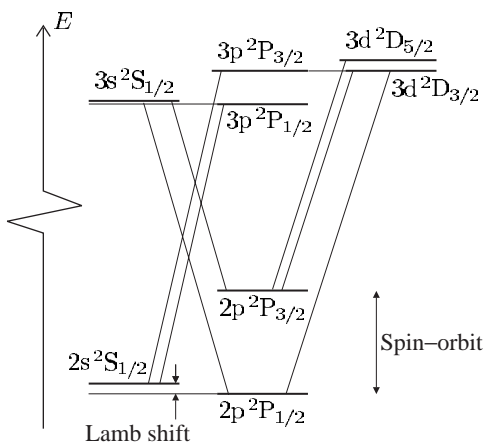


**Fig. 2.7** The fine structure of the  $n = 2$  and  $n = 3$  shells of hydrogen and the allowed transitions between the levels. According to the Dirac equation, the  $2\text{S}_{1/2}$  and  $2\text{P}_{1/2}$  levels should be degenerate, but they are not. The measured positions show that the  $2\text{s}^2\text{S}_{1/2}$  level is shifted upwards relative to the position  $E_{\text{Dirac}} (n = 2, j = 1/2)$  and is therefore not degenerate with the  $2\text{p}^2\text{P}_{1/2}$  level. Such a shift occurs for all the s-electrons (but the size of the energy shift decreases with increasing  $n$ ). The explanation of this shift takes us beyond relativistic quantum mechanics into the realm of quantum electrodynamics (QED)—the quantum field theory that describes electromagnetic interactions.

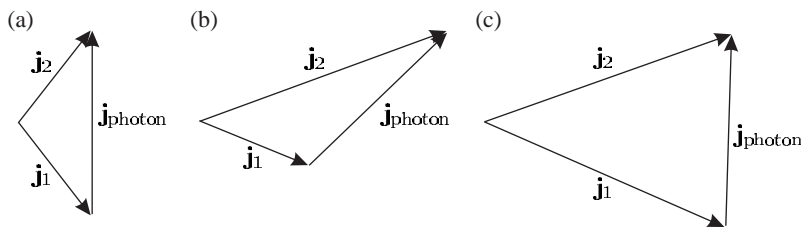


**Fig. 2.8** The conservation of total angular momentum in electric dipole transitions that gives the selection rule in eqn 2.59 can be represented as vector addition. The photon has one unit of angular momentum, and so to go from level  $j_1$  to  $j_2$  the vectors must form a triangle, as shown for the case of (a)  $j_1 = 1/2$  to  $j_2 = 1/2$ , (b)  $j_1 = 1/2$  to  $j_2 = 3/2$  and (c)  $j_1 = 3/2$  to  $j_2 = 3/2$ .

surement of a large frequency. Nowadays this can be achieved by laser spectroscopy (Chapter 8) but the near degeneracy of the two  $j = 1/2$  levels with  $n = 2$  was crucial in Lamb's experiment.<sup>58</sup> Another important feature in that experiment was the metastability of the  $2\text{S}_{1/2}$  level, whose lifetime was given in Section 2.2.3. That level decays  $\sim 10^8$  times more slowly than that of  $2\text{P}_{1/2}$ . In an atomic beam of hydrogen (at room temperature) the atoms have typical velocities of about  $3000 \text{ m s}^{-1}$  and atoms excited into the 2p configuration travel an average distance of only  $5 \times 10^{-6} \text{ m}$  before decaying with the emission of Lyman- $\alpha$  radiation. In contrast, metastable atoms travel the full length of the apparatus ( $\simeq 1 \text{ m}$ ) and are de-excited when they collide with a detector (or the wall of the vacuum chamber). Hydrogen, and hydrogenic systems, are still used for experimental tests of fundamental theory because their simplicity allows very precise predictions.

### 2.3.5 Transitions between fine-structure levels

Transitions in hydrogen between the fine-structure levels with principal quantum numbers  $n = 2$  and 3 give the components of the Balmer- $\alpha$  line shown in Fig. 2.7; in order of increasing energy, the seven allowed

<sup>58</sup> Higher shells have smaller shifts between the  $j = 1/2$  levels.

transitions between the levels with different  $j$  are as follows:

$$\begin{aligned} & 2P_{3/2} - 3S_{1/2}, \\ & 2P_{3/2} - 3D_{3/2}, \\ & 2P_{3/2} - 3D_{5/2}, \\ & 2S_{1/2} - 3P_{1/2}, \\ & 2P_{1/2} - 3S_{1/2}, \\ & 2S_{1/2} - 3P_{3/2}, \\ & 2P_{1/2} - 3D_{3/2}. \end{aligned}$$

These obey the selection rule  $\Delta l = \pm 1$  but an additional rule prevents a transition between  $2P_{1/2}$  and  $3D_{5/2}$ , namely that the change of the total angular momentum quantum number in an electric dipole transition obeys

$$\Delta j = 0, \pm 1. \quad (2.59)$$

This selection rule may be explained by angular momentum conservation (as mentioned in Section 2.2.2). This rule can be expressed in terms of vector addition, as shown in Fig. 2.8; the conservation condition is equivalent to being able to form a triangle from the three vectors representing  $\mathbf{j}$  of the initial state, the final state, and a unit vector for the (one unit of) angular momentum carried by the photon. Hence, this selection rule is sometimes referred to as the triangle rule. The projection of  $\mathbf{j}$  along the  $z$ -axis can change by  $\Delta m_j = 0, \pm 1$ . (Appendix C gives a summary of all selection rules.)

## Further reading

Much of the material covered in this chapter can be found in the introductory quantum mechanics and atomic physics texts listed in the References. For particular topics the following are useful: Segrè (1980) gives an overview of the historical development, and Series (1988) reviews the work on hydrogen, including the important Lamb shift experiment.

## Exercises

### (2.1) Angular-momentum eigenfunctions

- (a) Verify that all the eigenfunctions with  $l = 1$  are orthogonal to  $Y_{0,0}$ .
- (b) Verify that all the eigenfunctions with  $l = 1$  are orthogonal to those with  $l = 2$ .

### (2.2) Angular-momentum eigenfunctions

- (a) Find the eigenfunction with orbital angular momentum quantum number  $l$  and magnetic quantum number  $m = l - 1$ .
- (b) Verify that  $Y_{l,l-1}$  is orthogonal to  $Y_{l-1,l-1}$ .

(2.3) *Radial wavefunctions*

Verify eqn 2.23 for  $n = 2$ ,  $l = 1$  by calculating the radial integral (for  $Z = 1$ ).

(2.4) *Hydrogen*

For a hydrogen atom the normalised wavefunction of an electron in the 1s state, assuming a point nucleus, is

$$\psi(r) = \left( \frac{1}{\pi a_0^3} \right)^{1/2} e^{-r/a_0},$$

where  $a_0$  is the Bohr radius. Find an approximate expression for the probability of finding the electron in a small sphere of radius  $r_b \ll a_0$  centred on the proton. What is the electronic charge density in this region?

(2.5) *Hydrogen*

The Balmer- $\alpha$  spectral line is observed from a (weak) discharge in a lamp that contains a mixture of hydrogen and deuterium at room temperature. Comment on the feasibility of carrying out an experiment using a Fabry-Pérot étalon to resolve (a) the isotope shift, (b) the fine structure and (c) the Lamb shift.

(2.6) *Transitions*

Estimate the lifetime of the excited state in a two-level atom when the transition wavelength is (a) 100 nm and (b) 1000 nm. In what spectral regions do these wavelengths lie?

(2.7) *Selection rules*

By explicit calculation of integrals over  $\theta$ , for the case of  $\pi$ -polarization only, verify that p to d transitions are allowed, but not s to d.

(2.8) *Spin-orbit interaction*

The spin-orbit interaction splits a single-electron configuration into two levels with total angular momentum quantum numbers  $j = l + 1/2$  and  $j' = l - 1/2$ . Show that this interaction does not shift the mean energy (centre of gravity) of all the states given by  $(2j+1)E_j + (2j'+1)E_{j'}$ .

(2.9) *Selection rule for the magnetic quantum number*

Show that the angular integrals for  $\sigma$ -transitions contain the factor

$$\int_0^{2\pi} e^{i(m_{l_1}-m_{l_2}\pm 1)\phi} d\phi.$$

Hence derive the selection rule  $\Delta m_l = \pm 1$  for this polarization. Similarly, derive the selection rule for the  $\pi$ -transitions.

(2.10) *Transitions*

An atom in a superposition of two states has the

wavefunction

$$\Psi(t) = A\psi_1(\mathbf{r})e^{-iE_1t/\hbar} + B\psi_2(\mathbf{r})e^{-iE_2t/\hbar}.$$

The distribution of electronic charge is given by

$$-e|\Psi(t)|^2 = -e\{ |A\psi_1|^2 + |B\psi_2|^2 \\ + |2A^*B\psi_1^*\psi_2| \cos(\omega_{12}t - \phi) \}.$$

Part of this oscillates at the (angular) frequency of the transition  $\omega_{12} = \omega_2 - \omega_1 = (E_2 - E_1)/\hbar$ .

- (a) A hydrogen atom is in a superposition of the 1s ground state,  $\psi_1 = R_{1,0}(r)Y_{0,0}(\theta, \phi)$ , and the  $m_l = 0$  state of the 2p configuration,  $\psi_2 = R_{2,1}(r)Y_{1,0}(\theta, \phi)$ ;  $A \approx 0.995$  and  $B = 0.1$  (so the term containing  $B^2$  can be ignored). Sketch the form of the charge distribution for one cycle of oscillation.

- (b) The atom in a superposition state may have an oscillating electric dipole moment

$$-e\mathbf{D}(t) = -e\langle\Psi^*(t)\mathbf{r}\Psi(t)\rangle.$$

What are the conditions on  $\psi_1$  and  $\psi_2$  for which  $\mathbf{D}(t) \neq 0$ ?

- (c) Show that an atom in a superposition of the same states as in part (a) has a dipole moment of

$$-e\mathbf{D}(t) = -e|2A^*B|\mathcal{I}_{\text{ang}} \\ \times \left\{ \int rR_{2,1}(r)R_{1,0}(r)r^2 dr \right\} \cos(\omega_{12}t)\hat{\mathbf{e}}_z,$$

where  $\mathcal{I}_{\text{ang}}$  is an integral with respect to  $\theta$  and  $\phi$ . Calculate the amplitude of this dipole, in units of  $ea_0$ , for  $A = B = 1/\sqrt{2}$ .

- (d) A hydrogen atom is in a superposition of the 1s ground state and the  $m_l = 1$  state of the 2p configuration,  $\psi_2 = R_{2,1}(r)Y_{1,1}(\theta, \phi)$ . Sketch the form of the charge distribution at various points in its cycle of oscillation.

- (e) Comment on the relationship between the time dependence of the charge distributions sketched in this exercise and the motion of the electron in the classical model of the Zeeman effect (Section 1.8).

(2.11) *Angular eigenfunctions*

We shall find the angular momentum eigenfunctions using ladder operators, by assuming that for some value of  $l$  there is a maximum value of the magnetic quantum number  $m_{\text{max}}$ . For this case  $Y_{l,m_{\text{max}}} \propto \Theta(\theta)e^{im_{\text{max}}\phi}$  and the function  $\Theta(\theta)$  can be found from

$$l_+\Theta(\theta)\exp(im_{\text{max}}\phi) = 0.$$

- (a) Show that  $\Theta(\theta)$  satisfies the equation

$$\frac{1}{\Theta(\theta)} \frac{\partial \Theta(\theta)}{\partial \theta} = m_{\max} \frac{\cos \theta}{\sin \theta}.$$

- (b) Find the solution of the equation for  $\Theta(\theta)$ . (Both sides have the form  $f'(\theta)/f(\theta)$  whose integral is  $\ln\{f(\theta)\}$ .) By substituting this solution into eqn 2.5 to show that  $b = m_{\max}(m_{\max} + 1)$ , or otherwise, obtain eqn 2.10.

(2.12) *Parity and selection rules*

Show that eqn 2.42 implies that  $l_2 - l_1$  is odd.

Hence, or otherwise, prove that  $\mathcal{I}_{\text{ang}}$  is zero unless the initial and final states have opposite parity.

(2.13) *Selection rules in hydrogen*

Hydrogen atoms are excited (by a pulse of laser light that drives a multi-photon process) to a specific configuration and the subsequent spontaneous emission is resolved using a spectrograph. Infrared and visible spectral lines are detected *only* at the wavelengths  $4.05 \mu\text{m}$ ,  $1.87 \mu\text{m}$  and  $0.656 \mu\text{m}$ . Explain these observations and give the values of  $n$  and  $l$  for the configurations involved in these transitions.

Web site:

<http://www.physics.ox.ac.uk/users/foot>

This site has answers to some of the exercises, corrections and other supplementary information.

# Helium

# 3

Helium has only two electrons but this simplicity is deceptive. To treat systems with two particles requires new concepts that also apply to multi-particle systems in many branches of physics, and it is very worthwhile to study them carefully using the example of helium. There is truth in the saying that atomic physicists count ‘one, two, many’ and a detailed understanding of the two-electron system is sufficient for much of the atomic structure in this book.<sup>1</sup>

## 3.1 The ground state of helium

Two electrons in the Coulomb potential of a charge  $Ze$ , e.g. the nucleus of an atom, obey a Schrödinger equation of the form

$$\left\{ \frac{-\hbar^2}{2m} \nabla_1^2 + \frac{-\hbar^2}{2m} \nabla_2^2 + \frac{e^2}{4\pi\epsilon_0} \left( -\frac{Z}{r_1} - \frac{Z}{r_2} + \frac{1}{r_{12}} \right) \right\} \psi = E\psi. \quad (3.1)$$

Here  $r_{12} = |\mathbf{r}_1 - \mathbf{r}_2|$  is the distance between electron 1 and electron 2 and the electrostatic repulsion of electrons is proportional to  $1/r_{12}$ . Neglecting this mutual repulsion for the time being, we can write the equation as

$$(H_1 + H_2)\psi = E^{(0)}\psi, \quad (3.2)$$

where

$$H_1 \equiv \frac{-\hbar^2}{2m} \nabla_1^2 - \frac{Ze^2}{4\pi\epsilon_0 r_1} \quad (3.3)$$

and  $H_2$  is a similar expression for electron 2. Writing the atomic wavefunction as a product of the wavefunctions for each electron,  $\psi = \psi(1)\psi(2)$ , allows us to separate eqn 3.2 into two single-electron Schrödinger equations:

$$H_1\psi(1) = E_1\psi(1) \quad (3.4)$$

and a similar equation for  $\psi(2)$  with energy  $E_2$ . The solutions of these one-electron equations are hydrogenic wavefunctions with energies given by the Rydberg formula. Helium has  $Z = 2$  and in its ground state both electrons have energy  $E_1 = E_2 = -4hcR_\infty = -54.4\text{ eV}$ . Thus the total energy of the atom (neglecting repulsion) is

$$E^{(0)} = E_1 + E_2 = -109\text{ eV}. \quad (3.5)$$

|  |    |
|--|----|
| 3.1 The ground state of helium               | 45 |
| 3.2 Excited states of helium                 | 46 |
| 3.3 Evaluation of the integrals<br>in helium | 53 |
| Further reading                              | 56 |
| Exercises                                    | 58 |

<sup>1</sup>This book considers only those multi-electron systems with one, or two, valence electrons ‘outside’ a spherically-symmetric core of charge.

Now we need to calculate the perturbation produced by the electron-electron repulsion. The system has the spatial wavefunction

$$\psi_{1s^2} = R_{1s}^{Z=2}(r_1) R_{1s}^{Z=2}(r_2) \times \frac{1}{4\pi}, \quad (3.6)$$

<sup>2</sup> $1/\sqrt{4\pi}$  is the angular part of an s-electron wavefunction.

where radial wavefunctions are defined in Table 2.2.<sup>2</sup> The expectation value of the repulsion is (see Section 3.3)

$$\frac{e^2}{4\pi\epsilon_0} \int_0^\infty \int_0^\infty \psi_{1s^2}^* \frac{1}{r_{12}} \psi_{1s^2} r_1^2 dr_1 r_2^2 dr_2 = 34 \text{ eV}. \quad (3.7)$$

Adding this to the (zeroth-order) estimate  $E^{(0)}$  gives an energy of  $E(1s^2) = -109 + 34 = -75 \text{ eV}$ . It takes an energy of 75 eV to remove both electrons from a helium atom leaving a bare helium nucleus  $\text{He}^{++}$ —the second ionization energy. To go from  $\text{He}^+$  to  $\text{He}^{++}$  takes 54.4 eV, so this estimate suggests that the first ionization energy (required to remove one electron from He to create  $\text{He}^+$ ) is  $\text{IE}(\text{He}) \simeq 75 - 54 \simeq 21 \text{ eV}$ . But the expectation value in eqn 3.7 is not small compared to the binding energy and therefore the perturbation has a significant effect on the wavefunctions. The necessary adjustment of the wavefunctions can be accounted for by the variational method.<sup>3</sup> This method gives a value close to the measured ionization energy 24.6 eV. Helium has the highest first ionization energy of all elements because of its closed  $n = 1$  shell. For a plot of the ionization energies of the elements see Grant and Phillips (2001, Chapter 11, Fig. 18).<sup>4</sup>

<sup>3</sup>This is a standard quantum mechanical technique whose mathematical details are given in quantum texts. The essential principle of this technique is to find an expression for the energy in terms of a parameter—an effective atomic number in the case of helium—and then minimise the energy with respect to this parameter, i.e. study the variation in the energy as a function of the chosen parameter.

<sup>4</sup>This is accessible at <http://wwwoup.co.uk/best.textbooks/physics/ephys/illustrations/> along with other illustrations of elementary quantum ideas.

<sup>5</sup>It is often said that ‘one electron is in a spin-up state and the other is spin-down’; what this really means is defined in the discussion of spin for the excited states of helium.

According to the Pauli exclusion principle, two electrons cannot have the same set of quantum numbers. Therefore there must be some additional quantum number associated with the two 1s-electrons in the ground state of helium—this is their **spin** (introduced in Section 2.3.1). The observed filling-up of the atomic (sub-)shells in the periodic table implies that two spin states are associated with each set of spatial quantum numbers  $n, l, m_l$ .<sup>5</sup> However, electrostatic energies do not depend on spin and we can find the spatial wavefunctions separately from the problem of finding the spin eigenfunctions.

## 3.2 Excited states of helium

To find the energy of the excited states we use the same procedure as for the ground state—at first we neglect the mutual repulsion term and separate eqn 3.1 into two one-electron equations that have solutions<sup>6</sup>

$$u_{1s}(1) = R_{1s}(r_1) \times \frac{1}{\sqrt{4\pi}},$$

$$u_{nl}(2) = R_{nl}(r_2) Y_{l,m}(\theta_2, \phi_2)$$

for the configuration  $1snl$ . The spatial part of the atomic wavefunction is the product

$$\psi_{\text{space}} = u_{1s}(1)u_{nl}(2). \quad (3.8)$$

<sup>6</sup>The spatial wavefunction  $u$  contains both radial and angular parts but the energy does not depend on the magnetic quantum number, so we drop  $m$  as a subscript on  $u$ . The repulsion from a spherically-symmetric 1s wavefunction does not depend on the orientation of the other electron. To show this mathematically we could carry  $m$  through all the calculations and examine the resulting angular integrals, but this is cumbersome.

Another wavefunction has the same energy, namely

$$\psi_{\text{space}} = u_{1s}(2)u_{nl}(1). \quad (3.9)$$

These two states are related by a permutation of the labels on the electrons,  $1 \leftrightarrow 2$ ; the energy cannot depend on the labeling of identical particles so there is exchange degeneracy. To consider the effect of the repulsive term on this pair of wavefunctions with the same energy (degenerate states) we need degenerate perturbation theory. There are two approaches. The look-before-you-leap approach is first to form eigenstates of the perturbation from linear combinations of the initial states.<sup>7</sup> In this new basis the determination of the eigenenergies of the states is simple. It is instructive, however, simply to press ahead and go through the algebra once.<sup>8</sup>

We rewrite the Schrödinger equation (eqn 3.1) as

$$(H_0 + H') \psi = E\psi, \quad (3.10)$$

where  $H_0 = H_1 + H_2$ , and we consider the mutual repulsion of the electrons  $H' = e^2/4\pi\epsilon_0 r_{12}$  as a perturbation. We also rewrite eqn 3.2 as

$$H_0\psi = E^{(0)}\psi, \quad (3.11)$$

where  $E^{(0)} = E_1 + E_2$  is the unperturbed energy. Subtraction of eqn 3.11 from eqn 3.10 gives the energy change produced by the perturbation,  $\Delta E = E - E^{(0)}$ , as

$$H'\psi = \Delta E \psi. \quad (3.12)$$

A general expression for the wavefunction with energy  $E^{(0)}$  is a linear combination of expressions 3.8 and 3.9, with arbitrary constants  $a$  and  $b$ ,

$$\psi = a u_{1s}(1)u_{nl}(2) + b u_{1s}(2)u_{nl}(1). \quad (3.13)$$

Substitution into eqn 3.12, multiplication by either  $u_{1s}^*(1)u_{nl}^*(2)$  or  $u_{1s}^*(2)u_{nl}^*(1)$ , and then integration over the spatial coordinates for each electron ( $r_1, \theta_1, \phi_1$  and  $r_2, \theta_2, \phi_2$ ) gives two coupled equations that we write as

$$\begin{pmatrix} J & K \\ K & J \end{pmatrix} \begin{pmatrix} a \\ b \end{pmatrix} = \Delta E \begin{pmatrix} a \\ b \end{pmatrix}. \quad (3.14)$$

This is eqn 3.12 in matrix form. The direct integral is

$$\begin{aligned} J &= \frac{1}{4\pi\epsilon_0} \iint |u_{1s}(1)|^2 \frac{e^2}{r_{12}} |u_{nl}(2)|^2 d\mathbf{r}_1^3 d\mathbf{r}_2^3 \\ &= \frac{1}{4\pi\epsilon_0} \iint \frac{\rho_{1s}(r_1)\rho_{nl}(r_2)}{r_{12}} d\mathbf{r}_1^3 d\mathbf{r}_2^3, \end{aligned} \quad (3.15)$$

where  $\rho_{1s}(1) = -e|u_{1s}(1)|^2$  is the charge density distribution for electron 1, and similarly for  $\rho_{nl}(2)$ . This direct integral represents the Coulomb repulsion of these charge clouds (Fig. 3.1). The exchange integral is

$$K = \frac{1}{4\pi\epsilon_0} \iint u_{1s}^*(1)u_{nl}^*(2) \frac{e^2}{r_{12}} u_{1s}(2)u_{nl}(1) d\mathbf{r}_1^3 d\mathbf{r}_2^3. \quad (3.16)$$

<sup>7</sup>This is guided by looking for eigenstates of symmetry operators that commute with the Hamiltonian for the interaction, as in Section 4.5.

<sup>8</sup>In the light of this experience one can take the short cut in future.

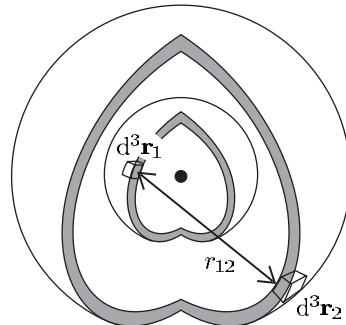


**Fig. 3.1** The direct integral in a 1sns configuration of helium corresponds to the Coulomb repulsion between two spherically-symmetric charge clouds made up of shells of charge like those shown.

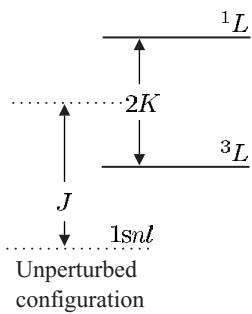


**Fig. 3.2** The effect of the direct and exchange integrals on a 1snl configuration in helium. The singlet and triplet terms have an energy separation of twice the exchange integral ( $2K$ ).

<sup>9</sup> It is easy to check which wavefunction corresponds to which eigenvalue by substitution into the original equation.

<sup>10</sup> Another example is the classical treatment of the normal Zeeman effect.

Unlike the direct integral, this does not have a simple classical interpretation in terms of charge (or probability) distributions—the exchange integral depends on interference of the amplitudes. The spherical symmetry of the 1s wavefunction makes the integrals straightforward to evaluate (Exercises 3.6 and 3.7).

The eigenvalues  $\Delta E$  in eqn 3.14 are found from

$$\begin{vmatrix} J - \Delta E & K \\ K & J - \Delta E \end{vmatrix} = 0. \quad (3.17)$$

The roots of this determinantal equation are  $\Delta E = J \pm K$ . The direct integral shifts both levels together but the exchange integral leads to an energy splitting of  $2K$  (see Fig. 3.2). Substitution back into eqn 3.14 gives the two eigenvectors in which  $b = a$  and  $b = -a$ . These correspond to symmetric (S) and antisymmetric (A) wavefunctions:

$$\begin{aligned} \psi_{\text{space}}^{\text{S}} &= \frac{1}{\sqrt{2}} \{ u_{1s}(1)u_{nl}(2) + u_{1s}(2)u_{nl}(1) \}, \\ \psi_{\text{space}}^{\text{A}} &= \frac{1}{\sqrt{2}} \{ u_{1s}(1)u_{nl}(2) - u_{1s}(2)u_{nl}(1) \}. \end{aligned}$$

The wavefunction  $\psi_{\text{space}}^{\text{A}}$  has an eigenenergy of  $E^{(0)} + J - K$ , and this is lower than the energy  $E^{(0)} + J + K$  for  $\psi_{\text{space}}^{\text{S}}$ . (For the 1snl configurations in helium  $K$  is positive.)<sup>9</sup> This is often interpreted as the electrons ‘avoiding’ each other, i.e.  $\psi_{\text{space}}^{\text{A}} = 0$  for  $r_1 = r_2$ , and for this wavefunction the probability of finding electron 1 close to electron 2 is small (see Exercise 3.3). This anticorrelation of the two electrons makes the expectation of the Coulomb repulsion between the electrons smaller than for  $\psi_{\text{space}}^{\text{S}}$ .

The occurrence of symmetric and antisymmetric wavefunctions has a classical analogue illustrated in Fig. 3.3. A system of two oscillators, with the same resonance frequency, that interact (e.g. they are joined together by a spring) has antisymmetric and symmetric normal modes as illustrated in Fig. 3.3(b) and (c). These modes and their frequencies are found in Appendix A as an example of the application of degenerate perturbation theory in *Newtonian mechanics*.<sup>10</sup>

The exchange integral decreases as  $n$  and  $l$  increase because of the reduced overlap between the wavefunctions of the excited electron and

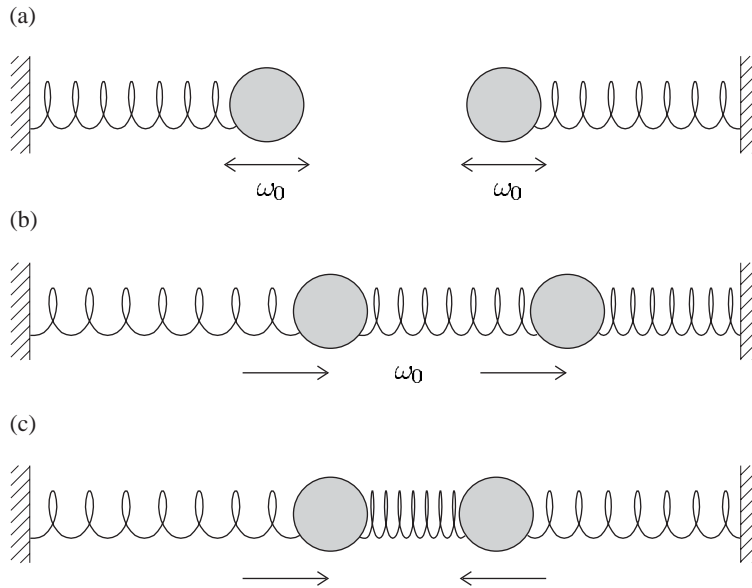


**Fig. 3.3** An illustration of degenerate perturbation in a classical system. (a) Two harmonic oscillators with the same oscillation frequency  $\omega_0$ —each spring has a mass on one end and its other end is attached to a rigid support. An interaction, represented here by another spring that connects the masses, couples the motions of the two masses. The normal modes of the system are (b) an in-phase oscillation at  $\omega_0$ , in which the spring between the masses does not change length, and (c) an out-of-phase oscillation at a higher frequency. Appendix A gives the equations for this system of two masses and three springs, and also for the equivalent system of three masses joined by two springs that models a triatomic molecule, e.g. carbon dioxide.

the 1s-electron. These trends are an obvious consequence of the form of the wavefunctions: the excited electron's average orbit radius increases with energy and hence with  $n$ ; the variation with  $l$  arises because the effective potential from the angular momentum ('centrifugal' barrier) leads to the wavefunction of the excited electron being small at small  $r$ . However, in the treatment as described above, the direct integral does not tend to zero as  $n$  and  $l$  increase, as shown by the following physical argument. The excited electron 'sees' the nuclear charge of  $+2e$  surrounded by the 1s electronic charge distribution, i.e. in the region far from the nucleus where  $nl$ -electron's wavefunction has a significant value it experiences a Coulomb potential of charge  $+1e$ . Thus the excited electron has an energy similar to that of an electron in the hydrogen atom, as shown in Fig. 3.4. But we have started with the assumption that both the 1s- and  $nl$ -electrons have an energy given by the Rydberg formula for  $Z = 2$ . The direct integral  $J$  equals the difference between these energies.<sup>11</sup> This work was an early triumph for wave mechanics since previously it had not been possible to calculate the structure of helium.<sup>12</sup>

In this section we found the wavefunctions and energy levels in helium by direct calculation but looking back we can see how to anticipate the answer by making use of symmetry arguments. The Hamiltonian for the electrostatic repulsion, proportional to  $1/r_{12} \equiv 1/|\mathbf{r}_1 - \mathbf{r}_2|$ , commutes with the operator that interchanges the particle labels 1 and 2, i.e. the swap operation  $1 \leftrightarrow 2$ . (Although we shall not give this operator a symbol it is obvious that it leaves the value of  $1/r_{12}$  unchanged.) Commuting operators have simultaneous eigenfunctions. This prompts us

<sup>11</sup>This can also be seen from eqn 3.15. The integration over  $r_1$ ,  $\theta_1$  and  $\phi_1$  leads to a repulsive Coulomb potential  $\sim e/4\pi\epsilon_0 r_2$  that cancels part of the attractive potential of the nucleus, when  $r_2$  is greater than the values of  $r_1$  where  $\psi_1$  is appreciable.

<sup>12</sup>For hydrogen, the solution of Schrödinger's equation reproduced the energy levels calculated by the Bohr-Sommerfeld theory. However, wave mechanics does give more information about hydrogen than the old quantum theory, e.g. it allows the detailed calculation of transition rates.

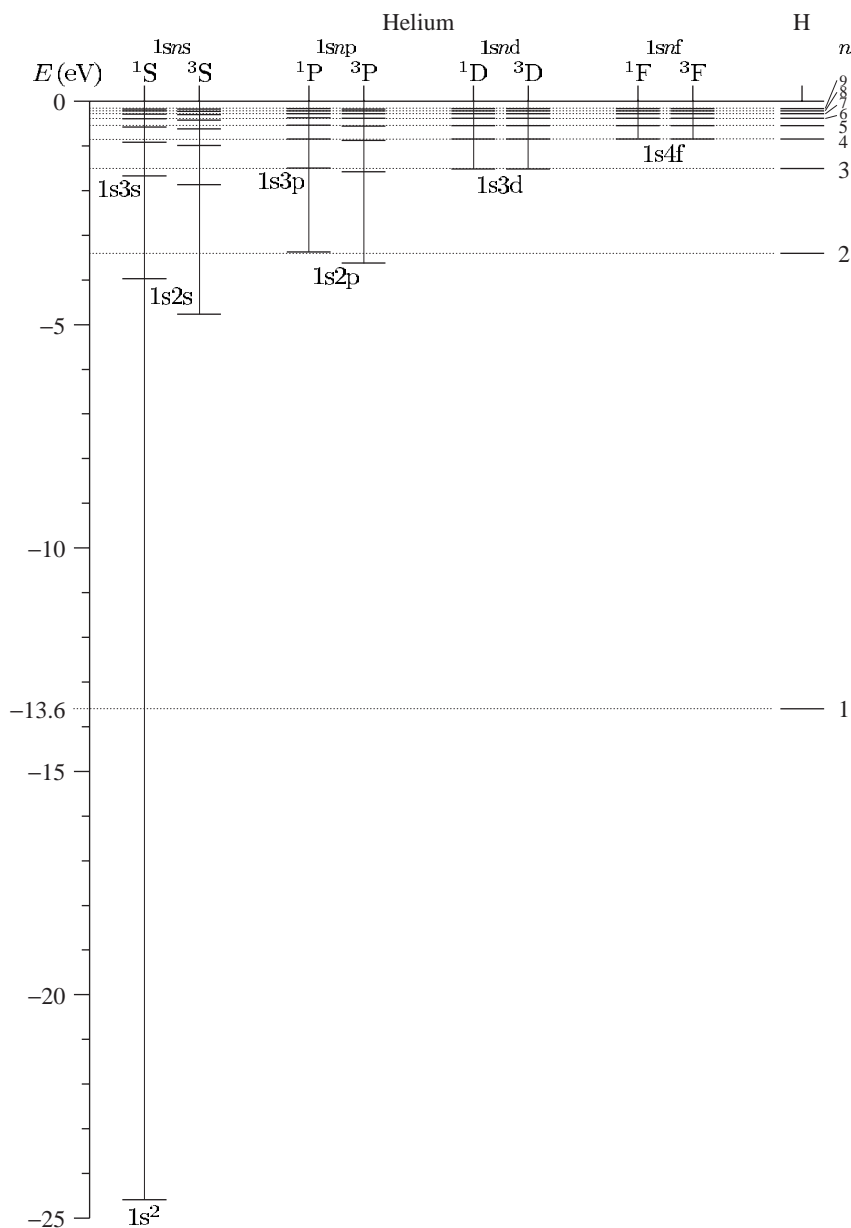


**Fig. 3.4** The energy levels of the helium atom with those of hydrogen for comparison. The  $1s^2$  ground configuration is tightly bound. For the excited configurations of helium the  $1s$ -electron screens the outer electron from the nuclear charge so that the  $1snl$  configurations in helium have similar energy to the shell with principal quantum number  $n$  in hydrogen. The hydrogenic levels are indicated on the right. The interval between the  $^1L$  and  $^3L$  terms (equal to twice the exchange integral) is clear for the  $1s2s$ ,  $1s2p$ ,  $1s3s$ ,  $1s3p$  and  $1s4s$  configurations but it is smaller for higher  $n$  and  $l$ .

to construct the symmetrised wavefunctions  $\psi_{\text{space}}^{\text{A}}$  and  $\psi_{\text{space}}^{\text{S}}$ .<sup>13</sup> In this basis of eigenstates it is simple to calculate the effect of the electrostatic repulsion.

### 3.2.1 Spin eigenstates

The electrostatic repulsion between the two electrons leads to the wavefunctions  $\psi_{\text{space}}^{\text{S}}$  and  $\psi_{\text{space}}^{\text{A}}$  in the excited states of the helium atom. The ground state is a special case where both electrons have the same spatial wavefunction, so only a symmetric solution exists. We did not consider spin since electrostatic interactions depend on the charge of the particle, not their spin. Neither  $H_0$  nor  $H'$  contains any reference to the spin of the electrons. Spin does, however, have a profound effect on atomic wavefunctions. This arises from the deep connection between spin and the *symmetry* of the wavefunction of indistinguishable particles.<sup>14</sup> Note that here we are considering the total wavefunction in the systems that includes both the spatial part (found in the previous section) and the spin. Fermions have wavefunctions that are antisymmetric with respect to particle-label interchange, and bosons have symmetric ones. As a consequence of this symmetry property, fermions and bosons fill up the levels of a system in different ways, i.e. they obey different quantum statistics.

Electrons are fermions so atoms have total wavefunctions that are antisymmetric with respect to permutation of the electron labels. This requires  $\psi_{\text{space}}^{\text{S}}$  to associate with an antisymmetric spin function  $\psi_{\text{spin}}^{\text{A}}$ , and the other way round:

$$\psi = \psi_{\text{space}}^{\text{S}} \psi_{\text{spin}}^{\text{A}} \quad \text{or} \quad \psi_{\text{space}}^{\text{A}} \psi_{\text{spin}}^{\text{S}}. \quad (3.18)$$

These **antisymmetrised** wavefunctions that we have constructed fulfil the requirement of having particular symmetry with respect to the interchange of indistinguishable particles. Now we shall find the spin eigenfunctions explicitly. We use the shorthand notation where  $\uparrow$  and  $\downarrow$  represent  $m_s = 1/2$  and  $-1/2$ , respectively. Two electrons have four possible combinations: the three symmetric functions,

$$\begin{aligned} \psi_{\text{spin}}^{\text{S}} &= |\uparrow\uparrow\rangle \\ &= \frac{1}{\sqrt{2}} \{ |\uparrow\downarrow\rangle + |\downarrow\uparrow\rangle \} \\ &= |\downarrow\downarrow\rangle, \end{aligned} \quad (3.19)$$

corresponding to  $S = 1$  and  $M_S = +1, 0, -1$ ; and an antisymmetric function

$$\psi_{\text{spin}}^{\text{A}} = \frac{1}{\sqrt{2}} \{ |\uparrow\downarrow\rangle - |\downarrow\uparrow\rangle \}, \quad (3.20)$$

corresponding to  $S = 0$  (with  $M_S = 0$ ).<sup>15</sup> Spectroscopists label the eigenstates of the electrostatic interactions with the symbol  ${}^{2S+1}L$ , where  $S$  is the total spin and  $L$  is the total orbital angular momentum quantum number. The  $1snl$  configurations in helium  $L = l$ , so the allowed terms

<sup>13</sup>For two electrons, swapping the particle labels twice brings us back to where we started, so  $\psi(1, 2) = \pm\psi(2, 1)$ . Therefore the two possible eigenvalues are 1 for  $\psi_{\text{space}}^{\text{S}}$  and  $-1$  for  $\psi_{\text{space}}^{\text{A}}$ .

<sup>14</sup>Indistinguishable means that the particles are identical and have the freedom to exchange positions, e.g. atoms in a gas which obey Fermi–Dirac or Bose–Einstein statistics depending on their spin. In contrast, atoms in a solid can be treated as distinguishable, even if they are identical, because they have fixed positions—we could label the atoms 1, 2, etc. and still know which is which at some later time.

<sup>15</sup>These statements about the result of adding two  $s = 1/2$  angular momenta can be proved by formal angular momentum theory. Simplified treatments describe  $S = 0$  as having one electron with ‘spin-up’ and the other with ‘spin-down’; but both  $M_S = 0$  states are linear combinations of the states  $|m_{s1} = +1/2, m_{s2} = -1/2\rangle$  and  $|m_{s1} = -1/2, m_{s2} = +1/2\rangle$ .

<sup>16</sup>The letter ‘S’ appears over-used in this established notation but no ambiguity arises in practice. The symbol  $S$  for the total spin is italic because this is a variable, whereas the symbols  $S$  for  $L = 0$  and  $s$  for  $l = 0$  are not italic.

are  $^1L$  and  $^3L$ , e.g. the  $1s2s$  configuration in helium gives rise to the terms  $^1S$  and  $^3S$ , where  $S$  represents  $L = 0$ .<sup>16</sup>

In summary, we have calculated the structure of helium in two distinct stages.

- (1) **Energies** Degenerate perturbation theory gives the space wavefunctions  $\psi_{\text{space}}^S$  and  $\psi_{\text{space}}^A$  with energies split by twice the exchange integral. In helium the degeneracy arises because the two electrons are identical particles so there is exchange degeneracy, but the treatment is similar for systems where a degeneracy arises by accident.
- (2) **Spin** We determined the spin associated with each energy level by constructing symmetrised wavefunctions. The product of the spatial functions and the spin eigenstates gives the total atomic wavefunction that must be antisymmetric with respect to particle-label interchange.

Exchange degeneracy, exchange integrals, degenerate perturbation theory and symmetrised wavefunctions all occur in helium and their interrelationship is not straightforward so that misconceptions abound. A common misinterpretation is to infer that because levels with different total spin,  $S = 0$  and  $1$ , have different energies then there is a spin-dependent interaction—this is *not* correct, but sometimes in condensed matter physics it is useful to pretend that it is! (See Blundell 2001.) The interactions that determine the gross structure of helium are entirely *electrostatic* and depend only on the charge and position of the particles. Also, degenerate perturbation theory is sometimes regarded as a mysterious quantum phenomenon. Appendix A gives further discussion and shows that symmetric and antisymmetric normal modes occur when two classical systems, with similar energy, interact, e.g. two coupled oscillators.

### 3.2.2 Transitions in helium

To determine which transitions are allowed between the energy levels of helium we need a selection rule for spin: the total spin quantum number does not change in electric dipole transitions. In the matrix element  $\langle \psi_{\text{final}} | r | \psi_{\text{initial}} \rangle$  the operator  $r$  does not act on spin; therefore, if the  $\psi_{\text{final}}$  and  $\psi_{\text{initial}}$  do not have the same value of  $S$ , then their spin functions are orthogonal and the matrix element equals zero.<sup>17</sup> This selection rule gives the transitions shown in Fig. 3.5.

<sup>17</sup>This anticipates a more general discussion of this and other selection rules for the  $LS$ -coupling scheme in a later chapter.

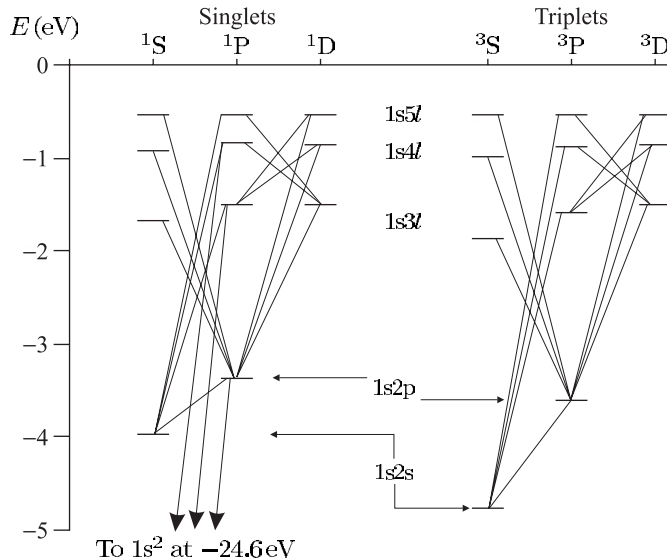


**Fig. 3.5** The allowed transitions between the terms of helium are governed by the selection rule  $\Delta S = 0$  in addition to the rule  $\Delta l = \pm 1$  found previously. Since there are no transitions between singlets and triplets it is convenient to draw them as two separate systems. Notice that in the radiative decay of helium atoms excited to high-lying levels there are bottlenecks in the metastable  $1s2s\ ^1S$  and  $1s2s\ ^3S$  terms.

### 3.3 Evaluation of the integrals in helium

In this section we shall calculate the direct and exchange integrals to make quantitative predictions for some of the energy levels in the helium atom, based on the theory described in the previous sections. This provides an example of the use of atomic wavefunctions to carry out a calculation where there are no corresponding classical orbits and gives an indication of the complexities that arise in systems with more than one electron. The evaluation of the integrals requires care and some further details are given in Appendix B. The important point to be learnt from this section, however, is not the mathematical techniques but rather to see that the integrals arise from the Coulomb interaction between electrons treated by straightforward quantum mechanics.

#### 3.3.1 Ground state

To calculate the energy of the  $1s^2$  configuration we need to find the expectation value of  $e^2/4\pi\epsilon_0 r_{12}$  in eqn 3.1—this calculation is the same as the evaluation of the mutual repulsion between two charge distributions in classical electrostatics, as in eqn 3.15 with  $\rho_{1s}(r_1)$  and  $\rho_{nl}(r_2) = \rho_{1s}(r_2)$ . The integral can be considered in different ways. We could calculate the energy of the charge distribution of electron 1 in the potential created by electron 2, or the other way around. This section does neither; it uses a method that treats each electron symmetrically (as in Appendix B), but of course each approach gives the same numerical result. Electron 1 produces an electrostatic potential at radial distance  $r_2$  given by

$$V_{12}(r_2) = \int_0^{r_2} \frac{1}{4\pi\epsilon_0 r_{12}} \rho(r_1) d^3\mathbf{r}_1. \quad (3.21)$$

The spherical symmetry of s-electrons means that the charge in the region  $r_1 < r_2$  acts like a point charge at the origin, so that

$$V_{12}(r_2) = \frac{Q(r_2)}{4\pi\epsilon_0 r_2},$$

where  $Q(r_2)$  is the charge within a radius of  $r_2$  from the origin, which is given by<sup>18</sup>

$$Q(r_2) = \int_0^{r_2} \rho(r_1) 4\pi r_1^2 dr_1. \quad (3.22)$$

The electrostatic energy that arises from the repulsion equals

$$E_{12} = \int_0^\infty V_{12}(r_2) \rho(r_2) 4\pi r_2^2 dr_2. \quad (3.23)$$

For the  $1s^2$  configuration there is an exactly equal contribution to the energy from  $V_{21}(r_1)$ , the (partial) potential at  $r_1$  produced by electron 2. Thus the total energy of the repulsion between the electrons is twice that in eqn 3.23.<sup>19</sup> Using the radial wavefunction for a  $1s$ -electron, we find

$$\begin{aligned} J_{1s^2} &= 2 \times \frac{e^2}{4\pi\epsilon_0} \int_0^\infty \left\{ \int_0^{r_2} \frac{1}{r_1} 4Z^3 e^{-(Z/a_0)2r_1} r_1^2 dr_1 \right\} 4Z^3 e^{-(Z/a_0)2r_2} r_2^2 dr_2 \\ &= \frac{e^2/4\pi\epsilon_0}{2a_0} \frac{5}{4} Z = (13.6 \text{ eV}) \times \frac{5}{4} Z. \end{aligned} \quad (3.24)$$

For helium this gives  $J_{1s^2}^{Z=2} = 34 \text{ eV}$ .

### 3.3.2 Excited states: the direct integral

A  $1snl$  configuration of helium has an energy close to that of an  $nl$ -electron in hydrogen, e.g. in the  $1s2p$  configuration the  $2p$ -electron has a similar binding energy to the  $n = 2$  shell of hydrogen. The obvious explanation, in Bohr's model, is that the  $2p$ -electron lies outside the  $1s$ -orbit so that the inner electron screens the outer one from the full nuclear charge. Applying an analogous argument to the quantum treatment of helium leads to the Hamiltonian  $H = H_{0a} + H'_a$ , where<sup>20</sup>

$$H_{0a} = -\frac{\hbar^2}{2m} (\nabla_1^2 + \nabla_2^2) - \frac{e^2}{4\pi\epsilon_0} \left( \frac{2}{r_1} + \frac{1}{r_2} \right) \quad (3.25)$$

and

$$H'_a = \frac{e^2}{4\pi\epsilon_0} \left( \frac{1}{r_{12}} - \frac{1}{r_2} \right). \quad (3.26)$$

<sup>20</sup>The effect of the repulsion proportional to  $1/r_{12}$  can be considered in terms of potentials like that in eqn 3.21 (and Appendix B). The potential at the position of the outer electron  $r_2$  arising from the charge distribution of electron 1 accounts for a large portion of the total repulsion:  $V_{12}(r_2) \simeq e^2/4\pi\epsilon_0 r_2$  in the region where  $\rho_{nl}(r_2)$  has an appreciable value. Hence it makes sense to include  $e^2/4\pi\epsilon_0 r_2$  in the zeroth-order Hamiltonian  $H_{0a}$  and treat the (small) part left over as a perturbation  $H'_a$ .

In the expression for  $H_{0a}$ , electron 2 experiences the Coulomb attraction of a charge  $+1e$ . In  $H'_a$  the subtraction of  $e^2/4\pi\epsilon_0 r_2$  from the mutual repulsion means that the perturbation tends to zero at a large distance from the nucleus (which is intuitively reasonable). This decomposition differs from that in Section 3.1. The different treatment of the two electrons makes the perturbation theory a little tricky, but Heisenberg

did the calculation as described in Bethe and Salpeter (1957) or Bethe and Salpeter (1977); he found the direct integral

$$J_{1snl} = \frac{e^2}{4\pi\epsilon_0} \iint \left( \frac{1}{r_{12}} - \frac{1}{r_2} \right) |u_{1s}(1)|^2 |u_{nlm}(2)|^2 d^3\mathbf{r}_1 d^3\mathbf{r}_2. \quad (3.27)$$

This must be evaluated with the appropriate wavefunctions, i.e.  $u_{nlm}^{Z=1}$  rather than  $u_{nlm}^{Z=2}$ , and  $u_{1s}^{Z=2}$  as before.<sup>21</sup> For the excited electron  $u_{nlm} = R_{nl}(r)Y_{lm}(\theta, \phi)$ , where  $R_{nl}(r)$  is the radial function for  $Z = 1$ . We write the direct integral as

$$J_{1snl} = \frac{e^2}{4\pi\epsilon_0} \int_0^\infty \int_0^\infty J(r_1, r_2) R_{10}^2(r_1) R_{nl}^2(r_2) r_1^2 dr_1 r_2^2 dr_2, \quad (3.28)$$

where the angular parts are contained in the function<sup>22</sup>

$$\begin{aligned} J(r_1, r_2) &= \int_0^{2\pi} \int_0^\pi \int_0^{2\pi} \int_0^\pi \left( \frac{1}{r_{12}} - \frac{1}{r_2} \right) \frac{1}{4\pi} |Y_{lm}(\theta_2, \phi_2)|^2 \\ &\quad \times \sin \theta_1 d\theta_1 d\phi_1 d\phi_2 \sin \theta_2 d\theta_2 d\phi_2. \end{aligned} \quad (3.29)$$

The calculation of this integral requires the expansion of  $1/r_{12}$  in terms of spherical harmonics:<sup>23</sup>

$$\frac{1}{r_{12}} = \frac{1}{r_2} \sum_{k=0}^{\infty} \left( \frac{r_1}{r_2} \right)^k \frac{4\pi}{2k+1} \sum_{q=-k}^k Y_{k,q}^*(\theta_1, \phi_1) Y_{k,q}(\theta_2, \phi_2) \quad (3.30)$$

for  $r_2 > r_1$  (and  $r_1 \leftrightarrow r_2$  when  $r_1 > r_2$ ). Only the term for  $k = 0$  survives in the integration over angles in eqn 3.29 to give<sup>24</sup>

$$J(r_1, r_2) = \begin{cases} 0 & \text{for } r_1 < r_2, \\ 1/r_1 - 1/r_2 & \text{for } r_1 > r_2. \end{cases}$$

When  $r_1 < r_2$  the original screening argument applies and eqn 3.25 gives a good description. When  $r_1 > r_2$  the appropriate potential is proportional to  $-2/r_2 - 1/r_1$  and  $J(r_1, r_2)$  accounts for the difference between this and  $-2/r_1 - 1/r_2$  used in  $H_{0a}$ . Thus we find

$$J_{1snl} = \frac{e^2}{4\pi\epsilon_0} \int_0^\infty \left\{ \int_{r_2}^\infty \left( \frac{1}{r_1} - \frac{1}{r_2} \right) R_{10}^2(r_1) r_1^2 dr_1 \right\} R_{nl}^2(r_2) r_2^2 dr_2. \quad (3.31)$$

Evaluation of this integral for the 1s2p configuration (in Exercise 3.6) gives  $J_{1s2p} = -2.8 \times 10^{-2}$  eV—three orders of magnitude smaller than  $J_{1s^2}^{Z=2}$  in eqn 3.7 (evaluated from eqn 3.24). The unperturbed wavefunction for  $Z = 1$  has energy equal to that of the corresponding level in hydrogen and the small negative direct integral accounts for the incompleteness of the screening of the  $nl$ -electron by the inner electron.

### 3.3.3 Excited states: the exchange integral

The exchange integral has the same form as eqn 3.16 but with  $u_{nlm}^{Z=1}$  rather than  $u_{nlm}^{Z=2}$  (and  $u_{1s}^{Z=2}$  as before). Within the spatial wavefunction

<sup>21</sup>We have not derived this integral rigorously but it has an intuitively reasonable form.

<sup>22</sup> $Y_{00}(\theta_1, \phi_1) = 1/\sqrt{4\pi}$ .

<sup>23</sup> $Y_{k,q}^*(\theta_1, \phi_1) = (-1)^q Y_{k,-q}(\theta_1, \phi_1)$ .

<sup>24</sup>When  $k \neq 0$  the integral of the function  $Y_{k,q}^*(\theta_1, \phi_1)$  over  $\theta_1$  and  $\phi_1$  equals zero.

$u_{nlm} = R_{nl}(r)Y_{lm}(\theta, \phi)$  only the radial part depends on  $Z$ . We write the exchange integral as (cf. eqn 3.28)

$$K_{1snl} = \frac{e^2}{4\pi\epsilon_0} \iint K(r_1, r_2) R_{1s}(r_1) R_{nl}(r_1) R_{1s}(r_2) R_{nl}(r_2) r_1^2 dr_1 r_2^2 dr_2. \quad (3.32)$$

The function  $K(r_1, r_2)$  containing the angular integrals is (cf. eqn 3.29)

$$\begin{aligned} K(r_1, r_2) = & \iiint \frac{1}{r_{12}} Y_{lm}^*(\theta_1, \phi_1) \frac{1}{4\pi} Y_{lm}(\theta_2, \phi_2) \\ & \times \sin \theta_1 d\theta_1 d\phi_1 \sin \theta_2 d\theta_2 d\phi_2. \end{aligned} \quad (3.33)$$

For the  $1snp$  configuration only the second term of the expansion in eqn 3.30, with  $k = 1$ , survives in the integration because of the orthogonality of the spherical harmonic functions (see Exercise 3.7), to give

$$K(r_1, r_2) = \begin{cases} r_1/3r_2^2 & \text{for } r_1 < r_2, \\ r_2/3r_1^2 & \text{for } r_2 < r_1. \end{cases} \quad (3.34)$$

Carrying out the integration over the radial wavefunctions in eqn 3.32 for the  $1s2p$  configuration gives the splitting between  ${}^3P$  and  ${}^1P$  as  $2K_{1s2p} \simeq 0.21$  eV (close to the measured value of 0.25 eV).

The assumption that the excited electron lies outside the  $1s$  wavefunction does not work so well for  $1sns$  configurations since  $\psi_{ns}(0)$  has a finite value and the above method of calculating  $J$  and  $K$  is less accurate.<sup>25</sup> The  $1s2s$  configuration of helium has a singlet–triplet separation of  $E({}^1S) - E({}^3S) = 2K_{1s2s} \simeq 0.80$  eV and the direct integral is also larger than that for  $1s2p$ —these trends are evident in Fig. 3.4 (see also Exercise 3.7).<sup>26</sup>

In some respects, helium is a more typical atom than hydrogen. The Schrödinger and Dirac equations can be solved exactly for the one-electron system, but not for helium or other atoms with more electrons. Thus in a careful study of helium we encounter the approximations needed to treat multi-electron atoms, and this is very important for understanding atomic structure in general. Helium also gives a good example of the influence of identical particles on the occupation of the states in quantum systems. The energy levels of the helium atom (and the existence of exchange integrals) do not depend on the fact that the two electrons are identical, as demonstrated in Exercises 3.3 and 3.4; however, this is a common point of confusion. The books recommended for further reading give clear and accurate descriptions of helium that reward careful study.

## Further reading

The recommended books are divided into two categories corresponding to the two main themes in this chapter: (a) a description of how to calculate the electrostatic energy in an atom with more than one electron, which introduces principles that can be used in atoms with more

<sup>25</sup>At small  $r$  the wavefunction of an  $ns$ -electron deviates significantly from  $u_{ns}^{Z=1}$ ; for this reason  $1s2p$  was chosen as an example above.

<sup>26</sup>The overlap of the  $1s$  and  $nl$  wavefunctions becomes smaller as  $n$  and  $l$  increase. In Heisenberg's treatment where screening is taken into account, the direct integral gives the deviation from the hydrogenic levels (which could be characterised by a quantum defect as in the alkalis, see Chapter 4). For electrons with  $l \neq 0$  the term  $\hbar^2 l(l+1)/2mr^2$  in the Schrödinger equation causes the electron's wavefunction to lie almost entirely outside the region where  $u_{1s}^{Z=2} = R_{1s}(r)/\sqrt{4\pi}$  has a significant value.

electrons; and (b) a discussion of the influence of identical particles on the statistics of a quantum system that is important throughout physics. The influence of identical particles on the occupation of the quantum levels of a system with many particles, i.e. Bose–Einstein and Fermi–Dirac statistics, is discussed in statistical mechanics texts. Clear descriptions of helium may be found in the following textbooks: Cohen-Tannoudji *et al.* (1977), Woodgate (1980) and Mandl (1992). The calculation of the direct and exchange integrals in Section 3.3 is based on the definitive work by Bethe and Salpeter (1957), or see Bethe and Jackiw (1986).

A very instructive comparison can be made between the properties of the two electrons in helium and the nuclear spin statistics of homonuclear diatomic molecules<sup>27</sup> described in Atkins (1983, 1994).<sup>28</sup> There are diatomic molecules with nuclei that are identical bosons, identical fermions and cases of two similar but not identical particles, and their study gives a wider perspective than the study of helium alone. The nuclei of the two atoms in a hydrogen molecule are protons which are fermions (like the two electrons in helium).<sup>29</sup> For reasons explained in the above references, we can consider only those parts of the molecular wavefunction that describe the rotation  $\psi_{\text{rot}}$  and the nuclear spin states  $\psi_I$ —these are spatial and spin wavefunctions, respectively. For  $\text{H}_2$  the wavefunction must have overall antisymmetry with respect to an interchange of particle labels since the nuclei are protons, each with a spin of  $1/2$ . This requires that a rotational must pair with a spin function of the opposite symmetry:

$$\psi_{\text{molecule}} = \psi_{\text{rot}}^S \psi_I^A \quad \text{or} \quad \psi_{\text{rot}}^A \psi_I^S. \quad (3.35)$$

This is analogous to eqn 3.18 for helium; as described in Section 3.2.1, the two spin- $1/2$  nuclei in a hydrogen molecule give a total (nuclear) spin of 0 and 1, with one state and three states, respectively. The 1 to 3 ratio of the number of nuclear spins associated with the energy levels for  $\psi_{\text{rot}}^S$  and  $\psi_{\text{rot}}^A$ , respectively, influences the populations of these rotational energy levels in a way that is directly observed in molecular spectra (the intensity of the lines in spectra depends on the population of the initial level). The molecule HD made from hydrogen and deuterium does not have identical nuclei so there is no overall symmetry requirement, but it has similar energy levels to those of  $\text{H}_2$  apart from the mass dependence. This gives a real physical example where the statistics depends on whether the particles are identical or not, but the energy of the system does not. Exercise 3.4 discusses an artificial example: a helium-like system that has the same energy levels as a helium atom and hence the same direct and *exchange* integrals, even though the constituent particles are not identical.

<sup>27</sup>Molecules made up of two atoms with identical nuclei.

<sup>28</sup>These books also summarise the helium atom and the quantum mechanics of these molecular systems is very closely related to atomic physics.

<sup>29</sup>The wavefunction of the hydrogen molecule has exchange symmetry—crudely speaking, the molecule looks the same when rotated through  $180^\circ$ .

## Exercises

More advanced problems are indicated by a \*.

(3.1) *Estimate of the binding energy of helium*

- (a) Write down the Schrödinger equation for the helium atom and state the physical significance of each of the terms.
- (b) Estimate the equilibrium energy of an electron bound to a charge  $+Ze$  by minimising

$$E(r) = \frac{\hbar^2}{2mr^2} - \frac{Ze^2}{4\pi\epsilon_0 r}.$$

- (c) Calculate the repulsive energy between the two electrons in helium assuming that  $r_{12} \sim r$ . Hence estimate the ionization energy of helium.
- (d) Estimate the energy required to remove a further electron from the helium-like ion  $\text{Si}^{12+}$ , taking into account the scaling with  $Z$  of the energy levels and the expectation value for the electrostatic repulsion. The experimental value is 2400 eV. Compare the accuracy of your estimates for  $\text{Si}^{12+}$  and helium. ( $\text{IE}(\text{He}) = 24.6 \text{ eV}$ )

(3.2) *Direct and exchange integrals for an arbitrary system*

- (a) Verify that for

$$\begin{aligned}\psi^A(r_1, r_2) \\ = \frac{1}{\sqrt{2}} \{ u_\alpha(r_1)u_\beta(r_2) - u_\alpha(r_2)u_\beta(r_1) \}\end{aligned}$$

and  $H' = e^2/4\pi\epsilon_0 r_{12}$  the expectation value  $\langle \psi^A | H' | \psi^A \rangle$  has the form  $J - K$  and give the expressions for  $J$  and  $K$ .

- (b) Write down the wavefunction  $\psi^S$  that is orthogonal to  $\psi^A$ .
- (c) Verify that  $\langle \psi^A | H' | \psi^S \rangle = 0$  so that  $H'$  is diagonal in this basis.

(3.3) *Exchange integrals for a delta-function interaction*  
A particle in a square-well potential, with  $V(x) = 0$  for  $0 < x < \ell$  and  $V(x) = \infty$  elsewhere, has normalised eigenfunctions  $u_0(x) = \sqrt{2/\ell} \sin(\pi x/\ell)$  and  $u_1(x) = \sqrt{2/\ell} \sin(2\pi x/\ell)$ .

- (a) What are the eigenenergies  $E_0$  and  $E_1$  of these two wavefunctions for a particle of mass  $m$ ?

- (b) Two particles of the same mass  $m$  are both in the ground state so that the energy of the whole system is  $2E_0$ . Calculate the perturbation produced by a point-like interaction described by the potential  $a\delta(x_1 - x_2)$ , with  $a$  constant.
- (c) Show that, when the two interacting particles occupy the ground and first excited states, the direct and exchange integrals are equal. Also show that the delta-function interaction produces no energy shift for the antisymmetric spatial wavefunction and explain this in terms of correlation of the particles. Calculate the energy of the other level of the perturbed system.
- (d) For the two energy levels found in part (c), sketch the spatial wavefunction as a function of the coordinates of the two particles  $x_1$  and  $x_2$ . The particles move in one dimension but the two-particle wavefunction exists in a two-dimensional Hilbert space—draw either a contour plot in the  $x_1x_2$ -plane or attempt a three-dimensional sketch (by hand or computer).
- (e) The two particles are identical and have spin  $1/2$ . What is the total spin quantum number  $S$  associated with each of the energy levels found in part (c)?
- (f) Discuss qualitatively the energy levels of this system for two particles that have slightly different masses  $m_1 \neq m_2$ , so that they are distinguishable? [Hint. The spin has not been given because it is not important for non-identical particles.]

*Comment.* The antisymmetric spatial wavefunction in part (c) clearly has different properties from a straightforward product  $u_0u_1$ . The exchange integral is a manifestation of the entanglement of the multiple-particle system.

- (3.4) *A helium-like system with non-identical particles*  
Imagine that there exists an exotic particle with the same mass and charge as the electron but spin  $3/2$  (so it is not identical to the electron). This particle and an electron form a bound system with a helium nucleus. Compare the energy levels of this system with those of the helium atom. Describe the energy levels of a system with two of the ex-

otic particles bound to a helium nucleus (and no electrons). [Hint. It is not necessary to specify the values of total spin associated with the levels.]

(3.5) *The integrals in helium*

- (a) Show that the integral in eqn 3.24 gives the value stated in eqn 3.7.
- (b) Estimate the ground-state energy of helium using the variational principle. (The details of this technique are not given in this book; see the section on further reading.)

(3.6) *Calculation of integrals for the 1s2p configuration*

- (a) Draw a scale diagram of  $R_{1s}^{Z=2}(r)$ ,  $R_{2s}^{Z=1}(r)$  and  $R_{2p}^{Z=1}(r)$ . (See Table 2.2.)
- (b) Calculate the direct integral in eqn 3.31 and show that it gives

$$J_{1s2p} = -\frac{e^2/4\pi\epsilon_0}{2a_0} \frac{13}{2 \times 5^5}.$$

Give the numerical value in eV (cf. that given in the text).

(3.7) *Expansion of  $1/r_{12}$*

For  $r_1 < r_2$  the binomial expansion of

$$\frac{1}{r_{12}} = (r_1^2 + r_2^2 - 2r_1r_2 \cos \theta_{12})^{-1/2}$$

Web site:

<http://www.physics.ox.ac.uk/users/foot>

This site has answers to some of the exercises, corrections and other supplementary information.

is

$$\begin{aligned} \frac{1}{r_{12}} &= \frac{1}{r_2} \left\{ 1 - 2\frac{r_1}{r_2} \cos \theta_{12} + \left(\frac{r_1}{r_2}\right)^2 \right\}^{-1/2} \\ &\simeq \frac{1}{r_2} \left\{ 1 + \frac{r_1}{r_2} \cos \theta_{12} + \dots \right\}. \end{aligned} \quad (3.36)$$

(When  $r_1 > r_2$  we must interchange  $r_1$  and  $r_2$  to obtain convergence.) The cosine of the angle between  $\mathbf{r}_1$  and  $\mathbf{r}_2$  is

$$\begin{aligned} \cos \theta_{12} &= \hat{\mathbf{r}}_1 \cdot \hat{\mathbf{r}}_2 \\ &= \cos \theta_1 \cos \theta_2 + \sin \theta_1 \sin \theta_2 \cos (\phi_1 - \phi_2). \end{aligned}$$

- (a) Show that the first two terms in the binomial expansion agree with the terms with  $k = 0$  and 1 in eqn 3.30.
- (b) The repulsion between a 1s- and an  $nl$ -electron is independent of  $m$ . Explain why, physically or mathematically.
- (c) Show that eqn 3.32 leads to eqn 3.34 for  $l = 1$ .
- (d) For a  $1snl$  configuration, the quantity  $K(r_1, r_2)$  in eqn 3.34 is proportional to  $r_1^l/r_2^{l+1}$  when  $r_1 < r_2$ . Explain this in terms of mathematical properties of the  $Y_{l,m}$  functions.

# 4

# The alkalis

|   |    |
|---|----|
| 4.1 Shell structure and the periodic table                    | 60 |
| 4.2 The quantum defect  | 61 |
| 4.3 The central-field approximation                           | 64 |
| 4.4 Numerical solution of the Schrödinger equation            | 68 |
| 4.5 The spin-orbit interaction: a quantum mechanical approach | 71 |
| 4.6 Fine structure in the alkalis                             | 73 |
| Further reading   | 75 |
| Exercises   | 76 |

<sup>1</sup> Also referred to by its original German name as the *Aufbau* principle. An extensive discussion of the atomic structure that underlies the periodic table can be found in chemistry texts such as Atkins (1994).

<sup>2</sup> Most of the arrangement of elements in a periodic table was determined by chemists, such as Mendeleev, in the nineteenth century. A few inconsistencies in the ordering were resolved by Moseley's measurements of X-ray spectra (see Chapter 1).

<sup>3</sup> The configuration of an atom is specified by a list of  $nl$  with the occupancy as an exponent. Generally, we do not need to list the full configuration and it is sufficient to say that a sodium atom in its ground state has the configuration 3s. A sodium 'atom' with one electron in the 3s level, and no others, is an excited state of the highly-charged ion  $\text{Na}^{+10}$ —this esoteric system can be produced in the laboratory but confusion with the common sodium atom is unlikely.

## 4.1 Shell structure and the periodic table

For multi-electron atoms we cannot solve the Hamiltonian analytically, but by making appropriate approximations we can explain their structure in a physically meaningful way. To do this, we start by considering the elementary ideas of atomic structure underlying the periodic table of the elements. In the ground states of atoms the electrons have the configuration that minimises the energy of the whole system. The electrons do not all fall down into the lowest orbital with  $n = 1$  (the K-shell) because the Pauli exclusion principle restricts the number of electrons in a given (sub-)shell—two electrons cannot have the same set of quantum numbers. This leads to the 'building-up' principle: electrons fill up higher and higher shells as the atomic number  $Z$  increases across the periodic table.<sup>1</sup> Full shells are found at atomic numbers  $Z = 2, 10, \dots$  corresponding to helium and the other inert gases. These inert gases, in a column on the right-hand side of the periodic table (see inside front cover), were originally grouped together because of their similar chemical properties, i.e. the difficulty in removing an electron from closed shells means that they do not readily undergo chemical reactions.<sup>2</sup> However, inert gas atoms can be excited to higher-lying configurations by bombardment with electrons in a gas discharge, and such processes are very important in atomic and laser physics, as in the helium-neon laser.

The ground states of the alkalis have the following electronic configurations:<sup>3</sup>

|           |    |           |           |
|-----------|----|-----------|-----------|
| lithium   | Li | $1s^2$    | $2s$ ,    |
| sodium    | Na | $1s^2$    | $2s^2$    |
|           |    | $2p^6$    | $3s$ ,    |
| potassium | K  | $1s^2$    | $2s^2$    |
|           |    | $2p^6$    | $3s^2$    |
|           |    | $3p^6$    | $4s$ ,    |
| rubidium  | Rb | $1s^2$    | $2s^2$    |
|           |    | $2p^6$    | $3s^2$    |
|           |    | $3p^6$    | $3d^{10}$ |
|           |    | $4s^2$    | $4p^6$    |
| caesium   | Cs | $1s^2$    | $2s^2$    |
|           |    | $2p^6$    | $3s^2$    |
|           |    | $3p^6$    | $3d^{10}$ |
|           |    | $4s^2$    | $4p^6$    |
|           |    | $4d^{10}$ | $5s^2$    |
|           |    | $5p^6$    | $6s$ .    |

The alert reader will notice that the sub-shells of the heavier alkalis are not filled in the same order as the hydrogenic energy levels, e.g. electrons occupy the 4s level in potassium before the 3d level (for reasons that emerge later in this chapter). Thus, strictly speaking, we should say that the inert gases have full sub-shells, e.g. argon has the electronic

**Table 4.1** Ionization energies of the inert gases and alkalis.

| Element | Z  | IE (eV) |
|---------|----|---------|
| He      | 2  | 24.6    |
| Li      | 3  | 5.4     |
| Ne      | 10 | 21.6    |
| Na      | 11 | 5.1     |
| Ar      | 18 | 15.8    |
| K       | 19 | 4.3     |
| Kr      | 36 | 14.0    |
| Rb      | 37 | 4.2     |
| Xe      | 54 | 12.1    |
| Cs      | 55 | 3.9     |

configuration  $1s^2 2s^2 2p^6 3s^2 3p^6$  with the 3d sub-shell unoccupied.<sup>4</sup>

Each alkali metal comes next to an inert gas in the periodic table and much of the chemistry of the alkalis can be explained by the simple picture of their atoms as having a single unpaired electron outside a core of closed electronic sub-shells surrounding the nucleus. The unpaired valence electron determines the chemical bonding properties; since it takes less energy to remove this outer electron than to pull an electron out of a closed sub-shell (see Table 4.1), thus the alkalis can form singly-charged positive ions and are chemically reactive.<sup>5</sup> However, we need more than this simple picture to explain the details of the spectra of the alkalis and in the following we shall consider the wavefunctions.

## 4.2 The quantum defect

The energy of an electron in the potential proportional to  $1/r$  depends only on its principal quantum number  $n$ , e.g. in hydrogen the 3s, 3p and 3d configurations all have the same gross energy. These three levels are not degenerate in sodium, or any atom with more than one electron, and this section explains why. Figure 4.1 shows the probability density of 3s-, 3p- and 3d-electrons in sodium. The wavefunctions in sodium have a similar shape (number of nodes) to those in hydrogen. The 3d wavefunction has a single lobe outside the core so that it experiences almost the same potential as in a hydrogen atom; therefore this electron, and other d configurations in sodium with  $n > 3$ , have binding energies similar to those in hydrogen, as shown in Fig. 4.2. In contrast, the wavefunctions for the s-electrons have a significant value at small  $r$ —they penetrate inside the core and ‘see’ more of the nuclear charge. Thus the screening of the nuclear charge by the other electrons in the atom is less effective for ns configurations than for nd, and s-electrons have lower energy than d-electrons with the same principal quantum number. (The np-electrons lie between these two.<sup>6</sup>) The following modified form of

<sup>4</sup>This book takes a shell to be all energy levels of the same principal quantum number  $n$ , but the meaning of *shell* and *sub-shell* may be different elsewhere. We use sub-shell to denote all energy levels with specific values of  $n$  and  $l$  (in a shell with a given value of  $n$ ). We used these definitions in Chapter 1; the inner atomic electrons involved in X-ray transitions follow the hydrogenic ordering.

<sup>5</sup>For a plot of the ionization energies of all the elements see Grant and Phillips (2001, Chapter 11, Fig. 18). This figure is accessible at <http://www.oup.co.uk/best.textbooks/physics/ephys/illustrations/>.

<sup>6</sup>This dependence of the energy on the quantum number  $l$  can also be explained in terms of the elliptical orbits of Bohr–Sommerfeld quantum theory rather than Schrödinger’s wavefunctions; however, we shall use only the ‘proper’ wavefunction description since the detailed correspondence between the elliptical classical trajectories and the radial wavefunctions can lead to confusion.

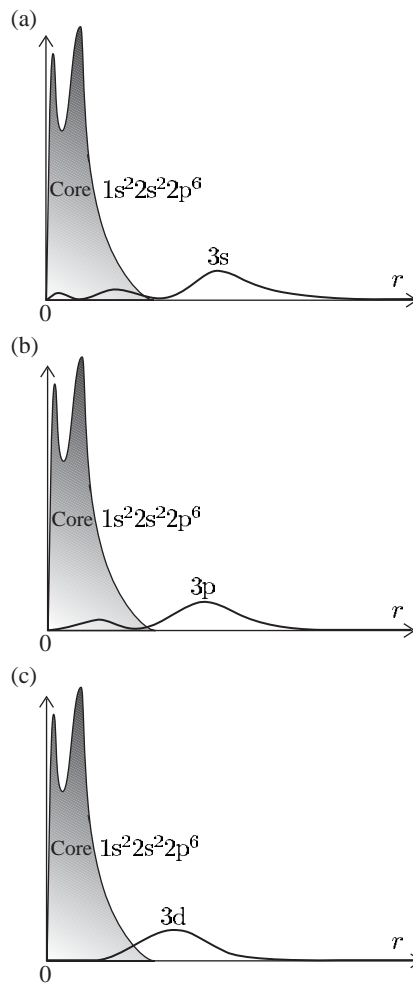


**Fig. 4.1** The probability density of the electrons in a sodium atom as a function of  $r$ . The electrons in the  $n = 1$  and  $n = 2$  shells make up the core, and the probability density of the unpaired outer electron is shown for the  $n = 3$  shell with  $l = 0, 1$  and  $2$ . The probability is proportional to  $|P(r)|^2 = r^2|R(r)|^2$ ; the  $r^2$  factor accounts for the increase in volume of the spherical shell between  $r$  and  $r + dr$  (i.e.  $4\pi r^2 dr$ ) as the radial distance increases. The decreasing penetration of the core as  $l$  increases can be seen clearly—the 3d-electron lies mostly outside the core with a wavefunction and binding energy very similar to those for the 3d configuration in hydrogen. These wavefunctions could be calculated by the simple numerical method described in Exercise 4.10, making the ‘frozen core’ approximation, i.e. that the distribution of the electrons in the core is not affected by the outer electron—this gives sufficient accuracy to illustrate the qualitative features. (The iterative method described in Section 4.4 could be used to obtain more accurate numerical wavefunctions.)

Bohr’s formula works amazingly well for the energy levels of the alkalis:

$$E(n, l) = -hc \frac{R_\infty}{(n - \delta_l)^2}. \quad (4.1)$$

<sup>7</sup>This differs from the modification used for X-ray transitions in Chapter 1—hardly surprising since the physical situation is completely different for the inner and outer electrons.

A quantity  $\delta_l$ , called the **quantum defect**, is subtracted from the principal quantum number to give an effective principal quantum number  $n^* = n - \delta_l$ .<sup>7</sup> The values of the quantum defects for each  $l$  can be estimated by inspecting the energy levels shown in Fig. 4.2. The d-electrons have a very small quantum defect,  $\delta_d \approx 0$ , since their energies are nearly hydrogenic. We can see that the 3p configuration in sodium has comparable energy to the  $n = 2$  shell in hydrogen, and similarly for 4p and  $n = 3$ , etc.; thus  $\delta_p \sim 1$ . It is also clear that the quantum defect for s-electrons is greater than that for p-electrons. A more detailed analysis shows that all the energy levels of sodium can be parametrised by the above formula and only three quantum defects:

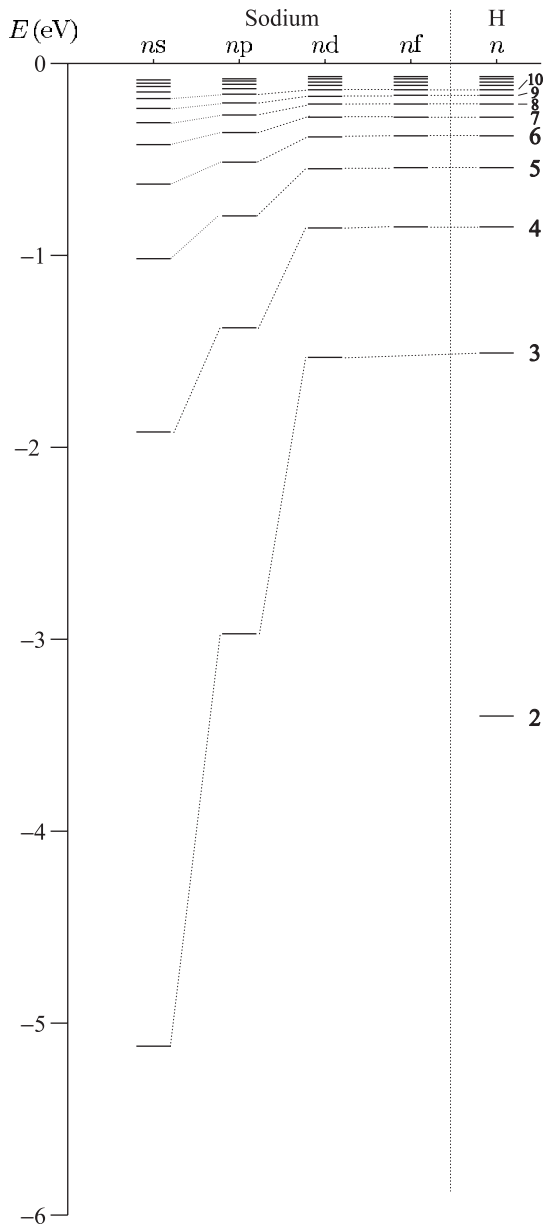


**Fig. 4.2** The energies of the s, p, d and f configurations in sodium. The energy levels of hydrogen are marked on the right for comparison. The guidelines link configurations with the same  $n$  to show how the energies become closer to the hydrogenic values as  $l$  increases, i.e. the quantum defects decrease so that  $\delta_l \simeq 0$  for f-electrons (and for the configurations with  $l > 3$  that have not been drawn).

$$\delta_s = 1.35, \quad \delta_p = 0.86, \quad \delta_d = 0.01, \quad \delta_l \simeq 0.00 \quad \text{for } l > 2.$$

There is a small variation with  $n$  (see Exercise 4.3). Having examined the variation in the quantum defects with orbital angular momentum quantum number for a given element, now let us compare the quantum defects in different alkalis. The data in Table 4.1 show that the alkalis have similar ionization energies despite the variation in atomic number. Thus the effective principal quantum numbers  $n^* = (13.6 \text{ eV}/\text{IE})^{1/2}$

**Table 4.2** The effective principal quantum numbers and quantum defects for the ground configuration of the alkalis. Note that the quantum defects do depend slightly on  $n$  (see Exercise 4.3), so the value given in this table for the 3s-electron in sodium differs slightly from the value given in the text ( $\delta_s = 1.35$ ) that applies for  $n > 5$ .

| Element | Configuration | $n^*$ | $\delta_s$ |
|---------|---------------|-------|------------|
| Li      | 2s            | 1.59  | 0.41       |
| Na      | 3s            | 1.63  | 1.37       |
| K       | 4s            | 1.77  | 2.23       |
| Rb      | 5s            | 1.81  | 3.19       |
| Cs      | 6s            | 1.87  | 4.13       |

(from eqn 4.1) are remarkably similar for all the ground configurations of the alkalis, as shown in Table 4.2.

In potassium the lowering of the energy for the s-electrons leads to the 4s sub-shell filling before 3d. By caesium (spelt cesium in the US) the 6s configuration has lower energy than 4f ( $\delta_f \simeq 0$  for Cs). The exercises give other examples, and quantum defects are tabulated in Kuhn (1969) and Woodgate (1980), amongst others.

### 4.3 The central-field approximation

The previous section showed that the modification of Bohr's formula by the quantum defects gives reasonably accurate values for the energies of the levels in alkalis. We described an alkali metal atom as a single electron orbiting around a core with a net charge of  $+1e$ , i.e. the nucleus surrounded by  $N - 1$  electrons. This is a top-down approach where we consider just the energy required to remove the valence electron from the rest of the atom; this binding energy is equivalent to the ionization energy of the atom. In this section we start from the bottom up and consider the energy of all the electrons. The Hamiltonian for  $N$  electrons in the Coulomb potential of a charge  $+Ze$  is

$$H = \sum_{i=1}^N \left\{ -\frac{\hbar^2}{2m} \nabla_i^2 - \frac{Ze^2/4\pi\epsilon_0}{r_i} + \sum_{j>i}^N \frac{e^2/4\pi\epsilon_0}{r_{ij}} \right\}. \quad (4.2)$$

The first two terms are the kinetic energy and potential energy for each electron in the Coulomb field of a nucleus of charge  $Z$ . The term with  $r_{ij} = |\mathbf{r}_i - \mathbf{r}_j|$  in the denominator is the electrostatic repulsion between the two electrons at  $\mathbf{r}_i$  and  $\mathbf{r}_j$ . The sum is taken over all electrons with  $j > i$  to avoid double counting.<sup>8</sup> This electrostatic repulsion is too large to be treated as a perturbation; indeed, at large distances the repulsion cancels out most of the attraction to the nucleus. To proceed further we make the physically reasonable assumption that a large part of the repulsion between the electrons can be treated as a central potential

<sup>8</sup>For example, lithium has three interactions between the three electrons, inversely proportional to  $r_{12}$ ,  $r_{13}$  and  $r_{23}$ ; summing over all  $j$  for each value of  $i$  would give six terms.

$S(r)$ . This follows because the closed sub-shells within the core have a spherical charge distribution, and therefore the interactions between the different shells and between shells and the valence electron are also spherically symmetric. In this **central-field approximation** the total potential energy depends only on the radial coordinate:

$$V_{\text{CF}}(r) = -\frac{Ze^2/4\pi\epsilon_0}{r} + S(r). \quad (4.3)$$

In this approximation the Hamiltonian becomes

$$H_{\text{CF}} = \sum_{i=1}^N \left\{ -\frac{\hbar^2}{2m} \nabla_i^2 + V_{\text{CF}}(r_i) \right\}. \quad (4.4)$$

For this form of potential, the Schrödinger equation for  $N$  electrons,  $H\psi = E_{\text{atom}}\psi$ , can be separated into  $N$  one-electron equations, i.e. writing the total wavefunction as a product of single-electron wavefunctions, namely

$$\psi_{\text{atom}} = \psi_1 \psi_2 \psi_3 \cdots \psi_N, \quad (4.5)$$

leads to  $N$  equations of the form

$$\left\{ -\frac{\hbar^2}{2m} \nabla_1^2 + V_{\text{CF}}(r_1) \right\} \psi_1 = E_1 \psi_1, \quad (4.6)$$

and similar for electrons  $i = 2$  to  $N$ . This assumes that all the electrons see the same potential, which is not as obvious as it may appear. This symmetric wavefunction is useful to start with (cf. the treatment of helium before including the effects of exchange symmetry); however, we know that the overall wavefunction for electrons, including spin, should be antisymmetric with respect to an interchange of the particle labels. (Proper antisymmetric wavefunctions are used in the Hartree–Fock method mentioned later in this chapter.) The total energy of the system is  $E_{\text{atom}} = E_1 + E_2 + \dots + E_N$ . The Schrödinger equations for each electron (eqn 4.6) can be separated into parts to give wavefunctions of the form  $\psi_i = R(r_i)Y_{l_i, m_i}\psi_{\text{spin}}(1)$ . Angular momentum is conserved in a central field and the angular equation gives the standard orbital angular momentum wavefunctions, as in hydrogen. In the radial equation, however, we have  $V_{\text{CF}}(r)$  rather than a potential proportional to  $1/r$  and so the equation for  $P(r) = rR(r)$  is

$$\left\{ -\frac{\hbar^2}{2m} \frac{d^2}{dr^2} + V_{\text{CF}}(r) + \frac{\hbar^2 l(l+1)}{2mr^2} \right\} P(r) = EP(r). \quad (4.7)$$

To solve this equation we need to know the form of  $V_{\text{CF}}(r)$  and compute the wavefunctions numerically. However, we can learn a lot about the behaviour of the system by thinking about the form of the solutions, without actually getting bogged down in the technicalities of solving the equations. At small distances the electrons experience the full nuclear charge so that the central electric field is

$$\mathbf{E}(r) \rightarrow \frac{Ze}{4\pi\epsilon_0 r^2} \hat{\mathbf{r}}. \quad (4.8)$$

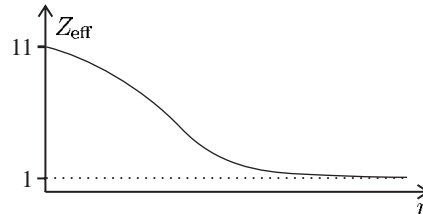


**Fig. 4.3** The change-over from the short- to the long-range is not calculated but is drawn to be a reasonable guess, using the following criteria. The typical radius of the 1s wavefunction around the nucleus of charge  $+Ze = +11e$  is about  $a_0/11$ , and so  $Z_{\text{eff}}$  will start to drop at this distance. We know that  $Z_{\text{eff}} \sim 1$  at the distance at which the 3d wavefunction has appreciable probability since that eigenstate has nearly the same energy as in hydrogen. The form of the function  $Z_{\text{eff}}(r)$  can be found quantitatively by the Thomas–Fermi method described in Woodgate (1980).

At large distances the other  $N - 1$  electrons screen most of the nuclear charge so that the field is equivalent to that of charge  $+1e$ :

$$\mathbf{E}(r) \rightarrow \frac{e}{4\pi\epsilon_0 r^2} \hat{\mathbf{r}}. \quad (4.9)$$

These two limits can be incorporated in a central field of the form

$$\mathbf{E}_{\text{CF}}(r) \rightarrow \frac{Z_{\text{eff}} e}{4\pi\epsilon_0 r^2} \hat{\mathbf{r}}. \quad (4.10)$$

<sup>9</sup>This is not necessarily the best way to parametrise the problem for numerical calculations but it is useful for understanding the underlying physical principles.

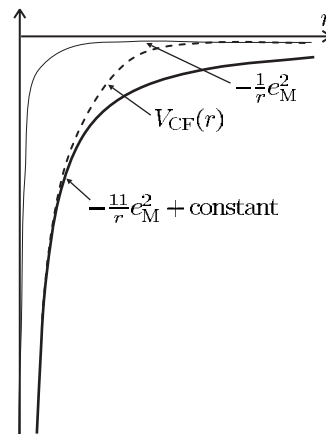
The effective atomic number  $Z_{\text{eff}}(r)$  has limiting values of  $Z_{\text{eff}}(0) = Z$  and  $Z_{\text{eff}}(r) \rightarrow 1$  as  $r \rightarrow \infty$ , as sketched in Fig. 4.3.<sup>9</sup> The potential energy of an electron in the central field is obtained by integrating from infinity:

$$V_{\text{CF}}(r) = e \int_{\infty}^r |\mathbf{E}_{\text{CF}}(r')| dr'. \quad (4.11)$$

The form of this potential is shown in Fig. 4.4.

So far, in our discussion of the sodium atom in terms of the wavefunction of the valence electron in a central field we have neglected

**Fig. 4.4** The form of the potential energy of an electron in the central-field approximation ( $e_M^2 = e^2/4\pi\epsilon_0$ ). This approximate sketch for a sodium atom shows that the potential energy crosses over from  $V_{\text{CF}}(r) = -e_M^2/r$  at long range to  $-11e_M^2/r + V_{\text{offset}}$ ; the constant  $V_{\text{offset}}$  comes from the integration in eqn 4.11 (if  $Z_{\text{eff}}(r) = 11$  for all  $r$  then  $V_{\text{offset}} = 0$  but this is not the case). For electrons with  $l > 0$  the effective potential should also include the term that arises from the angular momentum, as shown in Fig. 4.5.



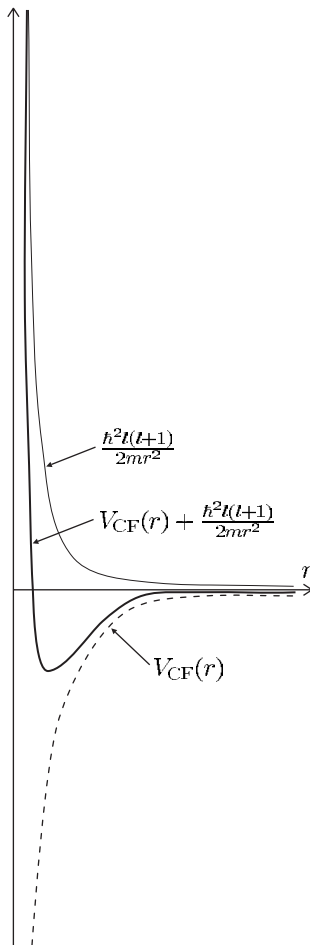


**Fig. 4.5** The total potential in the central-field approximation including the term that is proportional to  $l(l+1)/r^2$  drawn here for  $l = 2$  and the same approximate electrostatic  $V_{CF}(r)$  as shown in Fig. 4.4. The angular momentum leads to a ‘centrifugal barrier’ that tends to keep the wavefunctions of electrons with  $l > 0$  away from  $r = 0$  where the central-field potential is deepest.

the fact that the central field itself depends on the configuration of the electrons in the atom. For a more accurate description we must take into account the effect of the outer electron on the other electrons, and hence on the central field. The energy of the whole atom is the sum of the energies of the individual electrons (in eqn 4.6), e.g. a sodium atom in the 3s configuration has energy  $E(1s^2 2s^2 2p^6 3s) = 2E_{1s} + 2E_{2s} + 6E_{2p} + E_{3s} = E_{\text{core}} + E_{3s}$ . This is the energy of the neutral atom relative to the bare nucleus ( $\text{Na}^{11+}$ ).<sup>10</sup> It is more useful to measure the binding energy relative to the singly-charged ion ( $\text{Na}^+$ ) with energy  $E(1s^2 2s^2 2p^6) = 2E'_{1s} + 2E'_{2s} + 6E'_{2p} = E'_{\text{core}}$ . The dashes are significant—the ten electrons in the ion and the ten electrons in the core of the atom have slightly different binding energies because the central field is not the same in the two cases. The ionization energy is  $\text{IE} = E_{\text{atom}} - E_{\text{ion}} = (E_{\text{core}} - E'_{\text{core}}) + E_{3s}$ . From the viewpoint of valence electrons, the difference in  $E_{\text{core}}$  between the neutral atom and the ion can be attributed to **core polarization**, i.e. a change in the distribution of charge in the core produced by the valence electron.<sup>11</sup> To calculate the energy of multi-

<sup>10</sup>This is a crude approximation, especially for inner electrons.

<sup>11</sup>This effect is small in the alkalis and it is reasonable to use the **frozen core** approximation that assumes  $E_{\text{core}} \approx E'_{\text{core}}$ . This approximation becomes more accurate for a valence electron in higher levels where the influence on the core becomes smaller.

electron atoms properly we should consider the energy of the whole system rather than focusing attention on only the valence electron. For example, neon has the ground configuration  $1s^22s^22p^6$  and the electric field changes significantly when an electron is excited out of the  $2p$  subshell, e.g. into the  $1s^22s^22p^53s$  configuration.

Quantum defects can be considered simply as empirical quantities that happen to give a good way of parametrising the energies of the alkalis but there is a physical reason for the form of eqn 4.1. In any potential that tends to  $1/r$  at long range the levels of bound states bunch together as the energy increases—at the top of the well the classically allowed region gets larger and so the intervals between the eigenenergies and the stationary solutions get smaller.<sup>12</sup> More quantitatively, in Exercise 1.12 it was shown, using the correspondence principle, that such a potential has energies  $E \propto 1/k^2$ , with  $\Delta k = 1$  between energy levels, but  $k$  is not itself necessarily an integer. For the special case of a potential proportional to  $1/r$  for all distances,  $k$  is an integer that we call the principal quantum number  $n$  and the lowest energy level turns out to be  $n = 1$ . For a general potential in the central-field approximation we have seen that it is convenient to write  $k$  in terms of the integer  $n$  as  $k = n - \delta$ , where  $\delta$  is a non-integer (quantum defect). To find the actual energy levels of an alkali and hence  $\delta$  (for a given value of  $l$ ) requires the numerical calculation of the wavefunctions, as outlined in the following section.

## 4.4 Numerical solution of the Schrödinger equation

Before describing particular methods of solution, let us look at the general features of the wavefunction for particles in potential wells. The radial equation for  $P(r)$  has the form

$$\frac{d^2P}{dr^2} = -\frac{2m}{\hbar^2} \{E - V(r)\} P, \quad (4.12)$$

where the potential  $V(r)$  includes the angular momentum term in eqn 4.7. Classically, the particle is confined to the region where  $E - V(r) > 0$  since the kinetic energy must be positive. The positions where  $E = V(r)$  are the classical turning points where the particle instantaneously comes to rest, cf. at the ends of the swing of a pendulum. The quantum wavefunctions are oscillatory in the classically allowed region, with the curvature and number of nodes both increasing as  $E - V(r)$  increases, as shown in Fig. 4.6. The wavefunctions penetrate some way into the classically forbidden region where  $E - V(r) < 0$ ; but in this region the solutions decay exponentially and the probability falls off rapidly.

How can we find  $P(r)$  in eqn 4.12 without knowing the potential  $V(r)$ ? The answer is firstly to find the wavefunctions for a potential  $V_{CF}(r)$  that is ‘a reasonable guess’, consistent with eqn 4.11 and the limits on the central electric field in the previous equations. Then, secondly, we

<sup>12</sup>This is in contrast to an infinite square well where confinement to a region of fixed dimensions gives energies proportional to  $n^2$ , where  $n$  is an integer.

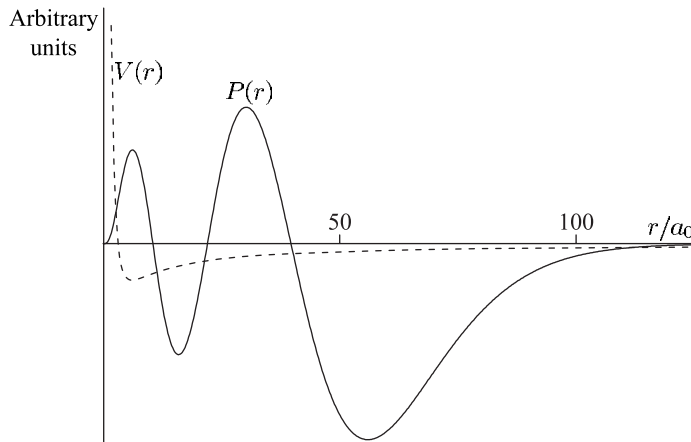


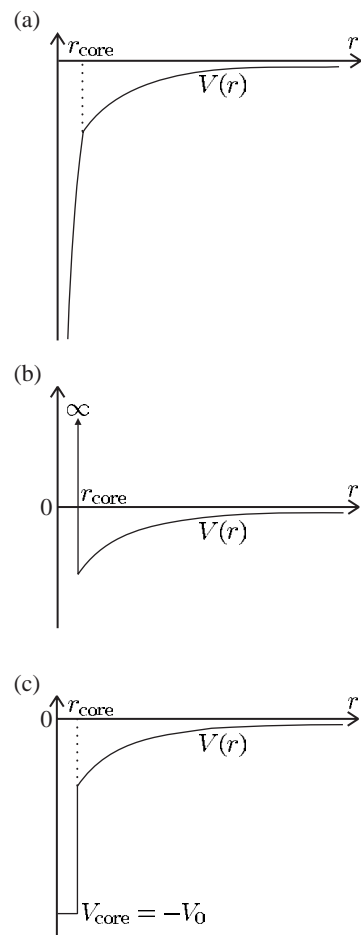
**Fig. 4.6** The potential in the central-field approximation including the term that is proportional to  $l(l + 1)/r^2$  is drawn here for  $l = 2$  and the same approximate electrostatic  $V_{\text{CF}}(r)$  as shown in Fig. 4.4. The function  $P(r) = rR(r)$  was drawn for  $n = 6$  and  $l = 2$  using the method described in Exercise 4.10.

make the assumed potential correspond closely to the real potential, as described in the next section. Equation 4.12 is a second-order differential equation and we can numerically calculate  $P(r)$ , the value of the function at  $r$ , from two nearby values, e.g.  $u(r - \delta r)$  and  $u(r - 2\delta r)$ .<sup>13</sup> Thus, working from near  $r = 0$ , the method gives the numerical value of the function at all points going out as far as is necessary. The region of the calculation needs to extend beyond the classical turning point(s) by an amount that depends on the energy of the wavefunction being calculated. These general features are clearly seen in the plots produced in Exercise 4.10. Actually, that exercise describes a method of finding the radial wavefunction  $R(r)$  rather than  $P(r) = rR(r)$  but similar principles apply.<sup>14</sup> If you carry out the exercise you will find that the behaviour at large  $r$  depends very sensitively on the energy  $E$ —the wavefunction diverges if  $E$  is not an eigenenergy of the potential—this gives a way of searching for those eigenenergies. If the wavefunction diverges upwards for  $E'$  and downwards for  $E''$  then we know that an eigenenergy of the system  $E_k$  lies between these two values,  $E' < E_k < E''$ . Testing further values between these upper and lower bounds narrows the range and gives a more precise value of  $E_k$  (as in the Newton–Raphson method for finding roots). This so-called ‘shooting’ method is the least sophisticated method of computing wavefunctions and energies, but it is adequate for illustrating the principles of such calculations. Results are not given here since they can readily be calculated—the reader is strongly encouraged to implement the numerical method of solution, using a spreadsheet program, as described in Exercise 4.10. This shows how to find the wavefunctions for an electron in an arbitrary potential and verifies that the energy levels obey a quantum defect formula such as eqn 4.1 in any potential that is proportional to  $1/r$  at long range (see Fig. 4.7).

<sup>13</sup>The step size  $\delta r$  must be small compared to the distance over which the wavefunction varies; but the number of steps must not be so large that round-off errors begin to dominate.

<sup>14</sup>In a numerical method there is no reason why we should not calculate the wavefunction directly;  $P(r)$  was introduced to make the equations neater in the analytical approach.

**Fig. 4.7** Simple modifications of the potential energy that could be used for the numerical solution of the Schrödinger equation described in Exercise 4.10. For all these potentials  $V(r) = -e^2/4\pi\epsilon_0 r$  for  $r \geq r_{\text{core}}$ . (a) Inside the radial distance  $r_{\text{core}}$  the potential energy is  $V(r) = -Ze^2/4\pi\epsilon_0 r + V_{\text{offset}}$ , drawn here for  $Z = 3$  and an offset chosen so that  $V(r)$  is continuous at  $r = r_{\text{core}}$ . This corresponds to the situation where the charge of the core is an infinitely thin shell. The deep potential in the inner region means that the wavefunction has a high curvature, so small steps must be used in the numerical calculation (in this region). The hypothetical potentials in (b) and (c) are useful for testing the numerical method and for showing why the eigenenergies of any potential proportional to  $1/r$  at long range obey a quantum defect formula (like eqn 4.1). The form of the solution depends sensitively on the energy in the outer region  $r \geq r_{\text{core}}$ , but in the inner region where  $|E| \ll |V(r)|$  it does not, e.g. the number of nodes ('wiggles') in this region changes slowly with energy  $E$ . Thus, broadly speaking, the problem reduces to finding the wavefunction in the outer region that matches boundary conditions, at  $r = r_{\text{core}}$ , that are almost independent of the energy—the potential energy curve shown in (b) is an extreme example that gives useful insight into the behaviour of the wavefunction for more realistic central fields.



#### 4.4.1 Self-consistent solutions

The numerical method described above, or a more sophisticated one, can be used to find the wavefunctions and energies for a given potential in the central-field approximation. Now we shall think about how to determine  $V_{\text{CF}}$  itself. The potential of the central field in eqn 4.2 includes the electrostatic repulsion of the electrons. To calculate this mutual repulsion we need to know where the electrons are, i.e. their wavefunctions, but to find the wavefunctions we need to know the potential. This argument is circular. However, going round and round this loop can be useful in the following sense. As stated above, the method starts by making a reasonable estimate of  $V_{\text{CF}}$  and then computing the electronic wavefunctions for this potential. These wavefunctions are then used to calculate a new average potential (using the central-field approximation) that is more realistic than the initial guess. This improved potential is then used to calculate more accurate wavefunctions, and so on. On suc-

cessive iterations, the changes in the potential and wavefunctions should get smaller and converge to a **self-consistent solution**, i.e. where the wavefunctions give a certain  $V_{\text{CF}}(r)$ , and solving the radial equation for that central potential gives back the same wavefunctions (within the required precision).<sup>15</sup> This self-consistent method was devised by Hartree. However, the wavefunctions of multi-electron atoms are not simply products of individual wavefunctions as in eqn 4.5. In our treatment of the excited configurations of helium we found that the two-electron wavefunctions had to be antisymmetric with respect to the permutation of the electron labels. This symmetry requirement for identical fermions was met by constructing symmetrised wavefunctions that were linear combinations of the simple product states (i.e. the spatial part of these functions is  $\psi_{\text{space}}^{\text{A}}$  and  $\psi_{\text{space}}^{\text{S}}$ ). A convenient way to extend this symmetrisation to  $N$  particles is to write the wavefunction as a **Slater determinant**:

$$\Psi = \frac{1}{\sqrt{N!}} \begin{vmatrix} \psi_a(1) & \psi_a(2) & \cdots & \psi_a(N) \\ \psi_b(1) & \psi_b(2) & \cdots & \psi_b(N) \\ \psi_c(1) & \psi_c(2) & \cdots & \psi_c(N) \\ \vdots & \vdots & \ddots & \vdots \\ \psi_x(1) & \psi_x(2) & \cdots & \psi_x(N) \end{vmatrix}.$$

Here  $a, b, c, \dots, x$  are the possible sets of quantum numbers of the individual electrons,<sup>16</sup> and  $1, 2, \dots, N$  are the electron labels. The change of sign of a determinant on the interchange of two columns makes the wavefunction antisymmetric. The Hartree–Fock method uses such symmetrised wavefunctions for self-consistent calculations and nowadays this is the standard way of computing wavefunctions, as described in Bransden and Joachain (2003). In practice, numerical methods need to be adapted to the particular problem being considered, e.g. numerical values of the radial wavefunctions that give accurate energies may not give a good value for a quantity such as the expectation value  $\langle 1/r^3 \rangle$  that is very sensitive to the behaviour at short range.

<sup>15</sup>The number of iterations required, before the changes when going round the loop become very small, depends on how well the initial potential is chosen, but the final self-consistent solution should not depend on the initial choice. In general, it is better to let a computer do the work rather than expend a lot of effort improving the starting point.

<sup>16</sup>Including both space and spin.

## 4.5 The spin–orbit interaction: a quantum mechanical approach

The spin–orbit interaction  $\beta \mathbf{s} \cdot \mathbf{l}$  (see eqn 2.49) splits the energy levels to give fine structure. For the single valence in an alkali we could treat this interaction in exactly the same way as for hydrogen in Chapter 2, i.e. use the vector model that treats the angular momenta as vectors obeying classical mechanics (supplemented with rules such as the restriction of the angular momentum to integer or half-integer values). However, in this chapter we shall use a quantum mechanical treatment and regard the vector model as a useful physical picture that illustrates the behaviour of the quantum mechanical operators. The previous discussion of fine structure in terms of the vector model had two steps that require further justification.

<sup>17</sup>The wavefunction for an alkali metal atom in the central-field approximation is a product of a radial wavefunction (which does not have an analytical expression) and angular momentum eigenfunctions (as in hydrogen).

<sup>18</sup>More explicitly, we have  $|l m_l s m_s\rangle \equiv Y_{l,m_l} \psi_{\text{spin}}$ , where  $\psi_{\text{spin}} = |m_s = +1/2\rangle$  or  $|m_s = -1/2\rangle$ .

<sup>19</sup>Proof of these commutation relations:  $[s_x l_x + s_y l_y + s_z l_z, l_z] = s_x [l_x, l_z] + s_y [l_y, l_z] = -is_x l_y + is_y l_x \neq 0$ . Similarly,  $[s_x l_x + s_y l_y + s_z l_z, s_z] = -is_y l_x + is_x l_y \neq 0$ . Note that  $[\mathbf{s} \cdot \mathbf{l}, l_z] = -[\mathbf{s} \cdot \mathbf{l}, s_z]$  and hence  $\mathbf{s} \cdot \mathbf{l}$  commutes with  $l_z + s_z$ .

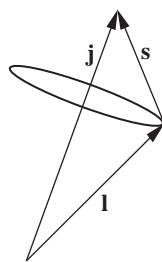


**Fig. 4.8** The total angular momentum of the atom  $\mathbf{j} = \mathbf{l} + \mathbf{s}$  is a fixed quantity in the absence of an external torque. Thus an interaction between the spin and orbital angular momenta  $\beta \mathbf{s} \cdot \mathbf{l}$  causes these vectors to rotate (precess) around the direction of  $\mathbf{j}$  as shown.

<sup>20</sup>As for helium in Section 3.2 and in the classical treatment of the normal Zeeman effect in Section 1.8.

<sup>21</sup>These commutation relations for the operators correspond to the conservation of the total angular momentum, and its component along the  $z$ -axis. Only an external torque on the atom affects these quantities. The spin-orbit interaction is an internal interaction.

- (a) The possible values of the total angular momentum obtained by the addition of the electron's spin,  $s = 1/2$ , and its orbital angular momentum are  $j = l + 1/2$  or  $l - 1/2$ . This is a consequence of the rules for the addition of angular momentum in quantum mechanics (vector addition but with the resultant quantised).
- (b) The vectors have squared magnitudes given by  $\mathbf{j}^2 = j(j+1)$ ,  $\mathbf{l}^2 = l(l+1)$  and  $\mathbf{s}^2 = 3/4$ , where  $j$  and  $l$  are the relevant angular momentum quantum numbers.

Step (b) arises from taking the expectation values of the quantum operators in the Hamiltonian for the spin-orbit interaction. This is not straightforward since the atomic wavefunctions  $R(r)|l m_l s m_s\rangle$  are not eigenstates of this operator<sup>17</sup>—this means that we must face the complications of degenerate perturbation theory. This situation arises frequently in atomic physics and merits a careful discussion.

We wish to determine the effect of an interaction of the form  $\mathbf{s} \cdot \mathbf{l}$  on the angular eigenfunctions  $|l m_l s m_s\rangle$ . These are eigenstates of the operators  $\mathbf{l}^2$ ,  $l_z$ ,  $\mathbf{s}^2$  and  $s_z$  labelled by the respective eigenvalues.<sup>18</sup> There are  $2(2l+1)$  degenerate eigenstates for each value of  $l$  because the energy does not depend on the orientation of the atom in space, or the direction of its spin, i.e. energy is independent of  $m_l$  and  $m_s$ . The states  $|l m_l s m_s\rangle$  are not eigenstates of  $\mathbf{s} \cdot \mathbf{l}$  because this operator does not commute with  $l_z$  and  $s_z$ :  $[\mathbf{s} \cdot \mathbf{l}, l_z] \neq 0$  and  $[\mathbf{s} \cdot \mathbf{l}, s_z] \neq 0$ .<sup>19</sup> Quantum operators only have simultaneous eigenfunctions if they commute. Since  $|l m_l s m_s\rangle$  is an eigenstate of  $l_z$  it cannot simultaneously be an eigenstate of  $\mathbf{s} \cdot \mathbf{l}$ , and similarly for  $s_z$ . However,  $\mathbf{s} \cdot \mathbf{l}$  does commute with  $\mathbf{l}^2$  and  $\mathbf{s}^2$ :  $[\mathbf{s} \cdot \mathbf{l}, \mathbf{l}^2] = 0$  and  $[\mathbf{s} \cdot \mathbf{l}, \mathbf{s}^2] = 0$  (which are easy to prove since  $s_x$ ,  $s_y$ ,  $s_z$ ,  $l_x$ ,  $l_y$  and  $l_z$  all commute with  $\mathbf{s}^2$  and  $\mathbf{l}^2$ ). So  $l$  and  $s$  are good quantum numbers in fine structure. Good quantum numbers correspond to constants of motion in classical mechanics—the magnitudes of  $\mathbf{l}$  and  $\mathbf{s}$  are constant but the orientations of these vectors change because of their mutual interaction, as shown in Fig. 4.8. If we try to evaluate the expectation value using wavefunctions that are not eigenstates of the operator then things get complicated. We would find that the wavefunctions are mixed by the perturbation, i.e. in the matrix formulation of quantum mechanics the matrix representing the spin-orbit interaction in this basis has *off-diagonal* elements. The matrix could be diagonalised by following the standard procedure for finding the eigenvalues and eigenvectors,<sup>20</sup> but a p-electron gives six degenerate states so the direct approach would require the diagonalisation of a  $6 \times 6$  matrix. It is much better to find the eigenfunctions at the outset and work in the appropriate eigenbasis. This 'look-before-you-leap' approach requires some preliminary reasoning.

We define the operator for the total angular momentum as  $\mathbf{j} = \mathbf{l} + \mathbf{s}$ . The operator  $\mathbf{j}^2$  commutes with the interaction, as does its component  $j_z$ :  $[\mathbf{s} \cdot \mathbf{l}, \mathbf{j}^2] = 0$  and  $[\mathbf{s} \cdot \mathbf{l}, j_z] = 0$ . Thus  $j$  and  $m_j$  are good quantum numbers.<sup>21</sup> Hence suitable eigenstates for calculating the expectation value of  $\mathbf{s} \cdot \mathbf{l}$  are  $|l s j m_j\rangle$ . Mathematically these new eigenfunctions can be expressed as combinations of the old basis set:

$$|lsjm_j\rangle = \sum_{m_l, m_s} C(lsjm_j; m_l, m_s) |l m_l s m_s\rangle.$$

Each eigenfunction labelled by  $l$ ,  $s$ ,  $j$  and  $m_j$  is a linear combination of the eigenfunctions with the same values of  $l$  and  $s$  but various values of  $m_l$  and  $m_s$ . The coefficients  $C$  are the Clebsch–Gordan coefficients and their values for many possible combinations of angular momenta are tabulated in more advanced books. Particular values of Clebsch–Gordan coefficients are not needed for the problems in this book but it is important to know that, in principle, one set of functions can be expressed in terms of another complete set—with the same number of eigenfunctions in each basis.

Finally, we use the identity<sup>22</sup>  $\mathbf{j}^2 = \mathbf{l}^2 + \mathbf{s}^2 + 2\mathbf{s} \cdot \mathbf{l}$  to express the expectation value of the spin–orbit interaction as

$$\begin{aligned} \langle lsjm_j | \mathbf{s} \cdot \mathbf{l} | lsjm_j \rangle &= \frac{1}{2} \langle lsjm_j | \mathbf{j}^2 - \mathbf{l}^2 - \mathbf{s}^2 | lsjm_j \rangle \\ &= \frac{1}{2} \{j(j+1) - l(l+1) - s(s+1)\}. \end{aligned}$$

The states  $|lsjm_j\rangle$  are eigenstates of the operators  $\mathbf{j}^2$ ,  $\mathbf{l}^2$  and  $\mathbf{s}^2$ . The importance of the proper quantum treatment may not yet be apparent since all we appear to have gained over the vector model is being able to write the wavefunctions symbolically as  $|lsjm_j\rangle$ . We will, however, need the proper quantum treatment when we consider further interactions that perturb these wavefunctions.

## 4.6 Fine structure in the alkalis

The fine structure in the alkalis is well approximated by an empirical modification of eqn 2.56 called the Landé formula:

$$\Delta E_{\text{FS}} = \frac{Z_i^2 Z_o^2}{(n^*)^3 l(l+1)} \alpha^2 h c R_\infty. \quad (4.13)$$

In the denominator the effective principal quantum number cubed  $(n^*)^3$  (defined in Section 4.2) replaces  $n^3$ . The effective atomic number  $Z_{\text{eff}}$ , which was defined in the discussion of the central-field approximation, tends to the inner atomic number  $Z_i \sim Z$  as  $r \rightarrow 0$  (where the electron ‘sees’ most of the nuclear charge); outside the core the field corresponds to an outer atomic number  $Z_o \simeq 1$  (for neutral atoms). The Landé formula can be justified by seeing how the central-field approximation modifies the calculation of the fine structure in hydrogen (Section 2.3.2). The spin–orbit interaction depends on the electric field that the electron moves through; in an alkali metal atom this field is proportional to  $Z_{\text{eff}}(r)\mathbf{r}/r^3$  rather than  $\mathbf{r}/r^3$  as in hydrogen.<sup>23</sup> Thus the expectation value of the spin–orbit interaction depends on

$$\left\langle \frac{Z_{\text{eff}}(r)}{r^3} \right\rangle \equiv \left\langle \frac{1}{er} \frac{\partial V_{\text{CF}}(r)}{\partial r} \right\rangle$$

<sup>22</sup>This applies both for vector operators, where  $\mathbf{j}^2 = j_x^2 + j_y^2 + j_z^2$ , and for classical vectors where this is simply  $\mathbf{j}^2 = |\mathbf{j}|^2$ .

<sup>23</sup>This modification is equivalent to using  $V_{\text{CF}}$  in place of the hydrogenic potential proportional to  $1/r$ .

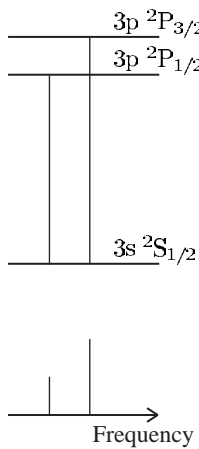


**Fig. 4.9** The fine-structure components of a p to s transition, e.g. the  $3S_{1/2}$ – $3P_{1/2}$  and  $3S_{1/2}$ – $3P_{3/2}$  transitions in sodium. (Not to scale.) The statistical weights of the upper levels lead to a 1:2 intensity ratio.

<sup>24</sup>The rates of the allowed transitions depend on integrals involving the radial wavefunctions (carried out numerically for the alkalis) and the integrals over the angular part of the wavefunction given in Section 2.2.1, where we derived the selection rules.

<sup>25</sup>This shortened form of the full *LS*-coupling scheme notation gives all the necessary information for a single electron, cf.  $3s\ 2S_{1/2}$ – $3p\ 2P_{3/2}$ .

<sup>26</sup>This must be true for the physical reason that the decay rate is the same whatever the spatial orientation of the atom, and similarly for the spin states. All the different angular states have the same radial integral, i.e. that between the 3p and 3s radial wavefunctions.

<sup>27</sup>This normal situation for fine structure may be modified slightly in a case like caesium where the large separation of the components means that the frequency dependence of the lifetime (eqn 1.24) leads to differences, even though the matrix elements are similar.

rather than  $\langle 1/r^3 \rangle$  as in hydrogen (eqn 2.51). This results in fine structure for the alkalis, given by the Landé formula, that scales as  $Z^2$ —this lies between the dependence on  $Z^4$  for hydrogenic ions (no screening) and the other extreme of no dependence on atomic number for complete screening. The effective principal quantum number  $n^*$  is remarkably similar across the alkalis, as noted in Section 4.2.

As a particular numerical example of the scaling, consider the fine structure of sodium ( $Z = 11$ ) and of caesium ( $Z = 55$ ). The 3p configuration of sodium has a fine-structure splitting of  $1700\text{ m}^{-1}$ , so for a  $Z^2$ -dependence the fine structure of the 6p configuration of caesium should be (using  $n^*$  from Table 4.2)

$$1.7 \times 10^3 \times \left(\frac{55}{11}\right)^2 \times \left(\frac{2.1}{2.4}\right)^3 = 28.5 \times 10^3 \text{ m}^{-1}.$$

This estimate gives only half the actual value of  $55.4 \times 10^3 \text{ m}^{-1}$ , but the prediction is much better than if we had used a  $Z^4$  scaling. (A logarithmic plot of the energies of the gross and fine structure against atomic number is given in Fig. 5.7. This shows that the actual trend of the fine structure lies close to the  $Z^2$ -dependence predicted.)

The fine structure causes the familiar yellow line in sodium to be a doublet comprised of the two wavelengths  $\lambda = 589.0\text{ nm}$  and  $589.6\text{ nm}$ . This, and other doublets in the emission spectrum of sodium, can be resolved by a standard spectrograph. In caesium the transitions between the lowest energy configurations (6s–6p) give spectral lines at  $\lambda = 852\text{ nm}$  and  $894\text{ nm}$ —this ‘fine structure’ is not very fine.

#### 4.6.1 Relative intensities of fine-structure transitions

The transitions between the fine-structure levels of the alkalis obey the same selection rules as in hydrogen since the angular momentum functions are the same in both cases. It takes a considerable amount of calculation to find absolute values of the transition rates<sup>24</sup> but we can find the relative intensities of the transitions between different fine-structure levels from a simple physical argument. As an example we shall look at p to s transitions in sodium, as shown in Fig. 4.9. The  $3S_{1/2}$ – $3P_{1/2}$  transition has half the intensity of the  $3S_{1/2}$ – $3P_{3/2}$  transition.<sup>25</sup> This 1:2 intensity ratio arises because the strength of each component is proportional to the statistical weight of the levels  $(2j + 1)$ . This gives 2:4 for  $j = 1/2$  and  $3/2$ . To explain this we first consider the situation without fine structure. For the 3p configuration the wavefunctions have the form  $R_{3p}(r)|lm_lsm_s\rangle$  and the decay rate of these states (to 3s) is independent of the values of  $m_l$  and  $m_s$ .<sup>26</sup> Linear combinations of the states  $R(r)|lm_lsm_s\rangle$  with different values of  $m_l$  and  $m_s$  (but the same values of  $n$ ,  $l$  and  $s$ , and hence the same lifetime) make up the eigenstates of the fine structure,  $|lsjm_j\rangle$ . Therefore an alkali atom has the same lifetime for both values of  $j$ .<sup>27</sup>

If each state has the same excitation rate, as in a gas discharge lamp for example, then all the states will have equal populations and the intensity of a given component of the line is proportional to the number of contributing  $m_j$  states. Similarly, the fine structure of transitions from s to p configurations, e.g.  $3\text{P}_{3/2}-5\text{S}_{1/2}$  and  $3\text{P}_{1/2}-5\text{S}_{1/2}$ , have an intensity ratio of 2:1—in this case the lower frequency component has twice the intensity of the higher component, i.e. the opposite of the p to s transition shown in Fig. 4.9 (and such information can be used to identify the lines in an observed spectrum). More generally, there is a sum rule for intensities: the sum of the intensities to, or from, a given level is proportional to its degeneracy; this can be used when both upper and lower configurations have fine structure (see Exercise 4.8).

The discussion of the fine structure has shown that spin leads to a splitting of energy levels of a given  $n$ , of which  $l$  levels have different  $j$ . These fine-structure levels are degenerate with respect to  $m_j$ , but an external magnetic field removes this degeneracy. The calculation of the effect of an external magnetic field in Chapter 1 was a classical treatment that led to the normal Zeeman effect. This does not accurately describe what happens for atoms with one valence electron because the contribution of the spin magnetic moment leads to an **anomalous Zeeman effect**. The splitting of the fine-structure level into  $2j + 1$  states (or Zeeman sub-levels) in an applied field is shown in Fig. 4.10. It is straightforward to calculate the Zeeman energy for an atom with a single valence electron, as shown in quantum texts, but to avoid repetition the standard treatment is not given here; in the next chapter we shall derive a general formula for the Zeeman effect on atoms with any number of valence electrons that covers the single-electron case (see Exercise 5.13). We also look at the Zeeman effect on hyperfine structure in Chapter 6.

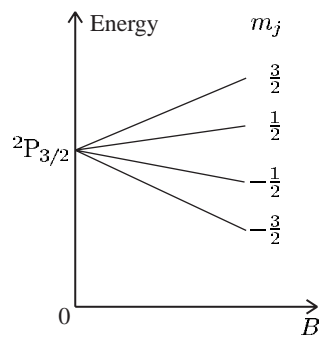


**Fig. 4.10** In an applied magnetic field of magnitude  $B$  the four states of different  $m_j$  of the  $^2\text{P}_{3/2}$  level have energies of  $E_{\text{Zeeman}} = g_j \mu_B B m_j$ —the factor  $g_j$  arises from the projection of the contributions to the magnetic moment from  $\mathbf{l}$  and  $\mathbf{s}$  onto  $\mathbf{j}$  (see Exercise 5.13).

## Further reading

This chapter has concentrated on the alkalis and mentioned the neighbouring inert gases; a more general discussion of the periodic table is given in *Physical chemistry* by Atkins (1994).

The self-consistent calculations of atomic wavefunctions are discussed in Hartree (1957), Slater (1960), Cowan (1981), in addition to the textbook by Bransden and Joachain (2003).

The numerical solution of the Schrödinger equation for the bound states of a central field in Exercise 4.10 is discussed in French and Taylor (1978), Eisberg and Resnick (1985) and Rioux (1991). Such numerical methods can also be applied to particles with positive energies in the potential to model scattering in quantum mechanics, as described in Greenhow (1990). The numerical method described in this book has deliberately been kept simple to allow quick implementation, but the Numerov method is more precise for this type of problem.

## Exercises

(4.1) *Configuration of the electrons in francium*

Write down the full electronic configuration of francium (atomic number  $Z = 87$ ). This element comes below caesium in the periodic table.

(4.2) *Finding the series limit for sodium*

Eight ultraviolet absorption lines in sodium have wavenumbers of

$$\begin{array}{cccc} 38\,541, & 39\,299, & 39\,795, & 40\,137, \\ 40\,383, & 40\,566, & 40\,706, & 40\,814, \end{array}$$

in units of  $\text{cm}^{-1}$ . Devise an extrapolation procedure to find the ionization limit of sodium with a precision justified by the data. Convert the result into electron volts. (You may find a spreadsheet program useful for manipulating the numbers.) What is the effective principal quantum number  $n^*$  of the valence electron in the ground configuration?

(4.3) *Quantum defects of sodium*

The binding energies of the 3s, 4s, 5s and 6s configurations in sodium are 5.14 eV, 1.92 eV, 1.01 eV and 0.63 eV, respectively. Calculate the quantum defects for these configurations and comment on what you find.

Estimate the binding energy of the 8s configuration and make a comparison with the  $n = 8$  shell in hydrogen.

(4.4) *Quantum defect*

Estimate the wavelength of laser radiation that excites the 5s  $^2\text{S}_{1/2}$ –7s  $^2\text{S}_{1/2}$  transition in rubidium by simultaneous absorption of two photons with the same frequency ( $\text{IE(Rb)} = 4.17 \text{ eV}$ ). (Two-photon spectroscopy is described in Section 8.4 but specific details are not required here.)

(4.5) *Application of quantum defects to helium and helium-like ions*

| Configuration | Binding energy ( $\text{cm}^{-1}$ ) |
|---------------|-------------------------------------|
| 1s2s          | 35 250                              |
| 1s2p          | 28 206                              |
| 1s3s          | 14 266                              |
| 1s3p          | 12 430                              |
| 1s3d          | 12 214                              |

(a) Calculate the wavelength of the 1s2p–1s3d line in helium and compare it with the Balmer- $\alpha$  line in hydrogen.

(b) Calculate the quantum defects for the configurations of helium in the table. Estimate the binding energies of the 1s4l configurations.

(c) The levels belonging to the 1s4f configuration of the  $\text{Li}^+$  ion all lie at an energy of 72.24 eV above the ion's ground state. Estimate the second ionization energy of this ion. Answer: 75.64 eV.

(4.6) *Quantum defects and fine structure of potassium*

An atomic vapour of potassium absorbs light at the wavelengths (in nm): 769.9, 766.5, 404.7, 404.4, 344.7 and 344.6. These correspond to the transitions from the ground configuration 4s. Explain these observations as fully as you can and estimate the mean wavelength of the next doublet in the series, and its splitting. (Potassium has  $\text{IE} = 4.34 \text{ eV}$ ).<sup>28</sup>

(4.7) *The Z-scaling of fine structure*

Calculate the fine-structure splitting of the 3p configuration of the hydrogen-like ion  $\text{Na}^{+10}$  (in eV). Explain why it is larger than the fine structure of the same configuration in the neutral sodium (0.002 eV) and hydrogen ( $1.3 \times 10^{-5} \text{ eV}$ ).

(4.8) *Relative intensities of fine-structure components*

(a) An emission line in the spectrum of an alkali has three fine-structure components corresponding to the transitions  ${}^2\text{P}_{3/2}$ – ${}^2\text{D}_{3/2}$ ,  ${}^2\text{P}_{3/2}$ – ${}^2\text{D}_{5/2}$  and  ${}^2\text{P}_{1/2}$ – ${}^2\text{D}_{3/2}$ . These components have intensities  $a$ ,  $b$  and  $c$ , respectively, that are in the ratio 1 : 9 : 5. Show that these satisfy the rule that the sum of the intensities of the transitions to, or from, a given level is proportional to its statistical weight ( $2J + 1$ ).

(b) Sketch an energy-level diagram of the fine-structure levels of the two terms  $nd$   ${}^2\text{D}$  and  $n'f$   ${}^2\text{F}$  (for  $n' > n$ ). Mark the three allowed electric dipole transitions and find their relative intensities.

<sup>28</sup>For a discussion of how to determine the quantum defect for a series of lines by an iterative method see Softley (1994).

(4.9) *Spherical symmetry of a full sub-shell*

The sum  $\sum_{m=-l}^l |Y_{l,m}|^2$  is spherically symmetric. Show this for the specific case of  $l = 1$  and comment on the relevance of the general expression, that is true for all values of  $l$ , to the central-field approximation.

(4.10) *Numerical solution of the Schrödinger equation*

This exercise goes through a method of finding the wavefunctions and their energies for a potential (in the central-field approximation). This shows how numerical calculations are carried out in a simple case that can be implemented easily on a computer with readily available spreadsheet programs.<sup>29</sup> Of course, the properties of hydrogen-like atoms are well known and so the first stage really serves as a way of testing the numerical method (and checking that the formulae have been typed correctly). It is straightforward to extend the numerical method to deal with other cases, e.g. the potentials in the central-field approximation illustrated in Fig. 4.7.<sup>30</sup>

(a) *Derivation of the equations*

Show from eqn 2.4, and other equations in Chapter 2, that

$$\frac{d^2R}{dx^2} + \frac{2}{x} \frac{dR}{dx} + (\tilde{E} - \tilde{V}(x)) R(x) = 0, \quad (4.14)$$

where the position and energy have been turned into dimensionless variables:  $x = r/a_0$  and  $\tilde{E}$  is the energy in units of  $e^2/8\pi\epsilon_0 a_0 = 13.6 \text{ eV}$  (equal to half the atomic unit of energy used in some of the references).<sup>31</sup> In these units the effective potential is

$$\tilde{V}(x) = \frac{l(l+1)}{x^2} - \frac{2}{x}, \quad (4.15)$$

where  $l$  is the orbital angular momentum quantum number.

The derivatives of a function  $f(x)$  can be approximated by

$$\begin{aligned} \frac{df}{dx} &= \frac{f(x+\delta/2) + f(x-\delta/2)}{\delta}, \\ \frac{d^2f}{dx^2} &= \frac{f(x+\delta) + f(x-\delta) - 2f(x)}{\delta^2}, \end{aligned}$$

<sup>29</sup>With a spreadsheet it is very easy to make changes, e.g. to find out how different potentials affect the eigenenergies and wavefunctions.

<sup>30</sup>It is intended to put more details on the web site associated with this book, see introduction for the address.

<sup>31</sup>The electron mass  $m_e = 1$  in these units. Or, more strictly, its reduced mass.

<sup>32</sup>This abbreviation should not be confused with the quantum defect.

<sup>33</sup>This example is an exception to the general requirement that the solution of a second-order differential equation, such as that for a harmonic oscillator, requires a knowledge of the function at two points to define both the value of the function and its derivative.

where  $\delta$  is a small step size.<sup>32</sup>

Show that the second derivative follows by applying the procedure used to obtain the first derivative twice. Show also that substitution into eqn 4.14 gives the following expression for the value of the function at  $x + \delta$  in terms of its value at the two previous points:

$$R(x + \delta) = \left\{ 2R(x) + (\tilde{V}(x) - \tilde{E}) R(x)\delta^2 - \left(1 - \frac{\delta}{x}\right) R(x - \delta) \right\} / \left(1 + \frac{\delta}{x}\right). \quad (4.16)$$

If we start the calculation near the origin then

$$R(2\delta) = \frac{1}{2} \left\{ 2 + (\tilde{V}(\delta) - \tilde{E}) \delta^2 \right\} R(\delta),$$

$$R(3\delta) = \frac{1}{3} \left\{ 2R(2\delta) + (\tilde{V}(2\delta) - \tilde{E}) R(2\delta) \delta^2 + R(\delta) \right\},$$

etc. Note that in the first equation the value of  $R(x)$  at  $x = 2\delta$  depends only on  $R(\delta)$ —it can easily be seen why by inspection of eqn 4.16 for the case of  $x = \delta$  (for this value of  $x$  the coefficient of  $R(0)$  is zero). Thus the calculation starts at  $x = \delta$  and works outwards from there.<sup>33</sup> At all other positions ( $x > \delta$ ) the value of the function depends on its values at the two preceding points. From these recursion relations we can calculate the function at all subsequent points.

The calculated functions will not be normalised and the starting conditions can be multiplied by an arbitrary constant without affecting the eigenenergies, as will become clear from looking at the results. In the following  $R(\delta) = 1$  is the suggested choice but any starting value works.

(b) *Implementation of the numerical method using a spreadsheet program*  
Follow these instructions.

- Type the given text labels into cells A1, B1, C1, D2, E2 and F2 and the three numbers into cells D1, E1 and F1 so that it has the following form:

| A | B | C    | D   | E    | F      |
|---|---|------|-----|------|--------|
| 1 | x | V(x) | psi | 0.02 | -0.25  |
| 2 |   |      |     | step | energy |

Column A will contain the  $x$ -coordinates, the potential will be in column B and the function in column C. Cells D1, E1 and F1 contain the step size, energy and orbital angular momentum quantum number ( $l = 1$ ), respectively.

2. Put 0 into A2 and the formula `=A2+$D$1` into A3. Copy cell A3 to the block A4:A1002. (Or start with a smaller number of steps and adjust D1 accordingly.)
3. The potential diverges at  $x = 0$  so type `inf.` into B2 (or leave it blank, remembering not to refer to it).

Put the formula

$$=-2/A3 +$F$1*($F$1+1)/(A3*A3)$$

into cell B3 (as in eqn 4.15). Copy B3 into the block B4:B1002.

4. This is the crucial stage that calculates the function. Type the number 1 into cell C3. (We leave C2 blank since, as explained above, the value of the function at  $x = 0$  does not affect the solution given by the recursion relation in eqn 4.16.) Now move to cell C4 and enter the following formula for the recursion relation:

$$=(2*C3+(B3-$E$1)*C3*$D$1*$D$1 - (1-$D$1/A3)*C2) / (1+$D$1/A3).$$

Copy this into the block C5:C1002. Create an  $xy$ -plot of the wavefunction (with data points connected by smooth lines and no markers); the  $x$  series is A2:A1002 and the  $y$  series is C2:C1002. Insert this graph on the sheet.

5. Now play around with the parameters and observe the effect on the wavefunction for a particular energy.
  - (i) Show that the initial value of the function does not affect its shape, or the eigenenergy, by putting 0.1 (or any number) into cell C3.
  - (ii) Change the energy, e.g. put -0.251 into cell E1, then -0.249, and observe the change in behaviour at large

*x.* (The divergence is exponential, so even a small energy discrepancy gives a large effect.) Try the different energies again with bigger and smaller step sizes in D1. It is important to search for the eigenenergy using an appropriate range of  $x$ . The eigenenergy lies between the two values of the trial energy that give opposite divergence, i.e. upwards and downwards on the graph.

- (iii) Change F1 to 0 and find a solution for  $l = 0$ .
6. Produce a set of graphs labelled clearly with the trial energy that illustrate the principles of the numerical solution, for the two functions with  $n = 2$  and two other cases. Compare the eigenenergies with the Bohr formula.

Calculate the effective principal quantum number for each of the solutions, e.g. by putting `=SQRT(-1/E1)` in G1 (and the label `n*` in G2).

(The search for eigenenergies can be automated by exploiting the spreadsheet's ability to optimise parameters subject to constraints (e.g. the 'Goal Seek' command, or similar). Ask the program to make the last value of the function (in cell C1002) have the value of zero by adjusting the energy (cell E1). This procedure can be recorded as a macro that searches for the eigenenergies with a single button click.)

7. Implement one, or more, of the following suggestions for improving the basic method described above.
  - (i) Find the eigenenergies for a potential that tends to the Coulomb potential ( $-2/x$  in dimensionless units) at long range, like those shown in Fig. 4.7, and show that the quantum defects for that potential depend on  $l$  but only weakly on  $n$ .
  - (ii) For the potential shown in Fig. 4.7(c) compare the wavefunction in the inner and outer regions for several different energies. Give a qualitative explanation of the observed behaviour.
  - (iii) Calculate the function  $P(r) = rR(r)$  by putting `A3*C3` in cell D3 and copying this to the rest of the column.

Make a plot of  $P(r)$ ,  $R(r)$  and  $V(r)$  for at least two different values of  $n$  and  $l$ . Adjust the value in C3, as in stage 5(i), to scale the functions to convenient values for plotting on the same axes as the potential.

- (iv) Attempt a semi-quantitative calculation of the quantum defects in the lithium atom, e.g. model  $V_{\text{CF}}(r)$  as in Fig. 4.7(a) for some reasonable choice of  $r_{\text{core}}$ .<sup>34</sup>
- (v) Numerically calculate the sum of  $r^2 R^2(r) \delta$  for all the values of the function and divide through by its square root to normalise the wavefunction. With normalised functions (stored in a column of the spread-

sheet) you can calculate the electric dipole matrix elements (and their ratios), e.g.  $|\langle 3p | r | 2s \rangle|^2 / |\langle 3p | r | 1s \rangle|^2 = 36$ , as in Exercise 7.6 (not forgetting the  $\omega^3$  factor from eqn 7.23).

- (vi) Assess the accuracy of this numerical method by calculating some eigenenergies using different step sizes. (More sophisticated methods of numerical integration provided in mathematical software packages can be compared to the simple method, if desired, but the emphasis here is on the atomic physics rather than the computation. Note that methods that calculate higher derivatives of the function cannot cope with discontinuities in the potential.)

Web site:

<http://www.physics.ox.ac.uk/users/foot>

This site has answers to some of the exercises, corrections and other supplementary information.

<sup>34</sup>This simple model corresponds to all the inner electron charge being concentrated on a spherical shell. Making the transition from the inner to outer regions smoother does not make much difference to the qualitative behaviour, as you can check with the program.

# 5

## The *LS*-coupling scheme

|   |           |
|---|-----------|
| <b>5.1 Fine structure in the <i>LS</i>-coupling scheme</b>                | <b>83</b> |
| <b>5.2 The <i>jj</i>-coupling scheme</b>                                  | <b>84</b> |
| <b>5.3 Intermediate coupling: the transition between coupling schemes</b> | <b>86</b> |
| <b>5.4 Selection rules in the <i>LS</i>-coupling scheme</b>               | <b>90</b> |
| <b>5.5 The Zeeman effect</b>  | <b>90</b> |
| <b>5.6 Summary</b>  | <b>93</b> |
| <b>Further reading</b>  | <b>94</b> |
| <b>Exercises</b>  | <b>94</b> |

In this chapter we shall look at atoms with two valence electrons, e.g. alkaline earth metals such as Mg and Ca. The structures of these elements have many similarities with helium, and we shall also use the central-field approximation that was introduced for the alkalis in the previous chapter. We start with the Hamiltonian for  $N$  electrons in eqn 4.2 and insert the expression for the central potential  $V_{\text{CF}}(r)$  (eqn 4.3) to give

$$H = \sum_{i=1}^N \left[ -\frac{\hbar^2}{2m} \nabla_i^2 + V_{\text{CF}}(r_i) + \left\{ \sum_{j>i}^N \frac{e^2/4\pi\epsilon_0}{r_{ij}} - S(r_i) \right\} \right].$$

This Hamiltonian can be written as  $H = H_{\text{CF}} + H_{\text{re}}$ , where the central-field Hamiltonian  $H_{\text{CF}}$  is that defined in eqn 4.4 and

$$H_{\text{re}} = \sum_{i=1}^N \left\{ \sum_{j>i}^N \frac{e^2/4\pi\epsilon_0}{r_{ij}} - S(r_i) \right\} \quad (5.1)$$

<sup>1</sup>Choosing  $S(r)$  to account for all the repulsion between the spherically-symmetric core and the electrons outside the closed shells, and also within the core, leaves the repulsion between the two valence electrons, i.e.  $H_{\text{re}} \simeq e^2/4\pi\epsilon_0 r_{12}$ . This approximation highlights the similarity with helium (although the expectation value is evaluated with different wavefunctions). Although it simplifies the equations nicely, this is not the best approximation for accurate calculations— $S(r)$  can be chosen to include most of the direct integral (cf. Section 3.3.2). For alkali metal atoms, which we studied in the last chapter, the repulsion between electrons gives a spherically-symmetric potential, so that  $H_{\text{re}} = 0$ .

<sup>2</sup>For two p-electrons we cannot ignore  $m_l$  as we did in the treatment of  $1snl$  configurations in helium. Configurations with one, or more, s-electrons can be treated in the way already described for helium but with the radial wavefunctions calculated numerically.

is the residual electrostatic interaction. This represents that part of the repulsion not taken into account by the central field. One might think that the field left over is somehow non-central. This is not necessarily true. For configurations such as  $1s2s$  in He, or  $3s4s$  in Mg, both electrons have spherically-symmetric distributions but a central field cannot completely account for the repulsion between them—a potential  $V_{\text{CF}}(r)$  does not include the effect of the correlation of the electrons' positions that leads to the exchange integral.<sup>1</sup> The residual electrostatic interaction perturbs the electronic configurations  $n_1 l_1 n_2 l_2$  that are the eigenstates of the central field. These angular momentum eigenstates for the two electrons are products of their orbital and spin functions  $|l_1 m_{l_1} s_1 m_{s_1}\rangle |l_2 m_{l_2} s_2 m_{s_2}\rangle$  and their energy does not depend on the atom's orientation so that all the different  $m_l$  states are degenerate, e.g. the configuration  $3p4p$  has  $(2l_1 + 1)(2l_2 + 1) = 9$  degenerate combinations of  $Y_{l_1, m_1} Y_{l_2, m_2}$ .<sup>2</sup> Each of these spatial states has four spin functions associated with it, but we do not need to consider thirty-six degenerate states since the problem separates into spatial and spin parts, as in helium. Nevertheless, the direct approach would require diagonalising matrices of larger dimensions than the simple  $2 \times 2$  matrix whose determinant was given in eqn 3.17. Therefore, instead of that brute-force approach, we use the ‘look-before-you-leap’ method that starts by finding the eigenstates of the perturbation  $H_{\text{re}}$ . In that representation,  $H_{\text{re}}$  is a diagonal matrix with the eigenvalues as its diagonal elements.

The interaction between the electrons, from their electrostatic repulsion, causes their orbital angular momenta to change, i.e. in the vector model  $\mathbf{l}_1$  and  $\mathbf{l}_2$  change direction, but their magnitudes remain constant. This internal interaction does not change the total orbital angular momentum  $\mathbf{L} = \mathbf{l}_1 + \mathbf{l}_2$ , so  $\mathbf{l}_1$  and  $\mathbf{l}_2$  move (or precess) around this vector, as illustrated in Fig. 5.1. When no external torque acts on the atom,  $\mathbf{L}$  has a fixed orientation in space so its  $z$ -component  $M_L$  is also a constant of the motion ( $m_{l_1}$  and  $m_{l_2}$  are not good quantum numbers). This classical picture of conservation of total angular momentum corresponds to the quantum mechanical result that the operators  $L^2$  and  $L_z$  both commute with  $H_{\text{re}}$ :<sup>3</sup>

$$[L^2, H_{\text{re}}] = 0 \quad \text{and} \quad [L_z, H_{\text{re}}] = 0. \quad (5.2)$$

Since  $H_{\text{re}}$  does not depend on spin it must also be true that

$$[S^2, H_{\text{re}}] = 0 \quad \text{and} \quad [S_z, H_{\text{re}}] = 0. \quad (5.3)$$

Actually,  $H_{\text{re}}$  also commutes with the individual spins  $\mathbf{s}_1$  and  $\mathbf{s}_2$  but we chose eigenfunctions of  $\mathbf{S}$  to antisymmetrise the wavefunctions, as in helium—the spin eigenstates for two electrons are  $\psi_{\text{spin}}^A$  and  $\psi_{\text{spin}}^S$  for  $S = 0$  and 1, respectively.<sup>4</sup> The quantum numbers  $L, M_L, S$  and  $M_S$  have well-defined values in this Russell–Saunders or *LS*-coupling scheme. Thus the eigenstates of  $H_{\text{re}}$  are  $|LM_LSM_S\rangle$ . In the *LS*-coupling scheme the energy levels labelled by  $L$  and  $S$  are called **terms** (and there is degeneracy with respect to  $M_L$  and  $M_S$ ). We saw examples of  ${}^1L$  and  ${}^3L$  terms for the  $1snl$  configurations in helium where the *LS*-coupling scheme is a very good approximation. A more complex example is an  $nnp'n'p$  configuration, e.g.  $3p4p$  in silicon, that has six terms as follows:

$$\begin{aligned} l_1 &= 1, & l_2 &= 1 \quad \Rightarrow \quad L = 0, 1 \text{ or } 2, \\ s_1 &= \frac{1}{2}, & s_2 &= \frac{1}{2} \quad \Rightarrow \quad S = 0 \text{ or } 1; \\ \text{terms:} \quad 2S+1L &= {}^1S, {}^1P, {}^1D, {}^3S, {}^3P, {}^3D. \end{aligned}$$

The direct and exchange integrals that determine the energies of these terms are complicated to evaluate (see Woodgate (1980) for details) and here we shall simply make some empirical observations based on the terms diagrams in Figs 5.2 and 5.3. The  $(2l_1 + 1)(2l_2 + 1) = 9$  degenerate states of orbital angular momentum become the  $1 + 3 + 5 = 9$  states of  $M_L$  associated with the S, P and D terms, respectively. As in helium, linear combinations of the four degenerate spin states lead to triplet and one singlet terms but, unlike helium, triplets do not necessarily lie below singlets. Also, the  $3p^2$  configuration has fewer terms than the  $3p4p$  configuration for equivalent electrons, because of the Pauli exclusion principle (see Exercise 5.6).

In the special case of *ground* configurations of *equivalent electrons* the spin and orbital angular momentum of the lowest-energy term follow some empirical rules, called **Hund's rules**: the lowest-energy term has the largest value of  $S$  consistent with the Pauli exclusion principle.<sup>5</sup> If

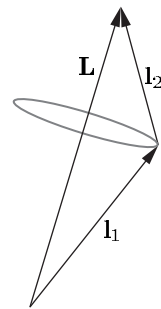


**Fig. 5.1** The residual electrostatic interaction causes  $\mathbf{l}_1$  and  $\mathbf{l}_2$  to precess around their resultant  $\mathbf{L} = \mathbf{l}_1 + \mathbf{l}_2$ .

<sup>3</sup>The proof is straightforward for the quantum operator:  $L_z = l_{1z} + l_{2z}$  since  $m_{l_1} = q$  always occurs with  $m_{l_2} = -q$  in eqn 3.30.

<sup>4</sup>The Hamiltonian  $H$  commutes with the exchange (or swap) operator  $X_{ij}$  that interchanges the labels of the particles  $i \leftrightarrow j$ ; thus states that are simultaneously eigenfunctions of both operators exist. This is obviously true for the Hamiltonian of the helium atom in eqn 3.1 (which looks the same if  $1 \leftrightarrow 2$ ), but it also holds for eqn 5.1. In general, swapping particles with the same mass and charge does not change the Hamiltonian for the electrostatic interactions of a system.

<sup>5</sup>Two electrons cannot both have the same set of quantum numbers.

**Fig. 5.2** The terms of the 3p4p configuration in silicon all lie about 6 eV above the ground state. The residual electrostatic interaction leads to energy differences of  $\sim 0.2$  eV between the terms, and the fine-structure splitting is an order of magnitude smaller, as indicated for the  $^3P$  and  $^3D$  terms. This structure is well described by the *LS*-coupling scheme.

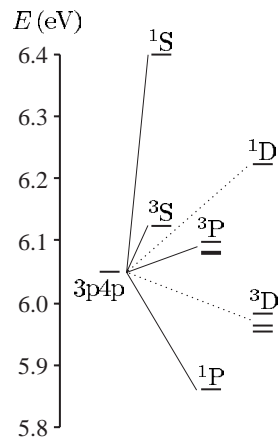
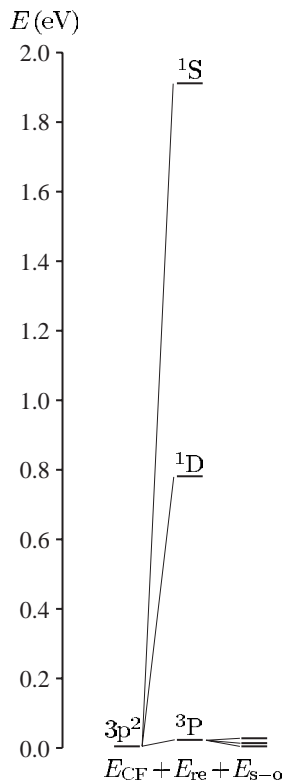


**Fig. 5.3** The energies of terms of the  $3p^2$  configuration of silicon. For equivalent electrons the Pauli exclusion principle restricts the number of terms—there are only three compared to the six in Fig. 5.2. The lowest-energy term is  $^3P$ , in accordance with Hund's rules, and this is the ground state of silicon atoms.

<sup>6</sup>Hund's rules are so commonly misapplied that it is worth spelling out that they only apply to the *lowest term* of the *ground configuration* for cases where there is only one incomplete subshell.

<sup>7</sup>The large total spin has important consequences for magnetism (Blundell 2001).



there are several such terms then the one with the largest  $L$  is lowest. The lowest term in Fig. 5.3 is consistent with these rules;<sup>6</sup> the rule says nothing about the ordering of the other terms (or about any of the terms in Fig. 5.2). Configurations of equivalent electrons are especially important since they occur in the ground configuration of elements in the periodic table, e.g. for the  $3d^6$  configuration in iron, Hund's rules give the lowest term as  $^5D$  (see Exercise 5.6).<sup>7</sup>

## 5.1 Fine structure in the LS-coupling scheme

Fine structure arises from the spin-orbit interaction for each of the unpaired electrons given by the Hamiltonian

$$H_{s-o} = \beta_1 \mathbf{s}_1 \cdot \mathbf{l}_1 + \beta_2 \mathbf{s}_2 \cdot \mathbf{l}_2.$$

For atoms with two valence electrons  $H_{s-o}$  acts as a perturbation on the states  $|LM_L S M_S\rangle$ . In the vector model, this interaction between the spin and orbital angular momentum causes  $\mathbf{L}$  and  $\mathbf{S}$  to change direction, so that neither  $L_z$  nor  $S_z$  remains constant; but the total electronic angular momentum  $\mathbf{J} = \mathbf{L} + \mathbf{S}$ , and its  $z$ -component  $J_z$ , are both constant because no external torque acts on the atom. We shall now evaluate the effect of the perturbation  $H_{s-o}$  on a term using the vector model. In the vector-model description of the  $LS$ -coupling scheme,  $\mathbf{l}_1$  and  $\mathbf{l}_2$  precess around  $\mathbf{L}$ , as shown in Fig. 5.4; the components perpendicular to this fixed direction average to zero (over time) so that only the component of these vectors along  $\mathbf{L}$  needs to be considered, e.g.  $\mathbf{l}_1 \rightarrow \{(\mathbf{l}_1 \cdot \mathbf{L}) / |\mathbf{L}|^2\} \mathbf{L}$ . The time average  $\bar{\mathbf{l}}_1 \cdot \mathbf{L}$  in the vector model becomes the expectation value  $\langle \mathbf{l}_1 \cdot \mathbf{L} \rangle$  in quantum mechanics; also we have to use  $L(L+1)$  for the magnitude-squared of the vector. Applying the same projection procedure to the spins leads to

$$\begin{aligned} H_{s-o} &= \beta_1 \frac{\langle \mathbf{s}_1 \cdot \mathbf{S} \rangle}{S(S+1)} \mathbf{S} \cdot \frac{\langle \mathbf{l}_1 \cdot \mathbf{L} \rangle}{L(L+1)} \mathbf{L} + \beta_2 \frac{\langle \mathbf{s}_2 \cdot \mathbf{S} \rangle}{S(S+1)} \mathbf{S} \cdot \frac{\langle \mathbf{l}_2 \cdot \mathbf{L} \rangle}{L(L+1)} \mathbf{L} \\ &= \beta_{LS} \mathbf{S} \cdot \mathbf{L}. \end{aligned} \quad (5.4)$$

The derivation of this equation by the vector model that argues by analogy with classical vectors can be fully justified by reference to the theory of angular momentum. It can be shown that, in the basis  $|JM_J\rangle$  of the eigenstates of a general angular momentum operator  $\mathbf{J}$  and its component  $J_z$ , the matrix elements of any vector operator  $\mathbf{V}$  are proportional to those of  $\mathbf{J}$ , i.e.  $\langle JM_J | \mathbf{V} | JM_J \rangle = c \langle JM_J | \mathbf{J} | JM_J \rangle$ .<sup>8</sup> Figure 5.5 gives a pictorial representation of why it is only the component of  $\mathbf{V}$  along  $\mathbf{J}$  that is well defined. We want to apply this result to the case where  $\mathbf{V} = \mathbf{l}_1$  or  $\mathbf{l}_2$  in the basis of eigenstates  $|LM_L\rangle$ , and analogously for the spins. For  $\langle LM_L | \mathbf{l}_1 | LM_L \rangle = c \langle LM_L | \mathbf{L} | LM_L \rangle$  the constant  $c$  is determined by taking the dot product of both sides with  $\mathbf{L}$  to give

$$c = \frac{\langle LM_L | \mathbf{l}_1 \cdot \mathbf{L} | LM_L \rangle}{\langle LM_L | \mathbf{L} \cdot \mathbf{L} | LM_L \rangle};$$

hence

$$\langle LM_L | \mathbf{l}_1 | LM_L \rangle = \frac{\langle \mathbf{l}_1 \cdot \mathbf{L} \rangle}{L(L+1)} \langle LM_L | \mathbf{L} | LM_L \rangle. \quad (5.5)$$

This is an example of the projection theorem and can also be applied to  $\mathbf{l}_2$  and to  $\mathbf{s}_1$  and  $\mathbf{s}_2$  in the basis of eigenstates  $|SM_S\rangle$ . It is clear that, for diagonal matrix elements, these quantum mechanical results give the same result of the vector model.

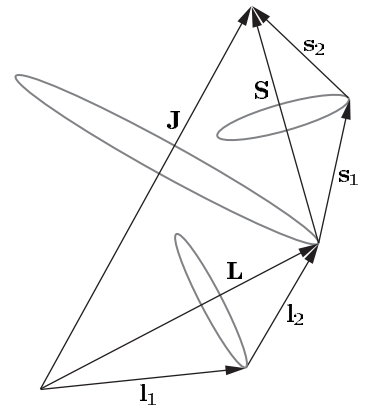


**Fig. 5.4** In the  $LS$ -coupling scheme the orbital angular momenta of the two electrons couple to give total angular momentum  $\mathbf{L} = \mathbf{l}_1 + \mathbf{l}_2$ . In the vector model  $\mathbf{l}_1$  and  $\mathbf{l}_2$  precess around  $\mathbf{L}$ ; similarly,  $\mathbf{s}_1$  and  $\mathbf{s}_2$  precess around  $\mathbf{S}$ .  $\mathbf{L}$  and  $\mathbf{S}$  precess around the total angular momentum  $\mathbf{J}$  (but more slowly than the precession of  $\mathbf{l}_1$  and  $\mathbf{l}_2$  around  $\mathbf{L}$  because the spin-orbit interaction is ‘weaker’ than the residual electrostatic interaction).

<sup>8</sup>This is a particular case of a more general result called the Wigner-Eckart theorem which is the cornerstone of the theory of angular momentum. This powerful theorem also applies to off-diagonal elements such as  $\langle JM_J | \mathbf{V} | JM'_J \rangle$ , and to more complicated operators such as those for quadrupole moments. It is used extensively in advanced atomic physics—see the ‘Further reading’ section in this chapter.

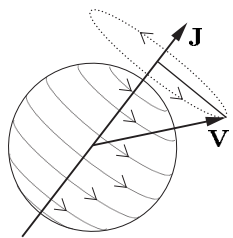


**Fig. 5.5** A pictorial representation of the project theorem for an atom, where  $\mathbf{J}$  defines the axis of the system.

Equation 5.4 has the same form as the spin-orbit interaction for the single-electron case but with capital letters rather than  $\mathbf{s} \cdot \mathbf{l}$ . The constant  $\beta_{LS}$  that gives the spin-orbit interaction for each term is related to that for the individual electrons (see Exercise 5.2). The energy shift is

$$E_{s-o} = \beta_{LS} \langle \mathbf{S} \cdot \mathbf{L} \rangle. \quad (5.6)$$

To find this energy we need to evaluate the expectation value of the operator  $\mathbf{L} \cdot \mathbf{S} = (\mathbf{J} \cdot \mathbf{J} - \mathbf{L} \cdot \mathbf{L} - \mathbf{S} \cdot \mathbf{S})/2$  for each term  $^{2S+1}L$ . Each term has  $(2S+1)(2L+1)$  degenerate states. Any linear combination of these states is also an eigenstate with the same electrostatic energy and we can use this freedom to choose suitable eigenstates and make the calculation of the (magnetic) spin-orbit interaction straightforward. We shall use the states  $|LSJM_J\rangle$ ; these are linear combinations of the basis states  $|LM_LSM_S\rangle$  but we do not need to determine their exact form to find the eigenenergies.<sup>9</sup> Evaluation of eqn 5.6 with the states  $|LSJM_J\rangle$  gives

$$E_{s-o} = \frac{\beta_{LS}}{2} \{ J(J+1) - L(L+1) - S(S+1) \}. \quad (5.7)$$

Thus the energy interval between adjacent  $J$  levels is

$$\Delta E_{FS} = E_J - E_{J-1} = \beta_{LS} J. \quad (5.8)$$

This is called the **interval rule**. For example, a  $^3P$  term ( $L=1=S$ ) has three  $J$  levels:  $^{2S+1}L_J = ^3P_0, ^3P_1, ^3P_2$  (see Fig. 5.6); and the separation between  $J=2$  and  $J=1$  is twice that between  $J=1$  and  $J=0$ . The existence of an interval rule in the fine structure of a two-electron system generally indicates that the  $LS$ -coupling scheme is a good approximation (see the ‘Exercises’ in this chapter); however, the converse is not true. The  $LS$ -coupling scheme gives a very accurate description of the energy levels of helium but the fine structure does not exhibit an interval rule (see Example 5.2 later in this chapter).

It is important not to confuse  $LS$ -coupling (or Russell–Saunders coupling) with the interaction between  $\mathbf{L}$  and  $\mathbf{S}$  given by  $\beta_{LS} \mathbf{S} \cdot \mathbf{L}$ . In this book the word *interaction* is used for real physical effects described by a Hamiltonian and *coupling* refers to the forming of linear-combination wavefunctions that are eigenstates of angular momentum operators, e.g. eigenstates of  $\mathbf{L}$  and  $\mathbf{S}$ . The  $LS$ -coupling scheme breaks down as the strength of the interaction  $\beta_{LS} \mathbf{S} \cdot \mathbf{L}$  increases relative to that of  $H_{re}$ .<sup>10</sup>

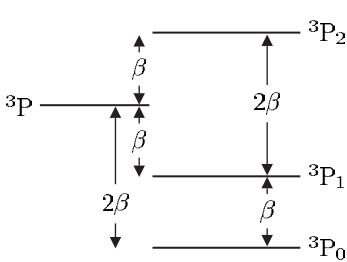


**Fig. 5.6** The fine structure of a  $^3P$  term obeys the interval rule.

<sup>10</sup>In classical mechanics the word ‘coupling’ is commonly used more loosely, e.g. for coupled pendulums, or coupled oscillators, the ‘coupling between them’ is taken to mean the ‘interaction between them’ that leads to their motions being coupled. (This coupling may take the form of a physical linkage such as a rod or spring between the two systems.)

<sup>11</sup> $E_{s-o} \sim \beta_{LS}$  and  $E_{re}$  is comparable to the exchange integral.

## 5.2 The $jj$ -coupling scheme

To calculate the fine structure in the  $LS$ -coupling scheme we treated the spin-orbit interaction as a perturbation on a term,  $^{2S+1}L$ . This is valid when  $E_{re} \gg E_{s-o}$ , which is generally true in light atoms.<sup>11</sup> The spin-orbit interaction increases with atomic number (eqn 4.13) so that it can be similar to  $E_{re}$  for heavy atoms—see Fig. 5.7. However, it is only in cases with particularly small exchange integrals that  $E_{s-o}$  exceeds  $E_{re}$ , so that the spin-orbit interaction must be considered before the residual

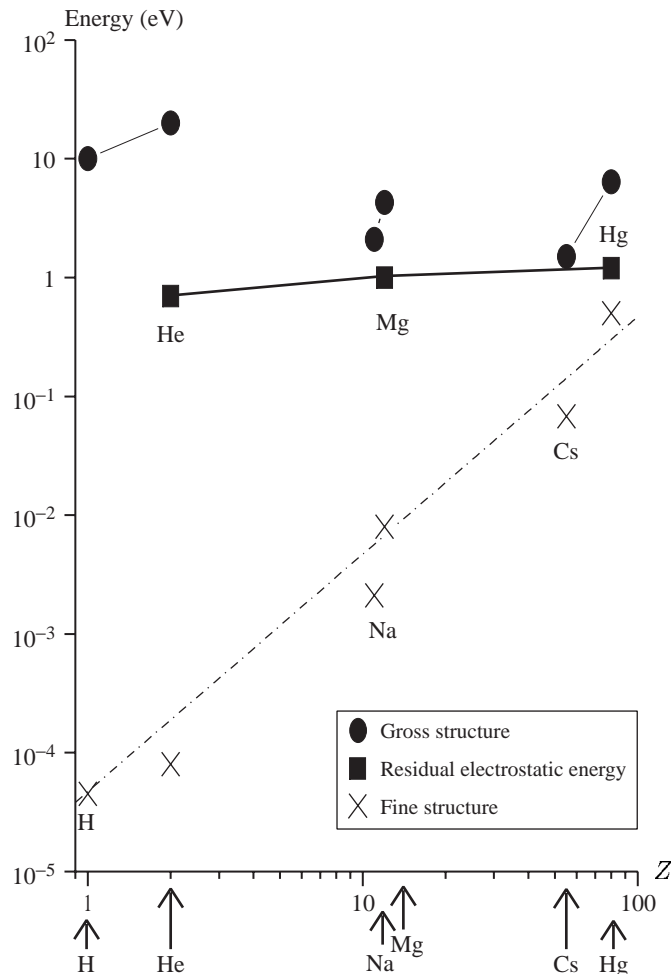


**Fig. 5.7** A plot of typical energies as a function of the atomic number  $Z$  (on logarithmic scales). A characteristic energy for the gross structure is taken as the energy required to excite an electron from the ground state to the first excited state—this is less than the ionization energy but has a similar variation with  $Z$ . The residual electrostatic interaction is the singlet–triplet separation of the lowest excited configuration in some atoms with two valence electrons. The fine structure is the splitting of the lowest p configuration. For all cases the plotted energies are fairly close to the maximum for that type of structure in neutral atoms—higher-lying configurations have smaller values.

electrostatic interaction. When  $H_{s-o}$  acts directly on a configuration it causes the  $\mathbf{l}$  and  $\mathbf{s}$  of each individual electron to be coupled together to give  $\mathbf{j}_1 = \mathbf{l}_1 + \mathbf{s}_1$  and  $\mathbf{j}_2 = \mathbf{l}_2 + \mathbf{s}_2$ ; in the vector model this corresponds to  $\mathbf{l}$  and  $\mathbf{s}$  precessing around  $\mathbf{j}$  independently of the other electrons. In this  $jj$ -coupling scheme each valence electron acts on its own, as in alkali atoms. For an sp configuration the s-electron can only have  $j_1 = 1/2$  and the p-electron has  $j_2 = 1/2$  or  $3/2$ ; so there are two levels, denoted by  $(j_1, j_2) = (1/2, 1/2)$  and  $(1/2, 3/2)$ . The residual electrostatic interaction acts as a perturbation on the  $jj$ -coupled levels; it causes the angular momenta of the electrons to be coupled to give total angular momentum  $\mathbf{J} = \mathbf{j}_1 + \mathbf{j}_2$  (as illustrated in Fig. 5.8). Since there is no external torque on the atom,  $M_J$  is also a good quantum number. For an sp configuration there are pairs of  $J$  levels for each of the two original  $jj$ -coupled levels, e.g.  $(j_1, j_2)_J = (1/2, 1/2)_0$ ,  $(1/2, 1/2)_1$  and  $(1/2, 3/2)_1$ ,  $(1/2, 3/2)_2$ . This doublet structure, shown in Fig. 5.10, contrasts with the singlets and triplets in the LS-coupling scheme.

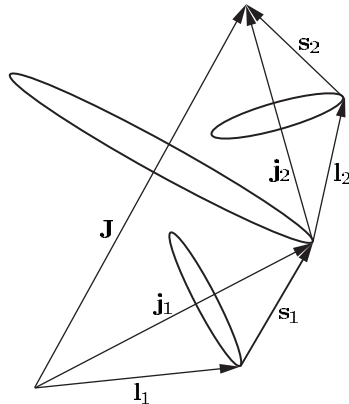


**Fig. 5.8** The  $jj$ -coupling scheme. The spin-orbit interaction energy is large compared to the  $E_{\text{re}}$ . (Cf. Fig. 5.4 for the  $LS$ -coupling scheme.)

<sup>12</sup>In both of these cases we assume an isolated configuration, i.e. that the energy separation of the different configurations in the central field is greater than the perturbation produced by either  $E_{\text{s-o}}$  or  $E_{\text{re}}$ .

In summary, the conditions for  $LS$ - and  $jj$ -coupling are as follows:<sup>12</sup>

$$\begin{aligned} LS\text{-coupling scheme: } & E_{\text{re}} \gg E_{\text{s-o}}, \\ jj\text{-coupling scheme: } & E_{\text{s-o}} \gg E_{\text{re}}. \end{aligned}$$

### 5.3 Intermediate coupling: the transition between coupling schemes

In this section we shall look at examples of angular momentum coupling schemes in two-electron systems. Figure 5.9 shows energy-level diagrams of Mg and Hg and the following example looks at the structure of these atoms.

#### Example 5.1

| 3s3p, Mg | 6s6p, Hg |
|----------|----------|
| 2.1850   | 3.76     |
| 2.1870   | 3.94     |
| 2.1911   | 4.40     |
| 3.5051   | 5.40     |

The table gives the energy levels, in units of  $10^6 \text{ m}^{-1}$  measured from the ground state, for the 3s3p configuration in magnesium ( $Z = 12$ ) and 6s6p in mercury ( $Z = 80$ ). We shall use these data to identify the levels and assign further quantum numbers.

For an sp configuration we expect  ${}^1\text{P}$  and  ${}^3\text{P}$  terms. In the case of magnesium we see that the spacings between the three lowest levels are  $2000 \text{ m}^{-1}$  and  $4100 \text{ m}^{-1}$ ; these are close to the 1 to 2 ratio expected from the interval rule for the levels with  $J = 0, 1$  and 2 that arise from the triplet. The  $LS$ -coupling scheme gives an accurate description because

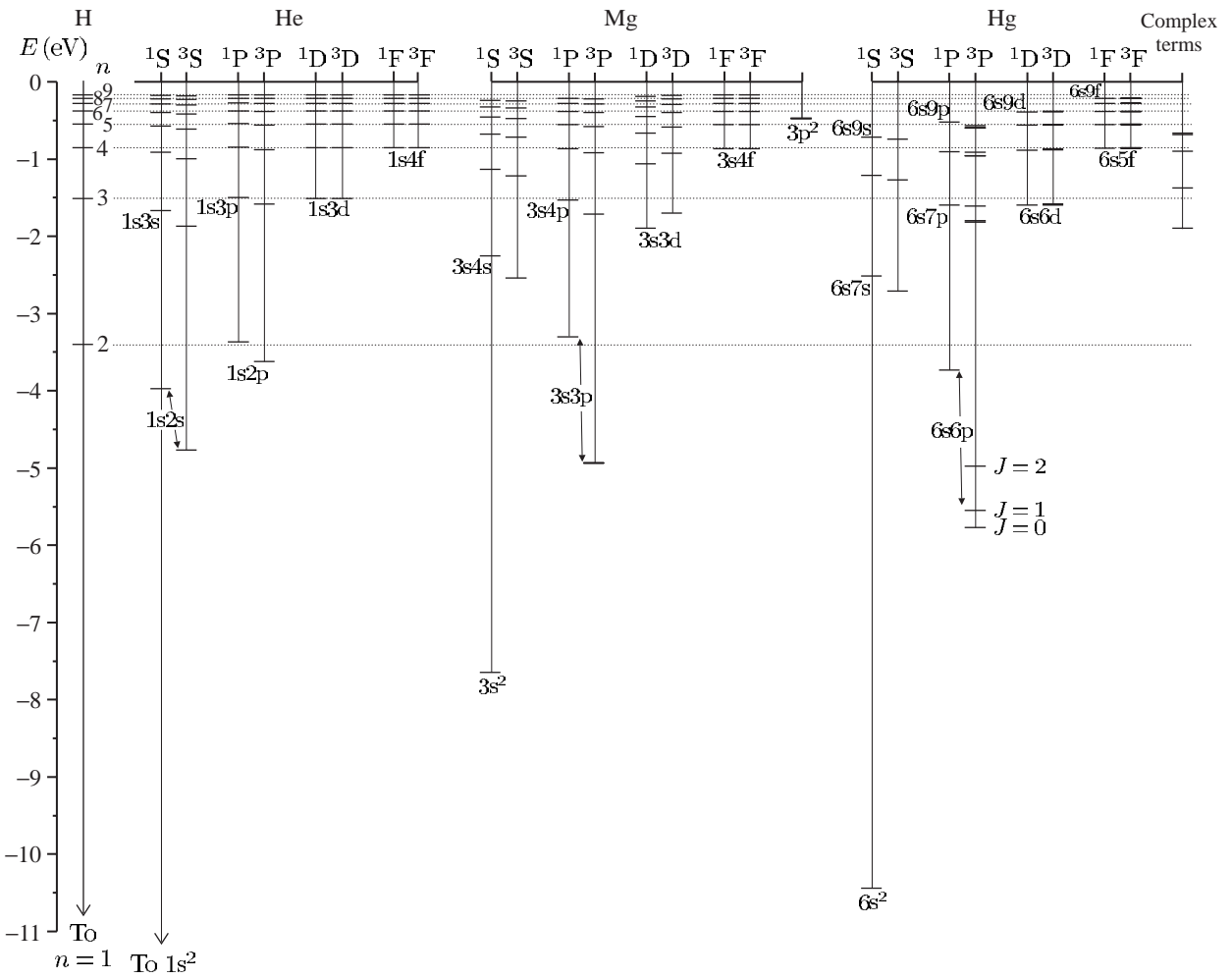


**Fig. 5.9** The terms of helium, magnesium and mercury are plotted on the same energy scale (with hydrogen on the left for comparison). The fine structure of the lighter atoms is too small to be seen on this scale and the  $LS$ -coupling scheme gives a very accurate description. This scheme gives an approximate description for the low-lying terms of mercury even though it has a much larger fine structure, e.g. for the  $6s6p$  configuration the  $E_{re} > E_{s-o}$  but the interval rule is not obeyed because the spin-orbit interaction is not very small compared to the residual electrostatic interaction. The  $1s^2$  configuration of helium is not shown; it has a binding energy of  $-24.6$  eV (see Fig. 3.4). The  $1s2s$  and  $1s2p$  configurations of helium lie close to the  $n = 2$  shell in hydrogen, and similarly the  $1s3l$  configurations lie close to the  $n = 3$  shell. In magnesium, the terms of the  $3snf$  configurations have very similar energies to those in hydrogen, but the differences get larger as  $l$  decreases. The energies of the terms in mercury have large differences from the hydrogen energy levels. Much can be learnt by carefully studying this term diagram, e.g. there is a  ${}^1P$  term which has similar energy in the three configurations:  $1s2p$ ,  $3s3p$  and  $6s6p$  in He, Mg and Hg, respectively—thus the effective quantum number  $n^*$  is similar despite the increase in  $n$ . Complex terms arise when both valence electrons are excited in Mg, e.g. the  $3p^2$  configuration, and the  $5d^96s^26p$  configuration in Hg.

<sup>13</sup>This identification of the levels is supported by other information, e.g. determination of  $J$  from the Zeeman effect and the theoretically predicted behaviour of an sp configuration shown in Fig. 5.10.

the fine structure is much smaller than the energy separation ( $E_{\text{re}} \sim 1.3 \times 10^6 \text{ m}^{-1}$ ) between the  ${}^3\text{P}$  term at  $\sim 2.2 \times 10^6 \text{ m}^{-1}$  and the  ${}^1\text{P}_1$  level at  $3.5 \times 10^6 \text{ m}^{-1}$ . In mercury the spacings of the levels, going down the table, are 0.18, 0.46 and 1.0 (in units of  $10^6 \text{ m}^{-1}$ ); these levels are not so clearly separated into a singlet and triplet. Taking the lowest three levels as  ${}^3\text{P}_0$ ,  ${}^3\text{P}_1$  and  ${}^3\text{P}_2$  we see that the interval rule is not well obeyed since  $0.46/0.18 = 2.6$  (not 2).<sup>13</sup> This deviation from the LS-coupling scheme is hardly surprising since this configuration has a spin-orbit interaction only slightly smaller than the singlet-triplet separation. However, even for this heavy atom, the LS-coupling scheme gives a closer approximation than the  $jj$ -coupling scheme.

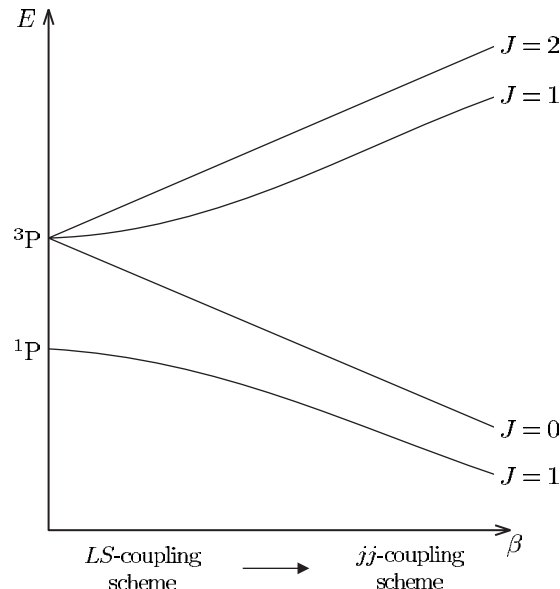


**Fig. 5.10** A theoretical plot of the energy levels that arise from an sp configuration as a function of the strength of the spin-orbit interaction parameter  $\beta$  (of the p-electron defined in eqn 2.55). For  $\beta = 0$  the two terms,  ${}^3\text{P}$  and  ${}^1\text{P}$ , have an energy separation equal to twice the exchange integral; this residual electrostatic energy is assumed to be constant and only  $\beta$  varies in the plot. As  $\beta$  increases the fine structure of the triplet becomes observable. As  $\beta$  increases further the spin-orbit and residual electrostatic interactions become comparable and the LS-coupling scheme ceases to be a good approximation: the interval rule and (LS-coupling) selection rules break down (as in mercury, see Fig. 5.9). At large  $\beta$  the  $jj$ -coupling scheme is appropriate. The operator  $\mathbf{J}$  commutes with  $H_{\text{s-o}}$  (and  $H_{\text{re}}$ ); therefore  $H_{\text{s-o}}$  only mixes levels of the same  $J$ , e.g. the two  $J = 1$  levels in this case. (The energies of the  $J = 0$  and 2 levels are straight lines because their wavefunctions do not change.) Exercise 5.8 gives an example of this transition between the two coupling schemes for  $np(n+1)s$  configurations with  $n = 3$  to 5 (that have small exchange integrals).

**Example 5.2** The 1s2p configuration in helium

| $J$ | $E$ ( $\text{m}^{-1}$ ) |
|-----|-------------------------|
| 2   | 16 908 687              |
| 1   | 16 908 694              |
| 0   | 16 908 793              |
| 1   | 17 113 500              |

The table gives the values of  $J$  and the energy, in units of  $\text{m}^{-1}$  measured from the ground state, for the levels of the 1s2p configuration in helium. The  ${}^3\text{P}$  term has a fine-structure splitting of about  $100 \text{ m}^{-1}$  that is much smaller than the singlet–triplet separation of  $10^6 \text{ m}^{-1}$  from the electrostatic interaction (twice the exchange integral). Thus the  $LS$ -coupling scheme gives an excellent description of the helium atom and the selection rules in Table 5.1 are well obeyed. But the interval rule is not obeyed—the intervals between the  $J$  levels are  $7 \text{ m}^{-1}$  and  $99 \text{ m}^{-1}$  and the fine structure is inverted. This occurs in helium because spin–spin and spin–other-orbit interactions have an energy comparable with that of the spin–orbit interaction.<sup>14</sup> However, for atoms other than helium, the rapid increase in the strength of the spin–orbit interaction with  $Z$  ensures that  $H_{\text{s–o}}$  dominates over the others. Therefore the fine structure of atoms in the  $LS$ -coupling scheme usually leads to an interval rule.

<sup>14</sup>The spin–spin interaction arises from the interaction between two magnetic dipoles (independent of any relative motion). See eqn 6.12 and its explanation.

Further examples of energy levels are given in the exercises at the end of this chapter. Figure 5.10 shows a theoretical plot of the transition from the  $LS$ - to the  $jj$ -coupling scheme for an sp configuration. Conservation of the total angular momentum means that  $J$  is a good quantum number even in the intermediate coupling regime and can always be used to label the levels. The notation  ${}^{2S+1}L_J$  for the  $LS$ -coupling scheme is often used even for systems in the intermediate regime and also for one-electron systems, e.g. 1s  ${}^2\text{S}_{1/2}$  for the ground state of hydrogen.

**Table 5.1** Selection rules for electric dipole (E1) transitions in the  $LS$ -coupling scheme. Rules 1–4 apply to all electric dipole transitions; rules 5 and 6 are obeyed only when  $L$  and  $S$  are good quantum numbers. The right-hand column gives the structure to which the rule applies.

|   |                         |   |               |
|---|-------------------------|---|---------------|
| 1 | $\Delta J = 0, \pm 1$   | $(J = 0 \leftrightarrow J' = 0)$                                | Level         |
| 2 | $\Delta M_J = 0, \pm 1$ | $(M_J = 0 \leftrightarrow M_{J'} = 0 \text{ if } \Delta J = 0)$ | State         |
| 3 | Parity changes          |   | Configuration |
| 4 | $\Delta l = \pm 1$      | One electron jump   | Configuration |
| 5 | $\Delta L = 0, \pm 1$   | $(L = 0 \leftrightarrow L' = 0)$                                | Term          |
| 6 | $\Delta S = 0$          |   | Term          |

## 5.4 Selection rules in the *LS*-coupling scheme

Table 5.1 gives the selection rules for electric dipole transitions in the *LS*-coupling scheme (listed approximately in the order of their strictness). The rule for  $J$  reflects the conservation of this quantity and is strictly obeyed; it incorporates the rule for  $\Delta j$  in eqn 2.59, but with the additional restriction  $J = 0 \leftrightarrow J' = 0$  that affects the levels with  $J = 0$  that occur in atoms with more than one valence electron. The rule for  $\Delta M_J$  follows from that for  $\Delta J$ : the emission, or absorption, of a photon cannot change the component along the  $z$ -axis by more than the change in the total atomic angular momentum. (This rule is relevant when the states are resolved, as in the Zeeman effect described in the following section.)<sup>15</sup> The requirement for an overall change in parity and the selection rule for orbital angular momentum were discussed in Section 2.2. In a configuration  $n_1 l_1 n_2 l_2 n_3 l_3 \dots n_x l_x$  only one electron changes its value of  $l$  (and may also change  $n$ ). The rule for  $\Delta L$  allows transitions such as  $3p4s\ ^3P_1 - 3p4p\ ^3P_1$ . The selection rule  $\Delta S = 0$  arises because the electric dipole operator does not act on spin, as noted in Chapter 3 on helium; as a consequence, singlets and triplets form two unconnected sets of energy levels, as shown in Fig. 3.5. Similarly, the singlet and triplet terms of magnesium shown in Fig. 5.9 could be rearranged. In the mercury atom, however, transitions with  $\Delta S = 1$  occur, such as  $6s^2\ ^1S_0 - 6s6p\ ^3P_1$ , that gives a so-called intercombination line with a wavelength of 254 nm.<sup>16</sup> This arises because this heavy atom is not accurately described by the *LS*-coupling scheme and the spin-orbit interaction mixes some  $^1P_1$  wavefunction into the wavefunction for the term that has been labelled  $^3P_1$  (this being its major component). Although not completely forbidden, the rate of this transition is considerably less than it would be for a fully-allowed transition at the same wavelength; however, the intercombination line from a mercury lamp is strong because many of the atoms excited to triplet terms will decay back to the ground state via this transition (see Fig. 5.9).<sup>17</sup>

<sup>15</sup>There is no simple physical explanation of why an  $M_J = 0$  to  $M_{J'} = 0$  transition does not occur if  $J = J'$ ; it is related to the symmetry of the dipole matrix element  $\langle \gamma J M_J = 0 | r | \gamma' J' M_J = 0 \rangle$ , where  $\gamma$  and  $\gamma'$  represent the other quantum numbers. The particular case of  $J = J' = 1$  and  $\Delta M_J = 0$  is discussed in Budker *et al.* (2003).

<sup>16</sup>This line comes from the second level in the table given in Example 5.1, since  $0.254 \mu\text{m} = 1/(3.941 \times 10^6 \text{ m}^{-1})$ .

<sup>17</sup>Intercombination lines are not observed in magnesium and helium. The relative strength of the intercombination lines and allowed transitions are tabulated in Kuhn (1969).

## 5.5 The Zeeman effect

The Zeeman effect for atoms with a single valence electron was not presented in earlier chapters to avoid repetition and that case is covered by the general expression derived here for the *LS*-coupling scheme.<sup>18</sup> The atom's magnetic moment has orbital and spin contributions (see Blundell 2001, Chapter 2):

$$\boldsymbol{\mu} = -\mu_B \mathbf{L} - g_s \mu_B \mathbf{S}. \quad (5.9)$$

The interaction of the atom with an external magnetic field is described by  $H_{ZE} = -\boldsymbol{\mu} \cdot \mathbf{B}$ . The expectation value of this Hamiltonian can be calculated in the basis  $|LSJM_J\rangle$ , provided that  $E_{ZE} \ll E_{s-o} \ll E_{re}$ , i.e. the interaction can be treated as a perturbation to the fine-structure

<sup>18</sup>Most quantum mechanics texts describe the anomalous Zeeman effect for a single valence electron that applies to the alkalis and hydrogen.

levels of the terms in the  $LS$ -coupling scheme. In the vector model we project the magnetic moment onto  $\mathbf{J}$  (see Fig. 5.11) following the same rules as are used in treating fine structure in the  $LS$ -coupling scheme (and taking  $\mathbf{B} = B\hat{\mathbf{e}}_z$ ). This gives

$$H_{ZE} = -\frac{\langle \mu \cdot \mathbf{J} \rangle}{J(J+1)} \mathbf{J} \cdot \mathbf{B} = \frac{\langle \mathbf{L} \cdot \mathbf{J} \rangle + g_s \langle \mathbf{S} \cdot \mathbf{J} \rangle}{J(J+1)} \mu_B B J_z. \quad (5.10)$$

In the vector model the quantities in angled brackets are time averages.<sup>19</sup> In a quantum description treatment the quantities  $\langle \dots \rangle$  are expectation values of the form  $\langle J M_J | \dots | J M_J \rangle$ .<sup>20</sup> In the vector model

$$E_{ZE} = g_J \mu_B B M_J, \quad (5.11)$$

where the Landé  $g$ -factor is  $g_J = \{ \langle \mathbf{L} \cdot \mathbf{J} \rangle + g_s \langle \mathbf{S} \cdot \mathbf{J} \rangle \} / \{ J(J+1) \}$ . Assuming that  $g_s \simeq 2$  (see Section 2.3.4) gives

$$g_J = \frac{3}{2} + \frac{S(S+1) - L(L+1)}{2J(J+1)}. \quad (5.12)$$

Singlet terms have  $S = 0$  so  $\mathbf{J} = \mathbf{L}$  and  $g_J = 1$  (no projection is necessary). Thus singlets all have the same Zeeman splitting between  $M_J$  states and transitions between singlet terms exhibit the normal Zeeman effect (shown in Fig. 5.12). The  $\Delta M_J = \pm 1$  transitions have frequencies shifted by  $\pm \mu_B B / h$  with respect to the  $\Delta M_J = 0$  transitions.

In atoms with two valence electrons the transitions between triplet terms exhibit the anomalous Zeeman effect. The observed pattern depends on the values of  $g_J$  and  $J$  for the upper and lower levels, as shown in Fig. 5.13. In both the normal and anomalous effects the  $\pi$ -transitions ( $\Delta M_J = 0$ ) and  $\sigma$ -transitions ( $\Delta M_J = \pm 1$ ) have the same polarizations as in the classical model in Section 1.8. Other examples in Exercises 5.10 to 5.12 show how observation of the Zeeman pattern gives information about the angular momentum coupling in the atom. (The Zeeman effect observed for the  $^2P_{1/2}-^2S_{1/2}$  and  $^2P_{3/2}-^2S_{1/2}$  transitions that arise between the fine-structure components of the alkalis and hydrogen is treated in Exercise 5.13.) Exercise 5.14 goes through the Paschen–Back effect that occurs in a strong external magnetic field—see Fig. 5.14.

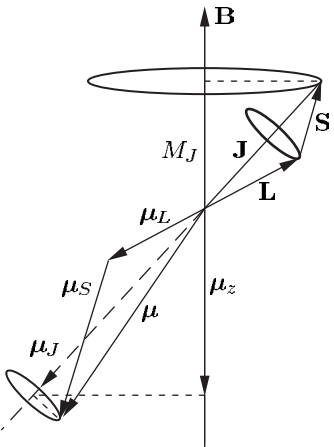


**Fig. 5.11** The projection of the contributions to the total magnetic moment from the orbital motion and the spin are projected along  $\mathbf{J}$ .

<sup>19</sup> Components perpendicular to  $\mathbf{J}$  time-average to zero.

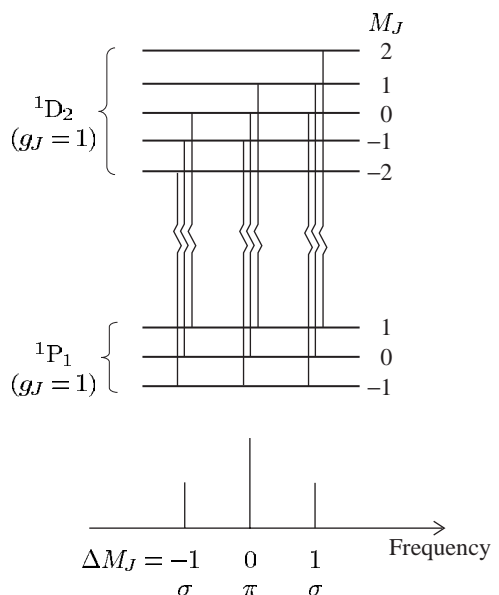
<sup>20</sup>This statement is justified by the projection theorem (Section 5.1), derived from the more general Wigner–Eckart theorem. The theorem shows that the expectation value of the vector operator  $\mathbf{L}$  is proportional to that of  $\mathbf{J}$  in the basis of eigenstates  $|JM_J\rangle$ , i.e.

$$\langle JM_J | \mathbf{L} | JM_J \rangle \propto \langle JM_J | \mathbf{J} | JM_J \rangle,$$

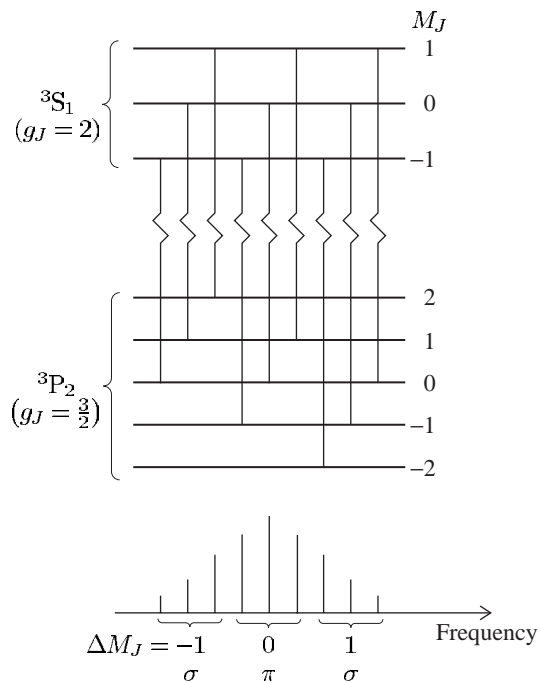
and similarly for the expectation value of  $\mathbf{S}$ . The component along the magnetic field is found by taking the dot product with  $\mathbf{B}$ :

$$\begin{aligned} \langle JM_J | \mathbf{L} \cdot \mathbf{B} | JM_J \rangle &\propto \langle JM_J | \mathbf{J} \cdot \mathbf{B} | JM_J \rangle \\ &\propto \langle JM_J | J_z | JM_J \rangle = M_J. \end{aligned}$$

**Fig. 5.12** The normal Zeeman effect on the  $1s2p\ ^1P_1$ – $1s3d\ ^1D_2$  line in helium. These levels split into three and five  $M_J$  states, respectively. Both levels have  $S = 0$  and  $g_J = 1$  so that the allowed transitions between the states give the same pattern of three components as the classical model (in Section 1.8)—this is the historical reason why it is called the normal Zeeman effect. Spectroscopists called any other pattern an anomalous Zeeman effect, although such patterns have a straightforward explanation in quantum mechanics and arise whenever  $S \neq 0$ , e.g. all atoms with one valence electron have  $S = 1/2$ . The  $\pi$ - and  $\sigma$ -components arise from  $\Delta M_J = 0$  and  $\Delta M_J = \pm 1$  transitions, respectively. (In this example of the normal Zeeman effect each component corresponds to three allowed electric dipole transitions with the *same* frequency but they are drawn with a slight horizontal separation for clarity.)



**Fig. 5.13** The anomalous Zeeman effect for the  $6s6p\ ^3P_2$ – $6s7s\ ^3S_1$  transition in Hg. The lower and upper levels both have the same number of Zeeman sub-levels (or  $M_J$  states) as the levels in Fig. 5.12, but give rise to nine separate components because the levels have different values of  $g_J$ . (The  $6s7s$  configuration happens to have higher energy than  $6s6p$ , as shown in Fig. 5.9, but the Zeeman pattern does not depend on the relative energy of the levels.)



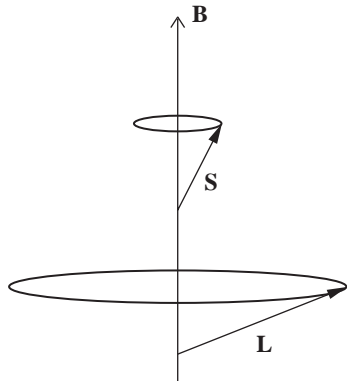


**Fig. 5.14** The Paschen–Back effect occurs in a strong external magnetic field. The spin and orbital angular momentum precess independently about the magnetic field. The states have energies given by  $E_{PB} = \mu_B B(M_L + 2M_S)$ .

## 5.6 Summary

Figure 5.15 shows the different layers of structure in a case where the  $LS$ -coupling scheme is a good approximation, i.e. the residual electrostatic interaction dominates the two magnetic interactions (spin-orbit and with an external magnetic field). The spin-orbit interaction splits terms into different  $J$  levels. The Zeeman effect of a weak magnetic field splits the levels into states of given  $M_J$ , that are also referred to as Zeeman sub-levels.

There are various ways in which this simple picture can break down.

- (a) Configuration mixing occurs if the residual electrostatic interaction

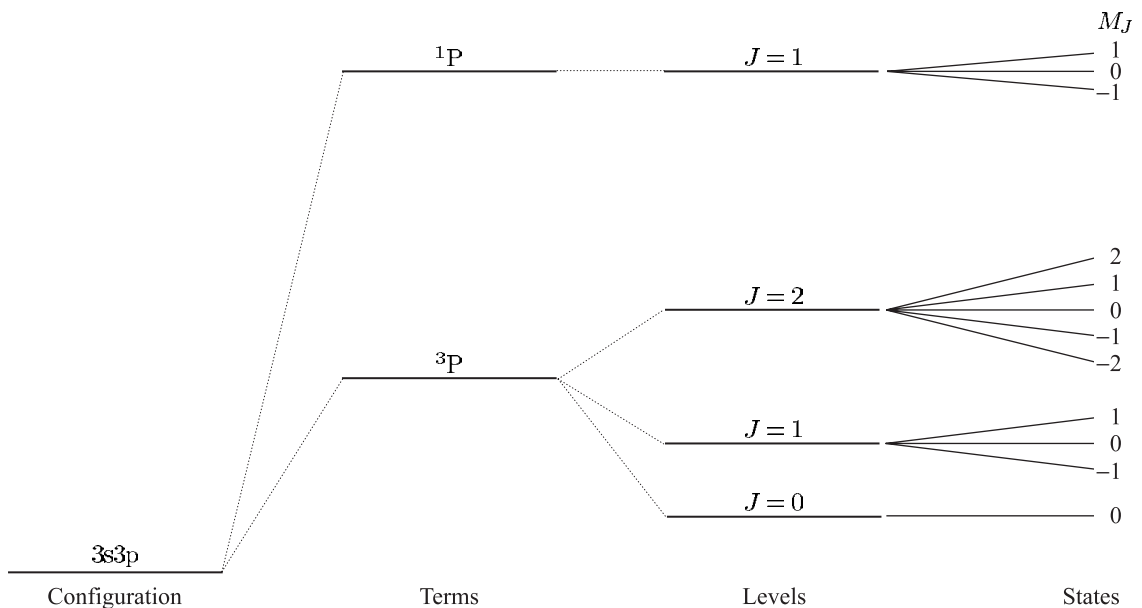


**Fig. 5.15** The hierarchy of atomic structure for the 3s3p configuration of an alkaline earth metal atom.

is not small compared to the energy gap between the configurations—this is common in atoms with complex electronic structure.

- (b) The  $jj$ -coupling scheme is a better approximation than  $LS$ -coupling or Russell–Saunders coupling when the spin–orbit interaction is greater than the residual electrostatic interaction.
- (c) The Paschen–Back effect arises when the interaction with an external magnetic field is stronger than the spin–orbit interaction (with the internal field). This condition is difficult to achieve except for atoms with a low atomic number and hence small fine structure. Similar physics arises in the study of the Zeeman effect on hyperfine structure where the transition between the low-field and high-field regimes occurs at values of the magnetic field that are easily accessible in experiments (see Section 6.3).

## Further reading

The mathematical methods that describe the way in which angular momenta couple together form the backbone of the theory of atomic structure. In this chapter the quantum mechanical operators have been treated by analogy with classical vectors (the vector model) and the Wigner–Eckart theorem was mentioned to justify the projection theorem. Graduate-level texts give a more comprehensive discussion of the quantum theory of angular momentum, e.g. Cowan (1981), Brink and Satchler (1993) and Sobelman (1996).

## Exercises

### (5.1) Description of the LS-coupling scheme

Explain what is meant by the central-field approximation and show how it leads to the concept of electron configurations. Explain how perturbations arising from (a) the residual electrostatic interactions, and (b) the magnetic spin–orbit interactions, modify the structure of an isolated multi-electron configuration in the  $LS$ -coupling limit.

### (5.2) Fine structure in the LS-coupling scheme

Show from eqn 5.4 that the  $J$  levels of the  ${}^3P$  term in the  $3s4p$  configuration have a separation given by eqn 5.8 with  $\beta_{LS} = \beta_{4p}/2$  (where  $\beta_{4p}\mathbf{s} \cdot \mathbf{l}$  is the spin–orbit interaction of the 4p-electron).

### (5.3) The LS-coupling scheme and the interval rule in calcium

Write down the ground configuration of calcium ( $Z = 20$ ). The line at 610 nm in the spectrum

of neutral calcium consists of three components at relative positions 0, 106 and 158 (in units of  $\text{cm}^{-1}$ ). Identify the terms and levels involved in these transitions.

The spectrum also contains a multiplet of six lines with wavenumbers 5019, 5033, 5055, 5125, 5139 and 5177 (in units of  $\text{cm}^{-1}$ ). Identify the terms and levels involved. Draw a diagram of the relevant energy levels and the transitions between them. What further experiment could be carried out to check the assignment of quantum numbers?

### (5.4) The LS-coupling scheme in zinc

The ground configuration of zinc is  $4s^2$ . The seven lowest energy levels of zinc are 0, 32 311, 32 501, 32 890, 46 745, 53 672 and 55 789 (in units of  $\text{cm}^{-1}$ ). Sketch an energy-level diagram that shows these levels with appropriate quantum numbers. What evidence do these levels provide that

the *LS*-coupling scheme describes this atom. Show the electric dipole transitions that are allowed between the levels.

(5.5) *The LS-coupling scheme*

| 3s3p, Mg | 3s3p, Fe <sup>14+</sup> |
|----------|-------------------------|
| 2.1850   | 23.386                  |
| 2.1870   | 23.966                  |
| 2.1911   | 25.378                  |
| 3.5051   | 35.193                  |

The table gives the energy levels, in units of  $10^6 \text{ m}^{-1}$  measured from the ground state, of the 3s3p configuration in neutral magnesium ( $Z = 12$ ) and the magnesium-like ion  $\text{Fe}^{14+}$ . Suggest, with reasons, further quantum numbers to identify these levels. Calculate the ratio of the spin-orbit interaction energies in the 3s3p configuration of Mg and  $\text{Fe}^{14+}$ , and explain your result. Discuss the occurrence in the solar spectrum of a strong line at 41.726 nm that originates from  $\text{Fe}^{14+}$ . Would you expect a corresponding transition in neutral Mg?

(5.6) *LS-coupling for configurations with equivalent electrons*

- (a) List the values of the magnetic quantum numbers  $m_{l_1}$ ,  $m_{s_1}$ ,  $m_{l_2}$  and  $m_{s_2}$  for the two electrons in an  $np^2$  configuration to show that fifteen degenerate states exist within the central-field approximation. Write down the values of  $M_L = m_{l_1} + m_{l_2}$  and  $M_S = m_{s_1} + m_{s_2}$  associated with each of these states to show that the only possible terms in the *LS*-coupling scheme are  ${}^1\text{S}$ ,  ${}^3\text{P}$  and  ${}^1\text{D}$ .
- (b) The  $1\text{s}^2 2\text{s}^2 2\text{p}^2$  configuration of doubly-ionized oxygen has levels at relative positions 0, 113, 307, 20271 and 43184 (in units of  $\text{cm}^{-1}$ ) above the ground state, and its spectrum contains weak emission lines at  $19964 \text{ cm}^{-1}$  and  $20158 \text{ cm}^{-1}$ . Identify the quantum numbers for each of the levels and discuss the extent to which the *LS*-coupling scheme describes this multiplet.
- (c) For six d-electrons, in the same sub-shell, write a list of the values of the  $m_s$  and  $m_l$  for the individual electrons corresponding to  $M_S = 2$  and  $M_L = 2$ . Briefly discuss why this is the maximum value of  $M_S$ , and why  $M_L \leq 2$  for this particular value of  $M_S$ . (Hence from

Hund's rules the  ${}^5\text{D}$  term has the lowest energy.) Specify the lowest-energy term for each of the five configurations  $nd$ ,  $nd^2$ ,  $nd^3$ ,  $nd^4$  and  $nd^5$ .

(5.7) *Transition from LS- to jj-coupling*

| 3p4s, Si |                                  | 3p7s, Si |                                  |
|----------|----------------------------------|----------|----------------------------------|
| $J$      | Energy ( $10^6 \text{ m}^{-1}$ ) | $J$      | Energy ( $10^6 \text{ m}^{-1}$ ) |
| 0        | 3.968                            | 0        | 6.154                            |
| 1        | 3.976                            | 1        | 6.160                            |
| 2        | 3.996                            | 2        | 6.182                            |
| 1        | 4.099                            | 1        | 6.188                            |

The table gives  $J$ -values and energies (in units of  $10^6 \text{ m}^{-1}$  measured from the ground state) of the levels in the 3p4s and 3p7s configurations of silicon. Suggest further quantum numbers to identify the levels.

Why do the two configurations have nearly the same value of  $E_{J=2} - E_{J=0}$  but quite different energy separations between the two  $J = 1$  states?

(5.8) *Angular-momentum coupling schemes*

| 4p5s, germanium |                                  | 5p6s, tin |                                  |
|-----------------|----------------------------------|-----------|----------------------------------|
| $J$             | Energy ( $10^6 \text{ m}^{-1}$ ) | $J$       | Energy ( $10^6 \text{ m}^{-1}$ ) |
| 0               | 3.75                             | 0         | 3.47                             |
| 1               | 3.77                             | 1         | 3.49                             |
| 2               | 3.91                             | 2         | 3.86                             |
| 1               | 4.00                             | 1         | 3.93                             |

The table gives the  $J$ -values and energies (in units of  $10^6 \text{ m}^{-1}$  measured from the ground state) of the levels in the configurations 4p5s in Ge and 5p6s in Sn. Data for the 3p4s configuration in Si are given in the previous exercise. How well does the *LS*-coupling scheme describe the energy levels of the  $np(n+1)s$  configurations with  $n = 3, 4$  and  $5$ ? Give a physical reason for the observed trends in the energy levels.

One of the  $J = 1$  levels in Ge has a Landé  $g$ -factor of  $g_J = 1.06$ . Which level would you expect this to be and why?

(5.9) *Selection rules in the LS-coupling scheme*

State the selection rules that determine the configurations, terms and levels that can be connected by an electric dipole transition in the *LS*-coupling approximation. Explain which rules are rigorous, and which depend on the validity of the coupling

scheme. Give a physical justification for three of these rules.

Which of the following are allowed for electric dipole transitions in the *LS*-coupling scheme:

- (a)  $1s2s\ ^3S_1 - 1s3d\ ^3D_1$ ,
- (b)  $1s2p\ ^3P_1 - 1s3d\ ^3D_3$ ,
- (c)  $2s2p\ ^3P_1 - 2p^2\ ^3P_1$ ,
- (d)  $3p^2\ ^3P_1 - 3p^2\ ^3P_2$ ,
- (e)  $3p^6\ ^1S_0 - 3p^53d\ ^1D_2$ ?

The transition  $4d^95s^2\ ^2D_{5/2} - 4d^{10}5p\ ^2P_{3/2}$  satisfies the selection rules for  $L$ ,  $S$  and  $J$  but it appears to involve two electrons jumping at the same time. This arises from configuration mixing—the residual electrostatic interaction may mix configurations.<sup>21</sup> The commutation relations in eqns 5.2 and 5.3 imply that  $H_{re}$  only mixes terms of the same  $L$ ,  $S$  and  $J$ . Suggest a suitable configuration that gives rise to a  $^2P_{3/2}$  level that could mix with the  $4d^{10}5p$  configuration to cause this transition.

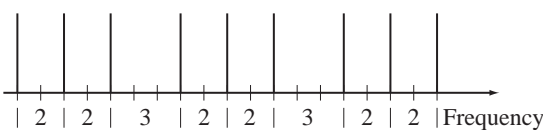
(5.10) *The anomalous Zeeman effect*

What selection rule governs  $\Delta M_J$  in electric dipole transitions? Verify that the  $^3S_1 - ^3P_2$  transition leads to the pattern of nine equally-spaced lines shown in Fig. 5.13 when viewed perpendicular to a weak magnetic field. Find the spacing for a magnetic flux density of 1 T.

(5.11) *The anomalous Zeeman effect*

Draw an energy-level diagram for the states of  $^3S_1$  and  $^3P_1$  levels in a weak magnetic field. Indicate the allowed electric dipole transitions between the Zeeman states. Draw the pattern of lines observed perpendicular to the field on a frequency scale (marked in units of  $\mu_B B/h$ ).

(5.12) *The anomalous Zeeman effect*



The above Zeeman pattern is observed for a spectral line that originates from one of the levels of a  $^3P$  term in the spectrum of a two-electron system; the numbers indicate the relative separations of the lines, observed perpendicular to the direction of the applied magnetic field. Identify  $L$ ,  $S$  and  $J$  for the two levels in the transition.<sup>22</sup>

(5.13) *The anomalous Zeeman effect in alkalis*

Note that atoms with one valence electron are not discussed explicitly in the text.

(a) Give the value of  $g_J$  for the one-electron levels  $^2S_{1/2}$ ,  $^2P_{1/2}$  and  $^2P_{3/2}$ .

(b) Show that the Zeeman pattern for the  $3s\ ^2S_{1/2} - 3p\ ^2P_{3/2}$  transition in sodium has six equally-spaced lines when viewed perpendicular to a weak magnetic field. Find the spacing (in GHz) for a magnetic flux density of 1 T. Sketch the Zeeman pattern observed along the magnetic field.

(c) Sketch the Zeeman pattern observed perpendicular to a weak magnetic field for the  $3s\ ^2S_{1/2} - 3p\ ^2P_{1/2}$  transition in sodium.

(d) The two fine-structure components of the  $3s - 3p$  transition in sodium in parts (b) and (c) have wavelengths of 589.6 nm and 589.0 nm, respectively. What magnetic flux density produces a Zeeman splitting comparable with the fine structure?<sup>23</sup>

(5.14) *The Paschen–Back effect*

In a strong magnetic field  $\mathbf{L}$  and  $\mathbf{S}$  precess independently about the field direction (as shown in Fig. 5.14), so that  $J$  and  $M_J$  are not good quantum numbers and appropriate eigenstates are  $|LM_LSM_S\rangle$ . This is called the Paschen–Back effect. In this regime the *LS*-coupling selection rules are  $\Delta M_L = 0, \pm 1$  and  $\Delta M_S = 0$  (because the electric dipole operator does not act on the spin).<sup>24</sup> Show that the Paschen–Back effect leads to a pattern of three lines with the same spacing as in the normal Zeeman effect (i.e. the same as if we completely ignore spin).<sup>25</sup>

<sup>21</sup>In the discussion of the *LS*-coupling scheme we treated  $H_{re}$  as a perturbation on a configuration and assumed that  $E_{re}$  is small compared to the energy separation between the configurations in the central field. This is rarely true for high-lying configurations of complex atoms.

<sup>22</sup>The relative intensities of the components have not been indicated.

<sup>23</sup>This value is greater than 1 T so the assumption of a weak field in part (b) is valid.

<sup>24</sup>The rules for  $J$  and  $M_J$  are not relevant in this regime.

<sup>25</sup>The Paschen–Back effect occurs when the valence electrons interact more strongly with the external magnetic field than with the orbital field in  $H_{s-o}$ . The *LS*-coupling scheme still describes this system, i.e.  $L$  and  $S$  are good quantum numbers.

# Hyperfine structure and isotope shift

# 6

## 6.1 Hyperfine structure

Up to this point we have regarded the nucleus as an object of charge  $+Ze$  and mass  $M_N$ , but it has a magnetic moment  $\mu_I$  that is related to the nuclear spin  $\mathbf{I}$  by

$$\mu_I = g_I \mu_N \mathbf{I}. \quad (6.1)$$

Comparing this to the electron's magnetic moment  $-g_s \mu_B \mathbf{s}$  we see that there is no minus sign.<sup>1</sup> Nuclei have much smaller magnetic moments than electrons; the nuclear magneton  $\mu_N$  is related to the Bohr magneton  $\mu_B$  by the electron-to-proton mass ratio:

$$\mu_N = \mu_B \frac{m_e}{M_p} \simeq \frac{\mu_B}{1836}. \quad (6.2)$$

The interaction of  $\mu_I$  with the magnetic flux density created by the atomic electrons  $\mathbf{B}_e$  gives the Hamiltonian

$$H_{\text{HFS}} = -\mu_I \cdot \mathbf{B}_e. \quad (6.3)$$

This gives rise to hyperfine structure which, as its name suggests, is smaller than fine structure. Nevertheless, it is readily observable for isotopes that have a nuclear spin ( $I \neq 0$ ).

The magnetic field at the nucleus is largest for s-electrons and we shall calculate this case first. For completeness the hyperfine structure for electrons with  $l \neq 0$  is also briefly discussed, as well as other effects that can have similar magnitude.

### 6.1.1 Hyperfine structure for s-electrons

We have previously considered the atomic electrons as having a charge distribution of density  $-e|\psi(r)|^2$ , e.g. in the interpretation of the direct integral in helium in eqn 3.15 (see also eqn 6.22). To calculate magnetic interactions we need to consider an s-electron as a distribution of magnetisation given by

$$\mathbf{M} = -g_s \mu_B \mathbf{s} |\psi(r)|^2. \quad (6.4)$$

This corresponds to the total magnetic moment of the electron  $-g_s \mu_B \mathbf{s}$  spread out so that each volume element  $d^3\mathbf{r}$  has a fraction  $|\psi(r)|^2 d^3\mathbf{r}$

|   |     |
|---|-----|
| 6.1 Hyperfine structure                   | 97  |
| 6.2 Isotope shift                         | 105 |
| 6.3 Zeeman effect and hyperfine structure | 108 |
| 6.4 Measurement of hyperfine structure    | 112 |
| Further reading                           | 119 |
| Exercises                                 | 120 |

<sup>1</sup>Nuclear magnetic moments can be parallel, or anti-parallel, to  $\mathbf{I}$ , i.e.  $g_I$  can have either sign depending on the way that the spin and orbital angular momenta of the protons and neutrons couple together inside the nucleus. The proton (that forms the nucleus of a hydrogen atom) has  $g_P > 0$  because of its positive charge. More generally, nuclear magnetic moments can be predicted from the shell model of the nucleus.

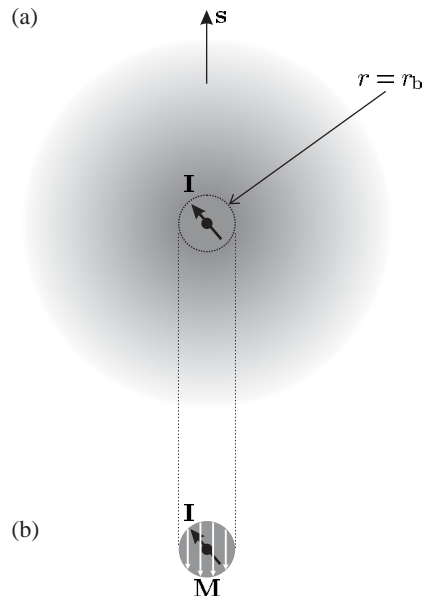


**Fig. 6.1** (a) An illustration of a nucleus with spin  $\mathbf{I}$  surrounded by the spherically-symmetric probability distribution of an s-electron. (b) That part of the s-electron distribution in the region  $r < r_b$  corresponds to a sphere of magnetisation  $\mathbf{M}$  anti-parallel to the spin  $\mathbf{s}$ .

<sup>2</sup>See Blundell (2001) or electromagnetism texts.

<sup>3</sup>This spherical boundary at  $r = r_b$  does not correspond to anything physical in the atom but is chosen for mathematical convenience. The radius  $r_b$  should be greater than the radius of the nucleus  $r_N$  and it easy to fulfil the conditions  $r_N \ll r_b \ll a_0$  since typical nuclei have a size of a few fermi ( $10^{-15}$  m), which is five orders of magnitude less than atomic radii.

<sup>4</sup>The magnetisation is a function of  $r$  only and therefore each shell has a uniform magnetisation  $\mathbf{M}(r)$  between  $r$  and  $r + dr$ . The proof that these shells do not produce a magnetic flux density at  $r = 0$  does not require  $\mathbf{M}(r)$  to be the same for all the shells, and clearly this is not the case. Alternatively, this result can be obtained by integrating the contributions to the field at the origin from the magnetic moments  $\mathbf{M}(r) d^3\mathbf{r}$  over all angles ( $\theta$  and  $\phi$ ).

of the total. For s-electrons this distribution is spherically symmetric and surrounds the nucleus, as illustrated in Fig. 6.1. To calculate the field at  $r = 0$  we shall use the result from classical electromagnetism<sup>2</sup> that inside a *uniformly* magnetised sphere the magnetic flux density is

$$\mathbf{B}_e = \frac{2}{3}\mu_0 \mathbf{M}. \quad (6.5)$$

However, we must be careful when applying this result since the distribution in eqn 6.4 is not uniform—it is a function of  $r$ . We consider the spherical distribution in two parts.

- (a) A sphere of radius  $r = r_b$ , where  $r_b \ll a_0$  so that the electronic wavefunction squared has a constant value of  $|\psi(0)|^2$  throughout this inner region, as indicated on Fig. 6.2.<sup>3</sup> From eqn 6.5 the field inside this uniformly magnetised sphere is

$$\mathbf{B}_e = -\frac{2}{3}\mu_0 g_s \mu_B |\psi_{ns}(0)|^2 \mathbf{s}. \quad (6.6)$$

- (b) The part of the distribution outside the sphere  $r > r_b$  produces no field at  $r = 0$ , as shown by the following argument. Equation 6.5 for the field inside a sphere does not depend on the radius of that sphere—it gives the same field for a sphere of radius  $r$  and a sphere of radius  $r+dr$ . Therefore the contribution from each shell of thickness  $dr$  is zero. The region  $r > r_b$  can be considered as being made up of many such shells that give no additional contribution to the field.<sup>4</sup>

Putting this field and  $\mu_I$  from eqn 6.1 into eqn 6.3 gives

$$H_{\text{HFS}} = g_I \mu_N \mathbf{I} \cdot \frac{2}{3}\mu_0 g_s \mu_B |\psi_{ns}(0)|^2 \mathbf{s} = A \mathbf{I} \cdot \mathbf{s}. \quad (6.7)$$

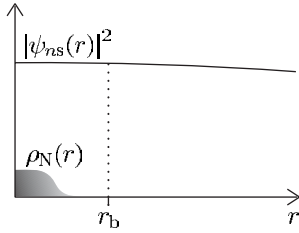


**Fig. 6.2** (a) The probability density  $|\psi(r)|^2$  of an s-electron at small distances ( $r \ll a_0$ ) is almost constant. The distribution of nuclear matter  $\rho_N(r)$  gives an indication of the nuclear radius  $r_N$ . To calculate the interaction of the nuclear magnetic moment with an s-electron the region is divided into two parts by a boundary surface of radius  $r = r_b \gg r_N$  (as also shown in Fig. 6.1). The inner region corresponds to a sphere of uniform magnetisation that produces a flux density  $\mathbf{B}_e$  at  $r = 0$ . The nuclear magnetic moment interacts with this field.

This is called the **Fermi contact interaction** since it depends on  $|\psi_{ns}(0)|^2$  being finite. It can also be expressed as

$$H_{\text{HFS}} = A \mathbf{I} \cdot \mathbf{J} \quad (6.8)$$

because  $\mathbf{J} = \mathbf{s}$  for  $l = 0$ . It is useful to write down this more general form at an early stage since it turns out that an interaction proportional to  $\mathbf{I} \cdot \mathbf{J}$  is also obtained when  $l \neq 0$ .

We have already considered the effect of an interaction proportional to a dot product of two angular momenta when looking at the spin-orbit interaction  $\beta \mathbf{S} \cdot \mathbf{L}$  (eqn 5.4). In the same way the hyperfine interaction in eqn 6.8 causes  $\mathbf{I}$  and  $\mathbf{J}$  to change direction but the total angular momentum of the atom  $\mathbf{F} = \mathbf{I} + \mathbf{J}$  remains constant. The quantities  $\mathbf{I} \cdot \mathbf{B}$  and  $\mathbf{J} \cdot \mathbf{B}$  are not constant in this precession of  $\mathbf{I}$  and  $\mathbf{J}$  around  $\mathbf{F}$ . Therefore  $M_I$  and  $M_J$  are not good quantum numbers; we use  $F$  and  $M_F$  instead and the eigenstates of  $H_{\text{HFS}}$  are  $|IJFM_F\rangle$ .<sup>5</sup> The expectation value of eqn 6.8 gives

$$E_{\text{HFS}} = A \langle \mathbf{I} \cdot \mathbf{J} \rangle = \frac{A}{2} \{F(F+1) - I(I+1) - J(J+1)\}. \quad (6.9)$$

### Example 6.1 Hyperfine structure of the 1s ${}^2\text{S}_{1/2}$ ground state of hydrogen

The lowest level of the hydrogen atom is 1s  ${}^2\text{S}_{1/2}$ , i.e.  $J = \frac{1}{2}$  and the proton has spin  $I = 1/2$  so that  $F = 0$  and 1 and these hyperfine levels have energies

$$E_{\text{HFS}} = \frac{A}{2} \{F(F+1) - I(I+1) - J(J+1)\} = \begin{cases} A/4 & \text{for } F = 1, \\ -3A/4 & \text{for } F = 0. \end{cases}$$

The splitting between the hyperfine levels is  $\Delta E_{\text{HFS}} = A$  (see Fig. 6.3). Substituting for  $|\psi_{ns}(0)|^2$  from eqn 2.22 gives

$$A = \frac{2}{3} \mu_0 g_s \mu_B g_I \mu_N \frac{Z^3}{\pi a_0^3 n^3}. \quad (6.10)$$

<sup>5</sup>This should be compared with the  $LS$ -coupling scheme where combinations of the eigenstates  $|LM_LSM_S\rangle$  form eigenstates of the spin-orbit interaction  $|LSJM_J\rangle$ . The same warning issued for  $LS$ -coupling and the spin-orbit interaction  $\beta \mathbf{S} \cdot \mathbf{L}$  also applies. It is important not to confuse  $IJ$ -coupling and the interaction  $A \mathbf{I} \cdot \mathbf{J}$ . In the  $IJ$ -coupling scheme  $I$  and  $J$  are good quantum numbers and the states are  $|IJM_IM_J\rangle$  or  $|IJFM_F\rangle$ . The latter are eigenstates of the interaction  $A \mathbf{I} \cdot \mathbf{J}$ .

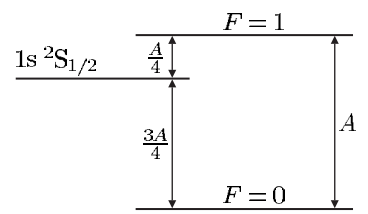


**Fig. 6.3** The splitting between the hyperfine levels in the ground state of hydrogen.

The proton has a  $g$ -factor of  $g_I = 5.6$ , so for  $n = 1 = Z$  we have

$$\frac{\Delta E_{\text{HFS}}}{h} = 1.42 \text{ GHz}.$$

<sup>6</sup>This hyperfine transition in hydrogen is the one detected in radio astronomy, where it is commonly referred to by its wavelength as the 21 cm line.

This is very close to the measured value of  $1\ 420\ 405\ 751.7667 \pm 0.0009 \text{ Hz}$ . This frequency has been measured to such extremely high precision because it forms the basis of the hydrogen maser, described below.<sup>6</sup>

### 6.1.2 Hydrogen maser

Maser stands for microwave amplification by stimulated emission of radiation and such devices were the precursors of lasers, although nowadays they are less widespread than the devices using light. Actually, lasers are usually operated as oscillators rather than amplifiers but the acronym with ‘o’ instead of ‘a’ is not so good. A schematic of a hydrogen maser is shown in Fig. 6.4; it operates in the following way.

- Molecular hydrogen is dissociated in an electrical discharge.
- Atoms effuse from the source to form a beam in an evacuated chamber.
- The atoms pass through a region with a strong magnetic field gradient (from a hexapole magnet) that focuses atoms in the upper hyperfine level ( $F = 1$ ) into a glass bulb. The atomic beam contains atoms in both hyperfine levels but the state selection by the magnet<sup>7</sup> leads to a

<sup>7</sup>This works on the same basic principle as the Stern–Gerlach experiment in Section 6.4.

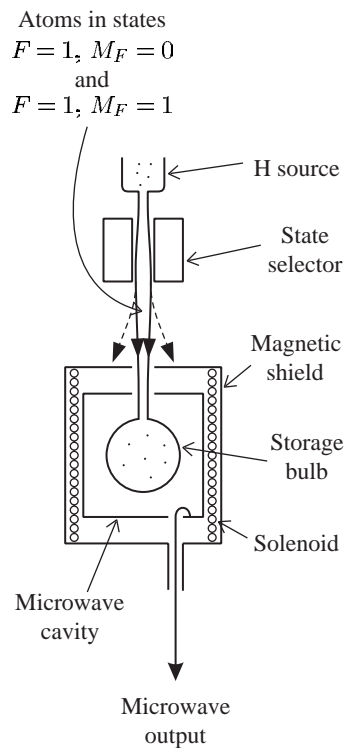


**Fig. 6.4** The hydrogen maser. The principle of operation is described in the text. A magnetic shield excludes external fields and the solenoid creates a small stable magnetic field. In this way the frequency shift produced by the Zeeman effect on the hyperfine structure is controlled (in the same way as in the atomic clock described in Section 6.4.2).

population inversion in the bulb, i.e. the population in  $F = 1$  exceeds that in  $F = 0$ ; this gives more stimulated emission than absorption and hence gain, or amplification of radiation at the frequency of the transition.

- The atoms bounce around inside the bulb—the walls have a ‘non-stick’ coating of teflon so that collisions do not change the hyperfine level.
- The surrounding microwave cavity is tuned to the 1.42 GHz hyperfine frequency and maser action occurs when there are a sufficient number of atoms in the upper level. Power builds up in a microwave cavity, some of which is coupled out through a hole in the wall of the cavity.

The maser frequency is very stable—much better than any quartz crystal used in watches. However, the output frequency is not precisely equal to the hyperfine frequency of the hydrogen atoms because of the collisions with the walls (see Section 6.4).

### 6.1.3 Hyperfine structure for $l \neq 0$

Electrons with  $l \neq 0$ , orbiting around the nucleus, give a magnetic field

$$\mathbf{B}_e = \frac{\mu_0}{4\pi} \left\{ \frac{-e\mathbf{v} \times (-\mathbf{r})}{r^3} - \frac{\boldsymbol{\mu}_e - 3(\boldsymbol{\mu}_e \cdot \hat{\mathbf{r}})\hat{\mathbf{r}}}{r^3} \right\}, \quad (6.11)$$

where  $-\mathbf{r}$  gives the position of the nucleus with respect to the orbiting electron. The first term arises from the orbital motion.<sup>8</sup> It contains the cross-product of  $-e\mathbf{v}$  with  $-\mathbf{r}$ , the position vector of the nucleus relative to the electron, and  $-e\mathbf{r} \times \mathbf{v} = -2\mu_B \mathbf{l}$ . The second term is just the magnetic field produced by the spin dipole moment of the electron  $\boldsymbol{\mu}_e = -2\mu_B \mathbf{s}$  (taking  $g_s = 2$ ) at a position  $-\mathbf{r}$  with respect to the dipole.<sup>9</sup> Thus we can write

$$\mathbf{B}_e = -2 \frac{\mu_0 \mu_B}{4\pi r^3} \left\{ \mathbf{l} - \mathbf{s} + \frac{3(\mathbf{s} \cdot \mathbf{r})\mathbf{r}}{r^2} \right\}. \quad (6.12)$$

This combination of orbital and spin-dipolar fields has a complicated vector form.<sup>10</sup> However, we can again use the argument (in Section 5.1) that in the vector model there is rapid precession around  $\mathbf{J}$ , and any components perpendicular to this quantisation axis average to zero, so that only components along  $\mathbf{J}$  have a non-zero time-averaged value.<sup>11</sup> The projection factor can be evaluated exactly (Woodgate 1980) but we shall assume that it is approximately unity giving

$$\mathbf{B}_e \sim -2 \frac{\mu_0}{4\pi} \left\langle \frac{\mu_B}{r^3} \right\rangle \mathbf{J}. \quad (6.13)$$

Thus from eqns 6.1 and 6.3 we find that the hyperfine interaction for electrons with  $l \neq 0$  has the same form  $A\mathbf{l} \cdot \mathbf{J}$  as eqn 6.8. This form of interaction leads to the following interval rule for hyperfine structure:

$$E_F - E_{F-1} = AF. \quad (6.14)$$

This interval rule is derived in the same way as eqn 5.8 for fine structure but with  $I$ ,  $J$  and  $F$  instead of  $L$ ,  $S$  and  $J$ , as shown in Exercise 6.5.

<sup>8</sup>This resembles the Biot–Savart law of electromagnetism:

$$\mathbf{B} = \frac{\mu_0}{4\pi} \frac{I d\mathbf{s} \times \mathbf{r}}{r^3}.$$

Roughly speaking, the displacement along the direction of the current is related to the electron’s velocity by  $d\mathbf{s} = \mathbf{v} dt$ , where  $dt$  is a small increment of time, and the current is related to the charge by  $I dt = Q$ .

The spin-orbit interaction can be very crudely ‘justified’ in a similar way, by saying that the electron ‘sees’ the nucleus of charge  $+Ze$  moving round it; for a hydrogenic system this simplistic argument gives

$$\mathbf{B}_{\text{orbital}} = -2Z \frac{\mu_0}{4\pi} \frac{\mu_B}{r^3} \mathbf{l}.$$

The Thomas precession factor does not occur in hyperfine structure because the frame of reference is not rotating.

<sup>9</sup>See Blundell (2001).

<sup>10</sup>The same two contributions to the field also occur in the fine structure of helium; the field produced at the position of one electron by the orbital motion of the other electron is called the spin-other-orbit interaction, and a spin–spin interaction arises from the field produced by the magnetic dipole of one electron at the other electron.

<sup>11</sup>In quantum mechanics this corresponds to saying that the matrix elements of any vector operator in the eigenbasis  $|JM_J\rangle$  are proportional to  $\mathbf{J}$ , i.e.  $\langle JM_J | \mathbf{B}_e | JM_J \rangle \propto \langle JM_J | \mathbf{J} | JM_J \rangle$ . This is a consequence of the Wigner–Eckart theorem that was mentioned in Section 5.1.

**Table 6.1** Comparison of fine and hyperfine structures.

|                        | Fine structure in the<br><i>LS</i> -coupling scheme   | Hyperfine structure in the<br><i>IJ</i> -coupling scheme           |
|------------------------|---|--|
| Interaction            | $\beta \mathbf{L} \cdot \mathbf{S}$                   | $A \mathbf{I} \cdot \mathbf{J}$                                    |
| Total angular momentum | $\mathbf{J} = \mathbf{L} + \mathbf{S}$                | $\mathbf{F} = \mathbf{I} + \mathbf{J}$                             |
| Eigenstates            | $ LSJM_J\rangle$                                      | $ IJFM_F\rangle$   |
| Energy, $E$            | $\frac{\beta}{2} \{ J(J+1) - L(L+1) - S(S+1) \}$      | $\frac{A}{2} \{ F(F+1) - I(I+1) - J(J+1) \}$                       |
| Interval rule          | $E_J - E_{J-1} = \beta J$<br>(if $E_{s-o} < E_{re}$ ) | $E_F - E_{F-1} = AF$<br>(if $A \gg \Delta E_{\text{Quadrupole}}$ ) |

<sup>12</sup>This interval rule for magnetic dipole hyperfine structure can be disrupted by the quadrupole interaction. Some nuclei are not spherical and their charge distribution has a quadrupole moment that interacts with the gradient of the electric field at the nucleus. This electric quadrupole interaction turns out to have an energy comparable to the interaction of the magnetic dipole moment  $\mu_I$  with  $\mathbf{B}_e$ . Nuclei, and atoms, do not have static electric dipole moments (for states of definite parity).

That exercise also shows how this rule can be used to deduce  $F$  and hence the nuclear spin  $I$  from a given hyperfine structure.<sup>12</sup>

The hyperfine-structure constant  $A(n, l, j)$  is smaller for  $l > 0$  than for  $l = 0$  and the same  $n$ . Exact calculation shows that the hyperfine-structure constants of the hydrogenic levels np  $^2\text{P}_{1/2}$  and ns  $^2\text{S}_{1/2}$  are in the ratio

$$\frac{A(n^2\text{P}_{1/2})}{A(n^2\text{S}_{1/2})} = \frac{1}{3}. \quad (6.15)$$

This ratio is smaller in the alkalis, e.g.  $\sim 1/10$  in the examples below, because the closed shells of electrons screen the nuclear charge more effectively for p-electrons than for s-electrons.

### 6.1.4 Comparison of hyperfine and fine structures

The analogy between hyperfine and fine structures is summarised in Table 6.1.

For fine structure in the alkalis we found the Landé formula (eqn 4.13)

$$E_{\text{FS}} \sim \frac{Z_i^2 Z_o^2}{(n^*)^3} \alpha^2 hc R_\infty. \quad (6.16)$$

The  $Z^4$  scaling for a hydrogenic system is reduced to  $E_{\text{FS}} \propto Z^2$  for neutral atoms since the effective outer atomic number is  $Z_o = 1$ , and  $Z_i \sim Z$  gives a reasonable approximation in the inner region. Applying similar considerations to the hyperfine structure shows that the dependence on  $Z^3$  in eqn 6.10 reduces to

$$E_{\text{HFS}} \sim \frac{Z_i Z_o^2}{(n^*)^3} \frac{m_e}{M_p} \alpha^2 hc R_\infty. \quad (6.17)$$

The mass ratio arises from  $\mu_N/\mu_B = m_e/M_p$ . Hyperfine structure scales as  $Z$ , whereas fine structure scales as  $Z^2$ ; thus  $E_{\text{HFS}}$  varies much less than  $E_{\text{FS}}$ , as the following comparison of the splittings for Na and Cs shows.

| Na, $Z = 11$                           | Cs, $Z = 55$                           |
|--|--|
| $E(3p\ ^2P_{3/2}) - E(3p\ ^2P_{1/2}),$ | $E(6p\ ^2P_{3/2}) - E(6p\ ^2P_{1/2}),$ |
| $\Delta f_{FS} = 510 \text{ GHz}$      | $\Delta f_{FS} = 16\,600 \text{ GHz}$  |
| For the ground state $3s\ ^2S_{1/2},$  | For the ground state $6s\ ^2S_{1/2},$  |
| $\Delta f_{HFS} = 1.8 \text{ GHz}$     | $\Delta f_{HFS} = 9.2 \text{ GHz}$     |
| For $3p\ ^2P_{1/2},$                   | For $6p\ ^2P_{1/2},$                   |
| $\Delta f_{HFS} = 0.18 \text{ GHz}$    | $\Delta f_{HFS} = 1.2 \text{ GHz}$     |

The hyperfine splitting of the ground states and the fine-structure splitting of the first excited states are indicated on the plot of energies against  $Z$  in Fig. 6.5. The values shown are only a guideline; e.g. different

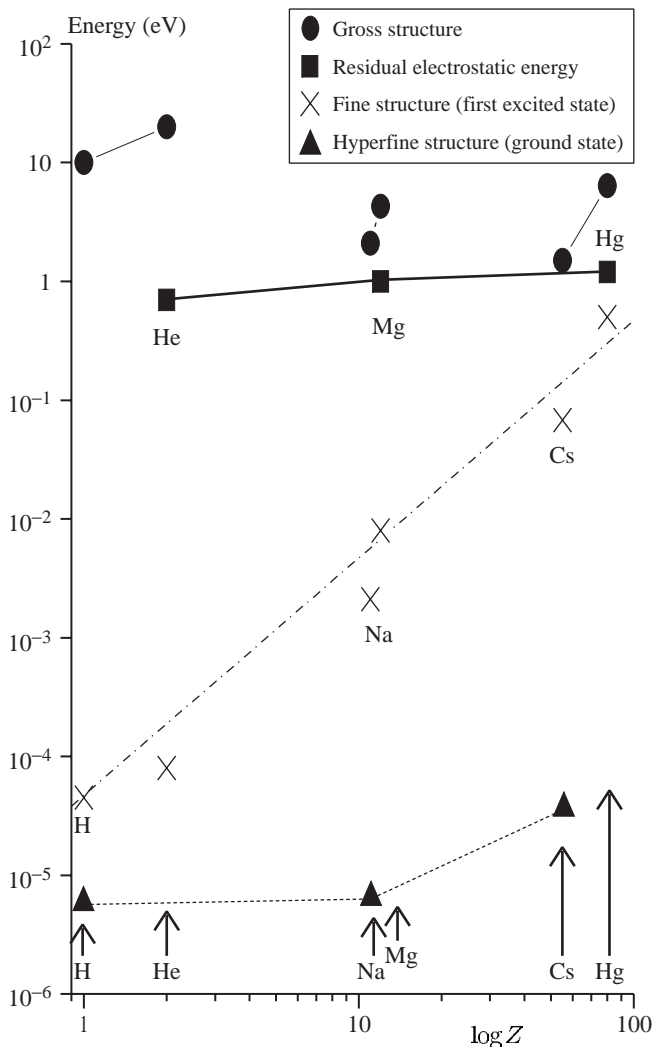


**Fig. 6.5** A logarithmic plot of the energy of various structures against atomic number  $Z$ ; the hyperfine splitting of the ground state is plotted with data from Fig. 5.7. All the points are close to the maximum values of that quantity for low-lying configurations, terms, levels and hyperfine levels (as appropriate) of neutral atoms with one or two valence electrons, and these illustrate how these quantities vary with  $Z$ . This is only a rough guideline in particular cases; higher-lying configurations in neutral atoms have smaller values and in highly-ionized systems the structures have higher energies.

<sup>13</sup>Two-photon spectroscopy is explained in Section 8.4

<sup>14</sup>It is straightforward to apply the interval rule even when both the lower and upper levels have hyperfine structure.

isotopes of the same element have different hyperfine splittings because the magnetic moment  $\mu_I$  depends on the nuclear structure. The ground state of hydrogen has an especially large hyperfine structure that is greater than that of lithium ( $Z = 3$ ), see Exercise 6.3.

### Example 6.2 Hyperfine structure of europium

Figure 6.6 shows an experimental trace of a  $4f^76s^2\ ^8S_{7/2} - 4f^76s6d\ ^8D_{11/2}$  transition in europium obtained by Doppler-free laser spectroscopy (Kronfeldt and Weber 1991).<sup>13</sup> The ground level ( $4f^76s^2\ ^8S_{7/2}$ ) has a small hyperfine structure, from the unpaired f-electrons, that causes the small splitting of the peaks labelled 3, 4, 5, 6 and 7 (barely resolved for peak 3); however, this detail will not be considered further in the following analysis,<sup>14</sup> which concentrates on the much larger hyperfine structure of the  $4f^76s6d\ ^8D_{11/2}$  level that arises mainly from the unpaired s-electron. The spectrum has a dozen main peaks. Since  $J = 11/2$  a naive analysis might suppose that  $I \geq J$  and so the observed peaks arise from transitions to the  $2J + 1 = 12$  hyperfine levels expected in this case, i.e.  $F = I + J, I + J - 1, \dots, I - J + 1$  and  $I - J$ . This is obviously wrong for various reasons: it is clear that the pattern of all twelve peaks does not fit any simple rule and also this element has two stable isotopes  $^{151}\text{Eu}$  and  $^{153}\text{Eu}$ . As indicated by their similar shape, the peaks labelled 3, 4, 5, 6 and 7 all belong to same isotope ( $^{151}\text{Eu}$ ) and this can be verified by the interval rule as shown in the following table.

| I<br>Peak | II<br>Position (GHz) | III<br>$\frac{E_F-1-E_F}{h}$ (GHz) | IV<br>Ratio of differences, $x$ | V<br>$\frac{x}{x-1}$ |
|-----------|----------------------|------------------------------------|---------------------------------|----------------------|
| 3         | 21.96                | —                                  | —                               | —                    |
| 4         | 19.14                | 2.82                               | —                               | —                    |
| 5         | 15.61                | 3.53                               | 1.252                           | 5.0                  |
| 6         | 11.37                | 4.24                               | 1.201                           | 6.0                  |
| 7         | 6.42                 | 4.95                               | 1.167                           | 7.0                  |
| g         | 0.77                 | 5.65                               | 1.141                           | 8.1                  |

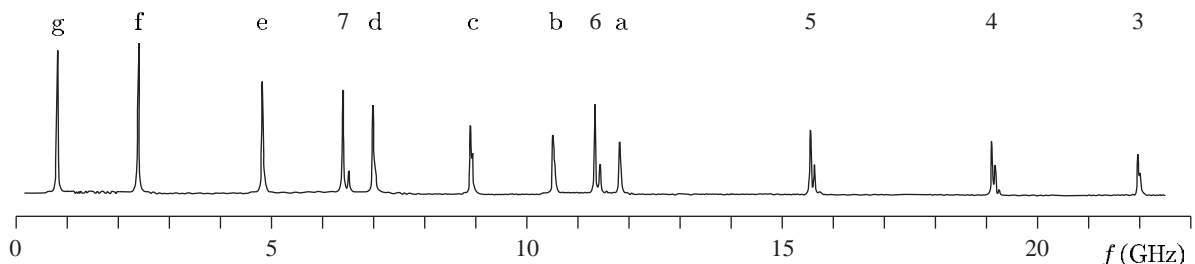


**Fig. 6.6** An experimental trace of a  $4f^76s^2\ ^8S_{7/2} - 4f^76s6d\ ^8D_{11/2}$  transition in europium obtained by Doppler-free laser spectroscopy (Kronfeldt and Weber 1991). Copyright 1991 by the American Physical Society.

Column II in this table gives the positions of the peaks<sup>15</sup> measured from Fig. 6.6. Column III gives the difference between the frequencies in column II (the intervals between the peaks), e.g.  $21.96 - 19.14 = 2.82$ . Column IV gives the ratio of the intervals in column III, e.g.  $3.53/2.82 = 1.252$ . The interval rule for hyperfine structure in eqn 6.14 predicts that

$$x = \frac{E_F - E_{F-1}}{E_{F-1} - E_{F-2}} = \frac{AF}{A(F-1)} = \frac{F}{F-1}. \quad (6.18)$$

Rearrangement gives the total angular momentum  $F$  in terms of  $x$  as

$$F = \frac{x}{x-1}. \quad (6.19)$$

The numerical values of this quantity in column V (that have been calculated from the data by the above procedure) confirm that  $F$  has the value used to label the peaks. Moreover, we find that peak g fits the interval rule with  $F = 8$ . Thus, since this level has  $J = 11/2$ , this isotope ( $^{151}\text{Eu}$ ) must have a nuclear spin of  $I = 5/2$ —this follows from the rules for the addition of angular momentum which allow values of  $F$  between  $F_{\max} = I + J = 8$  and  $F_{\min} = |I - J| = 3$ .<sup>16</sup> Exercise 6.5 shows that the other six peaks a to f also obey an interval rule and they all belong to another isotope ( $^{153}\text{Eu}$ ).

<sup>15</sup>The highest peak in the case of the closely-spaced pairs.

## 6.2 Isotope shift

In addition to the (magnetic dipole) hyperfine interaction in eqn 6.8 there are several other effects that may have a comparable magnitude (or might even be larger).<sup>17</sup> This section describes two effects that lead to a difference in the frequency of the spectral lines emitted by different isotopes of an element.

<sup>16</sup>The proof of this result using operators can be found in quantum mechanics texts. It can be justified by analogy with vector addition: the maximum value occurs when the two angular momentum vectors point in the same direction and the minimum value when they are anti-parallel.

### 6.2.1 Mass effects

In Chapter 1 we saw that, in the Bohr model, energies are proportional to the reduced mass of the electron, given in eqn 1.13, and this scaling also applies to the solutions of the Schrödinger equation. Thus a transition between two levels of energies  $E_1$  and  $E_2$  has a wavenumber  $\tilde{\nu} = (E_2 - E_1)/hc$  that is related to  $\tilde{\nu}_\infty$ , the value for a ‘theoretical’ atom with a nucleus of infinite mass, by

$$\tilde{\nu} = \tilde{\nu}_\infty \times \frac{M_N}{m_e + M_N}, \quad (6.20)$$

where  $M_N$  is the mass of the nucleus. However,  $\tilde{\nu}_\infty$  cannot be measured. What we can observe is the difference in wavenumbers between two isotopes of an element, e.g. hydrogen and deuterium for  $Z = 1$ . In general, for two isotopes with atomic masses  $A'$  and  $A''$ , we can make the approximation  $M_N = A'M_p$  or  $A''M_p$ , so that<sup>18</sup>

<sup>17</sup>The quadrupole interaction was noted in Table 6.1, but will not be discussed further.

<sup>18</sup>Strictly, atomic mass units should be used rather than  $M_p$ . The difference between the mass of an atom and its nucleus equals the mass of the electrons including the contribution from their binding energy. However, for this estimate we do not need to know  $M_N$  precisely.

$$\begin{aligned}\Delta\tilde{\nu}_{\text{Mass}} &= \tilde{\nu}_{A''} - \tilde{\nu}_{A'} = \frac{\tilde{\nu}_\infty}{1 + m_e/A''M_p} - \frac{\tilde{\nu}_\infty}{1 + m_e/A'M_p} \\ &\simeq \tilde{\nu}_\infty \left\{ 1 - \frac{m_e}{A''M_p} - \left( 1 - \frac{m_e}{A'M_p} \right) \right\} \\ &\simeq \frac{m_e}{M_p} \frac{\delta A}{A' A''} \tilde{\nu}_\infty.\end{aligned}\quad (6.21)$$

This is called the **normal mass shift** and the energy difference  $hc\Delta\tilde{\nu}_{\text{Mass}}$  is plotted in Fig. 6.7, assuming that  $\delta A = 1$ ,  $A \simeq A' \simeq 2Z$ , and that  $E_2 - E_1 \simeq 2\text{eV}$  for a visible transition. The mass shift is largest for hydrogen and deuterium where  $A'' = 2A' \simeq 2M_p$  (Exercise 1.1); it is larger than the fine structure in this case. For atoms with more than one electron there is also a **specific mass shift** that has the same order of magnitude as the normal mass effect, but is much harder to calculate.<sup>19</sup> Equation 6.20 shows that the mass shift always leads to the heavier isotope having a higher wavenumber—by definition the reduced mass of the electron is less than  $m_e$ , and as the atomic mass increases the energy levels become closer to those of the theoretical atom with a nucleus of infinite mass.

### 6.2.2 Volume shift

Although nuclei have radii which are small compared to the scale of electronic wavefunctions,  $r_N \ll a_0$ , the nuclear size has a measurable effect on spectral lines. This finite nuclear size effect can be calculated as a perturbation in two complementary ways. A simple method uses Gauss' theorem to determine how the electric field of the nuclear charge distribution differs from  $-Ze/4\pi\epsilon_0 r^2$  for  $r \lesssim r_N$  (see Woodgate 1980).

Alternatively, to calculate the electrostatic interaction of two overlapping charge distributions (as in eqn 3.15, for example) we can equally well find the energy of the nucleus in the potential created by the electronic charge distribution (in an analogous way to the calculation of the magnetic field at the nucleus created by s-electrons in Section 6.1.1). The charge distributions for an s-electron and a typical nucleus closely resemble those shown in Fig. 6.2.<sup>20</sup> In the region close to the nucleus there is a uniform electronic charge density

$$\rho_e = -e |\psi(0)|^2. \quad (6.22)$$

Using Gauss' theorem to find the electric field at the surface of a sphere of radius  $r$  in a region of uniform charge density shows that the electric field is proportional to  $r$ . Integration gives the electrostatic potential:

$$\phi_e(r) = -\frac{\rho_e r^2}{6\epsilon_0}. \quad (6.23)$$

The zero of the potential has been chosen to be  $\phi_e(0) = 0$ . Although this is not the usual convention the difference in energy that we calculate does not depend on this choice.<sup>21</sup> With this convention a point-like nucleus

<sup>19</sup>See Exercise 6.12 and also Woodgate (1980).

<sup>20</sup>For hyperfine structure we were concerned with the nuclear magnetic moment arising from the constituent protons and neutrons. To calculate the electrostatic effect of a finite nuclear size, however, we need to consider the charge distribution of the nucleus, i.e. the distribution of protons. This has a shape that is similar to, but not the same as, the distribution of nuclear matter (see nuclear physics texts). The essential point for atomic structure is that all the nuclear distributions extend over a distance small compared to the electronic wavefunctions, as illustrated in Fig. 6.2.

<sup>21</sup>If this worries you, then put an arbitrary constant  $\phi_0$  in the equation, arising from the integration of the electric field to give the electrostatic potential, and show that the answer does not depend on  $\phi_0$ .

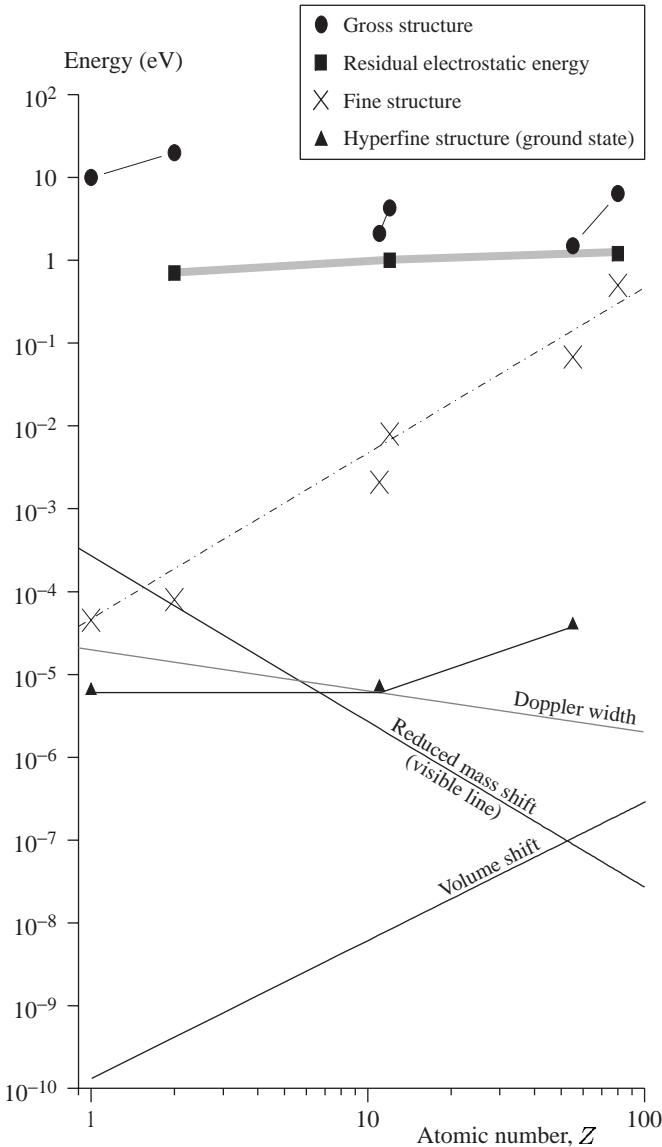


**Fig. 6.7** A plot of the energy of various structures against atomic number  $Z$ . This includes the data shown on Fig. 6.5, but the scale has been changed to show the effects of lower energy. The contributions to the isotope shift from the mass and volume effects are plotted using eqns 6.21 and 6.26, respectively. Although these effects arise from completely independent physical effects, they have a similar magnitude for medium-heavy elements (and can be comparable to the magnetic dipole hyperfine structure of an excited state, which is considerably smaller than the ground-state splitting). The Doppler width for a visible transition with energy 2 eV is plotted to indicate the typical experimental limit in spectroscopic measurements using light; the line has a slope of  $-1/2$  because  $\Delta f_D \propto 1/\sqrt{M}$  and the atomic mass  $A$  is approximately  $A \sim 2Z$ , so that  $\Delta f_D \propto Z^{-1/2}$  (see eqn 8.7). For hydrogen the Doppler width is almost equal to the fine-structure splitting (and much larger than hyperfine structure). The Doppler broadening of visible lines in sodium is comparable with its hyperfine structure; for heavier elements the ground-state hyperfine structure can be resolved in a vapour at room temperature. This gives an indication of the importance of Doppler-free techniques described in Chapter 8. The Zeeman effect of a magnetic flux density of  $B = 1$  T is equivalent to a frequency shift of 14 GHz.

has zero potential energy, and for a distribution of nuclear charge  $\rho_N(r)$  the potential energy is

$$\begin{aligned} E_{\text{Vol}} &= \iiint \rho_N \phi_e d^3r = \frac{e}{6\epsilon_0} |\psi(0)|^2 \iiint \rho_N r^2 d^3r \\ &= \frac{Ze^2}{6\epsilon_0} |\psi(0)|^2 \langle r_N^2 \rangle. \end{aligned} \quad (6.24)$$

The integral gives the mean-square charge radius of the nucleus  $\langle r_N^2 \rangle$  times the charge  $Ze$ . This volume effect only applies to configurations with s-electrons. The liquid drop model gives a formula for the radius

<sup>22</sup>More accurate calculations can be made directly from eqn 6.24 in individual cases, e.g. the 1s configuration in hydrogen has

$$E_{\text{Vol}} = \frac{4}{3} \frac{\langle r_N^2 \rangle}{a_0^2} hc R_\infty \simeq 5 \times 10^{-9} \text{ eV.}$$

The proton has a root-mean-square charge radius of  $\langle r_N^2 \rangle^{1/2} = 0.875 \text{ fm}$  (CODATA value).

<sup>23</sup>The size of the nucleus  $\langle r_N^2 \rangle$  generally increases with  $A$  following the trend in eqn 6.25 but there are exceptions, e.g. a nucleus that is particularly stable because it has closed shells of nucleons can be smaller than a lighter nucleus. Experimental measurements of isotope shifts, and the deduced values of the volume effect, are used to study such behaviour. (Similarly, for atoms, the shell structure makes inert gas atoms exceptionally small. More generally, the variation of atomic size with atomic mass is opposite to that of ionization energy—alkali atoms are larger than nearby atoms in the periodic table.)

of a nucleus as

$$r_N \simeq 1.2 \times A^{1/3} \text{ fm.} \quad (6.25)$$

Using this equation and making the same approximations for the wavefunction squared as in hyperfine structure (eqn 6.17), we can write the isotope shift caused by the volume effect as

$$\Delta \tilde{\nu}_{\text{Vol}} = \frac{\Delta E_{\text{Vol}}}{hc} \simeq \frac{\langle r_N^2 \rangle}{a_0^2} \frac{\delta A}{A} \frac{Z^2}{(n^*)^3} R_\infty. \quad (6.26)$$

This has been used to plot  $\Delta E_{\text{Vol}}$  as a function of  $Z$  in Fig. 6.7, assuming that  $\delta A = 1$ ,  $A \sim 2Z$  and  $n^* \sim 2$ .<sup>22</sup>

This volume effect decreases the binding energy of a given atomic level with respect to that of a ‘theoretical’ atom with a point charge. The resulting change in the transition depends on whether the effect occurs in the upper or lower level (see Exercise 6.9).<sup>23</sup>

### 6.2.3 Nuclear information from atoms

We have shown that the nucleus has an observable effect on atomic spectra. If hyperfine structure is observed then one immediately knows that the nucleus has spin and the number of hyperfine components sets a lower limit on  $I$  (Example 6.1). The values of  $F$ , and hence  $I$ , can be deduced by checking the interval rule, and the sum rule for relative intensities (similar to that for fine structure in Section 4.6.1). In principle, the magnetic moment of the nucleus  $\mu_I$  can be deduced from the hyperfine-structure constant  $A$ , e.g. calculations such as that in Section 6.1.1 are accurate for light atoms. For atoms with a higher  $Z$ , the relativistic effects are important for the electronic wavefunction near the nucleus and it is more difficult to calculate  $|\psi(0)|^2$ . However, the electronic factors cancel in ratios of the hyperfine-structure constants of isotopes of the same element to give accurate ratios of their magnetic moments, i.e. if the  $\mu_I$  is known for one isotope then it can be deduced for the other isotopes (see Exercise 6.4).

Similarly, isotope shifts give the difference in the nuclear sizes between isotopes,  $\Delta \langle r_N^2 \rangle$ , assuming that the mass effects are calculable.<sup>24</sup> To interpret this information, it is necessary to know the absolute value of the charge radius for one of the isotopes by another means, e.g. muonic X-rays. These transitions between the energy levels of a muon bound to an atomic nucleus have a very large volume effect, from which  $\langle r_N^2 \rangle$  can be deduced (see Exercise 6.13).<sup>25</sup>

## 6.3 Zeeman effect and hyperfine structure

The treatment of the Zeeman effect on hyperfine structure (in the  $IJ$ -coupling scheme) closely resembles that described in Section 5.5 for the  $LS$ -coupling scheme, and the detailed explanation of each step is not repeated here. The total atomic magnetic moment of the atom is the

<sup>24</sup>See Woodgate (1980) for further details.

<sup>25</sup>High-energy electron scattering experiments also probe the nuclear charge distribution.

sum of the electronic and nuclear moments (cf. eqn 5.9):

$$\boldsymbol{\mu}_{\text{atom}} = -g_J \mu_B \mathbf{J} + g_I \mu_N \mathbf{I} \simeq -g_J \mu_B \mathbf{J}. \quad (6.27)$$

Since  $\mu_N \ll \mu_B$  we can neglect the nuclear contribution (for all but the most precise measurements), so that the Hamiltonian for the interaction with an external field  $\mathbf{B}$  is just that for the electronic magnetic moment:

$$H = g_J \mu_B \mathbf{J} \cdot \mathbf{B}. \quad (6.28)$$

This interaction does not depend on the nuclear spin. However, its expectation value does depend on the hyperfine structure. We consider first the weak-field regime where the interaction with the external field is weaker than  $A \mathbf{I} \cdot \mathbf{J}$  so that it can be treated as a perturbation to the hyperfine structure. We then treat the strong-field regime, and also the intermediate situation.

### 6.3.1 Zeeman effect of a weak field, $\mu_B B < A$

If the interaction with the external field in eqn 6.28 is weaker than the hyperfine interaction  $A \mathbf{I} \cdot \mathbf{J}$ , then in the vector model  $\mathbf{J}$  and  $\mathbf{I}$  move rapidly about their resultant  $\mathbf{F}$ , as illustrated in Fig. 6.8, whilst  $\mathbf{F}$  itself precesses more slowly about the magnetic field ( $z$ -axis). In this regime  $F$  and  $M_F$  are good quantum numbers, but  $M_I$  and  $M_J$  are not. Taking the projection of the magnetic moments along  $\mathbf{F}$  gives the effective Hamiltonian

$$H = g_J \mu_B \frac{\langle \mathbf{J} \cdot \mathbf{F} \rangle}{F(F+1)} \mathbf{F} \cdot \mathbf{B} = g_F \mu_B \mathbf{F} \cdot \mathbf{B} = g_F \mu_B B F_z, \quad (6.29)$$

where

$$g_F = \frac{F(F+1) + J(J+1) - I(I+1)}{2F(F+1)} g_J. \quad (6.30)$$

Here the factor  $g_F$  arises from the projection of  $\mathbf{J}$  onto  $\mathbf{F}$ , as illustrated in Fig. 6.9, in the just same way as  $g_J$  is given by the projection of  $\mathbf{L}$  and  $\mathbf{S}$  onto  $\mathbf{J}$  in Section 5.5. The Zeeman energy is

$$E = g_F \mu_B B M_F. \quad (6.31)$$

As an example, consider the ground-state hyperfine levels in hydrogen ( $I = J = 1/2$  and  $g_J = g_s \simeq 2$ ). For  $F = 1$  we find  $g_F = 1$  so the three states  $M_F = -1, 0$  and  $1$  are spaced by  $\mu_B B$ . The  $F = 0, M_F = 0$  state has no first-order Zeeman shift (see Fig. 6.10).

In summary, the calculation of the Zeeman effect of a weak magnetic field on the hyperfine structure is simple because only the magnetic moment of the electron(s) along  $\mathbf{J}$  contributes, whereas in the  $LS$ -coupling scheme there are components along both  $\mathbf{L}$  and  $\mathbf{S}$ . However,  $I$  affects  $g_F$  because the nuclear angular momentum  $I$  is not small, and has a major effect on the  $IJF$ -triangle (thinking in terms of vectors as in Fig. 6.9), even though the nuclear magnetic moment is negligible.

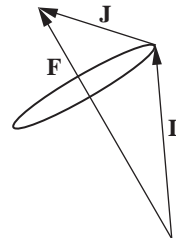
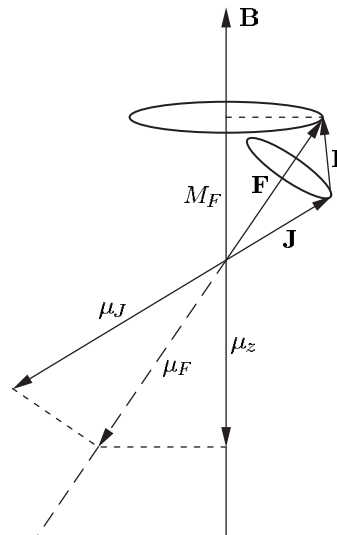
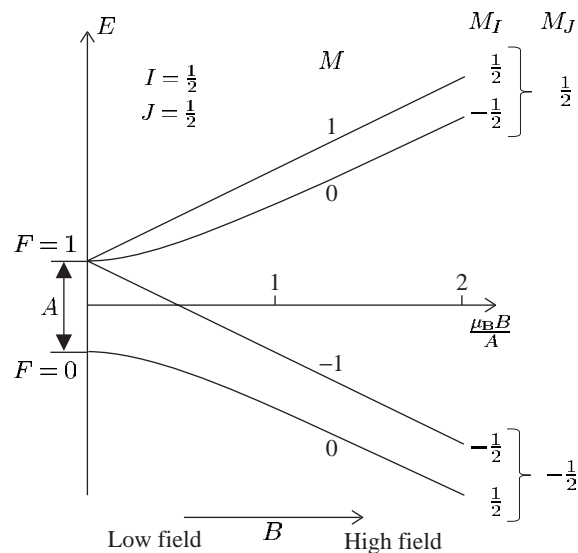


Fig. 6.8 The  $IJ$ -coupling scheme.



**Fig. 6.9** The projection of the contributions to the magnetic moment from the atomic electrons along  $\mathbf{F}$ . The magnetic moment of the nucleus is negligible in comparison.



**Fig. 6.10** The Zeeman effect on the hyperfine structure of the ground level of hydrogen 1s  $^2\text{S}_{1/2}$ . The interval between the  $F = 0$  and  $F = 1$  levels is  $A$ , as shown in Fig. 6.3. The zero of the energy scale has been chosen to be midway between the levels at zero field, which is convenient for the calculations in the text. (The two states with  $M_F = 0$  in the low-field regime are mixed by the perturbation and then move apart as the magnetic flux density increases.) The quantity  $x = \mu_B B / A$  is plotted on the horizontal axis and the low- and high-field regimes correspond to  $x \ll 1$  and  $x \gg 1$ .

### 6.3.2 Zeeman effect of a strong field, $\mu_B B > A$

A strong field is one where the interaction with the external field, in eqn 6.28, is greater than  $A \mathbf{I} \cdot \mathbf{J}$ . This can readily be achieved for hyperfine structures since the Zeeman energy  $\mu_B B$  in a field of 1 T is about  $6 \times 10^{-5}$  eV (corresponding to a frequency of 14 GHz), which is greater than all but the largest hyperfine structures in the ground configurations of heavy elements (see Fig. 6.7).<sup>26</sup> In this regime  $F$  is not a

<sup>26</sup>But smaller than the fine structure of the first excited state, except for the lightest elements. High-lying levels, however, have smaller fine structure.

good quantum number and  $\mathbf{J}$  precesses about  $\mathbf{B}$ .<sup>27</sup> The effect of the hyperfine interaction can be calculated as a perturbation on the  $|IM_IJM_J\rangle$  eigenstates, i.e.

$$E_{ZE} = g_J \mu_B B M_J + \langle IM_IJM_J | A \mathbf{I} \cdot \mathbf{J} | IM_IJM_J \rangle \quad (6.32)$$

$$= g_J \mu_B B M_J + A M_I M_J. \quad (6.33)$$

The first term is the same as eqn 5.11. In the second term,  $\mathbf{I} \cdot \mathbf{J} = I_x J_x + I_y J_y + I_z J_z$  and the  $x$ - and  $y$ -components average to zero in the precession about the field along the  $z$ -direction.<sup>28</sup>

An example of the energy levels in a strong field is shown in Fig. 6.10 for the hydrogen ground state. The two energy levels with  $M_J = \pm 1/2$  are both split into sub-levels with  $M_I = \pm 1/2$  by the hyperfine interaction; eqn 6.33 shows that these sub-levels have a separation of  $A/2$  (independent of the field strength).

### 6.3.3 Intermediate field strength

In Fig. 6.10 the low- and high-field energy levels follow the rule that two states never cross if they have the same value of  $M$ , where at low fields  $M = M_F$  and at high fields  $M = M_I + M_J$ . This implies that

$$\begin{array}{ccc} & M_J & M_I \\ F = 1, & M_F = 0 & \rightarrow +1/2, -1/2, \\ F = 0, & M_F = 0 & \rightarrow -1/2, +1/2. \end{array}$$

This rule can be justified by showing that the operator  $I_z + J_z$  commutes with all the interactions and it allows unambiguous connection of states even in more complex cases.<sup>29</sup> For the simple case of hydrogen the energy levels can be calculated at all fields by simple perturbation theory, as shown below.

#### Example 6.3 The Zeeman effect on the hyperfine structure of hydrogen for all field strengths

Figure 6.10 shows the energy levels for all field strengths. The Zeeman energies of the  $M = \pm 1$  states are  $\pm \mu_B B$  for all fields because their wavefunctions are not mixed ( $g_F = 1$  from eqn 6.30). The  $M_F = 0$  states have no first-order shift but the magnetic field mixes these two states in the  $F = 0$  and 1 hyperfine levels; the matrix element between them is

$$-\langle F = 1, M_F = 0 | \boldsymbol{\mu} \cdot \mathbf{B} | F = 0, M_F = 0 \rangle = \zeta \mu_B B.$$

Such (off-diagonal) matrix elements can be evaluated by angular momentum theory, but in this simple case we can get by without using Clebsch–Gordan coefficients (leaving  $\zeta$  as an undetermined constant for the time being). The Hamiltonian for the two-level system is

$$H = \begin{pmatrix} A/2 & \zeta \mu_B B \\ \zeta \mu_B B & -A/2 \end{pmatrix}. \quad (6.34)$$

<sup>27</sup>The nuclear angular momentum  $\mathbf{I}$  does not precess around  $\mathbf{B}$  because  $-\boldsymbol{\mu}_I \cdot \mathbf{B}$  is negligible. In this regime the interaction  $A \mathbf{I} \cdot \mathbf{J}$  makes  $\mathbf{I}$  precess about the mean direction of  $\mathbf{J}$ , which is parallel to  $\mathbf{B}$ . Thus effectively  $\mathbf{I}$  precesses about the axis defined by  $\mathbf{B}$  (but not because of  $-\boldsymbol{\mu}_I \cdot \mathbf{B}$ ). The vector model picture requires careful thought because of the subtle differences from the Paschen–Back effect (Fig. 5.14). In the quantum mechanical description this is taken into account by considering the relative magnitudes of the perturbations:  $|\boldsymbol{\mu}_e \cdot \mathbf{B}| > |A \mathbf{I} \cdot \mathbf{J}| > |\boldsymbol{\mu}_I \cdot \mathbf{B}|$ , where  $\boldsymbol{\mu}_e$  is the magnetic moment of the atomic electrons in eqn 5.9.

<sup>28</sup>This can be shown rigorously using the ladder operators

$$I_+ \equiv I_x + i I_y,$$

$$I_- \equiv I_x - i I_y,$$

and similarly for  $J_+$  and  $J_-$ . These ladder operators change the magnetic quantum numbers, e.g.

$$I_+ |IM_I\rangle \propto |IM_I + 1\rangle.$$

Since

$$I_x J_x + I_y J_y = \frac{1}{2} (I_+ J_- + I_- J_+),$$

the expectation value of this part of  $\mathbf{I} \cdot \mathbf{J}$  is zero (for states of given  $M_J$  and  $M_I$  as in eqn 6.32).

<sup>29</sup>At low fields,  $I_z + J_z \equiv F_z$ , which clearly commutes with the interaction in eqn 6.29. At high fields the relevant interactions are proportional to  $J_z$  and  $I_x J_x + I_y J_y + I_z J_z$ , both of which commute with  $I_z + J_z$ .

<sup>30</sup>Any choice for the point at which  $E = 0$  leads to the same result, e.g. taking the unperturbed energies as  $A/4$  and  $-3A/4$  as in Fig. 6.3.

<sup>31</sup>The avoided crossing of states that mix is a general feature of perturbation theory.

The energies are measured from the point midway between the hyperfine levels to streamline the algebra.<sup>30</sup> The energy eigenvalues are

$$E = \pm \sqrt{(A/2)^2 + (\zeta\mu_B B)^2}. \quad (6.35)$$

This exact solution for all fields is plotted in Fig. 6.10. The approximate solution for weak fields is

$$E_{\text{weak}} \simeq \pm \left\{ \frac{A}{2} + \frac{(\zeta\mu_B B)^2}{A} \right\}. \quad (6.36)$$

When  $B = 0$  the two unperturbed levels have energies  $\pm A/2$ . The term proportional to  $B^2$  is the usual second-order perturbation theory expression that causes the levels to *avoid* one another (hence the rule that states of the same  $M$  do not cross).<sup>31</sup>

For strong fields, where  $\mu_B B \gg A$ , eqn 6.35 gives the energy of the  $M = 0$  states as

$$E(F = \pm 1, M_F = 0) \simeq \pm \zeta\mu_B B. \quad (6.37)$$

In a strong field the energy levels of the system are given by  $g_J\mu_B B M_J$  and the two  $M_J = \pm 1/2$  states have Zeeman energies of  $g\mu_B B M_J = \pm \mu_B B$ . Comparison with eqn 6.37 shows that  $\zeta = 1$ , and so we have found the energies for all field strengths. The other two states have energies  $E(M = \pm 1) = \frac{1}{2}A \pm \mu_B B$  for all values of  $B$ .

A similar approach can be used when  $J = 1/2$  for arbitrary values of  $I$ , which applies to the ground states of the alkalis. For  $I > 1/2$  there are more states to consider than in hydrogen (where  $I = 1/2$ ), so the Hamiltonian will have larger dimensions than in eqn 6.34. Actually there were four basis states to consider in hydrogen, but because the perturbation mixes only two of them it was only necessary to diagonalise a  $2 \times 2$  matrix.

## 6.4 Measurement of hyperfine structure

An apparatus similar to that for measuring the Zeeman effect, shown in Fig. 1.7(a), can be used to observe hyperfine structure—a magnet is not required because hyperfine structure arises from an internal magnetic field of the atom. Figure 6.11 shows a typical experimental trace obtained from such an experiment with a pressure-scanned Fabry–Perot étalon for the  $5s5p\ ^3P_0 - 5s6s\ ^3S_1$  line in cadmium. The  $^3P_0$  level has no hyperfine structure (because  $J = 0$ ) and the observed splitting comes entirely from the  $5s6s\ ^3S_1$  level. Both s-electrons contribute to the field at the nucleus<sup>32</sup> so this level has an exceptionally large hyperfine splitting that is greater than the Doppler broadening.

The fact that the  $J = 1$  level only gives two hyperfine levels implies that  $I = 1/2$ . If  $I \geq 1$  then there would be three levels (by the rules for addition of angular momenta). One of these peaks might, however, be hidden underneath the large central peak? That this is not the case here

<sup>32</sup>The two spins are aligned in a triplet state so the 5s- and 6s-electrons produce fields in the same direction.

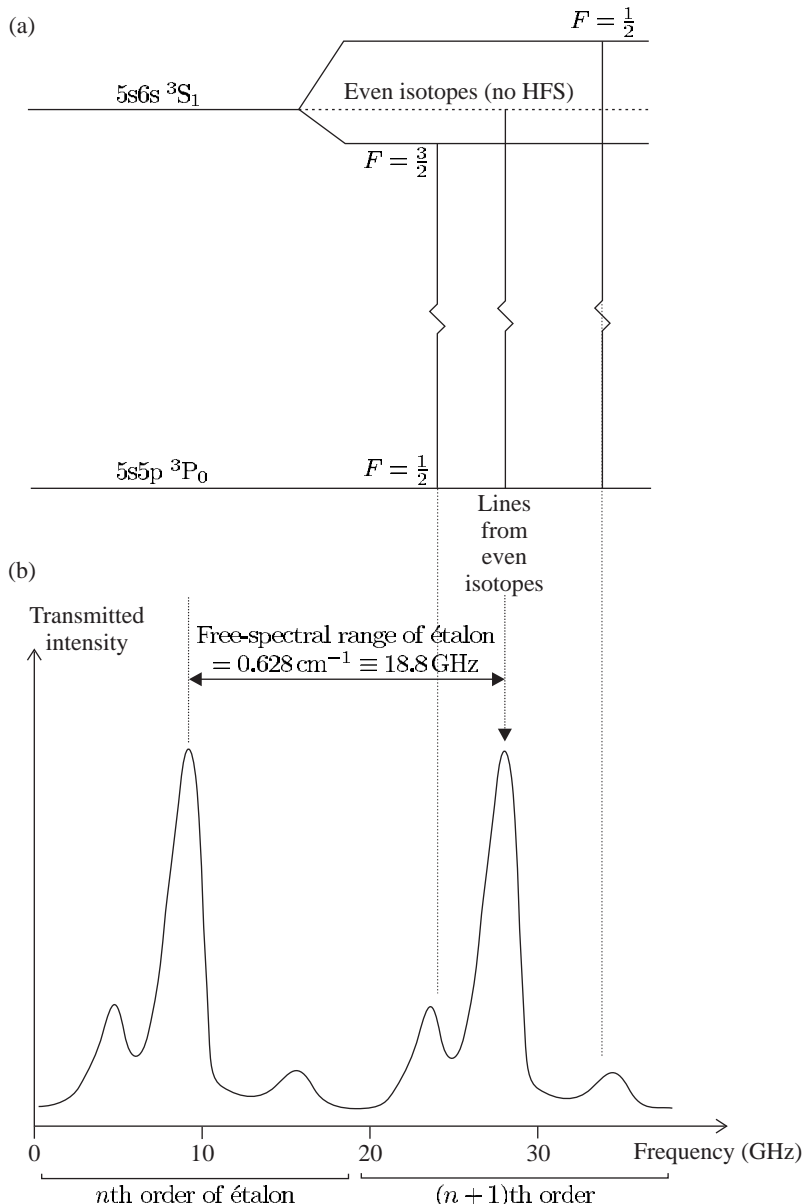


**Fig. 6.11** (a) The  $5s6s\ ^3S_1$  level in the odd isotopes of cadmium ( $^{111}\text{Cd}$  and  $^{113}\text{Cd}$ ) has a large hyperfine structure; the  $F = 3/2$  hyperfine level lies below  $F = 1/2$  because the nuclear  $g$ -factor is negative and similar in size for both odd isotopes. (The total magnetic field created by the unpaired s-electrons at the nucleus is anti-parallel to  $\mathbf{J}$ , as in the ground state of hydrogen and the alkalis.) (b) An experimental trace of the hyperfine structure for the  $5s5p\ ^3P_0$ – $5s6s\ ^3S_1$  line at a wavelength of 468 nm obtained with a pressure-scanned Fabry–Perot étalon (as in Fig. 1.7). There are three peaks in each order of the étalon: a large peak from the isotopes with no nuclear spin  $I = 0$  and hence no hyperfine structure (generally isotopes with an even number of nucleons so there are no unpaired spins within the nucleus); and two smaller peaks whose separation equals the hyperfine splitting of the  $5s6s\ ^3S_1$  level. (Data from the Oxford Physics Teaching Laboratory practical course; further details are in Lewis (1977).)

can be checked by verifying that the observed peaks have the expected displacements from their centre of gravity (which is approximately at the position of the even isotopes).<sup>33</sup>

It can be seen from Fig. 6.11 that optical spectroscopy is not generally suitable for measuring the Zeeman effect of hyperfine structure because spectral lines have a Doppler broadening that can be comparable with the hyperfine splitting. Thus in the low-field regime ( $\mu_B B < A$ ) the Zeeman splitting is too small to be resolved. To show this quantitatively

<sup>33</sup>This is not straightforward in this example because of the overlap of lines, but this could be done using a curve-fitting program on a computer. Additionally, there is a sum rule for the intensities as in fine structure.

we consider the Doppler width  $\Delta f_D$  of a line of wavelength  $\lambda$ :

$$\Delta f_D \simeq \frac{2u}{\lambda}, \quad (6.38)$$

<sup>34</sup>This gives a value of  $\Delta f_D$  that differs by only  $\sqrt{\ln 2} = 0.8$  from the exact result for the full width at half maximum (FWHM) derived in Chapter 8.

<sup>35</sup>The Zeeman splitting of a spectral line can only be resolved when the field is strong enough to give the Paschen–Back effect.

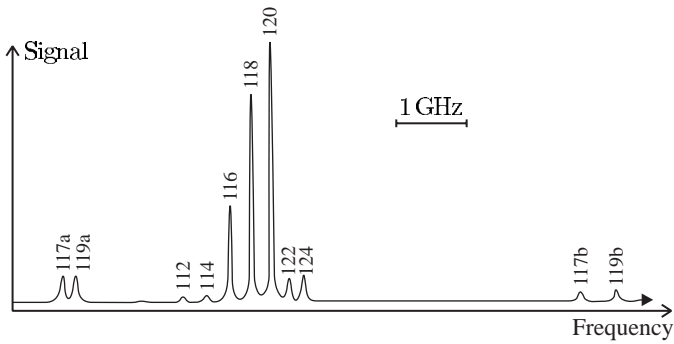
where  $u$  is a typical atomic velocity. The factor of 2 appears because atoms can move towards and away from the observer. For this estimate we shall use the most probable velocity  $u = \sqrt{2k_B T/m}$ .<sup>34</sup> For cadmium at  $T = 300$  K, we have  $u \simeq 200 \text{ m s}^{-1}$  and thus the Doppler width of the lines with a wavelength of  $\lambda = 468 \text{ nm}$  is  $\Delta f_D = 2u/\lambda = 0.9 \text{ GHz}$ , whereas  $A = 7.9 \text{ GHz}$  for the  $5s6s \ ^3S_1$  level. More generally, the Doppler width for a visible transition is plotted in Fig. 6.7 as a function of the atomic number. At room temperature the optical transitions of hydrogen, the lightest element, have a Doppler width slightly less than the fine-structure splitting of the first excited state, so in this case the low-field Zeeman effect cannot be observed even for fine structure (let alone hyperfine structure).<sup>35</sup> Figure 6.12 shows the results of an experimental observation of the hyperfine structure and isotope shift of tin by a technique of Doppler-free laser spectroscopy (that will be described in Section 8.2).

Doppler broadening is much less of a problem in direct measurements of the separation between hyperfine levels with microwave techniques (at frequencies of gigahertz), or the even smaller splitting of the Zeeman sub-levels that correspond to radio-frequency transitions. An example of a radio-frequency and microwave spectroscopy technique is outlined in the next section.

#### 6.4.1 The atomic-beam technique

An atomic-beam apparatus can be understood as an extension of the original Stern–Gerlach apparatus illustrated in Fig. 6.13. In the original Stern–Gerlach experiment a beam of silver atoms was sent through a region of strong gradient of the magnetic field and further downstream the atoms were deposited on a glass plate. Upon inspecting the plate, Stern and Gerlach found that the atoms appeared in two distinct places, showing that the atomic beam was split into two directions. This told them that angular momentum is quantised and that it can have values

**Fig. 6.12** Doppler-free laser spectroscopy of the  $5p^2 \ ^3P_0$ – $5p6s \ ^3P_1$  line of tin; the reduction in Doppler broadening (cf. Fig. 6.11) reveals the isotope shifts between the even isotopes, in addition to the hyperfine splitting of the odd isotopes. Each peak is labelled by the relative atomic mass. Each odd isotope gives rise to two peaks because of hyperfine structure (as in Fig. 6.11). For further details see Baird *et al.* (1983).



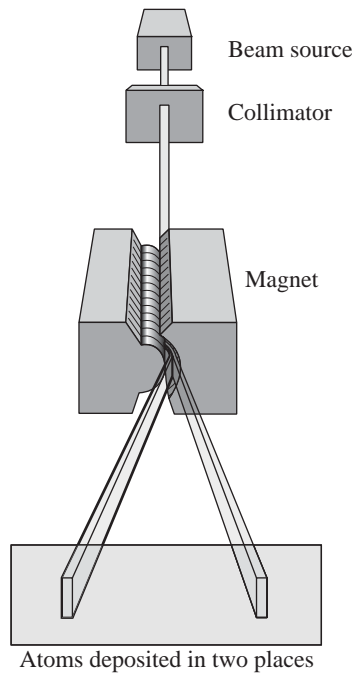


**Fig. 6.13** In the original Stern–Gerlach apparatus a beam of silver atoms was sent through a region of strong gradient of the magnetic field and further downstream the atoms were deposited on a glass plate. This simple experiment had a great influence on the development of quantum ideas and provides a very useful illustration of the concepts of quantisation (Feynman *et al.* 1963–1965).

that are half-integer multiples of  $\hbar$ . (Orbital angular momentum would give  $2l + 1$  components, with  $l$  an integer.) To interpret the experiment we consider an atom in a magnetic field  $\mathbf{B}$  with a gradient along the  $z$ -axis.<sup>36</sup> The force exerted on the atom is (using eqn 5.11)

$$\text{Force} = -\frac{dE_{ZE}}{dz} = g_J \mu_B \frac{dB}{dz} M_J. \quad (6.39)$$

The ground level of silver,  $5s\ ^2S_{1/2}$ , has  $l = 0$  and  $J = s = 1/2$ . Thus the force on atoms passing through the Stern–Gerlach magnet has the two values  $F = \pm \mu_B dB/dz$  for  $m_s = M_J = \pm \frac{1}{2}$ . This explains the separation of the atomic beam into two components and provides direct observational evidence for quantisation since the two emerging beams are well defined. For a classical vector the  $z$ -component of angular momentum would be spread over a range between the maximum and minimum values.

An atomic-beam apparatus has two Stern–Gerlach-type magnets, as shown in Fig. 6.14, that create an inhomogeneous field in the A and B regions to deflect atoms according to their  $M_J$  state. The A and B regions have a strong field ( $\mu_B B \gg A$ ), associated with the high gradient of magnetic field there, so  $M_J$  is a good quantum number and eqn 6.39 gives the force. The transition to be measured occurs in the C region between the two state-selecting magnets where, generally, the atoms are in the low-field regime. The principles of the operation of such an

<sup>36</sup>Since  $\nabla \cdot \mathbf{B} = 0$  we cannot have a gradient along the  $z$ -axis without there also being a gradient in another direction, but the effect of a gradient in a direction perpendicular to  $\mathbf{B}$  averages to zero as the magnetic moment precesses around the  $z$ -axis—for a more rigorous discussion see Chapter 10.

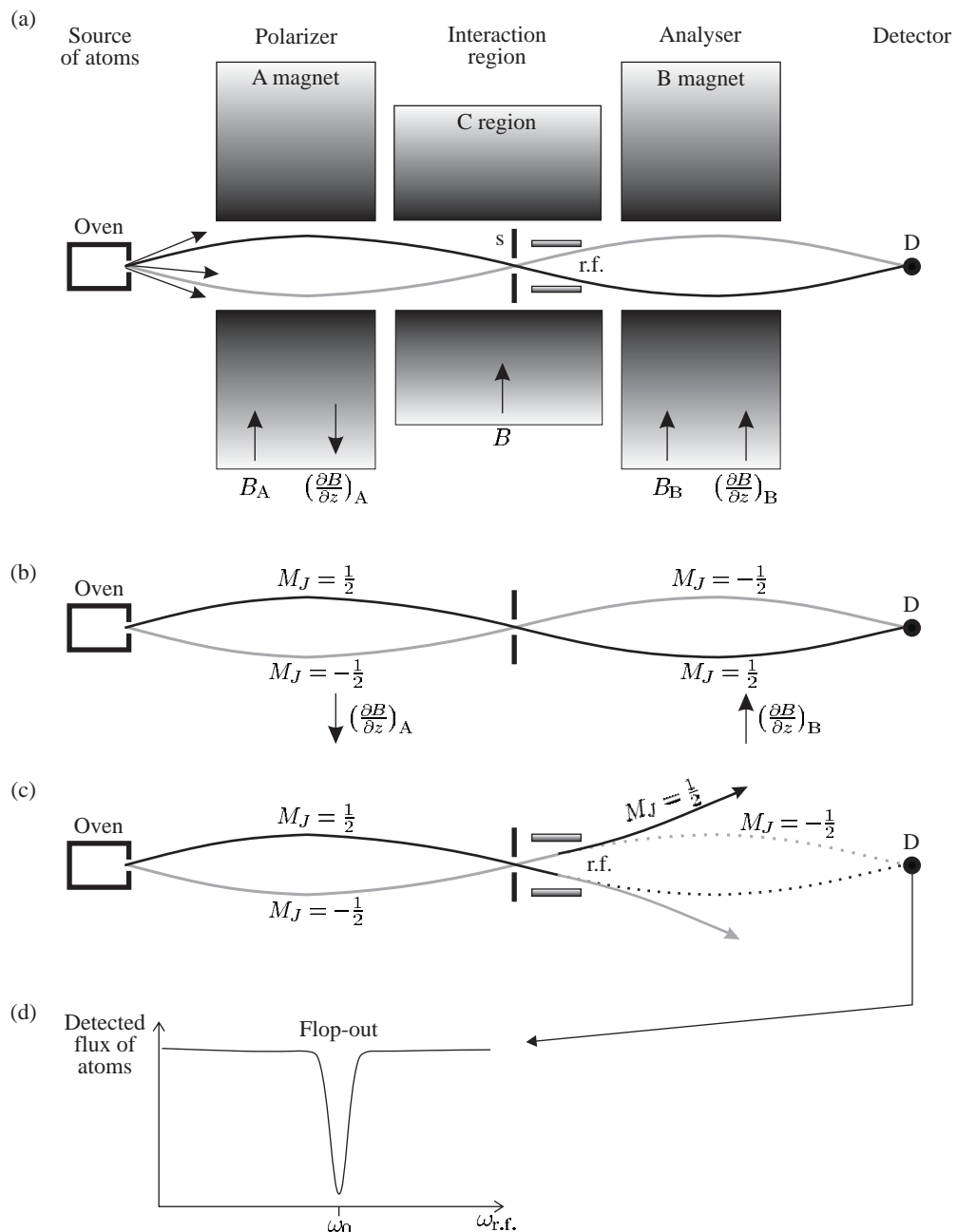


**Fig. 6.14** (a) The magnetic resonance technique in an atomic beam. Atoms emerge from an oven and travel through the collimating slit 's' to the detector. The deflection of atoms by the magnetic field gradient in the A and B regions depends on  $M_J$ , as indicated. (b) Atoms that stay in the same  $M_J$  state are refocused onto the detector when the A and B regions have gradients in opposite directions. (c) Resonant interaction with radio-frequency radiation in the C region can change the  $M_J$  quantum number,  $M_J = +\frac{1}{2} \leftrightarrow M_J = -\frac{1}{2}$ , so that atoms no longer reach the detector. (In a real apparatus the C region may be up to several metres long.) This is known as the flop-out arrangement and gives a signal as in (d). Further details are given in the text and in Corney (2000).

atomic-beam experiment are as follows.

- Atoms emerge from an oven to form an atomic beam in an evacuated chamber. The atoms have a mean free path much greater than the length of the apparatus (i.e. there are no collisions).
- The deflection of atoms in the A and B regions depends on  $M_J$ . If these two regions have magnetic field gradients in the same direction, as indicated in Fig. 6.15, then atoms only reach the detector if their  $M_J$  quantum number changes in the C region, i.e.  $M_J = +\frac{1}{2} \leftrightarrow M_J = -\frac{1}{2}$ . This is known as the flop-in arrangement.<sup>37</sup>
- As the atoms travel from A into the C region their state changes adiabatically to that in a low magnetic field as shown in Fig. 6.16 (and similarly as the field changes between the C and B regions). The transitions in the low-field region that can be observed are those that connect states with different values of  $M_J$  in the high-field regions, e.g. the transitions:

low frequency ( $\Delta F = 0$ ):

$$F = 1, \quad M_F = 0 \leftrightarrow F = 1, \quad M_F = -1 \quad \text{with} \quad \Delta E = g_F \mu_B B;$$

higher frequency ( $\Delta F = \pm 1$ ):

$$F = 0, \quad M_F = 0 \leftrightarrow F = 1, \quad M_F = 0 \quad \text{with} \quad \Delta E = A,$$

$$F = 0, \quad M_F = 0 \leftrightarrow F = 1, \quad M_F = 1 \quad \text{with} \quad \Delta E = A + g_F \mu_B B.$$

In this example, the  $M_F = 1 \leftrightarrow M_F = 0$  change between the Zeeman sub-levels of the upper  $F = 1$  level cannot be detected, but this

<sup>37</sup>The flop-out arrangement is shown in Fig. 6.14.

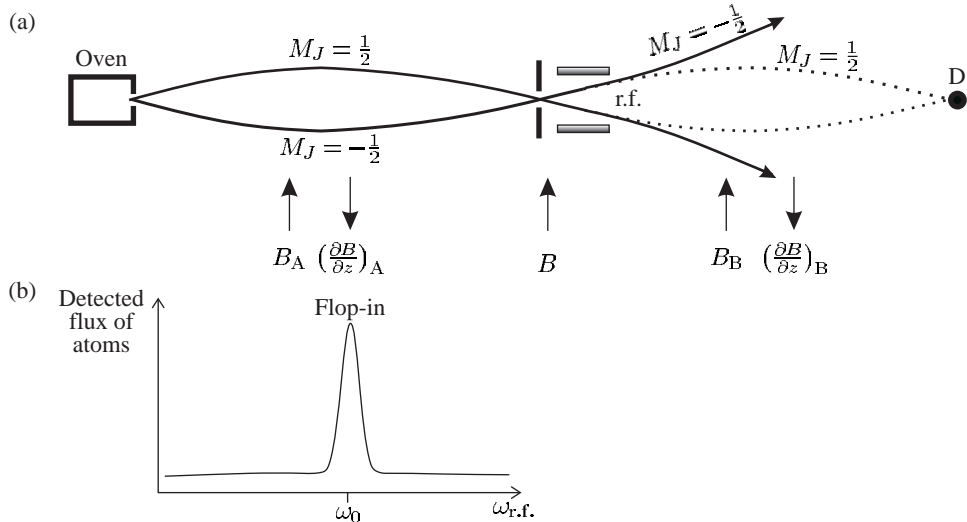
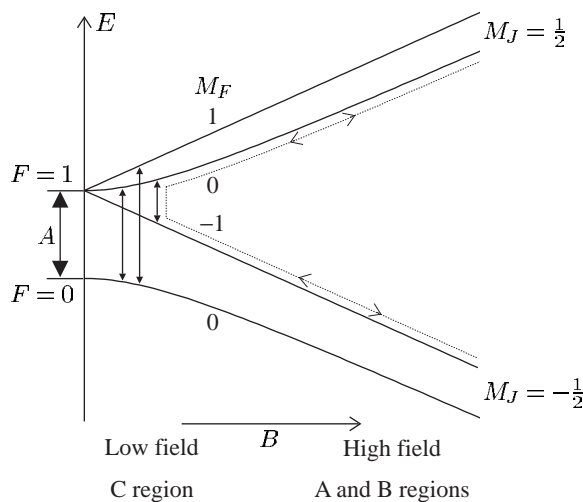


**Fig. 6.15** (a) The trajectories of atoms in an atomic-beam apparatus similar to that shown in Fig. 6.14, but magnetic field gradients in the A and B regions have the same direction. Atoms only reach the detector if their  $M_J$  quantum number is changed in the C region by the interaction with radio-frequency radiation. This is known as the flop-in arrangement and gives a signal as in (b).

**Fig. 6.16** The method of magnetic resonance in an atomic beam detects transitions that occur at low field (in the C region shown in Fig. 6.14) which cause a change in the quantum number  $M_J$  at high field (A and B regions). For example, an atom that follows the path indicated by the dotted line may start in the state  $M_J = +\frac{1}{2}$ , go adiabatically into the state  $F = 1, M_F = 0$  in the C region, where it undergoes a transition to the state with  $M_F = -1$  and then end up in the state  $M_J = -\frac{1}{2}$  in the B region (or it may follow the same path in the opposite direction). A strong magnetic field gradient (which is associated with a high field) is required in the A and B regions to give an observable deflection of the atomic trajectories.



does not lead to any loss of information since the hyperfine-structure constant  $A$  and  $g_F$  can be deduced from the other transitions.

These transitions at microwave- and radio-frequencies are clearly not electric dipole transitions since they occur between sub-levels of the ground configuration and have  $\Delta l = 0$  (and similarly for the maser). They are magnetic dipole transitions induced by the interaction of the oscillating magnetic field of the radiation with the magnetic dipole of the atoms. The selection rules for these M1 transitions are given in Appendix C.

### 6.4.2 Atomic clocks

An important application of the atomic-beam technique is atomic clocks, that are the primary standards of time. By international agreement the second is defined to be 9 192 631 770 oscillation periods of the hyperfine frequency in the ground state of  $^{133}\text{Cs}$  (the only stable isotope of this element). Since all stable caesium atoms are identical, precise measurements of this atomic frequency in the National Standards Laboratories throughout the world should agree with each other, within experimental uncertainties.<sup>38</sup>

The definition of the second is realised using the hyperfine frequency of the  $F = 3, M_F = 0 \leftrightarrow F = 4, M_F = 0$  transition in caesium. This transition between two  $M_F = 0$  states has no first-order Zeeman shift, but even the second-order shift has a significant effect at the level of precision required for a clock. The apparatus can be designed so that the dominant contribution to the line width comes from the finite interaction time  $\tau$  as atoms pass through the apparatus (transit time). Fourier transform theory gives the line width as<sup>39</sup>

$$\Delta f \sim \frac{1}{\tau} = \frac{v_{\text{beam}}}{l}, \quad (6.40)$$

<sup>38</sup>Such quantum metrology has been used to define other fundamental constants, with the exception of the kilogram which is still defined in terms of a lump of platinum kept in a vault in Paris.

<sup>39</sup>The next chapter gives a complete treatment of the interaction of atoms with radiation.

where  $v_{\text{beam}}$  is the typical velocity in the beam and  $l$  is the length of the interaction region. Therefore the atomic beams used as primary standards are made as long as possible. An interaction over a region 2 m long gives a line width of  $\Delta f = 100 \text{ Hz}$ .<sup>40</sup> Thus the quality factor is  $f/\Delta f \sim 10^8$ ; however, the centre frequency of the line can be determined to a small fraction of the line width.<sup>41</sup> As a result of many years of careful work at standards laboratories, atomic clocks have uncertainties of less than 1 part in  $10^{14}$ . This illustrates the incredible precision of radio-frequency and microwave techniques, but the use of slow atoms gives even higher precision, as we shall see in Chapter 10.<sup>42</sup> There is a great need for accurate timekeeping for the synchronisation of global telecommunications networks, and for navigation both on Earth through the global positioning system (GPS) and for satellites in deep space.

The atomic-beam technique has been described here because it furnishes a good example of the Zeeman effect on hyperfine structure, and it was also historically important in the development of atomic physics. The first atomic-beam experiments were carried out by Isador Rabi and he made numerous important discoveries. Using atomic hydrogen he showed that the proton has a magnetic moment of  $2.8 \mu_N$ , which was about three times greater than expected for a point-like particle (cf. the electron with  $\mu_B$ , i.e. one unit of the relevant magnetic moment). This was the first evidence that the proton has internal structure. Other important techniques of radio-frequency spectroscopy such as optical pumping are described elsewhere, see Thorne *et al.* (1999) and Corney (2000).

## Further reading

Further details of hyperfine structure and isotope shift including the electric quadrupole interaction can be found in Woodgate (1980). The discussion of magnetic resonance techniques in condensed matter (Blundell 2001) gives a useful complement to this chapter.

The classic reference on atomic beams is *Molecular beams* (Ramsey 1956). Further information on primary clocks can be found on the web sites of the National Physical Laboratory (for the UK), the National Institute of Standards and Technology (NIST, in the US), and similar sites for other countries. The two volumes by Vannier and Audouin (1989) give a comprehensive treatment of atomic clocks and frequency standards.

<sup>40</sup>Caesium atoms have velocities of  $v_{\text{Cs}} = (3k_B T/M_{\text{Cs}})^{1/2} = 210 \text{ m s}^{-1}$  at  $T = 360 \text{ K}$ .

<sup>41</sup>In a normal experiment it is hard to measure the centre of a line with an uncertainty of better than one-hundredth of the line width, i.e. a precision of only 1 in  $10^{10}$  in this case.

<sup>42</sup>The hydrogen maser achieves a long interaction time by confining the atoms in a glass bulb for  $\tau \sim 0.1 \text{ s}$  to give a line width of order 10 Hz—the atoms bounce off the walls of the bulb without losing coherence. Thus masers can be more precise than atomic clocks but this does not mean that they are more accurate, i.e. the frequency of a given maser can be measured to more decimal places than that of an atomic-beam clock, but the maser frequency is shifted slightly from the hyperfine frequency of hydrogen by the effect of collisions with the walls. This shift leads to a frequency difference between masers that depends on how they were made. In contrast, caesium atomic clocks measure the unperturbed hyperfine frequency of the atoms. (The use of cold atoms improves the performance of both masers and atomic clocks—the above remarks apply to uncooled systems.)

## Exercises

(6.1) *The magnetic field in fine and hyperfine structure*

Calculate the magnetic flux density  $B$  at the centre of a hydrogen atom for the  $1s\ ^2S_{1/2}$  level and also for  $2s\ ^2S_{1/2}$ .

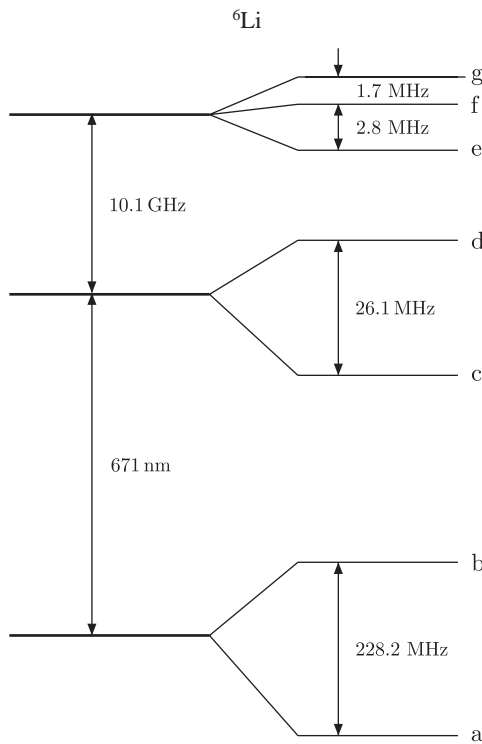
Calculate the magnitude of the orbital magnetic field experienced by a  $2p$ -electron in hydrogen (eqn 2.47).

(6.2) *Hypersfine structure of lithium*

The figure shows the energy levels of lithium involved in the  $2s$ - $2p$  transitions for the two isotopes  $^6\text{Li}$  and  $^7\text{Li}$ . (The figure is not to scale.)

Explain in simple terms why the hypersfine splitting is of order  $m_e/M_p$  smaller than the fine-structure splitting in the  $2p$  configuration of lithium.

Explain, using the vector model or otherwise, why the hypersfine interaction splits a given  $J$  level into  $2J + 1$  hypersfine levels if  $J \leq I$  and  $2I + 1$  levels if  $I \leq J$ . Hence, deduce the nuclear spin of  $^6\text{Li}$  and give the values of the quantum numbers  $L$ ,  $J$  and  $F$  for all its hypersfine levels. Verify that the



interval rule is obeyed in this case.

Determine from the data given the nuclear spin of  $^7\text{Li}$  and give the values of  $L$ ,  $J$  and  $F$  for each of the hypersfine levels on the figure. Calculate the hypersfine splitting of the interval marked X.

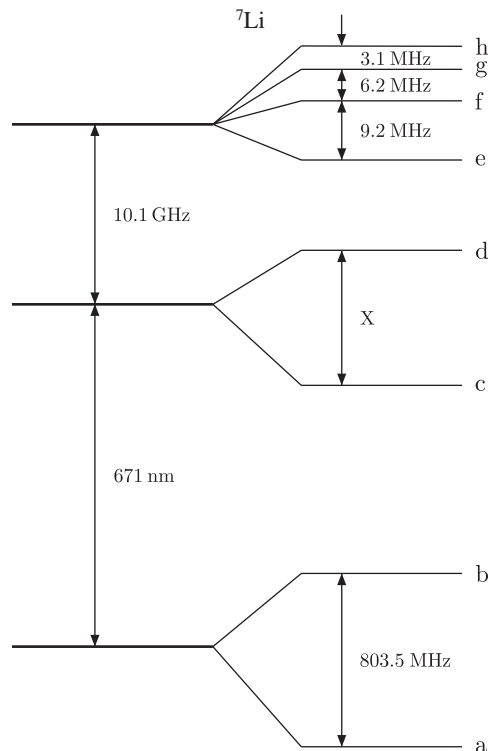
(For the hypersfine levels a to d the parameter  $A_{nlj}$  is positive for both isotopes.)

(6.3) *Hypersfine structure of light elements*

Use the approximate formula in eqn 6.17 to estimate the hypersfine structure in the ground states of atomic hydrogen and lithium. Comment on the difference between your estimates and the actual values given for hydrogen in Section 6.1.1 and for Li in Exercise 6.2.

(6.4) *Ratio of hypersfine splittings*

The spin and magnetic moment of the proton are  $(1/2, 2.79\mu_N)$ , of the deuteron  $(1, 0.857\mu_N)$  and of  $^3\text{He}$   $(1/2, -2.13\mu_N)$ . Calculate the ratio of the ground-state hypersfine splittings of (a) atomic hydrogen and deuterium and (b) atomic hydrogen and the hydrogen-like ion  $^3\text{He}^+$ .



## (6.5) Interval for hyperfine structure

- (a) Show that an interaction of the form  $A\mathbf{I} \cdot \mathbf{J}$  leads to an interval rule, i.e. the splitting between two sub-levels is proportional to the total angular momentum quantum number  $F$  of the sub-level with the larger  $F$ .
- (b)

| Peak | I<br>Position (GHz) | II |
|------|---------------------|----|
| a    | 11.76               |    |
| b    | 10.51               |    |
| c    | 8.94                |    |
| d    | 7.06                |    |
| e    | 4.86                |    |
| f    | 2.35                |    |

The table gives the positions of the six peaks in the spectrum shown in Fig. 6.6 that were not assigned quantum numbers in Example 6.2. It is the hyperfine structure of the upper level ( $^8D_{11/2}$ ) of the transition in the isotope  $^{153}\text{Eu}$  that determines the positions of these six peaks. What is the nuclear spin  $I$  of this isotope? Show that the spacing between these peaks obeys an interval rule and determine the quantum number  $F$  associated with each peak.

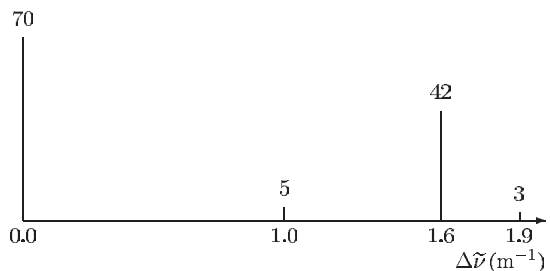
- (c) For the isotope  $^{151}\text{Eu}$ , whose hyperfine structure was analysed in Example 6.2, the lower level of the transition has a hyperfine structure constant of  $A(^8S_{7/2}) = 20\text{ MHz}$  (measured by the method of magnetic resonance in an atomic beam (Sandars and Woodgate 1960)). What is the hyperfine-structure constant of this  $^8S_{7/2}$  level for the isotope  $^{153}\text{Eu}$ , analysed in this exercise?

## (6.6) Interval for hyperfine structure

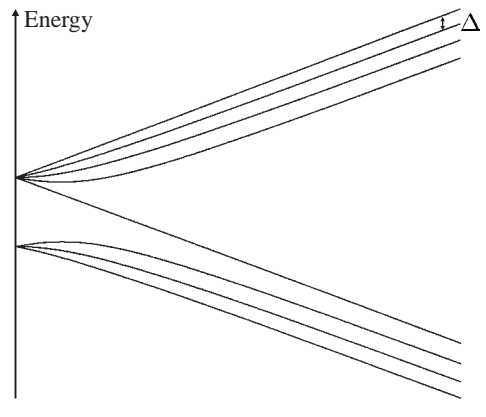
The  $3d^54s4p\ ^6P_{7/2}$  level of  $^{55}\text{Mn}$  is split by hyperfine interaction into six levels that have separations 2599, 2146, 1696, 1258 and 838 MHz. Deduce the nuclear spin of  $^{55}\text{Mn}$  and show that the separations confirm your value.

## (6.7) Hyperfine structure

When studied by means of high-resolution spectroscopy, the resonance line  $4s\ ^2S_{1/2}-4p\ ^2P_{1/2}$  of naturally-occurring potassium consists of four components with spacings and intensity ratios as shown in the following diagram.



Natural potassium is a mixture of  $^{39}\text{K}$  and  $^{41}\text{K}$  in the ratio 14 : 1. Explain the origin of the structure, and deduce the nuclear spins and the ratio of the magnetic moments of the two isotopes.



## (6.8) Zeeman effect on HFS at all field strengths

The figure shows the hyperfine structure of the ground level ( $5s\ ^2S_{1/2}$ ) of  $^{37}\text{Rb}$  (which has  $A/h = 3.4\text{ GHz}$ ), as a function of the magnetic flux density  $B$ .

- (a) Deduce the nuclear spin of this isotope of rubidium.
- (b) What are the appropriate quantum numbers for the states in both strong and weak fields (mark these on a copy of the figure)?
- (c) Show that in the weak-field regime the separation between states is the same in the upper and lower hyperfine levels.
- (d) In a strong field the energy of the states is given by eqn 6.33. Show that in this regime the four uppermost states have the same separation between them (marked  $\Delta$  on the figure) as the four lower-lying states.

- (e) Define what is meant by a ‘strong field’ when considering hyperfine structure. Give an approximate numerical value for the magnetic field at which the cross-over from the weak-field to the strong-field regime occurs in this example.

(6.9) *Isotope shift*

Estimate the contributions to the isotope shift between  $^{85}_{37}\text{Rb}$  and  $^{87}_{37}\text{Rb}$  that arise from the mass and volume effects for the following transitions:

- (a) 5s–5p at a wavelength of  $\sim 790\text{ nm}$ ; and
- (b) 5p–7s at a wavelength of  $\sim 730\text{ nm}$ .

Estimate the total isotope shift for both transitions, being careful about the sign of each contribution.

(6.10) *Volume shift*

Calculate the contribution of the finite nuclear size effect to the Lamb shift between the 2p  $^2\text{P}_{1/2}$  and 2s  $^2\text{S}_{1/2}$  levels in atomic hydrogen (using the information in Section 6.2.2). The measured value of the proton charge radius has an uncertainty of 1% and the Lamb shift is about 1057.8 MHz. What is the highest precision with which experimental measurement of the Lamb shift can test quantum electrodynamics (expressed as parts per million)?

(6.11) *Isotope shift*

Estimate the relative atomic mass  $A$  for which the volume and mass effect give a similar contribution to the isotope shift for  $n^* \sim 2$  and a visible transition.

(6.12) *Specific mass shift*

An atom with a nucleus of mass  $M_N$  and  $N$  elec-

trons has a kinetic energy  $T$  given by

$$T = \frac{\mathbf{p}_N^2}{2M_N} + \sum_{i=1}^N \frac{\mathbf{p}_i^2}{2m_e},$$

where  $\mathbf{p}_N$  is the momentum of the nucleus and  $\mathbf{p}_i$  is the momentum of the  $i$ th electron. The total of these momenta is zero in the centre-of-mass frame of the atom:

$$\mathbf{p}_N + \sum_{i=1}^N \mathbf{p}_i = 0.$$

Use this equation to express  $T$  in terms of electronic momenta only.

Answer the following for either (a) a lithium atom (with  $N = 3$ ) or (b) the general case of a multi-electron atom with a nucleus of finite mass (i.e. any real non-hydrogenic atom). Find the kinetic-energy terms that are  $\sim m_e/M_N$  times the main contribution: a normal mass effect (cf. eqn 6.21) and a specific mass effect that depends on products of the momenta  $\mathbf{p}_i \cdot \mathbf{p}_j$ .

(6.13) *Muonic atom*

A muon of mass  $m_\mu = 207m_e$  is captured by an atom of sodium ( $Z = 11$ ). Calculate the radius of the muon’s orbit for  $n = 1$  using Bohr theory and explain why the atomic electrons have little influence on the energy levels of the muonic atom. Calculate the binding energy of the muon for  $n = 1$ . Determine the volume effect on the 1s–2p transition in this system; express the difference between the frequency of the transition for a nucleus with a radius  $r_N$  (given by eqn 6.25) and the theoretical frequency for  $r_N = 0$  as a fraction of the transition frequency.

Web site:

<http://www.physics.ox.ac.uk/users/foot>

This site has answers to some of the exercises, corrections and other supplementary information.

# The interaction of atoms with radiation

7

To describe the interaction of a two-level atom with radiation we shall use a *semiclassical* treatment, i.e. the radiation is treated as a classical electric field but we use quantum mechanics to treat the atom. We shall calculate the effect of an oscillating electric field on the atom from first principles and show that this is equivalent to the usual time-dependent perturbation theory (TDPT) summarised by the golden rule (as mentioned in Section 2.2). The golden rule only gives the steady-state transition rate and therefore does not describe adequately spectroscopy experiments with highly monochromatic radiation, e.g. radio-frequency radiation, microwaves or laser light, in which the amplitudes of the quantum states evolve coherently in time. In such experiments the damping time may be less than the total measurement time so that the atoms never reach the steady state.

From the theory of the interaction with radiation, we will be able to find the conditions for which the equations reduce to a set of rate equations that describe the populations of the atomic energy levels (with a steady-state solution). In particular, for an atom illuminated by broad-band radiation, this approach allows us to make a connection with Einstein's treatment of radiation that was presented in Chapter 1; we shall find the Einstein  $B$  coefficient in terms of the matrix element for the transition. Then we can use the relation between  $A_{21}$  and  $B_{21}$  to calculate the spontaneous decay rate of the upper level. Finally, we shall study the roles of natural broadening and Doppler broadening in the absorption of radiation by atoms, and derive some results needed in later chapters such as the a.c. Stark shift.

## 7.1 Setting up the equations

We start from the time-dependent Schrödinger equation<sup>1</sup>

$$i\hbar \frac{\partial \Psi}{\partial t} = H\Psi. \quad (7.1)$$

The Hamiltonian has two parts,

$$H = H_0 + H_I(t). \quad (7.2)$$

That part of the Hamiltonian that depends on time,  $H_I(t)$ , describes the interaction with the oscillating electric field that perturbs the eigen-

|     |  |     |
|-----|--|-----|
| 7.1 | Setting up the equations                 | 123 |
| 7.2 | The Einstein $B$ coefficients            | 126 |
| 7.3 | Interaction with monochromatic radiation | 127 |
| 7.4 | Ramsey fringes                           | 132 |
| 7.5 | Radiative damping                        | 134 |
| 7.6 | The optical absorption cross-section     | 138 |
| 7.7 | The a.c. Stark effect or light shift     | 144 |
| 7.8 | Comment on semiclassical theory          | 145 |
| 7.9 | Conclusions                              | 146 |
|     | Further reading                          | 147 |
|     | Exercises                                | 148 |

<sup>1</sup>The operators do not have hats so  $H \equiv \hat{H}$ , as previously.

functions of  $H_0$ ; the unperturbed eigenvalues and eigenfunctions of  $H_0$  are just the atomic energy levels and wavefunctions that we found in previous chapters. We write the wavefunction for the level with energy  $E_n$  as

$$\Psi_n(\mathbf{r}, t) = \psi_n(\mathbf{r}) e^{-iE_n t/\hbar}. \quad (7.3)$$

For a system with only two levels, the spatial wavefunctions satisfy

$$\begin{aligned} H_0\psi_1(\mathbf{r}) &= E_1\psi_1(\mathbf{r}), \\ H_0\psi_2(\mathbf{r}) &= E_2\psi_2(\mathbf{r}). \end{aligned} \quad (7.4)$$

These atomic wavefunctions are not stationary states of the full Hamiltonian,  $H_0 + H_I(t)$ , but the wavefunction at any instant of time can be expressed in terms of them as follows:

$$\Psi(\mathbf{r}, t) = c_1(t)\psi_1(\mathbf{r})e^{-iE_1 t/\hbar} + c_2(t)\psi_2(\mathbf{r})e^{-iE_2 t/\hbar}, \quad (7.5)$$

or, in concise Dirac ket notation (shortening  $c_1(t)$  to  $c_1$ ,  $\omega_1 = E_1/\hbar$ , etc.),

$$\Psi(\mathbf{r}, t) = c_1|1\rangle e^{-i\omega_1 t} + c_2|2\rangle e^{-i\omega_2 t}. \quad (7.6)$$

Normalisation requires that the two time-dependent coefficients satisfy

$$|c_1|^2 + |c_2|^2 = 1. \quad (7.7)$$

### 7.1.1 Perturbation by an oscillating electric field

The oscillating electric field  $\mathbf{E} = \mathbf{E}_0 \cos(\omega t)$  of electromagnetic radiation produces a perturbation described by the Hamiltonian

$$H_I(t) = e\mathbf{r} \cdot \mathbf{E}_0 \cos(\omega t). \quad (7.8)$$

This corresponds to the energy of an electric dipole  $-e\mathbf{r}$  in the electric field, where  $\mathbf{r}$  is the position of the electron with respect to the atom's centre of mass.<sup>2</sup> Note that we have assumed that the electric dipole moment arises from a single electron but the treatment can easily be generalised by summing over all of the atom's electrons. The interaction mixes the two states with energies  $E_1$  and  $E_2$ . Substitution of eqn 7.6 into the time-dependent Schrödinger eqn 7.1 leads to

$$i\dot{c}_1 = \Omega \cos(\omega t) e^{-i\omega_0 t} c_2, \quad (7.9)$$

$$i\dot{c}_2 = \Omega^* \cos(\omega t) e^{i\omega_0 t} c_1, \quad (7.10)$$

where  $\omega_0 = (E_2 - E_1)/\hbar$  and the Rabi frequency  $\Omega$  is defined by

$$\Omega = \frac{\langle 1 | e\mathbf{r} \cdot \mathbf{E}_0 | 2 \rangle}{\hbar} = \frac{e}{\hbar} \int \psi_1^*(\mathbf{r}) \mathbf{r} \cdot \mathbf{E}_0 \psi_2(\mathbf{r}) d^3\mathbf{r}. \quad (7.11)$$

The electric field has almost uniform amplitude over the atomic wavefunction so we take the amplitude  $|\mathbf{E}_0|$  outside the integral.<sup>3</sup> Thus, for radiation linearly polarized along the  $x$ -axis,  $\mathbf{E} = |\mathbf{E}_0| \hat{\mathbf{e}}_x \cos(\omega t)$ , we obtain<sup>4</sup>

<sup>2</sup>Note that  $\mathbf{E}_0 \cos(\omega t)$  is not replaced by a complex quantity  $\mathbf{E}_0 e^{-i\omega t}$ , because a complex convention is built into quantum mechanics and we must not confuse one thing with another.

<sup>3</sup>This *dipole* approximation holds when the radiation has a wavelength greater than the size of the atom, i.e.  $\lambda \gg a_0$ , as discussed in Section 2.2.

<sup>4</sup>Section 2.2 on selection rules shows how to treat other polarizations.

$$\Omega = \frac{eX_{12}|\mathbf{E}_0|}{\hbar}, \quad (7.12)$$

where

$$X_{12} = \langle 1 | x | 2 \rangle. \quad (7.13)$$

To solve the coupled differential equations for  $c_1(t)$  and  $c_2(t)$  we need to make further approximations.

### 7.1.2 The rotating-wave approximation

When all the population starts in the lower level,  $c_1(0) = 1$  and  $c_2(0) = 0$ , integration of eqns 7.9 and 7.10 leads to

$$\begin{aligned} c_1(t) &= 1, \\ c_2(t) &= \frac{\Omega^*}{2} \left\{ \frac{1 - \exp[i(\omega_0 + \omega)t]}{\omega_0 + \omega} + \frac{1 - \exp[i(\omega_0 - \omega)t]}{\omega_0 - \omega} \right\}. \end{aligned} \quad (7.14)$$

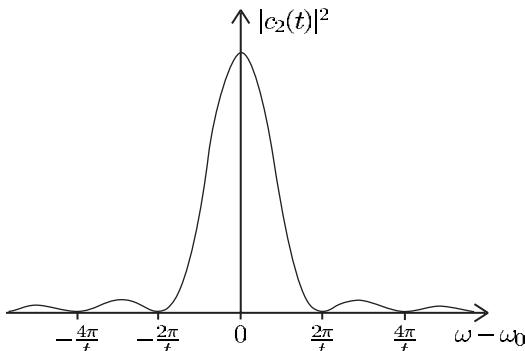
This gives a reasonable first-order approximation while  $c_2(t)$  remains small. For most cases of interest, the radiation has a frequency close to the atomic resonance at  $\omega_0$  so the magnitude of the detuning is small,  $|\omega_0 - \omega| \ll \omega_0$ , and hence  $\omega_0 + \omega \sim 2\omega_0$ . Therefore we can neglect the term with denominator  $\omega_0 + \omega$  inside the curly brackets. This is the **rotating-wave approximation**.<sup>5</sup> The modulus-squared of the co-rotating term gives the probability of finding the atom in the upper state at time  $t$  as

$$|c_2(t)|^2 = \left| \Omega \frac{\sin\{(\omega_0 - \omega)t/2\}}{\omega_0 - \omega} \right|^2, \quad (7.15)$$

or, in terms of the variable  $x = (\omega - \omega_0)t/2$ ,

$$|c_2(t)|^2 = \frac{1}{4} |\Omega|^2 t^2 \frac{\sin^2 x}{x^2}. \quad (7.16)$$

The sinc function  $(\sin x)/x$  has a maximum at  $x = 0$ , and the first minimum occurs at  $x = \pi$  or  $\omega_0 - \omega = \pm 2\pi/t$ , as illustrated in Fig. 7.1; the frequency spread decreases as the interaction time  $t$  increases.



<sup>5</sup>This is not true for the interaction of atoms with radiation at  $10.6 \mu\text{m}$  from a CO<sub>2</sub> laser. This laser radiation has a frequency closer to d.c. than to the resonance frequency of the atoms, e.g. for rubidium with a resonance transition in the near infra-red (780 nm) we find that  $\omega_0 \simeq 15\omega$ , hence  $\omega_0 + \omega \simeq \omega_0 - \omega$ . Thus the counter-rotating term must be kept. The quasi-electrostatic traps (QUEST) formed by such long wavelength laser beams are a form of the dipole-force traps described in Chapter 10.

**Fig. 7.1** The excitation probability function of the radiation frequency has a maximum at the atomic resonance. The line width is inversely proportional to the interaction time. The function  $\text{sinc}^2$  also describes the Fraunhofer diffraction of light passing through a single slit—the diffraction angle decreases as the width of the aperture increases. The mathematical correspondence between these two situations has a natural explanation in terms of Fourier transforms.

## 7.2 The Einstein $B$ coefficients

In the previous section we found the effect of an electric field  $\mathbf{E}_0 \cos(\omega t)$  on the atom. To relate this to Einstein's treatment of the interaction with broadband radiation we consider what happens with radiation of energy density  $\rho(\omega)$  in the frequency interval  $\omega$  to  $\omega + d\omega$ . This produces an electric field of amplitude  $E_0(\omega)$  given by  $\rho(\omega) d\omega = \epsilon_0 E_0^2(\omega) / 2$ . For this narrow (almost monochromatic) slice of the broad distribution eqn 7.12 gives

$$|\Omega|^2 = \left| \frac{e X_{12} E_0(\omega)}{\hbar} \right|^2 = \frac{e^2 |X_{12}|^2}{\hbar^2} \frac{2\rho(\omega) d\omega}{\epsilon_0}. \quad (7.17)$$

Integration of eqn 7.15 over frequency gives the excitation probability for the broadband radiation as

$$|c_2(t)|^2 = \frac{2e^2 |X_{12}|^2}{\epsilon_0 \hbar^2} \int_{\omega_0 - \Delta/2}^{\omega_0 + \Delta/2} \rho(\omega) \frac{\sin^2\{(\omega_0 - \omega)t/2\}}{(\omega_0 - \omega)^2} d\omega. \quad (7.18)$$

We integrate the squares of the amplitudes, rather than taking the square of the total amplitude, since contributions at different frequencies do not interfere.<sup>6</sup> The range of integration  $\Delta$  must be large compared to the extent of the sinc function, but this is easily fulfilled since as time increases this function becomes sharply peaked at  $\omega_0$ . (In the limit  $t \rightarrow \infty$  it becomes a Dirac delta function—see Loudon (2000).) Over the small range about  $\omega_0$  where the sinc function has an appreciable value, a smooth function like  $\rho(\omega)$  varies little, so we take  $\rho(\omega_0)$  outside the integral. A change of variable to  $x = (\omega - \omega_0)t/2$ , as in eqn 7.16, leads to

$$|c_2(t)|^2 \simeq \frac{2e^2 |X_{12}|^2}{\epsilon_0 \hbar^2} \rho(\omega_0) \times \frac{t}{2} \int_{-\phi}^{+\phi} \frac{\sin^2 x}{x^2} dx. \quad (7.19)$$

The integration has limits of  $x = \pm\phi = \pm\Delta t/4 \gg \pi$  and the integral approximates closely to  $\int_{-\infty}^{\infty} x^{-2} \sin^2 x dx = \pi$ . We make this assumption of a long interaction to find the steady-state excitation rate for broadband radiation. The probability of transition from level 1 to 2 increases linearly with time corresponding to a transition rate of

$$R_{12} = \frac{|c_2(t)|^2}{t} = \frac{\pi e^2 |X_{12}|^2}{\epsilon_0 \hbar^2} \rho(\omega_0). \quad (7.20)$$

Comparison with the upward rate  $B_{12}\rho(\omega)$  in Einstein's treatment of radiation (eqn 1.25) shows that

$$B_{12} = \frac{\pi e^2 |D_{12}|^2}{3\epsilon_0 \hbar^2}, \quad (7.21)$$

where  $|X_{12}|^2 \rightarrow |D_{12}|^2/3$ , and  $D_{12}$  is the magnitude of the vector

$$\mathbf{D}_{12} = \langle 1 | \mathbf{r} | 2 \rangle \equiv \int \psi_1^* \mathbf{r} \psi_2 d^3 r. \quad (7.22)$$

The factor of  $1/3$  arises from averaging of  $\mathbf{D} \cdot \hat{\mathbf{e}}_{\text{rad}}$ , where  $\hat{\mathbf{e}}_{\text{rad}}$  is a unit vector along the electric field, over all the possible spatial orientations of the atom (see Exercise 7.6). The relation between  $A_{21}$  and  $B_{12}$  in eqn 1.32 leads to

$$A_{21} = \frac{g_1}{g_2} \frac{4\alpha}{3c^2} \times \omega^3 |D_{12}|^2, \quad (7.23)$$

where  $\alpha = e^2 / (4\pi\epsilon_0\hbar c)$  is the fine-structure constant. The matrix element between the initial and final states in eqn 7.22 depends on an integral involving the electronic wavefunctions of the atom so, as emphasised previously, the Einstein coefficients are properties of the atom. For a typical allowed transition the matrix element has an approximate value of  $D_{12} \simeq 3a_0$  (this can be calculated analytically for hydrogenic systems). Using this estimate of  $D_{12}$  in the equation gives  $A_{21} \simeq 2\pi \times 10^7 \text{ s}^{-1}$  for a transition of wavelength  $\lambda = 6 \times 10^{-7} \text{ m}$  and  $g_1 = g_2 = 1$ . Although we have not given a physical explanation of spontaneous emission, Einstein's argument allows us to calculate its rate; he obtained the relation between  $A_{21}$  and  $B_{21}$  and we have used TDPT to determine  $B_{21}$  from the atomic wavefunctions. For a two-level atom with an allowed transition between the levels the quantum mechanical result corresponds closely to the treatment of radiative decay using classical electromagnetism in Section 1.6.

## 7.3 Interaction with monochromatic radiation

The derivation of eqns 7.14 assumed that the monochromatic radiation perturbed the atom only weakly so that most of the population stayed in the initial state. We shall now find a solution without assuming a weak field. We write eqn 7.9 as

$$i\dot{c}_1 = c_2 \left\{ e^{i(\omega - \omega_0)t} + e^{-i(\omega + \omega_0)t} \right\} \frac{\Omega}{2}, \quad (7.24)$$

and similarly for eqn 7.10. The term with  $(\omega + \omega_0)t$  oscillates very fast and therefore averages to zero over any reasonable interaction time—this is the rotating-wave approximation (Section 7.1.2) and it leads to

$$\begin{aligned} i\dot{c}_1 &= c_2 e^{i(\omega - \omega_0)t} \frac{\Omega}{2}, \\ i\dot{c}_2 &= c_1 e^{-i(\omega - \omega_0)t} \frac{\Omega^*}{2}. \end{aligned} \quad (7.25)$$

These combine to give

$$\frac{d^2 c_2}{dt^2} + i(\omega - \omega_0) \frac{dc_2}{dt} + \left| \frac{\Omega}{2} \right|^2 c_2 = 0. \quad (7.26)$$

The solution of this second-order differential equation for the initial conditions  $c_1(0) = 1$  and  $c_2(0) = 0$  gives the probability of being in the upper state as<sup>7</sup>

<sup>7</sup>For transitions between bound states the frequency  $\Omega$  is real, so  $|\Omega|^2 = \Omega^2$ .

$$|c_2(t)|^2 = \frac{\Omega^2}{W^2} \sin^2\left(\frac{Wt}{2}\right), \quad (7.27)$$

where

$$W^2 = \Omega^2 + (\omega - \omega_0)^2. \quad (7.28)$$

At resonance  $\omega = \omega_0$  and  $W = \Omega$ , so

$$|c_2(t)|^2 = \sin^2\left(\frac{\Omega t}{2}\right). \quad (7.29)$$

<sup>8</sup>This is partly a consequence of the dependence on  $\omega^3$  in eqn 7.23, but also because the magnetic dipole transitions have smaller matrix elements than electric dipole transitions. For electric dipole transitions in the optical region spontaneous emission washes out the Rabi oscillations on a time-scale of tens of nanoseconds ( $\tau = 1/A_{21}$ , assuming that the predominant decay is from 2 to 1, and we estimated  $A_{12}$  above). Nevertheless, experimenters have observed coherent oscillations by driving the transition with intense laser radiation to give a high Rabi frequency ( $\Omega\tau > 1$ ).

The population oscillates between the two levels. When  $\Omega t = \pi$  all the population has gone from level 1 into the upper state,  $|c_2(t)|^2 = 1$ , and when  $\Omega t = 2\pi$  the atom has returned to the lower state. This behaviour is completely different from that of a two-level system governed by rate equations where the populations tend to become equal as the excitation rate increases and population inversion cannot occur. These **Rabi oscillations** between the two levels are readily observed in radio-frequency spectroscopy, e.g. for transitions between Zeeman or hyperfine states. Radio-frequency and microwave transitions have negligible spontaneous emission so that, in most cases, the atoms evolve coherently.<sup>8</sup>

### 7.3.1 The concepts of $\pi$ -pulses and $\pi/2$ -pulses

A pulse of resonant radiation that has a duration of  $t_\pi = \pi/\Omega$  is called a  $\pi$ -pulse and from eqn 7.29 we see that  $\Omega t = \pi$  results in the complete transfer of population from one state to the other, e.g. an atom initially in  $|1\rangle$  ends up in  $|2\rangle$  after the pulse. This contrasts with illumination by broadband radiation where the populations (per state) become equal as the energy density  $\rho(\omega)$  increases. More precisely, a  $\pi$ -pulse swaps the states in a superposition:<sup>9</sup>

$$c_1|1\rangle + c_2|2\rangle \rightarrow -i\{c_1|2\rangle + c_2|1\rangle\}. \quad (7.30)$$

This swap operation is sometimes also expressed as  $|1\rangle \leftrightarrow |2\rangle$ , but the factor of  $-i$  is important in atom interferometry, as shown in Exercise 7.3.

Interferometry experiments also use  $\pi/2$ -pulses that have half the duration of a  $\pi$ -pulse (for the same Rabi frequency  $\Omega$ ). For an atom initially in state  $|1\rangle$ , the  $\pi/2$ -pulse puts its wavefunction into a superposition of states  $|1\rangle$  and  $|2\rangle$  with equal amplitudes (see Exercise 7.3).

### 7.3.2 The Bloch vector and Bloch sphere

In this section we find the electric dipole moment induced on a atom by radiation, and introduce a very powerful way of describing the behaviour of two-level systems by the Bloch vector. We assume that the electric field is along  $\hat{\mathbf{e}}_x$ , as in eqn 7.12. The component of the dipole along this direction is given by the expectation value

$$-eD_x(t) = -\int \Psi^\dagger(t) ex \Psi(t) d^3r. \quad (7.31)$$

<sup>9</sup>This can be shown by solving eqns 7.25 (and 7.26) for  $\omega = \omega_0$ .

Using eqn 7.5 for  $\Psi(t)$  gives this dipole moment of the atom as

$$\begin{aligned} D_x(t) &= \int (c_1 e^{-i\omega_1 t} \psi_1 + c_2 e^{-i\omega_2 t} \psi_2)^* x (c_1 e^{-i\omega_1 t} \psi_1 + c_2 e^{-i\omega_2 t} \psi_2) d^3 r \\ &= c_2^* c_1 X_{21} e^{i\omega_0 t} + c_1^* c_2 X_{12} e^{-i\omega_0 t}. \end{aligned} \quad (7.32)$$

Here  $\omega_0 = \omega_2 - \omega_1$ . The dipole moment is a real quantity since from eqn 7.13 we see that  $X_{21} = (X_{12})^*$ , and also  $X_{11} = X_{22} = 0$ . To calculate this dipole moment induced by the applied field we need to know the bilinear quantities  $c_1^* c_2$  and  $c_2^* c_1$ . These are some of the elements of the density matrix<sup>10</sup>

$$|\Psi\rangle\langle\Psi| = \begin{pmatrix} c_1 \\ c_2 \end{pmatrix} \begin{pmatrix} c_1^* & c_2^* \\ c_2 c_1^* & |c_2|^2 \end{pmatrix} = \begin{pmatrix} |c_1|^2 & c_1 c_2^* \\ c_2 c_1^* & |c_2|^2 \end{pmatrix} = \begin{pmatrix} \rho_{11} & \rho_{12} \\ \rho_{21} & \rho_{22} \end{pmatrix}. \quad (7.33)$$

Off-diagonal elements of the density matrix are called **coherences** and they represent the response of the system at the driving frequency (eqn 7.32). The diagonal elements  $|c_1|^2$  and  $|c_2|^2$  are the populations. We define the new variables

$$\tilde{c}_1 = c_1 e^{-i\delta t/2}, \quad (7.34)$$

$$\tilde{c}_2 = c_2 e^{i\delta t/2}, \quad (7.35)$$

where  $\delta = \omega - \omega_0$  is the detuning of the radiation from the atomic resonance. This transformation does not affect the populations ( $\tilde{\rho}_{11} = \rho_{11}$  and  $\tilde{\rho}_{22} = \rho_{22}$ ) but the coherences become  $\tilde{\rho}_{12} = \rho_{12} \exp(-i\delta t)$  and  $\tilde{\rho}_{21} = \rho_{21} \exp(i\delta t) = (\tilde{\rho}_{12})^*$ . In terms of these coherences the dipole moment is<sup>11</sup>

$$\begin{aligned} -eD_x(t) &= -eX_{12} \{ \rho_{12} e^{i\omega_0 t} + \rho_{21} e^{-i\omega_0 t} \} = -eX_{12} \{ \tilde{\rho}_{12} e^{i\omega t} + \tilde{\rho}_{21} e^{-i\omega t} \} \\ &= -eX_{12} (u \cos \omega t - v \sin \omega t). \end{aligned} \quad (7.36)$$

The coherences  $\tilde{\rho}_{12}$  and  $\tilde{\rho}_{21}$  give the response of the atom at  $\omega$ , the (angular) frequency of the applied field. The real and imaginary parts of  $\tilde{\rho}_{12}$  (multiplied by 2) are:

$$\begin{aligned} u &= \tilde{\rho}_{12} + \tilde{\rho}_{21}, \\ v &= -i(\tilde{\rho}_{12} - \tilde{\rho}_{21}). \end{aligned} \quad (7.37)$$

In eqn 7.36 we see that  $u$  and  $v$  are the in-phase and quadrature components of the dipole in a frame rotating at  $\omega$ . To find expressions for  $\tilde{\rho}_{12}$ ,  $\tilde{\rho}_{21}$  and  $\rho_{22}$ , and hence  $u$  and  $v$ , we start by writing eqns 7.25 for  $c_1$  and  $c_2$  in terms of  $\delta$  as follows:<sup>12</sup>

$$ic_1 = c_2 e^{i\delta t} \frac{\Omega}{2}, \quad (7.38)$$

$$ic_2 = c_1 e^{-i\delta t} \frac{\Omega}{2}. \quad (7.39)$$

Differentiation of eqn 7.34 yields<sup>13</sup>

<sup>10</sup>This is the outer product of  $|\Psi\rangle$  and its Hermitian conjugate  $\langle\Psi| \equiv |\Psi\rangle^\dagger$ , the transposed conjugate of the matrix representing  $|\Psi\rangle$ . This way of writing the information about the two levels is an extremely useful formalism for treating quantum systems. However, we have no need to digress into the theory of density matrices here and we simply adopt it as a convenient notation.

<sup>11</sup>We assume that  $X_{12}$  is real. This is true for transitions between two bound states of the atom—the radial wavefunctions are real and the discussion of selection rules shows that the integration over the angular momentum eigenfunctions also gives a real contribution to the matrix element—the integral over  $\phi$  is zero unless the terms containing powers of  $\exp(-i\phi)$  cancel.

<sup>12</sup>All the steps in this lengthy procedure cannot be written down here but enough information is given for meticulous readers to fill in the gaps.

<sup>13</sup>Spontaneous decay is ignored here—this section deals only with coherent evolution of the states.

$$\dot{\tilde{c}}_1 = \dot{c}_1 e^{-i\delta t/2} - \frac{i\delta}{2} c_1 e^{-i\delta t/2}. \quad (7.40)$$

Multiplication by  $i$  and the use of eqns 7.38, 7.34 and 7.35 yields an equation for  $\dot{\tilde{c}}_1$  (and similarly we can obtain  $\dot{\tilde{c}}_2$  from eqn 7.39):

$$\begin{aligned} i\dot{\tilde{c}}_1 &= \frac{1}{2} (\delta \tilde{c}_1 + \Omega \tilde{c}_2), \\ i\dot{\tilde{c}}_2 &= \frac{1}{2} (\Omega \tilde{c}_1 - \delta \tilde{c}_2). \end{aligned} \quad (7.41)$$

From these we find that the time derivatives  $\dot{\tilde{\rho}}_{12} = \dot{\tilde{c}}_1 \dot{\tilde{c}}_2^* + \dot{\tilde{c}}_1^* \dot{\tilde{c}}_2$ , etc. are

$$\begin{aligned} \frac{d\tilde{\rho}_{12}}{dt} &= \left( \frac{d\tilde{\rho}_{21}}{dt} \right)^* = -i\delta \tilde{\rho}_{12} + \frac{i\Omega}{2} (\rho_{11} - \rho_{22}), \\ \frac{d\rho_{22}}{dt} &= -\frac{d\rho_{11}}{dt} = \frac{i\Omega}{2} (\tilde{\rho}_{21} - \tilde{\rho}_{12}). \end{aligned} \quad (7.42)$$

The last equation is consistent with normalisation in eqn 7.7, i.e.

$$\rho_{22} + \rho_{11} = 1. \quad (7.43)$$

In terms of  $u$  and  $v$  in eqns 7.37 these equations become

$$\begin{aligned} \dot{u} &= \delta v, \\ \dot{v} &= -\delta u + \Omega (\rho_{11} - \rho_{22}), \\ \dot{\rho}_{22} &= \frac{\Omega v}{2}. \end{aligned} \quad (7.44)$$

<sup>14</sup>This is appropriate for calculating absorption. Alternatively,  $\rho_{22} - \rho_{11}$  could be chosen as a variable—this population inversion determines the gain in lasers.

We can write the population difference  $\rho_{11} - \rho_{22}$  as<sup>14</sup>

$$w = \rho_{11} - \rho_{22}, \quad (7.45)$$

so that finally we get the following compact set of equations:

$$\begin{aligned} \dot{u} &= \delta v, \\ \dot{v} &= -\delta u + \Omega w, \\ \dot{w} &= -\Omega v. \end{aligned} \quad (7.46)$$

These eqns 7.46 can be written in vector notation as:

$$\dot{\mathbf{R}} = \mathbf{R} \times (\Omega \hat{\mathbf{e}}_1 + \delta \hat{\mathbf{e}}_3) = \mathbf{R} \times \mathbf{W}, \quad (7.47)$$

by taking  $u$ ,  $v$  and  $w$  as the components of the Bloch vector

$$\mathbf{R} = u \hat{\mathbf{e}}_1 + v \hat{\mathbf{e}}_2 + w \hat{\mathbf{e}}_3, \quad (7.48)$$

and defining the vector

$$\mathbf{W} = \Omega \hat{\mathbf{e}}_1 + \delta \hat{\mathbf{e}}_3 \quad (7.49)$$

that has magnitude  $W = \sqrt{\Omega^2 + \delta^2}$  (cf. eqn 7.28). The cross-product of the two vectors in eqn 7.47 is orthogonal to both  $\mathbf{R}$  and  $\mathbf{W}$ . This implies

that  $\dot{\mathbf{R}} \cdot \mathbf{R} = 0$  so  $|\mathbf{R}|^2$  is constant—it is straightforward<sup>15</sup> to show that this constant is unity so that  $|\mathbf{R}|^2 = |u|^2 + |v|^2 + |w|^2 = 1$ . The Bloch vector corresponds to the position vector of points on the surface of a sphere with unit radius; this Bloch sphere is shown in Fig. 7.2.

It also follows from eqn 7.47 that  $\mathbf{R} \cdot \mathbf{W} = 0$  and so  $\mathbf{R} \cdot \mathbf{W} = RW \cos \theta$  is constant. For excitation with a fixed Rabi frequency and detuning the magnitude  $W$  is constant, and since  $R$  is also fixed the Bloch vector moves around a cone with  $\theta$  constant, as illustrated in Fig. 7.2(d). In this case  $\rho_{22}$  varies as in eqn 7.27 and

$$w = 1 - 2\rho_{22} = 1 - \frac{2\Omega^2}{W^2} \sin^2 \left( \frac{Wt}{2} \right).$$

This motion of the Bloch vector for the state of the atom resembles that of a magnetic moment in a magnetic field,<sup>16</sup> e.g. for adiabatic motion the

<sup>15</sup>  $|\mathbf{R}| = 1$  for the state  $u = v = 0$ ,  $w = 1$  and it always remains unity. This can also be proved by writing  $u$ ,  $v$  and  $w$  in terms of  $|c_1|^2$ ,  $|c_2|^2$ , etc.

<sup>16</sup> As described in Blundell (2001, Appendix G).

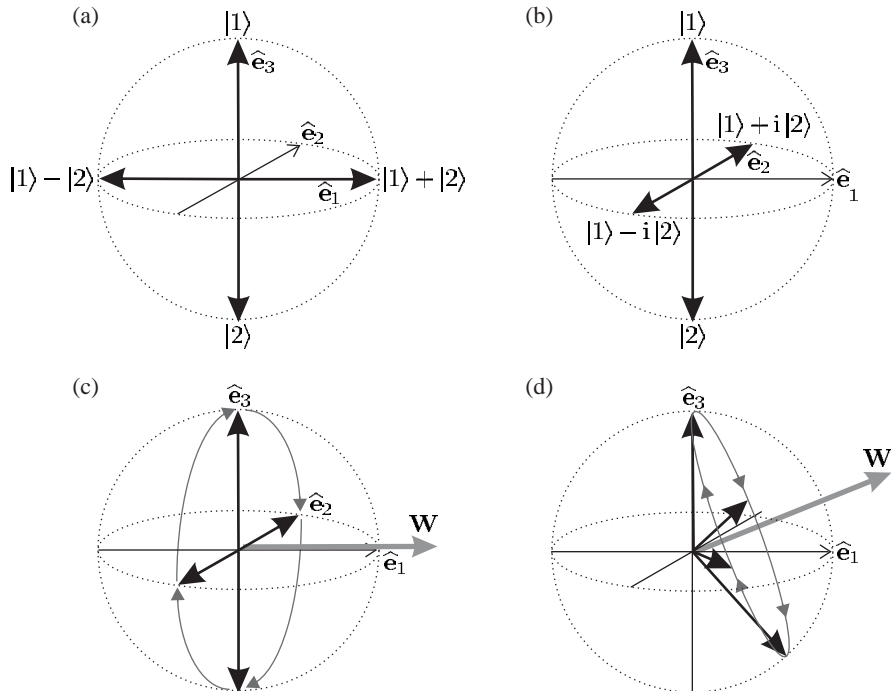


**Fig. 7.2** The Bloch sphere. The position vectors of points on its surface represent the states of a two-level system (in Hilbert space). Examples of states are shown in (a) and (b). At the poles of the sphere the Bloch vector is  $\mathbf{R} = w \hat{\mathbf{e}}_3$ , with  $w = \pm 1$  corresponding to the states  $|1\rangle$  and  $|2\rangle$ , respectively. States that lie on the equator of the Bloch sphere have the form  $\mathbf{R} = u \hat{\mathbf{e}}_1 + v \hat{\mathbf{e}}_2$ , e.g. the states for which  $\mathbf{R} = v \hat{\mathbf{e}}_2$  with  $u = 0$  and  $v = \pm 1$  are shown in (b) and these correspond to  $(|1\rangle \pm i|2\rangle)/\sqrt{2}$ , respectively (normalisation constants are not given in the figure for clarity). These examples illustrate an interesting property of this representation of quantum states, namely that diametrically-opposite states on the Bloch sphere are orthogonal. (c) The evolution of the Bloch vector for a system driven by a resonant field, i.e.  $\delta = 0$  so that  $\mathbf{W} = \Omega \hat{\mathbf{e}}_1$  in eqn 7.49. The evolution follows a great circle from  $|1\rangle$  at the north pole to  $|2\rangle$  at the south pole and back again, as described in Example 7.1. The Bloch vector remains perpendicular to  $\mathbf{W}$ . (d) When  $\delta \neq 0$  the Bloch vector also has a fixed angle with respect to  $\mathbf{W}$ , since  $\mathbf{R} \cdot \mathbf{W} = RW \cos \theta$  is constant, but  $\theta$  is not equal to  $\pi/2$ . (This quantum mechanical description of the two-level atom is equivalent to that for a spin-1/2 system.)

energy  $-\boldsymbol{\mu} \cdot \mathbf{B}$  is constant, and the magnetic moment precesses around the direction of the field  $\mathbf{B} = B\hat{\mathbf{e}}_z$ . In the Bloch description the fictitious magnetic field lies along  $\mathbf{W}$  and the magnitude  $W$  in eqn 7.28 determines the precession rate.

**Example 7.1** Resonant excitation ( $\delta = 0$ ) gives  $\mathbf{W} = \Omega\hat{\mathbf{e}}_1$  and  $\mathbf{R}$  describes a cone about  $\hat{\mathbf{e}}_1$ . An important case is when all the population starts in level 1 so that initially  $\mathbf{R} \cdot \hat{\mathbf{e}}_1 = 0$ ; in this case the Bloch vector rotates in the plane perpendicular to  $\hat{\mathbf{e}}_1$  mapping out a great circle on the Bloch sphere, as drawn in Fig. 7.2(c). This motion corresponds to the Rabi oscillations (eqn 7.29). In this picture a  $\pi/2$ -pulse rotates the Bloch vector through  $\pi/2$  about  $\hat{\mathbf{e}}_1$ . A sequence of two  $\pi/2$ -pulses gives a  $\pi$ -pulse that rotates the Bloch vector (clockwise) through  $\pi$  about  $\hat{\mathbf{e}}_1$ , e.g.  $w = 1 \rightarrow w = -1$  and this represents the transfer of all the population from level 1 to 2.<sup>17</sup> This is consistent with the more general statement given in eqn 7.30.

<sup>17</sup>In this particular example the final state is obvious by inspection, but clearly the same principles apply to other initial states, e.g. states of the form  $\{|1\rangle + e^{i\phi}|2\rangle\}/\sqrt{2}$  that lie on the equator of the sphere. The Bloch sphere is indispensable for thinking about more complex pulse sequences, such as those used in nuclear magnetic resonance (NMR).

The very brief introduction to the Bloch sphere given in this section shows clearly that a two-level atom's response to radiation does not increase indefinitely with the driving field—beyond a certain point an increase in the applied field (or the interaction time) does not produce a larger dipole moment or change in population. This ‘saturation’ has important consequences and makes the two-level system different from a classical oscillator (where the dipole moment is proportional to the field, as will be shown in Section 7.5).

## 7.4 Ramsey fringes

The previous sections in this chapter have shown how to calculate the response of a two-level atom to radiation. In this section we shall apply this theory to radio-frequency spectroscopy, e.g. the method of magnetic resonance in an atomic beam described in Chapter 6. However, the same principles are important whenever line width is limited by the finite interaction time, both within atomic physics and more generally. In particular, we shall calculate what happens to an atom subjected to two pulses of radiation since such a double-pulse sequence has favourable properties for precision measurements.

An atom that interacts with a square pulse of radiation, i.e. an oscillating electric field of constant amplitude from time  $t = 0$  to  $\tau_p$ , and  $E_0 = 0$  otherwise, has a probability of excitation as in eqn 7.15.<sup>18</sup> This excitation probability is plotted in Fig. 7.1 as a function of the radiation's frequency detuning from the (angular) resonance frequency  $\omega_0$ . As stated below eqn 7.16, the frequency spread given by the first minimum of the  $\text{sinc}^2$  function corresponds to a width<sup>19</sup>

$$\Delta f = \frac{\Delta\omega}{2\pi} = \frac{1}{\tau_p}. \quad (7.50)$$

<sup>18</sup>This assumes weak excitation:  $|c_2|^2 \ll 1$ .

<sup>19</sup>This is not the FWHM but it is close enough for our purposes.

<sup>20</sup>This expression is equivalent to eqn 6.40 that was used to calculate the line width for an atomic clock.

The frequency spread is inversely proportional to the interaction time,<sup>20</sup>

as expected from the Fourier transform relationship of the frequency and time domains.

We shall now consider what happens when an atom interacts with two separate pulses of radiation, from time  $t = 0$  to  $\tau_p$  and again from  $t = T$  to  $T + \tau_p$ . Integration of eqn 7.10 with the initial condition  $c_2 = 0$  at  $t = 0$  yields

$$c_2(t) = \frac{\Omega^*}{2} \left\{ \frac{1 - \exp[i(\omega_0 - \omega)\tau_p]}{\omega_0 - \omega} + \exp[i(\omega_0 - \omega)T] \frac{1 - \exp[i(\omega_0 - \omega)\tau_p]}{\omega_0 - \omega} \right\}. \quad (7.51)$$

This is the amplitude excited to the upper level after both pulses ( $t > T + \tau_p$ ). The first term in this expression is the amplitude arising from the first pulse and it equals the part of eqn 7.14 that remains after making the rotating-wave approximation.<sup>21</sup> Within this approximation, interaction with the second pulse produces a similar term multiplied by a phase factor of  $\exp[i(\omega_0 - \omega)T]$ . Either of the pulses acting alone would affect the system in the same way, i.e. the same excitation probability  $|c_2|^2$  as in eqn 7.15. When there are two pulses the amplitudes in the excited state interfere giving

$$\begin{aligned} |c_2|^2 &= \left| \Omega \frac{\sin\{(\omega_0 - \omega)\tau_p/2\}}{(\omega_0 - \omega)} \right|^2 \times |1 + \exp[i(\omega_0 - \omega)T]|^2 \\ &= \left| \frac{\Omega\tau_p}{2} \right|^2 \left[ \frac{\sin(\delta\tau_p/2)}{\delta\tau_p/2} \right]^2 \cos^2\left(\frac{\delta T}{2}\right), \end{aligned} \quad (7.52)$$

where  $\delta = \omega - \omega_0$  is the frequency detuning. The double-pulse sequence produces a signal of the form shown in Fig. 7.3. These are called Ramsey fringes after Norman Ramsey and they have a very close similarity to the interference fringes seen in a Young's double-slit experiment in optics—Fraunhofer diffraction of light with wavevector  $k$  from two slits of width  $a$  and separation  $d$  leads to an intensity distribution as a function of angle  $\theta$  given by<sup>22</sup>

$$I = I_0 \cos^2\left(\frac{1}{2}kd \sin \theta\right) \operatorname{sinc}^2\left(\frac{1}{2}ka \sin \theta\right). \quad (7.53)$$

The overall envelope proportional to  $\operatorname{sinc}^2$  comes from single-slit diffraction. The  $\cos^2$  function determines the width of the central peak in both eqns 7.53 and 7.52.<sup>23</sup>

For the atom excited by two pulses of radiation the excitation drops from the maximum value at  $\omega = \omega_0$  to zero when  $\delta T/2 = \pi/2$  (or to half the maximum at  $\pi/4$ ); so the central peak has a width (FWHM) of  $\Delta\omega = \pi/T$ , or equivalently

$$\Delta f = \frac{1}{2T}. \quad (7.54)$$

This shows that Ramsey fringes from two interactions separated by time  $T$  have half the width of the signal from a single long interaction of

<sup>21</sup>Neglecting terms with  $\omega_0 + \omega$  in the denominator.

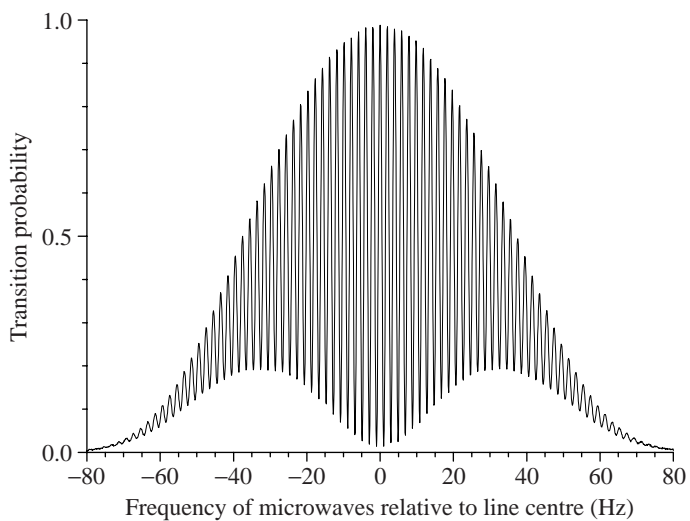
<sup>22</sup>See Section 11.1 and Brooker (2003).

<sup>23</sup>In both quantum mechanics and optics, the amplitudes of waves interfere constructively, or destructively, depending on their relative phase. Also, the calculation of Fraunhofer diffraction as a Fourier transform of amplitude in the plane of the object closely parallels the Fourier transform relationship between pulses in the time domain and the frequency response of the system.

**Fig. 7.3** Ramsey fringes from an atomic fountain of caesium, showing the transition probability for the  $F = 3, M_F = 0$  to  $F' = 4, M_{F'} = 0$  transition versus the frequency of the microwave radiation in the interaction region. The height of the fountain is 31 cm, giving a fringe width just below 1 Hz (i.e.  $\Delta f = 1/(2T) = 0.98$  Hz, see text)—the envelope of the fringes has a more complicated shape than that derived in the text, but this has little influence since, during operation as a frequency standard, the microwaves have a frequency very close to the centre which, by definition, corresponds to 9 192 631 770 Hz. This is real experimental data but the noise is not visible because the signal-to-noise ratio is about 1000 (near the centre), and with such an extremely high-quality signal the short-term stability of a microwave source referenced to the caesium transition is about  $1 \times 10^{-13}$  for 1 s of averaging. Courtesy of Dale Henderson, Krzysztof Szymaniec and Chalupczak Witold, National Physical Laboratory, Teddington, UK.

<sup>24</sup>Ramsey originally introduced two separated interactions in an atomic-beam experiment to avoid the line broadening by inhomogeneous magnetic fields. A small phase difference between the two interaction regions just causes a phase shift of the fringes, whereas if the atom interacts with the radiation throughout a region where the field varies then the contributions from each part of the interaction region do not add in phase. The phasor description, commonly used in optics, gives a good way of thinking about this—Young’s fringes have a high contrast when the two slits of separation  $d$  are illuminated coherently, but to achieve the diffraction limit from a single wide slit of width  $d$  requires a good wavefront across the whole aperture.

<sup>25</sup>In the Bloch sphere description this corresponds to the following path: the initial  $\pi/2$ -pulse causes  $\hat{\mathbf{e}}_3 \rightarrow \hat{\mathbf{e}}_2$ , then the accumulated phase causes the state vector to move around the equator of the sphere to  $-\hat{\mathbf{e}}_2$ , from whence the final  $\pi/2$ -pulse takes the system back up to  $\hat{\mathbf{e}}_3$  (see Fig. 7.2). This formalism allows quantitative calculation of the final state for any type of pulse.



duration  $T$  (cf. eqn 7.50); also, it is often preferable to have two separated interaction regions, e.g. for measurements in an atomic fountain as described in Chapter 8.<sup>24</sup>

In practice, microwave experiments use strong rather than weak excitation (as assumed above) to obtain the maximum signal, i.e.  $|c_2|^2 \simeq 1$ . This does not change the width of the Ramsey fringes, as shown by considering two  $\pi/2$ -pulses separated by time  $T$ . If no phase shift accumulates between the two pulses they add together to act as a  $\pi$ -pulse that transfers all the population to the upper state—from the north to the south pole of the Bloch sphere, as shown in Fig. 7.2(c). But if a relative phase shift of  $\pi$  accrues during the time interval  $T$  then there is destructive interference between the amplitudes in the upper state produced by the two pulses.<sup>25</sup> Thus the first minimum from the central fringe occurs for  $\delta T = \pi$ , which is the condition that gave eqn 7.54, and so that equation remains accurate.

## 7.5 Radiative damping

This section shows how damping affects the coherent evolution of the Bloch vector described in the previous section. It is shown by analogy with the description of a classical dipole that a damping term should be introduced into eqns 7.46. Ultimately, such an argument by analogy is only a justification that the equations have an appropriate form rather

than a derivation, but this approach does give useful physical insight.

### 7.5.1 The damping of a classical dipole

Damping by spontaneous emission can be introduced into the quantum treatment of the two-level atom, in a physically reasonable way, by comparison with the damping of a classical system. To do this we first review the damped harmonic oscillator and express the classical equations in a suitable form. For a harmonic oscillator of natural frequency  $\omega_0$ , Newton's second law leads to the equation of motion

$$\ddot{x} + \beta\dot{x} + \omega_0^2 x = \frac{F(t)}{m} \cos \omega t. \quad (7.55)$$

The driving force has amplitude  $F(t)$  that varies slowly compared to the oscillation at the driving frequency. (The friction force is  $F_{\text{friction}} = -\alpha\dot{x}$  and  $\beta = \alpha/m$ , where  $m$  is the mass.) To solve this we look for a solution of the form

$$x = \mathcal{U}(t) \cos \omega t - \mathcal{V}(t) \sin \omega t. \quad (7.56)$$

This anticipates that most of the time dependence of the solution is an oscillation at frequency  $\omega$ , and  $\mathcal{U}$  is the component of the displacement in-phase with the force, and the quadrature component  $\mathcal{V}$  has a phase lead<sup>26</sup> of  $\pi/2$  with respect to  $F \cos \omega t$ .<sup>27</sup> Substitution of eqn 7.56 into eqn 7.55 and equating terms that depend on  $\sin \omega t$  and  $\cos \omega t$  gives

$$\begin{aligned} \dot{\mathcal{U}} &= (\omega - \omega_0)\mathcal{V} - \frac{\beta}{2}\mathcal{U}, \\ \dot{\mathcal{V}} &= -(\omega - \omega_0)\mathcal{U} - \frac{\beta}{2}\mathcal{V} - \frac{F(t)}{2m\omega}, \end{aligned} \quad (7.57)$$

respectively. The amplitudes  $\mathcal{U}$  and  $\mathcal{V}$  change in time as the amplitude of the force changes, but we assume that these changes occur slowly compared to the fast oscillation at  $\omega$ . This slowly-varying envelope approximation has been used in the derivation of eqn 7.57, i.e.  $\dot{\mathcal{U}}$  and  $\dot{\mathcal{V}}$  have been neglected and  $\dot{\mathcal{V}} \ll \omega\mathcal{V}$  (see Allen and Eberly 1975). By setting  $\dot{\mathcal{U}} = \dot{\mathcal{V}} = 0$  we find the form of the solution that is a good approximation when the amplitudes and the force change slowly compared to the damping time of the system  $1/\beta$ :

$$\mathcal{U} = \frac{\omega_0 - \omega}{(\omega - \omega_0)^2 + (\beta/2)^2} \frac{F}{2m\omega}, \quad (7.58)$$

$$\mathcal{V} = \frac{-\beta/2}{(\omega - \omega_0)^2 + (\beta/2)^2} \frac{F}{2m\omega}. \quad (7.59)$$

The approximation  $\omega^2 - \omega_0^2 = (\omega + \omega_0)(\omega - \omega_0) \simeq 2\omega(\omega - \omega_0)$  has been used so these expressions are only valid close to resonance<sup>28</sup>—they give the wrong result for  $\omega \simeq 0$ . The phase is found from  $\tan \phi = \mathcal{V}/\mathcal{U}$  (see Exercise 7.7). The phase lies in the range  $\phi = 0$  to  $-\pi$  for a force of constant amplitude.<sup>29</sup>

<sup>26</sup>A phase lead occurs when  $\mathcal{V}(t) > 0$ , since  $-\sin \omega t = \cos(\omega t + \pi/2)$ , and  $\mathcal{V}(t) < 0$  corresponds to a phase lag.

<sup>27</sup>This method of considering the components  $\mathcal{U}$  and  $\mathcal{V}$  is equivalent to the phasor description which is widely used in the theory of a.c. circuits (made from capacitors, inductors and resistors) to represent the phase lag, or lead, between the current and an applied voltage of the form  $V_0 \cos \omega t$ .

<sup>28</sup>This is a very good approximation for optical transitions since typically  $\beta/\omega_0 \simeq 10^{-6}$ . The assumption of small damping is implicit in these equations and therefore the resonance frequency is very close to  $\omega_0$ .

<sup>29</sup>It is well known from the study of the harmonic oscillator with damping that the mechanical response lags behind the driving. At low frequencies the system closely follows the driving force, but above the resonance, where  $\omega > \omega_0$ , the phase shift lies in the range  $-\pi/2 < \phi < -\pi$ .

The sum of the kinetic energy  $\frac{1}{2}m\dot{x}^2$  and the potential energy  $\frac{1}{2}m\omega_0^2x^2$  gives the total energy  $E = \frac{1}{2}m\omega^2(\mathcal{U}^2 + \mathcal{V}^2)$  using the approximation  $\omega_0^2 \simeq \omega^2$ . This changes at the rate  $\dot{E} = m\omega^2(\mathcal{U}\dot{\mathcal{U}} + \mathcal{V}\dot{\mathcal{V}})$ , and hence from eqns 7.57 for  $\dot{\mathcal{U}}$  and  $\dot{\mathcal{V}}$  we find that

$$\dot{E} = -\beta E - F\mathcal{V}\frac{\omega}{2}. \quad (7.60)$$

<sup>30</sup>For light damping ( $\beta/\omega_0 \ll 1$ ) the decaying oscillations have angular frequency  $\omega' = \{\omega_0^2 - \beta^2/4\}^{1/2} \simeq \omega_0$ .

For no driving force ( $F = 0$ ) the energy decays away. This is consistent with the complementary function of eqn 7.55 (the solution for  $F = 0$ ) that gives the oscillator's transient response as<sup>30</sup>

$$x = x_0 e^{-\beta t/2} \cos(\omega' t + \varphi). \quad (7.61)$$

Energy is proportional to the amplitude of the motion squared, hence the  $\exp(-\beta t/2)$  dependence in eqn 7.61 becomes  $E \propto \exp(-\beta t)$ . The term  $F\mathcal{V}\omega/2$  in eqn 7.60 is the rate at which the driving force does work on the oscillator; this can be seen from the following expression for power as the force times the velocity:

$$\overline{P} = \overline{F(t) \cos(\omega t)} \dot{x}. \quad (7.62)$$

<sup>31</sup>We use the same slowly varying envelope approximation as for eqn 7.57, namely  $\mathcal{V} \ll \omega\mathcal{V}$ , etc.

<sup>32</sup>This is normally a positive quantity since  $r < 0$  (see eqn 7.59).

The overlining indicates an average over many periods of the oscillation at  $\omega$ , but the amplitude of the force  $F(t)$  may vary (slowly) on a longer time-scale. Differentiation of eqn 7.56 gives the velocity as<sup>31</sup>

$$\dot{x} \simeq -\mathcal{U}\omega \sin \omega t - \mathcal{V}\omega \cos \omega t, \quad (7.63)$$

and only the cosine term contributes to the cycle-averaged power:<sup>32</sup>

$$\overline{P} = -F(t)\mathcal{V}\frac{\omega}{2}. \quad (7.64)$$

This shows that absorption of energy arises from the quadrature component of the response  $\mathcal{V}$ .

In the classical model of an atom as an electron that undergoes simple harmonic motion the oscillating electric field of the incident radiation produces a force  $F(t) = -e|\mathbf{E}_0| \cos \omega t$  on the electron. Each atom in the sample has an electric dipole moment of  $D = -ex$  (along the direction of the applied field). The quadrature component of the dipole that gives absorption has a Lorentzian function of frequency as in eqn 7.59. The in-phase component of the dipole that determines the polarization of the medium and its refractive index (Fox 2001) has the frequency dependence given in eqn 7.58.<sup>33</sup>

When any changes in the driving force occur slowly eqn 7.60 has the following quasi-steady-state solution:

$$E = \frac{|F\mathcal{V}|\omega}{2\beta}. \quad (7.65)$$

<sup>33</sup>See Fig. 9.12.

This shows that the energy of the classical oscillator increases linearly with the strength of the driving force, whereas in a two-level system the energy has an upper limit when all the atoms have been excited to the upper level.

## 7.5.2 The optical Bloch equations

A two-level atom has an energy proportional to the excited-state population,  $E = \rho_{22}\hbar\omega_0$ . By analogy with eqn 7.60 for the energy of a classical oscillator, we introduce a damping term into eqn 7.44 to give

$$\dot{\rho}_{22} = -\Gamma\rho_{22} + \frac{\Omega}{2}v. \quad (7.66)$$

In the absence of the driving term ( $\Omega = 0$ ) this gives exponential decay of the population in level 2, i.e.  $\rho_{22}(t) = \rho_{22}(0)\exp(-\Gamma t)$ . In this analogy, between the quantum system and a classical oscillator,  $\Gamma$  corresponds to  $\beta$ . From eqns 7.57 we see that the coherences  $u$  and  $v$  have a damping factor of  $\Gamma/2$  and eqns 7.46 become the **optical Bloch equations**<sup>34</sup>

$$\begin{aligned} \dot{u} &= \delta v - \frac{\Gamma}{2}u, \\ \dot{v} &= -\delta u + \Omega w - \frac{\Gamma}{2}v, \\ \dot{w} &= -\Omega v - \Gamma(w - 1). \end{aligned} \quad (7.67)$$

For  $\Omega = 0$  the population difference  $w \rightarrow 1$ . These optical Bloch equations describe the excitation of a two-level atom by radiation close to resonance for a transition that decays by spontaneous emission. There is not room here to explore all of the features of these equations and their many diverse and interesting applications; we shall concentrate on the steady-state solution that is established at times which are long compared to the lifetime of the upper level ( $t \gg \Gamma^{-1}$ ), namely<sup>35</sup>

$$\begin{pmatrix} u \\ v \\ w \end{pmatrix} = \frac{1}{\delta^2 + \Omega^2/2 + \Gamma^2/4} \begin{pmatrix} \Omega\delta \\ \Omega\Gamma/2 \\ \delta^2 + \Gamma^2/4 \end{pmatrix}. \quad (7.68)$$

These show that a strong driving field ( $\Omega \rightarrow \infty$ ) tends to equalise the populations, i.e.  $w \rightarrow 0$ . Equivalently, the upper level has a steady-state population of

$$\rho_{22} = \frac{1-w}{2} = \frac{\Omega^2/4}{\delta^2 + \Omega^2/2 + \Gamma^2/4}, \quad (7.69)$$

and  $\rho_{22} \rightarrow 1/2$  as the intensity increases. This key result is used in Chapter 9 on radiation forces.

In the above, the optical Bloch equations have been justified by analogy with a damped classical oscillator but they also closely resemble the Bloch equations that describe the behaviour of a spin-1/2 particle in a combination of static and oscillating magnetic fields.<sup>36</sup> The reader familiar with magnetic resonance techniques may find it useful to make an analogy with that historically important case.<sup>37</sup> For times much shorter than any damping or relaxation time, the two-level atom and spin-1/2 system behave in the same way, i.e. they have a coherent evolution such as  $\pi$ - and  $\pi/2$ -pulses, etc. A steady-state solution of the optical Bloch equations has been presented (and nothing has been said about the different result for a spin-1/2 system).

<sup>34</sup>The main purpose of the rather lengthy discussion of the classical case was to highlight the correspondence between  $u$ ,  $v$  and  $U$ ,  $V$  to make this step seem reasonable. An auxiliary feature of this approach is to remind the reader of the classical electron oscillator model of absorption and dispersion (which is important in atomic physics).

<sup>35</sup>The steady-state solution is obtained by setting  $\dot{u} = \dot{v} = \dot{w} = 0$  in eqns 7.67 to give three simultaneous equations.

<sup>36</sup>The Zeeman effect leads to a splitting between states with  $m_s = \pm 1/2$  to give a two-level system, and the oscillating magnetic field drives *magnetic dipole* transitions between the levels. In atomic physics such transitions occur between Zeeman states and hyperfine levels (Chapter 6).

<sup>37</sup>The Bloch equations were well known from magnetic resonance techniques before lasers allowed the observation of coherent phenomena in optical transitions. Radio-frequency transitions have negligible spontaneous emission and the magnetic dipole of the whole sample decays by other mechanisms. Where the optical Bloch equations (eqns 7.67) have decay constants of  $\Gamma$  and  $\Gamma/2$  for the population and coherences, respectively, the Bloch equations have  $1/T_1$  and  $1/T_2$ . The decay rates  $1/T_1$  and  $1/T_2$  in magnetic resonance techniques are expressed in terms of  $T_1$  and  $T_2$ , the longitudinal and transverse relaxation times, respectively. Under some conditions the two relaxation times are similar, but in other cases  $T_2 \ll T_1$ .  $T_1$  describes the relaxation of the component of the magnetic moment parallel to the applied field  $\mathbf{B}$  which requires exchange of energy (e.g. with the phonons in a solid).  $T_2$  arises from the dephasing of individual magnetic moments (spins) so that the magnetisation of the sample perpendicular to  $\mathbf{B}$  decays. For further details see condensed matter texts, e.g. Kittel (2004).

## 7.6 The optical absorption cross-section

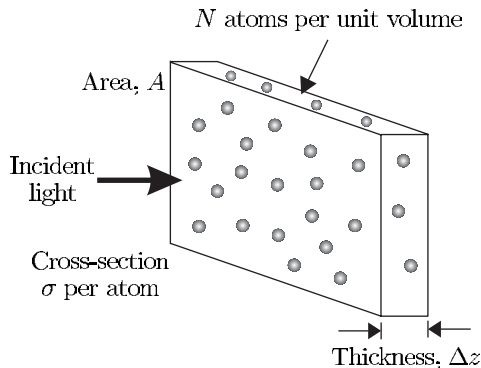
Monochromatic radiation causes an atom to undergo Rabi oscillations, but when the transition has damping the atom settles down to a steady state in which the excitation rate equals the decay rate. This has been shown explicitly above for an optical transition with spontaneous emission, but the same reduction of the coherent evolution of quantum amplitudes to a simple rate equation for populations (amplitudes squared) also occurs for other line-broadening mechanisms, e.g. Doppler broadening (Chapter 8) and collisions. Thus the equilibrium situation for monochromatic radiation is described by rate equations like those in Einstein's treatment of excitation by broadband radiation (eqns 1.25). It is convenient to write these rate equations in terms of an optical absorption cross-section defined in the usual way, as in Fig. 7.4. Consider a beam of particles (in this case photons) passing through a medium with  $N$  atoms per unit volume.<sup>38</sup> A slab of thickness  $\Delta z$  has  $N\Delta z$  atoms per unit area and the fraction of particles absorbed by the target atoms is  $N\sigma\Delta z$ , where  $\sigma$  is defined as the cross-section;  $N\sigma\Delta z$  gives the fraction of the target area covered by the atoms and this equals the probability that an incident particle hits an atom in the target (as it passes through the slab). The parameter  $\sigma$  that characterises the probability of absorption is equally well definable in quantum mechanics (in which photons and particles are delocalised, fuzzy objects) even though this cross-section generally has little relation to the physical size of the object (as we shall see). The probability of absorption equals the fraction of intensity lost,  $\Delta I/I = -N\sigma\Delta z$ , so the attenuation of the beam is described by

$$\frac{dI}{dz} = -\kappa(\omega) I = -N\sigma(\omega)I, \quad (7.70)$$

where  $\kappa(\omega)$  is the absorption coefficient at the angular frequency  $\omega$  of the incident photons. Integration gives an exponential decrease of the intensity with distance, namely

$$I(\omega, z) = I(\omega, 0) \exp\{-\kappa(\omega)z\}. \quad (7.71)$$

**Fig. 7.4** Atoms with number density  $N$  distributed in a slab of thickness  $\Delta z$  absorb a fraction  $N\sigma\Delta z$  of the incident beam intensity, where  $\sigma$  is defined as the cross-section (for absorption).  $N\Delta z$  is the number of atoms per unit area and  $\sigma$  represents the 'target' area that each atom presents. We assume that the motion of the target atoms can be ignored (Doppler broadening is treated in Exercise 7.9) and also that atoms in the next layer (of thickness  $\delta z$ ) cannot 'hide' behind these atoms (see Brooker 2003, Problem 3.26).



This formula, known as Beer's law (see Fox 2001), works well for absorption of low-intensity light that leaves most of the population in the ground state. Intense laser light significantly affects the populations of the atomic levels and we must take this into account. Atoms in level 2 undergo stimulated emission and this process leads to a gain in intensity (amplification) that offsets some of the absorption. Equation 7.70 must be modified to<sup>39</sup>

$$\frac{dI}{dz} = -\kappa(\omega) I(\omega) = -(N_1 - N_2)\sigma(\omega) I(\omega). \quad (7.72)$$

Absorption and stimulated emission have the same cross-section. For the specific case of a two-level atom this can be seen from the symmetry with respect to the exchange of the labels 1 and 2 in the treatment of the two-level atom in the early parts of this chapter; the oscillating electric field drives the transition from 1 to 2 at the same rate as the reverse process—only the spontaneous emission goes one way. This is an example of the general principle that a strong absorber is also a strong emitter.<sup>40</sup> This is also linked to the equality of the Einstein coefficients,  $B_{12} = B_{21}$ , for non-degenerate levels. The population densities in the two levels obey the conservation equation  $N = N_1 + N_2$ .<sup>41</sup> In the steady state conservation of energy per unit volume of the absorber requires that

$$(N_1 - N_2)\sigma(\omega) I(\omega) = N_2 A_{21} \hbar\omega. \quad (7.73)$$

On the left-hand side is the amount by which the rate of absorption of energy exceeds the stimulated emission, i.e. the net rate of energy absorbed per unit volume. On the right-hand side is the rate at which the atoms scatter energy out of the beam—the rate of spontaneous emission for atoms in the excited state times  $\hbar\omega$ .<sup>42</sup> The number densities are related to the variables in the optical Bloch equations by  $\rho_{22} = N_2/N$  and

$$w = \frac{N_2 - N_1}{N}, \quad (7.74)$$

and  $w$  and  $\rho_{22}$  are given in eqns 7.68 and 7.69, respectively. Hence

$$\sigma(\omega) = \frac{\rho_{22}}{w} \frac{A_{21} \hbar\omega}{I} = \frac{\Omega^2/4}{(\omega - \omega_0)^2 + \Gamma^2/4} \times \frac{A_{21} \hbar\omega}{I}. \quad (7.75)$$

Both  $I$  and  $\Omega^2$  are proportional to  $|E_0|^2$  so this cancels out, and further manipulation yields<sup>43</sup>

$$\sigma(\omega) = 3 \times \frac{\pi^2 c^2}{\omega_0^2} A_{21} g_H(\omega). \quad (7.76)$$

The Lorentzian frequency dependence is expressed by the line shape function

$$g_H(\omega) = \frac{1}{2\pi} \frac{\Gamma}{(\omega - \omega_0)^2 + \Gamma^2/4}, \quad (7.77)$$

where the subscript H denotes homogeneous, i.e. something that is the same for each atom, like the radiative broadening considered here.<sup>44</sup> The

<sup>39</sup>We do not try to include the degeneracy of the levels because illumination with intense polarized laser light usually leads to *unequal* populations of the states with different  $M_J$ , or  $M_F$ . This differs from the usual situation in laser physics where the excitation, or pumping mechanisms, populate all states in a given level at the same rate, so  $N_1/g_1$  and  $N_2/g_2$  can be taken as the population densities per state. Selective excitation of the upper level can give  $N_2/g_2 > N_1/g_1$ , and hence gain.

<sup>40</sup>The laws of thermodynamics require that an object stays in equilibrium with black-body radiation at the same temperature, hence the absorbed and emitted powers must balance.

<sup>41</sup>Compare this with eqns 1.26, 7.7 and 7.43.

<sup>42</sup>This assumes that atoms do not get rid of their energy in any other way such as inelastic collisions.

<sup>43</sup>Intensity is related to the electric field amplitude by  $I = \epsilon_0 c |E_0(\omega)|^2/2$ , and  $\Omega^2 = e^2 X_{12}^2 |E_0|^2/\hbar^2$  (eqn 7.12). Also  $X_{12}^2 = |D_{12}|^2/3 \propto A_{21}$  (eqn 7.23). The degeneracy factors are  $g_1 = g_2 = 1$  for the two-level atom, but see eqn 7.79.

<sup>44</sup>It is a general result that homogeneous broadening mechanisms give a Lorentzian line shape.

area under this line shape function equals unity:

$$\int_{-\infty}^{\infty} g_H(\omega) d\omega = 1. \quad (7.78)$$

The pre-factor of 3 in eqn 7.76 may have any value in the range 0 to 3. It has the maximum value of 3 for atoms with the optimum orientation to absorb a beam of polarized laser light (from a specific direction). However, if either the light is unpolarized or the atoms have a random orientation (i.e. they are uniformly distributed across all the  $M_J$  states or  $M_F$  states) then the pre-factor is 1 because  $|X_{12}|^2 = |D_{12}|^2/3$  as in eqn 7.21 (from the average of  $\cos^2 \theta$  over all angles), and this 1/3 cancels the pre-factor of 3.<sup>45</sup> Under these conditions the absorption does not depend on the magnetic state ( $M_J$  or  $M_F$ ) so a real atom with degenerate levels has a cross-section of

$$\sigma(\omega) = \frac{g_2}{g_1} \times \frac{\pi^2 c^2}{\omega_0^2} A_{21} g_H(\omega). \quad (7.79)$$

This equation, or eqn 7.76, applies to many experimental situations. Careful study of the following examples gives physical insight that can be applied to other situations.<sup>46</sup>

**Example 7.2** *Atoms in a specific  $M_F$  state interacting with a polarized laser beam, e.g. sodium atoms in a magnetic trap that absorb a circularly-polarized probe beam (Fig. 7.5)*

This gives effectively a two-level system and the polarization of the light matches the atom's orientation so eqn 7.76 applies (the pre-factor has the maximum value of 3). To drive the  $\Delta M_F = +1$  transition the

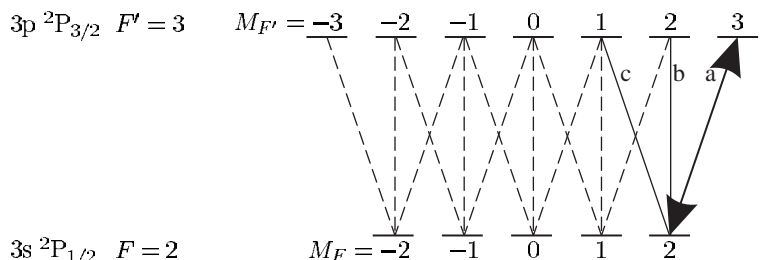


**Fig. 7.5** The Zeeman states of the  $3s\ 2P_{1/2}\ F = 2$  and  $3p\ 2P_{3/2}\ F' = 3$  hyperfine levels of sodium, and the allowed electric dipole transitions between them. The other hyperfine levels ( $F = 1$  and  $F' = 0, 1$  and  $2$ ) have not been shown. Excitation of the transition  $F = 2, M_F = 2$  to  $F' = 3, M_{F'} = 3$  (labelled a) gives a closed cycle that has similar properties to a two-level atom—the selection rules dictate that atoms in the  $F' = 3, M_{F'} = 3$  state spontaneously decay back to the initial state. (Circularly-polarized light that excites  $\Delta M_F = +1$  transitions leads to cycles of absorption and emission that tend to drive the population in the  $F = 2$  level towards the state of maximum  $M_F$ , and this optical pumping process provides a way of preparing a sample of atoms in this state.) When all the atoms have the correct orientation, i.e. they are in the  $F = 2, M_F = 2$  state for this example, then eqn 7.76 applies. Atoms in this state give less absorption for linearly-polarized light (transition b), or circular polarization of the wrong handedness (transition c).

circularly-polarized light must have the correct handedness and propagate along the atom's quantisation axis (defined by the magnetic field in this example).<sup>47</sup>

**Example 7.3** *The absorption of light on an s–p transition, e.g. the 3s–3p resonance line of sodium*

Light with a particular polarization and direction drives a transition to one magnetic sub-level in the upper level, as shown in Fig. 7.6(a). Since the lower level has only  $m_l = 0$  there is no averaging over the orientation and eqn 7.76 applies. Unpolarized light drives transitions to the three upper  $m_l$  states equally. For each transition the averaging gives a factor of 1/3 but all three transitions contribute equally to the absorption so the atoms have the same cross-section as for polarized light (eqn 7.79 with  $g_2/g_1 = 3$ ). Thus the s–p transition is a special case that gives the same absorption cross-section whatever the polarization of the light. Atoms with  $m_l = 0$  have no preferred direction and interact in the same way with light of any polarization (or direction). In contrast, for the p–s transition shown in Fig. 7.6(b), atoms in a given  $m_l$  state only interact with light that has the correct polarization to drive the transition to  $m_l = 0$ .

<sup>47</sup>The direction of the electric field at the atom depends on both the polarization and direction of the radiation, e.g. circularly-polarized light that propagates perpendicular to the quantisation axis drives  $\Delta M_F = 0$  and  $\pm 1$  ( $\pi$ - and  $\sigma$ -) transitions. This leads to a smaller cross-section than when the light propagates along the axis. Radiation that propagates in all directions does not produce a polarized electric field, e.g. isotropic radiation in a black-body enclosure.

### 7.6.1 Cross-section for pure radiative broadening

The peak absorption cross-section given by eqn 7.76, when  $\omega = \omega_0$ , is

$$\sigma(\omega_0) = 3 \times \frac{2\pi c^2}{\omega_0^2} \frac{A_{21}}{\Gamma}. \quad (7.80)$$

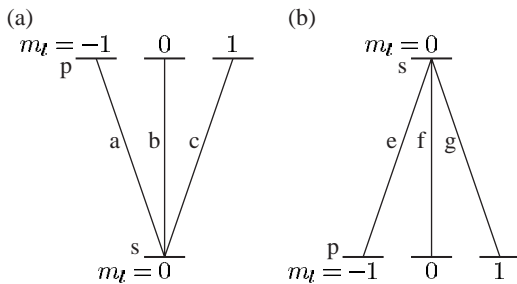


**Fig. 7.6** A comparison of s–p and p–s transitions. (a) The three transitions a, b and c between the s and p levels have equal strength. The physical reason for this is that the spontaneous decay rate of the upper  $m_l$  states cannot depend on the atom's orientation in space. Light linearly-polarized parallel to the z-axis drives  $\pi$ -transition b only, and spontaneous decay occurs back to the initial state since there are no other accessible states—this gives the equivalent of a two-level system. The s–p transition is a special case where the absorption does not depend on the polarization, e.g. unpolarized light gives equal excitation rates on the three transitions a, b and c, and this increases the absorption by the degeneracy factor  $g_2/g_1 = 3$ , thereby cancelling the 1/3 that arises in the orientational average. (b) In contrast, for the p–s transition the peak cross-section is one-ninth of that in (a).<sup>48</sup>

<sup>48</sup>Spin is ignored here. This applies when either the fine structure is not resolved, e.g. this may arise for the transition 2s–3p in hydrogen where the fine structure of the upper level is small, or to transitions between singlet terms, i.e.  ${}^1S$ – ${}^1P$  and  ${}^1P$ – ${}^1S$  (with  $m_l \rightarrow M_l$  in the figure).

In a two-level atom the upper level can only decay to level 1 so  $\Gamma = A_{21}$ , and for a transition of wavelength  $\lambda_0 = 2\pi c/\omega_0$  we find

$$\sigma(\omega_0) = 3 \times \frac{\lambda_0^2}{2\pi} \simeq \frac{\lambda_0^2}{2}. \quad (7.81)$$

This maximum cross-section is much larger than the size of the atom, e.g. the  $\lambda_0 = 589$  nm transition of sodium has  $\sigma(\omega_0) = 2 \times 10^{-13} \text{ m}^2$ , whereas in kinetic theory the atoms have a cross-section of only  $\pi d^2 = 3 \times 10^{-18} \text{ m}^{-2}$  for an atomic diameter of  $d = 0.3$  nm—‘collisions’ between atoms and photons have a large resonant enhancement. The optical cross-section decreases rapidly off resonance, e.g. light of wavelength 600 nm gives  $\Gamma/(\omega - \omega_0) = 10^{-6}$  for the sodium transition above, so that  $\sigma(\omega) = 10^{-12} \times \sigma(\omega_0) = 2 \times 10^{-25} \text{ m}^2$ . Clearly the absorption of radiation has little relation to the size of the electronic orbitals.

### 7.6.2 The saturation intensity

In the previous section we calculated the absorption cross-section starting from eqn 7.73 and we shall now use the same equation to determine the population difference; we can write eqn 7.73 as  $(N_1 - N_2) \times r = N_2$ , where the dimensionless ratio  $r = \sigma(\omega) I(\omega) / (\hbar\omega A_{21})$ . This equation and  $N_1 + N_2 = N$  give the difference in population densities as

$$N_1 - N_2 = \frac{N}{1 + 2r} = \frac{N}{1 + I/I_s(\omega)}, \quad (7.82)$$

where the saturation intensity is defined by

$$I_s(\omega) = \frac{\hbar\omega A_{21}}{2\sigma(\omega)}. \quad (7.83)$$

It is important to note that other definitions of saturation intensity are also used, such as the above expression without 2 in the denominator. From eqn 7.72 we find that the absorption coefficient depends on intensity as follows:<sup>49</sup>

$$\kappa(\omega, I) = \frac{N\sigma(\omega)}{1 + I/I_s(\omega)}. \quad (7.84)$$

The *minimum* value of  $I_{\text{sat}}(\omega)$  occurs on resonance where the cross-section is largest; this minimum value is often referred to as *the saturation intensity*,  $I_{\text{sat}} \equiv I_s(\omega_0)$ , given by<sup>50</sup>

$$I_{\text{sat}} = \frac{\pi}{3} \frac{hc}{\lambda^3 \tau}, \quad (7.85)$$

where  $\tau = \Gamma^{-1}$  is the lifetime for radiative broadening. For example, the resonance transition in sodium at  $\lambda = 589$  nm has a lifetime of  $\tau = 16$  ns and for an appropriate polarization (as in Fig. 7.5) the atom cycles on an effectively two-level transition. This leads to an intensity  $I_{\text{sat}} = 60 \text{ W m}^{-2}$ , or  $6 \text{ mW cm}^{-2}$ , that can easily be produced by a tunable dye laser.

<sup>49</sup>This equation is very similar to the formula for the saturation of gain in a homogeneously-broadened laser system since gain is negative absorption.

<sup>50</sup>Here  $I_{\text{sat}} = \hbar\omega A_{21} / (2\sigma(\omega_0))$  and  $\sigma(\omega_0)$  is given by eqn 7.81.

We can also obtain eqn 7.82 directly from the steady-state value of  $w = (N_1 - N_2)/N$  in eqn 7.68 if the saturation intensity is defined by

$$\frac{I}{I_{\text{sat}}} = \frac{2\Omega^2}{\Gamma^2}. \quad (7.86)$$

This is equivalent to eqn 7.85.<sup>51</sup> At saturation the Rabi frequency has a value comparable with  $\Gamma$ .

<sup>51</sup>As discussed after eqn 7.75,  $\Omega^2/I$  does not depend on the electric field.

### 7.6.3 Power broadening

Equation 7.84 for  $\kappa(\omega, I)$  contains two quantities that vary with frequency:  $\sigma(\omega)$  and  $I_s(\omega)$ .<sup>52</sup> Rearranging this equation to show the frequency dependence, and defining  $\sigma_0 \equiv \sigma(\omega_0)$  as the maximum cross-section in eqn 7.81, we find that

$$\begin{aligned} \kappa(\omega, I) &= N\sigma_0 \frac{\Gamma^2/4}{(\omega - \omega_0)^2 + \Gamma^2/4} \times \frac{1}{1 + \frac{I}{I_{\text{sat}}} \frac{\Gamma^2/4}{(\omega - \omega_0)^2 + \Gamma^2/4}} \\ &= N\sigma_0 \frac{\Gamma^2/4}{(\omega - \omega_0)^2 + \frac{1}{4}\Gamma^2(1 + I/I_{\text{sat}})}. \end{aligned} \quad (7.87)$$

The expression for the absorption coefficient  $\kappa(\omega, I)$  has a Lorentzian line shape with a full width at half maximum (FWHM) of

$$\Delta\omega_{\text{FWHM}} = \Gamma \left(1 + \frac{I}{I_{\text{sat}}}\right)^{1/2}. \quad (7.88)$$

The line width increases with intensity. This power broadening occurs because saturation reduces the absorption near the resonance while far from resonance the absorption changes little (see Fig. 7.7). The expression for the population in the upper level  $\rho_{22}$  in eqn 7.69 also has the same power-broadened line width, as in eqn 7.88.<sup>53</sup> The relationship between this absorption and the populations of the two levels is discussed in Exercise 7.11.

<sup>52</sup>In terms of the *minimum* value  $I_{\text{sat}} = I_s(\omega_0)$  we can rewrite eqn 7.83 as

$$\frac{I_s(\omega)}{I_{\text{sat}}} = \frac{\sigma_0}{\sigma(\omega)}.$$

We also have

$$\sigma(\omega) = \sigma_0 \frac{\Gamma^2/4}{(\omega - \omega_0)^2 + \Gamma^2/4}.$$

<sup>53</sup>This can be shown by rearrangement of the denominator of eqn 7.69 in terms of a line width

$$\begin{aligned} \Delta\omega &= \Gamma \left(1 + \frac{2\Omega^2}{\Gamma^2}\right)^{1/2} \\ &= \Gamma \left(1 + \frac{I}{I_{\text{sat}}}\right)^{1/2}. \end{aligned}$$

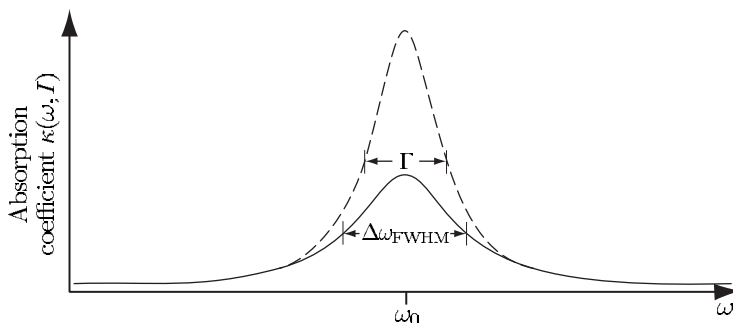


**Fig. 7.7** The absorption coefficient  $\kappa(\omega, I)$  is a Lorentzian function of the frequency that peaks at  $\omega_0$ , the atomic resonance. Saturation causes the absorption line shape to change from the curve for a low intensity ( $I \ll I_{\text{sat}}$ , dashed line), to a broader curve (solid line), with a lower peak value, described by the Lorentzian function in eqn 7.87.

## 7.7 The a.c. Stark effect or light shift

In addition to its effect on the populations, the perturbing radiation also changes the energy of the levels and we calculate this light shift in this section. We can write eqns 7.41 for  $\tilde{c}_1$  and  $\tilde{c}_2$  in matrix form as

$$i \frac{d}{dt} \begin{pmatrix} \tilde{c}_1 \\ \tilde{c}_2 \end{pmatrix} = \begin{pmatrix} \delta/2 & \Omega/2 \\ \Omega/2 & -\delta/2 \end{pmatrix} \begin{pmatrix} \tilde{c}_1 \\ \tilde{c}_2 \end{pmatrix}. \quad (7.89)$$

This has solutions of the form

$$\begin{pmatrix} \tilde{c}_1 \\ \tilde{c}_2 \end{pmatrix} = \begin{pmatrix} a \\ b \end{pmatrix} e^{-i\lambda t}. \quad (7.90)$$

The equation for the eigenvalues  $\lambda$  is

$$\begin{vmatrix} \delta/2 - \lambda & \Omega/2 \\ \Omega/2 & -\delta/2 - \lambda \end{vmatrix} = \lambda^2 - \left(\frac{\delta}{2}\right)^2 - \left(\frac{\Omega}{2}\right)^2 = 0. \quad (7.91)$$

Hence  $\lambda = \pm (\delta^2 + \Omega^2)^{1/2}/2$ . For  $\Omega = 0$  the unperturbed eigenvalues are  $\lambda = \pm \delta/2$ , corresponding to two levels  $\delta$  apart, as shown in Fig. 7.8. This result of time-dependent perturbation theory closely resembles the equations for a time-independent perturbation of two states with an energy separation of  $\delta$  (see Appendix A); the two states are the excited state at  $E_2$  and a level at energy  $E_1 + \hbar\omega$ , corresponding to the ground state plus a photon of the radiation field, see Fig. 7.9. This system of atom plus photon is called a ‘dressed atom’—see Cohen-Tannoudji *et al.* (1992) for a much more in-depth treatment.

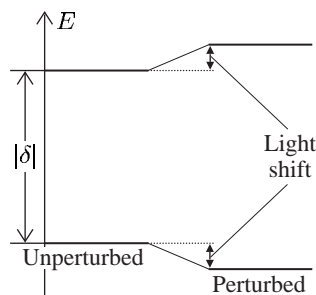
Normally light shifts are most important at large frequency detuning where the effect of absorption is negligible; in this case  $|\delta| \gg \Omega$  and the eigenvalues are

$$\lambda \simeq \pm \left( \frac{\delta}{2} + \frac{\Omega^2}{4\delta} \right). \quad (7.92)$$

The states are shifted from their unperturbed eigenfrequencies by the light shift  $\pm \Omega^2/4\delta$ . From eqn 7.89 we see that the amplitude  $\tilde{c}_1$  is associated with the state with unperturbed energy  $+\delta/2$  and lies above the other state when  $\delta > 0$ . This state with amplitude  $\tilde{c}_1$  has a light shift of

$$\Delta\omega_{\text{light}} = \frac{\Omega^2}{4\delta}. \quad (7.93)$$

**Fig. 7.8** The treatment of the interaction of a two-level atom with radiation by time-dependent perturbation theory leads to eqn 7.89, that looks similar to a time-independent perturbation (proportional to  $\Omega$ ) of two energy levels with an energy separation of  $\delta$ . The light shift is the difference between the unperturbed energies and energy eigenvalues of the system when it is perturbed by the radiation.



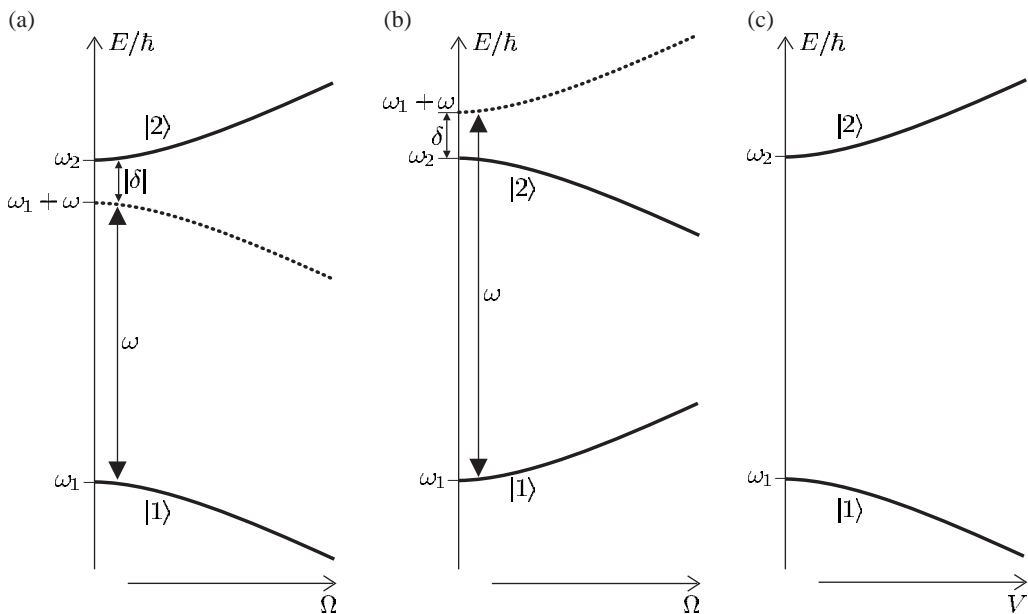


**Fig. 7.9** Eigenenergies of a two-level atom interacting with an external electric field. (a) and (b) show the a.c. Stark effect for negative and positive frequency detunings respectively, as a function of the Rabi frequency. (c) The d.c. Stark effect as a function of the applied field strength.

This equation is also valid for negative frequency detuning  $\delta < 0$  when the light shift of this state decreases its energy. The dependence of the light shift on the sign of  $\delta$  has important consequences for dipole-force traps for atoms, as described in Chapter 9. Figure 7.9 summarises the light shift and shows the d.c. Stark shift for comparison, and the eigenstates of the perturbation are discussed in Appendix A.

## 7.8 Comment on semiclassical theory

This chapter's treatment of the interaction of radiation with atoms is semiclassical—the energy of the atoms is quantised but the radiation is not (since  $E_0 \cos \omega t$  is a classical electric field). It is individual two-level atoms that absorb energy in lumps of  $\hbar\omega$  from the radiation; nevertheless, the quantity  $I/\hbar\omega$  is commonly referred to as the flux of photons. In addition to transitions between two bound quantum states of the atom, this semiclassical theory can also describe photo-ionization where light excites an electron from a bound state to an unbound state above the ionization limit. In such a transition the atom suddenly becomes an ion (plus a free electron) at a given time, like a quantum jump between bound states. The average of many such jumps corresponds to the rate predicted semiclassically.<sup>54</sup> Photo-ionization of individual atoms closely resembles the photoelectric effect that occurs at the surface of a metal with work function  $\Phi$  illuminated by light of frequency  $\omega$ . The sur-

<sup>54</sup>Similarly, in radioactivity the individual nuclei decay randomly but a large sample exhibits a smooth exponential decay.

face only emits electrons if  $\hbar\omega > \Phi$ . Semiclassical theory explains this observation if the least tightly bound energy level, or energy band, of electrons in the metal has a binding energy of  $\Phi$  (cf. the ionization energy of atoms). Electrons come off the surface with a maximum kinetic energy of  $\hbar\omega - \Phi$  because the oscillating field resonantly drives transitions that have angular frequencies close to  $\omega$  (see eqn 7.15), from a lower level in the metal to an upper unbound ‘level’; this explanation does not require quantisation of the light into photons, as often implied in elementary quantum physics. A common line of argument is that a purely classical theory cannot explain various aspects of the photoelectric effect and therefore the light must be quantised. The above discussion shows that this effect can be explained by quantisation of the atoms.<sup>55</sup>

<sup>55</sup>The prompt emission of electrons after the light hits the surface can also be explained semiclassically.

However, there are phenomena that do require quantisation of the radiation field, e.g. in the fluorescence from a single trapped ion it is found that two photons have a lower probability of arriving at the detector together (within the short time period of a measurement) than predicted for a totally random source of photons. This spreading out of the photons, or *anti-bunching*, occurs because it takes a time to excite the ion again after spontaneous emission. Such correlation of photons, or anticorrelation in this case, goes beyond the semiclassical theory presented here. Quantitative calculations of photon statistics require a fully quantum theory called quantum optics. The book on this subject by Loudon (2000) contains more fascinating examples, and also gives rigorous derivations of many results used in this chapter.

## 7.9 Conclusions

The treatment of the interaction of atoms with radiation that has been described in this chapter forms the foundation of spectroscopy, e.g. laser spectroscopy as described in Chapter 8 (and laser physics); it is also important in quantum optics. There are a variety of approaches to this subject and it is worthwhile summarising the particular route that has been followed here.

The introductory sections closely follow Loudon (2000), and Section 7.3 gave a terse account of the coherent evolution of a two-level system interacting with single-frequency radiation—the atom undergoes Rabi oscillations and we saw that the Bloch sphere gives a useful way of thinking about the effect of sequences of  $\pi$ - and  $\pi/2$ -pulses of the atom. In Section 7.5 the introduction of damping terms in the equations was justified by analogy with a behaviour of a classical dipole oscillator and this led to the optical Bloch equations. These equations give a complete description of the system and show how the behaviour at short times where damping has a negligible effect<sup>56</sup> is connected to what happens at longer times (much greater than the damping time) when a steady state has been established. We found that for radiative damping the system settles down to a steady-state solution described by a set of rate equations for the populations of the levels—this turns out to be a general

<sup>56</sup>In the radio-frequency region the damping time can easily be longer than the time of measurement (even if it lasts several seconds). For allowed optical transitions the coherent evolution lasts for only a few nanoseconds, but it can be observed using short pulses of laser radiation. Optical experiments have also been carried out with exceptionally long-lived two-photon transitions (Demtröder 1996).

feature for all broadening mechanisms.<sup>57</sup> In particular, this means that the steady-state populations for an atom illuminated by monochromatic (laser) radiation can be related to the case of illumination by broadband radiation and the rate equations that Einstein wrote down. The theory of the interaction between radiation and matter can also be developed by working ‘backwards’ from the rate equations in Einstein’s treatment of broadband radiation to find the rate equations for the case of monochromatic radiation by making ‘reasonable’ assumptions about the atomic line shape, etc. This approach avoids perturbation theory and is commonly adopted in laser physics; however, it gives no information about coherent phenomena (Rabi oscillations, etc.).<sup>58</sup>

Section 7.6 introduced the concept of an absorption cross-section and its use in the calculation of the absorption of radiation propagating through a gas with a certain number density of atoms.<sup>59</sup> The discussion of the cross-section provides a link between two different perspectives on the interaction of radiation with matter, namely (a) the effect of the radiation on the individual atoms, and (b) the effect of the atomic gas (medium) on the radiation, e.g. absorption.<sup>60</sup> The saturation of absorption as characterised by the saturation intensity forms the basis for a method of Doppler-free spectroscopy described in Chapter 8. From viewpoint (a), saturation arises because there is a maximum rate at which an atom can scatter radiation and this result for individual atoms is important in the discussion of radiation forces in Chapter 9. The formalism developed in this chapter allowed a straightforward derivation of the a.c. Stark effect on the atomic energy levels; this light shift is used in some of the methods of trapping and cooling atoms with laser radiation (also described in Chapter 9).

## Further reading

Loudon’s book on quantum optics gives more rigorous derivations of many formulae in this chapter.<sup>61</sup> Further properties of the optical Bloch equations are discussed by Cohen-Tannoudji *et al.* (1992) and Barnett and Radmore (1997). The treatment of the optical absorption cross-section of a gas closely resembles the calculation of the gain cross-section for a laser and further details can be found in books on laser physics including detailed discussion of broadening mechanisms, e.g. Davis (1996) and Corney (2000).

<sup>57</sup>Both for mechanisms that are homogeneous like radiative broadening, e.g. collisions as shown in Loudon (2000), and also for inhomogeneous mechanisms such as Doppler broadening (Exercise 7.9).

<sup>58</sup>Using time-dependent perturbation theory to describe the underlying behaviour of the two-level atom and finding the rate equations from them gives a clear understanding of the conditions under which these rate equations for the populations are valid.

<sup>59</sup>The inverse of absorption is gain; this is a critical parameter in laser systems that is calculated in terms of an optical cross-section in a very similar way to absorption. The gain also exhibits saturation.

<sup>60</sup>An important objective of this chapter was to show that both of these viewpoints embody the same physics.

<sup>61</sup>I have used similar notation, except  $\Gamma$  for the full width at half maximum (FWHM), whereas Loudon uses the half width  $\gamma = \Gamma/2$ .

## Exercises

(7.1) *Averaging over spatial orientations of the atom*

- (a) Light linearly polarized along the  $x$ -axis gives a dipole matrix element of  $X_{12} = \langle 2 | r | 1 \rangle \cos \phi \sin \theta$ . Show that the average over all solid angles gives a factor of  $1/3$ , as in eqn 7.21.
- (b) Either show explicitly that the same factor of  $1/3$  arises for light linearly polarized along the  $z$ -axis,  $\mathbf{E} = E_0 \hat{\mathbf{e}}_z \cos \omega t$ , or prove this by a general argument.

(7.2) *Rabi oscillations*

- (a) Prove that eqns 7.25 lead to eqn 7.26 and that this second-order differential equation has a solution consistent with eqn 7.27.
- (b) Plot  $|c_2(t)|^2$  for the cases of  $\omega - \omega_0 = 0$ ,  $\Omega$  and  $3\Omega$ .

(7.3)  $\pi$ - and  $\pi/2$ -pulses

- (a) For zero detuning,  $\omega = \omega_0$ , and the initial conditions  $c_1(0) = 1$  and  $c_2(0) = 0$ , solve eqns 7.25 to find both  $c_1(t)$  and  $c_2(t)$ .
- (b) Prove that a  $\pi$ -pulse gives the operation in eqn 7.30.
- (c) What is the overall effect of two  $\pi$ -pulses acting on  $|1\rangle$ ?
- (d) Show that a  $\pi/2$ -pulse gives  $|1\rangle \rightarrow \{|1\rangle - i|2\rangle\}/\sqrt{2}$ .
- (e) What is the overall effect of two  $\pi/2$ -pulses acting on  $|1\rangle$ ? When state  $|2\rangle$  experiences a phase shift of  $\phi$ , between the two pulses, show that the probabilities of ending up in states  $|1\rangle$  and  $|2\rangle$  are  $\sin^2(\phi/2)$  and  $\cos^2(\phi/2)$ , respectively.
- (f) Calculate the effect of the three-pulse sequence  $\pi/2 - \pi - \pi/2$ , with a phase shift of  $\phi$  between the second and third pulses. (The operators can be written as  $2 \times 2$  unitary matrices, although this is not really necessary for this simple case.)

*Comment.* Without the factors of  $-i$  the signals in the two output ports of the interferometer are not complementary. The fact that the identity operation is a  $4\pi$ -pulse rather than  $2\pi$  stems from

the isomorphism between the two-level atom and a spin- $1/2$  system.

(7.4) *The steady-state excitation rate with radiative broadening*

An alternative treatment of radiative decay simply introduces decay terms into eqn 7.25 to give

$$\dot{c}_1 = c_2 \frac{\Omega}{2} e^{i(\omega - \omega_0)t} + i \frac{\Gamma}{2} c_2, \quad (7.94)$$

$$\dot{c}_2 = c_1 \frac{\Omega}{2} e^{-i(\omega - \omega_0)t} - i \frac{\Gamma}{2} c_2. \quad (7.95)$$

This is a phenomenological model, i.e. a guess that works. The integrating factor  $\exp(\Gamma t/2)$  allows eqn 7.95 to be written as

$$\begin{aligned} \frac{d}{dt} \left\{ c_2 \exp \left( \frac{\Gamma t}{2} \right) \right\} \\ = -ic_1 \frac{\Omega^*}{2} \exp \left\{ -i \left( \omega - \omega_0 + \frac{i\Gamma}{2} \right) t \right\}. \end{aligned}$$

- (a) Show that for  $\Omega = 0$  eqn 7.95 predicts that

$$|c_2(t)|^2 = |c_2(t=0)|^2 e^{-\Gamma t}.$$

- (b) For the initial conditions  $c_1(0) = 1$  and  $c_2(0) = 0$ , integration of eqn 7.94 gives  $c_1 \approx 1$ . For these conditions and weak excitation ( $\Omega \ll \Gamma$ ) show that, after a time which is long compared to the radiative lifetime, level 2 has a steady-state population given by

$$|c_2|^2 = \frac{\Omega^2/4}{(\omega - \omega_0)^2 + \Gamma^2/4}.$$

(7.5) *Saturation of absorption*

The  $3s$ - $3p$  resonance line of sodium has a wavelength of  $\lambda = 589$  nm.

- (a) Sodium atoms in a magnetic trap form a spherical cloud of diameter 1 mm. The Doppler shift and the Zeeman effect of the field are both small compared to  $\Gamma$ . Calculate the number of atoms that gives a transmission of  $e^{-1} = 0.37$  for a weak resonant laser beam.
- (b) Determine the absorption of a beam with intensity  $I = I_{\text{sat}}$ .

(7.6) *The properties of some transitions in hydrogen*

The table gives the values of  $A_{21}$  for transitions from the  $n = 3$  shell of hydrogen to lower levels. (Spin and fine structure are ignored.)

| Transition | $A_{21} (\text{s}^{-1})$ |
|------------|--------------------------|
| 2p–3s      | $6.3 \times 10^6$        |
| 1s–3p      | $1.7 \times 10^8$        |
| 2s–3p      | $2.2 \times 10^7$        |
| 2p–3d      | $6.5 \times 10^7$        |

- (a) Draw an energy-level diagram for the  $n = 1, 2$  and 3 shells in hydrogen that shows the allowed electric dipole transitions between the orbital angular momentum levels. (Neglect transitions for which  $n$  does not change, e.g. 2s–2p.)
- (b) Calculate the lifetimes of the 3s, 3p and 3d configurations. What fraction of atoms that start in 3p end up in the 2s configuration?
- (c) An electron in the 2p configuration has a lifetime of only 1.6 ns. Why is this shorter than for the 3p configuration?
- (d) Calculate the radial matrix elements  $D_{12}$  in units of  $a_0$  for the transitions in the table, and for 1s–2p.
- (e) Calculate  $I_{\text{sat}}$  for the 2p–3s and 1s–3p transitions.

(7.7) *The classical model of atomic absorption*

- (a) A simple classical model of absorption assumes that an electron (in an atom) behaves like a damped simple harmonic oscillator of charge  $-e$  and mass  $m_e$  driven by the oscillating electric field of the radiation:  $E_0 \cos \omega t$ . The electron's equation of motion has the form of eqn 7.55 with a driving force of constant amplitude  $F_0 = -eE_0$ . Find a solution of this equation in the form  $x = \mathcal{U} \cos \omega t - \mathcal{V} \sin \omega t$  ( $\mathcal{U}$  and  $\mathcal{V}$  are not functions of time in the case considered here).
- (b) Show that the displacement of the electron has an amplitude

$$\begin{aligned}\sqrt{\mathcal{U}^2 + \mathcal{V}^2} &= \frac{F_0/m}{\sqrt{(\omega^2 - \omega_0^2)^2 + (\beta\omega)^2}} \\ &\approx \frac{F_0}{2m\omega} \left\{ (\omega - \omega_0)^2 + \frac{\beta^2}{4} \right\}^{-1/2}.\end{aligned}$$

Show that the angular frequency  $\omega$  at which this amplitude is maximum is very close to  $\omega_0$  for a narrow resonance.

- (c) Show that the phase is given by

$$\tan \phi = \frac{\mathcal{V}}{\mathcal{U}} = \frac{\beta\omega}{\omega^2 - \omega_0^2}.$$

How does this phase vary as the angular frequency  $\omega$  increases from  $\omega \ll \omega_0$  to  $\omega \gg \omega_0$ ?

- (d) For frequencies close to the atomic resonance ( $\omega \simeq \omega_0$ ), show that your expressions for  $\mathcal{U}$  and  $\mathcal{V}$  can be written in an approximate form that agrees with eqns 7.58 and 7.59 (that were derived using the slowly-varying envelope approximation in which the amplitude of the driving force may change slowly over time).
- (e) Show that in the steady state the power  $P$  absorbed by the electron is a Lorentzian function of  $\omega$ :

$$P \propto \frac{1}{(\omega - \omega_0)^2 + (\beta/2)^2}.$$

(7.8) *Oscillator strength*

This question shows the usefulness of a dimensionless parameter called the absorption oscillator strength, denoted by  $f_{12}$ .

- (a) Show that for the cross-section in eqn 7.79 we have

$$\int_{-\infty}^{\infty} \sigma(\omega) d\omega = 2\pi^2 r_0 c f_{12}, \quad (7.96)$$

where  $r_0 = 2.8 \times 10^{-15}$  m and  $f_{12} = 2m_e\omega D_{12}^2/(3\hbar)$ .

- (b) From the simple model of the atom as an oscillating electron in Exercise 7.7, find the classical absorption cross-section  $\sigma_{\text{cl}}(\omega)$  in terms of  $\beta$ ,  $\omega_0$  and fundamental constants.
- (c) Without the driving electric field, the oscillator undergoes damped harmonic motion  $x = x_0 e^{-\beta t/2} \cos(\omega' t - \varphi)$ . The power radiated by an oscillating dipole leads to a decay rate given by eqn 1.23 (from classical electromagnetism). Determine  $\beta$ .
- (d) Show that  $\sigma_{\text{cl}}(\omega)$  integrated over all frequencies gives  $2\pi^2 r_0 c$ .

*Comment.* This classical value is the maximum value for any transition, so  $f_{12} \leq 1$ . The absorption oscillator strength is a fraction of the integrated cross-section associated with a given transition.

- (e) Calculate  $f_{12}$  for the 3s–3p transition of sodium. ( $A_{21} = \Gamma = 2\pi \times 10^7 \text{ s}^{-1}$ .)
- (f) Calculate the absorption oscillator strength for the 1s–2p and 1s–3p transitions in hydrogen using the data from Exercise 7.6(d).

(7.9) *Doppler broadening*

The Maxwell–Boltzmann distribution of the velocities in a gas is a Gaussian function  $f(v)$ , as defined in eqn 8.3. Explain why for excitation by monochromatic radiation of angular frequency  $\omega$  the population in the upper level is given by

$$|c_2(t)|^2 = \frac{e^2 X_{12}^2}{\hbar^2} |E(\omega)|^2 \times \int_{-\infty}^{\infty} \frac{\sin^2 \{(\omega - \omega_0 + kv)t/2\}}{(\omega - \omega_0 + kv)^2} f(v) dv.$$

Assuming that the  $\text{sinc}^2$  in the integrand acts like a Dirac delta function (as explained in Section 7.2), show that  $|c_2|^2$  is proportional to  $g_D(\omega)$  in eqn 8.4.

*Comment.* Doppler broadening washes out the Rabi oscillations because their frequency depends on the velocity, giving an equation similar to that for broadband radiation. For all broadening mechanisms Rabi oscillations, and other coherent phenomena, are only seen on time-scales shorter than the reciprocal of the line width.

(7.10) *An example of the use of Fourier transforms*

Show that an oscillator whose amplitude decays exponentially according to  $x_0 e^{-\beta t/2} \cos(\omega t)$  radiates with a Lorentzian power spectrum.

(7.11) *The balance between absorption and spontaneous emission*

Explain why absorption and the population in the upper level are related by

$$\kappa(\omega, I) I = N_2 A_{21} \hbar \omega = N \rho_{22} A_{21} \hbar \omega. \quad (7.97)$$

Show that this is consistent with eqns 7.87 and 7.69 for  $\kappa(\omega, I)$  and  $\rho_{22}$ , respectively.

Web site:

<http://www.physics.ox.ac.uk/users/foot>

This site has answers to some of the exercises, corrections and other supplementary information.

*Comment.* An electric dipole does not radiate uniformly in all directions but this does not matter here; only a tiny fraction of the spontaneous emission goes along the direction of the incident beam. For example, in an experiment to measure the attenuation of a laser beam as it passes through a gas cell, a negligible fraction of the light scattered out of the beam falls on the photodetector that measures the power after the sample.

(7.12) *The d.c. Stark effect*

This exercise goes through a treatment of the d.c. Stark effect for comparison with the a.c. Stark effect.

- (a) An atom with two levels of energies  $E_2 > E_1$ , and a separation of  $\epsilon = E_2 - E_1$  is placed in a *static* electric field. Show that the Hamiltonian for the system has the form

$$\hat{H} = \begin{pmatrix} \epsilon/2 & V \\ V & -\epsilon/2 \end{pmatrix},$$

where the matrix element for the perturbation  $V$  is proportional to the magnitude of the electric field. Find the energy eigenvalues. The two levels move apart as shown in Fig. 7.9—this is a general feature of systems where a perturbation mixes the wavefunctions.

- (b) Show that ‘weak’ fields produce a quadratic Stark effect on the atom, equivalent to the usual second-order perturbation-theory expression for a perturbation  $H_I$ :

$$\Delta E_1 = -\frac{|\langle 2 | H_I | 1 \rangle|^2}{E_2 - E_1}.$$

A similar expression can be found for the energy shift  $\Delta E_2$  of the other level (in the opposite direction).

- (c) Estimate the Stark shift for the ground state of a sodium atom in a field of  $10^6 \text{ V m}^{-1}$  (e.g.  $10^4 \text{ V}$  between plates 1 cm apart).

# Doppler-free laser spectroscopy

## 8

Doppler broadening is usually the dominant contribution to the observed width of lines in atomic spectra, at room temperature. The techniques of Doppler-free laser spectroscopy overcome this limitation to give much higher resolution than, for example, a Fabry–Perot étalon analyzing the light from a discharge lamp, as shown in Fig. 1.7(a). This chapter describes three examples that illustrate the principles of Doppler-free techniques: the crossed-beam method, saturated absorption spectroscopy and two-photon spectroscopy. To use these high resolution techniques for precision measurements of atomic transition frequencies the laser frequency must be determined accurately. Thus the calibration is a crucial part of laser spectroscopy experiments, as discussed at the end of this chapter. Since it is important to understand the problem before looking at the solution, the chapter starts with an outline of Doppler broadening of spectral lines in gases.

### 8.1 Doppler broadening of spectral lines

The relationship between the angular frequency  $\omega$  of radiation in the laboratory frame of reference and the angular frequency seen in a frame of reference moving at velocity  $\mathbf{v}$ , as shown in Fig. 8.1, is

$$\omega' = \omega - kv, \quad (8.1)$$

where the wavevector of the radiation has magnitude  $k = \omega/c = 2\pi/\lambda$ . It is the component of the velocity along  $\mathbf{k}$  that leads to the Doppler effect and here it has been assumed that  $\mathbf{k} \cdot \mathbf{v} = kv$ .<sup>1</sup>

|  |     |
|--|-----|
| 8.1 Doppler broadening of spectral lines | 151 |
| 8.2 The crossed-beam method              | 153 |
| 8.3 Saturated absorption spectroscopy    | 155 |
| 8.4 Two-photon spectroscopy              | 163 |
| 8.5 Calibration in laser spectroscopy    | 168 |
| Further reading                          | 175 |
| Exercises                                | 175 |

<sup>1</sup>If necessary, this and other equations in this chapter could be generalised by replacing  $kv$  with the scalar product  $\mathbf{k} \cdot \mathbf{v}$ .

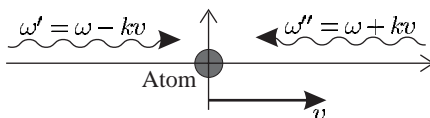


**Fig. 8.1** The Doppler effect on the observed frequency of radiation. Radiation that has an angular frequency of  $\omega$  in the laboratory frame of reference has the frequencies indicated in a reference frame moving with a speed  $v$ , e.g. the rest frame of an atom. Only the component of the velocity along the wavevector  $\mathbf{k}$  contributes to the first-order Doppler shift.

<sup>2</sup>Section 8.3 describes what happens when the atoms absorb a range of frequencies, given by the homogeneous width, in addition to any Doppler broadening. Absorption is considered here because of its relevance to laser spectroscopy, but Doppler broadening of an emission line arises in the same way—atoms emit at  $\omega_0$  in their rest frame and we see a frequency shift in the laboratory.

<sup>3</sup>This can easily be shown by differentiating the Maxwell speed distribution which is proportional to  $v^2$  times the velocity distribution, see Table 8.1.

<sup>4</sup>Note that  $\int_{-\infty}^{\infty} g(\omega) d\omega = 1$ .

In this section, we consider the Doppler effect on the absorption by a gas where each atom absorbs radiation at frequency  $\omega_0$  in its rest frame, i.e. when  $\omega' = \omega_0$ .<sup>2</sup> Thus atoms moving with velocity  $v$  absorb radiation when  $\delta = \omega - \omega_0 = kv$ , or equivalently

$$\frac{\delta}{\omega_0} = \frac{v}{c}. \quad (8.2)$$

In a gas the fraction of atoms with velocity in the range  $v$  to  $v + dv$  is

$$f(v) dv = \sqrt{\frac{M}{\pi 2k_B T}} \exp\left(-\frac{Mv^2}{2k_B T}\right) dv \equiv \frac{1}{u\sqrt{\pi}} \exp\left(-\frac{v^2}{u^2}\right) dv. \quad (8.3)$$

Here  $u = \sqrt{2k_B T/M}$  is the most probable speed for atoms of mass  $M$  at temperature  $T$ .<sup>3</sup> Relating  $v$  to the frequency via eqn 8.2, we find that the absorption has the Gaussian line shape function<sup>4</sup>

$$g_D(\omega) = \frac{c}{u\omega_0\sqrt{\pi}} \exp\left\{-\frac{c^2}{u^2} \left(\frac{\omega - \omega_0}{\omega_0}\right)^2\right\}. \quad (8.4)$$

The maximum value occurs at  $\omega = \omega_0$  and the function falls to half its maximum value at  $\omega - \omega_0 = \delta_{1/2}$ , where

$$\left(\frac{c\delta_{1/2}}{u\omega_0}\right)^2 = \ln 2. \quad (8.5)$$

The Doppler-broadened line has a full width at half maximum (FWHM) of  $\Delta\omega_D = 2\delta_{1/2}$  given by<sup>5</sup>

$$\frac{\Delta\omega_D}{\omega_0} = 2\sqrt{\ln 2} \frac{u}{c} \simeq 1.7 \frac{u}{c}. \quad (8.6)$$

Kinetic theory gives the most probable speed in a gas as

$$u = 2230 \text{ m s}^{-1} \times \sqrt{\frac{T}{300 \text{ K}}} \times \frac{1 \text{ a.m.u.}}{M}. \quad (8.7)$$

**Table 8.1** The characteristic velocities in a gas with a Maxwellian distribution of speeds and in an effusive atomic beam;  $u = \sqrt{2k_B T/M}$ , where  $T$  is the temperature and  $M$  is the mass. The extra factor of  $v$  in the distribution for a beam, as compared to that of a gas, arises from the way that atoms effuse through a small hole of area  $A$ . Atoms with speed  $v$  are incident on a surface of area  $A$  at a rate of  $N(v) vA/4$ , where  $N(v)$  is the number density of atoms with speeds in the range  $v$  to  $v + dv$ —faster atoms are more likely to pass through the hole. Integration over  $v$  leads to the well-known kinetic theory result  $N\bar{v}A/4$  for the flux that arrives at the surface, where  $N$  is the total number density. The mean speed  $\bar{v}$  has a value between the most probable and the root-mean-square velocities.

|                           | Gas                  | Beam                 |
|---------------------------|----------------------|----------------------|
| Distribution              | $v^2 \exp(-v^2/u^2)$ | $v^3 \exp(-v^2/u^2)$ |
| Most probable $v$         | $u$                  | $\sqrt{3/2} u$       |
| Root-mean-square velocity | $\sqrt{3/2} u$       | $\sqrt{2} u$         |

In the formula, the atomic mass  $M$  must be expressed in atom mass units, e.g.  $M = 1$  a.m.u. for atomic hydrogen. Numerical values of  $u$  are given below for hydrogen and a vapour of caesium, both at a temperature of  $T = 300\text{ K}$ .<sup>6</sup>

| $M$ (a.m.u.) | $u$ ( $\text{m s}^{-1}$ ) | $\Delta\omega_D/\omega_0$ | $\Delta f_D$ (GHz), for 600 nm |
|--------------|---------------------------|---------------------------|--------------------------------|
| H            | 1                         | $2230$                    | $1 \times 10^{-5}$             |
| Cs           | 133                       | 200                       | $1 \times 10^{-6}$             |

<sup>6</sup>In this table  $\Delta f_D = 1.7u/\lambda$ .

The values given for the fractional width  $\Delta\omega_D/\omega_0$  show that heavy elements have an order of magnitude smaller Doppler width than hydrogen. The Doppler shift of the frequency  $\Delta f_D$  is also given for a wavelength of 600 nm. (This wavelength does not correspond to actual transitions.<sup>7</sup>) These calculations show that Doppler broadening limits optical spectroscopy to a resolution of  $\sim 10^6$  even for heavy elements.<sup>8</sup>

The Doppler effect on the absorption of a gas is an example of an inhomogeneous broadening mechanism; each atom interacts with the radiation in a different way because the frequency detuning, and hence absorption and emission, depend on the velocity of the individual atom. In contrast, the radiative broadening by spontaneous decay of the excited level gives the same natural width for all atoms of the same species in a gas—this is a homogeneous broadening mechanism.<sup>9</sup> The difference between homogeneous and inhomogeneous broadening is crucially important in laser physics and an extensive discussion and further examples can be found in Davis (1996) and Corney (2000).<sup>10</sup>

## 8.2 The crossed-beam method

Figure 8.2 shows a simple way to reduce the Doppler effect on a transition. The laser beam intersects the atomic beam at right angles. A thin vertical slit collimates the atomic beam to give a small angular spread  $\alpha$ . This gives a spread in the component of the atomic velocity along the direction of the light of approximately  $\alpha v_{\text{beam}}$ . Atoms in the beam have slightly higher characteristic velocities than in a gas at the same temperature, as shown in Table 8.1, because faster atoms have a higher probability of effusing out of the oven. Collimation reduces the Doppler broadening to

$$\Delta f \simeq \frac{\alpha v_{\text{beam}}}{\lambda} \sim \alpha \Delta f_D, \quad (8.8)$$

where  $\Delta f_D$  is the Doppler width of a gas at the same temperature as the beam.<sup>11</sup>

**Example 8.1** Calculation of the collimation angle for a beam of sodium that gives a residual Doppler broadening comparable with the natural width  $\Delta f_N = 10\text{ MHz}$  (for the resonance transition at  $\lambda = 589\text{ nm}$ )

<sup>7</sup>The Doppler widths of optical transitions in other elements normally lie between the values for H and Cs. A useful way to remember the correct order of magnitude is as follows. The speed of sound in air is  $330\text{ m s}^{-1}$  (at  $0^\circ\text{C}$ ), slightly less than the speed of the air molecules. The speed of sound divided by the speed of light equals  $10^{-6}$ . Multiplication by a factor of 2 converts the half-width to a FWHM of  $\Delta\omega_D/\omega_0 \approx 2 \times 10^{-6}$ , which gives a reasonable estimate of the fractional Doppler shift of medium-heavy elements.

<sup>8</sup>The resolving power of a Fabry–Perot étalon can easily exceed  $\sim 10^6$  (Brooker 2003), so that normally the instrumental width does not limit the resolution, in the visible region.

<sup>9</sup>The different characteristics of the two types of broadening mechanism are discussed further in this chapter, e.g. see Fig. 8.3.

<sup>10</sup>The treatment of the saturation of gain in different classes of laser system is closely related to the discussion of saturation of absorption, both in principle and also in the historical development of these subjects.

<sup>11</sup>A numerical factor of  $0.7 \simeq 1.2/1.7$  has been dropped. To obtain a precise formula we would have to consider the velocity distribution in the beam and its collimation—usually the exit slit of the oven and the collimation slit have comparable widths.

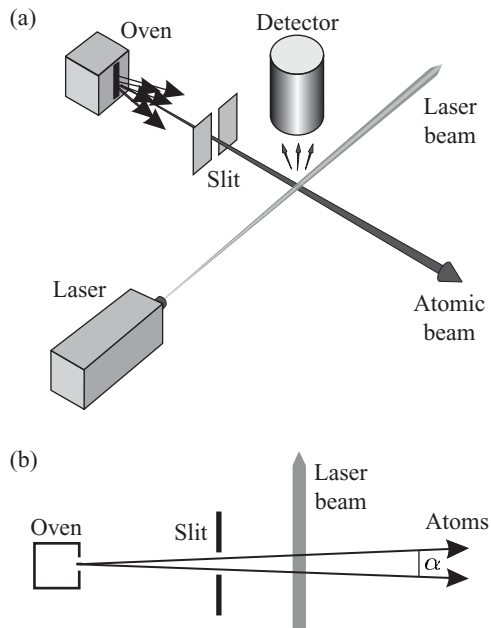


**Fig. 8.2** Laser spectroscopy of a collimated atomic beam. The component of atomic velocity along the laser beam has a small spread  $\alpha v_{\text{beam}}$ , where  $\alpha$  is the collimation angle shown on the plan view in (b).

Sodium vapour at 1000 K has a Doppler width of  $\Delta f_D = 2.5 \text{ GHz}$  and the most probable velocity in the beam is  $v_{\text{beam}} \simeq 1000 \text{ m s}^{-1}$ . Thus a suitable collimation angle for a beam of sodium effusing from an oven at this temperature is

$$\alpha = \frac{\Delta f_N}{\Delta f_D} = \frac{10}{2500} = 4 \times 10^{-3} \text{ rad}. \quad (8.9)$$

This angle corresponds to a slit 1 mm wide positioned 0.25 m from the oven. Collimation of the beam to a smaller angular spread would just throw away more of the atomic flux to give a weaker signal without reducing the observed line width.

In this experiment, atoms interact with the light for a time  $\Delta t \simeq d/v_{\text{beam}}$ , where  $d$  is the laser beam diameter. The finite interaction time leads to a spread in frequencies called transit-time broadening.<sup>12</sup> For a laser beam of diameter 1 mm we find

$$\Delta f_{\text{tt}} = \frac{v_{\text{beam}}}{d} = \frac{1000}{10^{-3}} \simeq 1 \text{ MHz}. \quad (8.10)$$

Thus this broadening mechanism does not have a significant effect in this experiment, compared to the natural width of the optical transition. (Transit time is an important consideration for the radio-frequency measurements with atomic beams described in Section 6.4.2.) Collision broadening has a negligible effect in the experiment shown in Fig 8.2 because of the low density of atoms in the atomic beam and also in the background gas in the vacuum chamber. An atomic-beam apparatus must have a high vacuum since even a glancing collision with a

<sup>12</sup>From eqn 7.50,  $\Delta f \simeq 1/\Delta t$ .

background gas molecule deflects an atom out of the highly-collimated beam.

**Example 8.2** Figure 6.12 in the chapter on hyperfine structure showed a spectrum of tin (Sn) obtained by the crossed-beam technique that illustrated isotope and hyperfine structure. Comparison with the Doppler-broadened spectrum emitted by a cadmium lamp clearly showed the advantages of the crossed-beam technique.<sup>13</sup>

Experimenters used highly-monochromatic light sources to demonstrate the principle of the crossed-beam method before the advent of lasers, but the two other techniques described in this chapter rely on the high-intensity and narrow-frequency bandwidth of laser light.

### 8.3 Saturated absorption spectroscopy

We derived the line shape for Doppler broadening in Section 8.1 on the assumption that an atom at rest absorbs radiation exactly at  $\omega_0$ . In reality the atoms absorb radiation over a range of frequencies given by the homogeneous width of the transition, e.g. the line width  $\Gamma$  caused by radiative broadening. In this section we shall reconsider absorption of monochromatic radiation in a way that includes homogeneous broadening together with the inhomogeneous broadening caused by the atom's motion. This approach leads naturally into a discussion of saturated absorption spectroscopy.

We consider a laser beam of intensity  $I(\omega)$  that travels through a sample of atoms, as shown in Fig. 7.4. In this chapter we consider the atoms as moving, whereas previously they were taken to be stationary.<sup>14</sup> Atoms with velocities in the velocity class  $v$  to  $v + dv$  see radiation with an effective frequency of  $\omega - kv$  in their rest frame, and for those atoms the absorption cross-section is  $\sigma(\omega - kv)$ , defined in eqn 7.76. The number density of atoms in this velocity class is  $N(v) = Nf(v)$ , where  $N$  is the total number density of the gas (in units of atoms m<sup>-3</sup>) and the distribution  $f(v)$  is given in eqn 8.3. Integration of the contributions from all the velocity classes gives the absorption coefficient as

$$\begin{aligned}\kappa(\omega) &= \int N(v) \sigma(\omega - kv) dv \\ &= \frac{g_2}{g_1} \frac{\pi^2 c^2}{\omega_0^2} A_{21} \times \int N(v) g_H(\omega - kv) dv \\ &= \frac{g_2}{g_1} \frac{\pi^2 c^2}{\omega_0^2} A_{21} \times N \int f(v) \frac{\Gamma/(2\pi)}{(\omega - \omega_0 - kv)^2 + \Gamma^2/4} dv.\end{aligned}\quad (8.11)$$

The integral is the convolution of the Lorentzian function  $g_H(\omega - kv)$  and the Gaussian function  $f(v)$ .<sup>15</sup> Except at very low temperatures the homogenous width is much less than the Doppler broadening,  $\Gamma \ll \Delta\omega_D$ , so that the Lorentzian is sharply peaked and acts like a delta function

<sup>13</sup>The spacings between the lines from different isotopes does not depend on the angle between the laser beam and the atomic beam, but for absolute measurements of transition frequencies the angle must be accurately set to 90°.

<sup>14</sup>At room temperature, the Doppler width usually exceeds natural and other homogeneous broadening mechanisms. Very cold atomic vapours in which the Doppler shifts are smaller than the natural width of allowed transitions can be prepared by the laser cooling techniques described in Chapter 9.

<sup>15</sup>In general, the convolution leads to a Voigt function that needs to be calculated numerically (Corney 2000 and Loudon 2000).

$g_H(\omega - kv) \equiv \delta(\omega - \omega_0 - kv)$  that picks out atoms moving with velocity

$$v = \frac{\omega - \omega_0}{k}. \quad (8.12)$$

<sup>16</sup>This is a convolution of the solution for a stationary atom with the velocity distribution (cf. Exercise 7.9).

Integration over  $v$  transforms  $f(v)$  into the Gaussian line shape function in eqn 8.4:<sup>16</sup>

$$g_D(\omega) = \int f(v) g_H(\omega - kv) dv. \quad (8.13)$$

Thus since  $\kappa(\omega) = N\sigma(\omega)$  (from eqn 7.70) we find from eqn 8.11 that the cross-section for Doppler-broadened absorption is

$$\sigma(\omega) = \frac{g_2}{g_1} \frac{\pi^2 c^2}{\omega_0^2} A_{21} g_D(\omega). \quad (8.14)$$

<sup>17</sup>The cross-section only has a significant value near  $\omega_0$ , so taking the lower limit of the integration to be 0 (which is realistic) or  $-\infty$  (which is easy to evaluate) makes little difference.

Integration of  $g_D(\omega)$  over frequency gives unity, as in eqn 7.78 for homogeneous broadening. Thus both types of broadening have the same integrated cross-section, namely<sup>17</sup>

$$\int_0^\infty \sigma(\omega) d\omega = \frac{g_2}{g_1} \frac{\lambda_0^2}{4} A_{21}. \quad (8.15)$$

The line broadening mechanisms spread this integrated cross-section out over a range of frequencies so that the peak absorption decreases as the frequency spread increases. The ratio of the peak cross-sections approximately equals the ratio of the line widths:

$$\frac{[\sigma(\omega_0)]_{\text{Doppler}}}{[\sigma(\omega_0)]_{\text{Homog}}} = \frac{g_D(\omega_0)}{g_H(\omega_0)} = \sqrt{\pi \ln 2} \frac{\Gamma}{\Delta\omega_D}. \quad (8.16)$$

The numerical factor  $\sqrt{\pi \ln 2} = 1.5$  arises in the comparison of a Gaussian to a Lorentzian. For the 3s–3p resonance line of sodium  $\Gamma/2\pi = 10$  MHz and at room temperature  $\Delta\omega_D/2\pi = 1600$  MHz, so the ratio of the cross-sections in eqn 8.16 is  $\simeq 1/100$ . The Doppler-broadened gas gives less absorption, for the same  $N$ , because only 1% of the atoms interact with the radiation at the line centre—these are the atoms in the velocity class with  $v = 0$  and width  $\Delta v \simeq \Gamma/k$ . For homogeneous broadening all atoms interact with the light in the same way, by definition.

### 8.3.1 Principle of saturated absorption spectroscopy

This method of laser spectroscopy exploits the saturation of absorption to give a Doppler-free signal. At high intensities the population difference between two levels is reduced as atoms are excited to the upper level, and we account for this by modifying eqn 8.11 to read

$$\kappa(\omega) = \int_{-\infty}^{\infty} \{N_1(v) - N_2(v)\} \sigma_{\text{abs}}(\omega - kv) dv. \quad (8.17)$$

This is the same as the modification we made in going from eqn 7.70 to 7.72 but applied to each velocity class within the distribution. Here  $N_1(v)$  and  $N_2(v)$  are the number densities in levels 1 and 2, respectively, for atoms with velocities between  $v$  and  $v+dv$ . At low intensities almost all the atoms stay in level 1, so  $N_1(v) \simeq N(v)$  has the Gaussian distribution in eqn 8.3 and  $N_2 \simeq 0$ , as illustrated in Fig. 8.3(a). For all intensities, the integral of the number densities in each velocity class equals the total number density in that level, i.e.

$$\int_{-\infty}^{\infty} N_1(v) dv = N_1, \quad (8.18)$$

and similarly for  $N_2$ . The total number density  $N = N_1 + N_2$ .<sup>18</sup>

In saturated absorption spectroscopy the quantity  $N_1(v) - N_2(v)$  is affected by interaction with a strong laser beam, as shown in Fig. 8.3(b) and Fig. 8.4 shows a typical experimental arrangement. The beam splitter divides the power of the laser beam between a weak probe and a stronger pump beam.<sup>19</sup> Both these beams have the same frequency  $\omega$  and the two beams go in opposite directions through the sample cell containing the atomic vapour. The pump beam interacts with atoms that have velocity  $v = (\omega - \omega_0)/k$  and excites many of them into the upper level, as shown in Fig. 8.3(b). This is referred to as **hole burning**. The hole burnt into the lower-level population by a beam of intensity  $I$  has a width

$$\Delta\omega_{\text{hole}} = \Gamma \left( 1 + \frac{I}{I_{\text{sat}}} \right)^{1/2}, \quad (8.19)$$

equal to the power-broadened homogeneous width in eqn 7.88.

When the laser has a frequency far from resonance,  $|\omega - \omega_0| \gg \Delta\omega_{\text{hole}}$ , the pump and probe beams interact with different atoms so the pump beam does not affect the probe beam, as illustrated on the left- and

<sup>18</sup>This treatment of saturation is restricted to two-level atoms. Real systems with degeneracy are more difficult to treat since, under conditions with significant saturation of the absorption, the atoms are usually not uniformly distributed over the sublevels (unless the light is unpolarized). Nevertheless, the expression  $N_1(v) - g_1 N_2(v)/g_2$  is often used for the difference in population densities in a given velocity class.

<sup>19</sup>Normally, we have  $I_{\text{probe}} \ll I_{\text{sat}}$  and  $I_{\text{pump}} \gtrsim I_{\text{sat}}$ .

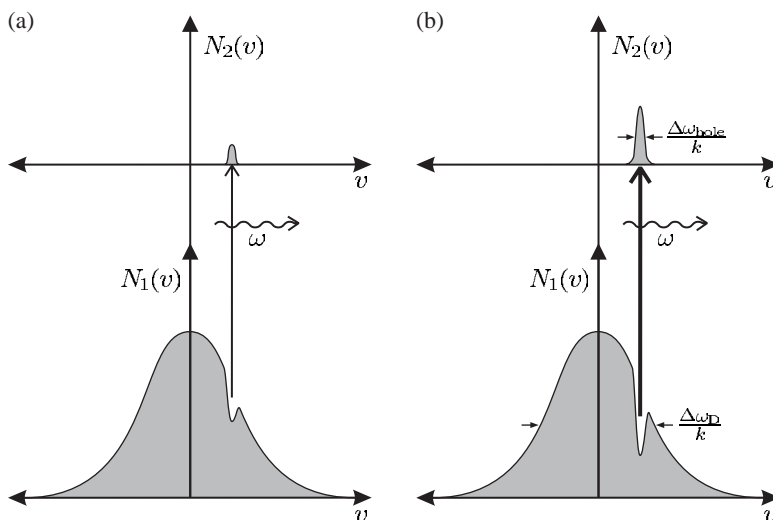


**Fig. 8.3** The saturation of absorption. (a) A weak beam does not significantly alter the number density of atoms in each level. The number density in the lower level  $N_1(v)$  has a Gaussian distribution of velocities characteristic of Doppler broadening of width  $\Delta\omega_D/k$ . The upper level has a negligible population,  $N_2(v) \simeq 0$ . (b) A high-intensity laser beam burns a deep hole—the population difference  $N_1(v) - N_2(v)$  tends to zero for the atoms that interact most strongly with the light (those with velocity  $v = (\omega - \omega_0)/k$ ). Note that  $N_1(v)$  does *not* tend to zero: strong pumping of a two-level system never gives population inversion. This figure also shows clearly that Doppler broadening is inhomogeneous so that atoms interact in different ways within the radiation.

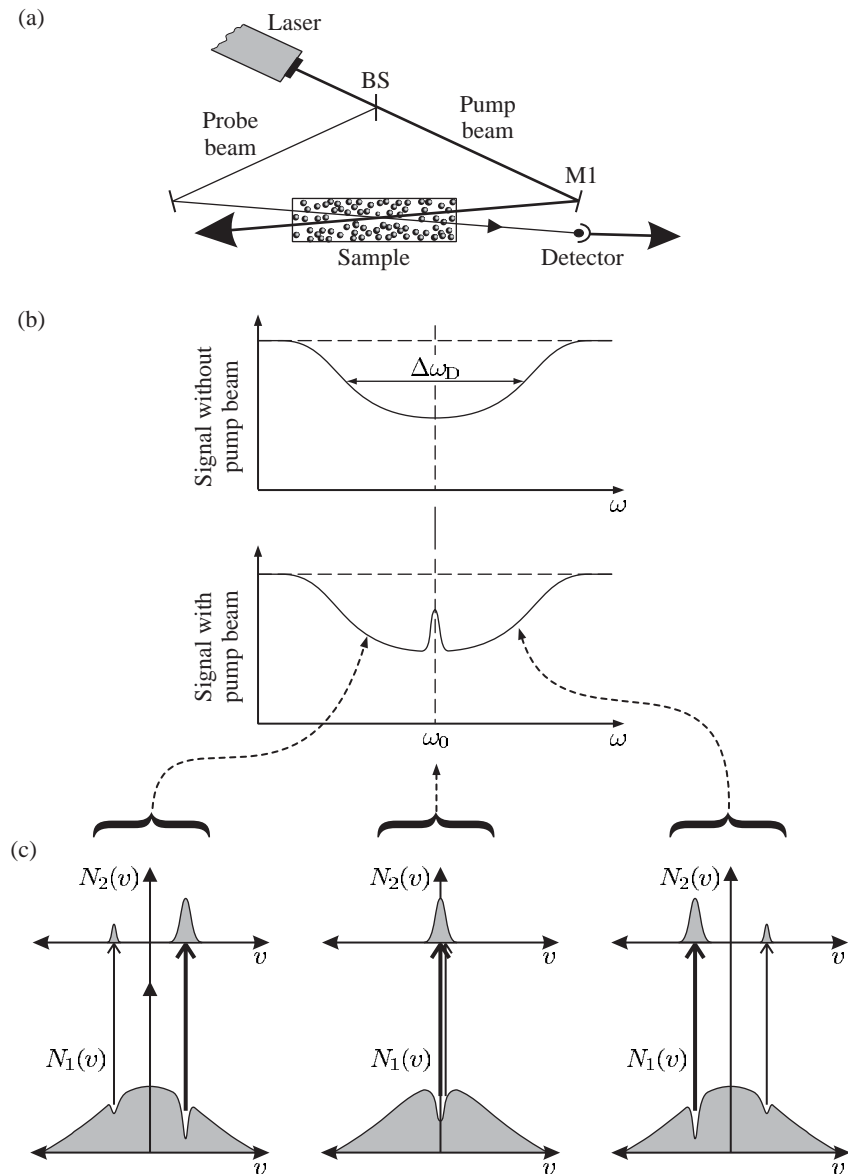


**Fig. 8.4** (a) A saturated absorption spectroscopy experiment. The beam splitter BS, e.g. a piece of glass, divides the laser power between a weak probe and a stronger pump beam. The figure shows a finite angle of intersection between the weak probe beam and the stronger pump beam in the sample; this arrangement makes it straightforward to detect the probe beam after the cell but it leaves some residual Doppler broadening. Therefore saturated absorption experiments often have the pump and probe beams exactly counter-propagating and use a partially-reflecting mirror at M1 to transmit some of the probe beam to the detector (while still reflecting enough of the pump beam). (b) A plot of the probe intensity transmitted through the sample as a function of the laser frequency. With the pump beam blocked the experiment gives a simple Doppler-broadened absorption, but in the presence of the pump beam a narrow peak appears at the atomic resonance frequency. (c) The population densities of the two levels  $N_1(v)$  and  $N_2(v)$  as a function of velocity for three different laser frequencies: below, equal to, and above the atomic resonance, showing the effect of the pump and probe beams.

right-hand sides of Fig. 8.4(c). Close to resonance,  $\omega \simeq \omega_0$ , both beams interact with atoms in the velocity class with  $v \simeq 0$ , and the hole burnt by the pump beam reduces the absorption of the probe beam. Thus saturation of the absorption by the pump beam leads to a narrow peak in the intensity of the probe beam transmitted through the sample, as shown in Fig. 8.4(b). Normally, the pump beam has an intensity of about the saturation intensity  $I_{\text{sat}}$ , so the saturated absorption peaks always have a line width greater than the natural width. The *velocity class* of atoms that interact with the light has a velocity spread  $\Delta v = \Delta\omega_{\text{hole}}/k$ .

This section shows how saturation spectroscopy picks out a signal from the atoms in the velocity class centred at  $v = 0$  to give a signal at the atomic resonance frequency. It is the homogeneous broadening of these stationary atoms that determines the widths of the peaks. Exercise 8.8 goes through a detailed calculation of this width. Many experiments use this Doppler-free technique to give a stable reference, e.g. to set the laser frequency a few line widths below resonance in laser cooling experiments with the optical molasses technique (described in the next chapter).<sup>20</sup>

<sup>20</sup>Nowadays, inexpensive semiconductor diode lasers make saturation spectroscopy a feasible experiment in undergraduate teaching laboratories, using the alkali elements rubidium or caesium that have sufficient vapour pressure at room temperature that a simple glass cell can be used as the sample (Wieman *et al.* 1999).

### 8.3.2 Cross-over resonances in saturation spectroscopy

In a saturated absorption spectrum, peaks appear at frequencies midway between pairs of transitions that have energy levels in common (and a separation less than the Doppler width), e.g. for the three-level atom shown in Fig. 8.5(a). To explain these **cross-over resonances** we need to consider the situation shown in Fig. 8.5(b), where the pump beam burns two holes in the velocity distribution. These holes give rise to two peaks in the spectrum when the laser frequency corresponds to the frequencies of the two transitions—the ‘expected’ saturated absorption signals for these two transitions. However, an additional peak appears when the hole burnt by one transition reduces the absorption for the other transition. As illustrated by Fig. 8.5(b), the symmetry of this situation means that cross-overs occur exactly midway between two saturated absorption peaks. This property allows experimenters to identify the cross-overs in a saturated absorption spectrum (see the exercises at the end of this chapter), and these extra peaks do not generally cause confusion.

The spectral lines of atomic hydrogen have large Doppler widths because it is the lightest element, but physicists want to measure the energy levels of this simple atom precisely to test atomic physics theory and to determine the Rydberg constant.

Figure 8.6 shows a spectrum of the Balmer- $\alpha$  line ( $n = 2$  to  $n = 3$ ) that is limited by Doppler broadening. This red line of atomic hydrogen, at a wavelength of  $\lambda = 656$  nm, has a Doppler width of  $\Delta f_D = 6$  GHz at room temperature (Section 8.1); this is less than the 11 GHz interval between the  $j = 1/2$  and  $3/2$  fine-structure levels in the  $n = 2$  shell. Using the isotope deuterium (which has twice the atomic mass of hydrogen) in a discharge cooled to 100 K reduces the Doppler width to  $\Delta f_D = 2.3$  GHz,<sup>21</sup> where one factor arises from the mass and the other from the

<sup>21</sup>As calculated by scaling the value for hydrogen. The ratio of the Doppler widths for H at  $T = 300$  K and D at  $T = 100$  K is  $\sqrt{6} = \sqrt{2} \times \sqrt{3}$ .

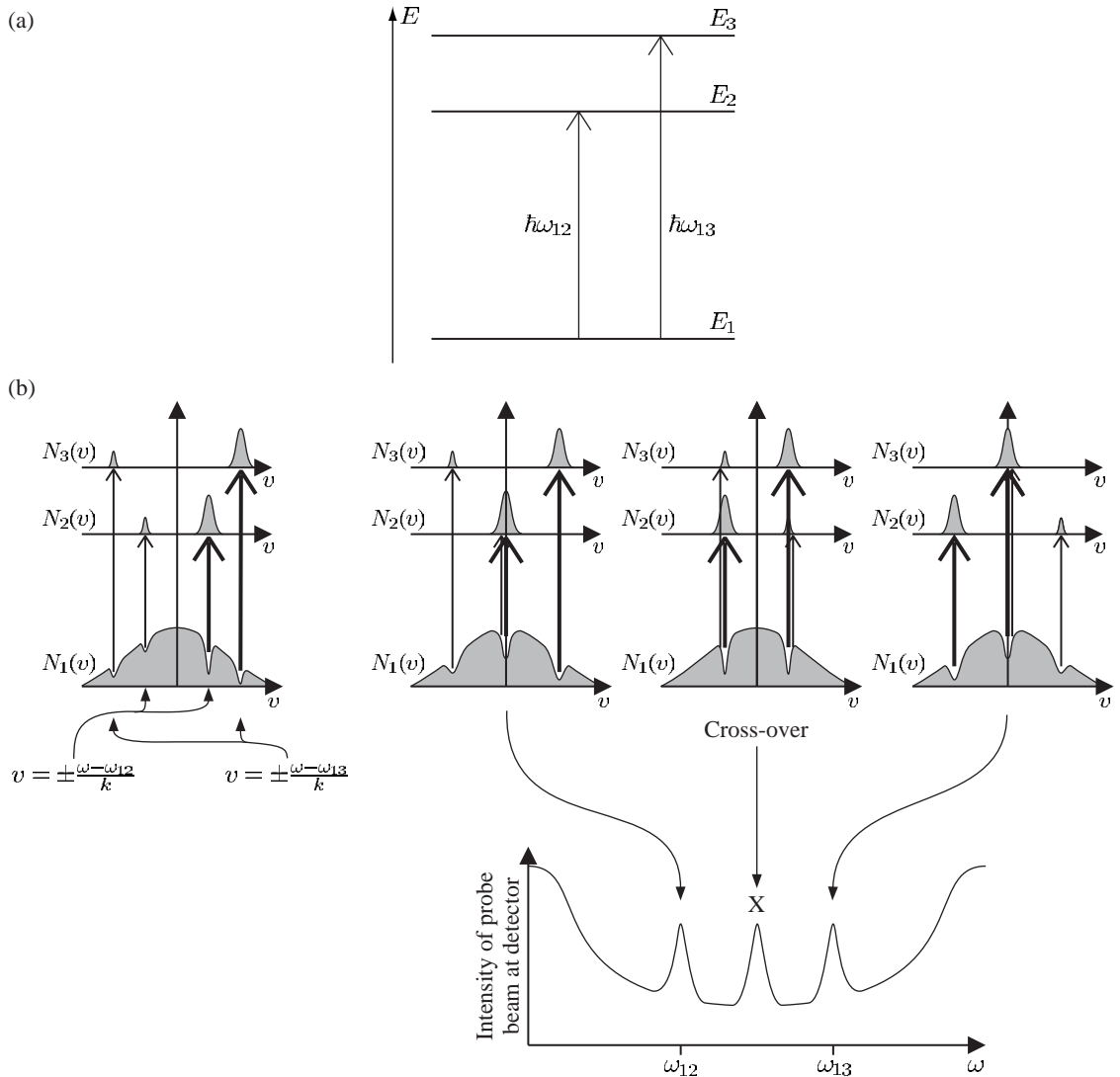


**Fig. 8.5** The formation of a cross-over resonance. (a) A three-level atom with two allowed transitions at angular frequencies  $\omega_{12}$  and  $\omega_{13}$ . (b) A cross-over resonance occurs at X, midway between two saturated absorption peaks corresponding to transitions at angular frequencies  $\omega_{12}$  and  $\omega_{13}$ . At the cross-over the hole burnt by the pump beam acting on transition  $1 \leftrightarrow 2$  reduces the probe beam absorption on transition  $1 \leftrightarrow 3$ , and vice versa.

<sup>22</sup>The expectation value of the spin-orbit interaction scales as  $1/n^3$  (in eqn 2.56) and hence the splitting for  $n = 3$  is  $8/27 \simeq 0.3$  times that for  $n = 2$ .

temperature. This makes it possible to observe components separated by the 3.3 GHz interval between the  $j = 1/2$  and  $3/2$  fine-structure levels in the  $n = 3$  shell—see Figs 8.6(c) and 8.7(a).<sup>22</sup> Structure on the scale of the 1 GHz corresponding to the Lamb shift cannot be resolved by conventional Doppler-limited techniques.

Figure 8.7 shows the spectacular improvement in resolution obtained with Doppler-free spectroscopy. The saturated absorption spectrum shown in Fig. 8.7(c) was obtained in a room-temperature discharge of

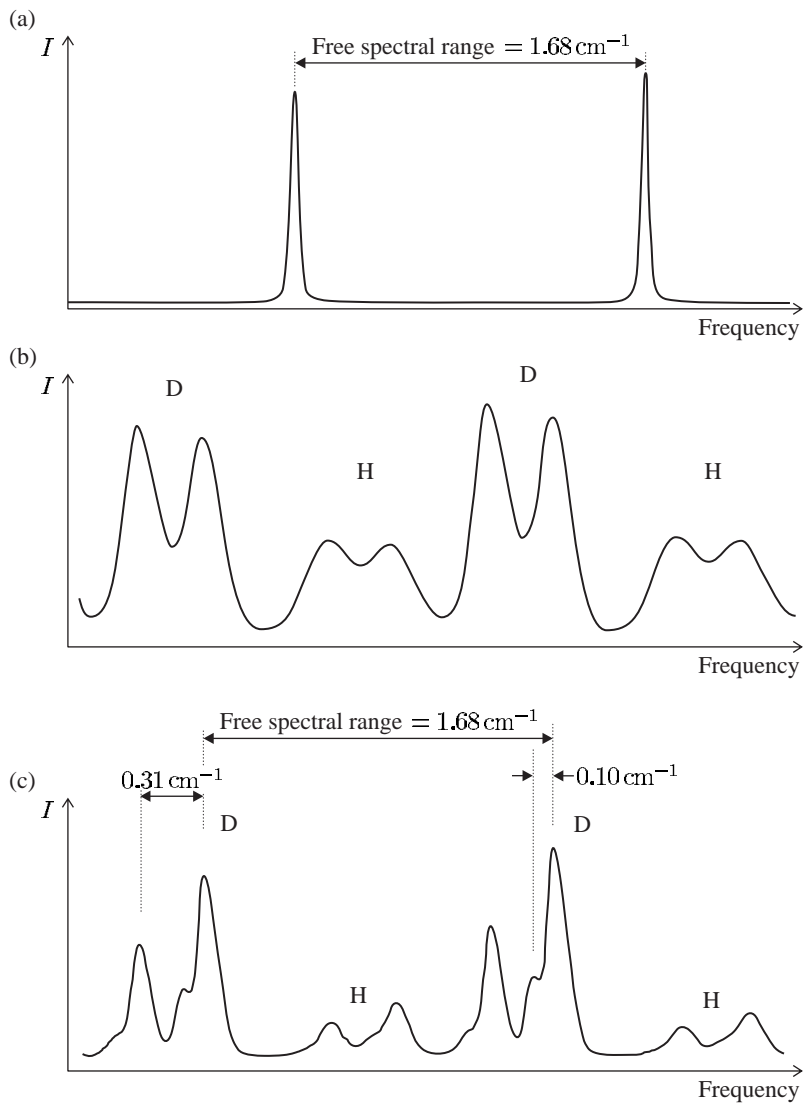
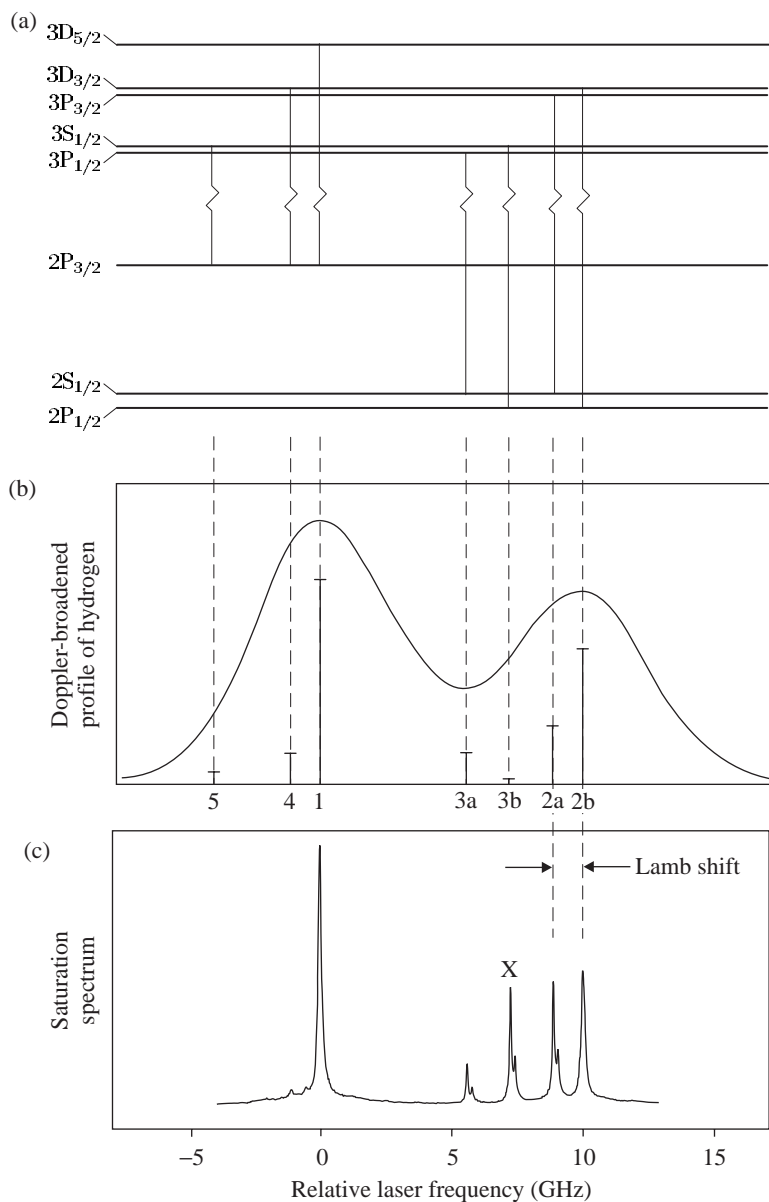


**Fig. 8.6** Spectroscopy of the Balmer- $\alpha$  line, carried out with an apparatus similar to that in Fig. 1.7(a), has a resolution limited by the Doppler effect. (a) The transmission peaks of a pressure-scanned Fabry-Perot étalon obtained with a highly-monochromatic source (helium-neon laser). The spacing of the peaks equals the free-spectral range of the étalon given by  $FSR = 1/2l = 1.68 \text{ cm}^{-1}$ , where  $l$  is the distance between the two highly-reflecting mirrors. The ratio of the FSR to the width of the peaks (FWHM) equals the finesse of the étalon, which is about 40 in this case. (The difference in height of the two peaks in this trace of real data arises from changes in laser intensity over time.) In all the traces, (a) to (c), the étalon was scanned over two free-spectral ranges. (b) The spectrum from a discharge of hydrogen, H, and deuterium, D, at room temperature. For each isotope, the two components have a separation approximately equal to the interval between the fine-structure levels with  $n = 2$ . This splitting is slightly larger than the Doppler width for hydrogen. The isotope shift between the hydrogen and deuterium lines is about 2.5 times larger than the free-spectral range, so that adjacent peaks for H and D come from different orders of the étalon. (The étalon length has been carefully chosen to avoid overlap whilst giving high resolution.) (c) The spectrum of hydrogen and deuterium cooled to around 100 K by immersing the discharge tube in liquid nitrogen. (The relative intensities change with discharge conditions.) The fine structure of the 3p configuration is not quite resolved, even for deuterium, but leads to observable shoulders on the left of each peak—the relevant energy levels are shown in Fig. 8.7. Courtesy of Dr John H. Sanders, Physics department, University of Oxford.

atomic hydrogen and part of the spectrum in Fig. 8.6(b) is shown for comparison.<sup>23</sup> The saturated absorption technique gives clearly resolved peaks from the 2a and 2b transitions with a separation equal to the Lamb shift—the QED contributions shift the energy of the 2s  $^2S_{1/2}$  level upwards relative to 2p  $^2P_{1/2}$ . Lamb and Rutherford had measured this shift by a radio-frequency method using a metastable beam of hydrogen

<sup>23</sup>The first saturated absorption spectrum of hydrogen was obtained by Professor Theodor Hänsch and co-workers at Stanford University (around 1972). In those pioneering experiments the width of the observed peaks was limited by the bandwidth of the pulsed lasers used. Continuous-wave lasers have lower bandwidth.

**Fig. 8.7** Spectroscopy of the Balmer- $\alpha$  transition. (a) The levels with principal quantum numbers  $n = 2$  and  $n = 3$  and the transitions between them. Relativistic quantum mechanics (the Dirac equation) predicts that energies depend only on  $n$  and  $j$ , leading to the five transitions labelled 1 to 5 in order of decreasing strength (proportional to the square of the matrix element). In reality, some of these levels are not degenerate because of QED effects, e.g. the Lamb shift between  $2s\ ^2S_{1/2}$  and  $2p\ ^2P_{1/2}$  that gives two components in transitions 2 and 3. Thus there are seven optical transitions (that were listed in Section 2.3.5). (The allowed transition between the  $2s\ ^2S_{1/2}$  and  $2p\ ^2P_{1/2}$  levels, and other radio-frequency transitions are not marked.) (b) The Doppler-broadened profile of the Balmer- $\alpha$  line in a room-temperature discharge containing atomic hydrogen shows only two clear components separated by about 10 GHz (slightly less than the fine-structure splitting of the  $2p$  configuration—see the caption of Fig. 8.6). (c) The saturated absorption spectrum obtained with a continuous-wave laser. The Lamb shift between the 2a and 2b components is clearly resolved. The  $2s\ ^2S_{1/2}$  level has a hyperfine splitting of 178 MHz and this leads to the double-peaked profile of 2a, 3a and the cross-over resonance X midway between them. (In addition to their relative positions, further evidence that peak X is the cross-over resonance between 2a and 3a comes from their similar line shape, which strongly indicates that they share a common level; the weak transition 3b is obscured.) Transition 4 is also seen on the far left and the cross-over resonance between 4 and 1 is just visible as a small bump on the base of peak 1. The scale gives the laser frequency relative to an arbitrary point (transition 1). Data shown in (c) was obtained by Dr John R. Brandenberger and the author.



(atoms in  $2s\ ^2S_{1/2}$  level) but it was not resolved by optical techniques before the invention of Doppler-free laser spectroscopy.

## 8.4 Two-photon spectroscopy

Two-photon spectroscopy uses two counter-propagating laser beams, as shown in Fig. 8.8. This arrangement has a superficial similarity to saturated absorption spectroscopy experiments (Fig. 8.4) but these two Doppler-free techniques differ fundamentally in principle. In two-photon spectroscopy the simultaneous absorption of two photons drives the atomic transition. If the atom absorbs one photon from each of the counter-propagating beams then the Doppler shifts cancel in the rest frame of the atom (Fig. 8.9(a)):

$$\omega \left(1 + \frac{v}{c}\right) + \omega \left(1 - \frac{v}{c}\right) = 2\omega. \quad (8.20)$$

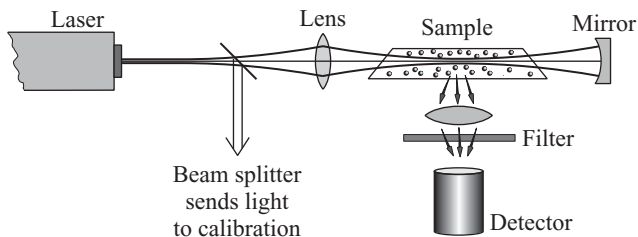


**Fig. 8.8** A two-photon spectroscopy experiment. The lens focuses light from the tunable laser into the sample and a curved mirror reflects this beam back on itself to give two counter-propagating beams that overlap in the sample. For this example, the photons spontaneously emitted after a two-photon absorption have different wavelengths from the laser radiation and pass through a filter that blocks scattered laser light. Usually, only one of the wavelengths corresponding to the allowed transitions at frequencies  $\omega_{1i}$  or  $\omega_{i2}$  (in the cascade shown in Fig. 8.9(a)) reaches the detector (a photomultiplier or photodiode). The beam splitter picks off some laser light to allow measurement of its frequency by the methods discussed in Section 8.5.

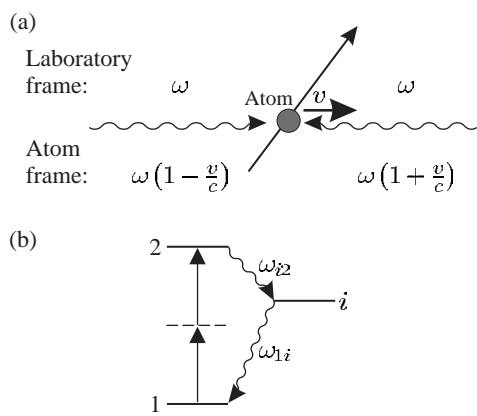


**Fig. 8.9** (a) The atom has a component of velocity  $v$  along the axis of the laser beams (the light has frequency  $\omega$ ). The atoms sees an equal and opposite Doppler shift for each beam. So these shifts cancel out in the sum of the frequencies of the two counter-propagating photons absorbed by the atom (eqn 8.20). The sum of the frequencies does not depend on  $v$  so resonance occurs for all atoms when  $2\omega = \omega_{12}$ . (b) A two-photon transition between levels 1 and 2. The atom decays in two steps that each emit a single photon with frequencies  $\omega_{i2}$  and  $\omega_{1i}$ .

When twice the laser frequency  $\omega$  equals the atomic resonance frequency  $2\omega = \omega_{12}$  all the atoms can absorb two photons; whereas in saturation spectroscopy the Doppler-free signal comes only from those atoms with zero velocity.

For the energy-level structure shown in Fig. 8.9(b) the atom decays in two steps that each emit a single photon (following the two-photon absorption). Some of these photons end up at the detector. A brief consideration of this cascade process illustrates the distinction between a two-photon process and two single-photon transitions. It would be possible to excite atoms from 1 to 2 using *two* laser beams with frequencies  $\omega_{L1} = \omega_{1i}$  and  $\omega_{L2} = \omega_{i2}$  resonant with the two electric dipole transitions, but this two-step excitation has a completely different nature to the direct two-photon transition. The transfer of population via the intermediate level  $i$  occurs at the rate determined by the rates of the two individual steps, whereas the two-photon transition has a virtual intermediate level with no transitory population in  $i$ . (Equation 8.20 shows that to get a Doppler-free signal the two counter-propagating beams must have the same frequency.) This distinction between single- and two-photon transitions shows up clearly in the theory of these processes (see Section E.2 of Appendix E) and it is worthwhile to summarise some of the results here. Time-dependent perturbation theory gives the rate of transitions to the upper level induced by an oscillating electric field  $\mathbf{E}_0 \cos \omega t$ . The calculation of the rate of two-photon transitions requires second-order time-dependent perturbation theory. Resonant enhancement of the second-order process occurs when  $2\omega = \omega_{12}$  but this still gives a rate which is small compared to an allowed single-photon transition. Therefore, to see any second-order effects, the first-order terms must be far off resonance; the frequency detuning from the intermediate level  $\omega - \omega_{1i}$  must remain large (of the same order of magnitude as  $\omega_{1i}$  itself, as drawn in the Fig. 8.9(b)). Two-photon absorption has many similarities with stimulated Raman scattering—a process of simultaneous absorption and stimulated emission of two photons via a virtual intermediate level, as shown in Fig. 8.10 (see Appendix E).

Finally, although the difference between two sequential electric dipole transitions (E1) and a two-photon transition has been strongly emphasised above, these processes do link the same levels. So from the E1 selection rules ( $\Delta l = \pm 1$  between levels of opposite parity) we deduce the two-photon selection rules:  $\Delta l = 0, \pm 2$  and no change of parity, e.g. s-s or s-d transitions.

Two-photon spectroscopy was first demonstrated on the 3s–4d transition of atomic sodium which has a line width dominated by the natural width of the upper level. The 1s–2s transition in atomic hydrogen has an extremely narrow two-photon resonance, and the line width observed in experiments arises from the various broadening mechanisms that we study in the next section.

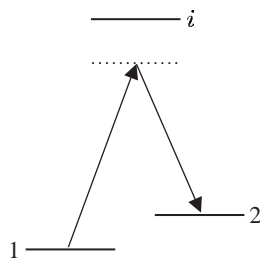


**Fig. 8.10** A stimulated Raman transition between levels 1 and 2, via a virtual level. Level  $i$  is not resonantly excited in this coherent process.

**Example 8.3** *Two-photon spectroscopy of the 1s–2s transition in atomic hydrogen*

The 1s–2s two-photon transition in atomic hydrogen has an intrinsic natural width of only 1 Hz because the 2s configuration is metastable. An atom in the 2s energy level has a lifetime of 1/8 s, in the absence of any external perturbations, since there are no p configurations of significantly lower energy (see Fig. 2.2).<sup>24</sup> In contrast, the 2p configuration has a lifetime of only 1.6 ns because of the strong Lyman- $\alpha$  transition to the ground state (with a wavelength of 121.5 nm in the vacuum ultraviolet). This huge difference in lifetimes of the levels in  $n = 2$  gives an indication of the relative strengths of single- and two-photon transitions. The 1s–2s transition has an intrinsic quality factor of  $Q = 10^{15}$ , calculated from the transition frequency  $\frac{3}{4}cR_\infty$  divided by its natural width. To excite this two-photon transition the experiments required ultraviolet radiation at wavelength  $\lambda = 243$  nm.<sup>25</sup>

Figure 8.11 shows a Doppler-free spectrum of the 1s–2s transition. A resolution of 1 part in  $10^{15}$  has not yet been achieved because the various mechanisms listed below limit the experimental line width.

- (a) *Transit time* Two-photon absorption is a nonlinear process<sup>26</sup> with a rate proportional to the square of the laser beam intensity,  $I^2$  (see Appendix E). Thus to give a high signal experimenters focus the counter-propagating beams down to a small size in the sample, as indicated in Fig. 8.8. For a beam diameter of  $d = 0.5$  mm transit-time broadening gives a contribution to the line width of

$$\Delta f_{\text{tt}} = \frac{\Delta\omega_{\text{tt}}}{2\pi} \simeq \frac{u}{d} = \frac{2200 \text{ m s}^{-1}}{5 \times 10^{-4} \text{ m}} = 4 \text{ MHz}, \quad (8.21)$$

where  $u$  is a typical velocity for hydrogen atoms (see eqn 8.7).

- (b) *Collision broadening (also called pressure broadening)* Collisions with other atoms, or molecules, in the gas perturb the atom (interacting with the radiation) and lead to a broadening and frequency shift of the observed spectral lines. This homogeneous broadening mechanism causes an increase in the line width that depends on the collision rate  $1/\tau_{\text{coll}}$ , where  $\tau_{\text{coll}}$  is the average time between collisions. In a simple treatment, the homogeneous width of a transition whose natural width is  $\Gamma$  becomes  $\Delta\omega_{\text{homog}} = \Gamma + 2/\tau_{\text{coll}} = \Gamma + 2N\sigma\bar{v}$ , where  $\sigma$  is the collision cross-section and  $\bar{v}$  is the mean relative velocity, as described by Corney (2000)—see also Loudon (2000) or Brooker (2003). The number density of the perturbing species  $N$  is proportional to the pressure. For the 1s–2s transition frequency the pressure broadening was measured to be 30 GHz/bar for hydrogen atoms in a gas that is mostly hydrogen molecules ( $\text{H}_2$ ), and this gives a major contribution to the line width of the signal shown in Fig. 8.11 of about 8 MHz (at the frequency of the ultraviolet radiation near 243 nm).<sup>27</sup> Some further details are given in Exercise 8.7.

- (c) *Laser bandwidth* The first two-photon experiments used pulsed lasers to give high intensities and the laser bandwidth limited the

<sup>24</sup>The microwave transition from the 2s  $^2\text{S}_{1/2}$  level down to the 2p  $^2\text{P}_{1/2}$  level has negligible spontaneous emission.

<sup>25</sup>Such short-wavelength radiation cannot be produced directly by tunable dye lasers, but requires frequency doubling of laser light at 486 nm by second-harmonic generation in a nonlinear crystal (a process that converts two photons into one of higher energy). Thus the frequency of the laser light (at 486 nm) is exactly one-quarter of the 1s–2s transition frequency (when both the factors of 2 for the frequency-doubling process and two-photon absorption are taken into account); thus the laser light (at 486 nm) has a frequency very close to that of the Balmer- $\beta$  line ( $n = 2$  to  $n = 4$ ) because the energies are proportional to  $1/n^2$  in hydrogen.

<sup>26</sup>In contrast, single-photon scattering *well below saturation* is a linear process proportional to the intensity  $I$ . Saturated absorption spectroscopy is a nonlinear process.

<sup>27</sup>Collisions shift the 1s–2s transition frequency by  $-9 \text{ GHz/bar}$  and this pressure shift is more troublesome for precision measurements than the broadening of the line (see Boshier *et al.* 1989 and McIntyre *et al.* 1989).

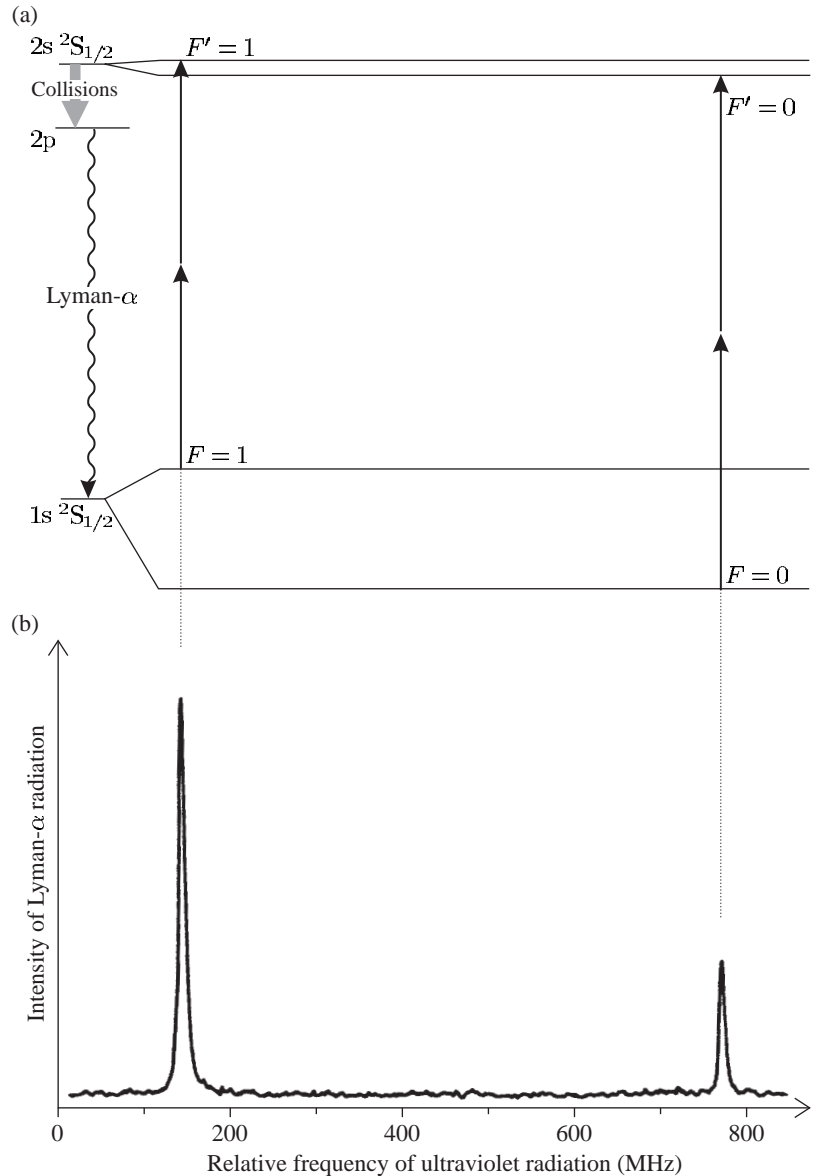


**Fig. 8.11** (a) The hyperfine structure of the  $1s$  and  $2s$  configurations of hydrogen (not to scale). The two-photon transitions obey the selection rule  $\Delta F = 0$ . This allows the transitions  $F = 0$  to  $F' = 0$  and  $F = 1$  to  $F' = 1$ . (b) A two-photon spectrum of the  $1s$ - $2s$  transition in atomic hydrogen. The recorded signal comes from photons emitted from the gas (following the two-photon excitation) that are detected by a photomultiplier, as shown in Fig. 8.8. This signal arises in a slightly different way to that shown in Fig. 8.9(b): the  $2s$  configuration in hydrogen decays very slowly since it has no allowed transition to  $1s$  but transfer from  $2s$  to  $2p$  occurs by collisions with atoms (or molecules) in the gas, and the  $2p$  configuration decays rapidly by the emission of Lyman- $\alpha$  photons. The scale gives the (relative) frequency of the ultraviolet radiation used to excite the two-photon transition (Foot *et al.* 1985). Copyright 1985 by the American Physical Society.

resolution. A laser with a pulse of duration  $\tau = 10$  ns has a lower limit to its bandwidth of

$$\Delta f_L \geq \frac{1}{\tau} \simeq 100 \text{ MHz}. \quad (8.22)$$

This Fourier transform limit assumes a perfectly shaped pulse and in practice pulsed lasers typically have a bandwidth an order of magnitude greater. Commercial continuous-wave dye lasers have bandwidths of 1 MHz but researchers use sophisticated electronic servo-control systems to reduce this. The best ion trap experiments

use a laser system that generates ultraviolet radiation with a bandwidth of only a few Hz to give a resolution approaching 1 in  $10^{15}$ .

- (d) *Second-order Doppler effect* Two-photon spectroscopy eliminates the first-order Doppler effect but not the second-order term that corresponds to time dilation in special relativity, namely

$$\Delta f_{D2} \sim \frac{u^2}{c^2} f_0 = 0.1 \text{ MHz}. \quad (8.23)$$

For hydrogen  $u/c = 7 \times 10^{-6}$  (see Section 8.1) and  $f_0 = 2.5 \times 10^{15}$  Hz for the 1s–2s transition.

Time dilation depends on the square of the atom's velocity and reduces the frequency of the emitted light seen by an observer in the laboratory, whichever direction the atom moves. This shifts the centre of the observed atomic line by an amount that depends on the velocity distribution of the atoms, and therefore causes uncertainty in precision measurements; it is worse than mechanisms that just broaden the line shape symmetrically about the atomic resonance frequency.

- (e) *Light shift* The light shift, or a.c. Stark effect (Section 7.7), affects two-photon spectroscopy experiments because of the high intensities required to give reasonable transition rates. The shift of the centre of the observed line shape causes problems in precision experiments for the same reason as the second-order Doppler effect.<sup>28</sup>

Detailed calculations of all systematic effects on the 1s–2s transition frequency are given in Boshier *et al.* (1989) and McIntyre *et al.* (1989). Table 8.2 is a check-list of effects that may broaden the peaks in Doppler-free spectroscopy (and in some cases cause frequency shifts).

In his original experiment, Lamb, and his student Rutherford, measured the shift between 2s  $^2S_{1/2}$  and 2p  $^2P_{1/2}$  directly with radio-frequency spectroscopy but the line width in their experiment was large

<sup>28</sup>The light shift does not significantly affect 1s–2s experiments because only low-power ultraviolet beams are generated by nonlinear mixing.

**Table 8.2** Summary of broadening mechanisms in Doppler-free spectroscopy.

- 
- (i) Natural broadening.
  - (ii) Collisions (pressure broadening).
  - (iii) Finite interaction time (transit-time broadening).
  - (iv) Second-order Doppler effect.
  - (v) Instrumental width—laser bandwidth.
  - (vi) External fields—Zeeman and Stark effects.
  - (vii) Residual Doppler broadening—if the beams are not exactly counter-propagating.
  - (viii) Power broadening—related to saturation of the transition (in saturation spectroscopy).
  - (ix) A.c. Stark effect—shift caused by the electric field of the light in two-photon spectroscopy.
-

because of the rapid decay of the 2p level (as mentioned at the beginning of this example). The 2p level has a natural width of 100 MHz—much larger than the line width in two-photon experiments. It is quite remarkable that the laser measurements of a transition frequency in the ultraviolet can exceed the precision of radio-frequency spectroscopy. Although the QED shifts represent only a very small part of the 1s–2s transition energy, the laser experiments determine these shifts accurately *if* the experimenters know the frequency of the laser. The following section describes methods used to measure the laser frequency and so calibrate the spectra.

## 8.5 Calibration in laser spectroscopy

Laser spectroscopy experiments use tunable lasers, i.e. laser systems whose frequency can be tuned over a wide range to find the atomic, or molecular, resonances. The early experiments used dye lasers in the visible region, e.g. the dye Rhodamine 6G gives the yellow light for experiments with sodium. The best dyes have a tunable range of over 50 nm and modern dyes exist that operate from the deep blue into the infra-red. However, the use of dyes in solution can be messy, and nowadays many experimenters prefer to use solid-state lasers that operate in the infra-red (Davis 1996); semiconductor diode lasers have a tuning range of about 10 nm, and the more general-purpose titanium-doped sapphire laser operates anywhere in the range 700–1000 nm. In comparison, the He–Ne laser only works within the Doppler profile of the neon transition; this has a Doppler width  $\sim 1$  GHz at 633 nm corresponding to a wavelength range of only 0.001 nm. This fixed and well-defined wavelength can be used as a frequency reference (and similarly for other lasers operating on atomic transitions).

The method of calibrating the laser frequency depends on whether the experiment requires absolute or relative measurements.

### 8.5.1 Calibration of the relative frequency

Experiments that measure the separations of the components within the spectrum require an accurate frequency scale for the laser scan, e.g. in the measurement of the isotope shifts and hyperfine splittings shown in Fig. 6.12. To calibrate the laser scan, experimenters send part of the laser beam through a Fabry–Perot étalon and record the transmission, as shown in Fig. 8.12 (cf. Fig. 8.6(a)). The observed fringes have a spacing equal to the étalon’s free-spectral range of  $c/2l$  and  $l$ , the length of the cavity, can be measured accurately. In practice these experiments do need some method that gives the approximate wavelengths of the laser light, in order to find the atomic lines.

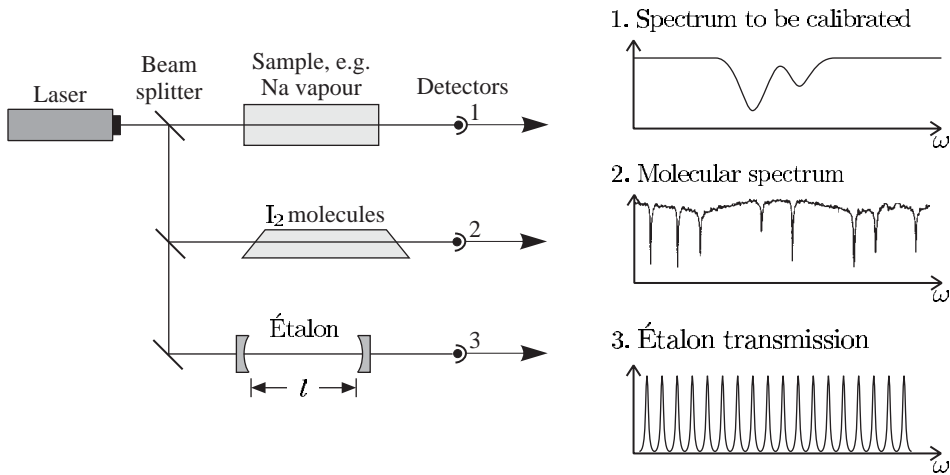


**Fig. 8.12** Calibration of a laser experiment. Three signals are recorded: (1) the spectrum to be calibrated, e.g. the absorption of an atomic vapour; (2) a molecular spectrum, e.g. the absorption spectrum of iodine; and (3) the intensity transmitted through a Fabry-Perot étalon gives fringes with a frequency spacing equal to its free-spectral range  $c/2l$ , where  $l$  is the length of the étalon. These reference fringes provide the frequency scale. Molecular spectra have a ‘forest’ of lines so that there will be lines near any arbitrary wavelength and the individual lines can be identified by comparison with a known spectrum. These molecular lines give the absolute frequency. (The sodium cell is heated to give a vapour pressure sufficient for an absorption experiment.)

### 8.5.2 Absolute calibration

To determine the absolute frequency of a spectral line it is compared to a nearby line of known frequency (or wavelength)—the same principle as in the use of a calibration lamp to produce fiducial lines on a spectrum obtained from a conventional prism spectrograph (or diffraction grating). Laser spectroscopists often use iodine to provide the reference lines because its molecular spectrum has many lines in the visible region and an atlas of iodine wavelengths has been compiled for this purpose (Gerstenkorn *et al.* 1993). Molecules have many more transitions than atoms and this gives a high probability of finding a suitable line near any frequency of interest. Iodine has sufficient vapour pressure at room temperature to give measurable absorption in a simple glass cell as shown in Fig. 8.12. The figure uses the Doppler-broadened absorption in sodium as an example of the spectrum to be measured. The iodine lines have much narrower Doppler widths because of the heavy molecular mass ( $I_2$  has molecular weight 254).

The calibration of Doppler-free spectra often requires narrower reference lines obtained by saturation spectroscopy on the iodine itself (see Corney 2000, Figs 13.13 and 13.14). The frequency of the 1s–2s transition in atomic hydrogen described in Example 8.3 has been measured relative to a line in the saturated absorption spectrum of tellurium,<sup>29</sup> as shown in Fig. 8.13. The experiment was calibrated by the following procedure. The saturation spectroscopy of  $Te_2$  was carried out with blue light of wavelength 486 nm and angular frequency  $\omega_L$ . Some of

<sup>29</sup> A heavy diatomic molecule like iodine, but  $Te_2$  happens to have lines in the blue region whereas  $I_2$  does not.

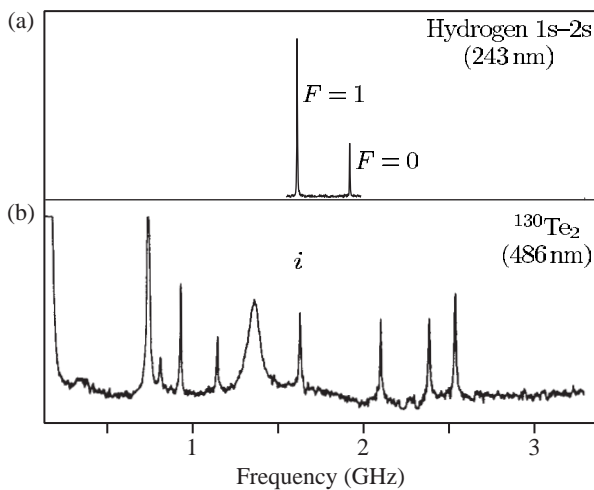


**Fig. 8.13** (a) A two-photon spectrum of the 1s–2s transition in atomic hydrogen as in Fig. 8.11 but on a different scale. (b) The saturated absorption spectrum of molecular tellurium used for calibration. The absolute frequency of the line labelled  $i$  was determined with an uncertainty of  $6 \times 10^{-10}$  (by auxiliary measurements). Adapted from McIntyre *et al.* (1989). Copyright 1989 by the American Physical Society.

this blue light was passed through a nonlinear crystal where the process of second-harmonic generation produced some radiation of frequency  $\omega = 2\omega_L$ . The frequency of this ultraviolet radiation at 243 nm was compared with the radiation (with a very similar frequency) that excited the 1s–2s transition. Thus the two-photon resonance condition in eqn 8.20 is  $\omega_{12} = 2\omega = 4\omega_L$ . The 1s  $^2\text{S}_{1/2}$   $F = 1$  to 2s  $^2\text{S}_{1/2}$   $F = 1$  transition has almost exactly four times the frequency of the line  $i$  in the spectrum of  $\text{Te}_2$ , and the small frequency offset can be measured precisely.

This method of calibration in terms of known spectral lines begs the question of how to determine the frequencies of the reference lines themselves in the first place. The short answer is that experimenters rely on the national standards laboratories around the world to measure suitable reference lines and to establish internationally agreed frequency standards, e.g. the particular iodine line that coincides with the output of the He–Ne laser at 633 nm has been measured very accurately. A helium–neon laser with its frequency controlled to be equal to that of the iodine line provides a portable frequency standard, i.e. one calibrated by the standard laboratory and then carried to the experimental laboratory to provide a reference (see Corney 2000, Section 13.10). The national standards laboratories must calibrate the secondary frequency standards in terms of the primary standard of time provided by the caesium atom clock at a frequency of 9 GHz (as described in Chapter 6). Until recently, a frequency chain was required to relate an optical frequency to a microwave frequency standard. A frequency chain comprises many oscillators, such as microwave sources and lasers, whose frequencies are multiples of each other, as indicated in Fig. 8.14. To go from 9 GHz up to around  $6 \times 10^{14}$  Hz (corresponding to visible light) required many different oscillators as links in the chain. All these devices must operate simultaneously and have their frequencies electronically controlled relative to those of neighbouring oscillators this makes such high precision

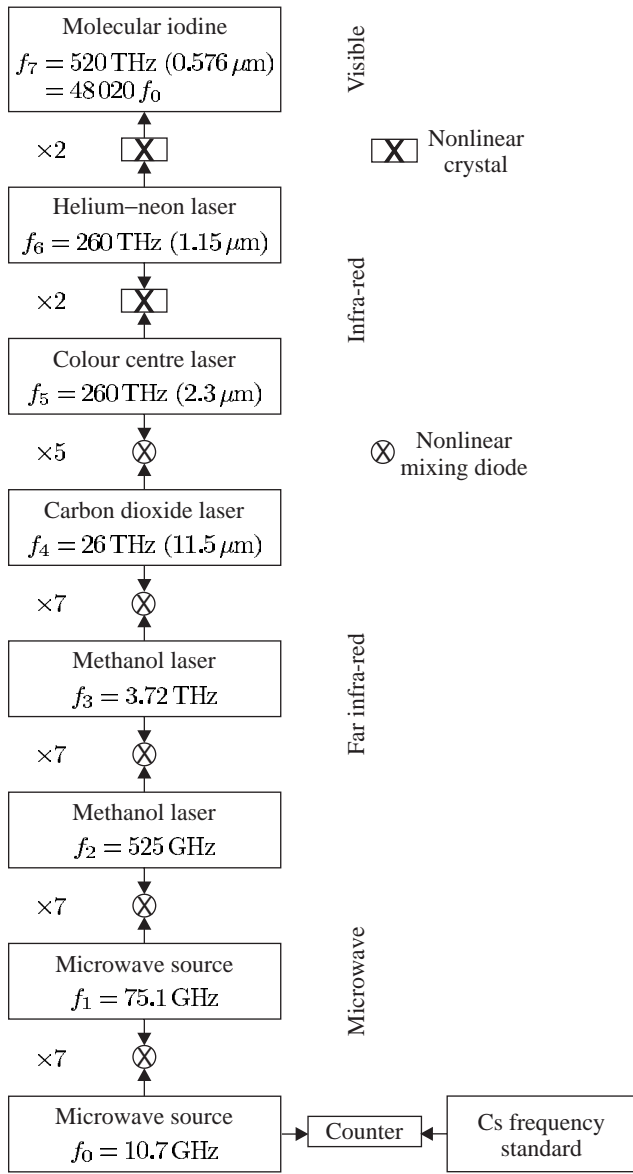


**Fig. 8.14** A frequency chain. The frequency of a line in the visible spectrum of molecular iodine is measured by setting up a chain of oscillators. The frequency of each oscillator is compared to a multiple or sum of the frequencies of the other oscillators. At the bottom of the chain is a microwave source whose frequency is measured with reference to a caesium frequency standard (the primary time standard as described in Section 6.4.2). A diode mixer produces a high number of harmonics of the microwaves, so that the first few stages achieve multiplication by a factor of 7. Nonlinear crystals are used for mixing mid-infra-red and visible radiation. The scheme shown here is one of the least complicated but it still involves a large number of devices. When the whole chain is operating it determines the multiplication factor that relates the optical frequency to the caesium frequency standard at 9 GHz. After Jennings *et al.* (1979).

measurements are a major undertaking. Recently, a new method has been invented that supersedes cumbersome frequency chains and makes the measurement of optical frequencies more straightforward.

### 8.5.3 Optical frequency combs

Recently, a new method of measuring optical frequencies has been invented that has revolutionised optical metrology. The new method relies on the ability to generate **frequency combs** using laser techniques, i.e. laser radiation that contains a set of regularly-spaced frequencies, as

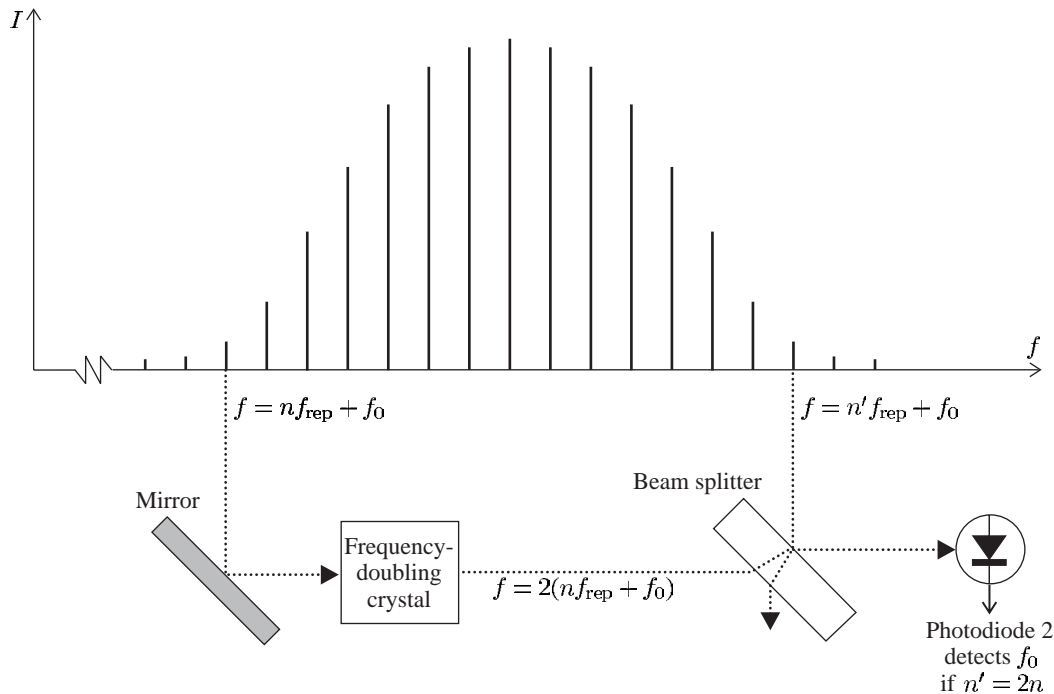


**Fig. 8.15** A frequency comb produced by a femtosecond laser system (and an optical fibre)—in reality there are many more regularly-spaced modes than are shown here. The frequencies spread over an octave so that modes on the low- and high-frequency wings can be compared, using second-harmonic generation in a nonlinear crystal, to determine the frequency offset of the comb as in eqn 8.25.

<sup>30</sup>A very short pulse of light propagates around the optical cavity of the laser formed by high-reflectivity mirrors. One of these mirrors is less reflective than the others so that it transmits a few per cent of the light. Each time the short pulse hits this output coupling mirror part of the pulse travels out of the cavity to give a steady train of short pulses that emerge from the laser with a time interval of  $t_{\text{rep}}$  between them. This time interval between pulses equals the round trip length of the laser cavity  $L$  divided by the speed of light:  $t_{\text{rep}} = L/c$ .

<sup>31</sup>This behaviour is closely analogous to the situation of light reflected from a diffraction grating, where the angular separation of the diffraction orders is inversely proportional to the spacing between the rulings, or slits for a transmission grating. For a detailed description of Fourier transforms and diffraction gratings see Brooker (2003).

illustrated in Fig. 8.15. The frequency comb contains the frequencies

$$f = f_0 + n f_{\text{rep}}, \quad (8.24)$$

where  $f_{\text{rep}}$  is the frequency interval and  $f_0$  is an offset from zero that we shall assume is smaller than  $f_{\text{rep}}$  (for this choice  $n$  will be a large positive integer). A laser produces such a frequency spectrum; however, there is not room here for a detailed description of the laser physics of such systems, see Davis (1996) or Meschede (2004).<sup>30</sup> The frequency spectrum is related by a Fourier transform to a train of short pulses in the time domain; the time interval between pulses  $t_{\text{rep}}$  and the spacing in the frequency are related by  $f_{\text{rep}} = 1/t_{\text{rep}}$ .<sup>31</sup>

The frequency span of the comb, i.e. the width of the spectrum's envelope in Fig. 8.15, is inversely proportional to the duration of each individual pulse. Actually, in the historical development of pulsed lasers this was viewed the other way around—the objective was to create the shortest pulses possible and this requires the laser medium to have gain over a wide spectral region. The titanium-doped sapphire laser used in the frequency comb experiments created pulses with a duration less than 100 fs ( $< 10^{-13}$  s, see Holzwarth *et al.* (2000)). Such femtosecond lasers have great technical importance, both for studying processes with

very high time resolution and for creating pulses of extremely high peak intensity (by compressing a high-energy pulse into a very short time).

The frequency  $f_{\text{rep}}$  is measured by directing some of the laser light onto a photodiode (see Fig. 8.16). The femtosecond laser does not produce a sufficiently wide spread in frequencies for the specific scheme illustrated in Figs 8.15 and 8.16. This is obtained by sending the output of the femtosecond laser along a special highly-dispersive optical fibre, as indicated schematically in Fig. 8.16. The combination of the femtosecond laser and this special fibre produces radiation with the frequency spectrum in eqn 8.24, that spans a large spectral range, e.g. from 520 nm to 1170 nm in the work of Udem *et al.* (2001), equivalent to a frequency range of 300 THz. For  $f_{\text{rep}} = 1 \text{ GHz}$  this range of values corresponds to  $n = 2.5$  to  $6 \times 10^6$ .

After the frequency comb has been generated, the next stage is to determine the offset  $f_0$  by an ingenious method devised by Professor Theodor Hänsch and co-workers, namely a comparison, or self-referencing, of the frequency of lines from different parts of the frequency comb. This is achieved by sending the light (from the low-frequency wing of the comb) through a frequency-doubling crystal; in this nonlinear optical medium some radiation is generated at the second harmonic of the input frequency. The light emerging from the crystal has frequency components  $2(n'f_{\text{rep}} + f_0)$ , where  $n'$  is an integer (the reason for introducing

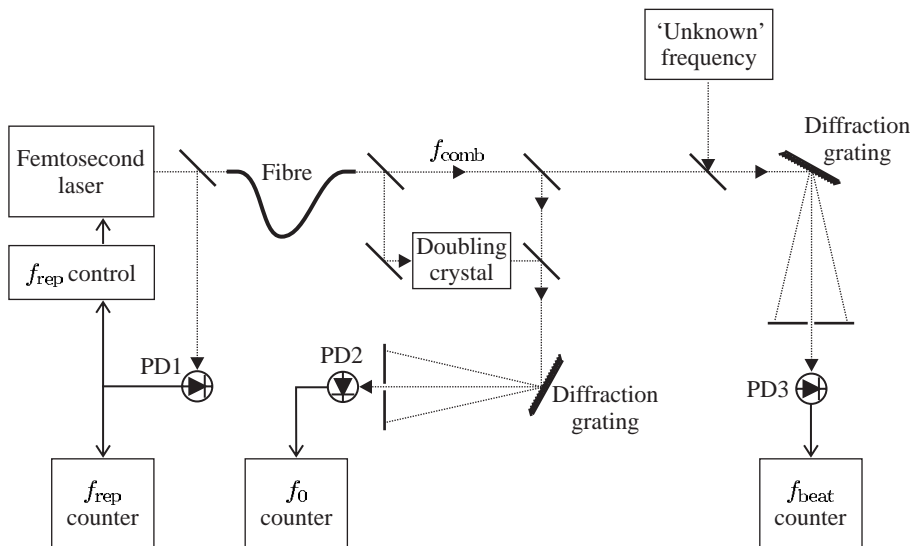


**Fig. 8.16** The experimental arrangement for the measurement of an optical frequency using a frequency comb from a femtosecond laser. Photodiode 1 measures the frequency interval between the laser modes,  $f_{\text{rep}}$  in eqn 8.24, and  $f_{\text{rep}}$  is maintained constant by electronic feedback from the frequency counter to the laser (the laser cavity length is kept fixed by adjusting the position of a mirror with a piezoelectric actuator). Photodiode 2 measures the beat frequency between modes in the low- and high-frequency wings of the comb (see Fig. 8.15). Photodiode 3 measures the frequency difference between one mode of the comb and the unknown laser frequency as in eqn 8.26. The diffraction gratings spread out the light so that only the relevant part of the frequency comb falls onto the detector, as explained in the text. Figure courtesy of Dr Helen Margolis, National Physical Laboratory; after Margolis *et al.* (2003).

both  $n'$  and  $n$  will become apparent shortly). This radiation mixes with some of the original light, whose frequency is given by eqn 8.24, on a photodiode. The signal from this detector contains the frequencies

$$f = 2(n' f_{\text{rep}} + f_0) - (n f_{\text{rep}} + f_0) = (2n' - n)f_{\text{rep}} + f_0. \quad (8.25)$$

<sup>32</sup>Other schemes have been demonstrated, e.g. choosing  $2n = 3n'$  so that the frequency comb does not have to be so wide and can be generated directly from a laser (eliminating the optical fibre in Fig. 8.16).

<sup>33</sup>A diffraction grating is used to spread out the light at different wavelengths so that only the high-frequency part of the spectral region where  $n = 2n'$  falls onto the detector. Light at other wavelengths produces unwanted background intensity that does not contribute to the signal.

<sup>34</sup>The beat frequencies with other components fall outside the bandwidth of the detector.

<sup>35</sup>This method has also been used to calibrate a selection of molecular iodine lines that can be used as secondary frequency standards, as described in the previous section (Holzwarth *et al.* 2000).

For a frequency comb that spans an octave there are frequency components with  $n = 2n'$ , i.e. high-frequency lines that have twice the frequency of lines on the low-frequency wing. For these lines eqn 8.25 reduces to  $f_0$ , and in this way the frequency offset is measured.<sup>32</sup> In Fig. 8.16 the photodiodes 1 and 2 measure precisely the radio frequencies  $f_{\text{rep}}$  and  $f_0$ , respectively, and hence determine the frequency of each line in the comb (eqn 8.24).<sup>33</sup>

The light from the calibrated frequency comb is mixed with some of the output of the continuous-wave laser whose frequency  $f_L$  is to be measured, whilst the remaining light from this second laser is used for experiments, e.g. high-resolution spectroscopy of atoms or molecules. The third photodiode measures the beat frequency, which is equal to the difference between  $f_L$  and the nearest component of the frequency comb:<sup>34</sup>

$$f_{\text{beat}} = |n'' f_{\text{rep}} + f_0 - f_L|. \quad (8.26)$$

This beat frequency is measured by a radio-frequency counter.

The unknown laser frequency is determined in terms of the three measured frequencies as  $f_L = n'' f_{\text{rep}} + f_0 \pm f_{\text{beat}}$ . It is assumed that  $f_L$  is known with an uncertainty less than  $f_{\text{rep}}$ , so that the value of the integer  $n''$  is determined, e.g. when  $f_{\text{rep}} = 1 \text{ GHz}$  (as above) and  $f_L \simeq 5 \times 10^{14}$  (corresponding to a visible wavelength) it is necessary to know  $f_L$  to a precision greater than 2 parts in  $10^6$ , which is readily achieved by other methods. The measurement of radio frequencies can be carried out extremely accurately and this frequency comb method has been used to determine the absolute frequency of very narrow transitions in atoms and ions,<sup>35</sup> e.g. Ca, Hg<sup>+</sup>, Sr<sup>+</sup> and Yb<sup>+</sup>—see Udem *et al.* (2001), Blythe *et al.* (2003) and Margolis *et al.* (2003). These experiments were limited by systematic effects such as perturbing electric and magnetic fields, that can be improved by further work. The uniformity of the spacing of the lines in the frequency comb has been verified to at least a few parts in  $10^{16}$ , and in the future it is anticipated that uncertainties in measurements of frequency of very narrow transitions in ions, trapped using the techniques described in Chapter 12, can be reduced to a few parts in  $10^{18}$ . At such an incredible level of precision new physical effects may show up. For example, it has been suggested that fundamental ‘constants’ such as the fine-structure constant  $\alpha$  may vary slowly on astrophysical time-scales, and this would lead to changes in atomic transition frequencies with time. If such variations do indeed occur, then an inter-comparison of frequency standards that depend on different powers of  $\alpha$  over many years is potentially a way to observe them.

## Further reading

This chapter has focused on just a few examples of Doppler-free laser spectroscopy and calibration to illustrate the important principles. Such measurements of the transition frequencies in atomic hydrogen give a precise value for the Rydberg constant and the QED shift. More details of the saturated absorption and two-photon methods are given in specialised books on laser spectroscopy by Letokhov and Chebotaev (1977), Demtröder (1996), Corney (2000) and Meschede (2004)—the last of these gives details of recent experiments on the 1s–2s transition in atomic hydrogen. Nowadays, laser spectroscopy is very widely used in more complex situations, e.g. liquids and solids.

The monograph by Series (1988) on the spectrum of atomic hydrogen gives a comprehensive description that includes Lamb and Rutherford's historic experiment and later refinements of the radio-frequency techniques, as well as laser spectroscopy. The series of proceedings of the biennial International Conference on Laser Spectroscopy (published by Springer-Verlag) gives an overview of the current state of the art and current applications. The measurement of the absolute frequency of light using optical frequency combs is a relatively new technique but already it has had an important impact on optical frequency metrology (Udem *et al.* 2002).

## Exercises

### (8.1) Doppler widths

Calculate the Doppler width of a spectral line with a wavelength of 589 nm for (a) sodium vapour at 1000 K, and (b) a vapour of molecular iodine at room temperature.

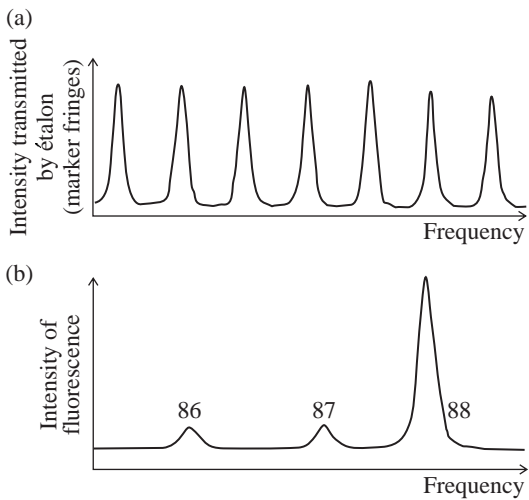
### (8.2) Doppler broadening

The two fine-structure components of the 2s–2p transition in a lithium atom have wavelengths of 670.961 nm and 670.976 nm (in a vacuum). Estimate the Doppler broadening of this line in a room-temperature vapour and comment on the feasibility of observing the weak-field Zeeman effect in lithium.

### (8.3) Crossed-beam technique

The figure shows the fluorescent signal obtained from a crossed-beam experiment like that presented in Fig. 8.2. Radiation of wavelength 243 nm excited a single-photon transition in strontium atoms from an oven at a temperature of 900 K. Each peak is labelled with the relative atomic mass of the isotope. The frequency scale was calibrated by sending some light through a Fabry–Perot étalon (cf. Fig. 8.12) to

produce marker fringes with a frequency spacing of 75 MHz.



Determine the line width of the peaks and the frequency shift between the even isotopes from the scan. The line width arises from residual Doppler broadening. Calculate the collimation angle of the atomic beam.

*Comment.* This line has a normal mass shift of 180 MHz between the two even isotopes. There are smaller contributions to the isotope shift from the specific mass and volume effects.

(8.4) *Hyperfine structure in laser spectroscopy*

What is the physical origin of the interaction that leads to hyperfine structure in atoms?

Show that hyperfine splittings obey an interval rule which can be expressed as

$$\Delta E_{F,F-1} = A_{nlj} F,$$

i.e. the splitting of two sub-levels is proportional to the total angular momentum quantum number  $F$  of the sub-level with the larger  $F$ .

The naturally-occurring isotope of caesium ( $^{133}\text{Cs}$ ) has a nuclear spin of  $I = 7/2$ . Draw a diagram showing the hyperfine sub-levels, labelled by the appropriate quantum number(s), that arise from the  $6\ ^2\text{S}_{1/2}$  and  $6\ ^2\text{P}_{3/2}$  levels in caesium, and the allowed electric dipole transitions between them. Explain the principle of Doppler-free saturation spectroscopy.

The figure shows the saturated absorption spectrum obtained from the  $6\ ^2\text{S}_{1/2}$ - $6\ ^2\text{P}_{3/2}$  transition in a vapour of atomic caesium, including the cross-over resonances which occur midway between all pairs of transitions whose frequency separation is less than the Doppler width. The relative positions of the saturated absorption peaks within each group are given below in MHz.

| A | B     | C     | D     | E     | F     |
|---|-------|-------|-------|-------|-------|
| 0 | 100.7 | 201.5 | 226.5 | 327.2 | 452.9 |
| a | b     | c     | d     | e     | f     |
| 0 | 75.8  | 151.5 | 176.5 | 252.2 | 353.0 |

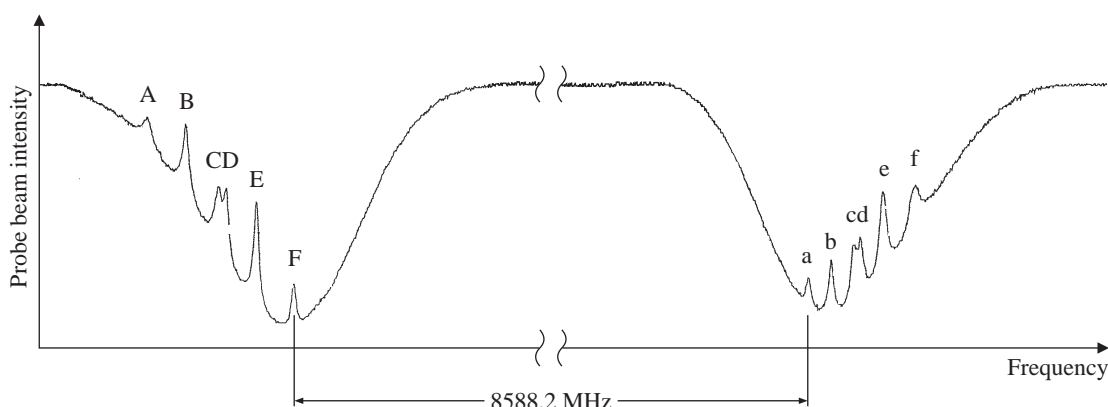
Using these data and the information in the diagram:

- (a) determine the extent to which the interval rule is obeyed in this case and deduce the hyperfine parameter  $A_{nlj}$  for the  $6\ ^2\text{S}_{1/2}$  and  $6\ ^2\text{P}_{3/2}$  levels;
- (b) estimate the temperature of the caesium vapour. (The wavelength of the transition is 852 nm.)

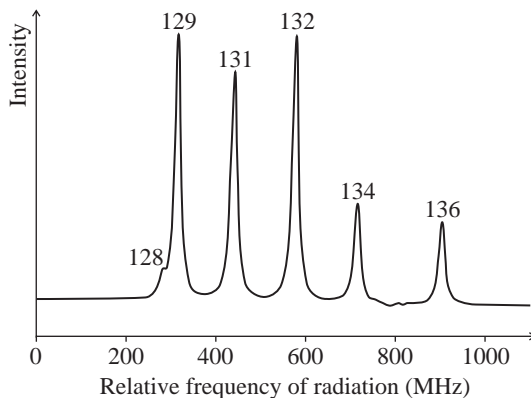
(8.5) *Hyperfine structure in laser spectroscopy*

The energy separation between the two hyperfine levels in the  $ns$  configurations of hydrogen is given by eqn 6.10, and for  $n = 1$  this corresponds to a hyperfine transition frequency of  $\Delta f_{\text{HFS}}(1s) = 1.4\ \text{GHz}$ .

- (a) Determine the separation of the hyperfine sub-levels in the  $2s\ ^2\text{S}_{1/2}$  level of hydrogen, and compare your answer to the value in the caption of Fig. 8.7.
- (b) Show that the peaks presented in Fig. 8.11 have an expected separation of  $\frac{7}{16}\Delta f_{\text{HFS}}(1s)$ . Compare the expected value with that in the figure (e.g. by measurement with a ruler and using the frequency scale given).



## (8.6) Two-photon experiment



The above experimental scan comes from a two-photon experiment like that shown in Fig. 8.8. The transition from the  $5p^6\ ^1S_0$  ground level of xenon to a  $J = 0$  level of the  $5p^56p$  configuration was excited by ultraviolet radiation with a wavelength of 249 nm and the scale gives the (relative) frequency of this radiation. This  $J = 0$  to  $J' = 0$  transition has no hyperfine structure and the peak for each isotope is labelled with its relative atomic mass. The xenon gas was at room temperature and a pressure of 0.3 mbar. Light from a blue dye laser with a frequency jitter of 1 MHz was frequency-doubled to generate the ultraviolet radiation and the counter-propagating beams of this radiation had a radius of 0.1 mm in the interaction region.

Estimate the contributions to the line width from (a) the transit time, (b) pressure broadening, (c) the instrumental width, and (d) the Doppler effect.

## (8.7) Collision broadening of a two-photon transition

The signal shown in Fig. 8.11 has a line width (FWHM) of about 10 MHz. From the data given in Example 8.3 determine the maximum pressure of hydrogen which could have been used in that experiment.

Web site:

<http://www.physics.ox.ac.uk/users/foot>

This site has answers to some of the exercises, corrections and other supplementary information.

Later experiments<sup>36</sup> measured the pressure broadening of the  $1s-2s$  transition frequency to be 20 GHz/bar for hydrogen atoms in a gas that is mostly helium atoms. Estimate the cross-section for collisions between metastable hydrogen and helium atoms. Comment on the size of this cross-section in relation to the size of atoms.

## (8.8) Convolution of Lorentzian line shapes

A simple quantitative model of saturated absorption spectroscopy is given in Appendix D and this exercise examines some of the mathematical details.

- (a) The convolution of two Lorentzian functions of equal width can be found using

$$\int_{-\infty}^{\infty} \frac{1}{1 + (2y - x)^2} \frac{1}{1 + x^2} dx = \frac{1}{2} \frac{\pi}{1 + y^2}. \quad (8.27)$$

Calculate the integral in eqn D.6. Hence prove eqn D.7.

- (b) The convolution of two Lorentzian functions of unequal widths is

$$\begin{aligned} & \int_{-\infty}^{\infty} \frac{1}{a^2 + (y + x)^2} \frac{1}{b^2 + (y - x)^2} dx \\ &= \left( \frac{a + b}{ab} \right) \frac{\pi}{(2y)^2 + (a + b)^2}. \end{aligned} \quad (8.28)$$

Use this to show that taking into account the power broadening of the hole burnt in populations by the pump beam leads to a predicted line width in saturation spectroscopy of

$$\Gamma' = \frac{1}{2} \Gamma \left( 1 + \sqrt{1 + \frac{I}{I_{\text{sat}}}} \right).$$

*Comment.* The proof of eqns 8.27 and 8.28 requires the residue theorem for complex path integrals.

<sup>36</sup>See Boshier *et al.* (1989) and McIntyre *et al.* (1989).

# 9

# Laser cooling and trapping

|                                      |     |
|--------------------------------------|-----|
| 9.1 The scattering force             | 179 |
| 9.2 Slowing an atomic beam           | 182 |
| 9.3 The optical molasses technique   | 185 |
| 9.4 The magneto-optical trap         | 190 |
| 9.5 Introduction to the dipole force | 194 |
| 9.6 Theory of the dipole force       | 197 |
| 9.7 The Sisyphus cooling technique   | 203 |
| 9.8 Raman transitions                | 208 |
| 9.9 An atomic fountain               | 211 |
| 9.10 Conclusions                     | 213 |
| Exercises                            | 214 |

<sup>1</sup>The inhomogeneous magnetic field deflects the atoms in the Stern–Gerlach experiment but has a negligible effect on the speed.

<sup>2</sup>This condition does not hold true for cold atoms moving through a standing wave of light where the intensity varies significantly over short distances (comparable with the optical wavelength, see Section 9.7).

In previous chapters we have seen how laser spectroscopy gives Doppler-free spectra and also how other older techniques of radio-frequency and microwave spectroscopy can resolve small splittings, e.g. hyperfine structure. These methods just observe the atoms as they go past,<sup>1</sup> but this chapter describes the experimental techniques that use the force exerted by laser light to slow the atomic motion and manipulate atoms. These techniques have become extremely important in atomic physics and have many applications, e.g. they have greatly improved the stability of the caesium atomic clocks that are used as primary standards of time around the world. We shall look at the forces that laser light exerts on an atom in some detail since this aspect contains most of the atomic physics. In many of the cases studied in this chapter, the atom’s motion follows straightforwardly from Newton’s laws once the force is known—an atom behaves like a classical particle, localised at a particular point in space, when the atomic wavepacket has a spread which is small compared to the distance over which the potential energy varies.<sup>2</sup>

The first laser cooling experiments were carried out on ions that were trapped by electric fields and then cooled by laser radiation. In contrast, it is difficult to confine atoms at room temperature, or above, because of the smaller electromagnetic forces on neutral particles. Therefore the pioneering experiments used light forces to slow atoms in an atomic beam and then confined the cold atoms with a magnetic field. The great success of laser cooling led to the award of the 1997 Nobel prize in physics to Steven Chu, Claude Cohen-Tannoudji and William Phillips. To describe the development of the subject we consider their contributions in the following order. We start from an explanation of the light force on atoms in terms of the scattering of photons. The research group of Phillips used this force to slow an atomic beam (Section 9.2). Chu and co-workers then demonstrated the method known as the optical molasses technique, that cools the motion of atoms in all three dimensions to give a very cold atomic vapour (Section 9.3). This led directly to the development of the so-called magneto-optical trap (Section 9.4) used in the majority of atom-trapping experiments today.

The interaction of the atoms with the light field turned out to be much more subtle than first supposed, and experiments showed that the optical molasses technique produced even lower temperatures than predicted. Cohen-Tannoudji and Jean Dalibard explained this behaviour by a new mechanism called Sisyphus cooling.<sup>3</sup> This mechanism is described towards the end of the chapter (Section 9.7) since it does not

<sup>3</sup>Chu and co-workers also developed a physically equivalent description.

fall neatly into either category of the radiation force, i.e. (a) the scattering force that arises from absorption of light and spontaneous emission, and (b) the dipole force, described in Section 9.6. The forces on microscopic particles have properties similar to the forces on individual atoms, and this analogy is used to introduce the dipole force in Section 9.5. Atoms that have been pre-cooled by the other laser cooling techniques described in this chapter can be cooled even further using Raman transitions (Section 9.8). Finally, Section 9.9 describes an atomic fountain which requires laser-cooled atoms.

## 9.1 The scattering force

The idea that radiation has momentum (and energy) goes back to James Clerk Maxwell in the nineteenth century. It follows from the conservation of momentum that when an object absorbs radiation its momentum changes. The force on the object equals the rate of change of momentum. Therefore the force equals the rate at which the light delivers momentum—this is the same as the rate at which the light delivers energy divided by the speed of light.<sup>4</sup> Therefore radiation of intensity  $I$  exerts a force on area  $A$  given by

$$F_{\text{rad}} = \frac{IA}{c}. \quad (9.1)$$

Equivalently, the radiation pressure is  $F_{\text{rad}}/A = I/c$ . The quantity  $IA$  equals the power absorbed, e.g. for  $IA = 1\text{W}$  the force is  $F = 3.3 \times 10^{-9}\text{N}$ . At a surface that reflects the radiation back on itself the momentum change is twice as large and gives twice the force in eqn 9.1. Although small, the radiation force has observable effects in astrophysics, e.g. the outward radiation pressure balances gravity in stars, and the tails of comets point away from the sun (rather than trailing behind as for shooting stars in the atmosphere). Note, however, that although radiation pressure does have some effect on the dust and ice particles that form the tail of a comet, the solar wind is also important—the stream of particles emanating from the sun hit the particles in the comet tail and even the relatively low pressure in space leads to a force comparable to that from radiation pressure.<sup>5</sup> Radiation forces have a dramatic effect on atoms because the peak absorption cross-section  $\sigma_{\text{abs}}(\omega_0)$  is much greater than the physical size of the atom (see eqn 7.81).<sup>6</sup>

Lasers produce well-collimated monochromatic beams of light that can slow atoms in an atomic beam, as illustrated in Fig. 9.1. A counter-propagating laser beam exerts a force of  $F = -\sigma_{\text{abs}}I/c$  on an atom, where the minus sign indicates a force in the opposite direction to the motion. This expression in terms of the absorption cross-section shows that the light does not have to be considered as quantised in order to calculate the force, but it is convenient to describe the processes in terms of photons. Each absorbed photon gives the atom a kick in the direction opposite to its motion and spontaneously-emitted photons go in all directions, so that the scattering of many photons gives an average

<sup>4</sup>The energy of radiation divided by its momentum equals  $c$ . For a photon

$$\frac{\text{energy}}{\text{momentum}} = \frac{\hbar\omega}{\hbar k} = \frac{\omega}{k} = c.$$

Of course, Maxwell showed this by classical electromagnetism, not in terms of photons. (The ratio does not depend on  $\hbar$ .) This and other aspects of the pressure due to electromagnetic radiation are discussed in Bleaney and Bleaney (1976, Section 8.8).

<sup>5</sup>The radiation from the sun has an intensity of  $1.4\text{ kW m}^{-2}$  at the Earth. Thus the radiation pressure at the Earth's orbit is  $5 \times 10^{-6}\text{ N m}^{-2}$ , or slightly less than  $\sim 10^{-10}$  times atmospheric pressure.

<sup>6</sup>Alkali atoms in a vapour have a large fraction of their absorption strength concentrated in a narrow range centred at the frequency of the resonance line.

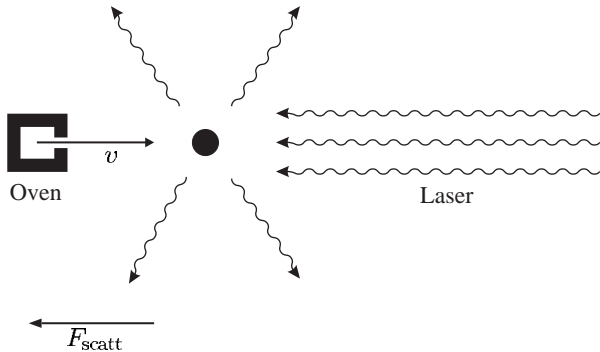


**Fig. 9.1** For an atom moving towards the laser, each absorbed photon gives the atom a kick in the direction opposite to its motion and the scattered photons go in random directions, resulting in a force that slows the atom.

force that slows the atom down. The magnitude of this scattering force equals the rate at which the absorbed photons impart momentum to the atom:

$$F_{\text{scatt}} = (\text{photon momentum}) \times (\text{scattering rate}). \quad (9.2)$$

The scattering rate is  $R_{\text{scatt}} = \Gamma \rho_{22}$ , and  $\rho_{22}$ , the fraction of the population in level 2, is given in eqn 7.69, so that

$$R_{\text{scatt}} = \frac{\Gamma}{2} \frac{\Omega^2/2}{\delta^2 + \Omega^2/2 + \Gamma^2/4}. \quad (9.3)$$

The frequency *detuning* from resonance  $\delta = \omega - \omega_0 + kv$  equals the difference between the laser frequency  $\omega$  and the atomic resonance frequency  $\omega_0$  taking into account the Doppler shift  $kv$ . The Rabi frequency and saturation intensity are related by  $I / I_{\text{sat}} = 2\Omega^2/\Gamma^2$  (see eqn 7.86)<sup>7</sup> and photons have momentum  $\hbar k$ , so that<sup>8</sup>

$$F_{\text{scatt}} = \hbar k \frac{\Gamma}{2} \frac{I / I_{\text{sat}}}{1 + I / I_{\text{sat}} + 4\delta^2/\Gamma^2}. \quad (9.4)$$

As  $I \rightarrow \infty$  the force tends to a limiting value of  $F_{\text{max}} = \hbar k \Gamma / 2$ . The rate of spontaneous emission from two-level atoms tends to  $\Gamma/2$  at high intensities because the populations in the upper and lower levels both approach 1/2. This follows from Einstein's equations for radiation interacting with a two-level atom that has degeneracy factors  $g_1 = g_2 = 1$ .

For an atom of mass  $M$  this radiation force produces a maximum acceleration that we can write in various forms as

$$a_{\text{max}} = \frac{F_{\text{max}}}{M} = \frac{\hbar k \Gamma}{M 2} = \frac{v_r}{2\tau}, \quad (9.5)$$

where  $\tau$  is the lifetime of the excited state. The recoil velocity  $v_r$  is the change in the atom's velocity for absorption, or emission, of a photon at wavelength  $\lambda$ ; it equals the photon momentum divided by the atomic mass:  $v_r = \hbar k/M \equiv h/(\lambda M)$ . For a sodium atom  $a_{\text{max}} = 9 \times 10^5 \text{ m s}^{-2}$ , which is  $10^5$  times the gravitational acceleration. For the situation shown in Fig. 9.1 the atom decelerates at a rate

$$\frac{dv}{dt} = v \frac{dv}{dx} = -a, \quad (9.6)$$

<sup>7</sup>Generally speaking, intensity is more directly related to experimental parameters than the Rabi frequency, but we shall use both  $I$  and  $\Omega$  in this chapter. As noted previously, there are other definitions of the saturation intensity in common use that differ by a factor of 2 from the one used here.

<sup>8</sup>This statement relies on the comprehensive description of two-level atoms interacting with radiation given in Chapter 7.

where  $a$  is positive. For constant deceleration from an initial velocity  $v_0$  at  $z = 0$ , integration gives the velocity as a function of distance:

$$v_0^2 - v^2 = 2az. \quad (9.7)$$

Typically, the deceleration is half the maximum value  $a = a_{\max}/2$  to ensure that atoms are not left behind.<sup>9</sup> Hence the stopping distance is

$$L_0 = \frac{v_0^2}{a_{\max}}. \quad (9.8)$$

A typical apparatus for slowing a sodium atom ( $M \simeq 23$  a.m.u.) uses the parameters in the following table, where the initial velocity  $v_0$  is taken to be the most probable velocity in a beam (given in Table 8.1).

|  |                       |                         |
|--|-----------------------|-------------------------|
| Most probable velocity in beam ( $T = 900$ K)              | $v_0$                 | $1000 \text{ m s}^{-1}$ |
| Resonance wavelength                                       | $\lambda$             | 589 nm                  |
| Lifetime of the excited state                              | $\tau$                | 16 ns                   |
| Recoil velocity  | $v_r = h/(\lambda M)$ | $3 \text{ cm s}^{-1}$   |
| Stopping distance (at half of<br>the maximum deceleration) | $2v_0^2\tau/v_r$      | 1.1 m                   |

A distance of 1 m is a convenient length for an experiment, and all alkali metals require surprisingly similar stopping distances. Although the heavier elements have a lower deceleration, they also have lower initial velocities because of their higher mass and the lower temperature required to give sufficient vapour pressure in an oven for a high-flux atomic beam, e.g. eqn 9.8 gives  $L_0 = 1.2$  m for rubidium and a most probable velocity of  $v_0 = v_{\text{beam}} = 360 \text{ ms}^{-1}$  at  $T = 450$  K (from the data in Table 9.1).

The majority of laser cooling experiments have been carried out with sodium or rubidium.<sup>10</sup>

The calculation of the stopping distance assumes a constant deceleration, but for a given laser frequency atoms only experience a strong force over a narrow range of velocities,  $\Delta v \sim \Gamma/k$ , for which the atoms have a

<sup>9</sup>Fluctuations of the force about its average value arise from the randomness in the number of photons scattered per unit time, as described in Section 9.3.1.

<sup>10</sup>Other elements such as magnesium (an alkaline earth metal) have ultraviolet transitions with shorter lifetimes that scatter photons of higher momentum. Thus the atoms stop in a shorter distance; however, it is technically more difficult to obtain continuous-wave ultraviolet radiation.

**Table 9.1** Properties of some elements used in laser cooling experiments.

| Element | Atomic mass<br>number | Wavelength of<br>resonance (nm) | Lifetime of the<br>excited state (ns) |
|---------|-----------------------|---------------------------------|---------------------------------------|
| H       | 1                     | 121.6                           | 1.6                                   |
| Li      | 7                     | 671                             | 27                                    |
| Na      | 23                    | 589                             | 16                                    |
| K       | 39                    | 767                             | 26                                    |
| Rb      | 85, 87                | 780                             | 27                                    |
| Cs      | 133                   | 852                             | 31                                    |

<sup>11</sup>This range is similar to the width of the hole burnt in the ground-state population in saturated absorption spectroscopy. In practice, power broadening makes the homogeneous width larger than the natural width.

range of Doppler shifts approximately equal to the homogeneous width of the transition.<sup>11</sup> Atoms that interact strongly with the laser light slow down until the change in their Doppler shift takes them out of resonance with the light. This change must be compensated for in order to keep the force close to its maximum value throughout the slowing process.

## 9.2 Slowing an atomic beam

The two pioneering laser cooling experiments used different methods to compensate for the change in Doppler shift as the atoms slowed down. William Phillips and co-workers used the ingenious method shown in Fig. 9.2 in which the atomic beam travels along the axis of a tapered solenoid; the Zeeman effect of the varying magnetic field perturbs the atomic energy levels so that the transition frequency matches a constant laser frequency. In the other method the laser frequency was changed and this so-called chirp cooling is described in the next section. From eqns 9.7 and 9.8 we see that during constant deceleration the velocity at distance  $z$  from the starting point is given by

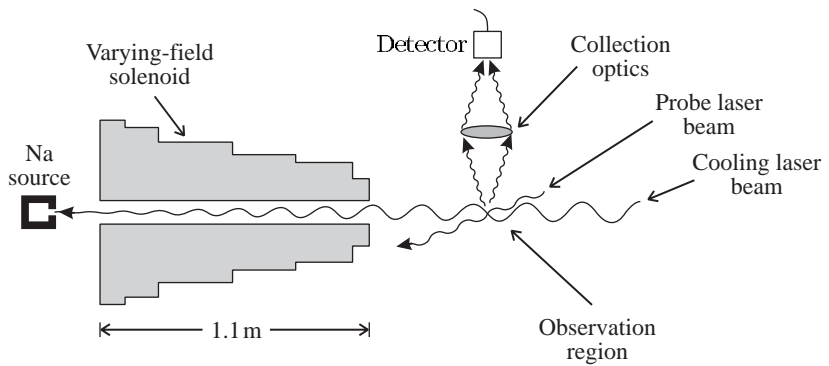
$$v = v_0 \left(1 - \frac{z}{L_0}\right)^{1/2}. \quad (9.9)$$

To compensate for the change in Doppler shift as the atoms slow down from  $v_0$  to the chosen final velocity, the frequency shift caused by the Zeeman effect needs to obey the condition

$$\omega_0 + \frac{\mu_B B(z)}{\hbar} = \omega + kv. \quad (9.10)$$

On the left-hand side, the Zeeman shift for an atomic magnetic moment  $\mu_B$  increases the atomic resonance frequency from  $\omega_0$ , its value at zero

**Fig. 9.2** The first Zeeman slowing experiment. The solenoid produces a magnetic field that varies with position along the atomic beam so that the Zeeman shift compensates for the change in the Doppler shift as atoms decelerate. A probe laser beam intersects the slow atomic beam at a point downstream and the laser frequency is scanned to give a fluorescent signal proportional to the velocity distribution, similar to that shown in Fig. 9.4 (from a different experiment). This procedure records the component of the atomic velocity along the probe beam and the angle of intersection must *not* be  $90^\circ$ . (Here we have the opposite requirement to that in Fig. 8.2.) Adapted from Phillips *et al.* (1985).



field; on the other side of the equation, the Doppler shift adds to the laser frequency  $\omega$ . Hence we find from eqn 9.9 that the required magnetic field profile is

$$B(z) = B_0 \left(1 - \frac{z}{L_0}\right)^{1/2} + B_{\text{bias}} \quad (9.11)$$

for  $0 \leq z \leq L_0$ , where

$$B_0 = \frac{\hbar v_0}{\lambda \mu_B}. \quad (9.12)$$

If  $\mu_B B_{\text{bias}} \simeq \hbar\omega - \hbar\omega_0$  then the atoms come to a complete stop at the end of the tapered solenoid; generally, it is more useful to leave the atoms with a small velocity so that they travel out of the tapered solenoid to a region where experiments, or further cooling, can be performed. Figure 9.3(a) shows the field profile for  $\omega \simeq \omega_0$  and  $B_{\text{bias}} \simeq 0$ , so that the maximum field at the entrance to the solenoid is about  $B_0$ ; Fig. 9.3(b) shows the field profile for a different choice of  $B_{\text{bias}}$  that requires a lower magnitude of the field.

**Example 9.1** For a transition between a state with quantum numbers  $F$  and  $M_F$  and an excited state with quantum numbers  $F'$  and  $M_{F'}$ , the Zeeman effect causes an (angular) frequency shift of  $(g_{F'} M_{F'} -$

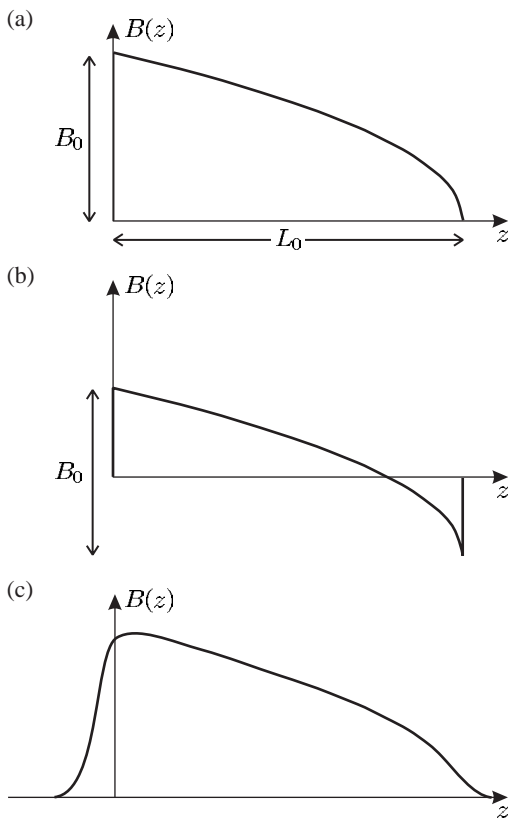


**Fig. 9.3** The magnetic field along the tapered solenoid in the first Zeeman slowing experiment (see Fig. 9.2) varied with position as shown in (a). This magnetic field is described by eqn 9.11. Nowadays, some experiments use the variant shown in (b) where the field drops to zero and then reverses; this gives the same decrease in velocity for a given change in field  $B_0$ , but has the following three advantages: (i) the field has a lower maximum value so that the coils need less current-turns; (ii) the ‘reverse slower’ produces less field at positions downstream,  $z > L_0$ , because the contributions from the coils with currents in opposite directions tend to cancel out; and (iii) the abrupt change in the field at the exit helps the atoms to leave the solenoid cleanly (the atoms see a sudden increase in the frequency detuning of the light from resonance that cuts off the radiation force). In a real solenoid the field changes gradually, as illustrated in (c). This smoothing has little influence on the overall length required because it does not significantly affect the early part of the slowing process.

$g_F M_F) \mu_B B / \hbar$ . For the  $3p\ ^2P_{3/2} - 3s\ ^2S_{1/2}$  line in sodium, the transition between the hyperfine levels  $F' = 3$ ,  $M_{F'} = 3$  and  $F = 2$ ,  $M_F = 2$  has  $g_{F'} M_{F'} - g_F M_F = 1$ , so its Zeeman shift is as assumed in eqn 9.10. This transition leads to a closed cycle of absorption and spontaneous emission because selection rules dictate that the excited state can only decay back to the initial state. This transition was used in the first slowing experiment shown in Fig. 9.2.<sup>12</sup> Hence for  $v_0 = 1000\text{ m s}^{-1}$  we find from eqn 9.12 that

$$B_0 = 0.12\text{ T}, \quad (9.13)$$

which is well within the capability of standard magnet coils. In this magnetic field a sodium atom has a Zeeman shift equal to the Doppler shift of  $\Delta f = v_0/\lambda = 1.7\text{ GHz}$  (cf. the natural width  $\Gamma/2\pi = 10\text{ MHz}$ ).

<sup>12</sup>Other alkalis have corresponding transitions between ‘fully-stretched’ states for which  $F$  has the maximum value for a given  $I$  and  $J$ ; and  $M_F = F$  or  $M_F = -F$ . Sodium has a nuclear spin of  $I = 3/2$ .

<sup>13</sup>From eqn 9.10 we see that the radiation exerts the strongest force on atoms with a velocity  $v_f$  at the end of the solenoid that is given by

$$kv_f \simeq \omega_0 + \frac{\mu_B B_{\text{bias}}}{\hbar} - \omega. \quad (9.14)$$

The actual final velocity will be lower than  $v_f$  because the atoms remain in the laser light after they have emerged from the solenoid and are slowed further. A rough estimate suggests that the atomic velocity is lower than  $v_f$  by an amount corresponding to a Doppler shift of several line widths (e.g.  $3\Gamma/k$ ), but this depends on the interaction time with the light (which itself depends on the velocity and distance travelled). It is difficult to obtain very low final velocities without stopping the atoms completely and pushing them back into the solenoid.

The important feature of the Zeeman slowing technique is that it reduces the velocity of a large fraction of the atoms in a beam to a low final value  $v_f$ . Any atoms that start with velocities within the range  $v_0$  to  $v_f$  interact with the laser radiation at some position along the solenoid and are swept along in the slowing process. The calculations in this section show how this works in principle, but the equations do not give the value of the final velocity  $v_f$  accurately for the following reason. The stopping distance is proportional to the square of the initial velocity (eqn 9.8), so during deceleration from  $v_0 = 100\text{ m s}^{-1}$  to  $v_f = 0\text{ m s}^{-1}$  the atoms only move 1 cm; and deceleration from  $v_0 = 33\text{ m s}^{-1}$  to zero occurs within 1 mm. Thus the final velocity depends critically on what happens at the end of the solenoid and in the fringing field that extends beyond.<sup>13</sup> In practice, the laser frequency is adjusted so that the atoms have sufficient velocity to continue along the apparatus. Various methods for extracting the atoms have been developed, such as that shown in Fig. 9.3(b) where the field changes abruptly at the end of the solenoid so the interaction with the light shuts off cleanly.

### 9.2.1 Chirp cooling

In the other pioneering experiment to laser cool a sodium beam, the laser frequency was changed to keep track of the Doppler shift as the atoms slowed down. This method has become known as chirp cooling—a chirped pulse is one in which the frequency sweeps rapidly. This name derives from an analogy with bird-song, where the pitch of the sound changes rapidly. We can calculate the sweep time from the number of photon kicks required to stop the atom:  $\mathcal{N} = v_0/v_r$ . An atom scatters photons at a maximum rate of  $\Gamma/2 = 1/(2\tau)$ . Therefore  $\mathcal{N}$  photons are scattered in a time of  $2\mathcal{N}\tau$ , or at half the maximum deceleration it takes twice as long, i.e.  $4\mathcal{N}\tau$ . For a beam of sodium atoms with parameters given in Example 9.1,  $\mathcal{N} = 34\,000$  and the sweep time is  $4\mathcal{N}\tau = 2 \times 10^{-3}\text{ s}$ . The frequency of the light must be swept over a range of more than 1 GHz in a few milliseconds. Tuneable dye lasers cannot scan this quickly and so the experimenters used electro-optic modulators and radio-frequency techniques to change the frequency of

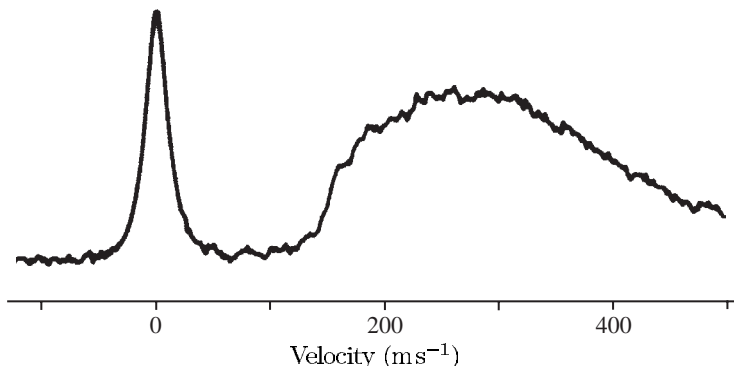


**Fig. 9.4** The atomic velocity distribution produced by chirp cooling caesium atoms with radiation from semiconductor diode lasers. The trace shows the experimentally observed fluorescence from the atoms as the laser frequency was scanned over a frequency range greater than the initial Doppler shift of the atoms in the atomic beam. From Steane (1991).

the light. Nowadays, chirp cooling of heavy alkalis such as rubidium and caesium can be carried out by directly scanning the frequency of infra-red semiconductor diode lasers—Fig. 9.4 shows the results of such an experiment. It can be seen that the laser cooling sweeps atoms to lower velocities to produce a narrow peak in the velocity distribution. It is the spread of the velocities within this peak that determines the final temperature, not the mean velocity of these atoms. The atoms have a much smaller spread of velocities than at room temperature so they are cold.

### 9.3 The optical molasses technique

In an atomic beam the collimation selects atoms moving in one direction that can be slowed with a single laser beam. Atoms in a gas move in all directions and to reduce their temperature requires laser cooling in all three directions by the configuration of three orthogonal standing waves shown in Fig. 9.5—the light along the Cartesian axes comes from the same laser and has the same frequency. At first, you might think that this symmetrical arrangement has no effect on an atom since there are equal and opposite forces on an atom. However, the radiation forces from the laser beams balance each other only for a stationary atom, which is what we want to achieve. For a moving atom the Doppler effect leads to an imbalance in the forces. Figure 9.5(b) shows the situation for a two-level atom in a pair of counter-propagating beams from a laser with a frequency below the atomic resonance frequency (red frequency detuning). Consider what happens in the reference frame of an atom moving towards the right, as shown in Fig. 9.5(c). In this frame the Doppler effect leads to an increase in the frequency of the laser beam propagating in the direction opposite to the atom's velocity. This Doppler shift brings the light closer to resonance with the atom and thereby increases the rate of absorption from this beam. This leads to a resultant force that slows the atom down.<sup>14</sup> Expressed mathematically, the difference between the force to the right and that to the left is

<sup>14</sup>A similar situation arises for movement in any direction.

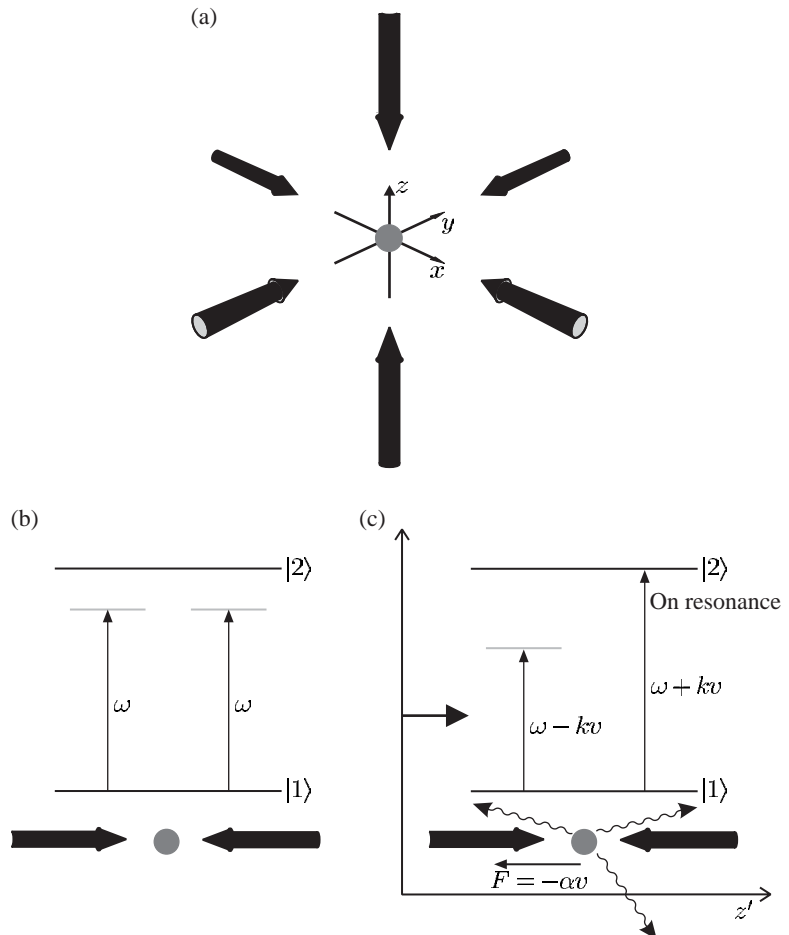


**Fig. 9.5** ‘Optical molasses’ is the name given to the laser cooling technique that uses the configuration of three orthogonal pairs of counter-propagating laser beams along the Cartesian axes shown in (a). The laser beams are derived from the same laser and have a frequency  $\omega$  that is slightly below the transition frequency between the two atomic levels 1 and 2. (b) A stationary atom in a pair of counter-propagating laser beams experiences no resultant force because the scattering is the same for each laser beam, but for a moving atom, as in (c), the Doppler effect leads to more scattering of the light propagating in the direction opposite to the atom’s velocity. (Part (c) is drawn in the rest frame of an atom moving at velocity  $v$ .) The imbalance in the forces occurs for all directions and damps the atomic motion.

$$\begin{aligned}
 F_{\text{molasses}} &= F_{\text{scatt}}(\omega - \omega_0 - kv) - F_{\text{scatt}}(\omega - \omega_0 + kv) \\
 &\simeq F_{\text{scatt}}(\omega - \omega_0) - kv \frac{\partial F}{\partial \omega} - \left[ F_{\text{scatt}}(\omega - \omega_0) + kv \frac{\partial F}{\partial \omega} \right] \\
 &\simeq -2 \frac{\partial F}{\partial \omega} kv. \tag{9.15}
 \end{aligned}$$

Low velocities,  $kv \ll \Gamma$ , have been assumed. This imbalance in the forces arising from the Doppler shift can be written as

$$F_{\text{molasses}} = -\alpha v. \tag{9.16}$$

<sup>15</sup>Strictly,

$$F_{\text{scatt}} = \hbar k R_{\text{scatt}} \equiv \hbar \frac{\omega}{c} R_{\text{scatt}},$$

so

$$\frac{\partial F}{\partial \omega} = \frac{\hbar}{c} \left( R_{\text{scatt}} + \omega \frac{\partial R_{\text{scatt}}}{\partial \omega} \right),$$

but typically the second term is about  $\omega/\Gamma \simeq 10^8$  larger than the first term.

The light exerts a frictional, or damping, force on the atom just like that on a particle in a viscous fluid. This analogy led the Americans who first demonstrated the effect (Chu *et al.* 1985) to call it the optical molasses technique (like treacle, or honey)—a name that seems to have stuck! Differentiation of eqn 9.4 gives the damping coefficient as<sup>15</sup>

$$\alpha = 2k \frac{\partial F}{\partial \omega} = 4\hbar k^2 \frac{I}{I_{\text{sat}}} \frac{-2\delta/\Gamma}{[1 + (2\delta/\Gamma)^2]^2}. \tag{9.17}$$

The term  $I / I_{\text{sat}} \ll 1$  has been neglected in the denominator because this simple treatment of the optical molasses technique is only valid for intensities well below saturation where the force from each beam acts independently.<sup>16</sup> Damping requires a positive value of  $\alpha$  and hence  $\delta = \omega - \omega_0 < 0$ , i.e. a red frequency detuning (in accordance with the physical explanation of the optical molasses technique given above). For this condition the plots of the force in Fig. 9.6 have a negative gradient  $\partial F/\partial v < 0$  at  $v = 0$ .

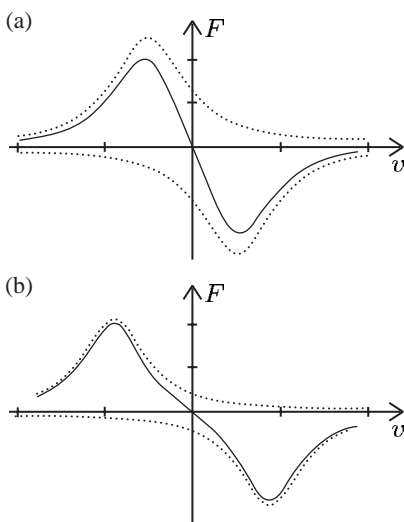
The above discussion of the optical molasses technique applies to one of pair of a counter-propagating laser beams. For the beams parallel to the  $z$ -axis, Newton's second law gives

$$\frac{d}{dt} \left( \frac{1}{2} M v_z^2 \right) = M v_z \frac{dv_z}{dt} = v_z F_{\text{molasses}} = -\alpha v_z^2. \quad (9.18)$$

The components of the velocity along the  $x$ - and  $y$ -directions obey similar equations, so that in the region where the three orthogonal pairs of laser beams intersect the kinetic energy  $E = \frac{1}{2}M(v_x^2 + v_y^2 + v_z^2)$  decreases:

$$\frac{dE}{dt} = -\frac{2\alpha}{M} E = -\frac{E}{\tau_{\text{damp}}}. \quad (9.19)$$

Under optimum conditions the damping time  $\tau_{\text{damp}} = M/(2\alpha)$  is a few microseconds (see Exercises 9.7 and 9.8). This gives the time-scale for the initial cooling of atoms that enter the laser beams with velocities within the capture range of the optical molasses technique, i.e. velocities for which the force has a significant value in Fig. 9.6. Equation 9.19 gives the physically unrealistic prediction that energy tends to zero because we have not taken into account the heating from fluctuations in the force.



<sup>16</sup>Saturation in two counter-propagating beams could be taken into account by the replacement  $I/I_{\text{sat}} \rightarrow 2I/I_{\text{sat}}$  in the denominator of the expression for  $\alpha$  (and also  $R_{\text{scatt}}$ ), although if  $I/I_{\text{sat}}$  is not negligible a simple rate equation treatment is not accurate. We will see that for real atoms, as opposed to theoretical two-level atoms, the light field needs to be considered as a standing wave even for low intensities.

**Fig. 9.6** The force as a function of the velocity in the optical molasses technique (solid lines) for (a)  $\delta = -\Gamma/2$ , and (b)  $\delta = -\Gamma$ . The damping is proportional to the slope of the force curve at  $v = 0$ . Note that the force is negative for  $v > 0$  and positive for  $v < 0$ , so the force decelerates atoms. The forces produced by each of the laser beams separately are shown as dotted lines—these curves have a Lorentzian line shape and they are drawn with an FWHM of  $\Gamma$  appropriate for low intensities. For  $\delta = 0$  (not shown in the figure) the forces from the two laser beams cancel each other for all velocities. The velocity capture range is approximately  $\pm\Gamma/k$ .

### 9.3.1 The Doppler cooling limit

We can write the force from a single laser beam as

$$\mathbf{F} = \mathbf{F}_{\text{abs}} + \delta\mathbf{F}_{\text{abs}} + \mathbf{F}_{\text{spont}} + \delta\mathbf{F}_{\text{spont}}. \quad (9.20)$$

The average of the force from the absorption of photons is the scattering force that we have already derived,  $\overline{\mathbf{F}}_{\text{abs}} = \mathbf{F}_{\text{scatt}}$ , and the random kicks from spontaneously-emitted photons average to zero, i.e.  $\overline{\mathbf{F}}_{\text{spont}} = 0$ . What we have not considered previously is the effect of the fluctuations in these two processes, i.e.  $\overline{\delta\mathbf{F}}_{\text{spont}}$  and  $\overline{\delta\mathbf{F}}_{\text{abs}}$ .

The spontaneous emission that always accompanies  $\mathbf{F}_{\text{scatt}}$  causes the atom to recoil in random directions. These recoil kicks lead to a random walk of the velocity, as shown in Fig. 9.7 (analogous to the Brownian motion of microscopic particles in air). A random walk of  $\mathcal{N}$  steps gives a mean displacement proportional to  $\sqrt{\mathcal{N}}$ , or equivalently the mean square displacement equals  $\mathcal{N}$  times the square of the step length. During a time  $t$  an atom scatters a mean number of photons

$$\mathcal{N} = R_{\text{scatt}} t. \quad (9.21)$$

Spontaneous emission causes the mean square velocity to increase as  $\overline{v^2} = R_{\text{scatt}} t \times v_r^2$ , or along the  $z$ -axis

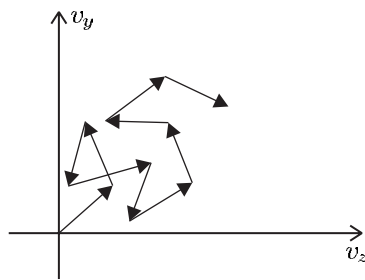
$$(\overline{v_z^2})_{\text{spont}} = \eta v_r^2 R_{\text{scatt}} t. \quad (9.22)$$

<sup>17</sup>The spontaneously-emitted photons that go in the  $x$ - and  $y$ -directions lead to heating in those directions, that must be taken into account in a full three-dimensional treatment. For isotropic spontaneous emission the heating would be the same in all directions, i.e.  $\overline{v_x^2}$  and  $\overline{v_y^2}$  would increase at the same rate as  $\overline{v_z^2}$ . Radiation from an electric dipole oscillator is not isotropic, but this turns out not to be important for reasons discussed below.

Each spontaneous photon gives a recoil kick in the  $z$ -direction of  $\hbar k \cos \theta$  and the factor  $\eta = \langle \cos^2 \theta \rangle$  is the angular average, e.g. for isotropic spontaneous emission  $\eta = 1/3$ .<sup>17</sup>

The fluctuations  $\overline{\delta\mathbf{F}}_{\text{abs}}$  arise because the atom does not always absorb the same number of photons in a time period  $t$ . Each absorption is followed by spontaneous emission and the mean number of such events in time  $t$  is given by eqn 9.21. Assuming that the scattering obeys Poissonian statistics, the fluctuations about the mean have a standard deviation of  $\sqrt{\mathcal{N}}$  and cause a random walk of the velocity along the laser beam, on top of the change in velocity (acceleration or deceleration) caused by the mean force. This one-dimensional random walk caused by the fluctuations  $\overline{\delta\mathbf{F}}_{\text{abs}}$  leads to an increase in the velocity spread similar

**Fig. 9.7** The recoil of an atom from each spontaneous emission causes the atomic velocity to change by the recoil velocity in a random direction. Thus the atom undergoes a random walk in velocity space with steps of length  $v_r$ . The equilibrium temperature is determined by the balance between this diffusive heating and the cooling. (For simplicity, only two directions are shown here.)



to that in eqn 9.22, but without the factor  $\eta$  (because all the absorbed photons have the same direction):

$$(\overline{v_z^2})_{\text{abs}} = v_r^2 R_{\text{scatt}} t. \quad (9.23)$$

This gives the effect of  $\overline{\delta F}_{\text{abs}}$  for a single laser beam. For an atom in two counter-propagating beams the radiation forces of the two beams tend to cancel (as in eqn 9.5) but the effect of the fluctuations is cumulative. The atom has an equal probability of absorbing photons from either beam (incident from the left and right, say) so it receives impulses that are randomly either to the left, or to the right, leading to a random walk of velocity along the beams.<sup>18</sup>

From eqns 9.22 and 9.23 we can find the heating arising from  $\overline{\delta F}_{\text{spont}}$  and  $\overline{\delta F}_{\text{abs}}$ , respectively. Inserting these terms into eqn 9.18, and assuming that for a pair of beams the scattering rate is  $2R_{\text{scatt}}$  (twice the rate for a single beam of intensity  $I$ ), we find

$$\frac{1}{2}M \frac{d\overline{v_z^2}}{dt} = (1 + \eta)E_r(2R_{\text{scatt}}) - \alpha\overline{v_z^2}, \quad (9.24)$$

where

$$E_r = \frac{1}{2}Mv_r^2 \quad (9.25)$$

is the recoil energy. Equation 9.24 describes the balance between heating and damping for an atom in a pair of counter-propagating beams, but in the optical molasses technique there are usually three orthogonal pairs of laser beams, as shown in Fig. 9.5. To estimate the heating in this configuration of six laser beams we shall assume that, in the region where the beams intersect, an atom scatters photons six times faster than in a single beam (this neglects any saturation). If the light field is symmetrical<sup>19</sup> then the spontaneous emission is isotropic. Thus averaging over angles gives  $\eta = 1/3$ , but the overall contribution from  $\overline{\delta F}_{\text{spont}}$  is three times greater than for a pair of the laser beams. Therefore the factor  $1 + \eta$  in eqn 9.24 becomes  $1 + 3\eta = 2$  for the three-dimensional configuration.<sup>20</sup> This gives the intuitively reasonable result that the kinetic energy increases by twice the recoil energy  $2E_r$  in each scattering event—this result can be derived directly from consideration of the conservation of energy and momentum in the scattering of photons (see Exercise 9.3).

Setting the time derivative equal to zero in eqn 9.24 gives the mean square velocity spread in the six-beam optical molasses configuration as

$$\overline{v_z^2} = 2E_r \frac{2R_{\text{scatt}}}{\alpha}, \quad (9.26)$$

and similarly along the other laser beam directions. The kinetic energy of the motion parallel to the  $z$ -axis is related to the temperature by  $\frac{1}{2}M\overline{v_z^2} = \frac{1}{2}k_B T$  (according to the equipartition theorem). Substitution for  $\alpha$  and  $R_{\text{scatt}}$  gives<sup>21</sup>

$$k_B T = \frac{\hbar\Gamma}{4} \frac{1 + (2\delta/\Gamma)^2}{-2\delta/\Gamma}. \quad (9.27)$$

<sup>18</sup> An underlying assumption here is that the absorption from the laser beams is uncorrelated, so that two laser beams produce twice as much diffusion as a single beam (given in eqn 9.23). This is only a reasonable approximation at low intensities ( $I \ll I_{\text{sat}}$ ) where saturation is not significant, and, as in the derivation of eqn 9.17, we shall ignore the factor  $I/I_{\text{sat}}$  in the denominator of  $R_{\text{scatt}}$ . A more comprehensive treatment is given by Cohen-Tannoudji *et al.* (1992).

<sup>19</sup> Theoretically, this might seem difficult to achieve since, even if all three pairs of beams have the same polarization, the resultant electric field depends on the relative phase between the pairs of beams. In practice, however, these phases normally vary randomly in time (and with position if the beams are not perfectly aligned), so assuming that the light field is symmetrical over an average of many measurements is not too bad.

<sup>20</sup> An alternative justification comes from considering the additional contribution along the  $z$ -axis from photons spontaneously emitted after absorption from the beams along the  $x$ - and  $y$ -axes. This contribution makes up for the fraction  $1 - \eta$  of the spontaneous emission that goes in other directions following absorption from beams parallel to the  $z$ -axis. There is detailed balancing between different directions because of the symmetry of the configuration.

<sup>21</sup> Equation 9.17 can be written as

$$\begin{aligned} \alpha &= 2\hbar k^2 \frac{\partial R_{\text{scatt}}}{\partial \omega} \\ &= 2\hbar k^2 \frac{-2\delta}{\delta^2 + \Gamma^2/4} R_{\text{scatt}}. \end{aligned}$$

This function of  $x = -2\delta/\Gamma$  has a minimum at  $\delta = \omega - \omega_0 = -\Gamma/2$  of

$$k_B T_D = \frac{\hbar\Gamma}{2}. \quad (9.28)$$

<sup>22</sup>Einstein pointed out in his fundamental work on radiative absorption and emission processes of atoms in a thermal radiation field that the momentum exchange between light and matter would bring the atoms into thermal equilibrium with the surroundings (Einstein 1917). When the radiation has a spectral distribution corresponding to 0 K (monochromatic light) the atom would be expected to approach this temperature.

<sup>23</sup>Narrow transitions with  $\hbar\Gamma < E_r$  give rise to a different behaviour, that has some similarities to the discussion of cooling using narrow Raman transitions in Section 9.8.

This key result is the *Doppler cooling limit*. It gives the lowest temperature expected in the optical molasses technique. On general grounds, we expect a limit of this magnitude for processes in a two-level atom since  $\hbar\Gamma = \hbar/\tau$  represents the smallest energy scale in the system.<sup>22</sup> For sodium  $T_D = 240 \mu\text{K}$ , which corresponds to a most probable velocity of  $0.5 \text{ m s}^{-1}$ . This velocity can be written as

$$v_D \simeq \left( \frac{\hbar\Gamma}{M} \right)^{1/2} = \left( \frac{\hbar k}{M} \cdot \frac{\Gamma}{k} \right)^{1/2} = (v_r v_c)^{1/2}, \quad (9.29)$$

where  $v_c \simeq \Gamma/k$  gives an estimate (to within a factor of 2) of the capture velocity for the optical molasses technique, i.e. the velocity range over which  $F_{\text{scatt}}$  has a significant value. For sodium  $v_r = 0.03 \text{ m s}^{-1}$  and  $v_c = 6 \text{ m s}^{-1}$ , and the above treatment of the optical molasses technique is valid for velocities within this range.<sup>23</sup>

The theory as presented so far was initially thought to describe the optical molasses technique until experimental measurements found much lower temperatures under certain conditions, in particular when the Earth's magnetic field was cancelled out. The two-level model of an atom cannot explain this *sub-Doppler cooling*. Real alkali atoms have degenerate energy levels ( $|IJFM\rangle$  states). Remarkably, this does not just complicate the situation but actually allows new cooling mechanisms to occur, as described in Section 9.7. This is a rare example in which things turned out to be much better than expected. The fact that Doppler cooling theory does not accurately describe the optical molasses experiments with alkali metal atoms gives an excuse for the rather cavalier treatment of saturation in this section.

## 9.4 The magneto-optical trap

In the optical molasses technique cold atoms accumulate in the region where the three orthogonal pairs of laser beams intersect because it takes a considerable time for atoms to diffuse out, e.g. several seconds for beams of 1 cm radius. With the correct choice of polarizations for the laser beams, this configuration can be turned into a trap by the addition of a magnetic field gradient, as illustrated in Figs 9.8 and 9.9; the two coils with currents in opposite directions produce a quadrupole magnetic field. This magnetic field is much weaker than in the purely magnetic traps described in Chapter 10 and *does not* confine atoms by itself. In the *magneto-optical trap* (MOT) the quadrupole magnetic field causes an imbalance in the scattering forces of the laser beams and it is the radiation force that strongly confines the atoms.<sup>24</sup> The principle of the MOT is illustrated in Fig. 9.9(a) for a simple  $J = 0$  to  $J = 1$  transition. At the point in the middle of the coils the magnetic fields

<sup>24</sup>The principal idea of magneto-optical trapping was suggested by Jean Dalibard and demonstrated at Bell Laboratories, USA in collaboration with a group from MIT.

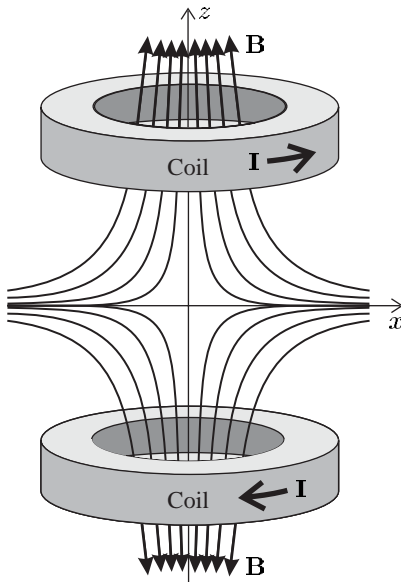


**Fig. 9.8** A pair of coils with currents in opposite directions produces a quadrupole magnetic field. The field is zero at the centre of the coils and its magnitude increases linearly in every direction for small displacements from the zero point.

produced by the coils cancel out, so that  $B = 0$ . Close to this zero of the field there is a uniform field gradient that perturbs the atomic energy levels; the Zeeman effect causes the energy of the three sub-levels (with  $M_J = 0, \pm 1$ ) of the  $J = 1$  level to vary linearly with the atom's position, as shown for the  $z$ -axis in Fig. 9.9(a).<sup>25</sup> The counter-propagating laser beams have circular polarization as shown in Fig. 9.9(b) and a frequency slightly less than the atomic resonance frequency. The Zeeman shift causes an imbalance in the radiation force in the following way. Consider an atom displaced from the centre of the trap along the  $z$ -axis with  $z > 0$ , so the  $\Delta M_J = -1$  transition moves closer to resonance with the laser frequency—the laser has a frequency below the atomic resonance in zero field to give damping by the optical molasses mechanism.<sup>26</sup> The selection rules lead to absorption of photons from the beam that excites the  $\sigma^-$  transition and this gives a scattering force that pushes the atom back towards the trap centre. A similar process occurs for a displacement in the opposite direction ( $z < 0$ ); in this case the Zeeman shift of the transition frequency and selection rules favour absorption from the beam propagating in the positive  $z$ -direction that pushes the atom back towards  $z = 0$ . Note that these beam polarizations and the quantisation axis of the atom have been defined relative to a fixed direction in space, i.e. the  $z$ -direction in this one-dimensional example. For  $z > 0$  this is the same as the direction of the magnetic field, but for  $z < 0$  the magnetic field points the opposite way; hence the  $M_J = -1$  state lies above +1 in this region, as shown in Fig. 9.9(a). Strictly speaking,  $\sigma^+$  and  $\sigma^-$  refer to transitions of the atom and labelling the radiation as  $\sigma^+$  is shorthand for circularly-polarized radiation of the handedness

<sup>25</sup>The energy levels also vary in the other directions. The Maxwell equation  $\text{div } \mathbf{B} = 0$  implies that

$$\frac{dB_x}{dx} = \frac{dB_y}{dy} = -\frac{1}{2} \frac{dB_z}{dz},$$

so the gradient in any radial direction is half of that along the  $z$ -direction.

<sup>26</sup>The MOT requires three orthogonal pairs of  $\sigma^+ - \sigma^-$  beams, but the optical molasses technique works with other polarization states, e.g. the Sisyphus cooling in Section 9.7 uses linearly-polarized beams.

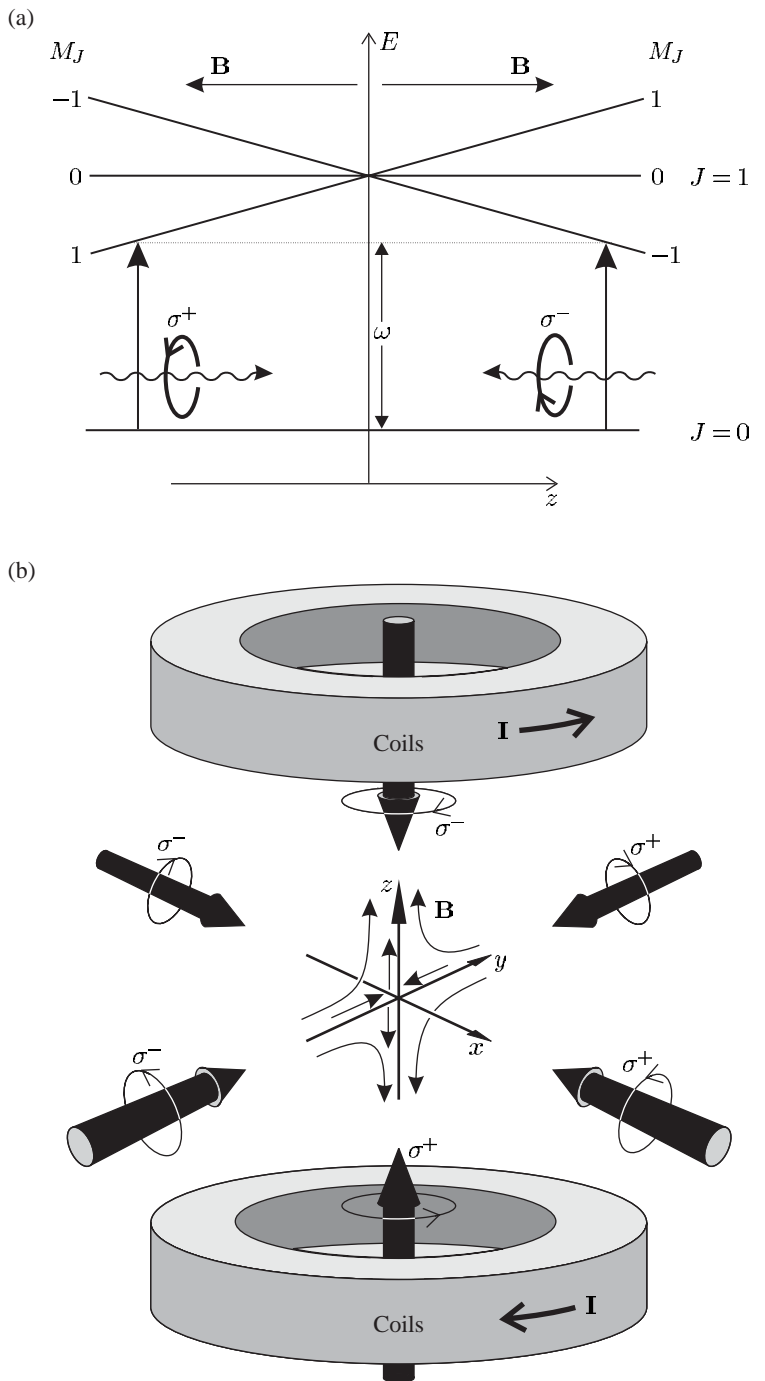


**Fig. 9.9** (a) The mechanism of a magneto-optical trap illustrated for the case of an atom with a  $J = 0$  to  $J = 1$  transition. In the magnetic field gradient the Zeeman splitting of the sub-levels depends on the atom's position. Two counter-propagating beams of circularly-polarized light illuminate the atom and the selection rules for transitions between the Zeeman states lead to an imbalance in the radiative force from the laser beams that pushes the atom back towards the centre of the trap. (Not to scale; the Zeeman energy is much smaller than the optical transition energy.) (b) A magneto-optical trap is formed from three orthogonal pairs of laser beams, as in the optical molasses technique, that have the requisite circular polarization states and intersect at the centre of a pair of coils with opposite currents. The small arrows indicate the direction of the quadrupole magnetic field produced by the coils (as shown in more detail in Fig 9.8).

that excites the  $\sigma^+$  transition (and similarly for  $\sigma^-$ ).<sup>27</sup> To describe the magneto-optical trap mathematically we can incorporate the frequency shift caused by the Zeeman effect into eqn 9.15 (that describes the optical molasses technique):<sup>28</sup>

$$\begin{aligned} F_{\text{MOT}} &= F_{\text{scatt}}^{\sigma^+} (\omega - kv - (\omega_0 + \beta z)) - F_{\text{scatt}}^{\sigma^-} (\omega + kv - (\omega_0 - \beta z)) \\ &\simeq -2 \frac{\partial F}{\partial \omega} kv + 2 \frac{\partial F}{\partial \omega_0} \beta z. \end{aligned} \quad (9.30)$$

The term  $\omega_0 + \beta z$  is the resonant absorption frequency for the  $\Delta M_J = +1$  transition at position  $z$ , and  $\omega_0 - \beta z$  is that for  $\Delta M_J = -1$ . The Zeeman shift at displacement  $z$  is

$$\beta z = \frac{g\mu_B}{\hbar} \frac{dB}{dz} z, \quad (9.31)$$

where  $g = g_J$  in this case.<sup>29</sup> The force depends on the frequency detuning  $\delta = \omega - \omega_0$ , so  $\partial F / \partial \omega_0 = -\partial F / \partial \omega$  and hence

$$\begin{aligned} F_{\text{MOT}} &= -2 \frac{\partial F}{\partial \omega} (kv + \beta z) \\ &= -\alpha v - \frac{\alpha \beta}{k} z. \end{aligned} \quad (9.32)$$

The imbalance in the radiation force caused by the Zeeman effect leads to a restoring force with spring constant  $\alpha\beta/k$  (which is written in this form to emphasise that it arises in a similar way to damping). Under typical operating conditions the atom undergoes over-damped simple harmonic motion, as shown in Exercise 9.9. Atoms that enter the region of intersection of the laser beams are slowed (as in the optical molasses technique) and the position-dependent force pushes the cold atoms to the trap centre. This combination of strong damping and trapping makes the magneto-optical trap easy to load and it is very widely used in laser cooling experiments.

A typical apparatus uses an MOT to collect cold atoms from a slowed atomic beam. When sufficient atoms have accumulated the magnetic field of the MOT is turned off to cool the atoms by the optical molasses technique before further experiments are carried out.<sup>30</sup> This procedure gives more atoms (at a higher density) than the optical molasses technique on its own because the MOT captures faster atoms than optical molasses. The magnetic field in the MOT changes the atom's absorption frequency in a similar way to the Zeeman slowing technique, e.g. if the magneto-optical trap has laser beams of radius 5 mm and we take this as the stopping distance in eqn 9.8 then the trap captures sodium atoms with velocities less than  $v_c(\text{MOT}) \simeq 70 \text{ m s}^{-1}$ . But atoms enter the MOT from all directions and the magnetic field varies linearly with position (a constant gradient), so the situation is not the same as the optimum case of an atom moving along the axis of a tapered solenoid with the counter-propagating laser beam (see Exercise 9.10). Nevertheless, an MOT captures atoms with much faster velocities than the optical

<sup>27</sup>This is a convenient convention for discussing the principles of laser cooling where the transitions that occur depend on the sense of rotation of the electric field around the quantization axis of the atom (whereas handedness depends on both the sense of the rotation and the direction of the propagation). The electric field of the circularly-polarized radiation drives the bound atomic electron(s) around in the same sense as the electric field; therefore, radiation labelled  $\sigma^+$  that imparts positive angular momentum about the quantization axis,  $\Delta M_J = +1$ , has an electric field that rotates clockwise when viewed along that quantization axis (see Fig. 9.9(b)), i.e. in the same direction as a particle with  $\langle L_z \rangle > 0$ . The magneto-optical trap also confines atoms along the  $x$ - and  $y$ -axes, and all other directions. In practice, these traps are extremely robust and only require the polarizations of the beams to be approximately correct—some atoms are trapped so long as none of the beams have the wrong handedness.

<sup>28</sup>This assumes a small Zeeman shift  $\beta z \ll \Gamma$  in addition to the small velocity approximation  $kv \ll \Gamma$ .

<sup>29</sup>More generally,  $g = g_{F'} M_{F'} - g_F M_F$  for a transition between the hyperfine-structure levels  $|F, M_F\rangle$  and  $|F', M_{F'}\rangle$ ; however,  $g \simeq 1$  for many of the transitions used for laser cooling—see Example 9.1.

<sup>30</sup>Atoms in the MOT have a higher temperature than in the optical molasses technique for several reasons: the sub-Doppler cooling mechanisms break down when the Zeeman shift exceeds the light shift and there is strong absorption of the laser beams as they pass through dense clouds of cold atoms (see Exercise 9.12).

<sup>31</sup>These elements have an appreciable vapour pressure at room temperature. The MOT captures the slowest atoms in the Maxwellian velocity distribution. The equilibrium number of atoms trapped directly into an MOT from a vapour is proportional to the fourth power of  $v_c(\text{MOT})$ , so the method is very sensitive to this parameter.

<sup>32</sup>Broadening from collisions and the Doppler effect is negligible and broadening caused by the inhomogeneous magnetic field is small, e.g. for a typical field gradient of  $0.1 \text{ T m}^{-1}$  and a cloud of radius 3 mm the variation in the Zeeman shift is  $\sim 4 \text{ MHz}$  (for  $g = 1$ ).

molasses technique, e.g. for sodium  $v_c(\text{MOT}) > v_c(\text{molasses}) \simeq 6 \text{ m s}^{-1}$  (eqn 9.29). This relatively large capture velocity makes it possible to load an MOT directly from a room temperature vapour, and this method can be used instead of slowing an atomic beam for the heavy alkalis rubidium and caesium (see Exercise 9.11).<sup>31</sup> Typically, an MOT loaded from a slow atomic beam contains up to  $10^{10}$  atoms. Experiments that capture atoms directly from a vapour usually have considerably less. Such general statements should be treated with caution, however, since there are various factors that limit number and density in different operating regimes, e.g. absorption of the laser light—the cold atoms that congregate in the centre of the MOT have close-to-the-maximum optical absorption cross-section<sup>32</sup>—absorption leads to a difference or an imbalance in the intensities of the laser beams propagating through the cloud of cold atoms that affects the trapping and cooling mechanisms.

At equilibrium each atom absorbs and emits the same amount of light. Therefore a large cloud of cold atoms in an MOT scatters a significant fraction of the incident light and the atoms can be seen with the naked eye as a bright glowing ball in the case of sodium; for rubidium the scattered infra-red radiation can easily be detected on a CCD camera. The MOT provides a source of cold atoms for a variety of experiments, e.g. loading the dipole-force traps (as described in the following sections) and magnetic traps (Chapter 10). Finally, it is worth highlighting the difference between magneto-optical and magnetic trapping. The force in the MOT comes from the radiation—the atoms experience a force close to the maximum value of the scattering force at large displacements from the centre. The magnetic field gradients in a magneto-optical trap (that tune the absorption frequency of the atoms) are much smaller than those used in magnetic traps. A typical MOT has a gradient of  $0.1 \text{ T m}^{-1}$  and when the light is switched off this produces a magnetic force that is not sufficient to support atoms against gravity.

## 9.5 Introduction to the dipole force

The scattering force equals the rate at which an object gains momentum as it absorbs radiation. Another type of radiation force arises from the refraction of light as illustrated in Fig. 9.10. A simple prism that deflects light through an angle  $\theta$  feels a force

$$F = \left( \frac{IA}{c} \right) 2 \sin \left( \frac{\theta}{2} \right), \quad (9.33)$$

where the quantity  $IA/c$  corresponds to the rate at which radiation with intensity  $I$  carries momentum through a cross-sectional area  $A$  (perpendicular to the direction of propagation); this quantity corresponds to the total force when the radiation is absorbed (eqn 9.1). When the beam is refracted the difference between the incoming and outgoing momentum flow leads to the factor  $2 \sin(\theta/2)$  by simple geometry. The angle and the resultant force increase with the refractive index.

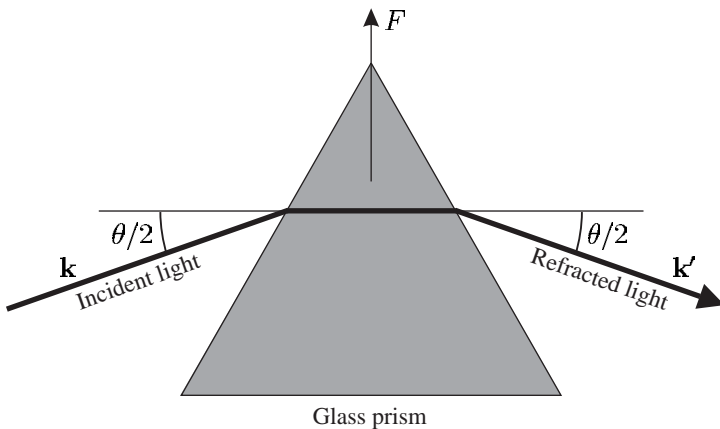


**Fig. 9.10** Radiation that is deflected by a glass prism (or a mirror) exerts a force on that object equal and opposite to the rate of change of momentum of the radiation.

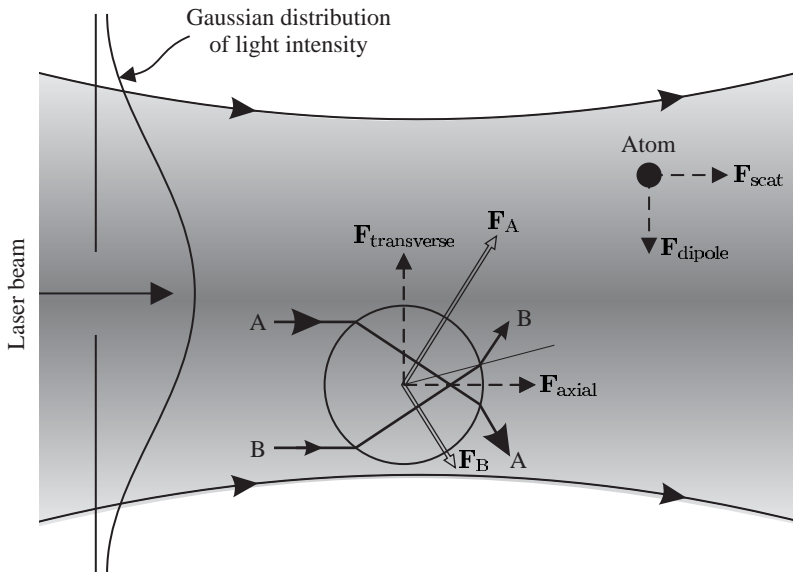


**Fig. 9.11** The refraction of light by a dielectric sphere with a refractive index greater than that of the surrounding medium. In a laser beam with a Gaussian profile the intensity along ray A is greater than for ray B. This leads to a resultant force on the sphere towards the region of high intensity (centre of the laser beam), in addition to an axial force pushing in the direction of the beam. Analogous forces arise on smaller particles such as atoms. After Ashkin (1997).

These simple considerations show that the forces associated with absorption and refraction by an object have similar magnitude but they have different characteristics; this can be seen by considering a small dielectric sphere that acts as a converging lens with a short focal length, as shown in Fig. 9.11. In a laser beam of non-uniform intensity, the difference in the intensity of the light refracted on opposite sides of the sphere leads to a resultant force that depends on the gradient of the intensity: a sphere with a refractive index greater than the surrounding medium,  $n_{\text{sphere}} > n_{\text{medium}}$ , feels a force in the direction of increasing intensity, whereas a sphere with  $n_{\text{sphere}} < n_{\text{medium}}$  is pushed away from the region of high intensity.<sup>33</sup> Thus the sign of this *gradient force* (also known as the *dipole force*) depends on  $n_{\text{sphere}}$ . The refractive index of materials varies with frequency in the characteristic way shown in Fig. 9.12. This behaviour can be understood in terms of a simple classi-

<sup>33</sup>The calculation of this force using geometrical optics is straightforward in principle, but integration over all the different rays and inclusion of reflection coefficients makes it complicated.

**Fig. 9.12** Absorption has a Lorentzian line shape with a peak at the resonance frequency  $\omega_0$ . The refractive index is zero on resonance, where it changes sign, and this characteristic dependence on frequency leads to dispersion.

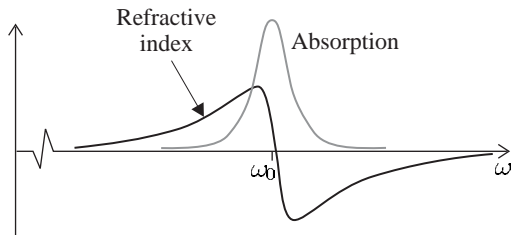
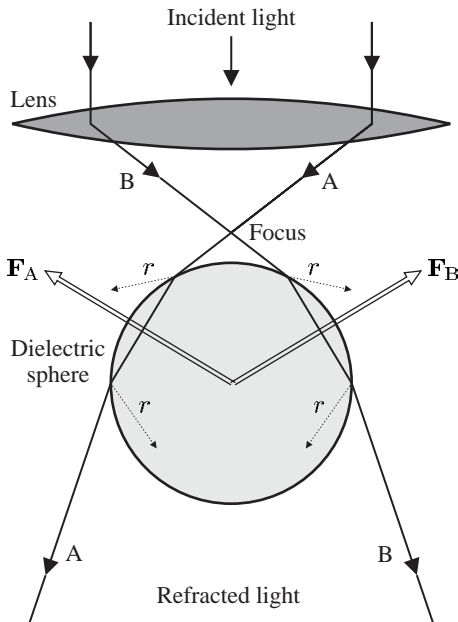


**Fig. 9.13** A tightly-focused beam of light exerts a radiation force on a dielectric sphere that pulls it towards the region of high intensity (at the focus). Not all of the light is transmitted at the interfaces and the reflected rays are indicated. After Ashkin (1997).



cal model in which bound electrons execute damped harmonic oscillation with resonance frequency  $\omega_0$ , see Section 7.5.1 and Fox (2001), but the relationship between the refractive index and absorption at the resonant frequency is very general (independent of any particular model). Dispersion and absorption are different facets of the same interaction of light with matter; strong absorption leads to large changes in refractive index. The variation in the refractive index extends over a larger frequency range than the absorption, e.g. although air and glass (of good optical quality) are both transparent at visible wavelengths they have refractive indices of 1.0003 and 1.5, respectively, associated with strong absorption in the ultraviolet region;  $n_{\text{glass}} - 1 \gg n_{\text{air}} - 1$  because a solid has a higher density of atoms than a gas.<sup>34</sup>

<sup>34</sup>Generally speaking, the effects of refraction are most apparent when they are not obscured by absorption, i.e. away from a resonance. A similar situation arises for forces on the individual atoms.

The force that attracts an object towards a region of high intensity has been used to manipulate microscopic objects in a technique called optical tweezers that was developed by Arthur Ashkin (Ashkin *et al.* 1986). The objective lens in an optical microscope is used to focus a laser beam tightly so that there is a strong gradient force along the axis, as shown in Fig. 9.13, in addition to trapping in the radial direction

shown in Fig. 9.11. As the laser beam is moved the particles remain trapped in the region of high intensity. The microscope is used to view the object through a filter that blocks the laser light. The objects are immersed in water and mounted on a microscope slide in a standard way. The liquid provides viscous damping of the motion.<sup>35</sup> Optical tweezers work, not just for simple spheres, but also for biological cells such as bacteria, and these living objects can withstand the focused intensity required to trap them without harm (the surrounding water prevents the cells from heating up). For example, experiments have been carried out where a bacterium is tethered to the surface of a glass microscope slide by its flagellum (or ‘tail’) and the body is moved around by optical tweezers. This gives a quantitative measure of the force produced by the microscopic biological motor that moves the flagellum to propel these organisms (see Ashkin (1997) and Lang and Bloch (2003) for reviews).

This section has introduced the concept of a radiation force called the gradient force, or dipole force, and the next section shows that a similar force occurs for atoms.<sup>36</sup>

## 9.6 Theory of the dipole force

Actually, this section does not just derive the dipole force on an atom from first principles but also the scattering force, and so demonstrates the relationship between these two types of radiation force. An electric field  $\mathbf{E}$  induces a dipole moment of  $-\mathbf{er} = \epsilon_0\chi_a\mathbf{E}$  on an atom with a (scalar) polarizability  $\epsilon_0\chi_a$ . The interaction energy of this dipole with the electric field is given by

$$U = -\frac{1}{2}\epsilon_0\chi_a E^2 = \frac{1}{2}\mathbf{er} \cdot \mathbf{E}, \quad (9.34)$$

where  $E$  is the amplitude of the electric field and  $U$  is used here to denote energy to avoid confusion with the electric field. This expression comes from the integration of  $dU = -\epsilon_0\chi_a\mathcal{E} d\mathcal{E}$  from  $\mathcal{E} = 0$  to  $\mathcal{E} = E$  (the factor of 1/2 does not occur for a permanent electric dipole). Differentiation gives the  $z$ -component of the force as

$$F_z = -\frac{\partial U}{\partial z} = \epsilon_0\chi_a E \frac{\partial E}{\partial z}, \quad (9.35)$$

and similarly for  $F_x$  and  $F_y$ . Radiation of angular frequency  $\omega$ , propagating along the  $z$ -direction, can be modelled as an electric field  $\mathbf{E} = E_0 \cos(\omega t - kz)\hat{\mathbf{e}}_x$ .<sup>37</sup> The gradient of the energy gives the  $z$ -component of the force as<sup>38</sup>

$$F_z = -ex \left\{ \frac{\partial E_0}{\partial z} \cos(\omega t - kz) + kE_0 \sin(\omega t - kz) \right\}. \quad (9.36)$$

The two parts of this force can be understood using either the classical or the quantum mechanical expressions for the dipole that were derived in Chapter 7. The classical model of the atom as an electron undergoing

<sup>35</sup>Laser radiation can levitate small objects in air, but this is less straightforward than the manipulation of objects floating in water.

<sup>36</sup>This analogy is not just of pedagogical interest—the first experiments on optical tweezers and the dipole-force trapping of atoms were carried out in the same place (Bell Laboratories in the USA).

<sup>37</sup>This particular field is linearly polarized parallel to  $\hat{\mathbf{e}}_x$ , as in Section 7.3.2, but the results derived here are quite general.

<sup>38</sup>This classical treatment gives the same result as the quantum mechanical derivation when the electric field varies slowly over the typical dimensions of an atomic wavepacket ( $\lambda_{dB} \ll \lambda_{light}$ ). Under these circumstances, classical equations of motion correspond to equations for the expectation values of the quantum operators, e.g. the rate of change of momentum equals the force corresponding to

$$\frac{d\langle \mathbf{p} \rangle}{dt} = -\langle \nabla U \rangle.$$

This is an example of Ehrenfest’s theorem in quantum mechanics. The quantum mechanical derivation of the dipole force is given in Cohen-Tannoudji *et al.* (1992).

<sup>39</sup> As shown in Section 7.5.1, the classical model does not account for saturation.

simple harmonic motion gives very useful insight into the frequency dependence of the force, but the quantum treatment is required to find the correct intensity dependence.<sup>39</sup> This section presents both approaches, starting with the classical one—because of the very close parallels between them this requires little extra effort.

Classically, the displacement of the electron  $x$  by an electric field is calculated by modelling the atom as a harmonic oscillator with a driving term. Expressing  $x$  in terms of its components in phase ( $\mathcal{U}$ ) and in quadrature ( $\mathcal{V}$ ) to the applied field (cf. eqn 7.56), we find

$$\begin{aligned} F_z = & -e \{ \mathcal{U} \cos(\omega t - kz) - \mathcal{V} \sin(\omega t - kz) \} \\ & \times \left\{ \frac{\partial E_0}{\partial z} \cos(\omega t - kz) + E_0 k \sin(\omega t - kz) \right\}. \end{aligned} \quad (9.37)$$

<sup>40</sup> Using  $\overline{\sin^2} = \overline{\cos^2} = \frac{1}{2}$ .

The time average over many oscillation periods gives<sup>40</sup>

$$\begin{aligned} \overline{F}_z = & \frac{-e}{2} \left\{ \mathcal{U} \frac{\partial E_0}{\partial z} - \mathcal{V} k E_0 \right\} \\ = & \frac{e^2}{4m\omega} \left\{ \frac{-(\omega - \omega_0)E_0}{(\omega - \omega_0)^2 + (\beta/2)^2} \frac{\partial E_0}{\partial z} + \frac{(\beta/2)kE_0^2}{(\omega - \omega_0)^2 + (\beta/2)^2} \right\}, \end{aligned} \quad (9.38)$$

using eqns 7.58 and 7.59 for  $\mathcal{U}$  and  $\mathcal{V}$ . The intensity of the light is  $I = \frac{1}{2}\epsilon_0 c E_0^2$  and, by a simple extension of the derivation given above to the  $x$ - and  $y$ -directions, the radiation force can be written in vector notation as

$$\overline{\mathbf{F}} = \frac{e^2}{2\epsilon_0 mc} \left\{ \frac{-(\omega - \omega_0)}{(\omega - \omega_0)^2 + (\beta/2)^2} \frac{\nabla I}{\omega} + \frac{\beta/2}{(\omega - \omega_0)^2 + (\beta/2)^2} \frac{I \mathbf{k}}{c |\mathbf{k}|} \right\}. \quad (9.39)$$

The in-phase component of the dipole ( $\mathcal{U}$ ) leads to a force proportional to the gradient of the intensity. The frequency dependence of this component follows a dispersive line shape that is closely related to the refractive index,<sup>41</sup> as shown in Fig. 9.12. (The dependence on  $1/\omega$  has a negligible effect on narrow transitions  $\beta \ll \omega_0$ .) At the atomic resonance frequency  $\omega = \omega_0$  the component  $\mathcal{U} = 0$ . The quadrature term, from  $\mathcal{V}$ , has a Lorentzian line shape and this force, arising from absorption, is proportional to  $I$  and points along the wavevector of the radiation  $\mathbf{k}$ . This classical model gives a simple way of understanding various important features of the forces on atoms and shows how they relate to radiation forces on larger objects (such as those discussed in the introductory Sections 9.1 and 9.5); however, we shall not use it for quantitative calculations.

To find the force quantum mechanically, we use eqn 7.36 for the dipole moment in terms of the components of the Bloch vector  $u$  and  $v$ . Substitution into eqn 9.36, and taking the time average as above, gives (cf. eqn 9.38)

$$\overline{F}_z = \frac{-eX_{12}}{2} \left\{ u \frac{\partial E_0}{\partial z} - v E_0 k \right\} \quad (9.40)$$

$$= F_{\text{dipole}} + F_{\text{scatt}}. \quad (9.41)$$

The force that depends on the in-phase component of the dipole  $u$  is the dipole force and the other part is the scattering force. Using the expressions for  $u$  and  $v$  given in eqn 7.68 and the Rabi frequency  $\Omega = eX_{12}E_0/\hbar$ , we find that

$$F_{\text{scatt}} = \hbar k \frac{\Gamma}{2} \frac{\Omega^2/2}{\delta^2 + \Omega^2/2 + \Gamma^2/4}, \quad (9.42)$$

which is consistent with eqn 9.4, and

$$F_{\text{dipole}} = -\frac{\hbar\delta}{2} \frac{\Omega}{\delta^2 + \Omega^2/2 + \Gamma^2/4} \frac{\partial\Omega}{\partial z}, \quad (9.43)$$

where  $\delta = \omega - \omega_0$  is the frequency detuning from resonance. The expression for the scattering force has been repeated here for ease of comparison with eqn 9.43. These forces have essentially the same frequency dependence as in the classical model, with a line width that is power broadened so that  $\beta \longleftrightarrow \Gamma(1 + 2\Omega^2/\Gamma^2)^{1/2}$ . The dipole force is zero on resonance ( $F_{\text{dipole}} = 0$  for  $\delta = 0$ ), and for  $|\delta| \gg \Gamma$  (and an intensity such that  $|\delta| \gg \Omega$ ) the dipole force equals the derivative of the light shift (eqn 7.93):

$$F_{\text{dipole}} \simeq -\frac{\partial}{\partial z} \left( \frac{\hbar\Omega^2}{4\delta} \right). \quad (9.44)$$

Thus the light shift, or a.c. Stark shift, for an atom in the ground state acts as a potential  $U_{\text{dipole}}$  in which the atom moves. More generally, in three dimensions

$$\mathbf{F}_{\text{dipole}} = - \left\{ \hat{\mathbf{e}}_x \frac{\partial}{\partial x} + \hat{\mathbf{e}}_y \frac{\partial}{\partial y} + \hat{\mathbf{e}}_z \frac{\partial}{\partial z} \right\} U_{\text{dipole}} = -\nabla U_{\text{dipole}}, \quad (9.45)$$

where

$$U_{\text{dipole}} \simeq \frac{\hbar\Omega^2}{4\delta} \equiv \frac{\hbar\Gamma}{8} \frac{\Gamma}{\delta} \frac{I}{I_{\text{sat}}}. \quad (9.46)$$

When  $\delta$  is positive ( $\omega > \omega_0$ ) this potential has a maximum where the intensity is highest—the atom is repelled from regions of high intensity. In the opposite case of frequency detuning to the red ( $\delta$  negative) the dipole force acts in the direction of increasing  $I$ , and  $U_{\text{dipole}}$  is an attractive potential—atoms in a tightly-focused laser beam are attracted towards the region of high intensity, both in the radial direction and along the axis of the beam. This dipole force confines atoms at the focus of a laser beam in an analogous way to optical tweezers to create a dipole-force trap.<sup>42</sup> Normally, dipole traps operate at large frequency detuning ( $|\delta| \gg \Gamma$ ), where to a good approximation eqn 9.3 becomes

$$R_{\text{scatt}} \simeq \frac{\Gamma}{8} \frac{\Gamma^2}{\delta^2} \frac{I}{I_{\text{sat}}}. \quad (9.47)$$

This scattering rate depends on  $I/\delta^2$ , whereas the trap depth is proportional to  $I/\delta$  (in eqn 9.46). Thus working at a sufficiently large frequency detuning reduces the scattering whilst maintaining a reasonable trap depth (for a high intensity at the focus of the laser beam). Usually

<sup>42</sup>The situation for an atom with detuning  $\delta < 0$  resembles that of a dielectric sphere with a refractive index greater than the surrounding medium.

there are two important criteria in the design of dipole-force traps: (a) the trap must be deep enough to confine the atoms at a certain temperature (that depends on the method of cooling); and (b) the scattering rate must be low to reduce heating.

### **Example 9.2** Dipole trapping of sodium atoms

<sup>43</sup>Whereas for scattering-force techniques the frequency of the laser must be tunable, so that it can be adjusted to within several line widths from an atomic transition frequency.

<sup>44</sup>This frequency detuning  $\delta \sim \frac{1}{2}\omega_0$ , so that the rotating-wave approximation is not very good.

The wavelength of the laser light used for a dipole-force trap depends mainly on practical considerations.<sup>43</sup> It is convenient to use a high-power solid-state laser such as a Neodymium:YAG laser that produces continuous-wave radiation at a fixed infra-red wavelength of  $\lambda = 1.06 \mu\text{m}$ . The frequency detuning of this laser radiation from the sodium resonance at  $\lambda_0 = 589 \text{ nm}$  is

$$\frac{\delta}{\Gamma} = \frac{2\pi}{\Gamma} \left\{ \frac{c}{\lambda_0} - \frac{c}{\lambda} \right\} = 2.3 \times 10^7, \quad (9.48)$$

in units of  $\Gamma$ , where  $1/\Gamma = \tau = 16 \text{ ns}$ .<sup>44</sup> Solid-state lasers can produce powers of many tens of watts, but in this example we use a conservative value of  $P = 1 \text{ W}$ . When focused to a waist of  $w_0 = 10 \mu\text{m}$  this laser beam has an intensity of  $I = 2P/(\pi w_0^2) = 6.4 \times 10^9 \text{ W m}^{-2} \equiv 1 \times 10^8 I_{\text{sat}}$ . Equation 9.46 gives

$$U_{\text{dipole}} = \frac{\hbar\Gamma}{2} \times 1.1 = 260 \mu\text{K}. \quad (9.49)$$

Thus atoms cooled below the Doppler cooling limit  $\hbar\Gamma/2$  can be trapped. For this laser intensity and frequency detuning, eqn 9.47 gives

$$R_{\text{scatt}} = 2.4 \times 10^{-8} \Gamma = 2 \text{ s}^{-1}. \quad (9.50)$$

<sup>45</sup>If atoms gain twice the recoil energy per scattering event, as in eqn 9.24, it takes many seconds before the atoms boil out of the trap. The fluctuations in the dipole force itself can cause heating and  $\mathbf{F}_{\text{dipole}} + \delta\mathbf{F}_{\text{dipole}}$  should be included in eqn 9.20. The fluctuations  $\overline{\delta\mathbf{F}_{\text{dipole}}}$  give comparatively small heating in a dipole-force trap with a large frequency detuning; however, there are circumstances where  $\overline{\delta\mathbf{F}_{\text{dipole}}}$  is the dominant cause of heating, e.g. for the Sisyphus effect described in Section 9.7.

<sup>46</sup>Writing eqn 9.50 as

$$R_{\text{scatt}} = 5 \times 10^{-8} (\Gamma/2),$$

where  $\Gamma/2$  is the maximum of  $R_{\text{scatt}}$ , shows that  $R_{\text{scatt}}$  is  $5 \times 10^{-8}$  times its maximum value.

A sodium atom only scatters a few photons per second which gives a low heating rate.<sup>45</sup> The scattering force is negligible for these conditions,<sup>46</sup> i.e. the force pushing in the direction of the light is weaker than the dipole force pulling the atom towards the high-intensity focus. The condition that the laser light has a frequency detuning far from the atomic resonance is not restrictive, and calculations along the same lines as that given here for sodium show that a laser with the above properties can be used for the dipole-force trapping of any alkali metal atom.

A force derived from a potential is conservative, i.e. the total energy remains constant during motion. Thus an atom that enters a dipole trap gains kinetic energy as it moves towards the bottom of the potential well and then it rides up the other side of the trap and escapes, because no energy is lost. To load a dipole trap there must be either some dissipation of energy by spontaneous emission (as in the MOT), or the atoms must be placed gently in the bottom of the trap. In the first experimental demonstration of a dipole trap for atoms the laser beam was focused into a cloud of atoms that were cooled by the optical molasses technique, see Fig. 9.14 (Chu *et al.* 1986). The trapped atoms were observed as a bright spot in the region of more diffuse fluorescence from

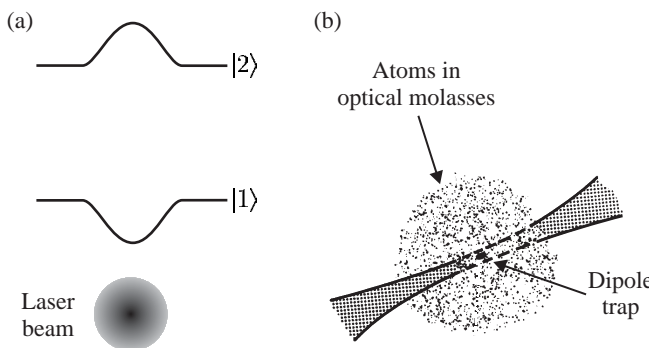


**Fig. 9.14** (a) An intense laser beam alters the energy levels of an atom, as illustrated for a radial direction across a laser beam propagating perpendicular to the plane of the figure. For a laser frequency less than the atomic resonance frequency the a.c. Stark effect forms a potential well in the ground-state energy and atoms are attracted towards regions of high intensity. (b) The dipole-force trap formed by a focused laser beam can be loaded with cold atoms produced by the optical molasses technique, as described in the text.

the region of optical molasses because the density of trapped atoms was greater. When the focused laser beam was first switched on the dipole trap contained relatively few atoms within its small volume, at a density comparable with that in the surrounding region, e.g.  $10^{10} \text{ cm}^{-3}$ . This was perceived to be a problem, but atoms that started off outside the trap executed a random walk<sup>47</sup> that took some of them into the dipole trap, where they remained. In this way atoms accumulated in the trap to give a high density.

A dipole-force trap formed by a single laser beam gives tight radial confinement, but it is weak in the axial direction. Therefore the atoms in such a trap form an elongated, cigar-shaped cloud. To obtain strong confinement in all directions, if necessary, one can form a dipole-force trap at the intersection of two laser beams.<sup>48</sup> Many other configurations are possible and the design of dipole traps is restricted only by the form of the intensity distributions that can be sculpted from laser light. Diffraction limits the minimum distance over which the intensity of the light changes. An ingenious way of creating a high-intensity gradient is shown in Fig. 9.15. A laser beam that is totally internally reflected at the surface of glass gives an evanescent wave in which the electric field falls off exponentially over a distance of the wavelength of the light.<sup>49</sup> For a laser frequency to the blue ( $\delta > 0$ ), the repulsive dipole force near the surface acts like a reflective coating for atoms. This creates a mirror that reflects low-energy atoms, as shown in Fig. 9.15.

### 9.6.1 Optical lattice

The dipole force is strong in a standing wave of light because the intensity changes from a maximum (at the anti-nodes) to zero (at the nodes) over a distance of  $\lambda/2$  to give a high gradient of intensity. The physical explanation for this strong force is stimulated scattering of radiation. In a standing wave, an atom absorbs light with wavevector  $\mathbf{k}$  from one beam and the laser beam in the opposite direction stimulates emission with wavevector  $\mathbf{k}' = -\mathbf{k}$ ; this gives the atom an impulse of  $2\mathbf{k}$ . The rate of this stimulated process does not saturate at high intensities.<sup>50</sup>

<sup>47</sup> A random walk in space leading to spatial diffusion, rather than the random walk of the velocity leading to heating that was used to calculate the Doppler cooling limit—both processes are caused by scattering.

<sup>48</sup> The dipole potential is proportional to the total intensity. Laser beams with orthogonal polarizations, or substantially different frequencies, do not interfere and the total intensity is the sum of the individual intensities.

<sup>49</sup> This behaviour of the light closely resembles the quantum reflection at a potential step that is higher than the energy of the incident particle. The wavefunction falls exponentially to zero in the classically forbidden region.

<sup>50</sup> More generally, the dipole force arises from a *stimulated* process of absorption of a photon of wavevector  $\mathbf{k}_1$  and stimulated emission with wavevector  $\mathbf{k}_2$ . In this process the atom receives an impulse  $\hbar(\mathbf{k}_1 - \mathbf{k}_2)$  that changes the atom's momentum. A tightly-focused laser beam contains a range of wavevectors and exerts a dipole force on an atom analogous to that in the optical tweezers technique. A dipole force cannot occur in a plane wave since the stimulated processes have  $\mathbf{k}_1 = \mathbf{k}_2$ .

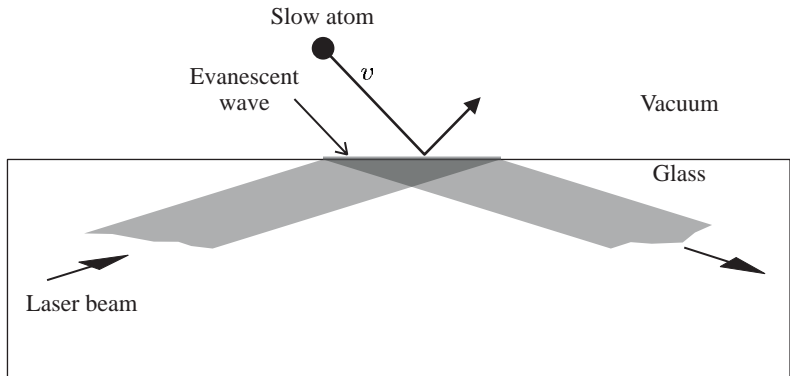


**Fig. 9.15** The evanescent wave, created when a laser beam is totally internally reflected, forms a mirror for atoms. For a light with a blue detuning ( $\omega > \omega_0$ ) the dipole force repels atoms from the region of high intensity close to the vacuum-glass interface. (The same principle applies if the surface is curved (e.g. concave) and such an arrangement can be used to focus the matter waves.)

The dipole potential associated with this force depends on the intensity of the light (cf. eqn 9.46 for a large frequency detuning). Two counter-propagating beams of linearly-polarized light produce an electric field given by

$$\begin{aligned}\mathbf{E} &= E_0 \{ \cos(\omega t - kz) + \cos(\omega t + kz) \} \hat{\mathbf{e}}_x \\ &= 2E_0 \cos(kz) \cos(\omega t) \hat{\mathbf{e}}_x.\end{aligned}\quad (9.51)$$

<sup>51</sup>This form is only true for large detunings,  $\delta \gg \Gamma, \Omega$ . If this inequality is satisfied then there is also little spontaneous scattering from the atoms.

<sup>52</sup>Interference will generally lead to a periodic arrangement of positions where atoms become localised (at intensity maxima for a frequency detuning to the red) in a three-dimensional standing wave of light, but the creation of a particular configuration of the optical lattice requires control of the polarization (and relative phase).

<sup>53</sup>The phase-space density at which BEC occurs is approximately equal to that at which there is one atom per well in the ground state of an optical lattice.

<sup>54</sup>As atoms pass through a standing wave of light they accumulate a phase shift of order  $\phi \simeq U_0 t / \hbar$  for an interaction time  $t$ . Light with either sign of frequency detuning can be used to give  $\phi \sim \pm\pi$ , and so create a phase grating with significant amplitude in the diffraction orders.

This standing wave gives a dipole potential of the form<sup>51</sup>

$$U_{\text{dipole}} = U_0 \cos^2(kz).\quad (9.52)$$

Here  $U_0$  is the light shift at the anti-nodes—these maxima have an intensity four times that of the individual beams. For a frequency detuning to the red, a standing wave of light traps atoms at the anti-nodes and gives confinement in the radial direction as in a single beam. This regular array of microscopic dipole traps is called an optical lattice. With more laser beams the interference between them can create a regular array of potential wells in three dimensions, e.g. the same configuration of six beams in the optical molasses technique shown in Fig. 9.5 (along  $\pm\hat{\mathbf{e}}_x$ ,  $\pm\hat{\mathbf{e}}_y$  and  $\pm\hat{\mathbf{e}}_z$ ) can create a regular cubic lattice of potential wells for suitable polarizations and a large frequency detuning.<sup>52</sup> The potential wells in this optical lattice have a spacing of  $\lambda/2$ , and so one atom per lattice site corresponds to a density of  $8/\lambda^3 \simeq 7 \times 10^{13} \text{ cm}^{-3}$  for  $\lambda = 1.06 \mu\text{m}$ . Therefore the sites will be sparsely populated when the atoms are loaded into the lattice after cooling by the optical molasses technique. (A typical number density in the optical molasses technique is a few times  $10^{10} \text{ cm}^{-3} \equiv 0.01 \text{ atoms } \mu\text{m}^{-3}$ .)

Experiments that load more than one atom in each potential well have been carried out by adiabatically turning on the light that creates an optical lattice in a region containing a sample of atoms that are in a Bose-Einstein condensate (see Chapter 10).<sup>53</sup> Moreover, these atoms go into the lowest vibrational level in each of the potential wells. The use of one-dimensional standing waves as diffraction gratings for matter waves is discussed in Chapter 11.<sup>54</sup>

## 9.7 The Sisyphus cooling technique

### 9.7.1 General remarks

The dipole force experienced by atoms in a light field can be stronger than the maximum scattering force because  $F_{\text{dipole}}$  does not saturate with increasing intensities (whereas  $F_{\text{scatt}}$  does), but stimulated processes alone cannot cool atoms. To dissipate energy there must be some spontaneous emission to carry away energy from the atoms—this is true for all cooling mechanisms, e.g. Doppler cooling by the scattering force, and it is particularly apparent for the process described in this section.

The first experimental evidence that Doppler cooling does not give a complete description of the laser cooling in a standing wave came from measurements of the velocity distribution of atoms by the direct time-of-flight method shown in Fig. 9.16. When William Phillips and co-workers carried out such measurements they were pleasantly surprised to find that the optical molasses technique can cool atoms below the Doppler

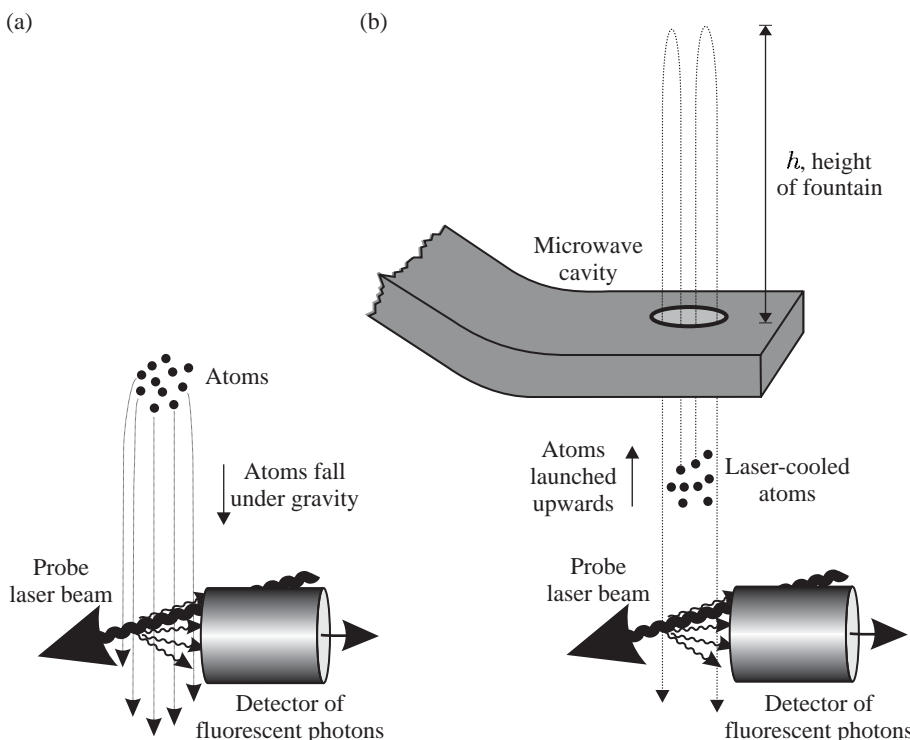


**Fig. 9.16** (a) The temperature of a sample of atoms that has been cooled by the optical molasses technique is measured by turning off the six laser beams (not shown) so that the cloud of cold atoms falls downwards to the bottom of the vacuum chamber (because of gravity). The expansion of the falling cloud depends on the initial spread of the velocities. To observe this expansion a horizontal probe laser beam is aligned several centimetres below the initial position of the cloud. This probe beam has a frequency close to the atomic resonance frequency  $\omega \approx \omega_0$  so that atoms scatter light as they pass through and this fluorescence signal is recorded (or absorption could be monitored). (b) Instead of just dropping the atoms, they can be launched upwards to form an atomic fountain. This configuration is used for precision measurements, as described in Section 9.9.

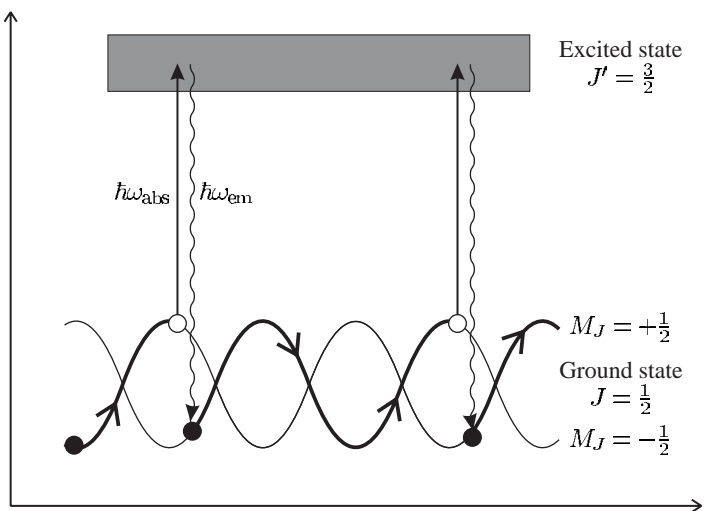
cooling limit in eqn 9.28. This *cannot* be understood in terms of a simple picture in which the scattering forces from each of the six laser beams add independently. Sodium, and other alkalis, have Zeeman structure in their ground states and this additional complexity, as compared to a simple two-level atom, allows new processes to occur.

A particularly important mechanism by which atoms dissipate energy as they move through a standing wave is the Sisyphus effect that was explained by Jean Dalibard and Claude Cohen-Tannoudji (1989), and this section follows the description given in that seminal paper. Steven Chu and co-workers also developed a model to explain sub-Doppler cooling based on the transfer of population between the different sub-levels of the ground configuration (optical pumping) as atoms move through the light field. This transfer of populations takes place on a time-scale  $\tau_{\text{pump}}$  that can be much longer than the spontaneous lifetime ( $\tau_{\text{pump}} \gg 1/\Gamma$ ). This longer time-scale gives better energy resolution than in a two-level atom and therefore allows cooling below the Doppler cooling limit, i.e.  $k_B T \simeq \hbar/\tau_{\text{pump}} < \hbar\Gamma/2$ . A specific example of this general argument is shown in Fig. 9.17, and the following section gives more details.

### 9.7.2 Detailed description of Sisyphus cooling

Consider an atom that has a lower level with angular momentum  $J = 1/2$  and an upper level with  $J' = 3/2$  that moves through a standing wave formed by two counter-propagating laser beams with orthogonal linear polarizations (e.g. along  $\hat{\mathbf{e}}_x$  and  $\hat{\mathbf{e}}_y$ ). The resultant polarization depends on the relative phase of the two laser beams and varies with position, as shown in Fig. 9.18(b). This polarization gradient causes the periodic modulation of the light shift of the states in the lower level. The strength of the interaction with the light depends on  $M_J$  and  $M_{J'}$  in the lower and upper levels, respectively. To understand this in detail, consider

**Fig. 9.17** The laser cooling mechanism in a standing wave with a spatially-varying polarization. The energy levels of the atom are perturbed by the light in a periodic way, so that the atoms travel up and down hills and valleys (maxima and minima) in the potential energy. Kinetic energy is lost when the atom absorbs laser light at the top of a hill and emits a spontaneous photon of higher frequency, so that it ends up in a valley. This has been called the Sisyphus effect and can be made more probable than the reverse process, so that there is strong laser cooling. Thus atoms in a standing wave are cooled below the Doppler cooling limit (the lowest temperature achievable with scattering force alone).



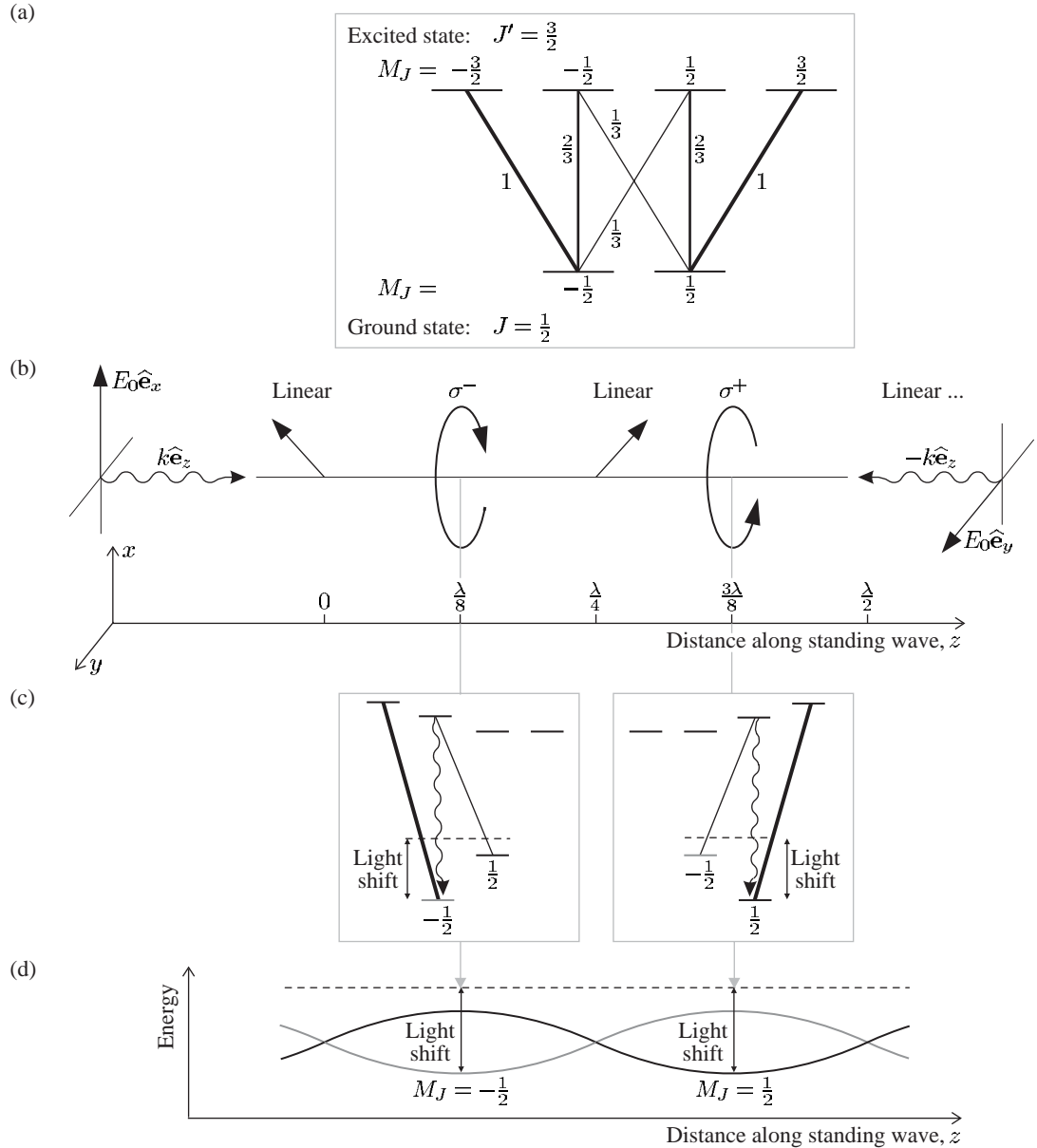
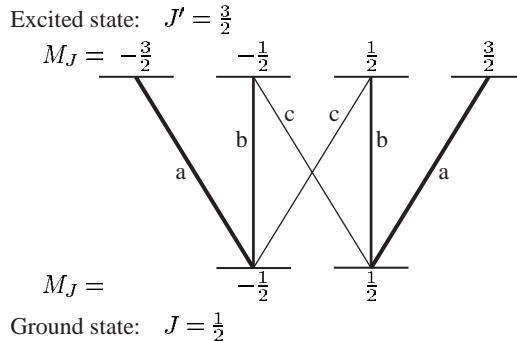


**Fig. 9.18** Details of the Sisyphus cooling mechanism. (a) The electric dipole transitions between two levels with angular momenta  $J = 1/2$  and  $J' = 3/2$ . The relative strength of each transition is indicated—this gives the relative intensity when the states in the upper level are equally populated (each state has the same radiative lifetime). (b) The polarization in a standing wave formed by two laser beams that propagate along  $\hat{e}_z$  and  $-\hat{e}_z$ , and have orthogonal linear polarizations along  $\hat{e}_x$  and  $\hat{e}_y$ , respectively. The resultant electric field is circularly polarized  $(\hat{e}_x \pm i\hat{e}_y)/\sqrt{2}$  at positions where the two counter-propagating beams have a phase difference of  $\pm\pi/2$ . The polarization changes from  $\sigma^+$  to  $\sigma^-$  over a distance of  $\Delta z = \lambda/4$ , and between these positions the light has elliptical or linear polarization. (c) The energies of the states at positions of  $\sigma^-$  and  $\sigma^+$  polarization (the unperturbed energy of the lower level is shown as a dotted line). Absorption of the circularly-polarized light followed by spontaneous emission transfers the population into the state with lowest energy (largest light shift). (d) The light shift varies with position and the optical pumping process, outlined in (c), transfers atoms from the top of a hill to the bottom of a valley (as shown in Fig. 9.17); or at least this process in which atoms lose energy happens more often than the other way around.

**Fig. 9.19** The intensities of the components of the  $J = 1/2$  to  $J = 3/2$  transition are represented by  $a$ ,  $b$  and  $c$  (as in Example 7.3) and their relative values can be determined from sum rules. The sum of the intensities from each of the upper states is the same:  $a = b + c$ ; because normally the lifetime of an atom does not depend on its orientation. (A similar rule applies to the states in the lower level but this does not yield any further information in this case.) When the states of the upper level are equally populated the atom emits unpolarized radiation; hence  $a + c = 2b$ . We now have two simultaneous equations whose solution is  $b = \frac{2}{3}a$  and  $c = \frac{1}{3}a$ , so the relative intensities are  $a : b : c = 3 : 2 : 1$ .

<sup>55</sup>This is the same convention for describing polarization that we used for the magneto-optical trap;  $\sigma^+$  and  $\sigma^-$  refer to transitions that the radiation excites in the atom,  $\Delta M_J = \pm 1$ , respectively. In laser cooling we are mainly interested in determining what transitions occur, and this depends on the sense of rotation of the electric field around the quantization axis of the atom (as described in Section 2.2). As stated previously, the electric field of the radiation drives the bound atomic electron(s) around in the same sense as the electric field; the circularly-polarized radiation travelling parallel to the quantization axis that is labelled  $\sigma^+$  imparts positive angular momentum to the atom. The handedness of the polarization can be deduced from this statement for a given direction of propagation, if necessary.



a position where the light has  $\sigma^+$  polarization;<sup>55</sup> here the interaction for the  $M_J = 1/2$  to  $M_{J'} = 3/2$  transition is stronger than that for the  $M_J = -1/2$  to  $M_{J'} = 1/2$ . (The squares of the Clebsch–Gordan coefficients are 2/3 and 1/3, respectively, for these two transitions, as determined from the sum rules as shown in Fig. 9.19). For light with a frequency detuning to the red ( $\delta < 0$ ), both of the  $M_J$  states in the lower level ( $J = 1/2$ ) are shifted downwards; the  $M_J = +1/2$  state is shifted to a lower energy than the  $M_J = -1/2$  state. Conversely, at a position of  $\sigma^-$  polarization the  $M_J = -1/2$  state is lower than the  $M_J = 1/2$  state. The polarization changes from  $\sigma^-$  to  $\sigma^+$  over a distance of  $\Delta z = \lambda/4$ , so that the light shift varies along the standing wave, as shown in Fig. 9.18(d). An atom moving over these hills and valleys in the potential energy speeds up and slows down as kinetic and potential energy interchange, but its total energy does not change if it stays in the same state.

To cool the atom there must be a mechanism for dissipating energy and this occurs through absorption and spontaneous emission—the process in which an atom absorbs light at the top of a hill and then decays spontaneously back down to the bottom of a valley has a higher probability than the reverse process. Thus the kinetic energy that the atom converts into potential energy in climbing the hill is lost (taken away by the spontaneously-emitted photon); the atom ends up moving more slowly, at the bottom of a valley. This was dubbed the ‘Sisyphus’ effect after a character in Greek mythology who was condemned by the gods

to repeatedly roll a stone to the top of a hill.<sup>56</sup>

To explain the transfer between the  $M_J$  states of the lower level let us again consider the details of what happens at a particular position where the light has  $\sigma^+$  polarization (see Fig. 9.18(d)). Absorption of  $\sigma^+$  light excites an atom from the state  $M_J = -1/2$  to  $M_{J'} = 1/2$ . An atom in this excited state may decay to either of the lower  $M_J$  states; if it returns to  $M_J = -1/2$  then the process restarts, but it may go into the  $M_J = +1/2$  state from which it cannot return (because  $\sigma^+$  light excites the transition from  $M_J = 1/2$  to  $M_{J'} = 3/2$  and the excited state of this transition only decays to  $M_J = +1/2$ ). Thus the  $\sigma^+$  light results in a one-way transfer  $M_J = -1/2$  to  $M_J = +1/2$  (via an excited state). This process in which absorption of light transfers population into a given state is known as optical pumping.<sup>57</sup> In Sisyphus cooling the optical pumping at a position of  $\sigma^+$  polarization takes an atom from the top of a hill, in the potential energy for the  $M_J = -1/2$  state, and transfers it down into a valley of the potential energy for the  $M_J = 1/2$  state. The atom continues its journey in the  $M_J = 1/2$  state until it gets optically pumped back to  $M_J = -1/2$  at a position of  $\sigma^-$  polarization.<sup>58</sup> In each transfer the atom loses an energy  $U_0$  approximately equal to the height of the hills (relative to the bottom of the valleys). This energy is roughly equal to the light shift in eqn 9.46.<sup>59</sup>

This physical picture can be used to estimate the rates of cooling and heating in the Sisyphus mechanism—the balance between these gives the equilibrium temperature (cf. the treatment of Doppler cooling in Section 9.3).<sup>60</sup> Such a treatment shows that atoms in a standing wave have a typical kinetic energy  $\sim U_0$ . This suggests that the Sisyphus mechanism works until atoms can no longer climb the hills and remain stuck in a valley (cf. an optical lattice). This simple picture predicts that the temperature is related to the intensity and frequency detuning by

$$k_B T \simeq U_0 \propto \frac{I}{|\delta|}, \quad (9.53)$$

which is borne out by more detailed calculation.

### 9.7.3 Limit of the Sisyphus cooling mechanism

In a typical optical molasses experiment there are the following two stages. Initially, the laser beams have a frequency several line widths below the atomic resonance ( $\delta \sim -\Gamma$ ) and intensities  $\sim I_{\text{sat}}$  to give a strong radiation force. Then the laser frequency is changed to be further from resonance (and the intensity may be reduced as well) to cool the atoms to lower temperatures below the Doppler limit. The initial stage of Doppler cooling, as described in Section 9.3, is essential because the sub-Doppler cooling mechanisms only operate over a very narrow range

<sup>56</sup>In addition to Sisyphus cooling, Dalibard and Cohen-Tannoudji found another sub-Doppler cooling mechanism called motion-induced orientation. This mechanism leads to an imbalance in scattering from counter-propagating beams that is much more sensitive to velocity, and hence produces a stronger damping than the imbalance caused by the Doppler effect in the ‘ordinary’ optical molasses technique. In a standing wave made from beams of opposite circular polarization ( $\sigma^+$  to  $\sigma^-$ ), a stationary atom has the population distributed over the magnetic sub-levels of the ground state in a symmetrical way, so that there is equal scattering from each beam and no net force. An atom moving through a gradient of polarization, however, sees a changing direction of the electric field and this causes a change in the distribution over the sub-levels (orientation by optical pumping) leading to a difference in the probability of absorption from each beam. In real optical molasses experiments, the three mutually-orthogonal pairs of laser beams create a complex three-dimensional pattern of polarization and a combination of sub-Doppler cooling mechanisms takes place.

<sup>57</sup>Optical pumping in atomic vapours at room temperature was used for very precise radio-frequency spectroscopy even before the laser was invented, e.g. to measure the splitting between the Zeeman sub-levels as described in Thorne (1999) and Corney (2000).

<sup>58</sup>The atom may travel over many hills and valleys between excitations, and the absorption and emission does not always remove energy, but averaged over many events this stochastic process dissipates energy.

<sup>59</sup>Actually, it is about two-thirds of the light shift for the case shown in Fig. 9.17.

<sup>60</sup>The heating arises from fluctuations in the dipole force—the direction of this force changes as an atom jumps from one  $M_J$  state to another. See Metcalf and van der Straten (1999) for a quantitative treatment.

<sup>61</sup>Broadly speaking, in Sisyphus cooling the force averages to zero for atoms that travel over many hills and valleys in an optical-pumping time. Thus this mechanism works for velocities  $v$  such that  $v\tau_{\text{pump}} \lesssim \lambda/2$ . This velocity range is less than the capture velocity for Doppler cooling by the ratio  $\tau/\tau_{\text{pump}}$ .

<sup>62</sup>This assumes that each degree of freedom has energy

$$\frac{1}{2}k_{\text{B}}T_{\text{r}} = E_{\text{r}}. \quad (9.54)$$

<sup>63</sup>Heavy alkalis such as Cs and Rb have a very low recoil limit and these elements can be laser cooled to a few  $\mu\text{K}$ . Such temperatures can only be achieved in practice when stray magnetic fields that would perturb the  $M_F$  states are carefully controlled—a Zeeman shift  $\mu_{\text{B}}B$  comparable with the light shift  $U_0$  will affect the Sisyphus cooling mechanism, i.e. if  $\mu_{\text{B}}B \sim U_0$ . For  $U_0/k_{\text{B}} = 3 \mu\text{K}$  this criterion implies that  $B < 5 \times 10^{-5} \text{ T}$ , which is an order of magnitude less than the Earth's magnetic field ( $5 \times 10^{-4} \text{ T}$ ).

<sup>64</sup>The assumption that the distribution has a Gaussian shape becomes worse at the lowest velocities of only a few times the recoil velocity—the smallest amount by which the velocity can change. Commonly, the distribution develops a sharp peak around  $v = 0$  with wide wings. In such cases the full distribution needs to be specified, rather than a single parameter such as the root-mean-square velocity, and the notion of a ‘temperature’ may be misleading. This remark is even more relevant for cooling below the recoil limit, as described in the following section.

<sup>65</sup>In a high-intensity standing wave, a combination of the dipole force and spontaneous scattering dissipates the energy of a two-level atom, as shown by Dalibard and Cohen-Tannoudji (1985). This high-intensity Sisyphus mechanism damps the atomic motion for a frequency detuning to the blue (and the opposite for the low-intensity effect), and the hills and valleys in the potential energy arise directly from the variation in intensity, as in an optical lattice, rather than a gradient of polarization.

of velocities.<sup>61</sup>

The equilibrium temperature in sub-Doppler cooling does not decrease indefinitely in proportion to  $I/|\delta|$ . Sisyphus cooling stops working when the loss in energy in going from the top of a hill (in the potential energy) to the valley bottom is balanced by the recoil energy acquired in spontaneous emission,  $U_0 \simeq E_{\text{r}}$ . For this condition there is no net loss of energy in optical pumping between  $M_J$  states. Thus the lowest temperatures achieved are equivalent to a few times the recoil energy,  $T \simeq E_{\text{r}}/k_{\text{B}}$ . At this recoil limit<sup>62</sup> the temperature is given by

$$k_{\text{B}}T_{\text{r}} = \frac{\hbar^2 k^2}{M} \equiv \frac{\hbar^2}{M\lambda^2}. \quad (9.55)$$

For sodium the temperature at the recoil limit is only  $2.4 \mu\text{K}$  (cf.  $T_{\text{D}} = 240 \mu\text{K}$ ). Typically, the optical molasses technique can reach temperatures that are an order of magnitude above the recoil limit, but still well below the Doppler cooling limit.<sup>63</sup>

The meaning of temperature must be considered carefully for dilute gas clouds. In a normal gas at room temperature and pressure the interatomic collisions establish thermal equilibrium and give a Maxwell–Boltzmann distribution of velocities. A similar Gaussian distribution is often obtained in laser cooling, where each atom interacts with the radiation field independently (for moderate densities, as in the optical molasses technique) and an equivalent temperature can be assigned that characterises the width of this distribution (see eqn 8.3).<sup>64</sup> From the quantum point of view, the de Broglie wavelength of the atom is more significant than the temperature. At the recoil limit the de Broglie wavelength roughly equals the wavelength of the cooling radiation,  $\lambda_{\text{dB}} \sim \lambda_{\text{light}}$ , because the atomic momentum equals that of the photons (and for both,  $\lambda = h/p$  is the relationship between wavelength and momentum  $p$ ).

This section has described the Sisyphus cooling that arises through a combination of the spatially-varying dipole potential, produced by the polarization gradients, and optical pumping. It is a subtle mechanism and the beautifully-detailed physical explanation was developed in response to experimental observations. It was surprising that the small light shift in a low-intensity standing wave has any influence on the atoms.<sup>65</sup> The recoil limit is an important landmark in laser cooling and the next section describes a method that has been invented to cool atoms below this limit.

## 9.8 Raman transitions

### 9.8.1 Velocity selection by Raman transitions

Raman transitions involve the simultaneous absorption and stimulated emission by an atom. This process has many similarities with the two-photon transition described in Section 8.4 (see Appendix E). A coherent Raman transition between two levels with an energy difference of  $\hbar\omega_{12}$

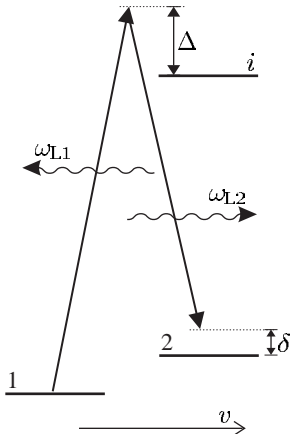


**Fig. 9.20** A Raman transition between levels 1 and 2 driven by two laser beams of (angular) frequencies  $\omega_{L1}$  and  $\omega_{L2}$ . For a resonant Raman process the frequency detuning  $\delta \simeq 0$ , and the detuning  $\Delta$  from the intermediate state remains large, so that excitation by single-photon absorption is negligible in comparison to the coherent transfer from  $|1\rangle$  to  $|2\rangle$ . In this example the atom has velocity  $v$  along the direction of the laser beam with frequency  $\omega_{L2}$ , and the laser beam with frequency  $\omega_{L1}$  propagates in the opposite direction.

is illustrated in Fig. 9.20. For two beams of frequencies  $\omega_{L1}$  and  $\omega_{L2}$  the condition for resonant excitation is

$$\omega_{L1} + k_1 v - (\omega_{L2} - k_2 v) = \omega_{L1} - \omega_{L2} + \frac{v}{c} (\omega_{L1} + \omega_{L2}) = \omega_{12}. \quad (9.56)$$

For counter-propagating beams the Doppler shifts add to make the Raman transition sensitive to the velocity—about twice as sensitive as a single-photon transition.<sup>66</sup> Direct excitation of the transition by radio-frequency radiation, or microwaves, at angular frequency  $\omega_{12}$  is insensitive to the motion. The great advantage of the Raman technique for velocity selection (and cooling) arises from its extremely narrow line width (comparable with that of radio-frequency methods) of Raman transitions between levels that have long lifetimes, e.g. hyperfine levels in the ground configuration of atoms for which spontaneous decay is negligible. To fully exploit the advantage of this narrow line width, the difference in frequency between the two laser beams  $\Delta\omega = \omega_{L1} - \omega_{L2}$  must be controlled very precisely. This can be achieved by taking two independent lasers and implementing sophisticated electronic servo-control of the frequency difference between them, but it is technically easier to pass a single laser beam through a phase modulator—the resultant frequency spectrum contains ‘sidebands’ whose difference from the original laser frequency equals the applied modulation frequency from a microwave source.<sup>67</sup> The selected velocity  $v$  is determined by

$$2kv = \omega_{12} - (\omega_{L1} - \omega_{L2}), \quad (9.57)$$

where  $k = (\omega_{L1} + \omega_{L2})/c$  is the mean wavevector.

Raman transitions between levels with negligible broadening from spontaneous decay or collisions have a line width determined by the interaction time: for a pulse of duration  $\tau_{\text{pulse}}$  the Fourier transform limit gives<sup>68</sup>

$$\frac{\Delta v}{\lambda} \simeq \frac{1}{\tau_{\text{pulse}}}. \quad (9.58)$$

For a visible transition with a wavelength of 600 nm<sup>69</sup> a pulse of duration

<sup>66</sup>In contrast, two counter-propagating laser beams of the same frequency give Doppler-free two-photon spectra:

$$\omega_L + kv + (\omega_L - kv) = 2\omega_L,$$

as in eqn 8.20. If a two-photon transition is excited by two laser beams with different frequencies then the Doppler shifts do not cancel exactly.

<sup>67</sup>For a laser beam with (angular) frequency  $\omega$ , phase modulation at frequency  $\Omega$  leads to a spectrum containing the frequencies  $\omega \pm n\Omega$ , with  $n$  integer. This can be used to carry out Raman excitation, e.g. with  $\omega_{L1} = \omega$  and  $\omega_{L2} = \omega - \Omega$ .

<sup>68</sup>Similar to that for the single-photon transition in Section 7.1.2.

<sup>69</sup>As in the case of sodium that was used in the first Raman experiments with cold atoms. In sodium, levels 1 and 2 are the hyperfine levels with  $F = 1$  and 2 of the 3s configuration, and the intermediate level  $i$  is  $3p\ ^2P_{3/2}$ .

<sup>70</sup>A useful comparison can be made with the method of reducing the Doppler broadening shown in Fig. 8.2, in which a narrow slit is used to collimate an atomic beam and so reduce the spread of transverse velocities.

$\tau_{\text{pulse}} = 600 \mu\text{s}$  selectively transfers atoms in a range of width  $\Delta v \simeq 1 \text{ mm s}^{-1}$ . This is about thirty times less than  $v_r$  and equivalent to a ‘temperature’ of  $T_r/900$  for the motion along the axis of the laser beams. This velocity selection does *not* produce any more cold atoms than at the start—it just separates the cold atoms from the others—so it has a different nature to the laser cooling processes described in the previous sections.<sup>70</sup>

### 9.8.2 Raman cooling

The previous section showed that Raman transitions give the precision of radio-frequency spectroscopy combined with a sensitivity to the Doppler shift twice that of single-photon (optical) transitions. Raman cooling exploits the extremely high velocity resolution of coherent Raman transitions to cool atoms below the recoil limit. The complete sequence of operations in Raman cooling is too lengthy to describe here, but the important principle can be understood by considering how atoms with a velocity distribution that is already below the recoil limit are cooled further. Figure 9.21 shows such an initial distribution in level 1 (the lower hyperfine level in the ground configuration of the atom; level 2 is the upper hyperfine level). Raman cooling uses the following steps.

- (a) Velocity selection by a Raman pulse that transfers atoms with velocities in the range from  $v - \Delta v/2$  to  $v + \Delta v/2$  up to level 2, where they have velocities centred about  $v - 2v_r$ . (The process of absorption and stimulated emission in the opposite direction changes the atom’s velocity by  $2v_r$ ).<sup>71</sup>
- (b) Atoms in level 2 are excited to level  $i$  by another laser beam and can decay back to level 1 with velocities centred around  $v - v_r$  (including the change in velocity produced by absorption). Spontaneous emission goes in all directions so that the atoms return to level 1 with velocities anywhere in the range  $v$  to  $v - 2v_r$ .<sup>72</sup>

<sup>71</sup>Equivalently, the atom’s momentum changes by  $\hbar\mathbf{k}_1 - \hbar\mathbf{k}_2 \simeq 2\hbar\mathbf{k}$ . (Here  $\omega_{12} \ll \omega_1 \simeq \omega_2$ .)

<sup>72</sup>Some atoms fall back into level 2 and are excited again until eventually they end up in level 1. Atoms that undergo more than one excitation receive additional impulses from the absorbed and emitted photons, which reduces the cooling efficiency but does not affect the principle.

<sup>73</sup>For velocity selection of atoms with  $v < 0$  the direction of the beams is reversed so that these atoms are distributed into the range  $v$  to  $v+2v_r$  (that includes  $v = 0$ ).

It might appear that this cycle of a velocity-selective Raman pulse followed by repumping has made things worse since the final spread of velocities is comparable to, if not greater than the initial spread. Crucially, however, some atoms fall back into level 1 with velocities very close to zero so the number of very slow atoms has increased, and increases further for each repetition of the cycle with different initial velocity.<sup>73</sup> Precise control of the Raman pulses ensures that atoms with velocities in the narrow range  $-\delta v < v < \delta v$  are never excited, so that after many cycles a significant fraction of the population accumulates in this narrow velocity class with  $\delta v \ll v_r$ . In this Raman cooling process the atomic velocity undergoes a random walk until either it falls into the desired velocity class around  $v = 0$ , and remains there, or diffuses away to higher velocities. The recoil limit is circumvented because atoms with  $v \simeq 0$  do not interact with the light and this sub-recoil cooling mechanism does not involve a radiation force (in contrast to the Doppler and sub-Doppler cooling mechanisms described in previous sections).

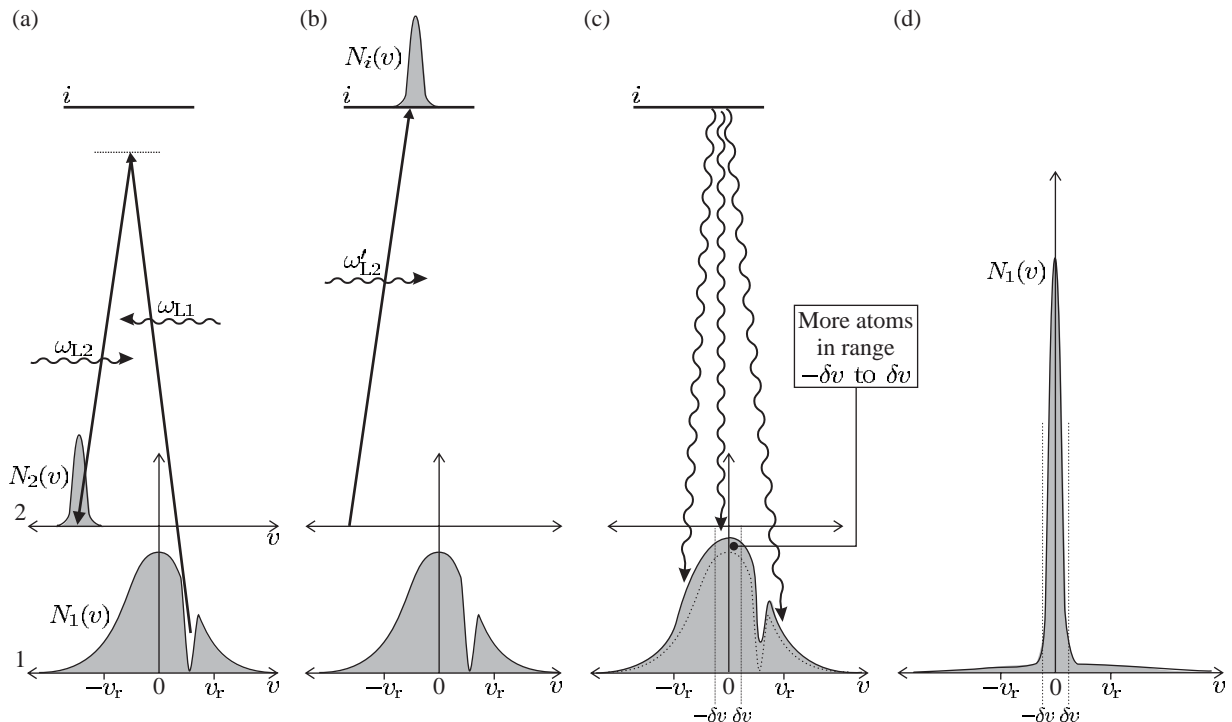


**Fig. 9.21** One step in the sequence of operations in Raman cooling. (a) Velocity selection by a Raman pulse that transfers atoms that have velocities within a certain narrow range from  $|1\rangle$  to  $|2\rangle$ —the process of absorption and stimulated emission changes the atomic velocity by  $-2v_r$ . (b) Atoms are excited from level 2 to level  $i$  by another laser beam—in this process the atomic velocity changes by  $v_r$ . (c) Atoms decay to level 1 by spontaneous emission—the recoil in a random direction means that the atoms return to level 1 with a component of velocity anywhere in the range  $v$  to  $v - 2v_r$ , where  $v$  is the initial velocity. There are more atoms in the narrow velocity class around  $v = 0$  than at the start of the sequence. (d) Repetition of the sequence with different initial velocities increases the number of atoms with  $v \approx 0$  until they are ‘piled’ up in a distribution whose width is much less than the recoil velocity  $v_r$ .

The time taken for atoms to fall (randomly) into a velocity class of width  $2\delta v$  increases as  $\delta v$  decreases and this determines the final velocity spread achievable by Raman cooling in practice.

Raman cooling works well in one dimension, but it is much less efficient in three dimensions where the target is to have all three components  $v_x$ ,  $v_y$  and  $v_z$  between  $\pm\delta v$ . Another method of sub-recoil cooling called velocity-selective coherent population trapping is also a stochastic process, see Metcalf and van der Straten (1999) and Bardou *et al.* (1991). Raman transitions are also used for matter-wave interferometry based on ultra-cold atoms (Chapter 10).

## 9.9 An atomic fountain

The slow atoms produced by laser cooling have led to a dramatic improvement in measurements whose resolution is limited by the interaction time. Cold atoms can be confined in dipole-force traps<sup>74</sup> for long

<sup>74</sup>Or magnetic traps as described in the next chapter.

<sup>75</sup>In principle, the perturbation can be calculated and corrected for, but without perfect knowledge of the trapping potential this leaves a large uncertainty. There are currently proposals for frequency standards based on transitions in optically-trapped atoms for which the light shift cancels out, i.e. the lower and upper levels of the narrow transition have very similar light shifts.

<sup>76</sup>In such an atomic fountain the atoms have an initial velocity of  $v_z = (2gh)^{1/2} = 4 \text{ m s}^{-1}$ .

<sup>77</sup>Caesium has a resonance wavelength of 852 nm and a relative atomic mass of 133.

<sup>78</sup>Only the spread in the radial direction leads to a loss of atoms, so velocity selection in two dimensions by Raman transitions, or otherwise, is useful.

<sup>79</sup>At the extraordinary precision of these experiments, collisions between ultra-cold caesium atoms cause an observable frequency shift of the hyperfine transition (proportional to the density of the atoms). Therefore it is undesirable for this density to change during the measurement.

periods of time; however, the trapping potential strongly perturbs the atomic energy levels and hinders accurate measurements of the transition frequencies.<sup>75</sup> The highest-accuracy measurements use atoms in free fall, as shown in Fig. 9.16. This apparatus launches cold atoms upwards with velocities of a few  $\text{m s}^{-1}$ , so that they travel upwards for a short distance before turning around and falling back down under gravity—this forms an atomic fountain.

A particularly important use of atomic fountains is to determine the frequency of the hyperfine-structure splitting in the ground configuration of caesium since this is used as the primary standard of time. Each atom passes through a microwave cavity on the way up and again on its way down, and these two interactions separated in time by  $T$  lead to Ramsey fringes (Fig. 7.3) with frequency width  $\Delta f = 1/(2T)$ , as described in Section 7.4. Simple Newtonian mechanics shows that a fountain of height  $h = 1 \text{ m}$  gives  $T = 2(2h/g)^{1/2} \simeq 1 \text{ s}$ , where  $g$  is the gravitational acceleration.<sup>76</sup> This is several orders of magnitude longer than the interaction time for a thermal atomic beam of caesium atoms (Section 6.4.2). This is because the measurement time on Earth is limited by gravity, and an obvious, but not simple, way to obtain further improvement is to put an apparatus into space, e.g. aboard a satellite or space station in orbit. Such an apparatus has the same components as an atomic fountain, but the atoms only pass once through the microwave interaction region and are detected on the other side—pushing the atoms gently so that they move very slowly through the microwave cavity gives measurement times exceeding 10 s.

Cold atoms obtained by laser cooling are essential for both the atomic fountain and atomic clocks in space, as shown by the following estimate for the case of a fountain. The entrance and exit holes of the microwave cavity have a diameter of about 1 cm. If the atoms that pass through the cavity on the way up have a velocity spread about equal to the recoil velocity  $v_r = 3.5 \text{ mm s}^{-1}$  for caesium,<sup>77</sup> then the cloud will have expanded by  $\sim 4 \text{ mm}$  by the time it falls back through the cavity.<sup>78</sup> Thus a reasonable fraction of these atoms, that have a temperature close to the recoil limit, pass back through the cavity and continue down to the detection region. Clearly, for a 10 s measurement time the effective temperature of the cloud needs to be well below the recoil limit.<sup>79</sup> These general considerations show the importance of laser cooling for the operation of an atomic fountain. Some further technical details are given below.

The atoms are launched upwards by the so-called ‘moving molasses’ technique, in which the horizontal beams in the six-beam configuration shown in Fig. 9.5 have angular frequency  $\omega$ , and the upward and downward beams have frequencies  $\omega + \Delta\omega$  and  $\omega - \Delta\omega$ , respectively. In a reference frame moving upwards with velocity  $\mathbf{v} = (\Delta\omega/k)\hat{\mathbf{e}}_z$  the Doppler shift is  $\Delta\omega$ , so that all the beams appear to have the same frequency. Therefore the optical molasses mechanisms damp the atomic velocity to zero with respect to this moving frame. These atoms have the same velocity spread about their mean velocity as atoms in the optical molasses technique with a stationary light field ( $\Delta\omega = 0$ ), so the

temperature is the same in both cases.<sup>80</sup>

In an atomic fountain the scheme for detecting that a microwave transition has occurred is very different to that in an atomic beam (Section 6.4). The ground configuration of caesium has  $J = 1/2$  (like all alkalis) and the two hyperfine levels are  $F = 3$  and  $4$  (for the only stable isotope that has nuclear spin  $I = 7/2$ ). If the atoms start in the lower level  $F = 3$  then the microwave radiation transfers a fraction of the atoms to the  $F = 4$  level. This fraction is determined when the atoms fall through a laser beam that detects atoms in the  $F = 4$  level, by exciting a transition from this level and monitoring the fluorescence, see Fig. 9.16. (Atoms in the  $F = 3$  level pass through undetected.<sup>81</sup>) Figure 7.3 shows a plot of the transition probability between the hyperfine levels as a function of the microwave frequency—so-called Ramsey fringes. The narrow line width means that the frequency of the microwave source used to drive the transition can be set very precisely to the caesium hyperfine frequency. Such an apparatus maintains the frequency of the microwave source stable to better than 1 part in  $10^{15}$ , or 32 ns per year. Many causes of perturbations that might give frequency shifts are small because of the atoms' low atomic velocity, but the Zeeman effect of magnetic fields remains a limitation. Experiments use the  $F = 3, M_F = 0$  to  $F = 4, M_F = 0$  transition because states with  $M_F = 0$  have no first-order Zeeman shift. Nowadays, such caesium fountain frequency standards play an important role in guiding the ensemble of clocks in national standards laboratories around the world that give agreed Universal Time.<sup>82</sup>

<sup>80</sup>These caesium atoms have a velocity spread of about  $3v_r \simeq 10 \text{ mm s}^{-1}$ . These atoms could be used directly if the measurement time is 0.3 s, but there would be a large loss of atoms in a higher fountain with  $T = 1$  s.

<sup>81</sup>To normalise the signal the atoms in the  $F = 3$  level are detected with a second probe laser beam (not shown in the figure).

<sup>82</sup>The important uses of such clocks were given in Section 6.4.2 and up-to-date information can be found on the web sites of national standards laboratories.

## 9.10 Conclusions

The techniques that have been developed to reduce the temperature of atoms from 1000 K to well below  $1 \mu\text{K}$  have had an enormous impact on atomic physics. Laser cooling has made it possible to manipulate neutral atoms in completely new ways and to trap them by magnetic and dipole forces. Some important applications of atom trapping have been mentioned, such as the great improvement in precision measurements, and others are given in later chapters, e.g. Bose–Einstein condensation and the laser cooling of trapped ions.

The important principles of radiation forces have been discussed, namely: the way in which the scattering force dissipates the energy of atoms and cools them to the Doppler cooling limit; the trapping of atoms by the dipole force in various configurations including optical lattices; and sub-Doppler cooling by the Sisyphus mechanism and sub-recoil cooling. This chapter greatly simplifies the real story of laser cooling for the sake of a clear presentation; the book *Laser cooling and trapping of atoms* by Metcalf and van der Straten (1999) gives a more comprehensive description of the important contributions made by many people and many references to other material—see also the review by Wieman

*et al.* (1999). Various internet resources and popular descriptions can be found on the web site of the Nobel foundation.

## Exercises

More advanced problems are indicated by a \*.

(9.1) *Radiation pressure*

What force does radiation exert on the head of a person wearing a black hat of radius 15 cm when the sun is directly overhead. Estimate the ratio of this radiation force to the weight of the hat.

(9.2) *An argument for photon momentum (due to Enrico Fermi)*

An atom moving at velocity  $v$  absorbs a photon propagating in the opposite direction (as in Fig. 9.1). In the laboratory frame of reference the photon has (angular) frequency  $\omega$  and momentum  $q_{\text{ph}}$ . In the rest frame of the atom the photon has (angular) frequency  $\omega_0$ , where  $\hbar\omega_0 = E_2 - E_1$  is the energy of the (narrow line width) transition between levels 1 and 2. After the absorption the system has a total energy of  $\frac{1}{2}M(v - \Delta v)^2 + \hbar\omega_0$ .

- (a) Write down the equations for conservation of energy and momentum.
- (b) Expand the equation for conservation of energy, neglecting the term of order  $(\Delta v)^2$ . (The change in velocity  $\Delta v$  is small compared to  $v$ .)
- (c) Use the usual expression for the fractional Doppler shift  $(\omega - \omega_0)/\omega = v/c$  to find an expression for the photon momentum  $q_{\text{ph}}$ .

(9.3) *Heating from photon recoil*

This exercise is based on a treatment of laser cooling by Wineland and Itano (1979). The angular frequencies of radiation absorbed and emitted by an atom are given by

$$\begin{aligned}\omega_{\text{abs}} &= \omega_0 + \mathbf{k}_{\text{abs}} \cdot \mathbf{v} - \frac{1}{2}\omega_0 \left(\frac{v}{c}\right)^2 + \frac{E_r}{\hbar}, \\ \omega_{\text{em}} &= \omega_0 + \mathbf{k}_{\text{em}} \cdot \mathbf{v}' - \frac{1}{2}\omega_0 \left(\frac{v'}{c}\right)^2 - \frac{E_r}{\hbar},\end{aligned}$$

where  $|\mathbf{k}_{\text{abs}}| = \omega_{\text{abs}}/c$  and  $|\mathbf{k}_{\text{em}}| = \omega_{\text{em}}/c$  are the wavevectors of the absorbed and emitted photons, respectively,  $\mathbf{v}$  is the velocity of the atom before the photon is absorbed, and similarly  $\mathbf{v}'$  is the velocity of the atom before emission. Prove these results from conservation of (relativistic) energy and

momentum (keeping terms of order  $(v/c)^2$  in the atomic velocity and  $E_r/\hbar\omega_0$  in the recoil energy). Averaged over many cycles of absorption and emission, the kinetic energy of the atom changes by

$$\Delta E_{\text{ke}} = \hbar(\omega_{\text{abs}} - \omega_{\text{em}}) = \hbar\mathbf{k}_{\text{abs}} \cdot \mathbf{v} + 2E_r$$

for each scattering event. Show that this result follows from the above equations with certain assumptions, that should be stated. Show that, when multiplied by the scattering rate  $R_{\text{scatt}}$ , the terms  $\hbar\mathbf{k}_{\text{abs}} \cdot \mathbf{v}$  and  $2E_r$  give cooling and heating at comparable rates to those derived in the text for the optical molasses technique.

(9.4) *The angular momentum of light*

An atom in a  ${}^1S_0$  level is excited to a state with  $L = 1$ ,  $M_L = 1$  by the absorption of a photon (a  $\sigma^+$  transition). What is the change in the atomic angular momentum?

A laser beam with a power of 1 W and a wavelength of 600 nm passes through a waveplate that changes the polarization of the light from linear to circular. What torque does the radiation exert on the waveplate?

(9.5) *Slowing H and Cs with radiation*

Atomic beams of hydrogen and caesium are produced by sources at 300 K and slowed by counter-propagating laser radiation. In both cases calculate (a) the stopping distance at half of the maximum deceleration, and (b) compare the Doppler shift at the initial velocity with the natural width of the transition. (Data are given in Table 9.1.)

(9.6) *The Doppler cooling and recoil limits*

Calculate the ratio  $T_D/T_r$  for rubidium (from eqns 9.28, 9.55 and the data in Table 9.1).

(9.7) *Damping in the optical molasses technique*

- (a) For the particular case of a frequency detuning of  $\delta = -\Gamma/2$  the slope of the force versus velocity curve, shown in Fig. 9.6, at  $v = 0$  equals the peak force divided by  $\Gamma/(2k)$ . Use this to

estimate  $\partial F/\partial v$  and hence to determine the damping coefficient  $\alpha$  for an atom in a pair of counter-propagating laser beams, under these conditions.

- (b) Estimate the damping time for a sodium atom in the optical molasses technique when each laser beam has intensity  $I_{\text{sat}}$  and  $\delta = -\Gamma/2$ .

(9.8) *Laser cooling of a trapped ion*

A trapped  $\text{Ca}^+$  ion undergoes simple harmonic motion with an oscillation frequency of  $\Omega = 2\pi \times 100 \text{ kHz}$ . The ion experiences a radiation force from laser light of wavelength 393 nm and intensity  $I$  that excites a transition with  $\Gamma = 2\pi \times 23 \times 10^6 \text{ s}^{-1}$ . The frequency detuning  $\delta$  does not depend on the ion's position within the trap.

- (a) Show that the force on the ion has the form  $F = -\kappa(z - z_0) - \alpha v$ . Describe the ion's motion.
- (b) Find the static displacement  $z_0$  of the ion from the centre of the harmonic potential, along the direction of the laser beam, for  $\delta = -\Gamma/2$  and  $I = 2I_{\text{sat}}$ .
- (c) Show that, to a good approximation, the damping coefficient can be written in the form

$$\alpha \propto \frac{xy}{(1+y+x^2)^2}, \quad (9.59)$$

where the variables  $x$  and  $y$  are proportional to  $\delta$  and  $I$ , respectively. Maximise this function of two variables and hence determine the intensity and frequency detuning that give the maximum value of  $\alpha$ .

- (d) The kinetic energy of small oscillations about  $z_0$  decays with a damping time of  $\tau_{\text{damp}} = M/\alpha$ . Show that this damping time is inversely proportional to the recoil energy.<sup>83</sup> Evaluate this minimum value of  $\tau_{\text{damp}}$  for a calcium ion of mass  $M \simeq 40 \text{ a.m.u.}$

*Comment.* This treatment of Doppler cooling for a single laser beam is accurate for any intensity (even above  $I_{\text{sat}}$ ), whereas the approximation that two laser beams (as in the optical molasses technique) give twice as much damping as a single beam is not accurate at high intensities.

(9.9) *The properties of a magneto-optical trap*

- (a) Obtain an expression for the damping coefficient  $\alpha$  for an atom in two counter-propagating laser beams (each of intensity  $I$ ),

taking into account saturation. (Use the results of the previous exercise with the modification  $I \rightarrow 2I$  in both the numerator and denominator, or otherwise.) Determine the minimum damping time (defined in eqn 9.19) of a rubidium atom in the optical molasses technique (with two laser beams).

- (b) The force on an atom in an MOT is given by eqn 9.30. Assume the worst-case scenario in the calculation of the damping and the restoring force, along a particular direction, i.e. that the radiation force arises from two counter-propagating laser beams (each of intensity  $I$ ) but the saturation of the scattering rate depends on the total intensity  $6I$  of all six laser beams. Show that the damping coefficient can be written in the form

$$\alpha \propto \frac{xy}{(1+y+x^2)^2},$$

where  $x = 2\delta/\Gamma$  and  $y = 6I/I_{\text{sat}}$ . Using the results of the previous exercise, or otherwise, determine the nature of the motion for a rubidium atom in an MOT with the values of  $I$  and  $\delta$  that give maximum damping, and a field gradient  $0.1 \text{ T m}^{-1}$  (in the direction considered).

(9.10) *Zeeman slowing in a magneto-optical trap*

- (a) Instead of the optimum magnetic field profile given in eqn 9.11, a particular apparatus to slow sodium atoms uses a linear ramp

$$B(z) = B_0 \left( 1 - \frac{z}{L} \right)$$

for  $0 \leq z \leq L$ , and  $B(z) = 0$  outside this range. Explain why a suitable value for  $B_0$  is the same as in eqn 9.12. Show that the minimum value of  $L$  is  $2L_0$ , where  $L_0$  is the stopping distance for the optimum profile.

- (b) The capture of atoms by a magneto-optical trap can be considered as Zeeman slowing in a uniform magnetic field gradient, as in part (a). In this situation the maximum velocity captured by an MOT with laser beams of radius 0.5 cm is equivalent to the velocity of atoms that come to rest in a distance of

<sup>83</sup>Surprisingly, the damping time does not depend on the line width of the transition  $\Gamma$ , but narrow transitions lead to a small velocity capture range.

$L_0 = 0.25$  cm for constant deceleration at half the maximum value. Use this simple model of a trap to calculate the capture velocity for rubidium atoms. What is a suitable value for the gradient of the magnetic field,  $B_0/L$  (where  $L = 2L_0$ )? (Data are given in Table 9.1.)

*Comment.* The magnetic field gradients in a magneto-optical trap are much less than those in magnetic traps (Chapter 10), but the force (from the radiation) is much stronger than the magnetic force.

(9.11) *The equilibrium number of atoms in an MOT*

The steady-state number of atoms that congregate at the centre of an MOT is determined by the balance between the loading rate and the loss caused by collisions. To estimate this equilibrium number  $\mathcal{N}$ , we consider the trapping region formed at the intersection of the six laser beams of diameter  $D$  as being approximately a cube with sides of length  $D$ . This trapping region is situated in a cell filled with a low-pressure vapour of number density  $N$ .

- (a) The loading rate can be estimated from the kinetic theory expression  $\frac{1}{4}NvAf(v)$  for the rate at which atoms with speed  $v$  hit a surface of area  $A$  in a gas;  $f(v)$  is the fraction of atoms with speeds in the range  $v$  to  $v + dv$  (eqn 8.3). Integrate this rate from  $v = 0$  up to the capture velocity  $v_c$  to obtain an expression for the rate at which the MOT captures atoms from the vapour. (The integration can be made simple by assuming that  $v_c \ll v_p$ .)
- (b) Atoms are lost ('knocked out of the trap') by collisions with fast atoms in the vapour at a rate  $\dot{\mathcal{N}} = -N\bar{v}\sigma$ , where  $\bar{v}$  is the mean velocity in the vapour and  $\sigma$  is a collision cross-section.

Show that the equilibrium number of atoms in the MOT is independent of the vapour pressure.

- (c) Atoms enter the trapping region over a surface area  $A = 6D^2$ . An MOT with  $D = 2$  cm has  $v_c \simeq 25$  m s<sup>-1</sup> for rubidium. Make a reasonable estimate of the cross-section  $\sigma$  for collisions between two atoms and hence find the equilibrium number of atoms captured from a low-pressure vapour at room temperature.<sup>84</sup>

(9.12) *Optical absorption by cold atoms in an MOT*

In a simplified model the trapped atoms are considered as a spherical cloud of uniform density, radius  $r$  and number  $\mathcal{N}$ .

- (a) Show that a laser beam of (angular) frequency  $\omega$  that passes through the cloud has a fractional change in intensity given by

$$\frac{\Delta I}{I_0} \simeq \frac{\mathcal{N}\sigma(\omega)}{2r^2}.$$

(The optical absorption cross-section  $\sigma(\omega)$  is given by eqn 7.76.)

- (b) Absorption will significantly affect the operation of the trap when  $\Delta I \simeq I_0$ . Assuming that this condition limits the density of the cloud for large numbers of atoms,<sup>85</sup> estimate the radius and density for a cloud of  $\mathcal{N} = 10^9$  rubidium atoms and a frequency detuning of  $\delta = -2\Gamma$ .

(9.13) *Laser cooling of atoms with hyperfine structure*

The treatment of Doppler cooling given in the text assumes a two-level atom, but in real experiments with the optical molasses technique, or the MOT, the hyperfine structure of the ground configuration causes complications. This exercise goes through

<sup>84</sup>The equilibrium number in the trap is independent of the background vapour pressure over a wide range, between (i) the pressure at which collisions with fast atoms knock cold atoms out of the trap before they settle to the centre of the trap, and (ii) the much lower pressure at which the loss rate from collisions between the cold atoms within the trap itself becomes important compared to collisions with the background vapour.

<sup>85</sup>*Comment.* Actually, absorption of the laser beams improves the trapping—for an atom on the edge of the cloud the light pushing outwards has a lower intensity than the unattenuated laser beam directed inwards—however, the spontaneously-emitted photons associated with this absorption do cause a problem when the cloud is 'optically thick', i.e. when most of the light is absorbed. Under these conditions a photon emitted by an atom near the centre of the trap is likely to be reabsorbed by another atom on its way out of the cloud—this scattering within the cloud leads to an outward radiation pressure (similar to that in stars) that counteracts the trapping force of the six laser beams. (The additional scattering also increases the rate of heating for a given intensity of the light.) In real experiments, however, the trapping force in the MOT is not spherically symmetric, and there may be misalignments or other imperfections of the laser beams, so that for conditions of high absorption the cloud of trapped atoms tends to become unstable (and may spill out of the trap).

some of the nitty-gritty details and tests understanding of hyperfine structure.<sup>86</sup>

- (a) Sodium has a nuclear spin  $I = 3/2$ . Draw an energy level diagram of the hyperfine structure of the  $3s\ ^2S_{1/2}$  and  $3p\ ^2P_{3/2}$  levels and indicate the allowed electric dipole transitions.
- (b) In a laser cooling experiment the transition  $3s\ ^2S_{1/2}, F = 2$  to  $3p\ ^2P_{3/2}, F' = 3$  is excited by light that has a frequency detuning of  $\delta = -\Gamma/2 \simeq -5$  MHz (to the red of this transition). Selection rules dictate that the excited state decays back to the initial state, so there is a nearly closed cycle of absorption and spontaneous emission, but there is some off-resonant excitation to the  $F' = 2$  hyperfine level which can decay to  $F = 1$  and be ‘lost’ from the cycle. The  $F' = 2$  level lies 60 MHz below the  $F' = 3$  level. Estimate the average number of photons scattered by an atom before it falls into the lower hyperfine level of the ground configuration. (Assume that the transitions have similar strengths.)
- (c) To counteract the leakage out of the laser cooling cycle, experiments use an additional laser beam that excites atoms out of the  $3s\ ^2S_{1/2}, F = 1$  level (so that they can get back into the  $3s\ ^2S_{1/2}, F = 2$  level). Suggest a suitable transition for this ‘repumping’ process and comment on the light intensity required.<sup>87</sup>

#### (9.14) The gradient force

Figure 9.11 shows a sphere, with a refractive index greater than the surrounding medium, that feels a force towards regions of high intensity. Draw a similar diagram for the case  $n_{\text{sphere}} < n_{\text{medium}}$  and indicate forces. (This object could be a small bubble of air in a liquid.)

#### (9.15) Dipole-force trap

A laser beam<sup>88</sup> propagating along the  $z$ -axis has an intensity profile of

$$I = \frac{2P}{\pi w(z)^2} \exp\left(-\frac{2r^2}{w(z)^2}\right), \quad (9.60)$$

where  $r^2 = x^2 + y^2$  and the waist size is  $w(z) = w_0(1+z^2/b^2)^{1/2}$  with  $b = \pi w_0^2/\lambda^2$ . This laser beam has a power of  $P = 1$  W at a wavelength of  $\lambda = 1.06 \mu\text{m}$ , and a spot size of  $w_0 = 10 \mu\text{m}$  at the focus.

- (a) Show that the integral of  $I(r, z)$  over any plane of constant  $z$  equals the total power of the beam  $P$ .
- (b) Calculate the depth of the dipole potential for rubidium atoms, expressing your answer as an equivalent temperature.
- (c) For atoms with a thermal energy much lower than the trap depth (so that  $r^2 \ll w_0^2$  and  $z^2 \ll b^2$ ), determine the ratio of the size of the cloud in the radial and longitudinal directions.
- (d) Show that the dipole force has a maximum value at a radial distance of  $r = w_0/2$ . Find the maximum value of the waist size  $w_0$  for which the dipole-force trap supports rubidium atoms against gravity (when the laser beam propagates horizontally).

#### (9.16) An optical lattice

In a standing wave of radiation with a wavelength of  $\lambda = 1.06 \mu\text{m}$ , a sodium atom experiences a periodic potential as in eqn 9.52 with  $U_0 = 100E_r$ , where  $E_r$  is the recoil energy (for light at the atom’s resonance wavelength  $\lambda_0 = 0.589 \mu\text{m}$ ). Calculate the oscillation frequency for a cold atom trapped near the bottom of a potential well in this one-dimensional optical lattice. What is the energy spacing between the low-lying vibrational levels?

#### (9.17) The potential for the dipole force

Show that the force in eqn 9.43 equals the gradient of the potential

$$U_{\text{dipole}} = -\frac{\hbar\delta}{2} \ln\left(1 + \frac{I}{I_{\text{sat}}} + \frac{4\delta^2}{\Gamma^2}\right).$$

For what conditions does eqn 9.46 give a good approximation for  $U_{\text{dipole}}$ ?

<sup>86</sup>The transfer between different hyperfine levels described here is distinct from the transfer between different Zeeman sublevels (states of given  $M_J$  or  $M_F$ ) in the Sisyphus effect.

<sup>87</sup>In the Zeeman slowing technique the magnetic field increases the separation of the energy levels (and also uncouples the nuclear and electronic spins in the excited state) so that ‘repumping’ is not necessary.

<sup>88</sup>This is a diffraction-limited Gaussian beam.

# 10

# Magnetic trapping, evaporative cooling and Bose–Einstein condensation

|   |     |
|---|-----|
| 10.1 Principle of magnetic trapping                       | 218 |
| 10.2 Magnetic trapping                                    | 220 |
| 10.3 Evaporative cooling                                  | 224 |
| 10.4 Bose–Einstein condensation                           | 226 |
| 10.5 Bose–Einstein condensation in trapped atomic vapours | 228 |
| 10.6 A Bose–Einstein condensate                           | 234 |
| 10.7 Properties of Bose-condensed gases                   | 239 |
| 10.8 Conclusions  | 242 |
| Exercises   | 243 |

Magnetic traps are used to confine the low-temperature atoms produced by laser cooling. If the initial atomic density is sufficiently high, the simple but extremely effective technique of evaporative cooling allows experiments to reach quantum degeneracy where the occupation of the quantum states approaches unity. This leads either to Bose–Einstein condensation (BEC) or to Fermi degeneracy, depending on the spin of the atoms. This chapter describes magnetic traps and evaporative cooling, using straightforward electromagnetism and kinetic theory, before giving an outline of some of the exciting new types of experiments that have been made possible by these techniques. The emphasis is on presenting the general principles and illustrating them with some relevant examples rather than attempting to survey the whole field in a qualitative way.

## 10.1 Principle of magnetic trapping

In their famous experiment, Otto Stern and Walter Gerlach used the force on an atom as it passed through a strong inhomogeneous magnetic field to separate the spin states in a thermal atomic beam. Magnetic trapping uses exactly the same force, but for cold atoms the force produced by a system of magnetic field coils bends the trajectories right around so that low-energy atoms remain within a small region close to the centre of the trap. Thus the principle of magnetic trapping of atoms has been known for many years but it only became widely used after the development of laser cooling.<sup>1</sup>

A magnetic dipole  $\mu$  in a field has energy

$$V = -\mu \cdot \mathbf{B}. \quad (10.1)$$

<sup>1</sup>There was early work on magnetic trapping of ultra-cold neutrons whose magnetic moment is only  $-1.9 \mu_N$ , and the nuclear magneton  $\mu_N$ , which is much smaller than the Bohr magneton  $\mu_B$ .

For an atom in the state  $|IJFM_F\rangle$  this corresponds to a Zeeman energy

$$V = g_F \mu_B M_F B. \quad (10.2)$$

The energy depends only the magnitude of the field  $B = |\mathbf{B}|$ . The energy does not vary with the direction of  $\mathbf{B}$  because as the dipole moves (adiabatically) it stays aligned with the field. From this we find the magnetic force along the  $z$ -direction:

$$F = -g_F \mu_B M_F \frac{dB}{dz}. \quad (10.3)$$

**Example 10.1** Estimate of the effect of the magnetic force on an atom of mass  $M$  that passes through a Stern-Gerlach magnet at speed  $v$ .

The atom takes a time  $t = L/v$  to pass through a region of high field gradient of length  $L$  (between the pole pieces of the magnet), where it receives an impulse  $Ft$ , in the transverse direction, that changes its momentum by  $\Delta p = Ft$ . An atom with momentum  $p = Mv$  along the beam has a deflection angle of

$$\theta = \frac{\Delta p}{p} = \frac{FL}{Mv^2} = \frac{FL}{2E_{\text{ke}}}. \quad (10.4)$$

The kinetic energy  $E_{\text{ke}} \simeq 2k_B T$  (from Table 8.1), where  $T$  is the temperature of the oven from which the beam effuses. An atom with a single valence electron has a maximum moment of  $\mu_B$  (when  $g_F M_F = 1$ ) and hence

$$\theta = \frac{\mu_B}{k_B} \times \frac{dB}{dz} \frac{L}{4T} = 0.67 \times \frac{3 \times 0.1}{4 \times 373} \simeq 1.4 \times 10^{-4} \text{ rad}. \quad (10.5)$$

This evaluation for a field gradient of  $3 \text{ T m}^{-1}$  over  $L = 0.1 \text{ m}$  and  $T = 373 \text{ K}$  makes use of the ratio of the Bohr magneton to the Boltzmann constant, given by

$$\frac{\mu_B}{k_B} = 0.67 \text{ K T}^{-1}. \quad (10.6)$$

Thus a well-collimated beam of spin-1/2 atoms that propagates for  $L = 1 \text{ m}$  after the magnet will be split into two components separated by  $2\theta L = 0.3 \text{ mm}$ .

For an atom with  $T \simeq 0.1 \text{ K}$  eqn 10.5 gives a deflection of  $0.5 \text{ rad}$ !<sup>2</sup> Although the equation is not valid for this large angle, it does indicate that magnetic forces have a strong influence on laser-cooled atoms and can bend their trajectories around. From eqn 10.6 we see directly that a magnetic trap where the field varies from 0 to  $0.03 \text{ T}$  has a depth of  $0.02 \text{ K}$ , e.g. a trap with a field gradient of  $3 \text{ T m}^{-1}$  over  $10 \text{ mm}$ , as described in the next section. Remember that the Doppler cooling limit for sodium is  $240 \mu\text{K}$ , so it is easy to capture atoms that have been laser cooled. Traps made with superconducting magnetic coils can have fields of over  $10 \text{ T}$  and therefore have depths of several kelvin; this enables researchers to trap species such as molecules that cannot be laser cooled.<sup>2</sup>

<sup>2</sup>Standard laser cooling does not work for molecules because repeated spontaneous emission causes the population to spread out over many vibrational and rotational levels. Superconducting traps operate at low temperatures with liquid helium cooling, or a dilution refrigerator, and molecules are cooled to the same temperature as the surroundings by buffer gas cooling with a low pressure of helium (cf. Section 12.4).

## 10.2 Magnetic trapping

### 10.2.1 Confinement in the radial direction

The estimate in the introduction shows that magnetic forces have a significant effect on cold atoms and in this section we examine the specific configuration used to trap atoms shown in Fig. 10.1. The four parallel wires arranged at the corners of a square produce a quadrupole magnetic field when the currents in adjacent wires flow in opposite directions. Clearly this configuration does not produce a field gradient along the axis ( $z$ -direction); therefore from Maxwell's relation  $\operatorname{div} \mathbf{B} = 0$  we deduce that

$$\frac{dB_x}{dx} = -\frac{dB_y}{dy} = b'.$$

These gradients have the same magnitude  $b'$ , but opposite sign. Therefore the magnetic field has the form

$$\mathbf{B} = b' (x\hat{\mathbf{e}}_x - y\hat{\mathbf{e}}_y) + \mathbf{B}_0. \quad (10.7)$$

Here we simply assume that  $b' = 3 \text{ T m}^{-1}$ ; that this is a realistic field gradient can be shown by using the Biot–Savart law to calculate the field produced by coils carrying reasonable currents (see caption of Fig. 10.1). In the special case of  $B_0 = 0$ , the field has a magnitude

$$|\mathbf{B}| = b'(x^2 + y^2)^{1/2} = b'r. \quad (10.8)$$

Thus the magnetic energy (eqn 10.2) has a linear dependence on the radial coordinate  $r = \sqrt{x^2 + y^2}$ . This conical potential has the V-shaped cross-section shown in Fig. 10.2(a), with a force in the radial direction of

$$\mathbf{F} = -\nabla V = -g_F \mu_B M_F b' \hat{\mathbf{e}}_r. \quad (10.9)$$

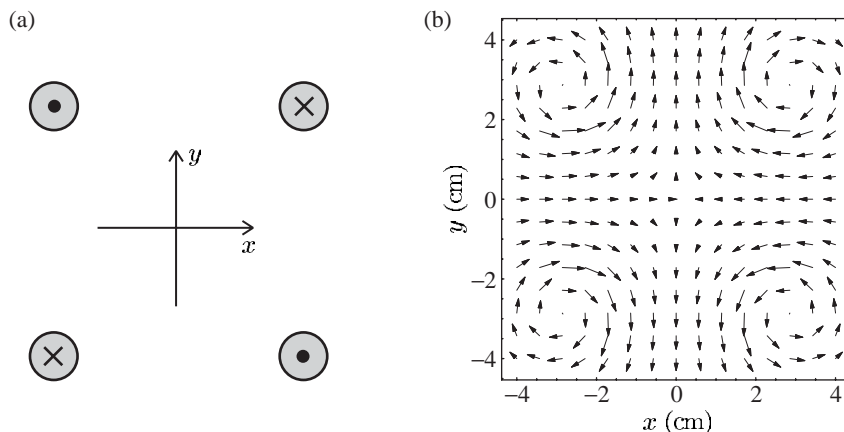


**Fig. 10.1** (a) A cross-section through four parallel straight wires, with currents into and out of the page as indicated. These give a magnetic quadrupole field. In a real magnetic trap, each ‘wire’ is generally made up of more than ten strands, each of which may conduct over 100 amps, so that the total current along each of the four wires exceeds 1000 amps. (b) The direction of the magnetic field around the wires—this configuration is a magnetic quadrupole.

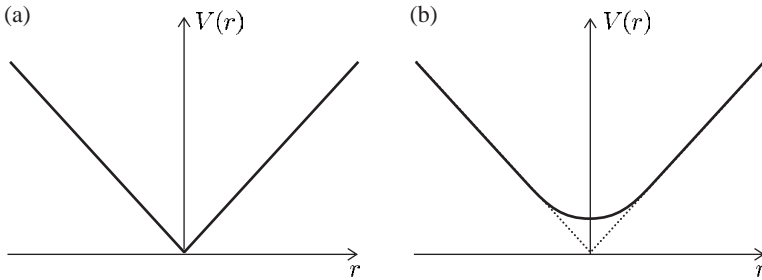


**Fig. 10.2** (a) A cross-section through the magnetic potential (eqn 10.8) in a radial direction, e.g. along the  $x$ - or  $y$ -axis. The cusp at the bottom of the conical potential leads to non-adiabatic transitions of the trapped atoms. (b) A bias field along the  $z$ -direction rounds the bottom of the trap to give a harmonic potential near the axis (in the region where the radial field is smaller than the axial bias field).

This force confines atoms in a low-field-seeking state, i.e. one with  $g_F M_F > 0$ , so that the magnetic energy decreases as the atom moves into a lower field (see Fig. 6.10, for example). However, a quadrupole field has a fundamental problem—the atoms congregate near the centre where  $B = 0$  and the Zeeman sub-levels ( $|IJFM_F\rangle$  states) have a very small energy separation. In this region of very low magnetic field the states with different magnetic quantum numbers mix together and atoms can transfer from one value of  $M_F$  to another (e.g. because of perturbations caused by noise or fluctuation in the field). These non-adiabatic transitions allow the atoms to escape and reduce the lifetime of atoms in the trap. The behaviour of atoms in this magnetic trap with a leak at the bottom resembles that of a conical funnel filled with water—a large volume of fluid takes a considerable time to pass through a funnel with a small outlet at its apex, but clearly it is desirable to plug the leak at the bottom of the trap.<sup>3</sup>

The loss by non-adiabatic transitions cannot be prevented by the addition of a uniform field in the  $x$ - or  $y$ -directions, since this simply displaces the line where  $\mathbf{B} = \mathbf{0}$ , to give the same situation as described above (at a different location). A field  $\mathbf{B}_0 = B_0 \hat{\mathbf{e}}_z$  along the  $z$ -axis, however, has the desired effect and the magnitude of the field in eqn 10.7 becomes

$$|\mathbf{B}| = \{B_0^2 + (b'r)^2\}^{1/2} \simeq B_0 + \frac{b'^2 r^2}{2B_0}. \quad (10.10)$$

This approximation works for small  $r$  where  $b'r \ll B_0$ . The bias field along  $z$  rounds the point of the conical potential, as illustrated in Fig. 10.2(b), so that near the axis the atoms of mass  $M$  see a harmonic potential. From eqn 10.2 we find

$$V(r) = V_0 + \frac{1}{2} M \omega_r^2 r^2. \quad (10.11)$$

The radial oscillation has an angular frequency given by

$$\omega_r = \sqrt{\frac{g_F \mu_B M_F}{M B_0}} \times b'. \quad (10.12)$$

### 10.2.2 Confinement in the axial direction

The *Ioffe* trap, shown in Fig. 10.3, uses the combination of a linear magnetic quadrupole and an axial bias field described above to give

<sup>3</sup>These losses prevent the spherical quadrupole field configuration of the two coils in the MOT being used directly as a magnetic trap—the MOT operates with gradients of  $0.1 \text{ T m}^{-1}$  so thirty times more current-turns are required in any case. We do not discuss the addition of a time-varying field to this configuration that leads to the TOP trap used in the first experimental observation of Bose–Einstein condensation in the dilute alkali vapours (Anderson *et al.* 1995).

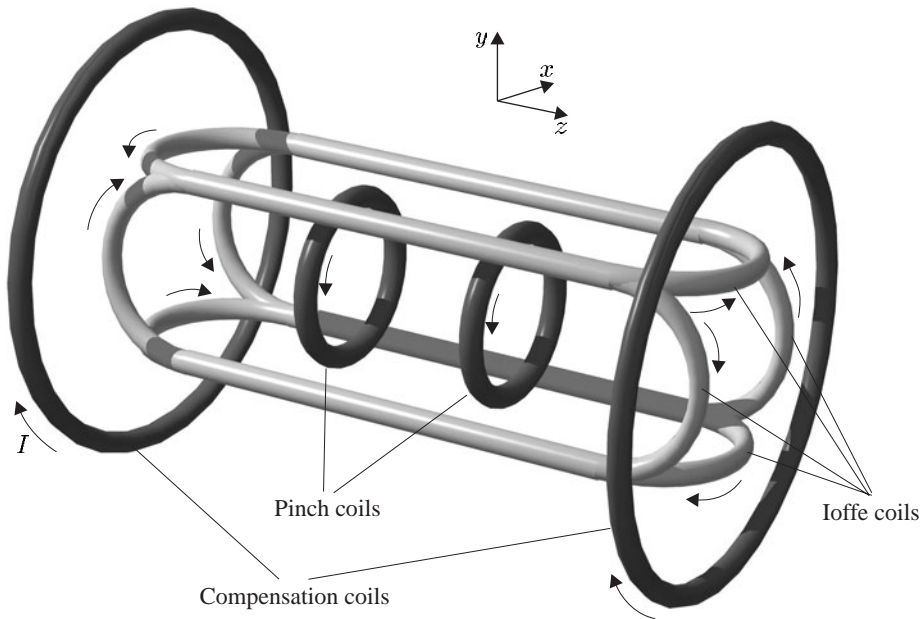


**Fig. 10.3** An Ioffe–Pritchard magnetic trap. The fields produced by the various coils are explained in more detail in the text and the following figures. This Ioffe trap is loaded with atoms that have been laser cooled in the way shown in Fig. 10.5. (Figure courtesy of Dr Kai Dieckmann.)

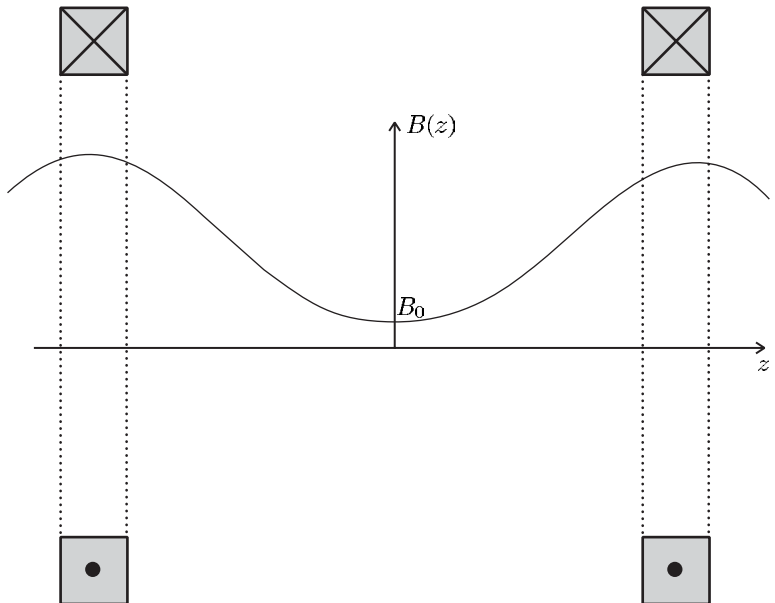


**Fig. 10.4** The pinch coils have currents in the same direction and create a magnetic field along the  $z$ -axis with a minimum midway between them, at  $z = 0$ . This leads to a potential well for atoms in low-field-seeking states along this axial direction. By symmetry, these coaxial coils with currents in the same direction give no gradient at  $z = 0$ .

radial confinement for atoms in low-field-seeking states. To confine these atoms in the axial direction the trap has two pairs of co-axial coils with currents that flow in the same direction to produce a field along the  $z$ -axis whose magnitude is shown in Fig. 10.4. These so-called pinch coils<sup>4</sup> have a separation greater than that of Helmholtz coils, so the field along  $z$  has a minimum midway between the coils (where  $dB_z/dz = 0$ ). The

<sup>4</sup>The term ‘pinch coils’ arises from the concept of pinching off the ‘magnetic tube’ containing the atoms. The Ioffe trap configuration was originally developed to confine plasma.

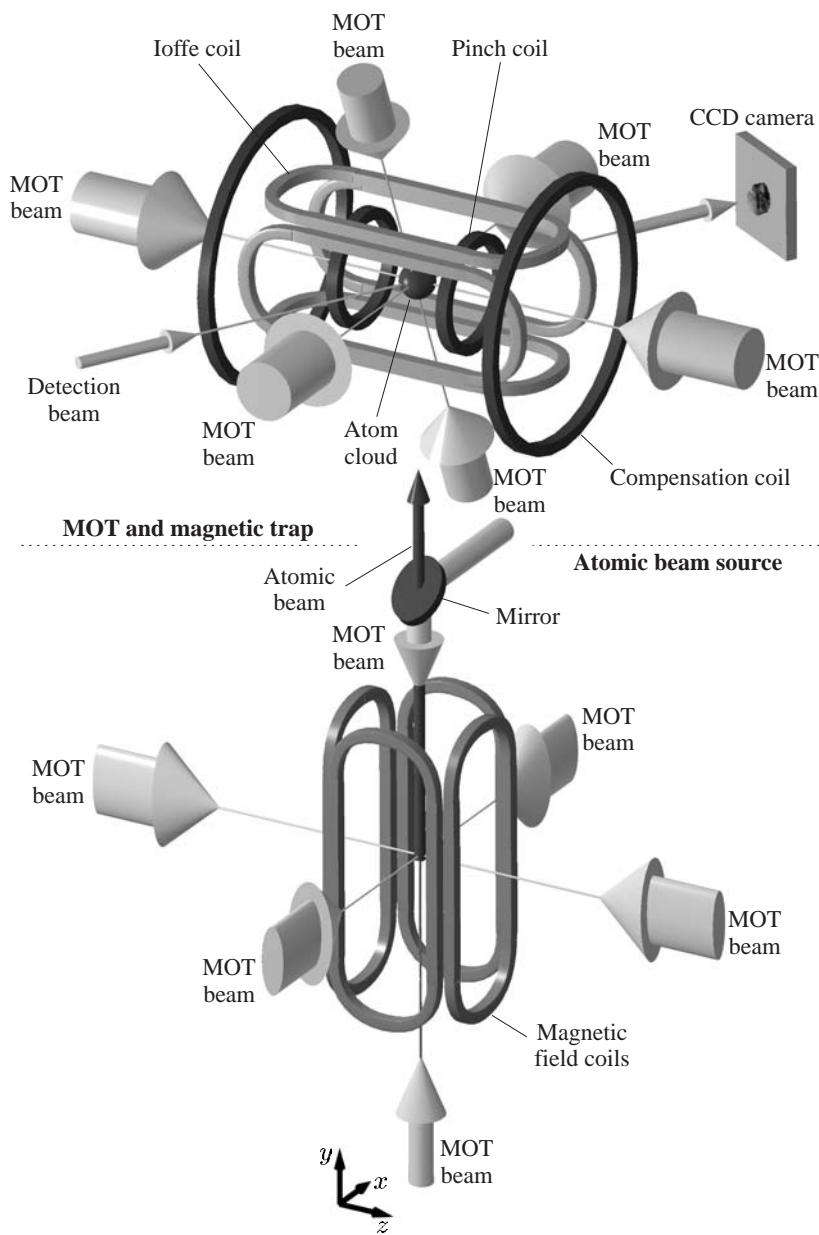


**Fig. 10.5** A general view of an apparatus to load an Ioffe–Pritchard magnetic trap with laser-cooled atoms from a magneto-optical trap. (The MOT has a different arrangement of coils to that described in Section 9.4 but the same principle of operation.) This experimental apparatus was constructed by the team of Professor Jook Walraven at the FOM Institute, Amsterdam. (Figure courtesy of Dr Kai Dieckmann, Dieckmann *et al.* (1998).) Copyright 1998 by the American Physical Society.

field has the form

$$B_{\text{pinch}}(z) = B_{\text{pinch}}(0) + \frac{d^2 B_z}{dz^2} \frac{z^2}{2}. \quad (10.13)$$

This gives a corresponding minimum in the magnetic energy and hence a harmonic potential along the  $z$ -axis. Typically, the Ioffe trap has an axial oscillation frequency  $\omega_z$  an order of magnitude lower than  $\omega_r$  ( $= \omega_x = \omega_y$ ), e.g.  $\omega_z/2\pi = 15$  Hz and  $\omega_r/2\pi = 250$  Hz (see Exercise 10.1). Thus the atoms congregate in a cigar-shaped cloud along the  $z$ -axis. The curvature of the magnetic field along  $z$  depends only on the dimensions of the pinch coils and their current. Therefore a uniform field along  $z$  does *not* affect  $\omega_z$ , but it does change  $\omega_r$  through the dependence on  $B_0$  in eqn 10.12. The pairs of compensation coils shown in Fig. 10.3 create a uniform field along the  $z$ -axis that opposes the field from the pinch coils. This allows experimenters to reduce  $B_0$  and make the trap stiff in the radial direction.<sup>5</sup>

To load the approximately spherical cloud of atoms produced by optical molasses, the Ioffe trap is adjusted so that  $\omega_r \simeq \omega_z$ . After loading, an increase in the radial trapping frequency, by reducing the bias field  $B_0$  (see eqn 10.12), squeezes the cloud into a long, thin cigar shape. This adiabatic compression gives a higher density and hence a faster collision rate for evaporative cooling.

### 10.3 Evaporative cooling

Laser cooling by the optical molasses technique produces atoms with a temperature below the Doppler limit, but considerably above the recoil limit. These atoms can easily be confined in magnetic traps (as shown in Section 10.1) and evaporative cooling gives a very effective way of reducing the temperature further. In the same way that a cup of tea loses heat as the steam carries energy away, so the cloud of atoms in a magnetic trap cools when the hottest atoms are allowed to escape. Each atom that leaves the trap carries away more than the average amount of energy and so the remaining gas gets colder, as illustrated in Fig. 10.6. A simple model that is useful for understanding this process (and for quantitative calculations in Exercise 10.4) considers evaporation as a sequence of steps. At the start of a step the atoms have a Boltzmann distribution of energies  $\mathcal{N}(E) = \mathcal{N}_0 \exp(-E/k_B T_1)$  characteristic of a temperature  $T_1$ . All atoms with energies greater than a certain value  $E > E_{\text{cut}}$  are allowed to escape, where  $E_{\text{cut}} = \eta k_B T_1$  and typically the parameter  $\eta$  lies in the range  $\eta = 3–6$ ; this truncated distribution has less energy per atom than before the cut so that, after collisions between the atoms have re-established thermal equilibrium, the new exponential distribution has a lower temperature  $T_2 < T_1$ .<sup>6</sup> The next step removes atoms with energies above  $\eta k_B T_2$  (a lower energy cut-off than in the first step) to give further cooling, and so on.<sup>7</sup> For many small steps this model gives a reasonable approximation to real experiments where evaporation proceeds by a continuous ramping down of  $E_{\text{cut}}$  that cuts away atoms at

<sup>5</sup>In practice, the compensation coils need not have exactly the Helmholtz spacing; the current in these coils together with pinch coil current gives two experimental parameters that allow the adjustment of the magnitude and field curvature along  $z$  to any desired value (limited by the maximum current through the pairs of coils). Neither pair of these coils gives a field gradient, by symmetry.

<sup>6</sup>Temperature is only defined at thermal equilibrium and in other situations the mean energy per atom should be used.

<sup>7</sup>An exponential distribution extends to infinity, and so for any value of  $E_{\text{cut}}$  (or  $\eta$ ) there is always some probability of atoms having a higher energy; however, the removal of a very small fraction of atoms has a little effect when averaged over the remaining atoms. Exercise 10.4 compares different depths of cut.

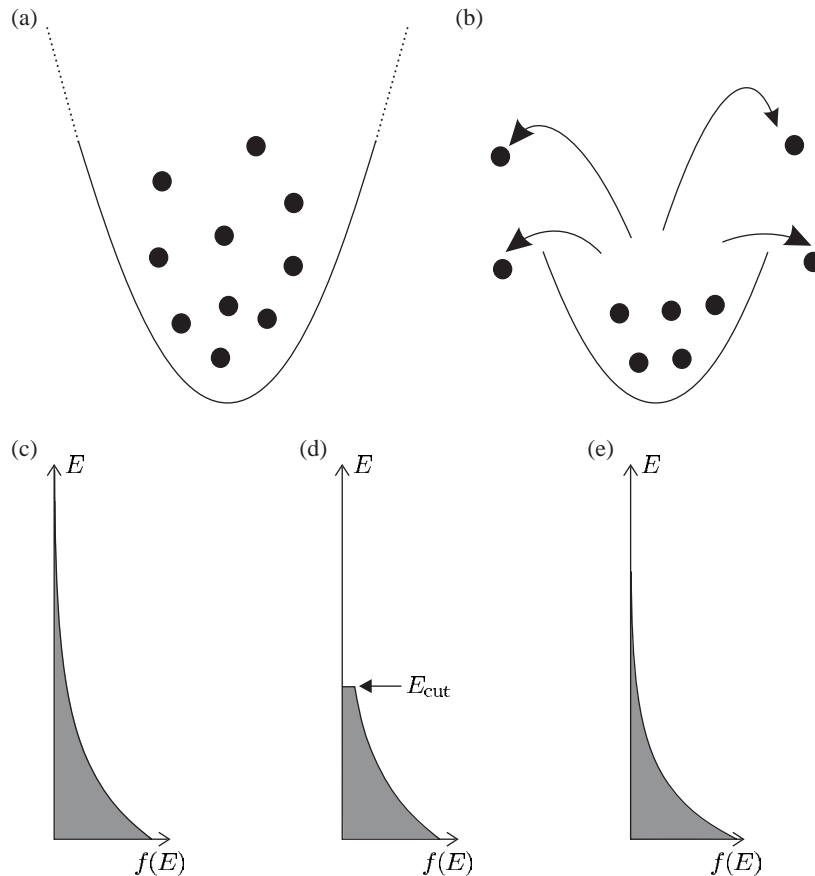


**Fig. 10.6** (a) A schematic representation of atoms confined in a harmonic potential. (b) The height of the potential is reduced so that atoms with above-average energy escape; the remaining atoms have a lower mean energy than the initial distribution. The evolution of the energy distribution is shown below: (c) shows the initial Boltzmann distribution  $f(E) = \exp(-E/k_B T_1)$ ; (d) shows the truncated distribution soon after the cut, when the hot atoms have escaped; and (e) shows the situation some time later, after collisions between the remaining atoms have re-established a Boltzmann distribution at a temperature  $T_2$  less than  $T_1$ . In practice, evaporative cooling in magnetic traps differs from this simplified picture in two respects. Firstly, the potential does not change but atoms leave the trap by undergoing radio-frequency transitions to untrapped states at a certain distance from the trap centre (or equivalently at a certain height up the sides of the potential). Secondly, cooling is carried out continuously rather than as a series of discrete steps.

the edge of the cloud (without stopping to allow rethermalisation). The rate of this evaporative cooling ramp depends on the rate of collisions between atoms in the trap.<sup>8</sup>

During evaporation in a harmonic trap the density *increases* (or at least stays constant) because atoms sink lower in the potential as they get colder. This allows *runaway evaporation* that reduces the temperature by many orders of magnitude, and increases the phase-space density to a value at which quantum statistics becomes important.<sup>9</sup>

Evaporation could be carried out by turning down the strength of the trap, but this reduces the density and eventually makes the trap too weak to support the atoms against gravity. (Note, however, that this method has been used successfully for Rb and Cs atoms in dipole-force traps.) In magnetic traps, precisely-controlled evaporation is carried out by using radio-frequency radiation to drive transitions between the trapped and untrapped states, at a given distance from the trap centre, i.e. radiation at frequency  $\omega_{\text{rf}}$  drives the  $\Delta M_F = \pm 1$  transitions at a radius  $r$  that satisfies  $g_F \mu_B b' r = \hbar \omega_{\text{rf}}$ . Hot atoms whose oscillations extend beyond this radius are removed, as shown in the following example.

<sup>8</sup>If the process is carried out too rapidly then the situation becomes similar to that for a non-interacting gas (with no collisions) where cutting away the hot atoms does not produce any more low-energy atoms than there are initially. It just selects the coldest atoms from the others.

<sup>9</sup>In contrast, for a square-well potential the density and collision rate decrease as atoms are lost, so that evaporation would grind to a halt. In the initial stages of evaporation in an Ioffe trap, the atoms spread up the sides of the potential and experience a linear potential in the radial direction. The linear potential gives a greater increase in density for a given drop in temperature than a harmonic trap, and hence more favourable conditions to start evaporation.

**Example 10.2** For an atom with  $g_F = 1/2$  (as in sodium) in a trap with  $b' = 3 \text{ T m}^{-1}$ , the frequency varies with position as  $g_F\mu_B b'/h = 21 \text{ GHz m}^{-1}$  ( $\mu_B \equiv 14 \text{ GHz T}^{-1}$ ). The application of radio-frequency radiation at 40 MHz removes atoms over a surface whose cross-section in the plane  $z = 0$  is a circle of radius  $r = 2 \text{ mm}$ . Sweeping the radio-frequency radiation down to 20 MHz reduces the radius to  $r = 1 \text{ mm}$ . This estimate assumes that the cutting surface (where the radio-frequency radiation removes atoms from the cloud) lies in the region where the magnetic field is linear  $b'r \gg B_0$ ; this is the *opposite* of the condition that gives the harmonic approximation in eqn 10.10. For a bias field of  $B_0 = 3 \times 10^{-4} \text{ T}$  and the field gradient  $b'$  above, the trapping potential is linear for  $r \gg 0.1 \text{ mm}$ , so our assumption of a linear field was valid. As evaporation proceeds, the atoms sink further down in the trap and the cross-over from a linear to a harmonic potential occurs when the cloud of atoms has a radius of  $r = B_0/b' = 0.1 \text{ mm}$  (see Fig. 10.2(b)). From eqn 10.6 we find that in a linear trap this would correspond to a cloud with a temperature of  $2 \times 10^{-4} \text{ K}$ .<sup>10</sup>

<sup>10</sup>This is approximately equal to the Doppler cooling limit for sodium (but see Exercise 10.2(c)).

<sup>11</sup>Good images were obtained from 2000 rubidium atoms in the first BEC experiment, and in principle it is possible to detect even a single atom.

<sup>12</sup>Contributions to the width of the radio-frequency transitions between Zeeman sub-levels arise from power broadening and fluctuations (noise) in the magnetic field. More usually, radio-frequency spectroscopy has a resolution limited by the interaction time, but this is less important for trapped atoms and continuous radiation.

Evaporative cooling has no fundamental lower limit and temperatures below 10 nK have been reached in magnetic traps. This is sufficient for the experiments discussed here, but let us consider briefly what limitations might arise in practice: (a) for a given set of starting conditions, it is not worthwhile to go beyond the point at which the number of trapped atoms becomes too low to detect;<sup>11</sup> (b) when the energy resolution of the radio-frequency transition is similar to the energy of the remaining atoms it is no longer possible to selectively remove hot atoms whilst leaving the cold atoms—colloquially, this is referred to as the radio-frequency ‘knife’ being blunt so that it cannot shave off atoms from the edges of the cloud;<sup>12</sup> and (c) in the case of fermions, it is difficult to cool atoms well below the Fermi temperature  $T_F$  at which quantum degeneracy occurs because, when almost all the states with energy below  $k_B T_F$  are filled (with the one atom in each state allowed by the Pauli exclusion principle), there is a very low probability of an atom going into an unoccupied state (‘hole’) in a collision. The case of bosons is discussed in the next section.

The temperature of a cloud of trapped atoms can be reduced by an adiabatic expansion of the cloud, but, by definition, an adiabatic process does not change the phase-space density (or equivalently the average number of atoms in each energy level of the system). Thus the parameter of overriding importance in trapped systems is the phase-space density rather than the temperature.

## 10.4 Bose–Einstein condensation

Bosons are gregarious particles that like to be together in the same state. In contrast, fermions refuse to go into an already occupied state, e.g. electrons obey the Pauli exclusion principle (which governs the struc-

ture of atoms). Statistical mechanics tells us that when a system of bosons reaches a critical phase-space density it undergoes a phase transition and the particles avalanche into the ground state. The standard textbook treatment of this Bose–Einstein condensation (BEC) applies almost exactly to dilute vapours of alkali metals in magnetic traps, and the relative simplicity of these systems was a strong motivation for these experiments. In comparison, superfluid helium is more complex since in this *liquid* the helium atoms interact much more strongly than the atoms in a dilute vapour.<sup>13</sup> Appendix F outlines a mathematical treatment of BEC that starts from the statistical mechanics of a ‘gas’ of photons in thermodynamic equilibrium, i.e. black-body radiation; this treatment shows clearly that BEC is a completely different sort of phase transition from the ‘ordinary’ condensation of a vapour into liquid caused by attractive forces between the atoms, or molecules. Quantum statistics becomes important when the occupation of quantum states approaches unity. At lower phase-space densities the particles hardly ever try to go into the same states, so they behave as classical objects; but when the states start to get crowded the particles behave differently, in a way that depends on their spin.

As shown in Appendix F, quantum effects arise when the number density  $n = \mathcal{N}/V$  reaches the value<sup>14</sup>

$$n = \frac{2.6}{\lambda_{dB}^3}, \quad (10.14)$$

where  $\lambda_{dB}$  is the value of the thermal de Broglie wavelength defined by

$$\lambda_{dB} = \frac{h}{\sqrt{2\pi M k_B T}}. \quad (10.15)$$

This definition corresponds to the usual expression  $\lambda_{dB} = h/Mv$  with a speed  $v$  characteristic of the gas. Simply speaking, the de Broglie wavelength gives a measure of the delocalisation of the atoms, i.e. the size of the region in which the atom would probably be found in a measurement of its position. This uncertainty in position increases as the momentum and associated kinetic energy decrease. Quantum effects become important when  $\lambda_{dB}$  becomes equal to the spacing between the atoms, so that the individual particles can no longer be distinguished.<sup>15</sup>

For an ideal Bose gas at the density of liquid helium ( $145 \text{ kg m}^{-3}$  at atmospheric pressure) eqns 10.14 and 10.15 predict a critical temperature of 3.1 K; this is close to the so-called  $\lambda$ -point at 2.2 K, where helium starts to become superfluid (see Annott 2004). The equations derived for a gas give quite accurate predictions because, although helium liquifies at 4.2 K, it has a lower density than other liquids (cf.  $10^3 \text{ kg m}^{-3}$  for water). Helium atoms have weak interactions because of their atomic structure—the closed shell of electrons leads to a small size and very low polarizability. The detailed properties of superfluid helium are, however, far from those of a weakly-interacting Bose-condensed gas. In contrast, trapped atomic gases have much lower densities so BEC occurs at temperatures of around one microkelvin. It is quite amazing that sodium

<sup>13</sup>Historically, the idea of BEC arose after the Indian physicist Satyendra Bose published a paper in 1924 that derived the Planck distribution for radiation in a new way, by looking at a statistical distribution of photons over the energy levels. Einstein realised that the same approach could be applied to particles (that we now call bosons), and he predicted the occurrence of Bose–Einstein condensation. Einstein wrote, ‘the theory is pretty but there may be some truth to it’, in a letter to Paul Ehrenfest.

<sup>14</sup>The symbol  $n$  is used for number density (as in most statistical mechanics texts) rather than  $N$  as in previous chapters. The number of atoms is  $\mathcal{N}$  and  $V$  is the volume.

<sup>15</sup>This very general criterion also applies to fermions but not with the same numerical coefficient as in eqn 10.14.

<sup>16</sup>In these systems the Bose-condensed gas is metastable; however, conditions can be reached where the condensate has a lifetime of many minutes. The ultra-cold molecules that form when cold atoms recombine are interesting to study in their own right. To achieve long lifetimes, limited by the recombination of atoms, the condensate must be held in an ultra-high vacuum to reduce the rate of collisions with molecules of the background gas in the apparatus.

and other alkalis can exist as atomic vapours at such low temperatures, and indeed this was doubted by many people before it was achieved in experiments. This is possible at very low densities because the processes that lead to recombination into molecules, and also heat the sample, occur slowly compared to the formation of a Bose–Einstein condensate.<sup>16</sup>

## 10.5 Bose–Einstein condensation in trapped atomic vapours

The usual textbook discussions of Bose–Einstein condensation consider a gas with a uniform density throughout a box of fixed volume, i.e. a homogeneous gas. However, the experiments with magnetically-trapped atoms correspond to a Bose gas in a harmonic potential and here we look at this inhomogeneous system. This section shows how to derive rough values of the important quantities in a way that gives a good physical understanding of the properties of the trapped Bose gas. A cloud of thermal atoms (i.e. not Bose-condensed) in a harmonic potential with a mean oscillation frequency  $\omega$  has a radius  $r$  given by

$$\frac{1}{2}M\omega^2r^2 \simeq \frac{1}{2}k_B T. \quad (10.16)$$

To the level of accuracy required we take the volume of the cloud as  $V \simeq 4r^3$  (a reasonable approximation to the volume of a sphere  $4\pi r^3/3$ ). This gives the number density as  $n \simeq \mathcal{N}/4r^3$ , which, when combined with eqn 10.14, gives

$$\mathcal{N}^{1/3} \simeq \frac{r}{\lambda_{dB}} = \frac{k_B T_C}{\hbar\omega}. \quad (10.17)$$

This result comes from substituting for  $r$  from eqn 10.16 and for  $\lambda_{dB}$  at the critical temperature,  $T_C$ , from eqn 10.15.<sup>17</sup> Fortunately, despite all our approximations, this expression lies within 10% of the value derived more carefully for a Gaussian distribution of atoms (see books by Pethick and Smith (2001) and Pitaevskii and Stringari (2003)). When the trapping potential does not have spherical symmetry, this result can be adapted by using the geometrical mean

$$\overline{\omega} = (\omega_x \omega_y \omega_z)^{1/3}. \quad (10.18)$$

For a cloud of  $\mathcal{N} = 4 \times 10^6$  atoms we find<sup>18</sup>

$$k_B T_C = \hbar \overline{\omega} \mathcal{N}^{1/3} = \hbar \overline{\omega} \times 160. \quad (10.19)$$

This result shows clearly that at the BEC transition the atoms occupy many levels of the trap and that it is quantum statistics which causes atoms to avalanche into the ground state.<sup>19</sup> A typical trap with  $\overline{\omega}/2\pi = 100$  Hz has a level spacing of  $\hbar \overline{\omega}/k_B \equiv 5$  nK (in temperature units). In this trap  $T_C \simeq 1 \mu\text{K}$ .<sup>20</sup> For  $4 \times 10^6$  sodium atoms in this trap, eqn 10.14 gives as the density at  $T_C$

$$n_C \simeq 40 \mu\text{m}^{-3} \equiv 4 \times 10^{13} \text{ cm}^{-3}.$$

<sup>17</sup>Neglecting a factor of  $10^{1/3} \simeq 2$ .

<sup>18</sup>This number at  $T_C$  has been chosen because after further evaporation it would lead to a condensate of roughly  $10^6$  atoms.

<sup>19</sup>Once a few bosons have accumulated in a particular state others want to join them. This cooperative behaviour arises because the constructive interference for bosons leads to a rate of stimulated transitions into a level proportional to the number in that level.

<sup>20</sup>This number of atoms gives a  $T_C$  close to the recoil limit for sodium (and  $T_C$  varies only slowly with  $\mathcal{N}$ ). Hence the atoms have a de Broglie wavelength comparable with that of laser cooling light. This coincidence gives a convenient way of remembering the approximate values. Note that  $T_C$  depends on the species of atom, since in a trap with a given magnetic field, limited by the maximum current through the coils, the oscillation frequencies of atoms are inversely proportional to  $\sqrt{M}$ .

The quantum statistics of identical particles applies to composite particles in the same way as for elementary particles, so long as the internal degrees of freedom are not excited. This condition is well satisfied for cold atoms since the energy required to excite the atomic electrons is much greater than the interaction energy.<sup>21</sup>

<sup>21</sup>P. Ehrenfest and J. R. Oppenheimer proved the spin-statistics relation for indistinguishable composite particles in ‘Note on the statistics of nuclei’, *Phys. Rev.*, **37**, 333 (1931).

### 10.5.1 The scattering length

The quantum theory of scattering is well described in most quantum mechanics texts, and the brief summary given here is only intended as a reminder of the salient points that are relevant for understanding the collisions between ultra-cold atoms in a gas. An important feature of very low-energy collisions is that, although the potential of the attractive interaction between two atoms has the shape shown in Fig. 10.7, the overall effect is the same as a hard-sphere potential. Thus we can model a low-temperature cloud of atoms as a gas of hard spheres,<sup>22</sup> in particular for the calculation of the contribution to the energy of the gas from interactions between the atoms.

This section gives a justification for this behaviour of ultra-cold atoms by simple physical arguments without mathematical details. The molecular potential (as in Fig. 10.7) has bound states that correspond to a diatomic molecule formed by the two atoms, and this part of the molecular wavefunction is a standing wave analogous to those that lead to the quantised energy levels of electrons in atoms.<sup>23</sup> It is the unbound states, however, that are appropriate for describing collisions between atoms in a gas and these correspond to travelling-wave solutions of the Schrödinger equation (illustrated in Figs 10.8 and 10.9). In the quantum mechanical treatment we need to solve the Schrödinger equation to determine what happens to an atomic wavepacket in the potential. The angular momentum of a particle in a radial potential  $V(r)$  is a conserved

<sup>22</sup>At least in most of the cases of interest for ultra-cold atoms.

<sup>23</sup>This part of the molecular wavefunction represents the vibrational motion of the molecule. Other aspects of molecular physics are described in Atkins (1994).

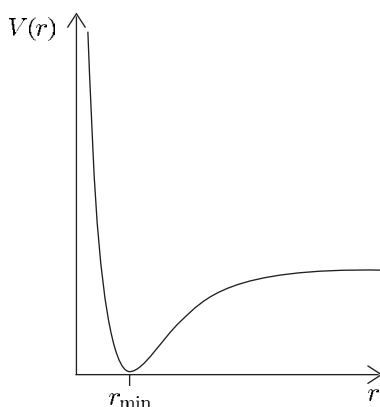


**Fig. 10.7** The potential  $V(r)$  for the interaction between two neutral atoms as a function of their separation  $r$ . At small separations the shells of electrons around each atom overlap and the strong electrostatic repulsion keeps the atoms apart, while at larger separations attractive van der Waals interactions dominate. These forces balance each other at the separation, where the potential is a minimum—this corresponds to the equilibrium separation of the diatomic molecule that is the bound state of the two atoms, e.g. the two sodium atoms are 0.3 nm apart in  $\text{Na}_2$ . This interatomic potential is called the molecular potential and it determines other properties of the molecule, e.g. its vibrational frequency (corresponding to oscillations in the potential well).

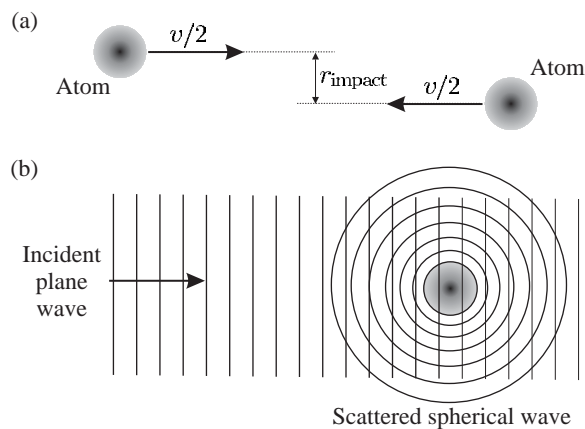
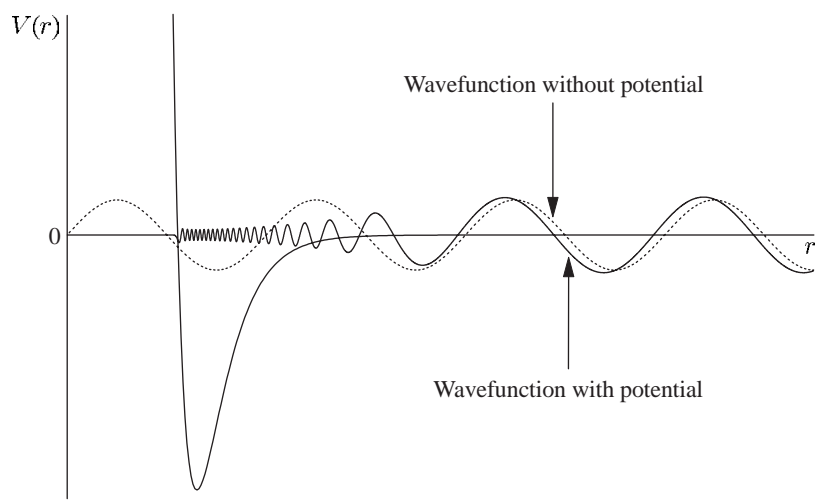


**Fig. 10.8** (a) A pair of colliding atoms with relative velocity  $v$  in their centre-of-mass frame. The impact parameter  $r_{\text{impact}}$  determines their relative orbital angular momentum (which is conserved). (b) In the quantum mechanical description of a low-energy scattering the solution of the Schrödinger equation is the sum of an incident plane wave  $e^{ikz}$  plus the wave scattered by the potential that expands outwards from  $r = 0$ , i.e. a wavefunction of the form  $\psi \propto e^{ikz} + f_k(\theta) e^{ikr}/r$ . This is an eigenstate with energy  $E = \hbar^2 k^2/M$  (for elastic scattering, i.e. no loss of energy). Only the scattering amplitude  $f_k(\theta)$  depends on the potential  $V(r)$ . For low energies the scattering amplitude is a constant,  $f \propto Y_{0,0}$ , and the condition in eqn 10.20 is fulfilled so that the phases  $kz$  and  $kr$  have a negligible variation across the region of interaction; hence  $\psi \simeq 1 + f/r$ . Writing the scattering amplitude as  $f = -a$  so that  $\psi(r) = 0$  on a spherical surface of radius  $r = a$ , shows that the scattered wave is a spherical wave that is equivalent to the scattering from a hard sphere of this radius. The comparison with a hard sphere is useful for positive values of  $a$ , but scattering theory allows negative values  $a < 0$  for which the outgoing wave is also spherical.

**Fig. 10.9** The solution of the Schrödinger equation for low-energy scattering from a molecular potential (cf. Fig. 10.7). The plot shows  $P(r)$ , where  $R(r) = P(r)/r$  is the radial wavefunction. At long range the overall effect of any potential (with a finite range) on the scattered wave is a phase shift (relative to a wave scattered from a point-like object at  $r = 0$ , shown as a dotted line)—in this region  $P(r) = \sin(kr - \phi)$  and the scattering is indistinguishable from that of a hard-sphere potential that gives the same phase shift. Potentials are characterised by the radius  $a$  of the equivalent hard-sphere potential. Radial wavefunctions can be calculated by the numerical method outlined in Exercise 4.10, and the extension of such a computational approach to study quantum scattering is described in Greenhow (1990). Figure from Butcher *et al.* (1999).



quantity, in both classical and quantum mechanics; thus the eigenstates of the angular part of the Schrödinger equation are the spherical harmonic functions, as in the central-field approximation for atoms. We can deduce the orbital angular momentum by correspondence with the following classical calculation.

A pair of colliding atoms has relative orbital angular momentum  $\hbar l \simeq M'vr_{\text{impact}}$ , where  $M'$  is the reduced mass,<sup>24</sup>  $v$  is their relative velocity and  $r_{\text{impact}}$  is the impact parameter (defined in Fig. 10.8). For a collision to happen  $r_{\text{impact}}$  must be less than the range of the interaction  $r_{\text{int}}$ . Thus we find that  $\hbar l \lesssim M'vr_{\text{int}} = hr_{\text{int}}/\lambda_{\text{dB}}$ , using the de Broglie relation. This implies that  $l \lesssim 2\pi r_{\text{int}}/\lambda_{\text{dB}}$  and therefore, when the energy is sufficiently low that

$$\frac{\lambda_{\text{dB}}}{2\pi} \gg r_{\text{int}}, \quad (10.20)$$

we have  $l = 0$ , i.e. the atoms have no relative orbital angular momentum. In this regime, the scattered wavefunction is a spherical wave proportional to  $Y_{l=0,m=0}$  no matter how complicated the actual potential. At the recoil limit of laser cooling the atoms and the photons of the laser light have a comparable wavelength  $\lambda_{\text{dB}} \simeq \lambda_{\text{light}}$ , because they have similar momentum, e.g. sodium atoms at  $T_{\text{recoil}} = 2 \mu\text{K}$  have  $\lambda_{\text{dB}}/2\pi \simeq 100 \text{ nm}$ .<sup>25</sup> This estimate indicates that the condition 10.20 is fulfilled at temperatures of a few microkelvin since the range of the interaction between neutral atoms is normally considerably less than 100 nm (equivalent to 2000 Bohr radii).<sup>26</sup> This spherical wave corresponding to the eigenfunction  $Y_{0,0}$  is called the s-wave, where s denotes zero relative orbital angular momentum (cf. s-orbitals that are bound states with  $l = 0$ ).<sup>27</sup>

The discussion of the s-wave scattering regime justifies the first part of the statement above that low-energy scattering from any potential looks the same as scattering from a hard-sphere potential when the radius of the sphere is chosen to give the same strength of scattering. The radius of this hard sphere is equivalent to a parameter that is usually called the scattering length  $a$ . This single parameter characterises the low-energy scattering from a particular potential.<sup>28</sup> For example, sodium atoms in the  $|F = 1, M_F = 1\rangle$  state have  $a = 2.9 \text{ nm}$ , which is about an order of magnitude greater than the size of the atom's electronic charge cloud and does not correspond to any physical feature in the real atom. In the following, the energy contribution from interactions between the atoms in a low-temperature gas is calculated assuming that the atoms act like hard spheres (which is just a useful fiction that is mathematically equivalent to the scattering from the actual potential). First, let us study a simple example that illustrates features that arise in the general case.

### Example 10.3 A particle in a spherical well

The Schrödinger equation for a particle in a spherically-symmetric potential can be separated into an angular equation and a radial equation that can be written in terms of  $P(r) = rR(r)$ , as in eqn 2.16. In this

<sup>24</sup>The difference between the reduced mass and the mass of the individual atoms is not particularly important in this rough estimate.

<sup>25</sup>Calculated in the laboratory frame of reference, i.e. not using the reduced mass.

<sup>26</sup>Molecular potentials, such as that shown in Fig. 10.7, do not have a sharply-defined cut-off. The determination of the minimum distance at which the atoms can pass with a negligible effect on each other requires a more general treatment.

<sup>27</sup>In the particular case of two identical bosons in the same internal state, the spatial wavefunction must be symmetric with respect to an interchange of the particle labels. Such wavefunctions have even orbital angular momentum quantum numbers  $l = 0, 2, 4$ , etc. Thus p-wave scattering cannot occur for collisions between identical bosons and the s-wave scattering regime extends up to the threshold energy for d-waves.

<sup>28</sup>There are many potentials that can give the same value of  $a$ .

example we shall examine the properties of wavefunctions with  $l = 0$  (corresponding to s-waves), so that the equation for  $P(r)$  is simply

$$\left[ -\frac{\hbar^2}{2M'} \frac{d^2}{dr^2} + V(r) \right] P(r) = EP(r), \quad (10.21)$$

where  $M'$  is the mass of the particle. For the potential  $V(r) = 0$  within the range  $a \leq r \leq b$  and  $V(r) = \infty$  elsewhere (for  $r < a$  and  $r > b$ ), this equation has the same form as that for an infinite square well in one dimension. The solution that satisfies the boundary condition  $\psi(r) = 0$  at  $r = a$  is

$$P = C \sin(k(r - a)), \quad (10.22)$$

where  $C$  is an arbitrary constant. The boundary condition that the wavefunction is zero at  $r = b$  requires that  $k(b - a) = n\pi$ , where  $n$  is an integer; hence the energy eigenvalues are given by<sup>29</sup>

$$E = \frac{\hbar^2 k^2}{2M'} = \frac{\hbar^2 \pi^2 n^2}{2M'(b - a)^2}. \quad (10.23)$$

To make a link with scattering theory we consider what happens when  $a \ll b$ , so that the wavefunction is contained in a spherical region of radius  $b$  but excluded from a small hard sphere of radius  $a$  at the origin; the energy of the lowest level ( $n = 1$ ) can be written as

$$E = \frac{\hbar^2 \pi^2}{2M' b^2} \left(1 - \frac{a}{b}\right)^{-2} \simeq E(a = 0) + \frac{\hbar^2 \pi^2 a}{M' b^3}. \quad (10.24)$$

This equals the energy for  $a = 0$  plus a small perturbation proportional to  $a$  which arises because the kinetic energy depends on the size of the region between  $r = a$  and  $b$ . (The expectation value of the potential energy is zero.) At short range where  $\sin(k(r - a)) \simeq k(r - a)$  the solution in eqn 10.22 reduces to

$$R(r) \simeq \frac{P(r)}{r} \propto 1 - \frac{a}{r}. \quad (10.25)$$

This is the general form for a wavefunction with a low energy ( $ka \ll 1$ ) near a hard sphere (in the region  $a < r \ll \lambda_{dB}/2\pi$ ) and the features illustrated by this example arise in the general case. The use of this situation to illustrate scattering might seem to contradict the above assertion that scattering involves wavefunctions that are unbound states, but we will see below that such waves have a similar increase in energy proportional to  $a$ . In any case, we will be applying the results to atoms that are confined (in the harmonic potential created by a magnetic trap).

A collision between a pair of atoms is described in their centre-of-mass frame as the scattering from a potential  $V(r)$  of a particle with a reduced mass given by<sup>30</sup>

$$M' = \frac{M_1 M_2}{M_1 + M_2}. \quad (10.26)$$

<sup>29</sup>This is the usual result for an infinite square well of length  $L$  rewritten with  $L = b - a$ .

<sup>30</sup>The reduced mass is used for the same reason as in the hydrogen atom, i.e. in one-electron atoms the electron and nucleus orbit around their centre-of-mass frame, and therefore it is the reduced mass of the electron  $m_e \times M_N/(m_e + M_N)$  that appears in the Schrödinger equation for the atom—the (slight) dependence of the electron's reduced mass on the nuclear mass  $M_N$  leads to the isotope shift of spectral lines (Chapter 6).

In a gas of identical particles, the two colliding atoms have the same mass  $M_1 = M_2 = M$  and therefore their reduced mass is  $M' = M/2$ .<sup>31</sup>

The discussion above showed that, in the s-wave regime, the scattering is the same for a hard-sphere potential and for the actual molecular potential (see also Fig. 10.9). Using the wavefunction in eqn 10.25, with an amplitude  $\chi$ , we find that the expectation value of the kinetic energy operator  $(-\hbar^2/2M')\nabla^2$ , with  $M' = M/2$ , is given by<sup>32</sup>

$$\begin{aligned} E_a &= \iiint \frac{-\hbar^2}{M} \left| \nabla \left\{ \chi \left( 1 - \frac{a}{r} \right) \right\} \right|^2 d^3 r \\ &= -\frac{4\pi\hbar^2}{M} |\chi|^2 \int_a^\infty \left| \frac{d}{dr} \left( 1 - \frac{a}{r} \right) \right|^2 r^2 dr \\ &= \frac{4\pi\hbar^2 a}{M} |\chi|^2. \end{aligned} \quad (10.27)$$

Taking the upper limit of integration over  $r$  as infinity gives a reasonable estimate of the energy (Pathra 1971).<sup>33</sup> This increase in energy caused by the interaction between atoms has the same scaling with  $a$  as in eqn 10.24, and arises from the same physical origin. We shall use this result to account for the interatomic interactions in a Bose–Einstein condensate in the following section.

Finally, we note a subtle modification of scattering theory for identical particles. The usual formula for the collision cross-section is  $4\pi a^2$ , but identical bosons have

$$\sigma = 8\pi a^2. \quad (10.28)$$

The additional factor of 2 arises because bosons constructively interfere with each other in a way that enhances the scattering.<sup>34</sup> This and the other features of collisions between ultra-cold bosons relevant to Bose–Einstein condensation are explained more fully in the books by Metcalf and van der Straten (1999), Pethick and Smith (2001), and Pitaevskii and Stringari (2003). These references also give a more careful definition of the scattering length that shows why this parameter can be positive  $a > 0$ , or negative  $a < 0$  (see Fig. 10.10). However, the majority of experimental work on Bose–Einstein condensation has been carried out with states of sodium and rubidium atoms that have positive scattering lengths, corresponding to the effectively repulsive hard-sphere interactions considered in this section. A full treatment of quantum scattering also allows a more rigorous derivation of the temperature below which there is only s-wave scattering, but the exact limits of the s-wave regime are not important for the purposes of this chapter since collisions between atoms at temperatures of a few microkelvin are normally well within this regime.<sup>35</sup>

<sup>31</sup>The transformation to the centre-of-mass frame and the use of reduced mass is very similar in classical and quantum mechanics.

<sup>32</sup>The integrand  $|\nabla\psi|^2 = \nabla\psi^*\nabla\psi$  is obtained from  $\psi^*\nabla^2\psi$  by integration by parts (as in the standard derivation of probability current in quantum mechanics).

<sup>33</sup>Most of the contribution to the integral comes from the region where  $a < r \ll \lambda_{dB}/2\pi$ , where eqn 10.25 is a good approximation to the wavefunction.

<sup>34</sup>The probability of bosons going into a particular quantum state is enhanced by a factor  $N + 1$ , where  $N$  is the number of particles in that state—for a two-body collision this increases the probability by a factor of 2. In contrast, two identical fermions cannot occupy the same state and therefore s-wave collisions, in which the particles have the same spatial state, are forbidden for fermions in the same spin state. (As noted previously, p-wave collisions do not occur for bosons.)

<sup>35</sup>Exceptions might occur where a resonance gives especially strong interactions between the atoms.

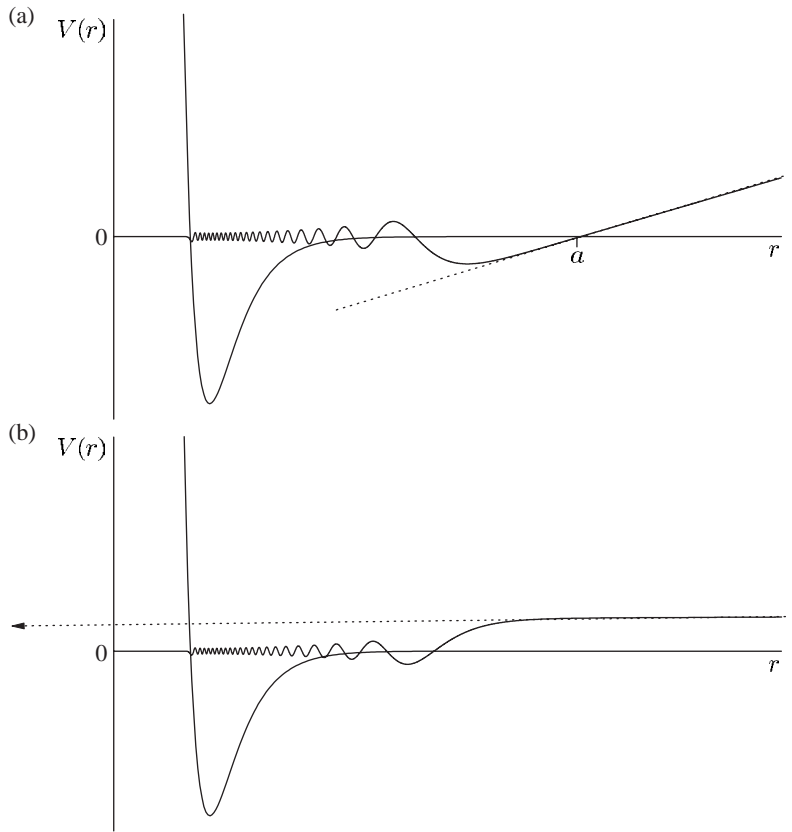


**Fig. 10.10** The wavefunction  $P(r) = rR(r)$  for very-low-energy scattering from slightly different molecular potentials with scattering lengths that are (a) positive and (b) negative with very large magnitude. From Butcher *et al.* (1999). The extrapolation of the wavefunction from at large  $r$  is drawn as a dashed line that crosses the horizontal axis at  $r = a$ .

## 10.6 A Bose–Einstein condensate

The interaction between atoms is taken into account by including a term in the Schrödinger equation that comes from eqn 10.27, proportional to the square of the wavefunction:

$$\left\{ -\frac{\hbar^2}{2M} \nabla^2 + V(\mathbf{r}) + g |\psi|^2 \right\} \psi = \mu \psi. \quad (10.29)$$

The extra energy from the interactions is proportional to  $|\psi|^2$ , the probability of finding a particle in a given region, and the coupling constant is

$$g = \frac{4\pi\hbar^2 N a}{M}. \quad (10.30)$$

<sup>36</sup>Actually, there are  $N - 1$  other atoms, but the difference from  $N$  is negligible for large numbers of atoms.

<sup>37</sup>This quantity turns out to be equivalent to the chemical potential in thermodynamics:  $\mu = \partial E / \partial N$  is the energy required to remove a particle from the system. This is not the same as the average energy per particle—see Exercise 10.7.

This comes from eqn 10.27 with  $|\chi|^2 \rightarrow N |\psi|^2$  that gives the interaction per atom in the presence of  $N$  atoms.<sup>36</sup> The symbol  $\mu$  is used (instead of  $E$ ) to represent the energy of an individual atom in the presence of all the others (cf. the central-field approximation in Chapter 4).<sup>37</sup> This nonlinear Schrödinger equation is called the Gross–Pitaevskii equation after the people who first (independently) wrote it down and a rigorous

derivation can be found in the book by Pitaevskii and Stringari (2003). Trapped atoms experience a harmonic potential

$$V(\mathbf{r}) = \frac{1}{2}M(\omega_x^2x^2 + \omega_y^2y^2 + \omega_z^2z^2). \quad (10.31)$$

For simplicity, we shall consider all three oscillation frequencies equal, i.e. the isotropic potential  $M\omega^2r^2/2$ , and use a variational method to estimate the energy. We choose a trial wavefunction that is a Gaussian function:

$$\psi = Ae^{-r^2/2b^2}. \quad (10.32)$$

Using this to calculate the expectation values of terms in eqn 10.29 gives

$$E = \frac{3}{4}\hbar\omega \left\{ \frac{a_{\text{ho}}^2}{b^2} + \frac{b^2}{a_{\text{ho}}^2} \right\} + \frac{g}{(2\pi)^{3/2}} \frac{1}{b^3}. \quad (10.33)$$

Differentiation of this expression shows that when  $g = 0$  the minimum energy occurs when  $b = a_{\text{ho}}$ , where

$$a_{\text{ho}} = \sqrt{\frac{\hbar}{M\omega}} \quad (10.34)$$

is the characteristic radius of the Gaussian ground-state wavefunction in the quantum harmonic oscillator. A sodium atom in a trap with oscillation frequency  $\omega/2\pi = 100$  Hz has  $a_{\text{ho}} = 2 \times 10^{-6}$  m. For this equilibrium value of  $b$ , the two terms representing the kinetic and potential energies give an equal contribution to the total energy which is  $E = (3/2)\hbar\omega$ , as expected for the ground state of the quantum harmonic oscillator.<sup>38</sup> The variational method gives exact results in this particular case because the trial wavefunction has the same Gaussian form as the actual solution for a harmonic oscillator.

Now we shall consider what happens when  $g > 0$ .<sup>39</sup> The ratio of the terms representing the atomic interactions and the kinetic energy is<sup>40</sup>

$$\frac{4}{3(2\pi)^{3/2}} \frac{g}{a_{\text{ho}}^3 \hbar\omega} \simeq \frac{\mathcal{N}a}{a_{\text{ho}}}. \quad (10.35)$$

The nonlinear term swamps the kinetic energy when  $\mathcal{N} > a_{\text{ho}}/a$ . This ratio equals  $a_{\text{ho}}/a = 700$  for  $a_{\text{ho}} = 2 \mu\text{m}$  and  $a = 3 \text{ nm}$ , and so in this case when the number of atoms in the condensate  $\mathcal{N} > 700$  we can neglect the kinetic energy.<sup>41</sup> We could estimate the condensate's size from eqn 10.33 by determining the value of  $r$  at which the confining potential balances the repulsive interactions, and this variational method is described in Exercise 10.6; but it is remarkably easy to solve the Gross–Pitaevskii equation when the kinetic energy term is neglected. In this so-called Thomas–Fermi regime eqn 10.29 becomes simply

$$\left\{ V(r) + g|\psi|^2 \right\} \psi = \mu\psi. \quad (10.36)$$

So for the region where  $\psi \neq 0$  we find

$$|\psi|^2 = \frac{\mu - V(r)}{g}. \quad (10.37)$$

<sup>38</sup>Each of the three degrees of freedom has a zero-point energy of  $\frac{1}{2}\hbar\omega$ .

<sup>39</sup>Small Bose–Einstein condensates with effectively attractive interactions have been created, but they collapse inward as the number of atoms grows (see Exercise 10.11).

<sup>40</sup>The factor of  $(4/3)(4\pi/(2\pi)^{3/2})$  that arises has a numerical value of about unity.

<sup>41</sup>Typically, experiments have  $\mathcal{N} > 10^5$  and the effectively repulsive interactions make the condensate much larger than  $a_{\text{ho}}$ . The interactions between the atoms in a dilute gas only have a small effect (< 10%) on the value of  $T_C$ .

Hence, the number density of atoms  $n(r) = \mathcal{N}|\psi(r)|^2$  in the harmonic potential has the form of an inverted parabola:

$$n(r) = n_0 \left( 1 - \frac{x^2}{R_x^2} - \frac{y^2}{R_y^2} - \frac{z^2}{R_z^2} \right), \quad (10.38)$$

where  $n_0$ , the number density at the centre of the condensate, is

$$n_0 = \frac{\mathcal{N}\mu}{g}. \quad (10.39)$$

The condensate has an ellipsoidal shape and the density goes to zero at points on the axes given by  $x = \pm R_x$ ,  $y = \pm R_y$  and  $z = \pm R_z$ , defined by

$$\frac{1}{2}M\omega_x^2 R_x^2 = \mu, \quad (10.40)$$

and similarly for  $R_y$  and  $R_z$ . In the Thomas–Fermi regime, the atoms fill up the trap to the level of the chemical potential as illustrated in Fig. 10.11, just like water in a trough. The chemical potential  $\mu$  is determined by the normalisation condition

$$1 = \iiint |\psi|^2 \, dx \, dy \, dz = \frac{\mu}{g} \frac{8\pi}{15} R_x R_y R_z. \quad (10.41)$$

A useful form for  $\mu$  is

$$\mu = \hbar\bar{\omega} \times \frac{1}{2} \left( \frac{15\mathcal{N}a}{a_{ho}} \right)^{2/5}. \quad (10.42)$$

The mean oscillation frequency is defined as  $\bar{\omega} = (\omega_x \omega_y \omega_z)^{1/3}$  and  $a_{ho}$  is calculated using this frequency in eqn 10.34. Typical values for an Ioffe trap are given in the following table together with the important properties of a BEC of sodium, calculated from the key formulae in eqns 10.42, 10.40 and 10.39 (in that order).

|  |                                    |                                    |
|--|------------------------------------|------------------------------------|
| Scattering length (for Na)                             | $a$                                | 2.9 nm                             |
| Radial oscillation frequency ( $\omega_x = \omega_y$ ) | $\omega_x/2\pi$                    | 250 Hz                             |
| Axial oscillation frequency                            | $\omega_z/2\pi$                    | 16 Hz                              |
| Average oscillation frequency                          | $\bar{\omega}/2\pi$                | 100 Hz                             |
| Zero-point energy (in temperature units)               | $\frac{1}{2}\hbar\bar{\omega}/k_B$ | 2.4 nK                             |
| Harmonic oscillator length (for $\bar{\omega}$ )       | $a_{ho}$                           | 2.1 $\mu$ m                        |
| Number of atoms in condensate                          | $\mathcal{N}_0$                    | $10^6$                             |
| Chemical potential                                     | $\mu$                              | 130 nK                             |
| Radial size of condensate                              | $R_x = R_y$                        | 15 $\mu$ m                         |
| Axial size of condensate                               | $R_z$                              | 95 $\mu$ m                         |
| Peak density of condensate                             | $n_0$                              | $2 \times 10^{14} \text{ cm}^{-3}$ |
| Critical temperature (for $4 \times 10^6$ atoms)       | $T_C$                              | 760 nK                             |
| Critical density (for $4 \times 10^6$ atoms)           | $n_C$                              | $4 \times 10^{13} \text{ cm}^{-3}$ |

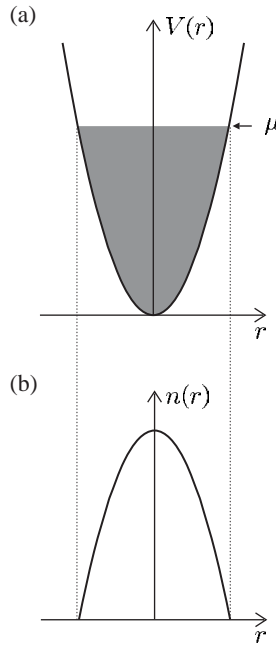


**Fig. 10.11** In the Thomas-Fermi regime the condensate has the same shape as the confining potential. (a) A harmonic potential. (b) The density of the atoms in a harmonic trap has an inverted-parabolic shape (along all three axes).

The critical temperature and density at the onset of Bose condensation are not properties of the condensate, but are calculated for a cloud of  $4 \times 10^6$  atoms (from eqn 10.19); this would lead to a condensate of roughly  $\mathcal{N}_0 \simeq 10^6$  atoms after evaporative cooling to  $T/T_C \simeq 0.5$  (where most atoms are in the condensate, see eqn F.16). Both  $\mu$  and  $T_C$  have a weak dependence on  $\mathcal{N}$  (eqns 10.19 and 10.42) and a similar (but not the same) dependence on  $\omega$ , so these quantities have a similar relative magnitude for many cases. Note, however, that  $\mu$  depends on

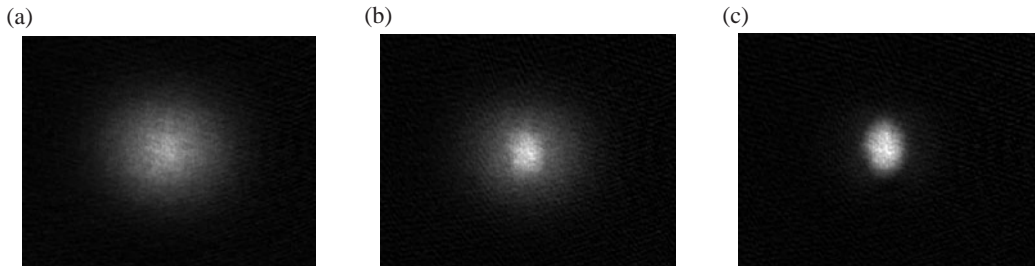


**Fig. 10.12** This sequence of images shows a Bose-Einstein condensate being born out of a cloud of evaporatively-cooled atoms in a magnetic trap. Each image was taken after a time-of-flight expansion. The cloud changes its size and shape as it undergoes a phase transition: (a) a thermal cloud just above the critical temperature  $T_C$  has a spherical shape (isotropic expansion); (b) a cloud of atoms at  $0.9 T_C$  has a Bose-condensed fraction in the centre surrounded by a halo of thermal atoms; and (c) well below the critical temperature ( $< 0.5 T_C$ ) most of the atoms are in the condensate (lowest energy state of the trap). These images come from a system that does not have the same aspect ratio as an Ioffe trap, but they illustrate the anisotropic expansion of the condensate wavefunction. See Fig. 10.13 for dimensions and other details. Data provided by Nathan Smith, Physics department, University of Oxford.

<sup>42</sup>The repulsive interactions prevent the much greater increase in the density that would occur if atoms congregated in a region of volume  $a_{ho}^3$ .

the strength of the interactions, whereas  $T_C$  does not. In this example the condensate has a density about a factor of 5 greater than the thermal cloud at the phase transition,<sup>42</sup> but the gas remains dilute because the average distance between atoms in the condensate is larger than the scattering length, that is  $na^3 \ll 1$  (for the data in the table  $n_0a^3 = 4 \times 10^{-6}$ ). Equation 10.40, and the similar equation for  $R_z$ , give the ratio of sizes as  $R_z/R_x = \omega_x/\omega_z = 16$  (and  $R_y = R_x$ ), so in this trap the condensate has the shape of a long, thin cigar.

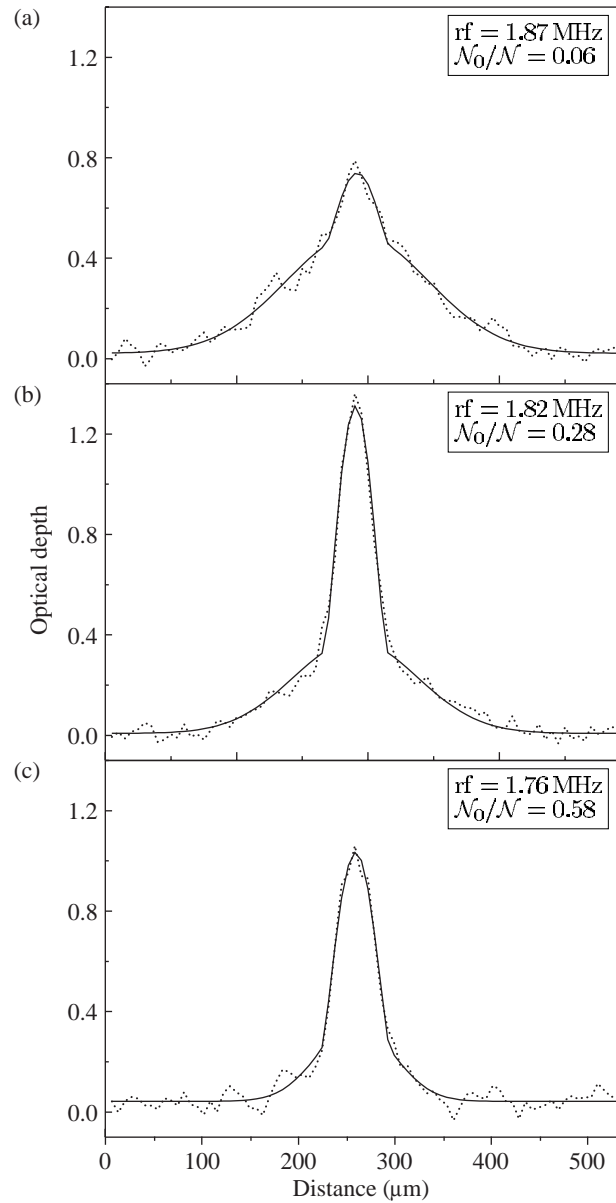


**Fig. 10.13** Cross-sections of the images similar to those shown in Fig. 10.12, but for different temperatures and a time of 12 ms after release from the magnetic trap. (a) Just below the critical temperature ( $0.99 T_C$ ) a small central peak appears on the Gaussian distribution of thermal atoms. (b) At  $0.82 T_C$  most of the atoms are in the condensate with some thermal atoms in the wings. (c) At  $0.63 T_C$  only a small thermal cloud remains. This narrowing of the distribution and change from a Gaussian to an inverted-parabolic shape occurs over a small range of temperatures which is a behaviour characteristic of a phase transition. From Hechenblaikner (2002), for a trap with  $\omega_x = \omega_y = 2\pi \times 126 \text{ Hz}$  and  $\omega_z = 2\pi \times 356 \text{ Hz}$ . The fraction of atoms in the condensate ( $N_0/N$ ) differs from that predicted by eqn F.16 because of interactions (see Maragò *et al.* 2001).

To observe the condensate experimenters record an image by illuminating the atoms with laser light at the resonance frequency.<sup>43</sup> Typically, the experiments have an optical resolution of about  $5\text{ }\mu\text{m}$ , so that the length of the condensate can be measured directly but its width is not precisely determined. Therefore the magnetic trap is turned off sharply so that the atoms expand and some time later a laser beam, that passes through the cloud of atoms onto a camera, is flashed on to record a shadow image of the cloud. The repulsion between atoms causes the cloud to expand rapidly after the confining potential is switched off (see Exercise 10.6). The cigar-shaped cloud expands more rapidly in the radial direction ( $x$  and  $y$ ) than along  $z$ , so that after several milliseconds the radial size becomes bigger than that along  $z$ , i.e. the aspect ratio inverts.<sup>44</sup> In contrast, the uncondensed atoms behave as a classical gas and expand isotropically to give a spherical cloud, since by definition the thermal equilibrium implies the same kinetic energy in each direction. Pictures such as Fig. 10.12 are the projection of the density distribution onto a two-dimensional plane, and show an obvious difference in shape between the elliptical condensate and the circular image of the thermal atoms. This characteristic shape was one of the key pieces of evidence for BEC in the first experiment, and it is still commonly used as a diagnostic in such experiments. Figure 10.13 shows the density profile of the cloud of atoms released from a magnetic trap for temperatures close to the critical point, and below.

## 10.7 Properties of Bose-condensed gases

Two striking features of Bose-condensed systems are superfluidity and coherence. Both relate to the microscopic description of the condensate as  $\mathcal{N}$  atoms sharing the same wavefunction, and for Bose-condensed gases they can be described relatively simply from first principles (as in this section). In contrast, the phenomena that occur in superfluid helium are more complex and the theory of quantum fluids is outside the scope of this book.

### 10.7.1 Speed of sound

To estimate the speed of sound  $v_s$  by a simple dimensional argument we assume that it depends on the three parameters  $\mu$ ,  $M$  and  $\omega$ , so that<sup>45</sup>

$$v_s \propto \mu^\alpha M^\beta \omega^\gamma. \quad (10.43)$$

This dimensional analysis gives<sup>46</sup>

$$v_s \simeq \sqrt{\frac{\mu}{M}}. \quad (10.44)$$

This corresponds to the actual result for a homogeneous gas (without us needing to insert any numerical factor), and gives a fairly good approximation in a trapped sample. The speed at which compression waves

<sup>43</sup>Generally, absorption gives a better signal than fluorescence but the optical system and camera are similar in both cases.

<sup>44</sup>This expansion of the wavefunction is predicted by including time dependence in the nonlinear Schrödinger equation.

<sup>45</sup>The size of the condensate  $R$  is not another independent parameter, see eqn 10.40.

<sup>46</sup>Comparing the dimensions of the terms in eqn 10.43 gives

$$\text{ms}^{-1} = [\text{kg m}^2 \text{s}^{-2}]^\alpha \text{kg}^\beta \text{s}^{-2\gamma}.$$

Hence  $\alpha = -\beta = 1/2$  and  $\gamma = 0$ .

travel in the gas has great significance for superfluidity. For motion slower than this speed the condensate flows smoothly around obstacles without exciting any particles out of the ground state of the quantum gases. This type of flow does not dissipate any energy and so it is frictionless and the gas is superfluid.

### 10.7.2 Healing length

The Thomas–Fermi approximation neglects the kinetic energy term in the Schrödinger equation. This leads to a physically unrealistic sharp edge at the surface of the condensate (see Fig. 10.11)—such a discontinuity in the gradient would make  $\nabla^2\psi$  infinite. Therefore we have to take kinetic energy into account at the boundary. To determine the shortest distance  $\xi$  over which the wavefunction can change we equate the kinetic term (that contains  $\nabla^2\psi \simeq \hbar^2/(2M\xi^2)$ ) to the energy scale of the system given by the chemical potential. Atoms with energy higher than  $\mu$  leave the condensate. Using  $n_0 = \mathcal{N}\mu/g$  (from eqn 10.39) and eqn 10.30 for  $g$ , we find that

$$\frac{\hbar^2}{2M\xi^2} \simeq \mu = \frac{gn_0}{\mathcal{N}} = \frac{4\pi\hbar^2an_0}{M}. \quad (10.45)$$

Hence  $\xi = 1/\sqrt{8\pi an_0}$ , e.g.  $\xi = 0.3\text{ }\mu\text{m}$  for a sodium condensate with  $n_0 = 2 \times 10^{14}\text{ cm}^{-3}$ . Typically,  $\xi \ll R_x$  and smoothing of the wavefunction only occurs in a thin boundary layer, and these surface effects give only small corrections to results calculated using the Thomas–Fermi approximation. This so-called healing length also determines the size of the vortices that form in a superfluid when the confining potential rotates (or a fast moving object passes through it). In these little ‘whirlpools’ the wavefunction goes to zero at the centre, and  $\xi$  determines the distance over which the density rises back up to the value in the bulk of the condensate, i.e. this healing length is the distance over which the superfluid recovers from a sharp change.

### 10.7.3 The coherence of a Bose–Einstein condensate

Figure 10.14 shows the result of a remarkable experiment carried out by the group led by Wolfgang Ketterle at MIT. They created two separate condensates of sodium at the same time. After the trapping potential was turned off the repulsion between the atoms caused the two clouds to expand and overlap with each other (as in the time-of-flight technique used to observe Bose–Einstein condensation, see Fig. 10.12). The two condensates interfere to give the fringes shown in the figure; there are no atoms at certain positions where the matter waves from the two sources interfere destructively—these atoms do not disappear, but they are redistributed to positions in the fringe pattern where the matter waves add constructively. Such interference is well known in optics; however, there is a very interesting difference between this experiment

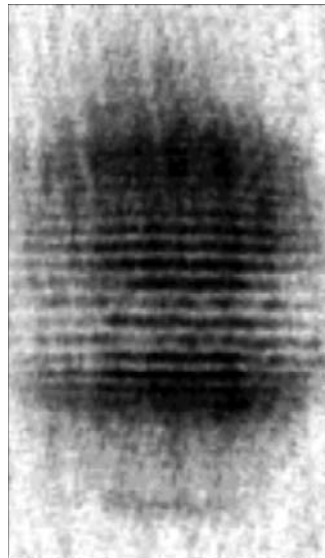


**Fig. 10.14** The interference fringes observed when two independent Bose condensates are released from nearby potential wells and the clouds of atoms expand and overlap. This experiment was carried out with sodium atoms by the team led by Wolfgang Ketterle at MIT (Andrews *et al.* 1997). Copyright 1997 by the American Association for the Advancement of Science.

and the usual double-slit experiments. In the MIT experiment there was no fixed relation between the phases of the two condensates and before the experiment was carried out it was hotly debated whether interference would be observed. Clear interference fringes were observed each time the experiment was carried out. However, the position of these fringes depended on the difference between the phases of the condensates in that particular run—the bright and dark fringes appeared at a different place each time the experiment was repeated; thus the fringe pattern would ‘wash out’ if averaged over many runs. The observation of the interference of two condensates relies on the ability to see interference fringes in a single shot.

The experiment was carried out with an Ioffe trap in which the atoms form a long, cigar-shaped cloud. At MIT they used a sheet of light to chop the cloud into two pieces of roughly half the original length. The light exerted a force that pushed the atoms out of the region of high intensity (because it had a blue frequency detuning as explained in Section 9.6). This configuration gave two separate potential wells. In practice, the following situations both give the same results: (a) when the two condensates are created independently; and (b) when a single large condensate is divided into two parts after it has formed. The process of turning on a sheet of light in the middle of an already-formed condensate produces such a strong perturbation that the two resulting condensates have almost random phases. Only recently has the controlled separation of a condensate into two parts whilst preserving the phase been demonstrated in a double-well dipole-force trap—a system that corresponds to a beam splitter for matter waves. (Atom optics is discussed further in Chapter 11.) However, the intriguing aspect of the interference of two independent condensates is its dissimilarity to previous experiments.

**Fig. 10.15** Atoms coupled out of a Bose–Einstein condensate fall downwards under gravity to form a well-collimated matter-wave beam, with analogous properties to the beam of light from a laser. Courtesy of Nathan Smith and William Heathcote, Physics department, University of Oxford.



#### 10.7.4 The atom laser

The phrase ‘atom laser’ has been used to describe the coherent beam of matter waves coupled out of a Bose–Einstein condensate (as shown in Fig. 10.15). After forming the condensate, the radio-frequency radiation was tuned to a frequency that drives a transition to an untrapped state (e.g.  $M_F = 0$ ) for atoms at a position inside the condensate. (This comes from the same source of radiation used for evaporative cooling.) These atoms fall downwards under gravity to form the beam seen in the figure. These matter waves coupled out of the condensate have a well-defined phase and wavelength like the light from a laser.<sup>47</sup> Many novel matter-wave experiments have been made possible by Bose–Einstein condensation, e.g. the observation of nonlinear processes analogous to nonlinear optics experiments that were made possible by the high-intensity light produced by lasers.

<sup>47</sup>The atoms accelerate as they fall under gravity so the wave propagation is different to that of light.

### 10.8 Conclusions

Bose–Einstein condensation in dilute alkali vapours was first observed in 1995 by groups at JILA (in Boulder, Colorado) and at MIT, using laser cooling, magnetic trapping and evaporation. This breakthrough, and the many subsequent new experiments that it made possible, led to the award of the Nobel prize to Eric Cornell, Carl Wieman and Wolfgang Ketterle in 2001 (and the Nobel prize web site has much useful information on this subject, with links to the web sites of the research groups). Recent BEC experiments have produced a wealth of beautiful images; however, the objective of this chapter has not been to cover everything but rather to explain the general principles of the underlying physics. The two books on BEC by Pethick and Smith (2001) and Pitaevskii and Stringari (2003) contain much more detail.

## Exercises

### (10.1) Magnetic trapping

An Ioffe–Pritchard trap has a radial gradient of  $b' = 3 \text{ T m}^{-1}$ , and the combination of Helmholtz and pinch coils gives a field along  $z$  with  $B_0 = 3 \times 10^{-4} \text{ T}$  and curvature  $b'' = 300 \text{ T m}^{-2}$ . Calculate the oscillation frequencies of sodium atoms in the trap.

### (10.2) Loading a trap

- (a) A spherical cloud of  $10^{10}$  sodium atoms with a density of around  $10^{10} \text{ cm}^{-3}$  and a temperature of  $T = 2.4 \times 10^{-4} \text{ K}$  is placed in a spherically-symmetric trapping potential. The temperature and density of the cloud are preserved during this loading if

$$\frac{1}{2} M \omega^2 r^2 = \frac{1}{2} k_B T. \quad (10.46)$$

Calculate the trapping frequency  $\omega$  that fulfils this mode-matching condition, and explain what happens if the trap is too stiff or too weak. (In a precise treatment  $r$  would be the root-mean-square radius of a cloud with a Gaussian density distribution.)

- (b) Calculate  $n\lambda_{dB}^3/2.6$  for the trapped cloud, i.e. the ratio of its phase-space density to that required for BEC (eqn 10.14).  
(c) After loading, an adiabatic compression of the trapped cloud changes the oscillation frequencies of the atoms to  $\omega_r/2\pi = 250 \text{ Hz}$  and  $\omega_z/2\pi = 16 \text{ Hz}$ . The phase-space density does not change during adiabatic processes, i.e.  $n\lambda_{dB}^3$  is constant. Show that this implies that  $TV^{2/3}$  is constant. Calculate the temperature and density of the cloud after compression.<sup>48</sup>

### (10.3) Magnetic trapping

- (a) Sketch the energy of the hyperfine levels of the  $3s\ ^2S_{1/2}$  ground level of sodium as a function of the applied magnetic field strength. (The hyperfine-structure constant of this level is  $A_{3s} = 886 \text{ MHz}$  and sodium has nuclear spin  $I = 3/2$ .)  
(b) What is meant by a ‘weak’ field in the context of hyperfine structure?  
(c) Show that for a weak magnetic field the states in both hyperfine levels have a splitting of  $7 \text{ GHz T}^{-1}$ .  
(d) Explain why the potential energy of an atom in a magnetic trap is proportional to the magnetic flux density  $|\mathbf{B}|$ .  
A magnetic trap has a field that can be approximated by

$$\mathbf{B} = b'(x\hat{\mathbf{e}}_x - y\hat{\mathbf{e}}_y)$$

in the region where  $r = (x^2 + y^2)^{1/2} \leq 10 \text{ mm}$ , and  $B = 0$  outside this radius. The field gradient  $b' = 1.5 \text{ T m}^{-1}$  and the  $z$ -axis of the trap is horizontal.

- (e) Calculate the ratio of the magnetic force on the atoms compared to that of gravity.  
(f) Estimate the maximum temperature of atoms that can be trapped in the (i) upper and (ii) lower hyperfine levels. State the  $M_F$  quantum number of the atoms in each case. (Assume that the confinement of atoms along the  $z$ -axis is not the limiting factor.)  
(g) For the clouds of trapped atoms in both (i) and (ii) of part (f), describe the effect of applying radio-frequency radiation with a frequency of  $70 \text{ MHz}$ .

<sup>48</sup>The relation between temperature and volume can also be derived from thermodynamics:  $TV^{\gamma-1}$  is constant for an adiabatic change in an ideal gas and a monatomic gas has a ratio of heat capacities  $\gamma = C_P/C_V = 5/3$ . Actually, the phase-space density only remains constant if the potential has the same shape throughout the adiabatic change. In the case of an Ioffe trap, the radial potential may change from harmonic to linear (see Example 10.2), giving a small increase in the phase-space density. This effect arises because the population of the energy levels stays the same but the distribution of the levels changes—the energy levels of a harmonic potential are equally spaced ( $\hbar\omega$  apart), whereas in a linear potential the intervals between levels decrease with increasing energy.

(10.4) *Evaporative cooling*

A cloud of atoms has a Boltzmann energy distribution  $\mathcal{N}(E) = Ae^{-\beta E}$ , where  $1/\beta = k_B T$  and the normalisation constant  $A$  is found from

$$\mathcal{N}_{\text{total}} = A \int_0^\infty e^{-\beta E} dE = \frac{A}{\beta}.$$

The cloud has a total energy given by

$$E_{\text{total}} = A \int_0^\infty E e^{-\beta E} dE = \frac{A}{\beta^2} = \mathcal{N}_{\text{total}} k_B T.$$

Hence each atom has a mean energy  $\bar{E} = k_B T$ . In an evaporative cooling step all atoms with energy greater than  $\epsilon$  escape.

- (a) Calculate the fraction of atoms lost  $\Delta\mathcal{N}/\mathcal{N}_{\text{total}}$ .
- (b) Calculate the fractional change in the mean energy per atom.
- (c) Evaluate your expressions for cuts with  $\beta\epsilon = 3$  and 6. Compare the ratio of energy lost and the number of atoms removed in the two cases and comment on the implications for evaporative cooling.
- (d) The collision rate between atoms in the cloud is  $R_{\text{coll}} = n\bar{v}\sigma$ . Assuming that the collision cross-section  $\sigma$  is independent of the energy, show that  $R_{\text{coll}} \propto \mathcal{N}_{\text{total}}/E_{\text{total}}$  in a harmonic trapping potential. Show that the collision rate increases during evaporation in such a potential.

(10.5) *The properties at the phase transition*

A cloud of  $10^6$  rubidium atoms is confined in a harmonic trap with oscillation frequencies of  $\omega_z/2\pi = 16$  Hz and  $\omega_r/2\pi = 250$  Hz (and axial symmetry). Calculate the critical temperature  $T_C$  and estimate the density of the cloud at the phase transition.

(10.6) *Properties of a Bose condensate*

The properties of a Bose condensate were calculated in the text using the Thomas–Fermi approximation, which gives accurate results for large condensates. This exercise shows that minimising the energy in eqn 10.33 (a variational calculation) to find the equilibrium size leads to similar results.

In a spherically-symmetric trapping potential, rubidium atoms ( $M = 87$  a.m.u.) have an oscillation frequency of  $\omega/2\pi = 100$  Hz and hence

$a_{ho} = 1 \mu\text{m}$ . The atoms have a scattering length of  $a = 5 \text{ nm}$ . Calculate the following for a condensate with  $\mathcal{N}_0 = 10^6$  atoms.

- (a) Show that the repulsive interactions give a much greater contribution to the total energy than the kinetic term.
- (b) Use eqn 10.33 to find an expression for the equilibrium size  $r$  and evaluate it.
- (c) What is the density of the condensate?
- (d) Show that the contribution to the energy from the repulsive interactions represents two-fifths of the total.
- (e) Find an expression for the energy  $E$  (in terms of  $\hbar\omega$ ). (Note that this expression should have the same dependence on the various parameters as in eqn 10.42, but with a different numerical factor.) Evaluate  $E/k_B$ .
- (f) When the trapping potential is switched off suddenly the potential energy goes to zero and the repulsive interaction between the atoms causes the condensate to expand. After a few milliseconds almost all this energy (from the repulsive interactions) is converted into kinetic energy. Estimate the velocity at which the atoms fly outwards and the size of the condensate 30 ms after the trap is switched off.<sup>49</sup>

*Comment.* These estimates of the important physical parameters show that, although interactions have little influence on the phase transition (Bose–Einstein condensation occurs because of quantum statistics and is completely different to the ‘ordinary’ condensation of a vapour into a liquid caused by molecular interactions, e.g. steam into water), the properties of the condensate itself do depend on the interactions between atoms, e.g. the energy of the condensate is much larger than the zero-point energy of the ground state of the quantum harmonic oscillator.

(10.7) *The chemical potential and mean energy per particle*

- (a) Show that eqn 10.42 follows from the preceding equations in Section 10.6.

<sup>49</sup>The small size of Bose condensates makes them difficult to view directly, although this has been done in certain experiments. Generally, the condensate is released from the trap and allowed to expand before an image (e.g. Fig. 10.12).

- (b) In thermodynamics the chemical potential is the energy required to remove a particle from the system  $\mu = \partial E / \partial \mathcal{N}$ , where  $E$  is the total energy of the system. Show that  $E = \frac{5}{7} \mathcal{N} \mu$ .
- (10.8) *Expansion of a non-interacting condensate*  
 Although experiments are not carried out with a non-interacting gas it is instructive to consider what happens when  $a = 0$ . In this case the condensate has the same size as the ground state of a quantum harmonic oscillator (for any  $\mathcal{N}_0$ ) and the initial momentum along each direction can be estimated from the uncertainty principle. For atoms of the same mass as sodium (but with  $a = 0$ ) released from a trap with a radial oscillation frequency of 250 Hz and a frequency of 16 Hz for axial motion, estimate roughly the time of flight at which the cloud is spherical.
- (10.9) *Excitations of a Bose condensate*  
 The vibrational modes of a condensate can be viewed as compression waves that form a standing wave within the condensate; hence these modes have frequencies of the order of the speed of sound divided by the size of the condensate  $v_s/R$ . Show that this collective motion of the condensate occurs at a comparable frequency to the oscillation of individual atoms in the magnetic trap.
- (10.10) *Derivation of the speed of sound*  
 The time-dependent Schrödinger equation for the wavefunction of an atom in a Bose–Einstein condensate in a uniform potential is

$$i\hbar \frac{d\psi}{dt} = -\frac{\hbar^2}{2M} \nabla^2 \psi + g|\psi|^2 \psi,$$

where, for simplicity, the potential has been taken as zero ( $V = 0$ ). The wavefunction  $\psi = \psi_0 e^{-i\mu t/\hbar}$  satisfies this equation with a chemical potential

$$\mu = g|\psi_0|^2.$$

The trial wavefunction with small fluctuations can be written as

$$\begin{aligned}\psi &= [\psi_0 + ue^{i(kx-\omega t)} + v^*e^{-i(kx-\omega t)}] e^{-i\mu t/\hbar} \\ &= \psi_0 e^{-i\mu t/\hbar} + \delta\psi(t),\end{aligned}$$

where the amplitudes  $|u|$  and  $|v|$  are small compared to  $|\psi_0|$ .

- (a) Show that substituting this function into the Schrödinger equation and making suitable

approximations leads to the same zeroth-order approximation for the chemical potential given above and

$$\begin{aligned}i\hbar \frac{d}{dt}(\delta\psi(t)) \\ = \frac{\hbar^2 k^2}{2M} \delta\psi(t) + g|\psi_0|^2 2\delta\psi(t) + g\psi_0^2 \delta\psi^*(t).\end{aligned}\quad (10.47)$$

- (b) Show that equating terms with the same time dependence leads to two coupled equations for  $u$  and  $v$  that, in matrix form, are

$$\begin{pmatrix} \epsilon_k + 2g|\psi_0|^2 - \mu & g\psi_0^2 \\ g(\psi_0^*)^2 & \epsilon_k + 2g|\psi_0|^2 - \mu \end{pmatrix} \begin{pmatrix} u \\ v \end{pmatrix} = \hbar\omega \begin{pmatrix} u \\ -v \end{pmatrix},$$

where  $\epsilon_k = \hbar^2 k^2 / 2M$ .

- (c) Hence show that  $u$  and  $v$  are solutions of the matrix equation

$$\begin{pmatrix} \epsilon_k + \mu - \hbar\omega & g\psi_0^2 \\ g(\psi_0^*)^2 & \epsilon_k + \mu + \hbar\omega \end{pmatrix} \begin{pmatrix} u \\ v \end{pmatrix} = 0.$$

From the determinant of this matrix, find the relation between the angular frequency of the small oscillations  $\omega$  and the magnitude of their wavevector  $k$  (the dispersion relation). Show that for low energies this gives the same expression for the speed of sound  $\omega/k$  found in Section 10.7.1.<sup>50</sup>

### (10.11) Attractive interactions

In certain hyperfine states, the scattering length  $a$  of alkali metal atoms changes with the applied magnetic field and this feature has been used to perform experiments in which the atoms have attractive interactions  $a < 0$ .

Show that eqn 10.33 can be written in the form

$$\frac{4}{3} \frac{E}{\hbar\omega} = x^{-2} + x^2 + Gx^{-3}.$$

By plotting graphs for various values of the parameter  $G$  between 0 and  $-1$ , estimate the lowest value of  $G$  for which there exists a minimum in the energy as a function of  $x$ . For an atomic species with a scattering length of  $a = -5 \text{ nm}$  in a trap where  $a_{ho} = 2 \mu\text{m}$ , estimate the maximum number of atoms that a Bose condensate can contain without collapsing.

<sup>50</sup>After problem devised by Professor Keith Burnett, Physics graduate class, University of Oxford.

# 11

## Atom interferometry

|  |     |
|--|-----|
| 11.1 Young's double-slit experiment    | 247 |
| 11.2 A diffraction grating for atoms   | 249 |
| 11.3 The three-grating interferometer  | 251 |
| 11.4 Measurement of rotation           | 251 |
| 11.5 The diffraction of atoms by light | 253 |
| 11.6 Conclusions                       | 257 |
| Further reading                        | 258 |
| Exercises                              | 258 |

The possibility of interferometry with atoms follows directly from wave–particle duality. The wave-like propagation of particles, such as atoms, means that they undergo interference and diffraction in an analogous way to light. This chapter explains how such matter waves have been used in interferometers that measure rotation and gravitational acceleration to a precision comparable with the best optical instruments. As in many important developments in physics, atom interferometry relies on simple principles—the first part of this chapter uses only elementary optics and the de Broglie relation

$$\lambda_{dB} = \frac{h}{p} \quad (11.1)$$

for the wavelength of the matter wave associated with a particle of momentum  $p = Mv$ . This relation between wavelength and momentum also applies to light waves and the momentum of photons, but here we shall use  $\lambda_{dB}$  exclusively for matter waves and  $\lambda$ , without a subscript, for the wavelength of light.

A sodium atom with velocity  $v = 1000 \text{ m s}^{-1}$  (typical of a thermal beam) has  $\lambda_{dB} = 2 \times 10^{-11} \text{ m}$ —about 1/30 000 times the wavelength of visible light, and comparable to that of X-ray radiation. Gratings with lines sufficiently close together to diffract such short wavelengths can now be made by nano-fabrication, i.e. techniques for making structures on scales smaller than  $1 \mu\text{m}$ .<sup>1</sup> Neutrons also have short de Broglie wavelengths but, unlike atoms, they pass through crystals and diffract from the closely-spaced planes of atoms. Electrons also diffract from crystals and their wave properties were observed long ago by Davisson and Germer in their classic experimental confirmation of wave–particle duality in quantum physics. This previous work with neutrons and electrons is mentioned here simply to show that matter-wave interferometry has a long history, and both neutron and electron diffraction are now highly-developed techniques used in condensed matter physics (Blundell 2001). The more recent matter-wave experiments with atoms described in this chapter should not be regarded as tests of already well-known quantum behaviour; rather their importance lies in their ability to make more precise measurements than other techniques in certain applications.

Consideration of the familiar Young's double-slit experiment provides a good introduction to the basic ideas of matter-wave experiments with atoms and gives a feeling for the size of the physical parameters. We shall then extend the treatment to a diffraction grating (multiple slits) and the design of an interferometer that measures the rate of rotation by

<sup>1</sup> It might seem advantageous to use laser-cooled atoms with larger  $\lambda_{dB}$ , but we shall see that this is not true.

the Sagnac effect. These matter-wave experiments operate on the same principles as similar experiments with light because the atoms remain in the ground state and propagate as simple waves. It will be assumed that the reader understands the standard treatment of Fraunhofer diffraction in optics (Brooker 2003) and key results will be quoted here rather than derived. After the discussion of the work with nano-fabricated slits and gratings, we shall look at the use of laser light to manipulate the atom's momentum using methods closely related to laser cooling. These laser techniques make use of the atom's internal energy levels—something that is not possible for electrons or neutrons.

## 11.1 Young's double-slit experiment

Young originally carried out his double-slit experiment to test the wave nature of light and his simple arrangement still finds practical use in measurements of the coherence of light.<sup>2</sup> Figure 11.1 shows a typical experimental layout. Waves propagate from the source slit S through the two slits,  $\Sigma_1$  and  $\Sigma_2$ , to a point P in the detection plane.<sup>3</sup> The amplitude of the light at any point on the detection plane equals the sum of the electric field amplitudes that arrive at that point via slits  $\Sigma_1$  and  $\Sigma_2$ . In any interference or diffraction calculation the resultant amplitude at the final point is determined by summing the contributions from all possible paths *taking account of the phase*. For the double slits

<sup>2</sup>The double slits also form the basis of many theoretical discussions of fundamental issues in quantum mechanics, such as why we cannot know which slit the photon went through and still observe interference.

<sup>3</sup>Young's fringes are not localised on this plane but can be seen throughout the far-field region.

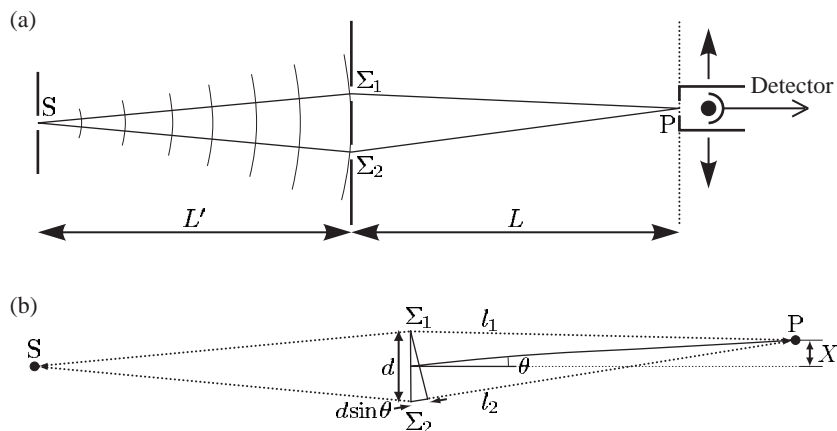


**Fig. 11.1** (a) The apparatus for observing interference from double slits. The light diffracted by the source slit propagates through the two slits  $\Sigma_1$  and  $\Sigma_2$  and onto the plane P. The interference fringes can be seen with the eye (with the aid of a magnifying eyepiece if necessary), but to further the analogy with atom optics experiments the apparatus is drawn with a detector such as a photodiode or photomultiplier. A narrow slit in front of the detector gives good spatial resolution; this slit and the detector scan across the fringes, as indicated. The light comes from a lamp, or laser; in a matter-wave experiment an atomic oven creates a beam of atoms collimated by the source slit (as shown in Fig. 11.2). (b) The difference in the distance from  $\Sigma_1$  to P and from  $\Sigma_2$  to P is  $d \sin \theta$ , where  $d$  is the slit separation. The angle  $\theta$  and the distance  $X$  in the detection plane are related by  $X = L \tan \theta$ . The transverse distances are drawn greatly exaggerated for clarity; for the typical conditions given in the text the fringes have an angular separation of  $2 \times 10^{-3}$  rad.

$$^4l_1 = \overline{S\Sigma_1} + \overline{\Sigma_1P}$$

and  $l_2 = \overline{S\Sigma_2} + \overline{\Sigma_2P}$ . we define  $l_1$  as the distance from S to P via  $\Sigma_1$ , and similarly  $l_2$  for the path through slit  $\Sigma_2$ , as shown by the dotted lines in Fig. 11.1(b).<sup>4</sup> Slits of the same size contribute equally to the total amplitude at a point on the plane P:

$$E_P \propto E_0 \left( e^{-i2\pi l_1/\lambda} + e^{-i2\pi l_2/\lambda} \right). \quad (11.2)$$

The intensity is proportional to the square of this amplitude,  $I \propto |E|^2$ , so that

$$I = I_0 \cos^2 \left( \frac{\phi}{2} \right). \quad (11.3)$$

Here  $\phi = 2\pi(\ell_2 - \ell_1)/\lambda$  is the phase difference between the two arms and  $I_0$  is the maximum intensity. Bright fringes occur at positions in the detection plane where the contributions from the two paths interfere constructively; these correspond to  $\phi = n2\pi$ , with  $n$  an integer, or equivalently

$$\ell_2 - \ell_1 = n\lambda. \quad (11.4)$$

To find the spacing of the fringes in the plane of observation we define the coordinate  $X$  measured perpendicular to the long axis of the slits in the plane P. In terms of the small angle defined in Fig. 11.1(b) this becomes

$$X = L \tan \theta. \quad (11.5)$$

A similar small angle approximation allows us to express the path length difference in Fig. 11.1(b) as

$$\ell_2 - \ell_1 = \Delta l + d \sin \theta. \quad (11.6)$$

<sup>5</sup>Elementary treatments often assume that the slits are equidistant from the source ( $\Delta l = 0$ ) so that the phase of the wave is the same at each slit (equivalent to having a plane wavefront before the slits). This assumption simplifies the algebra but it is *not* a necessary condition for Fraunhofer diffraction with light, or with matter waves. (A more detailed description of the assumptions such as  $L \gg d$  can be found in textbooks on optics, e.g. Brooker (2003).)

Here  $\Delta l = \overline{S\Sigma_1} - \overline{S\Sigma_2}$  is the path difference before the slits.<sup>5</sup> The path length difference from the two slits of separation  $d$  to P is  $d \sin \theta$ . The last three equations give the spacing of the fringes as

$$\Delta X = \frac{L \lambda}{d}. \quad (11.7)$$

For an experiment with visible light of wavelength  $\lambda = 6 \times 10^{-7}$  m, slits of separation  $d = 3 \times 10^{-4}$  m and  $L = 1$  m, the fringes have a spacing of  $\Delta X = 2$  mm and can be clearly seen by eye. The treatment so far assumes a small source slit at S that acts like a point source to illuminate the double slits coherently. The condition for this is that the double slits fall within the angular spread of the light diffracted from the source slit (Brooker 2003). The diffraction from a slit of width  $w_S$  has an angular spread  $\theta_{\text{diff}} \simeq \lambda/w_S$ . Therefore coherent illumination of two slits at a distance  $L'$  from this source slit requires  $L' \theta_{\text{diff}} \geq d$ , or

$$w_S \leq \frac{\lambda L'}{d}. \quad (11.8)$$

For  $L' = 0.1$  m and the values of  $\lambda$  and  $d$  used previously, we find  $w_S \leq 2 \times 10^{-4}$  m. Such slits are made by standard techniques and we know that Young's experiment with light is relatively straightforward to

carry out in the laboratory. Experiments with short-wavelength matter waves require the smallest available structures with slits on the scale of 100 nm.

A double-slit experiment was carried out with a beam of helium atoms in the metastable  $1s2s\ ^3S_1$  level that lies 20 eV above the ground state (Carnal and Mlynek 1991). This matter-wave experiment had the same layout as that shown in Fig. 11.1, although with atoms the interferometer has to be set up inside a vacuum chamber. Exercise 11.2 goes through the application of the equations given in this section to the calculation of the slit widths required to observe interference fringes with He\*. Metastable helium is very suitable for this experiment, firstly because it has a fairly long  $\lambda_{dB}$  and secondly when metastable atoms hit a surface they release sufficient energy to eject electrons; counting these charged particles allows the arrival of individual atoms to be detected with high efficiency. Further discussion of double-slit experiments can be found in the quantum mechanics book by Rae (1992); he uses a neutron interference experiment as an example of wave–particle duality.

## 11.2 A diffraction grating for atoms

Figure 11.2 shows an apparatus with a highly-collimated atom beam of sodium incident upon a transmission grating. The experimenters used a remarkable grating with slits only 50 nm wide, spaced 100 nm apart—equal widths of the bars and the gaps between them. Etching these very thin bars and their delicate support structure represents the state of the art in nano-fabrication. Figure 11.2(b) shows the diffraction pattern obtained with a mixture of sodium atoms and molecules, and Fig. 11.2(c) shows the diffraction of a beam of sodium molecules. The diffraction peaks of  $\text{Na}_2$  have about half the spacing of those for the Na atoms, as expected from the de Broglie relation for particles of twice the mass (for similar velocities).

Researchers recently exploited this property of these special gratings to make the first experimental observation of the very weakly-bound state of two helium atoms (Schöllkopf and Toennies 1994). Other methods of detection dissociate the very tenuously-bound  $\text{He}_2$  molecule. The gratings work well with helium and atomic beams of inert gases, since they do not clog the slits in the same way as sodium. However, despite the practical difficulties of working with these very fragile structures, a recent experiment used a grating to diffract  $\text{C}_{60}$  molecules—so-called Buckyballs (Arndt *et al.* 1999, Nairz *et al.* 2003). This demonstration of the wave-like nature of such massive particles prompts the following question: ‘What is the largest object for which such quantum interference can be observed?’<sup>6</sup> This question relates to Schrödinger’s well-known example of a cat that may be in a superposition of two states (‘alive’ and ‘dead’). To observe interference an object must exist in a superposition of the two states:  $|1\rangle$  in which it goes through slit  $\Sigma_1$  and  $|2\rangle$  the state where it goes through slit  $\Sigma_2$ . Nothing within standard

<sup>6</sup>This means quantum effects in the motion, or external degrees of freedom, and not quantisation of the internal energy levels.

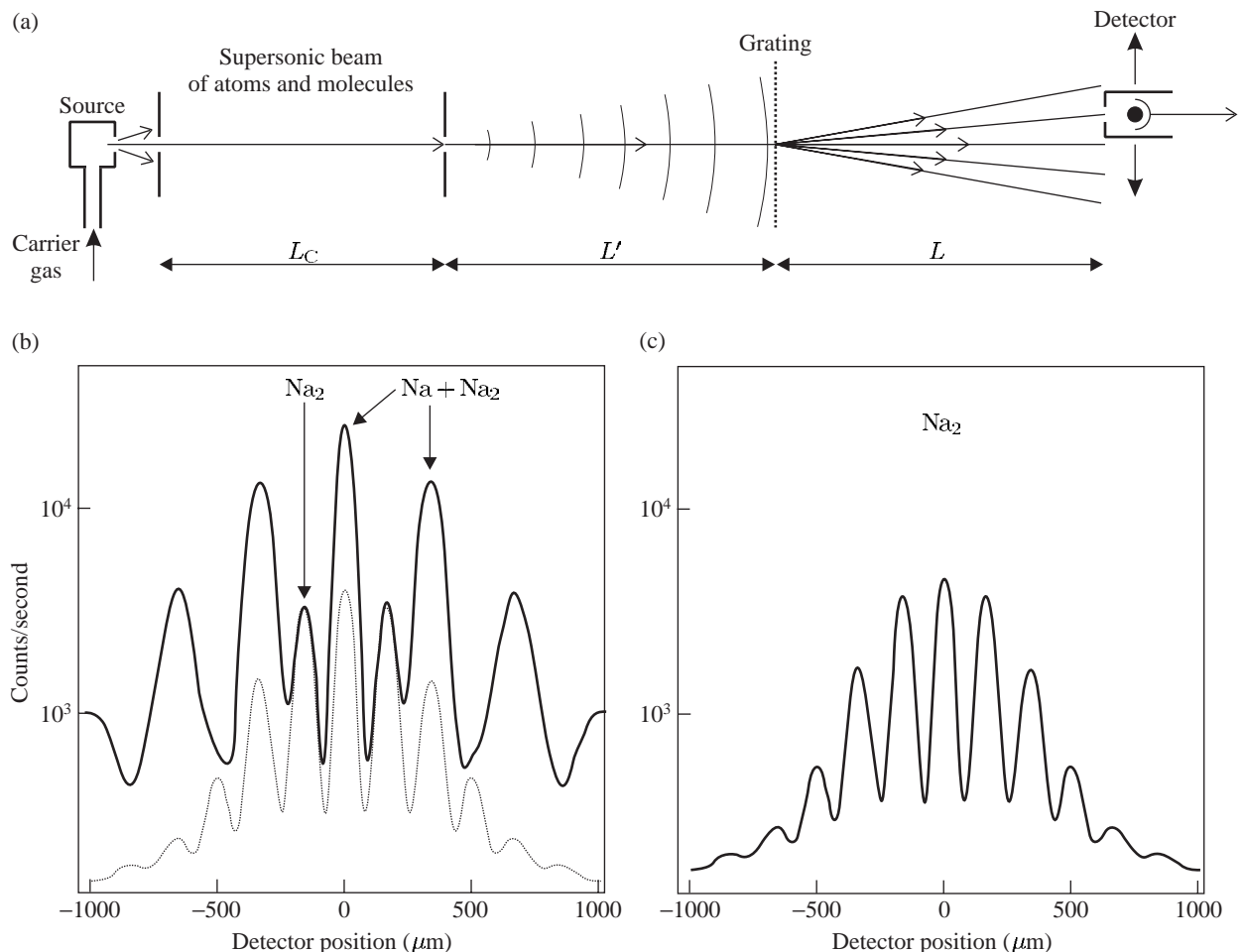


**Fig. 11.2** (a) Diffraction of a collimated atomic beam by a grating. To observe the diffraction of matter waves from the grating the source slit must be sufficiently narrow to make the matter waves coherent across several of the slits in the grating. This is the same requirement as described in the previous section for Young's double slits, and Exercise 11.1 looks at the relation of the pattern with multiple slits to that observed with just two slits. For the grating there is an additional requirement that the angular spread of the incident beam must be less than the angle between the diffracted orders, otherwise they cannot be distinguished. In this apparatus the slit widths were about  $20\ \mu\text{m}$ , the slits in the nano-fabricated grating had a spacing of  $100\ \text{nm}$  and all the distances  $L_C$ ,  $L'$  and  $L$  were about  $1\ \text{m}$ . (b) The diffraction of a collimated beam of sodium atoms and molecules by the grating. (c) The diffraction pattern for a beam that contains only  $\text{Na}_2$  molecules (this pattern is also shown as a dotted curve in (b)). The peaks for the molecules have half the spacing of those for the atoms as expected for twice the mass—the atoms and molecules have almost the same velocity in the supersonic flow because they are both carried along in a stream of krypton gas that flows through the heated oven containing sodium metal. This carrier gas gives a supersonic beam with a much lower velocity spread  $\Delta v/v \simeq 0.03$  than would be obtained from an effusive source of thermal atoms. The sodium atoms were removed from the beam by the resonant radiation pressure from a laser beam (not shown) perpendicular to the supersonic beam—scattering three or more photons was sufficient to deflect atoms out of the beam. From Chapman *et al.* (1995). Copyright 1995 by the American Physical Society.

quantum mechanics tells us that we cannot put something as large as a cat into a quantum superposition, if it is completely isolated from external perturbations. However, the heaviest object that can be used in a practical double-slit experiment in the foreseeable future is far lighter than a cat, but considerably heavier than what has been achieved so far. Continued work on matter-wave interference of larger and larger objects will be of great interest since it probes the boundary between quantum and classical physics.

### 11.3 The three-grating interferometer

Figure 11.3 shows an arrangement of three diffraction gratings a distance  $L$  apart. A highly-collimated beam of sodium atoms propagates through this three-grating interferometer onto a detector for atoms.<sup>7</sup> Diffraction at the first grating  $G_1$  splits the beam—only the zeroth- and first-order diffraction orders ( $0$  and  $\pm 1$  orders) have been drawn for simplicity. The second grating  $G_2$  gives diffraction through the same angles as  $G_1$ , so that some of the paths meet up at the plane of the third grating  $G_3$ , e.g. the  $0$  and  $+1$  orders from  $G_1$  are both diffracted by  $G_2$  to form the parallelogram  $ABPC$ , as shown in Fig. 11.3(a). The detector records the flux of atoms along one of the possible output directions coming from  $P$ . This arrangement closely resembles a Mach–Zehnder interferometer for light, with a smaller angle between the two arms because of the achievable grating spacing. For two-beam interference the signal has the same form as eqn 11.3. In these interferometers the sum of the fluxes of the atoms, or light, in the two possible output directions equals a constant, i.e. when a certain phase difference between the arms of the interferometer gives destructive interference at the detector then the flux in the other output direction has a maximum.

<sup>7</sup>The detector for sodium has a hot wire, heated by a current flowing through it, that runs parallel to the slits. The sodium atoms ionize when they hit the hot surface of the wire and the ejected electrons create a measurable current.

### 11.4 Measurement of rotation

The Mach–Zehnder interferometer for matter waves shown in Fig. 11.3 measures rotation precisely, as explained in this section.<sup>8</sup> To calculate the phase shift caused by rotation in a simple way we represent the interferometer as a circular loop of radius  $R$ , as in Fig. 11.4. The wave travelling at speed  $v$  from the point  $S$  takes a time  $t = \pi R/v$  to propagate around either arm of the interferometer to the point  $P$  diametrically opposite  $S$ . During this time the system rotates through an angle  $\Omega t$ , where  $\Omega$  is the angular frequency of rotation about an axis perpendicular to the plane of the interferometer. Thus the wave going one way round the loop has to travel  $\Delta l = 2\Omega R t$  further than the wave in the other arm of the interferometer. This corresponds to  $\Delta l/\lambda_{dB}$  extra wavelengths, or a phase shift of

$$\Delta\phi = \frac{2\pi}{\lambda_{dB}} \times 2\Omega R \times \frac{\pi R}{v}. \quad (11.9)$$

<sup>8</sup>For light a different configuration called a Sagnac interferometer is generally used to measure rotation but the principles are similar.

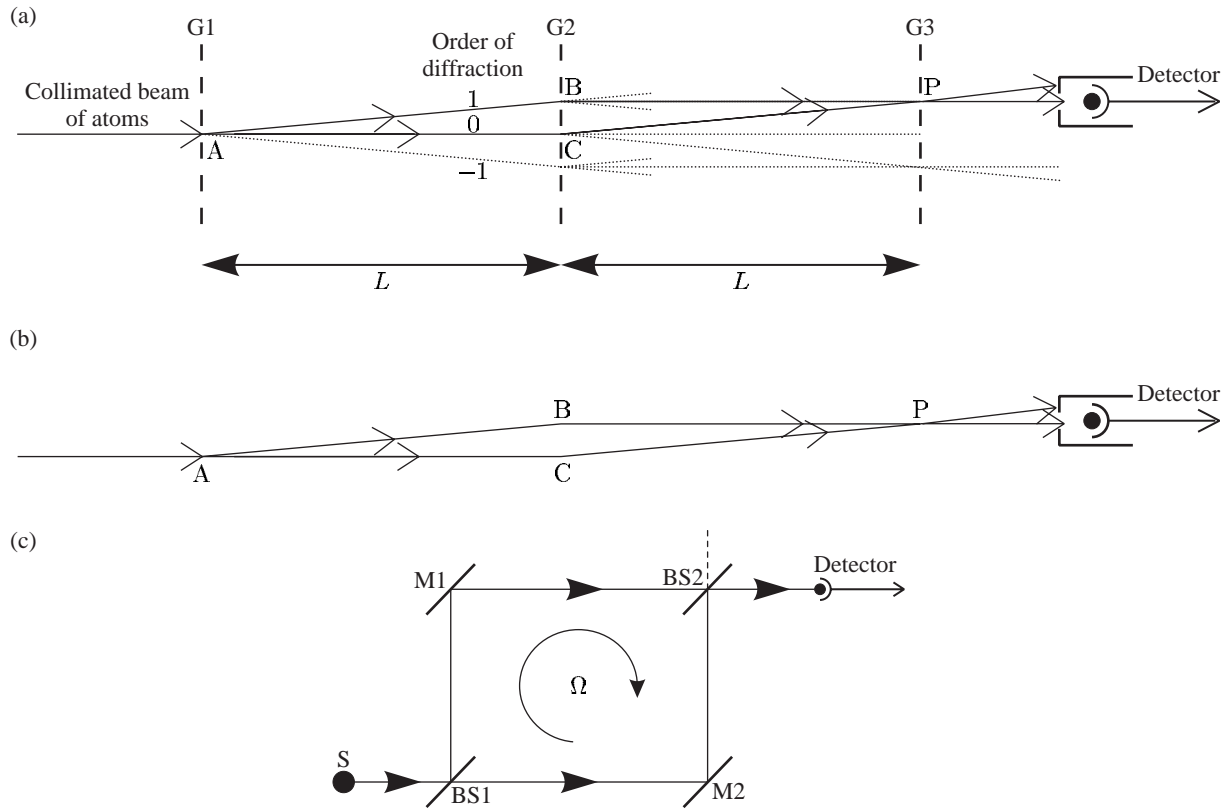


**Fig. 11.3** (a) An interferometer formed by three diffraction gratings spaced by a distance  $L$  along the atomic beam. A collimated beam of atoms is produced, as shown in Fig. 11.2. Waves diffracted at the first grating  $G_1$  split again at  $G_2$ , so that some of the paths meet at  $G_3$ . Only the 0 and  $\pm 1$  diffraction orders are shown and to further simplify the diagram some of the possible paths between  $G_2$  and  $G_3$  have not been drawn completely. Contributions to the amplitude at  $P$  arrive from  $A$ , via either  $B$  or  $C$ . The detector must be sufficiently far from  $G_3$  that it picks up only one of two possible output directions. (The parallelogram  $ABPC$  is just one of many closed loops formed by the three gratings; some others are indicated by dotted lines. With the detector at the position shown, the three gratings act as a Mach-Zehnder interferometer, as shown in (b). The diffraction gratings behave both as beam splitters and as deflectors (mirrors) for the matter waves (for small angles). (c) A Mach-Zehnder interferometer for light—the optical system equivalent to the three-grating interferometer. The incident wave hits beam splitter  $BS_1$  and the reflected and transmitted amplitudes reflect off mirrors  $M_1$  and  $M_2$ , respectively, so that their paths meet again at  $BS_2$ . Interference between the two paths leads to a detected intensity  $I_D = \frac{1}{2}I_0\{1 + \cos(\phi + \Delta\phi)\}$  (cf. eqn 11.3). The phase  $\phi$  that arises from path length differences and phase shifts on reflection at the mirrors is assumed to be fixed and  $\Delta\phi$  represents the extra phase that is measured; e.g. for an interferometer that rotates at angular frequency  $\Omega$  about an axis perpendicular to the plane of the instrument  $\Delta\phi \propto \Omega$ , so the instrument measures rotation, as shown in Section 11.4.

The loop has area  $A = \pi R^2$ , so that

$$\Delta\phi = \frac{4\pi}{\lambda_{dB}v} \times \Omega A. \quad (11.10)$$

A more rigorous derivation, by integration around a closed path, shows that this equation applies for an arbitrary shape, e.g. the square interferometer of Fig. 11.3(c). Comparison of this phase shift for matter waves of velocity  $v$  with that for light  $\Delta\phi_{\text{light}}$ , for an interferometer of the same

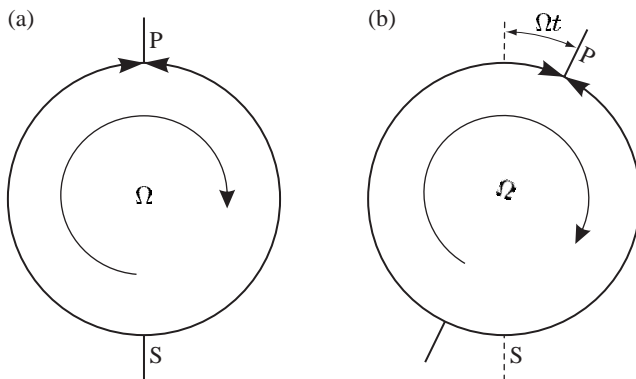


**Fig. 11.4** (a) A simplified diagram of an interferometer where the waves propagate from S to P. (b) Rotation at angular frequency  $\Omega$  about an axis perpendicular to the plane of the interferometer makes one path  $\Omega t$  longer and the other shorter by the same amount, where  $t$  is the time taken for a wave to travel from S to P. This leads to the phase shift in eqn 11.10.

area  $A$ , shows that

$$\Delta\phi = \frac{\lambda c}{\lambda_{dB} v} \times \Delta\phi_{\text{light}} = \frac{Mc^2}{\hbar\omega} \times \Delta\phi_{\text{light}}. \quad (11.11)$$

The ratio equals the rest mass of the atom divided by the energy of each photon and has a value of  $\Delta\phi/\Delta\phi_{\text{light}} \sim 10^{10}$  for sodium atoms and visible light. This huge ratio suggests that matter-wave interferometers have a great advantage, but at the present time they only achieve comparable results to conventional interferometers with light. Conventional interferometers with light make up the ground by:

- (a) having much larger areas, i.e. a distance between the arms of metres instead of a fraction of a millimetre achieved for matter waves;
- (b) the light goes around the loop many times;<sup>9</sup>
- (c) lasers give a much higher flux than the flux of atoms in a typical atomic beam. For example, in the scheme shown in Fig. 11.2 only a small fraction of the atoms emitted from the source end up in the highly-collimated atomic beam; as a source of matter waves the atomic oven is analogous to an incandescent tungsten light bulb rather than a laser.<sup>10</sup>

<sup>9</sup>Laser gyros use high-reflectivity mirrors or optical fibres.

<sup>10</sup>The atom interferometer based on Raman transitions (described in Section 11.5.1) does not require such a highly-collimated atomic beam, and that technique has achieved precise measurements of rotation.

## 11.5 The diffraction of atoms by light

A standing wave of light diffracts matter waves, as illustrated in Fig. 11.5. This corresponds to a role reversal as compared to optics in which matter, in the form of a conventional grating, diffracts light. This section explains how this light field created simply by the retro-reflection of a laser beam from a mirror is used in atom optics. The interaction of atoms with a standing wave leads to a periodic modulation of the atomic energy levels by an amount proportional to the intensity of the light, as explained in Section 9.6.<sup>11</sup> The light shift of the atomic energy levels in the standing wave introduces a phase modulation of the matter waves. An atomic wavepacket  $\psi(x, z, t)$  becomes  $\psi(x, z, t) e^{i\Delta\phi(x)}$  immediately after passing through the standing wave; it is assumed that

<sup>11</sup>The laser has a frequency  $\omega$  sufficiently far from the atom's transition frequency  $\omega_0$  that spontaneous emission has a negligible effect, yet close enough for the atoms to have a significant interaction with the light.

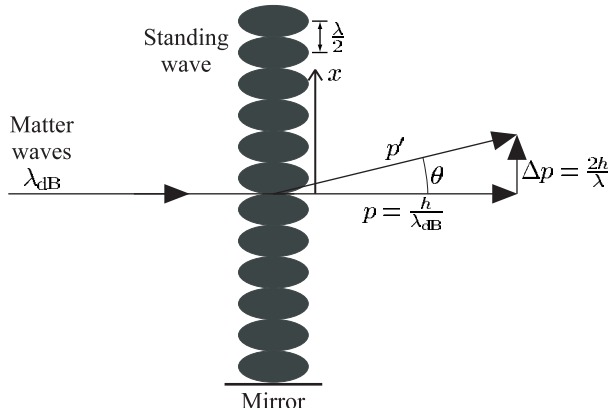


**Fig. 11.5** The diffraction of atoms by a standing wave light field. The angle of the first order of diffraction  $\theta$  is related to the grating period  $d$  by  $d \sin \theta = \lambda_{dB}$ . For the standing wave  $d = \lambda/2$ , so  $\sin \theta = 2\lambda_{dB}/\lambda$ . This diffraction can be regarded as a scattering process where an atom of momentum  $p$  receives an impulse that gives it transverse momentum  $\Delta p$  and deflects it by an angle  $\theta$  given by  $\tan \theta = \Delta p/p$ .

$\psi(x, z, t)$  changes smoothly over a length scale much greater than  $\lambda/2$ . This phase modulation has a spatial period of  $\lambda/2$ , where  $\lambda$  is the wavelength of the *light* not the matter waves. The matter waves accumulate an additional phase  $\Delta\phi(x) = \phi_0 \cos^2(2\pi x/\lambda)$  from the light shift. This phase grating diffracts the matter waves at angles determined by

$$d \sin \theta = n\lambda_{dB}, \quad (11.12)$$

<sup>12</sup>This is obvious from a treatment of diffraction by Fourier transforms (Brooker 2003).

where  $d = \lambda/2$ ,  $n$  is an integer and  $\lambda_{dB}$  gives the matter wavelength. Gratings with the same spacing  $d$  diffract waves by the same angles  $\theta$  whether they work by phase or amplitude modulation of the incident wave,<sup>12</sup> although not with the same relative intensities in different orders. Thus there is no fundamental difference between nano-fabricated absorption gratings and the use of standing waves. Interferometers that use three standing waves in the same arrangement as in Fig. 11.3 have similar properties to an instrument with three gratings etched from solid material. The mirrors that retro-reflect the light to form the standing waves must be mounted rigidly so that vibrations do not wash out the interference fringes (similarly, the nano-fabricated gratings must be held very stable). Standing waves of visible light give diffraction angles about three times less than those from the best nano-fabricated gratings; however, such gratings transmit all the atoms, whereas nano-fabricated gratings transmit much less than the 50% that might be expected for bars that have a width equal to the gaps between them—the very thin bars require an elaborate support structure of cross-bars that reduces the open area. Also, material gratings eventually get clogged up when used with alkali metals.

The diffraction of the matter waves by a standing wave has an alternative physical interpretation in terms of the scattering of light. The diffraction condition in eqn 11.12 can be written as  $\tan \theta \simeq n\hbar G/p$  (taking  $\tan \theta \simeq \sin \theta$  for small angles), where  $p$  is the longitudinal momentum of the atoms,  $G = 4\pi/\lambda$  is the characteristic wavevector of a structure with spacing  $\lambda/2$  (i.e. the grating) and  $\hbar G = 2h/\lambda$  equals the momentum of two photons. Thus, in the diffraction from the standing wave, atoms

receive a transverse kick from  $2n$  photons, as illustrated in Fig. 11.5, e.g. first order arises from absorption from one of the counter-propagating beams and stimulated emission into the other beam. This coherent process, with no spontaneous emission, has some similarities with the Raman transition shown in Fig. 11.6.<sup>13</sup>

### 11.5.1 Interferometry with Raman transitions

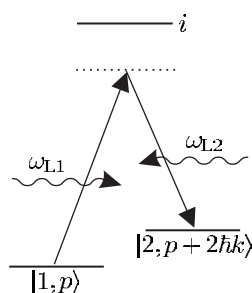
The description of the diffraction of two-level atoms by a standing wave, in the previous section, as a coherent scattering process that imparts twice the photon momentum  $2\hbar/\lambda$ , or multiples thereof, to the atom has links with the very powerful method for manipulating the atom's momentum by Raman transitions shown in Fig. 11.6. Two laser beams at frequencies  $\omega_{L1}$  and  $\omega_{L2}$  drive a coherent Raman transition between states  $|1\rangle$  and  $|2\rangle$  when

$$\hbar(\omega_{L1} - \omega_{L2}) = E_2 - E_1. \quad (11.13)$$

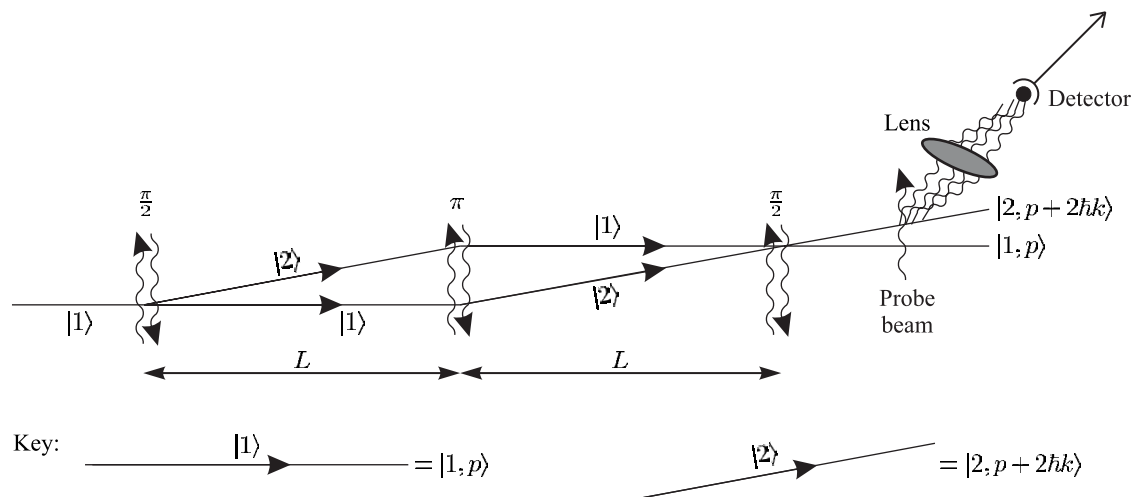
No population goes into the intermediate state  $|i\rangle$  in this coherent transition because neither of the two beams excites a single-photon transition (see Appendix E). The Raman transition couples states  $|1\rangle$  and  $|2\rangle$  and drives Rabi oscillations between them, e.g. when the atom starts in either  $|1\rangle$  or  $|2\rangle$ , a  $\pi/2$ -pulse creates a superposition of  $|1\rangle$  and  $|2\rangle$  with equal amplitudes. Raman laser beams propagating in opposite directions (as in Fig. 11.6) change the atom's momentum during the transition.<sup>14</sup> The absorption of a photon of wavevector  $\mathbf{k}_1$  and the stimulated emission of one in the opposite direction  $\mathbf{k}_2 \simeq -\mathbf{k}_1$  gives the atom two recoil kicks in the same direction. This process couples the state  $|1, p\rangle$  to  $|2, p + 2\hbar k\rangle$ . The bra(c)ket notation denotes the |internal state, momentum) of the atoms. The Raman resonance condition in eqn 11.13 depends sensitively on the atom's velocity  $v$  for counter-propagating beams and this provides the basis for the Raman cooling of atoms (Section 9.8). For interferometry this velocity selectivity is a complicating factor and we shall assume that the Raman pulses are sufficiently short<sup>15</sup> to drive transitions over the whole range of velocity components along the laser beam.

Figure 11.7 shows a complete Raman interferometer where the atoms start in  $|1, p\rangle$  and travel through three Raman interaction regions. In

<sup>13</sup>Scattering in a standing wave changes the atomic momentum (external state) but not the internal state.



**Fig. 11.6** A Raman transition with two laser beams of frequencies  $\omega_{L1}$  and  $\omega_{L2}$  that propagate in opposite directions. Equation 11.13 gives the resonance condition, ignoring the effects of the atom's motion (Doppler shift). The Raman process couples  $|1, p\rangle$  and  $|2, p + 2\hbar k\rangle$  so that an atom in a Raman interferometer has a wavefunction of the form  $\psi = A|1, p\rangle + B|2, p + 2\hbar k\rangle$  (usually with either  $B = 0$  or  $A = 0$  initially).



**Fig. 11.7** An interferometer formed by Raman transitions. As atoms traverse the three interaction regions they experience a  $\pi/2-\pi-\pi/2$  sequence of Raman pulses that split, deflect and recombine the atomic wavepackets. Each interaction region has two counter-propagating beams at frequencies  $\omega_{L1}$  and  $\omega_{L2}$ , as in Fig. 11.6. In this Mach-Zehnder interferometer the eigenstates with transverse momentum  $p$  and  $p + 2\hbar k$  are associated with the different internal atomic states  $|1\rangle$  and  $|2\rangle$ , respectively; as indicated at the bottom of the figure,  $|1\rangle$  is associated with  $p \approx 0$  (horizontal line) and  $|2\rangle$  with  $p \approx 2\hbar k$  (slanted line). Therefore at the output it is only necessary to measure the internal state of the atoms, e.g. by exciting a transition from  $|2\rangle$  and detecting the fluorescence, rather than allowing beams with different momenta to become spatially separated, as in Fig. 11.3. (The separation of the paths has been exaggerated for clarity.)

the first interaction the atom experiences a  $\pi/2$ -pulse that puts it into the superposition

$$|\psi\rangle = \{ |1, p\rangle + e^{i\phi_1} |2, p + 2\hbar k\rangle \}. \quad (11.14)$$

<sup>16</sup>This phase, and the other similar phases that arise at each interaction, lead to an offset in the final output which is not important. But these phases must remain constant in time, otherwise the interference ‘washes out’.

The phase factor depends on the relative phase of the two laser beams.<sup>16</sup> These two states separate, as shown in Fig. 11.7, and this first region corresponds to a beam splitter for matter waves. After a free-flight through a distance  $L$  the atom enters the middle interaction region where it undergoes a  $\pi$ -pulse that acts on both arms of the interferometer to swap the states  $|1, p\rangle \leftrightarrow |2, p + 2\hbar k\rangle$ . (In this apparatus the transit time for the atom to pass through the laser beams determines the duration of the Raman interaction.) The paths come back together after a further distance  $L$  and the final  $\pi/2$ -pulse acts as the beam splitter that mixes the wavepackets to give interference. The complete  $\pi/2-\pi-\pi/2$  sequence gives a Mach-Zehnder interferometer. A comparison of Figs 11.3 and 11.7 shows that the Raman scheme resembles the Mach-Zehnder interferometer more closely than the three-grating device; the Raman scheme does not direct any amplitude in unwanted directions and the middle interaction region in the Raman interferometer acts just like a mirror to change the direction (transverse momentum) of both paths through a small angle.<sup>17</sup>

A Raman pulse and standing light wave give the same opening angle between the arms for a given wavelength of laser light and both

<sup>17</sup>In a three-grating interferometer only a fraction of the amplitude goes in the required direction. Note, however, that the simple treatment of standing waves assumed the ‘thin’ grating approximation, but often the interaction between the matter waves and light takes place over a sufficiently long distance that Bragg diffraction occurs (as in crystals).

schemes use light whose frequency is detuned from the atomic transition to avoid spontaneous emission. A crucial difference between these methods arises in the detection. The three-grating apparatus, with standing waves or nano-fabricated structures, distinguishes the two outputs by their different directions. Therefore the three-grating devices require a highly-collimated atomic beam at the input whose angular divergence is less than the angle between the two output directions  $\theta_{\text{diff}}$ . The output channels of the Raman scheme are the two different states  $|1, p\rangle$  and  $|2, p + 2\hbar k\rangle$ , as shown in Fig. 11.7; thus experiments only need to determine the final state of the atom, e.g. using a laser beam that excites a transition from  $|2\rangle$  to another state that gives fluorescence for atoms in state  $|2\rangle$  but not for those in  $|1\rangle$ .<sup>18</sup> This means that Raman interferometers use more of the atoms from a given source because they do not need to have tight collimation.<sup>19</sup> Although the flux of atoms does not affect the size of the phase shift given by eqn 11.10, the strength of the measured signal determines how precisely that phase shift can be measured, i.e. the interferometer measures a smaller fraction of a fringe if the signal-to-noise ratio is higher.<sup>20</sup> Thus the type of Raman interferometer shown in Fig. 11.7 measures rotation more precisely than a three-grating device.

<sup>18</sup> As in the atomic fountain described in Section 9.9.

<sup>19</sup> The creation of the two Raman beams with a well-defined frequency difference, and other technical details, are described in Section 9.8.

<sup>20</sup> This argument assumes that it is purely statistical fluctuations (noise) that limit the precision, not systematic shifts.

## 11.6 Conclusions

Matter-wave interferometers for atoms are a modern use of the old idea of wave–particle duality and in recent years these devices have achieved a precision comparable to the best optical instruments for measuring rotation and gravitational acceleration. We have seen examples of experiments that are direct analogues of those carried out with light, and also the Raman technique for manipulating the momentum of atoms through their interaction with laser light, as in laser cooling. Laser cooling of the atom’s longitudinal velocity, however, only gives an advantage in certain cases (see the section on further reading).<sup>21</sup> Similarly, the high-coherence beams, or atom lasers, made from Bose condensates do not necessarily improve matter-wave devices—in contrast to the almost universal use of lasers in optical interferometers. Partly, this arises because of the interactions between the atoms themselves, as discussed in the derivation of the nonlinear Schrödinger equation in Chapter 10, which lead to phase shifts that depend on the atomic density. So far interferometry experiments that use BEC have been performed to find out more about the condensate itself, rather than as instruments for precision measurement of physical quantities. The interaction of atoms with the periodic potential produced by a standing wave gives a lot of interesting physics, in addition to the diffraction described here, and we have only scratched the surface of atom optics.

<sup>21</sup> The Ramsey fringes produced by atomic fountain clocks arise from interference of the internal (hyperfine) states of atoms, but in this chapter the ‘atom interferometer’ has been reserved for cases where there is spatial separation between the two arms.

## Further reading

<sup>22</sup>This journal is a useful source of similar articles.

The review in *Contemporary physics*<sup>22</sup> by Godun *et al.* (2001) surveys the field of atom interferometry at a level suitable for undergraduates, including important applications, such as the precision measurement of gravitational acceleration  $g$ , that have not been included here. The monograph *Atom interferometry* edited by Berman (1997) is a rich source of information on this subject.

## Exercises

(11.1) *Comparison of double- and multiple-slit diffraction*

- (a) Explain in simple physical terms why the diffraction orders of a grating occur at the same angles as the constructive interference between a pair of slits with the same spacing as those in the grating.
- (b) Monochromatic light passes through a transmission diffraction grating. Initially most of the grating is covered with opaque sheets of material so that the light illuminates only two adjacent slits in the middle of the grating. The grating is gradually uncovered until finally light falls on the whole grating. Describe how the intensity, spacing and shape of the observed far-field diffraction changes?

(11.2) *Young's slits with atoms*

- (a) Calculate  $\lambda_{dB}$  for metastable helium atoms from a source at 80 K.
- (b) Find the source slit width  $w_s$  such that the diffracted wave spreads out to coherently illuminate two slits separated by  $d = 8 \mu\text{m}$  when  $L' = 0.6 \text{ m}$  in Fig. 11.1 (the conditions for the experiment of Carnal and Mlynek (1991)).

Web site:

<http://www.physics.ox.ac.uk/users/foot>

This site has answers to some of the exercises, corrections and other supplementary information.

(11.3) *Measurement of the van der Waals interaction with a nano-fabricated grating*

Diffraction by a grating with slits of width  $a$  and spacing  $d$  gives an intensity distribution of<sup>23</sup>

$$I = I_0 \left( \frac{\sin(Nud/2)}{\sin(ud/2)} \right)^2 \left( \frac{\sin(ua/2)}{ua/2} \right)^2.$$

Here  $u = 2\pi \sin \theta / \lambda_{dB}$  and the angle is defined in Fig. 11.1. All of the parts of this exercise refer to a grating with  $d = 2a = 100 \text{ nm}$ .

- (a) Sketch the intensity distribution for  $0 \leq u \leq 10\pi/d$ .
- (b) What is the intensity of the second order?
- (c) An experimental observation of the diffraction of rare gas atoms from the grating found that the intensity of the second order is  $0.003 I_0$  for helium and  $0.05 I_0$  for krypton. The difference in these values was ascribed to the van der Waals force, which is strongest for large atoms. Therefore a krypton atom on a trajectory that goes close to the sides of the slit feels a force that deflects it through a large angle or causes it to crash into the grating. These processes effectively reduce the slit width from  $a$  to  $a - 2r$ , where  $r$  is the typical van der Waals range. Estimate  $r$  for krypton atoms.<sup>24</sup>

<sup>23</sup>Brooker (2003).

<sup>24</sup>Based on the experiment of Grisenti *et al.* (1999).

# Ion traps

# 12

This chapter describes the principal methods of building ion traps and a few of their many applications in physics. The examples illustrate the extremely high-resolution spectroscopy possible with microwave and laser radiation. The theme of precision measurement in an environment with very few perturbations continues in the next chapter on quantum computing—an application that has stimulated a new wave of research on trapped ions.

## 12.1 The force on ions in an electric field

Charged particles in electromagnetic fields experience much larger forces than neutral atoms. An ion with a single charge  $e = 1.6 \times 10^{-19} \text{ C}$  in an electric field of  $10^5 \text{ V m}^{-1}$  experiences a force

$$F_{\text{ion}} = eE \approx 10^{-14} \text{ N}. \quad (12.1)$$

This electric field corresponds to 500 V between electrodes which are 5 mm apart.<sup>1</sup> In comparison, a neutral atom with a magnetic moment of one Bohr magneton in a magnetic field gradient<sup>2</sup> of  $dB/dz = 10 \text{ T m}^{-1}$  experiences a force of magnitude

$$F_{\text{neutral}} = \mu_B \left| \frac{dB}{dz} \right| \simeq 10^{-22} \text{ N}. \quad (12.2)$$

Ions feel a force  $10^8$  times greater than magnetically-trapped neutrals. We also see this large difference in a comparison of trap depths. In a trap operating with a voltage of  $V_0 = 500 \text{ V}$ , singly-charged ions have a maximum ‘binding’ energy of order 500 eV.<sup>3</sup> This trap depth corresponds to the kinetic energy at a temperature of  $6 \times 10^6 \text{ K}$ . This is more than enough to trap ions, even if the ions do receive a large recoil kick during the ionization process—to load an ion trap experimenters send a weak (neutral) atomic beam through the trapping region where an electron beam ionizes a few of the atoms by knocking an electron off. These ions created by electron bombardment have much greater kinetic energy than the thermal energy of atoms at room temperature (equivalent to only 1/40 eV). It would be unwise to try to be more precise about the typical energy of an ion since it depends on the voltage used. In contrast, a magnetic trap for neutrals has a maximum depth of only 0.07 K. This was estimated in Section 10.1 by taking the magnetic energy  $\mu_B B$  for  $B = 0.1 \text{ T}$ , e.g. the force in eqn 12.2 over a distance of

|   |     |
|---|-----|
| 12.1 The force on ions in an electric field | 259 |
| 12.2 Earnshaw’s theorem                     | 260 |
| 12.3 The Paul trap                          | 261 |
| 12.4 Buffer gas cooling                     | 266 |
| 12.5 Laser cooling of trapped ions          | 267 |
| 12.6 Quantum jumps                          | 269 |
| 12.7 The Penning trap and the Paul trap     | 271 |
| 12.8 Electron beam ion trap (EBIT)          | 275 |
| 12.9 Resolved sideband cooling              | 277 |
| 12.10 Summary of ion traps                  | 279 |

|                 |     |
|-----------------|-----|
| Further reading | 279 |
| Exercises       | 280 |

<sup>1</sup>This assumes electrodes in the form of a parallel-plate capacitor. Although ion traps have a different geometry, this still gives a reasonable estimate and shows that the electrostatic force gives strong trapping for a voltage readily available in the laboratory.

<sup>2</sup>This value is typical of magnetic traps with coils wound with copper wire. Superconducting magnets give higher gradients.

<sup>3</sup>We consider ions with a single positive charge  $+e$  such as  $\text{Mg}^+$ ,  $\text{Ca}^+$  and  $\text{Hg}^+$ , since few experiments use species that acquire additional electrons to give negative ions. Section 12.8 deals with highly-charged ions.

10 mm. These estimates show that neutral atoms must be cooled before trapping but ion trapping requires only moderate electric fields to capture the charged particles directly. It is not straightforward, however, to find a suitable electric field configuration and, as in many advances within atomic physics, the success of ion trapping relies on some subtle ideas rather than a brute-force approach.

## 12.2 Earnshaw's theorem

<sup>4</sup>The theorem dates back to the nineteenth century and James Clerk Maxwell discussed it in his famous treatise on electromagnetism.

<sup>5</sup>The derivation of this equation from the Maxwell equation  $\text{div } \mathbf{D} = \rho_{\text{free}}$  assumes  $\rho_{\text{free}} = 0$  and a linear isotropic homogeneous medium in which  $\mathbf{D} = \epsilon_r \epsilon_0 \mathbf{E}$  with  $\epsilon_r$  constant. Ions are usually trapped in a vacuum, where  $\epsilon_r = 1$ .

Earnshaw proved that: *A charge acted on by electrostatic forces cannot rest in stable equilibrium in an electric field.*<sup>4</sup>

Thus it is not possible to confine an ion using a purely electrostatic field. Physicists have invented ingenious ways around this theorem but, before describing the principles of these ion traps, we need to think about the underlying physics. The theorem follows from the fact that an electric field has no divergence in a region with no free charge density,  $\text{div } \mathbf{E} = 0$ .<sup>5</sup> Zero divergence means that all the field lines going into a volume element must come out—there are no sources or sinks of field within the volume. Equivalently, Gauss' theorem tells us that the integral of the normal component of  $\mathbf{E}$  over the bounding surface equals the volume integral of  $\text{div } \mathbf{E}$ , which is zero:

$$\oint \oint \mathbf{E} \cdot d\mathbf{S} = \iiint \text{div } \mathbf{E} d^3 \mathbf{r} = 0. \quad (12.3)$$

Hence  $\mathbf{E} \cdot d\mathbf{S}$  cannot have the same sign over all of the surface. Where  $\mathbf{E} \cdot d\mathbf{S} < 0$  the electric field points inwards and a positive ion feels a force that pushes it back into the volume; but  $\mathbf{E} \cdot d\mathbf{S} > 0$  somewhere else on the surface and the ion escapes along that direction. A specific example of this is shown in Fig. 12.1 for the field produced by two equal positive charges with a fixed separation along the  $z$ -axis. Midway between the charges, at the point labelled P, the electric fields from the two charges cancel and the ion experiences no force, but this does not give stable equilibrium. The argument above holds true, so the electric field lines around the point P cannot all be directed inwards. When slightly displaced from P, a positive ion accelerates perpendicular to the axis, whereas a negative ion would be attracted towards one of the fixed charges. This behaviour can also be explained by the fact that the point P is a saddle point of the electrostatic potential  $\phi$ . The electrostatic potential energy  $e\phi$  of the ion has the same form as the gravitational potential energy of a ball placed on the saddle-shaped surface shown in Fig. 12.2—clearly the ball tends to roll off down the sides. In this alternative way of looking at Earnshaw's theorem in terms of electrostatic potential rather than the fields, stable trapping does not occur because the potential never has a minimum, or maximum, in free space.<sup>6</sup>

<sup>6</sup>It takes just a few lines of algebra to prove this from Laplace's equation.

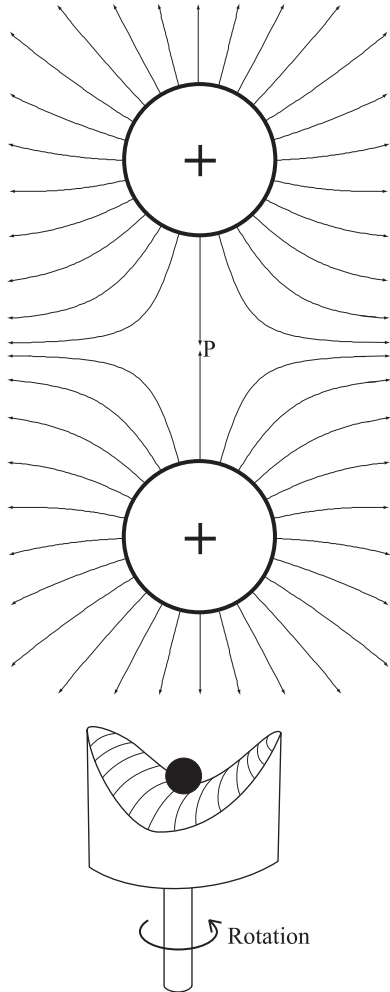


**Fig. 12.1** The electric field lines between two equal positive charges. Midway between the charges at the point P the electric fields from the two charges cancel. At this position the ion experiences no force but it is not in stable equilibrium. At all other positions the resultant electric field accelerates the ion.

**Fig. 12.2** A ball on a saddle-shaped surface has a gravitational potential energy that resembles the electrostatic potential energy of an ion in a Paul trap. Rotation of the surface about a vertical axis, at a suitable speed, prevents the ball rolling off the sides of the saddle and gives stable confinement.

## 12.3 The Paul trap

The analogy with a ball moving on the saddle-shaped surface shown in Fig. 12.2 provides a good way of understanding the method for confining ions invented by Wolfgang Paul. The gravitational potential energy of the ball on the surface has the same form as the potential energy of an ion close to a saddle point of the electrostatic potential. We assume here a symmetric saddle whose curvature has the same magnitude, but opposite sign, along the principal axes:

$$z = \frac{\kappa}{2} \left[ (x')^2 - (y')^2 \right], \quad (12.4)$$

where  $x' = r \cos \Omega t$  and  $y' = r \sin \Omega t$  are coordinates in a frame rotating with respect to the laboratory frame of reference. The time average of this potential is zero. Rotation of the saddle shape around the vertical axis turns the unstable situation into stable mechanical equilibrium, and

makes an impressive lecture demonstration. Such dynamic stabilisation cannot honestly be described as ‘well known’ so it is explained carefully here by an approximate mathematical treatment of ions in an a.c. field.

### 12.3.1 Equilibrium of a ball on a rotating saddle

In the mechanical analogue, the rotation of the saddle at a suitable speed causes the ball to undergo a wobbling motion; the ball rides up and down over the low-friction surface of the rotating saddle shape and the ball’s mean position only changes by a small amount during each rotation.<sup>7</sup> The amplitude of this wobbling increases as the ball moves further from the centre of the saddle. For this oscillatory motion the time-averaged potential energy is not zero and the total energy (potential plus kinetic) increases as the object moves away from the centre. Therefore the mean position of the object (averaged over many cycles of the rotation) moves as if it is in an effective potential that keeps the ball near the centre of the saddle. We will find that an ion jiggling about in an a.c. field has a similar behaviour: a fast oscillation at a frequency close to that of the applied field and a slower change of its mean position.

<sup>7</sup> Although we shall not analyse the mechanical system in detail, it is important to note that the wobbling motion is not entirely up and down but has radial and tangential components. Similarly, an object that floats on the surface of water waves does not just bob up and down but also oscillates back and forth along the direction of propagation of the waves, so its overall motion in space is elliptical. The discussion only applies for mechanical systems where friction has a negligible effect so that the ball slides smoothly over the surface.

### 12.3.2 The effective potential in an a.c. field

To explain the operation of the Paul trap, we first look at how an ion behaves in a.c. electric field  $\mathbf{E} = \mathbf{E}_0 \cos(\Omega t)$ . An ion of charge  $e$  and mass  $M$  feels a force  $\mathbf{F} = e\mathbf{E}_0 \cos(\Omega t)$ , and so Newton’s second law gives

$$M\ddot{\mathbf{r}} = e\mathbf{E}_0 \cos(\Omega t). \quad (12.5)$$

Two successive integrations give the velocity and displacement as

$$\begin{aligned} \dot{\mathbf{r}} &= \frac{e\mathbf{E}_0}{M\Omega} \sin(\Omega t), \\ \mathbf{r} &= \mathbf{r}_0 - \frac{e\mathbf{E}_0}{M\Omega^2} \cos(\Omega t). \end{aligned} \quad (12.6)$$

It has been assumed that the initial velocity is zero and  $\mathbf{r}_0$  is a constant of integration. The field causes the ion to oscillate at angular frequency  $\Omega$  with an amplitude proportional to the electric field. From this steady-state solution we see that the forced oscillation does not heat the ions.<sup>8</sup> (These simple steps form the first part of the well-known derivation of the *plasma frequency* for a cloud of electrons in an a.c. field, given in most electromagnetism texts.) The following section describes an example of this behaviour in which the amplitude of the electric field changes with position  $\mathbf{E}_0(\mathbf{r})$ .

### 12.3.3 The linear Paul trap

In a linear Paul trap the ion moves in the field produced by the electrodes shown in Fig. 12.3. The four rods lie parallel to the  $z$ -axis and at the corners of a square in the  $xy$ -plane. Each electrode is connected to the

<sup>8</sup> The a.c. field does not change the ion’s average total energy because the work done on the ion given by  $\mathbf{F} \cdot \dot{\mathbf{r}} \propto \cos(\Omega t) \sin(\Omega t)$  averages to zero over one cycle—the force and velocity have a phase difference of  $\pi/2$ .

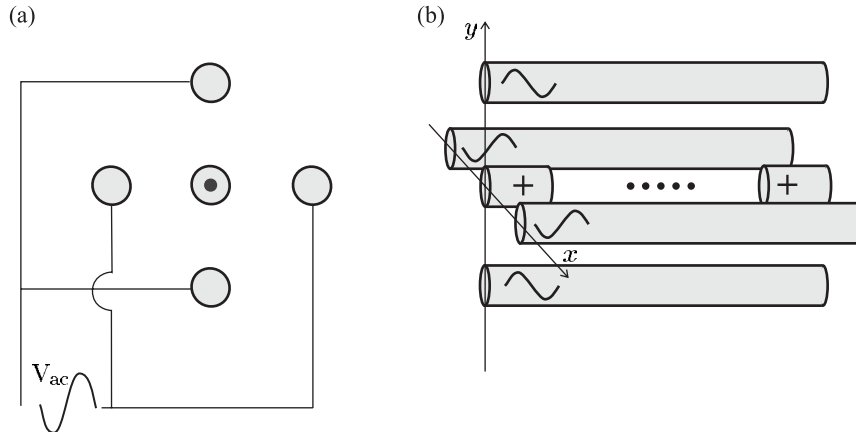


**Fig. 12.3** A linear Paul trap used to store a string of ions. (a) A view looking along the four rods with the end-cap electrode and ions in the centre. Each of the rods is connected to the one diagonally opposite so that a voltage between the pairs gives a quadrupole field. (b) A side view of the rod and end-cap electrodes which have a.c. and positive d.c. voltages, respectively. A string of trapped ions is indicated.

one diagonally opposite and the a.c. voltage  $V = V_0 \cos(\Omega t)$  is applied between the two pairs. Despite the fact that the voltages vary with time, we first find the potential by the usual method for electrostatic problems. The electrostatic potential  $\phi$  satisfies Laplace's equation  $\nabla^2 \phi = 0$  (because  $\text{div } \mathbf{E} = 0$  and  $\mathbf{E} = -\nabla \phi$ ). A suitable solution for the potential close to the  $z$ -axis, that matches the symmetry of the voltages on the electrodes, has the form of a quadrupole potential

$$\phi = a_0 + a_2(x^2 - y^2). \quad (12.7)$$

The coefficients  $a_0$  and  $a_2$  are determined from the boundary conditions. There are no terms linear in  $x$  or  $y$  because of the symmetry under reflection in  $x = 0$  and  $y = 0$ . The terms in  $x^2$  and  $y^2$  have opposite signs, and the variation with  $z$  is negligible for rods much longer than their separation  $2r_0$ . The potential must match the boundary conditions

$$\begin{aligned} \phi &= \phi_0 + \frac{V_0}{2} \cos(\Omega t) && \text{at} && x = \pm r_0, y = 0, \\ \phi &= \phi_0 - \frac{V_0}{2} \cos(\Omega t) && \text{at} && x = 0, y = \pm r_0. \end{aligned} \quad (12.8)$$

These conditions are satisfied by the potential<sup>9</sup>

$$\phi = \phi_0 + \frac{V_0}{2r_0^2} \cos(\Omega t) (x^2 - y^2). \quad (12.9)$$

To solve Laplace's equation we have simply made a reasonable guess, taking into account the symmetry. This is perfectly justified since the uniqueness theorem says that a solution that fits the boundary conditions is the only valid solution (see electromagnetism texts). The usual

<sup>9</sup>This ignores the finite size of the electrodes and that the inner surfaces of the electrodes would need to be hyperbolic, e.g. a surface given by  $x^2 - y^2 = \text{const.}$ , to match the equipotentials. However, by symmetry this potential has the correct form for  $r \ll r_0$ , no matter what happens near to the electrodes.

<sup>10</sup>This method would not be appropriate for shorter wavelengths, e.g. microwave radiation with frequencies of GHz.

<sup>11</sup>The two-dimensional quadrupole field between the four rods looks superficially like the quadrupole field with cylindrical symmetry in Fig. 12.1 and the analogy with a rotating saddle applies to both. A comparison of the potentials for the two cases in eqn 12.9 and eqn 12.23 shows that they are different. Note also that the electrostatic potential oscillates ‘up and down’ rather than rotating as in the mechanical analogy.

<sup>12</sup>The Mathieu equation arises in a variety of other physical problems, e.g. the inverted pendulum. A pendulum is normally considered as hanging down from its pivot point and undergoing simple harmonic motion with a small amplitude. In an inverted pendulum a rod, that is pivoted at one end, initially points vertically upwards; any slight displacement from this unstable position causes the rod to fall and swing about the stable equilibrium position (pointing straight down), but if the pivot point oscillates rapidly up and down then the rod remains upright whilst executing a complicated motion—the rod can make quite large-angle excursions from the vertical direction without falling over. The mathematical textbook by Acheson (1997) gives further details of the complexities of this fascinating system and numerical simulations can be seen on the web site associated with that book.

<sup>13</sup>This corresponds to the motion of an ion in a trap that has no d.c. voltage. In practice, ion traps may have some d.c. voltage because of stray electric fields but this can be cancelled by applying a suitable d.c. voltage to the electrodes (or additional electrodes near the four rods). The solution of the Mathieu equation with  $a_x \neq 0$  is discussed in the book on ion traps by Ghosh (1995).

<sup>14</sup>More detailed mathematical treatments of the Mathieu equation can be found in Morse and Feshbach (1953) and Mathews and Walker (1964).

method for solving an electrostatic problem applies even though the voltage on the electrodes changes because at the radio-frequencies (used in ion traps) the radiation has a wavelength much greater than the dimensions of the electrodes, e.g. a wavelength of 30 m for  $\Omega = 2\pi \times 10$  MHz.<sup>10</sup> The potential energy  $e\phi$  of an ion has a saddle point in the middle of these electrodes that looks like the saddle shape shown in Fig. 12.2—a potential ‘hill’ in the  $x$ -direction and a ‘valley’ in the  $y$ -direction, or the other way around.<sup>11</sup> From the gradient of potential we find the electric field

$$\begin{aligned}\mathbf{E} &= \mathbf{E}_0(\mathbf{r}) \cos(\Omega t) \\ &= -\frac{V_0}{r_0^2} \cos(\Omega t) (x\hat{\mathbf{e}}_x - y\hat{\mathbf{e}}_y).\end{aligned}\quad (12.10)$$

The equation of motion in the  $x$ -direction is

$$M \frac{d^2x}{dt^2} = -\frac{eV_0}{r_0^2} \cos(\Omega t) x. \quad (12.11)$$

A change of variable to  $\tau = \Omega t/2$  leads to

$$\frac{d^2x}{d\tau^2} = -\frac{4eV_0}{\Omega^2 Mr_0^2} \cos(2\tau) x. \quad (12.12)$$

This is a simplified form of the Mathieu equation:<sup>12</sup>

$$\frac{d^2x}{d\tau^2} + (a_x - 2q_x \cos 2\tau) x = 0 \quad (12.13)$$

with  $a_x = 0$ .<sup>13</sup> It is conventional to define the parameter in front of the oscillating term as  $2q_x$  (in anticipation of this  $e$  has been used for the ion’s charge), where

$$q_x = \frac{2eV_0}{\Omega^2 Mr_0^2}. \quad (12.14)$$

We look for a solution of the form

$$x = x_0 \cos A\tau \{1 + B \cos 2\tau\}. \quad (12.15)$$

The arbitrary constant  $A$  gives the angular frequency of the overall motion and  $B$  is the amplitude of the fast oscillation at close to the driving frequency. The justification for choosing this form is that we expect an oscillating driving term to produce a periodic solution and substitution of a function containing  $\cos A\tau$  into the equation leads to terms with  $\cos A\tau \cos 2\tau$ .<sup>14</sup> Substitution into the equation (with  $a_x = 0$ ) gives

$$\begin{aligned}x_0 [-4B \cos A\tau \cos 2\tau + 4AB \sin A\tau \sin 2\tau - A^2 \cos A\tau \{1 + B \cos 2\tau\}] \\ = 2q_x x_0 \cos 2\tau \cos A\tau \{1 + B \cos 2\tau\}.\end{aligned}\quad (12.16)$$

We shall assume that  $A \ll 1$ , so that the function  $\cos A\tau$  corresponds to a much slower oscillation than  $\cos 2\tau$ , and also that the amplitude  $B \ll 1$  (both of these assumptions are discussed below). Thus the terms

proportional to  $\cos A\tau \cos 2\tau$  dominate on each side, and equating their coefficients gives  $-4B = 2q_x$  or

$$B = -\frac{q_x}{2} = -\frac{eV_0}{M\Omega^2 r_0^2}. \quad (12.17)$$

This amplitude of the fast oscillation is consistent with the result for a uniform electric field in eqn 12.6.<sup>15</sup> This fast oscillation is called the micromotion. To determine the angular frequency  $A$  we consider how the mean displacement changes on a time-scale longer than the micromotion: the time-average of  $\cos^2 2\tau = 1/2$  so eqn 12.16 yields  $-A^2 \cos A\tau = q_x B \cos A\tau$ ,<sup>16</sup> hence  $A = q_x/\sqrt{2}$  and an approximate solution is

$$x = x_0 \cos \left( \frac{q_x \tau}{\sqrt{2}} + \theta_0 \right) \left\{ 1 + \frac{q_x}{2} \cos 2\tau \right\}, \quad (12.18)$$

where  $q_x$  is defined in eqn 12.14.<sup>17</sup> We assumed that  $q_x \ll 1$  but it turns out that this approximation works better than 1% for  $q_x \leq 0.4$  (Wuerker *et al.* 1959). Since  $\tau = \Omega t/2$  the mean displacement undergoes simple harmonic motion at an angular frequency given by

$$\omega_x = \frac{q_x \Omega}{2\sqrt{2}} = \frac{eV_0}{\sqrt{2}\Omega M r_0^2}. \quad (12.19)$$

A more detailed treatment shows that ions remain trapped for

$$q_x \leq 0.9 \quad (12.20)$$

or  $\omega_x \leq 0.3 \Omega$ . For a radio-frequency field oscillating at  $\Omega = 2\pi \times 10$  MHz the ion must have a radial oscillation frequency  $\omega_x \leq 2\pi \times 3$  MHz. If we choose  $\omega_x = 2\pi \times 1$  MHz (a convenient round number) then eqn 12.19 gives the numerical values  $V_0 = 500$  V and  $r_0 = 1.9$  mm for trapping  $Mg^+$  ions.<sup>18</sup> To get this high trapping frequency the ion trap has electrodes closer together than we assumed in the introduction. By symmetry, the same considerations apply for motion in the  $y$ -direction, and so we define a radial frequency  $\omega_r \equiv \omega_x = \omega_y$ . The Paul trap has a sharp transition from stable trapping to no trapping in the radial direction when  $q_r$  equals the maximum value of  $q_x$  in eqn 12.20. Paul used this feature to determine the charge-to-mass ratio  $e/M$  of the ions and hence perform mass spectroscopy—generally the charge state is known (e.g. it is  $e$  or  $2e$ , etc.) and hence  $M$  is determined.

So far we have only described confinement in the  $xy$ -plane. There are several ways to extend trapping to all three directions. For example, Fig. 12.3(b) shows a trap with two additional electrodes at  $z = \pm z_0$  that repel the ions. For positive ions both of these end-cap electrodes have the same positive voltage to give a field similar to that shown in Fig. 12.1, with a minimum in the electrostatic potential along the  $z$ -axis—in the radial direction the static potential has a negligible effect compared to the a.c. trapping. When the linear Paul trap has axial confinement weaker than that in the radial direction, i.e.  $\omega_z \ll \omega_x = \omega_y$ , the ions tend to lie in a string along the  $z$ -axis with only a small micromotion

<sup>15</sup>Equation 12.10 shows that the component of the electric field in this direction is  $\mathbf{E}_0(\mathbf{r}) \cdot \hat{\mathbf{e}}_x = -V_0 x/r_0^2$ .

<sup>16</sup>The term  $4AB \sin A\tau \cos 2\tau$  time-averages to zero.

<sup>17</sup>An arbitrary initial phase  $\theta_0$  has been included to make the expression more general but this does not affect the argument above.

<sup>18</sup>In comparison, neutral atoms in magnetic traps oscillate at frequencies in the range 10–1000 Hz.

in the radial direction; there is no axial micromotion because it is a d.c. electric field along the  $z$ -direction. We will see that after cooling the ions sit very close to the trap axis where the a.c. field causes very small perturbations. In the later discussion of laser cooling the trapped ions are considered simply as harmonic oscillators (neglecting micromotion).

## 12.4 Buffer gas cooling

Trapping of ions requires a vacuum, but the presence of a small background of helium gas at a pressure ( $\sim 10^{-4}$  mbar) gives very effective cooling of hot ions. The ions dissipate their kinetic energy through collisions with the buffer gas atoms and this quickly brings the ions into thermal equilibrium with the gas at room temperature. For ions that start off above room temperature the buffer gas cooling actually *reduces* the perturbations on the ions. Any slight broadening and shift of the ions' energy levels by the collisions is outweighed by the reduction in the ions' micromotion—the ions stay closer to the trap centre where they see smaller a.c. fields.

Buffer gas cooling can be compared to having a vacuum flask that has partially ‘lost its vacuum’—hot coffee in the flask cools down because the low pressure of gas between the walls provides much less thermal insulation than a good vacuum. It follows from this argument that ions can only be cooled far below room temperature in a good vacuum, e.g. a pressure of  $10^{-11}$  mbar in the laser cooling experiments described later (otherwise collisions with the hot background gas atoms heat the ions). This case corresponds to having a good vacuum flask; dewars in the laboratory work on the same principle to keep things such as liquid helium at temperatures much colder than the surroundings.

Buffer gas cooling finds widespread application in instruments that need to operate reliably over long periods, such as the mercury ion clock developed at NASA’s Jet Propulsion Laboratory in Pasadena, California. The linear Paul trap contains a cloud of mercury ions and microwaves drive the transition at 40 GHz between the two hyperfine levels in the ground state of the ions. By reference to the resonance frequency of the ions, the electronic servo-control system maintains the frequency of the microwave source stable to 1 part in  $10^{14}$  over long periods. This ion trap provides a very good frequency reference and has been used for navigation in deep space, where the accurate timing of signals transmitted to and from the probe determine its distance from a transmitter/receiver on Earth.<sup>19</sup> Paul traps with buffer gas cooling are also used to give long ion storage times in some commercial mass spectrometers.

There is a method analogous to buffer gas cooling that works at much lower temperatures. In **sympathetic cooling** a trap confines two species of ions at the same time, e.g.  $\text{Be}^+$  and  $\text{Mg}^+$ . Laser cooling one species, as described in the next section, e.g. the  $\text{Be}^+$  ions, produces a cloud of cold ions that acts as the ‘buffer gas’ to cool the  $\text{Mg}^+$  ions through collisions. The ions interact through their strong long-range Coulomb

<sup>19</sup>See Berkeland *et al.* (1998) for a description of a state-of-the-art laser-cooled mercury ion frequency standard.

repulsion, so they never come close enough together to react—in this sense the collisions between ions are benign (whereas neutral atoms in magnetic traps undergo some inelastic collisions leading to trap loss).

## 12.5 Laser cooling of trapped ions

The cooling of ions uses the same scattering force as the laser cooling of neutral atoms, and historically David Wineland and Hans Dehmelt proposed the idea of laser cooling for ions before any of the work on neutral atoms. The long confinement time in ion traps makes experiments straightforward in principle; but, in practice, ions have resonance lines in the blue or ultraviolet regions, so they often require more complicated laser systems than for neutral atoms with resonance lines at longer wavelengths.<sup>20</sup> This difference arises because in ions the valence electron sees a more highly-charged core than in the isoelectronic neutral atoms, i.e. the atom with the same electronic configuration. The shorter wavelengths for ions also means that they generally have larger natural widths than neutral atoms since  $\Gamma$  depends on the cube of the transition frequency. This high scattering rate for resonant laser light leads to a strong radiative force on the ions and also allows the detection of single ions, as shown below.

Each trapped ion behaves as a three-dimensional simple harmonic oscillator but a single laser beam damps the motion in all directions. To achieve this, experimenters tune the laser frequency slightly below resonance (red frequency detuning, as in the optical molasses technique), so the oscillating ion absorbs more photons as it moves towards the laser beam than when it moves away. This imbalance in the scattering during the oscillations slows the ion down. This Doppler cooling works in much the same way as in optical molasses but there is no need for a counter-propagating laser beam because the velocity reverses direction in a bound system. The imbalance in scattering arises from the Doppler effect so the lowest energy is the Doppler cooling limit  $k_B T = \hbar\Gamma/2$  (see Exercise 12.1). To cool the ion's motion in all three directions the radiative force must have a component along the direction corresponding to each degree of freedom, i.e. the laser beam does not go through the trap along any of the axes of symmetry. During laser cooling the spontaneously emitted photons go in all directions and this strong fluorescence enables even single ions to be seen! Here I do not mean detectable, but actually seen with the naked eye; a  $\text{Ba}^+$  ion with a visible transition appears as a tiny bright dot between the electrodes when you peer into the vacuum system. The resonance transition in the barium ion has a longer wavelength than most other ions at 493 nm in the green region of the visible spectrum. More generally, experiments use CCD cameras to detect the blue or ultraviolet radiation from the ions giving pictures such as Fig. 12.4. To calculate the signal from a  $\text{Ca}^+$  ion with a transition at a wavelength of 397 nm and  $\Gamma = 2\pi \times 23 \times 10^6 \text{ s}^{-1}$ , we use eqn 9.3 with

<sup>20</sup>The generation of continuous-wave radiation at 194 nm for laser cooling  $\text{Hg}^+$  requires several lasers and frequency mixing by nonlinear optics, but nowadays radiation at a wavelength of 397 nm for laser cooling  $\text{Ca}^+$  is produced by small semiconductor diode lasers.

**Fig. 12.4** A string of calcium ions in a linear Paul trap. The ions have an average separation of  $10\ \mu\text{m}$  and the strong fluorescence enables each ion to be detected individually. The minimum size of the image for each ion is determined by the spatial resolution of the imaging system. Courtesy of Professor Andrew Steane and co-workers, Physics department, University of Oxford.

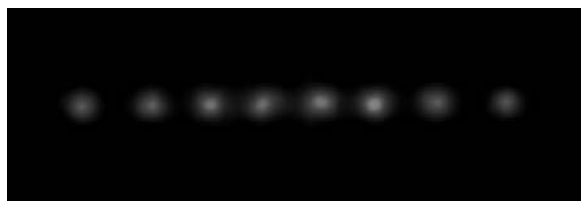
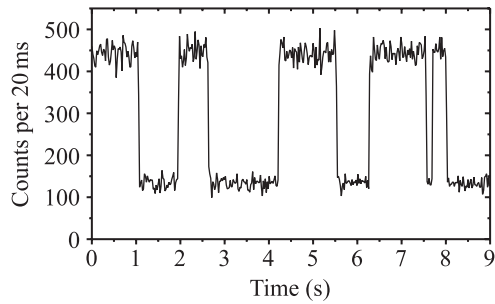


**Fig. 12.5** The fluorescence signal from a single calcium ion undergoing quantum jumps. The ion gives a strong signal when it is in the ground state and it is ‘dark’ while the ion is shelved in the long-lived metastable state. Data courtesy of Professors Andrew Steane and Derek Stacey, David Lucas and co-workers, Physics department, University of Oxford.



$\delta = -\Gamma/2$  and  $I = 2I_{\text{sat}}$ , so that

$$\mathcal{R}_{\text{scatt}} \simeq \frac{\Gamma}{4} \simeq 4 \times 10^7 \text{ photons s}^{-1}. \quad (12.21)$$

In a typical experiment the lens that images the fluorescence onto the detector has an *f*-number (ratio of focal length to diameter) of about 2, so it collects 1.6% of the total number of fluorescence photons (the solid angle subtended over  $4\pi$ ). A reasonable detector could have an efficiency of 20%, giving an experimental signal of  $S = 0.016 \times 0.2 \times \mathcal{R}_{\text{scatt}} = 10^5 \text{ photon s}^{-1}$  that can easily be measured on a photomultiplier as in Fig. 12.5. (The signal is lower than the estimate because fluorescent photons are lost by reflection at the surfaces of optical elements, e.g. windows or lenses.)

Laser cooling on a strong transition reduces the ion’s energy to the Doppler cooling limit  $\hbar\Gamma/2$ . In a trap with a spacing of  $\hbar\omega_{\text{trap}}$  between vibrational energy levels, the ions occupy about  $\sim \Gamma/\omega_{\text{trap}}$  vibrational levels; typically this corresponds to many levels. The minimum energy occurs when the ions reside in the lowest quantum level of the oscillator where they have just the zero-point energy of the quantum harmonic oscillator. To reach this fundamental limit experiments use more sophisticated techniques that drive transitions with narrow line widths, as described in Section 12.9.

## 12.6 Quantum jumps

In addition to the strong resonance transition of natural width  $\Gamma$  used for laser cooling, ions have many other transitions and we now consider excitation of a weak optical transition with a natural width  $\Gamma'$ , where  $\Gamma' \ll \Gamma$ . Figure 12.6 shows both of the transitions and the relevant energy levels. The first application described here simply uses a narrow transition to measure the temperature accurately. We shall look at high-resolution laser spectroscopy later.

A simple calculation shows that probing on a narrow transition is necessary to measure the temperature of ions at the Doppler cooling limit of the strong transition. Multiplying the velocity spread in eqn 9.29 by a factor of  $2/\lambda$ , as in eqn 6.38, gives the Doppler-broadening at the Doppler cooling limit as

$$\Delta f_D \simeq \frac{2v_D}{\lambda} = 2\sqrt{\frac{\hbar\Gamma}{M\lambda^2}}. \quad (12.22)$$

For the transition in the calcium ion whose parameters were given in the previous section this evaluates to  $\Delta f_D = 2$  MHz, which is only 0.07 times the natural width ( $\Delta f_N = 23$  MHz). Therefore the line has a width only slightly greater than the natural width and measurements of this line width cannot determine the temperature accurately. This difficulty disappears for a much narrower transition where Doppler broadening dominates the observed line width, but this scheme presents a practical problem—the low rate of scattering of photons on the weak transition makes it hard to observe the ion.

Ion trappers have developed a clever way to simultaneously obtain a good signal and a narrow line width. This experimental technique requires radiation at two frequencies so that both a strong and weak transition can be excited. When both laser frequencies illuminate the ions the fluorescence signal looks like that shown in Fig. 12.5. The fluorescence switches off and on suddenly at the times when the valence electron jumps up or down from the long-lived excited state—the average time between the switching in this *random telegraph signal* depends on the lifetime of the upper state. These are the quantum jumps between allowed energy levels postulated by Bohr in his model of the hydrogen

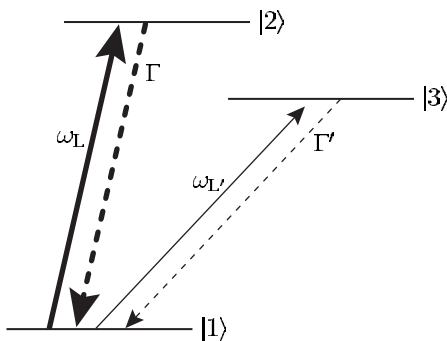


**Fig. 12.6** Three energy levels of an ion. The allowed transition between levels 1 and 2 gives a strong fluorescence signal when excited by laser light. The weak transition between 1 and 3 means that level 3 has a long lifetime and  $\Gamma' \ll \Gamma$  (a metastable state).

atom, and the direct observation of such jumps for a single ion provides new ways of testing quantum mechanics. Previous experiments measured the ensemble average of an observable, i.e. its average value for a collection particles, but ion traps allow repeated measurements on a single object. In quantum language, each absorption and emission of a photon on the strong transition constitutes a measurement of the state of the ion—it is found to be in either the ground state or the long-lived excited state, and these two outcomes correspond to the two eigenvalues of the observable. The fluorescence signal in Fig. 12.5 represents a sequence of such measurements that gives a record of the state of the ion. In addition to giving an insight into the nature of quantum mechanics, the excitation of very narrow resonances has a very practical use in optical frequency standards.

The observation of a highly forbidden transition in the ytterbium ion at the National Physical Laboratory at Teddington, London furnishes an extreme example of high-resolution spectroscopy. An  $^2F_{7/2}$  level in  $\text{Yb}^+$  can only decay to the ground level  $^2S_{1/2}$  by an octupole transition<sup>21</sup> with a calculated natural lifetime of 10 years (Roberts *et al.* 1997). Even though excited ions are forced to decay more quickly to make experiments feasible, the rate of spontaneous emission on this transition is tiny. To detect this weak transition experiments use the scheme shown in Fig. 12.6. In addition to the weak  $^2S_{1/2}-^2F_{7/2}$  transition between levels 1 and 3 there is a strong  $^2S_{1/2}-^2P_{1/2}$  transition between levels 1 and 2. Laser radiation at frequency  $\omega_L'$  drives the weak transition for a time  $t_w$ ; then laser light resonant with a strong transition ( $\omega_L \simeq \omega_{12}$ ) turns on for a period  $t_{\text{det}}$  to determine the state of the ion. If the ion was excited to the long-lived upper level during  $t_w$  then it does not fluoresce. If it remains in the ground state, however, photons arrive at the detector at a rate  $\mathcal{R}_{\text{obs}} \simeq 10^5 \text{ s}^{-1}$ , as estimated below eqn 12.21 (for a strong transition in a calcium ion). In a period  $t_{\text{det}} = 2 \times 10^{-2} \text{ s}$  there are  $\mathcal{R}_{\text{obs}} t_{\text{det}} = 2000$  photons detected. Repetition of these two stages of the measurement procedure as  $\omega_L$  scans over the frequency range around the narrow resonance at  $\omega_{13}$  produces a plot of the probability of exciting the narrow transition (in time  $t_w$ ) versus laser frequency. The line width of the observed resonance depends on the measurement time, since other broadening mechanisms are negligible. Fourier transform theory shows that the frequency width of a pulse is inversely proportional to its duration,  $\Delta\omega_{\text{obs}} \sim 1/t_w$ —the same relation used in transit-time broadening (eqn 7.50). This corresponds to counting the number of cycles of the laser radiation,  $f_{L'} t_w$  to within  $\pm \frac{1}{2}$  of a cycle ( $f_{L'} = \omega_{L'}/2\pi$ ). Frequency standards use this detection scheme with alternate periods of probing and measurement because the weak transition must not be perturbed by having a strong interaction at the same time.<sup>22</sup>

<sup>21</sup>This is an E3 transition in notation, where E1 and E2 signify electric dipole and quadrupole transitions, respectively.

<sup>22</sup>The logic of this method is reminiscent of a case solved by the famous detective Sherlock Holmes. From the observation that the dog did not bark in the night he deduced that the murderer was not a stranger. It is deduced that the ion has been excited when it is not observed.

## 12.7 The Penning trap and the Paul trap

For experiments with several ions the linear Paul trap has the advantage that the ions lie like a string of beads along the trap axis, with little micromotion. However, most of the pioneering experiments on ion traps used the electrode configuration shown in Fig. 12.7. The cylindrical symmetry of these electrodes imposes boundary conditions on the electrostatic potential, as in Section 12.3.3. Solutions of Laplace's equation that satisfy these conditions have the form

$$\phi = \phi_0 + a_2 \left( z^2 - \frac{x^2 + y^2}{2} \right). \quad (12.23)$$

The surfaces of constant potential have a hyperbolic cross-section in any radial plane, e.g.  $y = 0$ ; in many experiments the electrodes match the shape of these equipotentials so that the potential corresponds to eqn 12.23 right out to the electrode surfaces, but any cylindrically-

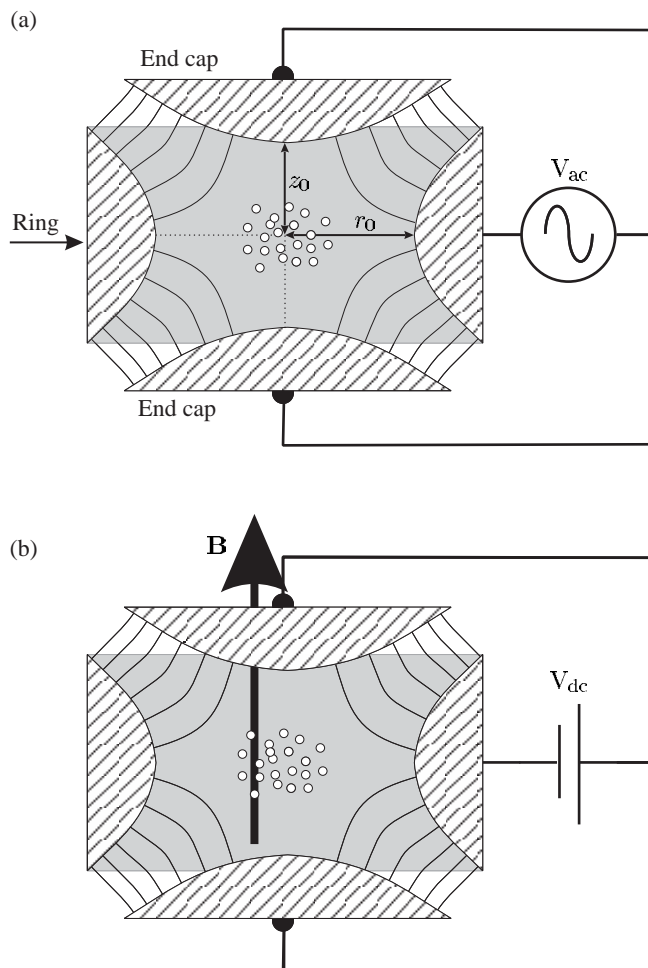


**Fig. 12.7** The electrode configuration of (a) the Paul trap and (b) the Penning trap, shown in cross-section. The lines between the end caps and ring electrode indicate the electric field lines; the Paul trap has an oscillating electric field but the Penning trap has static electric and magnetic fields. The electrodes shown have a hyperbolic shape (hyperbolae rotated about the  $z$ -axis), but for a small cloud of ions confined near to the centre any reasonable shape with cylindrical symmetry will do. Small ion traps with dimensions  $\sim 1$  mm generally have simple electrodes with cylindrical or spherical surfaces (cf. Fig. 12.3). Courtesy of Michael Nasse.

<sup>23</sup>The higher-order terms  $x^4$ ,  $x^2y^2$ , etc. have negligible influence near the origin.

symmetric electrodes work well for laser cooling experiments since the cold ions remain close to the trap centre, where symmetry constrains the potential to have the form of eqn 12.23.<sup>23</sup> An a.c. voltage between the ring electrode and the two end caps gives a Paul trap that works on the same principle as the two-dimensional trapping described in Section 12.3.3. For cylindrical symmetry the trap has an electric field gradient along  $z$  whose magnitude is twice as large as the gradient along  $x$  or  $y$ . This difference from the linear quadrupole field means that the region of stable Paul trapping occurs at slightly different voltages (values of the parameter  $q$ , defined in eqn 12.14), as described in the book on ion traps by Ghosh (1995).

The Paul trap principle can be used to confine charged particles in air, e.g. dust, or charged droplets of glycerin of diameter 10–100  $\mu\text{m}$ . In this demonstration apparatus, the strong damping of the motion by the air at atmospheric pressure helps to confine charged particles over a large range of a.c. voltages (see Nasse and Foot (2001), which contains references to earlier work). In comparison, the well-known Millikan oil drop experiment just levitates particles by balancing gravity with an electrostatic force.

### 12.7.1 The Penning trap

The Penning trap has the same electrode shape as the Paul trap (as shown in Fig. 12.7) but uses static fields. The Paul trap is generally assumed to have cylindrical symmetry unless specifically stated as being a linear Paul trap. In a Penning trap for positive ions, both end caps have the same positive voltage (with respect to the ring electrode) to repel the ions and prevent them escaping along the axis (cf. the trap in Fig. 12.3). With only a d.c. electric field the ions fly off in the radial direction, as expected from Earnshaw's theorem, but a strong magnetic field along the  $z$ -axis confines the ions. The effect of this axial magnetic field can be understood by considering how a charged particle moves in crossed electric and magnetic fields. In an electric field  $\mathbf{E} = E\hat{\mathbf{e}}_x$  the force  $\mathbf{F} = e\mathbf{E}$  accelerates the positive ion along the  $x$ -axis. In a region where there is a uniform magnetic field  $\mathbf{B} = B\hat{\mathbf{e}}_z$  the Lorentz force  $\mathbf{F} = e\mathbf{v} \times \mathbf{B}$  causes the ion to execute circular motion at the cyclotron frequency<sup>24</sup>

$$\omega_c = \frac{eB}{M}. \quad (12.24)$$

In a region of crossed electric and magnetic fields the solution of the equations of motion gives<sup>25</sup>

$$\begin{aligned} x &= \frac{E}{\omega_c B} (1 - \cos \omega_c t), \\ y &= -\frac{E}{\omega_c B} (\omega_c t - \sin \omega_c t), \\ z &= 0 \end{aligned} \quad (12.25)$$

for the initial conditions  $x = y = z = \dot{x} = \dot{y} = \dot{z} = 0$ . The trajectory

<sup>24</sup>As shown in Fig. 1.6 for the classical model of the Zeeman effect. This assumes zero velocity along the  $z$ -axis. See also Blundell (2001).

<sup>25</sup>See Bleaney and Bleaney (1976, Problem 4.10).

of the ion is a cycloid: a combination of circular motion at  $\omega_c$  and drift at velocity  $E/B$  in the  $y$ -direction,<sup>26</sup> as illustrated in Fig. 12.8(c). The counter-intuitive drift of the ion's average position in the direction *perpendicular* to  $\mathbf{E}$  is the key to the operation of the Penning trap. The drift of the ion perpendicular to the radial electric field gives a tangential component of velocity and causes the ion to move slowly around the  $z$ -axis (direction of  $\mathbf{B}$ ) at the magnetron frequency  $\omega_m$  whilst at the same time undergoing cyclotron orbits,<sup>27</sup> as shown in Fig. 12.8(d). The electrode structure shown in Fig. 12.7 gives a radial field in the plane  $z = 0$ . In addition to  $\omega_c$  and  $\omega_m$ , the ion's motion has a third characteristic frequency  $\omega_z$  associated with oscillations along the  $z$ -axis of the trap (analogous to the axial motion between the two d.c. electrodes at either end of the linear Paul trap). Usually the three frequencies have widely

<sup>26</sup>It is easily seen that  $E/B$  has the dimensions of a velocity by looking at the expressions for the electric and magnetic forces given above.

<sup>27</sup>In a magnetron, a beam of electrons in crossed E- and B-fields moves in a similar way to that shown in Fig. 12.8, but much faster than ions because of the smaller mass and higher electric field. These electrons radiate electromagnetic radiation at  $\omega_m$  in the microwave region, e.g. at 2.5 GHz for the magnetrons in domestic microwave ovens (Bleaney and Bleaney 1976, Section 21.5).

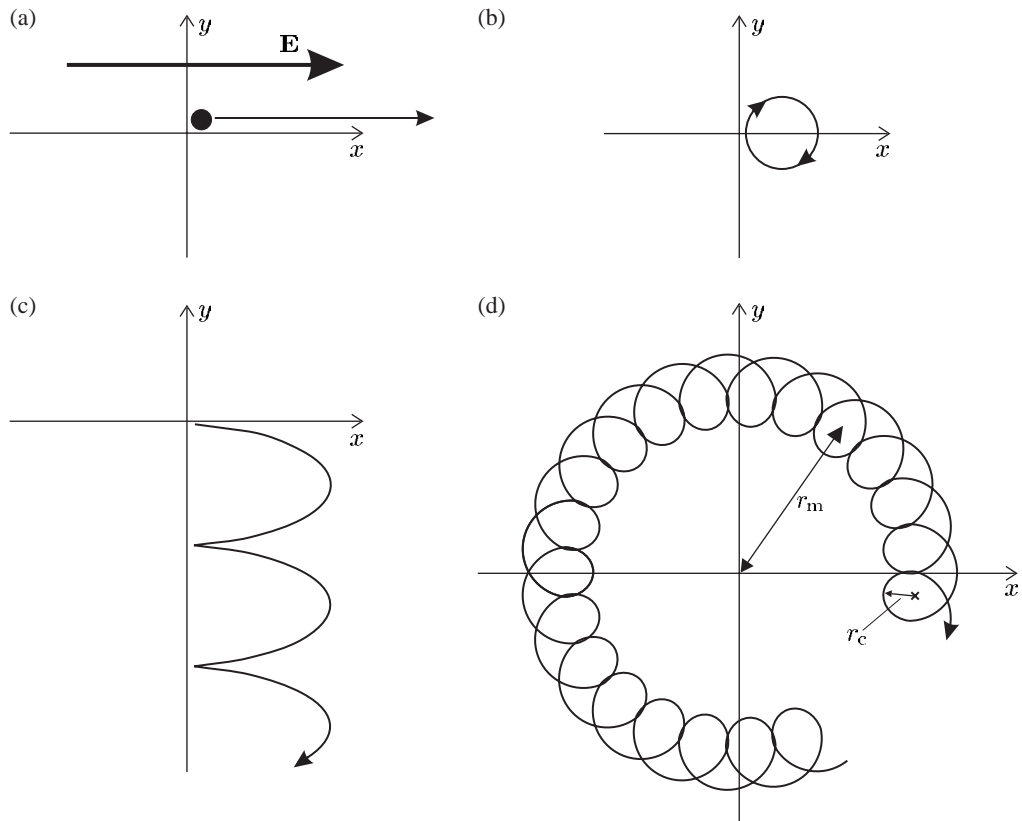


**Fig. 12.8** The motion of a positively-charged ion in various configurations of electric and magnetic fields. (a) A uniform electric field along the  $x$ -direction accelerates the ion in that direction. (b) A uniform magnetic flux density  $\mathbf{B}$  along the  $z$ -direction (out of the page) leads to a circular motion in the plane perpendicular to  $\mathbf{B}$ , at the cyclotron frequency  $\omega_c$ . (c) In a region of crossed electric and magnetic fields ( $E_x$  and  $B_z$ , respectively) the motion described by eqns 12.25 is drift at velocity  $E/B$  *perpendicular* to the uniform electric field in addition to the cyclotron orbits. (The ion is initially stationary.) (d) In a Penning trap the combination of a radial electric field and axial magnetic field causes the ion to move around in a circle at the magnetron frequency. (If  $B = 0$  then the ion would move radially outwards and hit the ring electrode.)

different values  $\omega_z \ll \omega_m \ll \omega_c$  (Exercise 12.4).

### 12.7.2 Mass spectroscopy of ions

The determination of the mass of ions by means of eqn 12.20 for Paul trapping has been mentioned earlier. Alternatively, measurement of the ratio of cyclotron frequencies of two different species of ion in the same Penning trap gives their mass ratio:

$$\frac{\omega'_c}{\omega_c} = \frac{eB/M'}{eB/M} = \frac{M}{M'}. \quad (12.26)$$

This assumes the simplest case with two species of equal charge, but the ratio of the charges is always known exactly. Superconducting magnets give very stable fields so that the cancellation of  $B$  in the above equation introduces very little uncertainty and in this way masses can be compared to better than 1 part in  $10^8$ .

### 12.7.3 The anomalous magnetic moment of the electron

The advantages of the Penning trap have been exploited to make precise measurements of the magnetic moment of the electron (confined in the same way as ions but with a negative voltage on the end caps). From an atomic physics perspective, this can be viewed as a measurement of the Zeeman effect for an electron bound in a trap rather than one bound in an atom (Dehmelt 1990), but the splitting between the two magnetic states  $m_s = \pm 1/2$  is the same in both situations, corresponding to a frequency  $\Delta\omega = g_s\mu_B B/\hbar = g_s eB/2m_e$ . Measurement of this frequency gives the gyromagnetic ratio for spin  $g_s$ . To determine  $B$  accurately they measured the cyclotron frequency  $\omega_c = eB/m_e$  and found the ratio

$$\frac{\Delta\omega}{\omega_c} = \frac{g_s}{2}. \quad (12.27)$$

The relativistic theory of quantum mechanics developed by Dirac predicts that  $g_s$  should be exactly equal to 2, but the incredibly precise measurement by Van Dyck *et al.* (1986) found

$$\frac{g_s}{2} = 1.0011596521884(4).$$

The accuracy is better than 4 in  $10^{12}$ . Often this is quoted as a measurement of  $g - 2$  for the electron and the difference from 2 arises from quantum electrodynamic (QED) effects. For the electron the theoretical calculation gives

$$\frac{g_s}{2} = 1 + \frac{\alpha}{2\pi} + A_2 \left(\frac{\alpha}{\pi}\right)^2 + A_3 \left(\frac{\alpha}{\pi}\right)^3 + A_4 \left(\frac{\alpha}{\pi}\right)^4 + \dots \quad (12.28)$$

The very detailed calculations give the coefficients  $A_2 = -0.328478965$ ,  $A_3 = 1.17611$  and  $A_4 = -0.99$ . The numerical value of this expression

agrees well with the experimental value given above and this provides a very stringent test of the theory.<sup>28</sup> Actually, at the time of the first measurements the fine-structure constant  $\alpha$  was not known to enough decimal places, so the argument was turned around—the theory was assumed to be correct and used to deduce the value of  $\alpha$ . Writing the theoretical value as coefficients multiplying various powers of  $\alpha$  (in this case  $\alpha/\pi$ ) reflects the way theorists carry out QED calculations. Each power corresponds to perturbations of a given order. To match the accuracy of the experiment required evaluation of the contribution from all orders of perturbation up to and including the fourth order.<sup>29</sup> As might be imagined, it took many years of careful work to match the phenomenal precision of the experiment.

Similar experiments have also been carried out for the positron, the antimatter counterpart of the electron, and the comparison of the properties of particles and antiparticles gives interesting tests of the fundamental symmetry principles of particle physics. The very accurate theoretical calculations of the magnetic moments can only be made for simple particles without internal structure (leptons). Other QED experiments provide complementary information; for example, the measurements of the Lamb shift in hydrogen, and highly-ionized hydrogenic ions test the theory for an electron in a bound state where the calculations are considerably more complicated than for a free electron. It is very important to understand how to apply field theories like QED to bound systems.

## 12.8 Electron beam ion trap

The electron beam ion trap (EBIT) was developed to confine ions that have lost many electrons and which have energies much higher than those in typical experiments with Paul and Penning traps.

Figure 12.9 shows a schematic layout of an EBIT. Such a device is physically much larger than the other types of trap, but still much smaller than the particle accelerators that were previously used to produce highly-ionized ions.<sup>30</sup> The EBIT confines positive ions by their strong electrostatic attraction to the high negative charge density in an electron beam along the axis of the trap—the ions stay within this electron beam most of the time. The electrons emanate from an electron gun with a high current density over a small area, but the space charge in the beam tends to cause divergence. A strong axial magnetic field counteracts this spreading to keep the electrons tightly focused. This magnetic field acts as in a Penning trap to prevent the electrons moving radially outwards under the influence of the radial electric field—the same field that confines positive ions pushes electrons outwards.<sup>31</sup> Electrodes with a d.c. voltage of several kilovolts restrict the motion of the ions along the electron beam. (In comparison, the Penning trap only has a few volts on the end caps.)

In addition to trapping, the EBIT also produces the ions by the following ionization steps.<sup>32</sup> Atoms or ions in a low-charge state injected

<sup>28</sup>In 1998 CODATA recommended the value of  $\alpha = 1/137.0359979$ . The latest value may be found on the NIST web site.

<sup>29</sup>This required the evaluation of about 1000 contributions, each represented by different Feynman diagrams, and the calculations are still being refined by Kinoshita (1995) and Kinoshita and Nio (2003).

<sup>30</sup>The EBIT uses a hybrid of the techniques in ion trapping and accelerator physics to extend the precision of traps to higher energies.

<sup>31</sup>The magnetic field has a negligible effect directly on the ions, in comparison to the electrostatic force from the space charge of the electrons.

<sup>32</sup>It has the alternative name of an electron beam ion source or EBIS.

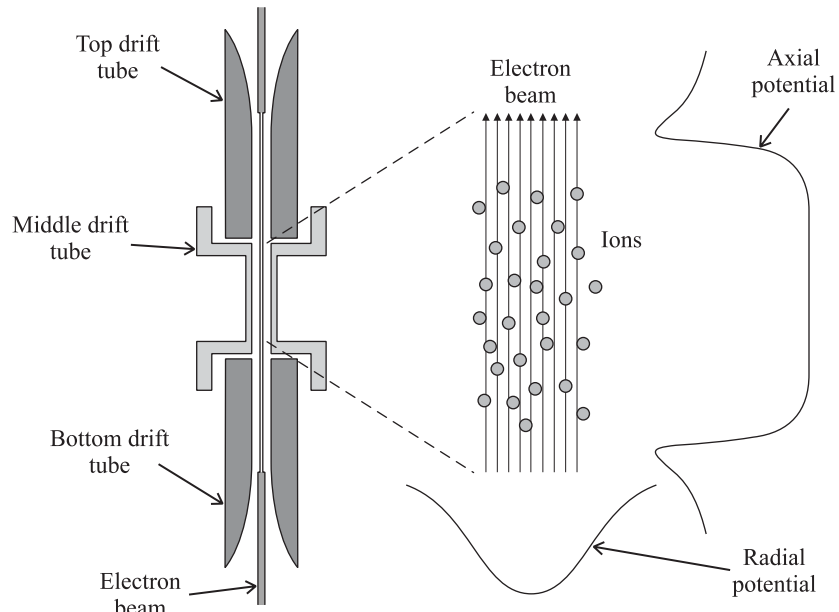


**Fig. 12.9** A cross-section of an electron beam ion trap that has cylindrical symmetry. The high-energy electron beam along the axis of the trap (that is obviously a negative space charge) attracts positive ions to give radial confinement and ionizes them further. The electrodes (called drift tubes by accelerator physicists) give confinement along the axis, i.e. the top and bottom drift tubes act like end caps as in a Penning trap but with much higher positive voltage. To the right is an enlarged view of the ions in the electron beam and the form of the electrostatic potentials along the radial and axial directions. Courtesy of Professor Joshua Silver and co-workers, Physics department, University of Oxford.

into the EBIT region have electrons knocked off by the electron beam to form positive ions. These ions become confined within the electron beam where bombardment by the high-energy electrons removes more and more electrons, so that the ions become more highly charged. This process continues until the electrons remaining on the ion have a binding energy greater than the energy of the incoming electrons. Thus the final charge state of the trapped ion is controlled by varying the accelerating voltage on the electron gun. As an extreme example, consider stripping all but one of the electrons off a uranium atom. The final stage of the ionization process to produce  $\text{U}^{+91}$  requires an energy of  $13.6 \times (92)^2 \sim 10^5$  eV, i.e. an accelerating voltage of 100 kV. These extreme conditions can be achieved but many EBIT experiments use more modest voltages on the electron gun of a few tens of kilovolts.

The transitions between the energy levels of highly-charged ions produce X-rays and the spectroscopic measurements of the wavelength of the radiation emitted from EBITs, use vacuum spectrographs (often with photographic film as the ‘detector’ since it has a high sensitivity at short wavelengths and gives good spatial resolution). Such traditional spectroscopic methods have lower precision than laser spectroscopy but QED effects scale up rapidly with increasing atomic number. The Lamb shift increases as  $(Z\alpha)^4$  whereas the gross energy scales as  $(Z\alpha)^2$ , so measurements of hydrogen-like ions with high  $Z$  allow the QED effects to be seen. It is important to test the QED calculations for bound states because, as mentioned in the previous section, they require distinctly different approximations and theoretical techniques to those used for free particles. Indeed, as  $Z$  increases the parameter  $Z\alpha$  in the expansions

used in the QED calculations becomes larger and higher orders start to make a greater contribution.

## 12.9 Resolved sideband cooling

Laser cooling on a strong transition of line width  $\Gamma$  rapidly reduces the energy of a trapped ion down to the Doppler cooling limit  $\hbar\Gamma/2$  of that transition. The laser cooling of an ion works in a very similar way to the Doppler cooling of a free atom (see Exercise 9.8). To go further narrower transitions are used. However, when the energy resolution of the narrow transition  $\hbar\Gamma'$  is less than the energy interval  $\hbar\omega_v$  between the vibrational levels of the trapped ion (considered as a quantum harmonic oscillator) the quantisation of the motion must be considered, i.e. in the regime where

$$\Gamma' \ll \omega_v \ll \Gamma. \quad (12.29)$$

We have seen that typically  $\Gamma/2\pi$  is tens of MHz and  $\omega_v/2\pi \simeq 1$  MHz. The vibrational energy levels have the same spacing  $\hbar\omega_v$  in both the ground and excited states of the ion since the vibrational frequency depends only on the charge-to-mass ratio of the ion and not its internal state, as illustrated in Fig. 12.10. The trapped ion absorbs light at the angular frequency of the narrow transition for a free ion  $\omega_0$ , and also at the frequencies  $\omega_L = \omega_0 \pm \omega_v$ ,  $\omega_0 \pm 2\omega_v$ ,  $\omega_0 \pm 3\omega_v$ , etc. that correspond to transitions in which the vibrational motion of the ion changes. The vibrational levels in the ground and excited states are labelled by the vibrational quantum numbers  $v$  and  $v'$ , respectively, and these sidebands correspond to transitions in which  $v' \neq v$ . The energy of the bound system is reduced by using laser light at frequency  $\omega_L = \omega_0 - \omega_v$  to excite the first sideband of lower frequency, so that the ion goes into the vibrational level with  $v' = v - 1$  in the upper electronic state. This excited state decays back to the ground state—the most probable spontaneous transition is the one in which the vibrational level does not change so that, on average, the ion returns to the ground electronic state in a lower vibrational level than it started. A detailed explanation of the change in  $v$  during spontaneous emission would need to consider the overlap of the wavefunctions for the different vibrational levels and is not given here.<sup>33</sup>

This sideband cooling continues until the ion has been driven into the lowest vibrational energy level. An ion in the  $v = 0$  level no longer absorbs radiation at  $\omega_0 - \omega_v$ , as indicated in Fig. 12.10—experiments use this to verify that the ion has reached this level by scanning the laser frequency to observe the sidebands on either side, as shown in Fig. 12.10(b); there is little signal at the frequency of the lower sideband, as predicted, but there is a strong signal at the frequency of the upper sideband.<sup>34</sup> The lower sideband arises for the population in the  $v = 1$  level (and any higher levels if populated), and the upper sideband comes from ions in  $v = 0$  that make a transition to the  $v' = 1$  level. Thus the ratio of the signals on these two sidebands gives a direct measure of the

<sup>33</sup>The situation closely resembles that in the Franck–Condon principle that determines the change in vibrational levels in transitions between electronic states of molecules—the relevant potentials for an ion, shown in Fig. 12.10, are simpler than those for molecules.

<sup>34</sup>It is easy to be misled into thinking that the number of sidebands observed depends on the occupation of the vibrational levels of the trapped ion (especially if you are familiar with the vibrational structure of electronic transitions in molecules). This example shows that this is not the case for ions, i.e. sidebands arise for an ion that is predominantly in the lowest vibrational level. Conditions can also arise where there is very weak absorption at the frequencies of the sidebands, even though many vibrational levels are occupied, e.g. for transitions whose wavelength is much larger than the region in which the ions are confined. Although sidebands have been explained here in terms of vibrational levels, they are not a quantum phenomenon—there is an alternative classical explanation of sidebands in terms of a classical dipole that emits radiation while it is vibrating to and fro.

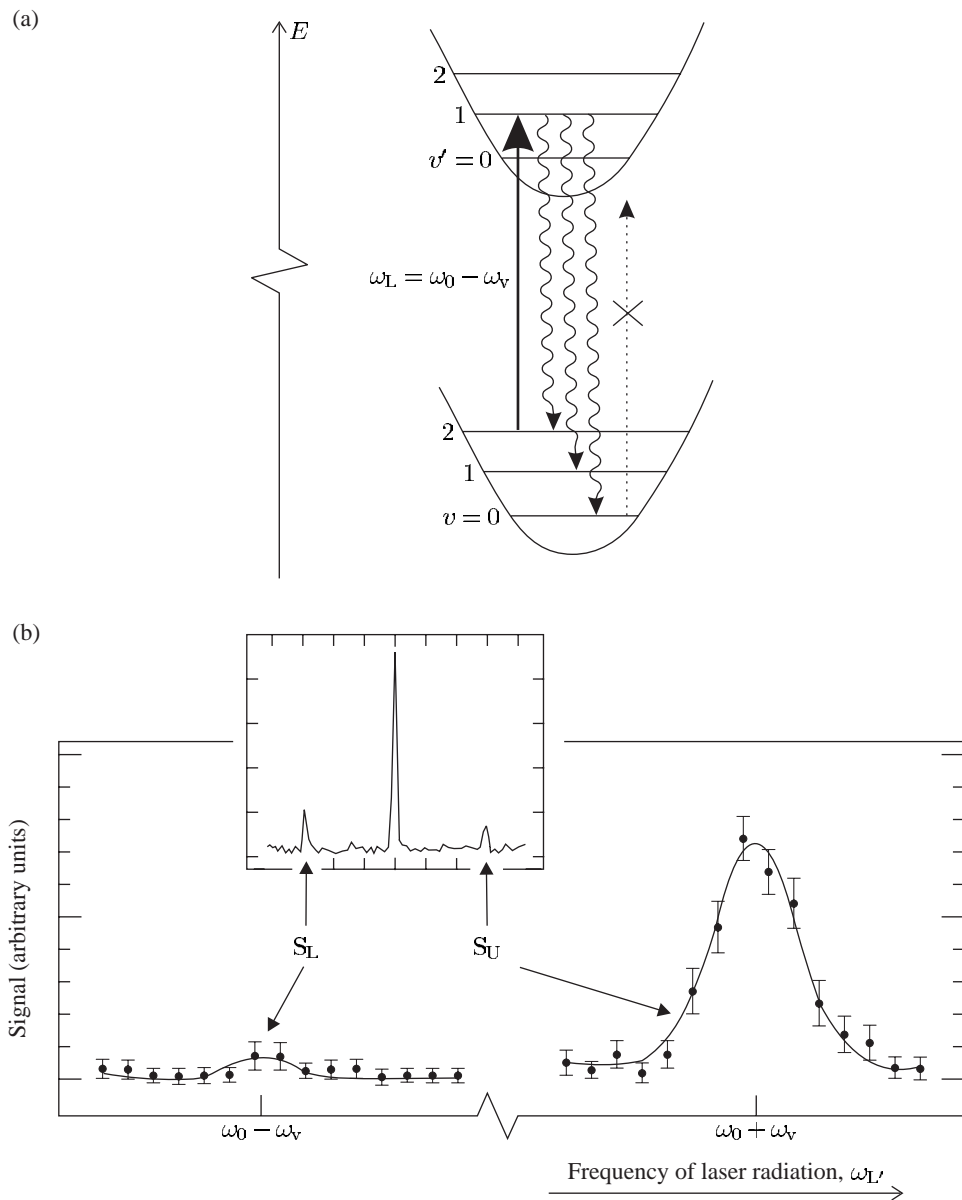


**Fig. 12.10** (a) The vibration levels of an ion in a harmonic trap have the same spacing for both the ground and excited electronic states. Excitation by light of frequency  $\omega_L = \omega_0 - \omega_v$ , followed by spontaneous emission, leads to a decrease in the vibrational quantum number, until the ion reaches the lowest level with  $v = 0$ , from whence there is no transition, as indicated by the dotted line at this frequency (but light at frequency  $\omega_0$  and  $\omega_0 + \omega_v$  would excite the ion in  $v = 0$ ). (b) The spectrum of a trapped ion shows sidebands on either side of the main transition. The inset figure shows the spectrum before sideband cooling. The enlarged part of the figure shows that after sideband cooling the signal on the upper sideband  $S_U$  at angular frequency  $\omega_0 + \omega_v$  is stronger than the lower one  $S_L$  at  $\omega_0 - \omega_v$ —this asymmetry indicates that the ion is mainly in the lowest vibrational state (i.e. vibrational quantum number much less than 1). The vertical axis gives the transition probability, or the probability of a quantum jump during the excitation of the narrow transition. After Diedrich *et al.* (1989). Part (b), copyright 1989 by the American Physical Society.

ratio of populations: in this example  $\mathcal{N}(v=1)/\mathcal{N}(v=0) = 0.05$  so the ion spends most of its time in the lowest level. Thus the ion has almost the minimum energy attainable in this system.

Single ion experiments such as optical frequency standards with extremely high resolution (Section 12.6) do not need to cool the ion to the very lowest level—they just pick out the transition at  $\omega_0$  from the well-resolved sidebands. The quantum computing experiments described in the next chapter, however, must have an initial state with all the ions in the lowest energy level of the trap (or very close to this ideal situation) to give complete control over the quantum state of the whole system. The preparation of all the trapped ions in the lowest vibrational level<sup>35</sup> is complicated by the collective modes of vibration of a system with more than one trapped ion (Exercise 12.1), and the achievement of this initial state stretches the capability of laser cooling methods to their very limits.<sup>36</sup>

## 12.10 Summary of ion traps

This chapter explored some of the diverse physics of ion trapping, ranging from the cooling of ions to temperatures of only  $10^{-3}$  K in small ion traps to the production of highly-charged ions in the EBIT. Trapping of positrons was mentioned in Section 12.7.3 and ion traps make good containers for storing other types of antimatter such as antiprotons produced at particle accelerators.<sup>37</sup> In recent experiments at CERN carried out by a large collaboration (Amoretti *et al.* 2002) these two antiparticles have been put together to produce anti-hydrogen. In the future it will be possible to do anti-atomic physics, e.g. to measure whether hydrogen and anti-hydrogen have the same spectra (a test of CPT invariance.) This high-energy trapping work has developed from accelerator-based experiments and probes similar physics.

At the opposite pole lies the work on the laser cooling of ions to extremely low energies. We have seen that the fundamental limit to the cooling of a bound system is quite different to the laser cooling of free atoms. Experimenters have developed powerful techniques to manipulate single ions and make frequency standards of extreme precision. The long decoherence times of trapped ions are now being exploited to carry out the manipulation of several trapped ions in experiments on quantum computation, which is the subject of the next chapter. Such experimental techniques give exquisite control over the state of the whole quantum system in a way that the founders of quantum mechanics could only dream about.

## Further reading

The book on ion trapping by Ghosh (1995) gives a detailed account of these techniques. See also the tutorial articles by Wayne Itano (Itano *et al.* 1995) and David Wineland (Wineland *et al.* 1995), and the Nobel

<sup>35</sup>For neutral particles in magnetic traps, quantum statistics causes the atoms to undergo Bose–Einstein condensation into the ground state, even though they have a mean thermal energy greater than the spacing between trap energy levels. Quantum statistics does not affect trapped ions because they are distinguishable—even if the ions are identical the mutual Coulomb repulsion keeps them far apart, as shown in Fig. 12.4, and the strong fluorescence enables the position of each ion to be determined.

<sup>36</sup>The alert reader may have noticed that we have not discussed the recoil limit, that plays such an important role for free particles. For stiff traps the spacing of the vibrational energy levels greatly exceeds the recoil energy  $\hbar\omega_v \gg E_{\text{rec}}$ , and the cooling limit of the trapped particle is determined by the zero-point energy.

<sup>37</sup>Just after its creation in high-energy collisions, the antimatter has an energy of MeV but it is moderated to energies of keV before trapping.

<sup>38</sup>On the web site of the Nobel prizes.

prize lecture of Wolfgang Paul.<sup>38</sup> The National Physical Laboratory in the UK and the National Institute of Standards and Technology in the US provide internet resources on the latest developments and research.

## Exercises

(12.1) *The vibrational modes of trapped ions*

Two calcium ions in a linear Paul trap lie in a line along the  $z$ -axis.

- (a) The two end-cap electrodes along the  $z$ -axis produce a d.c. potential as in eqn 12.23, with  $a_2 = 10^6 \text{ V m}^{-2}$ . Calculate  $\omega_z$ .
- (b) The displacements  $z_1$  and  $z_2$  of the two ions from the trap centre obey the equations

$$M\ddot{z}_1 = -M\omega_z^2 z_1 - \frac{e^2/4\pi\epsilon_0}{(z_2 - z_1)^2},$$

$$M\ddot{z}_2 = -M\omega_z^2 z_2 + \frac{e^2/4\pi\epsilon_0}{(z_2 - z_1)^2}.$$

Justify the form of these equations and show that the centre of mass,  $z_{\text{cm}} = (z_1 + z_2)/2$  oscillates at  $\omega_z$ .

- (c) Calculate the equilibrium separation  $a$  of two singly-charged ions.
- (d) Find the frequency of small oscillations of the relative position  $z = z_2 - z_1 - a$ .
- (e) Describe qualitatively the vibrational modes of three ions in the trap, and the relative order of their three eigenfrequencies.<sup>39</sup>

(12.2) *Paul trap*

- (a) For  $\text{Hg}^+$  ions in a linear Paul trap with dimensions  $r_0 = 3 \text{ mm}$ , calculate the maximum amplitude  $V_{\text{max}}$  of the radio-frequency voltage at  $\Omega = 2\pi \times 10 \text{ MHz}$ .
- (b) For a trap operating at a voltage  $V_0 = V_{\text{max}}/\sqrt{2}$ , calculate the oscillation frequency of an  $\text{Hg}^+$  ion. What happens to a  $\text{Ca}^+$  ion when the electrodes have the same a.c. voltage?
- (c) Estimate the depth of a Paul trap that has  $V_0 = V_{\text{max}}/\sqrt{2}$ , expressing your answer as a fraction of  $eV_0$ .

- (d) Explain why a Paul trap works for both positive and negative ions.

(12.3) *Investigation of the Mathieu equation*

Numerically solve the Mathieu equation and plot the solutions for some values of  $q_x$ . Give examples of stable and unstable solutions. By trial and error, find the maximum value of  $q_x$  that gives a stable solution, to a precision of two significant figures. Explain the difference between precision and accuracy. [Hint. Use a computer package for solving differential equations. The method in Exercise 4.10 does not work well when the solution has many oscillations because its numerical integration algorithm is too simple.]

(12.4) *The frequencies in a Penning trap*

A Penning trap confines ions along the axis by repulsion from the two end-cap electrodes; these have a d.c. positive voltage for positive ions that gives an axial oscillation frequency, as calculated in Exercise 12.1. This exercise looks at the radial motion in the  $z = 0$  plane. The electrostatic potential in eqn 12.23 with  $a_2 = 10^5 \text{ V m}^{-2}$  leads to an electric field that points radially outwards, but the ion does not fly off in this direction because of a magnetic field of induction  $B = 1 \text{ T}$  along the  $z$ -axis.

Consider a  $\text{Ca}^+$  ion.

- (a) Calculate the cyclotron frequency.
- (b) Find the magnetron frequency. [Hint. Work out the period of an orbit of radius  $r$  in a plane perpendicular to the  $z$ -axis by assuming a mean tangential velocity  $v = E(r)/B$ , where  $E(r)$  is the radial component of the electric field at  $r$ .]

<sup>39</sup>They resemble the vibrations of a linear molecule such as  $\text{CO}_2$ , described in Appendix A; however, a quantitative treatment would have to take account of the Coulomb repulsion between all pairs of ions (not just nearest neighbours).

(12.5) *Production of highly-charged ions in an EBIT*

- (a) Estimate the accelerating voltage required for an electron beam voltage that produces hydrogenic silicon  $\text{Si}^{13+}$  in an EBIT.
- (b) Calculate the radius of the first Bohr orbit ( $n = 1$ ) in hydrogenic uranium,  $\text{U}^{+91}$ .
- (c) Calculate the binding energy of the electron in  $\text{U}^{+91}$  and express it as a fraction of the atom's rest mass energy  $Mc^2$ .
- (d) QED effects contribute  $3 \times 10^{-5}$  eV to the

Web site:

<http://www.physics.ox.ac.uk/users/foot>

This site has answers to some of the exercises, corrections and other supplementary information.

binding energy of the 1s ground configuration of atomic hydrogen. Express this as a fraction of the hydrogen atom's rest mass. Estimate the magnitude of the QED contribution in the ground state of hydrogen-like uranium  $\text{U}^{+91}$  as a fraction of the rest mass. This fraction gives the precision  $\Delta M/M$  with which the ion's mass must be determined in order to measure QED effects. Discuss the feasibility of doing this in an ion trap.

# 13

# Quantum computing

|   |     |
|---|-----|
| 13.1 Qubits and their properties              | 283 |
| 13.2 A quantum logic gate                     | 287 |
| 13.3 Parallelism in quantum computing         | 289 |
| 13.4 Summary of quantum computers             | 291 |
| 13.5 Decoherence and quantum error correction | 291 |
| 13.6 Conclusion                               | 293 |
| Further reading                               | 294 |
| Exercises                                     | 294 |

<sup>1</sup>Quantum computing requires precise control of the motion of the ions, i.e. their external degrees of freedom, as well as their internal state  $|F, M_F\rangle$ .

Quantum computing will be a revolutionary new form of computation in the twenty-first century, able to solve problems inaccessible to classical computers. However, building a quantum computer is very difficult, and so far only simple logic gates have been demonstrated in experiments on ions in a linear Paul trap. The ideas of quantum computing have also been tested in experiments using nuclear magnetic resonance (NMR).

In the Paul trap, the ions sit in an ultra-high vacuum (pressure  $\sim 10^{-11}$  mbar) so that collisions rarely happen, and the ions are well isolated from the environment. We have seen that these conditions enable extremely high-resolution spectroscopy of single ions because of the very small perturbations to the energy levels. Quantum computing requires more than one ion in the trap, and all of these ions must be cooled to the lowest vibrational level to give a well-defined initial quantum state for the system.<sup>1</sup> This presents a much greater experimental challenge than the laser cooling of a single ion to reduce Doppler broadening, but it has been achieved in some experiments. The previous chapter describes the physics of the linear Paul trap but for the purposes of this chapter we simply assume that the trap produces a harmonic potential with strong confinement in the radial direction, so that the ions lie in a line along its  $z$ -axis, as shown in Fig. 13.1; their mutual electrostatic repulsion keeps the ions far enough apart for them to be seen separately.



**Fig. 13.1** A string of *four* ions in a linear Paul trap. Coulomb repulsion keeps the ions apart and the gap corresponds to an ion in the dark state. In this experiment two laser beams simultaneously excite strong and weak transitions to give quantum jumps, as described in Section 12.6, so that each ion flashes on and off randomly. This snapshot of the system at a particular time could be taken to represent the binary number 1101. A quantum logic gate requires much more sophisticated techniques in which laser pulses determine precisely the initial state of each individual ion in the chain, as described in this chapter. Courtesy of Professors A. M. Steane and D. N. Stacey, D. M. Lucas and co-workers, Physics department, University of Oxford.

## 13.1 Qubits and their properties

A classical computer uses bits with two values 0 or 1 to represent binary numbers, but a quantum computer stores information as quantum bits or qubits (pronounced Q-bits). Each qubit has two states, labelled  $|0\rangle$  and  $|1\rangle$  in the Dirac ket notation for quantum states. Most theoretical discussions of quantum computing consider the qubit as a spin-1/2 object, so the two states correspond to spin down  $|m_s = -1/2\rangle$  and spin up  $|m_s = +1/2\rangle$ . However, for a trapped ion the two states usually correspond to two hyperfine levels of the ground configuration, as illustrated in Fig. 13.2. In the following discussion,  $|1\rangle$  represents the ion in the upper hyperfine level and  $|0\rangle$  is used for the lower hyperfine level, but all of the arguments apply equally well to spin-1/2 particles since the principles of quantum computing clearly do not depend on the things used as qubits. Ions, and other physical qubits, give a compact way of storing information, e.g.  $|1101\rangle$  represents the binary number 1101 in Fig. 13.1, but the quantum features of this new way of encoding information only become apparent when we consider the properties of more than one qubit in Section 13.1.1. Even though a single qubit generally exists in a superposition of the two states, a qubit does not carry more classical information than a classical bit, as shown by the following argument. The superposition of the two states

$$\psi_{\text{qubit}} = a|0\rangle + b|1\rangle \quad (13.1)$$

obeys the normalisation condition  $|a|^2 + |b|^2 = 1$ . We write this superposition in the general form

$$\psi_{\text{qubit}} = \left\{ \cos\left(\frac{\theta}{2}\right)|0\rangle + e^{i\phi} \sin\left(\frac{\theta}{2}\right)|1\rangle \right\} e^{i\phi'} \quad (13.2)$$

The overall phase factor has little significance and the possible states correspond to vectors of unit length with direction specified by two angles  $\theta$  and  $\phi$ . These are the position vectors of points lying on the surface of a sphere, as in Fig. 13.3. The state  $|0\rangle$  lies at the north pole of this *Bloch sphere* and  $|1\rangle$  at the south pole; all other position vectors are superpositions of these two basis states. Since these position vectors correspond to a simple classical object such as a pointer in three-dimensional space, it follows that the information encoded by each qubit can be modelled in a classical way.

The analogy between a qubit and a three-dimensional pointer seems to imply that a qubit stores more information than a bit with two possible values 0 or 1, e.g. like one of the hands of an analogue clock that gives us information about the time by its orientation in two-dimensional space. Generally, however, this is not true because we cannot determine the orientation of a quantum object as precisely as the hands on a clock. Measurements can only distinguish quantum states, with a high probability, if the states are very different from each other, occupying well-separated positions on opposite sides of the Bloch sphere. A measurement on a

---


$$|1\rangle \equiv |F+1, M'\rangle$$

---


$$|0\rangle \equiv |F, M\rangle$$

**Fig. 13.2** The two hyperfine levels in the ground state of an ion. Generally, experiments use an ion with total angular momentum  $J = 1/2$  in the lowest electronic configuration, so that  $F = I \pm 1/2$ . The qubits  $|0\rangle$  and  $|1\rangle$  correspond to two particular Zeeman states in the two levels, e.g.  $|F, M\rangle$  and  $|F+1, M'\rangle$ , respectively.

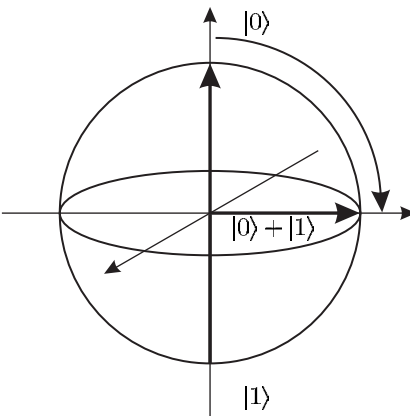


**Fig. 13.3** The state  $|0\rangle$  lies at the north pole of this *Bloch sphere* and  $|1\rangle$  at the south pole; all other position vectors are superpositions of these two basis states. The Bloch sphere lies in the Hilbert space spanned by the two eigenvectors  $|0\rangle$  and  $|1\rangle$ . The Hadamard transformation defined in eqn 13.3 takes  $|0\rangle \mapsto |0\rangle + |1\rangle$  (cf. Fig. 7.2).

spin-1/2 particle determines whether its orientation is up or down along a given axis. After that measurement the particle will be in one of those states since the act of measurement puts the system into an eigenstate of the corresponding operator. In the same way, a qubit will give either 0 or 1, and the read-out process destroys the superposition.

The Bloch sphere is very useful for describing how individual qubits transform under unitary operations. For example, the *Hadamard* transformation that occurs frequently in quantum computation (see the exercises at the end of this chapter) has the operator<sup>2</sup>

$$\begin{aligned}\hat{U}_H |0\rangle &\mapsto |0\rangle + |1\rangle , \\ \hat{U}_H |1\rangle &\mapsto |0\rangle - |1\rangle .\end{aligned}\quad (13.3)$$

This is equivalent to the matrix

$$\hat{U}_H = \frac{1}{\sqrt{2}} \begin{pmatrix} 1 & 1 \\ 1 & -1 \end{pmatrix}.$$

The effect of this unitary transformation of the state is illustrated in Fig. 13.3—it corresponds to a rotation in the Hilbert space containing the state vectors. This transformation changes  $|0\rangle$ , at the north pole, into the superposition given in eqn 13.3 that lies on the equator of the sphere.

### 13.1.1 Entanglement

We have already encountered some aspects of the non-intuitive behaviour of multi-particle quantum systems in the detailed description of the two electrons in the helium atom (Chapter 3), where the antisymmetric spin state  $[|\downarrow\uparrow\rangle - |\uparrow\downarrow\rangle]/\sqrt{2}$  corresponds to the wavefunction

$$\Psi = |01\rangle - |10\rangle \quad (13.4)$$

in the notation used in this chapter (without normalisation). This does not factorise into a product of single-particle wavefunctions:

$$\Psi \neq \psi_1 \psi_2 , \quad (13.5)$$

<sup>2</sup>In this chapter wavefunctions are written without normalisation, which is the common convention in quantum computation.

where

$$\psi_1\psi_2 = [a|0\rangle + b|1\rangle]_1 [c|0\rangle + d|1\rangle]_2. \quad (13.6)$$

Here  $c$  and  $d$  are additional arbitrary constants, and the futility of attempting to determine these constants quickly becomes obvious if you try it. Generally, we do not bother with the subscript used to denote the particle, so  $|0\rangle_1|1\rangle_2 \equiv |01\rangle$  and  $|1\rangle_1|1\rangle_2 \equiv |11\rangle$ , etc. Multiple-particle systems that have wavefunctions such as eqn 13.4 that cannot be written as a product of single-particle wavefunctions are said to be entangled. This entanglement in systems with two, or more, particles leads to quantum properties of a completely different nature to those of a system of classical objects—this difference is a crucial factor in quantum computing. Quantum computation uses qubits that are *distinguishable*, e.g. ions at well-localised positions along the axis of a linear Paul trap. We can label the two ions as Qubit 1 and Qubit 2 and know which one is which at any time. Even if they are identical, the ions remain distinguishable because they stay localised at certain positions in the trap. For a system of distinguishable quantum particles, any combination of the single-particle states is allowed in the wavefunction of the whole system:

$$\Psi = A|00\rangle + B|01\rangle + C|10\rangle + D|11\rangle. \quad (13.7)$$

The complex amplitudes  $A$ ,  $B$ ,  $C$  and  $D$  have arbitrary values. It is convenient to write down wavefunctions without normalisation, e.g.

$$\Psi = |00\rangle + |01\rangle + |10\rangle + |11\rangle, \quad (13.8)$$

$$\Psi = |00\rangle + 2|01\rangle + 3|11\rangle, \quad (13.9)$$

$$\Psi = |01\rangle + 5|10\rangle. \quad (13.10)$$

Two of these three wavefunctions possess entanglement (see Exercise 13.1). We encounter examples with three qubits later (eqn 13.12).

In the discussion so far, entanglement appears as a mathematical property of multiple-particle wavefunctions, but what does it mean physically? It is always dangerous to ask such questions in quantum mechanics, but the following discussion shows how entanglement relates to correlations between the particles (qubits), thus emphasising that entanglement is a property of the system *as a whole* and not the individual particles. As a specific example consider two trapped ions. To measure their state, laser light excites a transition from state  $|1\rangle$  (the upper hyperfine level) to a higher electronic level to give a strong fluorescence signal, so  $|1\rangle$  is a ‘bright state’, while an ion in  $|0\rangle$  remains dark.<sup>3</sup> Wavefunctions such as those in eqns 13.4 and 13.10 that contain only the terms  $|10\rangle$  and  $|01\rangle$  always give one bright ion and the other dark, i.e. an anticorrelation where a measurement always finds the ions in different states. To be more precise, this corresponds to the following procedure. First, prepare two ions so that the system has a certain initial wavefunction  $\Psi_{in}$ , then make a measurement of the state of the ions by observing their fluorescence. Then reset the system to  $\Psi_{in}$  before another measurement. The record of the state of the ions for a sequence

<sup>3</sup>This is similar to the detection of quantum jumps in Section 12.6, but typically quantum computing experiments use a separate laser beam for each ion to detect them independently.

of such measurements looks like: 10, 10, 01, 10, 10, ... Each ion gives a random sequence of 0s and 1s but always has the opposite state to the other ion.

This example does not illustrate the full subtlety of entanglement because we would get the same result if we prepared the two ions either in  $|01\rangle$  or  $|10\rangle$  randomly at the beginning. Such an apparatus produces correlated pairs of ions in a purely classical way that mimics the quantum situation. John Bell proved that we can make measurements that distinguish the ‘classical correlation’ from an entangled state. The above description shows that this cannot be done simply by making measurements along the axes defined by the basis states  $|0\rangle$  and  $|1\rangle$ , but it turns out that quantum entanglement and ‘classically-correlated’ particles give different results for measurements along other sets of axes. This was a very profound new insight into the nature of quantum mechanics that has stimulated much important theoretical and experimental work.<sup>4</sup>

<sup>4</sup>Bell considered the well-known EPR paradox and the system of two ions described above has the same properties as the two spin-1/2 particles usually used in quantum mechanics texts (Rae 1992).

‘Entanglement implies correlation but correlation does not imply entanglement’. In the following we shall concentrate mainly on the first half of this statement, i.e. two-particle systems encode quantum information as a *joint* property of the qubits and carry more information than can be stored on the component parts separately. The quantum information in an entangled state is very delicate and is easily destroyed by perturbations of the relative phase and amplitude of the qubits, e.g. in present-day ion traps it is difficult to maintain coherence between more than a few qubits; this decoherence is caused by random perturbations that affect each qubit in a different way.

The wavefunctions of the two electrons in helium are entangled but they do *not* give qubits useful for quantum computing. Nevertheless, since this is a book about atomic physics it is worthwhile to look back at helium. The antisymmetric state of the two spins has already been used as an example of entanglement. The symmetric spin wavefunction  $[|\downarrow\uparrow\rangle + |\uparrow\downarrow\rangle]/\sqrt{2}$  also has entanglement, but the two other symmetric wavefunctions factorise:  $|\uparrow\uparrow\rangle \equiv |\uparrow\rangle_1|\uparrow\rangle_2$ , and similarly for  $|\downarrow\downarrow\rangle$ . The two electrons are in these eigenstates of  $S$  because of the exchange symmetry. When the two electrons do not have the same quantum numbers,  $n$  and  $l$ , the spatial wavefunctions are symmetric and antisymmetric combinations of the single-electron wavefunctions and are entangled. These eigenstates of the residual electrostatic interaction also satisfy the requirement of exchange symmetry for identical particles. (Note that the energy levels and spatial wavefunctions would be the same even if the particles were not identical—see Exercise 3.4.) The exchange integrals in helium can be regarded as a manifestation of the entanglement of the spatial wavefunction of the two electrons that leads to a correlation in their positions, or an anticorrelation, making it more (or less) probable that the electrons will be found close together. From the quantum perspective, the energy difference for two different entangled wavefunctions does not seem strange because we do not expect them to have the same properties, even if they are made up of the same single-electron states.

## 13.2 A quantum logic gate

Quantum computing uses nothing more than standard quantum mechanics but it combines operations on the qubits and quantum measurements in sophisticated ways to give amazingly powerful new methods for computation. Here we consider just one example of the transformations of the qubits, or quantum logic gates, that form the elementary building blocks (primitives) of a quantum computer. The controlled-NOT gate (CNOT) transforms two qubits, as shown in Table 13.1.

The CNOT gate changes the value of the second qubit *if and only if* the first qubit has the value 1. The first qubit controls the effect of the gate on the second qubit. The truth Table 13.1 looks the same as that for ordinary logic, but a quantum logic gate corresponds to an operation that preserves the superposition of the input states. The quantum mechanical operator of the CNOT gate  $\hat{U}_{\text{CNOT}}$  acts on the wavefunction of the two qubits to give

$$\begin{aligned} \hat{U}_{\text{CNOT}} \{ &A |00\rangle + B |01\rangle + C |10\rangle + D |11\rangle \} \\ &\rightarrow A |00\rangle + B |01\rangle + C |11\rangle + D |10\rangle . \end{aligned} \quad (13.11)$$

Alternatively, the effect of this operation can be written as  $|10\rangle \leftrightarrow |11\rangle$ , with the other states unchanged. The complex numbers  $A$ ,  $B$ ,  $C$  and  $D$  represent the phase and relative amplitude of states within the superposition.

### 13.2.1 Making a CNOT gate

The CNOT gate is elementary but it turns out not to be the simplest gate to make in an ion trap quantum processor—it requires a sequence of several operations, as described in Steane (1997). So, despite the fact that quantum computing has been introduced into this book as an application of ion trapping, this section explains how to make a quantum logic gate for two spin-1/2 particles. This two-qubit system is not just a convenient theoretical case, but corresponds to actual quantum computing experiments carried out with the nuclear magnetic resonance (NMR) technique. Figure 13.4 shows the energy levels of the two interacting spins.

We do not need to go into all the details of how this energy-level structure arises to understand how to make a CNOT gate, but it is important

**Table 13.1** Truth table of the CNOT quantum logic gate.

|                                     |
|-------------------------------------|
| $ 00\rangle \rightarrow  00\rangle$ |
| $ 01\rangle \rightarrow  01\rangle$ |
| $ 10\rangle \rightarrow  11\rangle$ |
| $ 11\rangle \rightarrow  10\rangle$ |

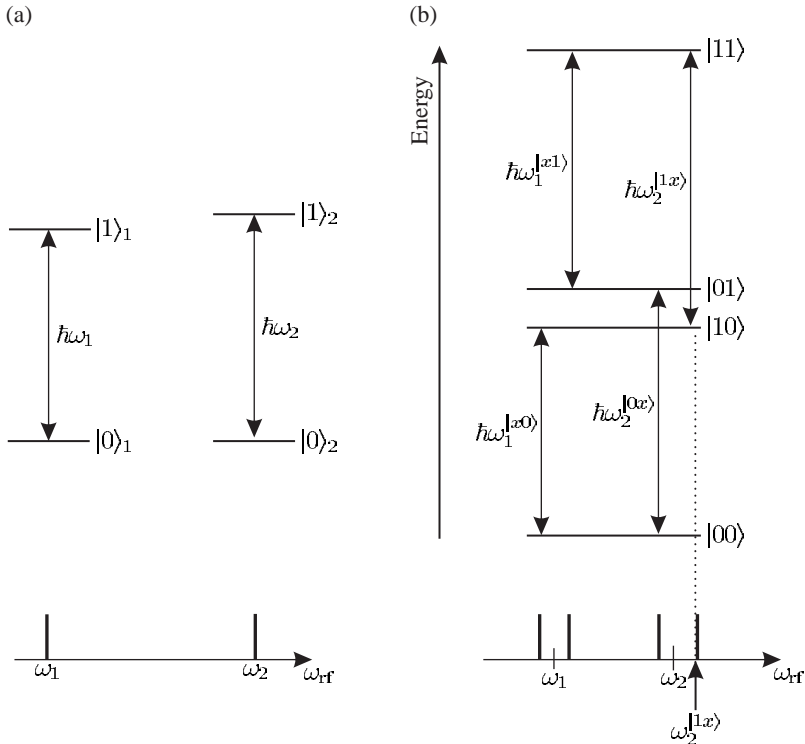


**Fig. 13.4** (a) The energy levels of two spin-1/2 particles which do not interact with each other. The frequencies that drive the transition between the levels of Qubit 1 and Qubit 2 are  $\omega_1$  and  $\omega_2$ , respectively. In NMR these levels correspond to the up and down orientations of two protons in a strong magnetic field, i.e. the states  $|m_I = \pm 1/2\rangle$  for each proton. The difference in the resonance frequencies  $\omega_1 \neq \omega_2$  arises from interaction with their surroundings (other nearby atoms in the molecule). (b) The energy levels of two interacting particles, or qubits. The interaction between the qubits makes the frequency required to change the orientation of Qubit 2 depend on the state of the other qubit (and similarly for Qubit 1). To denote this, the two new resonance frequencies close to  $\omega_2$  are labelled with the superscripts  $|0x\rangle$  and  $|1x\rangle$ . (Note this rather cumbersome notation is not generally used but it is useful in this introductory example.) The absorption spectrum is drawn below the corresponding transitions. A  $\pi$ -pulse of radio-frequency radiation at angular frequency  $\omega_2^{[1x]}$  switches Qubit 2 ( $|0\rangle_2 \leftrightarrow |1\rangle_2$ ) if and only if Qubit 1 is in  $|1\rangle_1$ . This gives the CNOT gate of Table 13.1. For details of the NMR technique see Atkins (1994). In NMR the interaction of the nuclear magnetic moment with a strong external magnetic field  $g_I \mu_B \mathbf{I} \cdot \mathbf{B}$  dominates. For a field of 10 T the protons at the centre of the hydrogen atoms in the sample have resonance frequencies of 400 MHz. This frequency corresponds to approximately  $\omega_1/2\pi \simeq \omega_2/2\pi$  in the figure. The *chemical shift* causes  $\omega_1$  and  $\omega_2$  to differ by only a few parts per million, but this is resolved by standard NMR equipment. Atkins (1994) describes how the fine structure in NMR spectra, shown in (b), arises from spin–spin coupling between the two nuclear spins.

<sup>5</sup>The amplitudes and phases of the states within the superposition must not change spontaneously, i.e. the decoherence must be very small over the time-scale of the experiment.

to know that spontaneous emission is negligible.<sup>5</sup> To make our discussion less abstract, it is also useful to know that in NMR experiments the energy differences between the levels shown in Fig. 13.4 arise from the orientation of the magnetic moment of the nuclei, proportional to their spin, in a strong magnetic field and that radio-frequency radiation drives transitions between the states. There is a splitting of  $\hbar\omega_1$  between the up and down states of the first qubit ( $|0\rangle$  and  $|1\rangle$ ) and  $\hbar\omega_2$  for the second qubit. Therefore a pulse of radio-frequency radiation at angular frequency  $\omega_1$  changes the orientation of the first spin (Qubit 1); for example, a  $\pi$ -pulse (as defined in Section 7.3.1) swaps the states of this

qubit  $|0\rangle \leftrightarrow |1\rangle$ , i.e.  $a|0\rangle + b|1\rangle \mapsto a|1\rangle + b|0\rangle$ . Similarly, pulses at angular frequency  $\omega_2$  manipulate the state of the other spin (Qubit 2). These changes in the state of each qubit independently are not sufficient for quantum computing. The qubits must interact with each other so that one qubit ‘controls’ the other qubit and influences its behaviour. A small interaction between the spin causes the shift of the energy levels indicated in going from Fig. 13.4(a) to (b)—the energy required to flip Qubit 2 now depends on the state of Qubit 1 (and vice versa). The energy levels in Fig. 13.4(b) give four separate transition frequencies between the four states of the two qubits; a pulse of radio-frequency radiation that drives one of these transitions can achieve the CNOT operation—it changes the state of Qubit 2 only if Qubit 1 has state  $|1\rangle$ .<sup>6</sup>

Although it seems simple for the spin-1/2 system, the implementation of a quantum logic gate represents a major step towards building a quantum computer. Rigorous proofs based on mathematical properties of unitary operators in quantum mechanics show that any unitary operation can be constructed from a few basic operators—it is sufficient to have just one gate which gives control of one qubit by another, such as the CNOT, in addition to the ability to manipulate the individual qubits in an arbitrary way.<sup>7</sup> These operators form a so-called universal set which generates all other unitary transformations of the qubits.

<sup>6</sup>The coupling between trapped ions arises from the mutual electrostatic repulsion of the ions, but this interaction between qubits does *not* give a level structure like that in Fig. 13.4.

<sup>7</sup>To rotate the nuclear spins to an arbitrary point on the Bloch sphere the NMR experiments use radio-frequency pulses. Experiments in ion traps use Raman pulses (Section 9.8).

### 13.3 Parallelism in quantum computing

A classical computer acts on binary numbers stored in the input register, or registers, to output another number also represented as bits with values 0 and 1. A quantum computer acts on the whole superposition of all the input information in the qubits of its input register, e.g. a string of ions in a linear Paul trap. This quantum register can be prepared in a superposition of all possible inputs at the same time, so that the quantum computing procedure transforms the entire register into a superposition of all possible outputs. For example, with  $N = 3$  qubits a general initial state containing all possible inputs has the wavefunction

$$\Psi = A|000\rangle + B|001\rangle + C|010\rangle + D|011\rangle + E|100\rangle + F|101\rangle + G|110\rangle + H|111\rangle. \quad (13.12)$$

Quantum computing corresponds to carrying out a transformation, represented by the quantum mechanical operator  $\hat{U}$ , to give the wavefunction  $\Psi' = \hat{U}\Psi$  that is a superposition of the outputs corresponding to each input

$$\Psi = A\hat{U}|000\rangle + B\hat{U}|001\rangle + C\hat{U}|010\rangle + \dots \quad (13.13)$$

Useful quantum algorithms combine different operations, such as  $\hat{U}_{\text{CNOT}}$ , to give an overall transformation  $\hat{U} = \hat{U}_m \cdots \hat{U}_2 \hat{U}_1$ , and these operations have the same advantage of parallelism as for the individual operations. It appears that, instead of laboriously calculating the output for each of the binary numbers 000 to 111, corresponding to 0

to 7 in decimals, the quantum computation does all eight calculations simultaneously. Herein lies the great power of quantum computing.

The number of combinations of the input states increases exponentially with the number of qubits; for a register of 100 qubits this means a transformation of  $2^{100} \equiv 10^{30}$  inputs in parallel—an astronomical number. But how can the correct answer be picked out from the enormous number of possible outputs? All the possibilities encoded in the multiple-particle wavefunction  $\Psi'$  *cannot* be turned into a list of the outputs for a given input, as given by a classical computer. Indeed, a simple quantum measurement just gives one of the outputs chosen randomly from all the possibilities. However, quantum mechanics allows measurements that give some information about all of the outputs, if we renounce the possibility of getting information about any particular output—just as the complementarity principle stops us knowing both the position and momentum of a particle precisely. As a trivial example that gives the flavour of this idea, but is in fact not strictly correct, consider the measurement of the state of the last qubit in the output register—if all the possible outputs are even numbers then this ion will be in  $|0\rangle$ . So we can establish something about all the possibilities in a single quantum computation, but this does not allow any more information to be extracted, i.e. if they are not all even we cannot find out which ones are odd (nor which input states gave these outputs). Similar ideas apply for more complicated quantum algorithms, e.g. finding the prime factors of numbers. (The real nature of quantum computation can only properly be appreciated by working through a quantum example, so the grossly simplified case given here must not be pushed too far.)

The factorisation of large numbers is often quoted as a ‘killer application’ of quantum computing, i.e. something that they can do which cannot be done on existing computers (within a realistic time). It is obviously easy to multiply two prime numbers together, e.g.  $37 \times 61 = 2257$ ; but it is much more difficult to go in the opposite direction, e.g. to find the prime factors of 1271 (try it for yourself). For the larger numbers a classical computer can easily do the multiplication, but the factorisation of a number of order  $10^{100}$  would take an exceedingly long time even with the fastest supercomputers and the most efficient classical algorithm to search for the prime factors. It has been proved rigorously that quantum algorithms exist to attack this type of problem—the algorithms act like a filter only letting through the sought-after combination of qubits from the input superposition state. The practical impossibility of factorising large numbers on present-day computers forms the foundation of the best methods of encryption.<sup>8</sup> A quantum computer has the ability to try many combinations in each computation and so quickly find the key. The possibility of cracking the best currently-used codes has prompted such hard-headed bodies as the government security agencies to investigate quantum computing and fund research on ion traps. One wonders what they think of the intrigue and mystery of quantum mechanics.

<sup>8</sup>The need for safe methods of encrypting information has always been crucial for the military, and nowadays it is important for confidential electronic transfer of data in business and to protect credit card numbers.

## 13.4 Summary of quantum computers

Qubits are quantum objects that store information and can exist in arbitrary superpositions  $a|0\rangle + b|1\rangle$ . A quantum computer is a set of qubits on which the following operations can be carried out.

- (1) Each qubit can be prepared in a given state, so the quantum registers of the computer have a well-defined initial state.
- (2) In quantum computation the quantum logic gates (unitary transformations) act on a chosen subset of the qubits. During these processes the system is in an entangled state where the information is encoded in the state of the entire quantum register. This cannot be reduced to a description of terms of the individual qubits, like a list of 0s and 1s for a classical computer. Some of these operations are control operations in which the change in the state of a qubit depends on the state of other qubits.
- (3) The final state of the qubits is read out by making a quantum measurement.

For quantum information processing with a string of trapped ions, the three stages of initialisation, quantum logic and read out correspond to the following operations:

- (1) Preparation of the initial state—all of the ions must be cooled to the ground vibrational state and be in the same internal state. Any state  $|F, M_F\rangle$  of a given hyperfine level will do and the choice is based on practical considerations.<sup>9</sup>
- (2) Raman transitions change both the internal and the vibrational states of the ions (qubits) to implement the operation of quantum gates.
- (3) Laser beams resonant with a strong transition determine which hyperfine level each ion is in at the end of the process (Section 12.6). The ions lie at least  $10\ \mu\text{m}$  apart, so that each one is seen individually (as in Fig. 13.1).

Quantum computing needs only a few basic types of quantum logic gate. A control gate between a single pair of qubits in a multiple-particle system can be combined with swap operations to effectively extend the operation to all pairs of qubits. These manipulations combined with arbitrary rotations of individual qubits give a universal set of operators from which all other unitary operators can be constructed.

## 13.5 Decoherence and quantum error correction

The power of quantum computing to solve important problems has been proved mathematically, but so far experiments have only used

<sup>9</sup>In the NMR experiments the preparation of the initial state, or the resetting of the device after a computation, are not straightforward since those systems do not have a dissipative process equivalent to laser cooling.

<sup>10</sup> At that time NMR experiments used up to seven qubits.

a few qubits to demonstrate the principle of some elementary operations. These experiments all use state-of-the-art techniques, but for large systems the external perturbations blur the entangled states so that they cannot be distinguished from each other, e.g. for ions in the Paul trap the electrical noise on the radio-frequency electrodes causes random changes of the phase of the states within a superposition. In the year 2000 the best ion trap experiment was limited to four qubits.<sup>10</sup> Decoherence quickly causes a system of many qubits to become so muddled up that it is impossible to pick out the required output. In contrast, in a classical computer errors which change 0 into 1, or the other way round, occur extremely rarely, and present-day computers have procedures for correcting errors so that they have a negligible effect.

Decoherence was thought to be an incurable disease in real quantum systems that would prevent quantum information processing from ever being carried out with enough qubits to make it really useful. However, a new cunning way of encoding information has been invented that cures the symptoms of decoherence. So-called quantum error correction (QEC) exploits the subtle features of the theory of quantum mechanics to get rid of the small amounts of the unwanted states that gradually get mixed into the states containing the quantum information by perturbations on the system. Broadly speaking, making a certain type of quantum measurement causes the wavefunction of the system of qubits to ‘collapse’, in a way that destroys any additional phase or amplitude introduced by decoherence. This measurement must be made with respect to a very carefully chosen basis of eigenstates to preserve the entanglement of the wavefunction. Clearly, it is not adequate to make a simple measurement that causes quantum superpositions to collapse into just one of the states within the superposition, since this would completely destroy the coherence between the states that we want to preserve.<sup>11</sup>

In the context of ion traps, the recent advances in quantum computing and QEC can be regarded as the latest steps in the evolution of spectroscopy and laser cooling, as illustrated by the following rough history.

- (1) The first spectroscopists observed light from discharge lamps, e.g. the Balmer lines in atomic hydrogen. They used spectrographs and étalons and the resolution was limited by Doppler broadening, together with collisions and other broadening mechanisms in the discharge.
- (2) Atomic beams allowed experimenters to change the population between the various energy levels of the atoms, using radio-frequency or microwave radiation to manipulate hyperfine and Zeeman levels in the ground state. (Optical pumping was applied to the ground states of certain atoms.) Atoms were deflected slightly in the Stern–Gerlach experiment but without a significant change in speed. The laser extended these techniques to the higher levels using optical transitions, so that, in principle, atomic physics experiments can manipulate the internal states of the atoms and put atoms into any

<sup>11</sup>QEC manages to make measurements on eigenstates that are in some sense orthogonal to those in the original superposition. These special quantum measurements cause the small admixture of other states introduced into the wavefunction by the noise to collapse to zero. The QEC measurements are performed on extra qubits entangled with the qubits in the quantum register; measurements made on these *ancillary* qubits do not reduce the size of the superposition state that stores quantum information (in the register), i.e. the number of qubits in the superposition is preserved in QEC. The technical details of this process are explained in Steane (1998). Some elementary aspects of QEC can be appreciated by analogy with the quantum Zeno effect described in Exercise 13.5.

desired energy level.

- (3) Ion traps confined the ions for long periods with buffer gas cooling.
- (4) The advent of laser cooling of atoms meant that spectroscopists were no longer passive observers, but could magnetically trap neutral atoms and control the atom's motion. Laser cooling of ions can put them into the ground state of the trap to give a completely defined external state.
- (5) Quantum computing techniques allow the manipulation of both the external and internal state of the trapped ion qubits with laser light, to put a system of many ions into a particular quantum state.
- (6) Quantum error correction can be regarded as a refined form of laser cooling. QEC puts the ions back into a coherent superposition of the desired states of the system (actually a particular sub-space of Hilbert space), rather than the lowest energy state as in conventional cooling. It was a real surprise that decoherence in quantum mechanics can be overcome in this way and actively stabilise quantum information.

## 13.6 Conclusion

At heart, quantum mechanics remains mysterious. Certain aspects of quantum behaviour seem strange to our intuition based on the classical world that we experience directly, e.g. the well-known examples of ‘which way the photon goes’ in a Young’s double-slit experiment and Schrödinger’s cat paradox.<sup>12</sup> These examples have provoked much discussion and thought over the years about the so-called quantum measurement problem. Nowadays, physicists do not regard the peculiarities of quantum systems as a problem at all, but rather as an opportunity. A proper appreciation of the profoundly different properties of multiple-particle systems and the nature of entanglement has shown how to use their unique behaviour in quantum computing. Just as a car mechanic uses her practical knowledge to get an engine working, without worrying about the details of internal combustion, so a quantum mechanic (or quantum state engineer) can design a quantum computer using the known rules of quantum mechanics without worrying too much about philosophical implications. Physicists, however, strive towards a better understanding of the quantum world and consideration of the profound and subtle ideas in quantum information theory sheds new light on aspects of quantum mechanics. In physics research there often exists a symbiotic relationship between theory and experimental work, with each stimulating the other; a prime example is quantum error correction which was not thought about until people started to face up to the fact that none of the systems used in existing experiments has any possibility of working reliably with a useful number of qubits (without error correction)—of course, the problem of decoherence has always been recognised but experimental results focused attention on this issue.

<sup>12</sup>See quotation from Heisenberg in the background reading section of the Preface.

The theoretical principles of quantum computing are well understood but there are many practical difficulties to overcome before it becomes a reality. All potential systems must balance the need to have interactions between the qubits to give coherent control and the minimisation of the interactions with the external environment that perturb the system. Trapped ions have decoherence times much longer than the time needed to execute quantum logic gates and this makes them one of the most promising possibilities. In quantum computing many new and interesting multiple-particle systems have been analysed and, even if they cannot be realised yet, thinking about them sharpens our understanding of the quantum world, just as the EPR paradox did for many years before it could be tested experimentally.

## Further Reading

The *Contemporary Physics* article by Cummins and Jones (2000) gives an introduction to the main ideas and their implementation by NMR techniques. The books by Nielsen and Chuang (2000) and Stolze and Suter (2004) give a very comprehensive treatment. The article on the ion-trap quantum information processor by Steane (1997) is also useful background for Chapter 12. Quantum computing is a fast-moving field with new possibilities emerging all the time. The latest information can be found on the World-Wide Web.

## Exercises

### (13.1) Entanglement

- (a) Show that the two-qubit state in eqn 13.8 is *not* entangled because it can be written as a simple product of states of the individual particles in the basis  $|0'\rangle = (|0\rangle - |1\rangle)/\sqrt{2}$  and  $|1'\rangle = (|0\rangle + |1\rangle)/\sqrt{2}$ .
- (b) Write the maximally-entangled state  $|00\rangle + |11\rangle$  in the new basis.
- (c) Is  $|00\rangle + |01\rangle - |10\rangle + |11\rangle$  an entangled state? [Hint. Try to write it in the form of eqn 13.6 and find the coefficients.]
- (d) Show that the two states given in eqns 13.9 and 13.10 are both entangled.

- (e) Discuss whether the three-qubit state  $\Psi = |000\rangle + |111\rangle$  possesses entanglement.

### (13.2) Quantum logic gates

This question goes through a particular example of the statement that any operation can be constructed from a combination of a control gate and arbitrary rotations of the individual qubits. For trapped ions the most straightforward logic gate to build is a controlled ‘rotation’ of Qubit 2 when Qubit 1 is  $|1\rangle$ , i.e.

$$\begin{aligned} \hat{U}_{\text{CROT}} \{ A |00\rangle + B |01\rangle + C |10\rangle + D |11\rangle \} \\ = A |00\rangle + B |01\rangle + C |10\rangle - D |11\rangle. \end{aligned}$$

- (a) Write  $\hat{U}_{\text{CROT}}$  as a  $4 \times 4$  matrix and show that it is unitary.
- (b) Equation 13.3 defines the Hadamard transformation. Write this transformation for Qubit 2,  $\hat{U}_H(2)$  as a  $4 \times 4$  matrix with the same basis states as in (a), and show that it is unitary.
- (c) Find the combination of  $\hat{U}_{\text{CROT}}$ ,  $\hat{U}_H(2)$  and  $\hat{U}_H^\dagger(2)$  that gives the CNOT gate (Table 13.1).
- (13.3) *Elementary operations with more than two qubits*  
 The CNOT gate where the state of Qubit 1 controls whether Qubit 2 switches (Table 13.1) corresponds to the operator  $\hat{U}_{\text{CNOT}}(1, 2)$ . Note that  $\hat{U}_{\text{CNOT}}(1, 2) \neq \hat{U}_{\text{CNOT}}(2, 1)$  and that these gates do not affect other qubits.
- (a) A system of three qubits has a quantum bus that enables operations that swap the states of any pair of qubits:  $\hat{U}_{\text{SWAP}}(1, 2)$  for  $1 \leftrightarrow 2$ ,  $\hat{U}_{\text{SWAP}}(2, 3)$  for  $2 \leftrightarrow 3$  and  $\hat{U}_{\text{SWAP}}(1, 3)$  for  $1 \leftrightarrow 3$ . What combination of  $\hat{U}_{\text{CNOT}}(1, 2)$  and SWAP operators gives  $\hat{U}_{\text{CNOT}}(1, 3)$ , a CNOT gate where Qubit 1 controls Qubit 3?
- (b) The operator  $\hat{U}_H(i)$  gives the transformation  $|0\rangle \mapsto (|0\rangle + |1\rangle)/\sqrt{2}$  for the  $i$ th qubit. Show that  $\hat{U}_H(3)\hat{U}_H(2)\hat{U}_H(1)$  acting on  $|000\rangle$  gives the three-qubit state with all coefficients equal, namely  $A = B = C = D = E = F = G = H$  in eqn 13.12.
- (c) The three operations in part (b) prepare eight input states, i.e. they put a three-qubit register into a superposition of the eight states. How many inputs are prepared by thirty such operations on thirty qubits. Is the initial state of the quantum register prepared in this way entangled?
- (13.4) *Grover's search algorithm*

Imagine trying to find a given number in the telephone directory when you have written down the number but not the name. There is no clever classical way of speeding up this tedious task but the massive parallelism of a quantum algorithm does make a big difference to this sort of problem. In

this question we consider finding a particular value of a two bit number  $x$  from the list of four possibilities, but the principles can be extended to larger numbers. To implement the search the quantum computer uses an operation in which the sign of the input changes for the specified value—if we assume the answer is  $x = |11\rangle$  then the operation causes  $|11\rangle \mapsto -|11\rangle$  but leaves the other states unchanged. Instead of a simple list, the assignment of  $x$  could be made on the basis of a solution to an algebraic problem, e.g. the operator changes the sign of the input  $x$  if some function of  $x$  has a particular value such as  $f(x) = 0$ . In order that the computer can implement the sign change efficiently it is only necessary that the function  $f(x)$  can be evaluated efficiently for some general  $x$ . This is a much easier task than finding the value of  $x$  for which  $f(x) = 0$ .

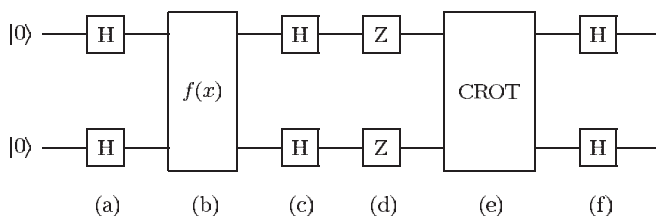
The figure shows the sequence of operations corresponding to Grover's algorithm, starting with two qubits in  $|00\rangle$ . The operators are defined in the following. The letters (a) to (f) indicate the part of this question corresponding to each stage. (Ignore normalisation factors throughout this question.)

- (a) Show that the Hadamard transformation (eqn 13.3) applied to each of the qubits of  $|00\rangle$  results in the superposition state

$$\Psi_{\text{in}} = |00\rangle + |01\rangle + |10\rangle + |11\rangle .$$

This is the initial state of the two qubits needed for the algorithm.

- (b) The box labelled  $f(x)$  represents the operation for the function, as described above. In this question this corresponds to a CROT gate (defined in Exercise 13.2). Write down  $\hat{U}_{\text{CROT}}\Psi_{\text{in}}$ .
- (c) The next step in the algorithm is another Hadamard transformation of each qubit. We have already worked out the effect on  $|00\rangle$  in part (a). Work out the effect on  $|01\rangle$ ,  $|10\rangle$  and  $|11\rangle$ . Show that the superposition is  $|00\rangle + |01\rangle + |10\rangle - |11\rangle$ .



- (d) The operator  $\hat{U}_Z$  corresponds to  $|0\rangle \mapsto |0\rangle$  and  $|1\rangle \mapsto -|1\rangle$ , for each qubit. Write down the resulting state of the system of two qubits.
- (e) Show that after another  $\hat{U}_{\text{CROT}}$  the state is  $|00\rangle - |01\rangle - |10\rangle + |11\rangle$ .
- (f) Show that a final Hadamard transformation yields the required answer.
- (g) Repeat the algorithm for another function with solution  $x = 10$ , to show that it picks out the required value, i.e.  $f(x)$  corresponds to  $|10\rangle \mapsto -|10\rangle$ .

*Comment.* This algorithm has a similar ‘one-way’ nature to the factorisation of numbers mentioned in the text—it is very time consuming to find the prime factors, but once possible solutions have been found by the quantum computation it is easy to verify whether they are indeed factors (or satisfy the equation) using a classical computer. Some more complex quantum algorithms do not always give the ‘correct’ answer but they are still useful in ‘winnowing the wheat from the chaff’; the algorithms pick out all the required answers (grains of wheat) along with a few unwanted numbers. This is not a problem since invalid numbers are thrown away after checking—the set of numbers to be checked is much smaller than the initial set of all possibilities, so the procedure is efficient.

### (13.5) The quantum Zeno effect

The ancient Greek philosopher Zeno proposed various arguments against motion, e.g. *Achilles and the tortoise* in which the logic leads to the paradoxical conclusion that the man cannot overtake the tortoise. In the quantum Zeno effect the evolution of a wavefunction is slowed down by repeated quantum measurements on the system, and this has been described by the colloquial phrase ‘a watched pot never boils’.

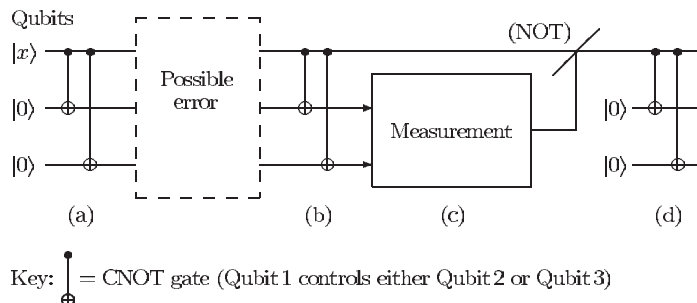
This question is based on the usual treatment of Rabi oscillations rewritten in terms of the states of a qubit that starts in  $|0\rangle$  at time  $t = 0$ . Transitions between the states are induced by a perturbation which is characterised by the Rabi frequency  $\Omega$ :

$$|\psi\rangle = \cos\left(\frac{\Omega t}{2}\right)|0\rangle - i \sin\left(\frac{\Omega t}{2}\right)|1\rangle.$$

- (a) The state of the qubit is measured after a short time  $\tau \ll 1/\Omega$ . Show that the probability that the qubit ends up in  $|1\rangle$  is  $(\Omega\tau/2)^2 \ll 1$ . What is the probability that the qubit is in  $|0\rangle$  after the measurement?
- (b) The state of the qubit is measured at time  $\tau/2$ . What are now the probabilities of  $|0\rangle$  and  $|1\rangle$ ?
- (c) After the measurement at time  $\tau/2$  the qubit will be in either  $|0\rangle$  or  $|1\rangle$ . The qubit then evolves for time  $\tau/2$  and its state is measured again at time  $\tau$ . Calculate the probability of the outcome  $|1\rangle$ .
- (d) For a sequence of  $n$  measurements with a time interval of  $\tau/n$  between them, the probability of having made a transition from  $|0\rangle$  to  $|1\rangle$  at time  $\tau$  is  $1/n$  times that in part (a). Verify this result for  $n = 3$  or, if you can, justify it for the general case.
- (e) Discuss the application of these results to the measurement of the frequency of a narrow transition by the quantum jump technique, as described in Section 12.6. The transition rate on the weak transition decreases as the measurement periods of excitation on the strong transition become more frequent. What effect does this have on the measured line width of the narrow transition?

### (13.6) Quantum error correction

Classical computers encode each number with more than the minimum number of bits necessary; the additional ‘check’ bits allow the system to detect whether any of the bits has undergone a random change (caused by noise). In these error correction codes the binary code for each number differs from the string of 0s and 1s for any other possible number by at least two bits, so a random change of a single bit leads to an invalid binary code that the computer rejects. In practice, error correction codes have the binary strings representing valid entries ‘further apart’ to protect against errors in several bits. Quantum error correction (QEC) uses extra qubits to make the computational states ‘further apart’ (in Hilbert space), so the system is more robust, i.e. it is harder for the computational states to become mixed.



The above figure shows a particular QEC scheme. On the left-hand side, Qubit 1 starts in  $|x\rangle$  and Qubits 2 and 3 both start in  $|0\rangle$ . The letters (a) to (d) indicate the part of this question corresponding to each stage.

- (a) To represent the qubit  $|x\rangle = a|0\rangle + b|1\rangle$  this quantum error correction code uses  $\Psi_{\text{in}} = a|000\rangle + b|111\rangle$ . Show that two CNOT gates acting on Qubits 2 and 3, with Qubit 1 as the control qubit in both cases, as indicated in the figure, encode  $|x\rangle$  in this way.
- (b) Suppose that a perturbation of Qubit 1 causes a bit-change error so that the state of the three qubits becomes  $\alpha(a|000\rangle + b|111\rangle) + \beta(a|100\rangle + b|011\rangle)$ . Here  $\beta$  is the amplitude of the unwanted state mixed into the original state (and normalisation determines  $\alpha$ ). Show that after another two CNOT gates we get  $(a|0\rangle + b|1\rangle)\alpha|00\rangle + (a|1\rangle + b|0\rangle)\beta|11\rangle$ .

- (c) The measurement of the states of Qubits 2 and 3 has two possible results. One possibility is to find  $|11\rangle$ , which means that Qubit 1 has changed and in this case the error is corrected by applying a (conditional) NOT operation to Qubit 1, i.e.  $|0\rangle \leftrightarrow |1\rangle$  if and only if the measurement of the other qubits gives  $|11\rangle$ . What is the other possible state of Qubits 2 and 3 resulting from the measurement? Verify that Qubit 1 ends up in the original state  $|x\rangle$  after this stage.
- (d) Qubits 2 and 3 are both reset to  $|0\rangle$ . Two further CNOT gates recreate  $\Psi_{\text{in}}$  from  $|x\rangle$ , just as in stage (a).

This scheme corrects ‘bit flip’ errors in any of the qubits. Show this by writing out what happens in stages (b), (c) and (d) for the state

$$\begin{aligned} & \alpha(a|000\rangle + b|111\rangle) + \beta(a|100\rangle + b|011\rangle) \\ & + \gamma(a|010\rangle + b|101\rangle) + \delta(a|001\rangle + b|110\rangle). \end{aligned}$$

Web site:

<http://www.physics.ox.ac.uk/users/foot>

This site has answers to some of the exercises, corrections and other supplementary information.

# A

# Appendix A: Perturbation theory

|   |     |
|---|-----|
| A.1 Mathematics of perturbation theory                          | 298 |
| A.2 Interaction of classical oscillators of similar frequencies | 299 |

Although degenerate perturbation theory is quite simple (cf. the series solution of differential equations used to find the eigenenergies of the hydrogen atom), it is often regarded as a ‘difficult’ and subtle topic in introductory quantum mechanics courses. Degenerate perturbation theory arises often in atomic physics, e.g. in the treatment of helium (eqn 3.14). Equations 6.34 and 7.89 in the treatment of the Zeeman effect on hyperfine structure and the a.c. Stark effect, respectively, also have a similar mathematical form, as can be appreciated by studying the general case in this appendix. Another aim of this appendix is to underline the point made in Chapter 3 that degenerate perturbation theory is not a mysterious quantum mechanical phenomenon (associated with exchange symmetry) and that a similar behaviour occurs when two classical systems interact with each other.

## A.1 Mathematics of perturbation theory

The Hamiltonian for a system of two levels of energies  $E_1$  and  $E_2$  (where  $E_2 > E_1$ ) with a perturbation given by  $H'$ , as in eqn 3.10, can be written in matrix form as

$$H_0 + H' = \begin{pmatrix} E_1 & 0 \\ 0 & E_2 \end{pmatrix} + \begin{pmatrix} H'_{11} & H'_{12} \\ H'_{21} & H'_{22} \end{pmatrix}. \quad (\text{A.1})$$

The matrix elements of the perturbation are  $H'_{12} = \langle \psi_1 | H' | \psi_2 \rangle$ , and similarly for the others. The expectation values  $\langle \psi_1 | H' | \psi_1 \rangle$  and  $\langle \psi_2 | H' | \psi_2 \rangle$  are the usual first-order perturbations. It is convenient to write the energies in terms of a mean energy  $J$  and an energy interval  $2\epsilon$  that takes into account the energy shift caused by the diagonal terms of the perturbation matrix:

$$\begin{aligned} E_1 + H'_{11} &= J - \epsilon, \\ E_2 + H'_{22} &= J + \epsilon. \end{aligned}$$

For simplicity, we assume that the off-diagonal terms are real, e.g. as for the case of exchange integrals in helium and the other examples in this book:<sup>1</sup>

$$H'_{12} = H'_{21} = K.$$

<sup>1</sup>This is normally the case when levels are bound states. We shall find that the eigenenergies depend on  $K^2$ , which would generalise to  $|K|^2$ .

When  $\epsilon = 0$  this leads to a matrix eigenvalue equation similar to that used in the treatment of helium (eqn 3.14), but the formalism given here enables us to treat both degenerate and non-degenerate cases as different limits of the same equations. This two-level system is described by the matrix equation

$$\begin{pmatrix} J + \epsilon & K \\ K & J - \epsilon \end{pmatrix} \begin{pmatrix} a \\ b \end{pmatrix} = E \begin{pmatrix} a \\ b \end{pmatrix}. \quad (\text{A.2})$$

The eigenenergies  $E$  are found from the determinantal equation (as in eqn 7.91 or eqn 3.17):

$$E = J \pm \sqrt{\epsilon^2 + K^2}. \quad (\text{A.3})$$

This exact solution is valid for all values of  $K$ , not just small perturbations. However, it is instructive to look at the approximate values for weak and strong interactions.

(a) *Degenerate perturbation theory,  $K \gg 2\epsilon$*

If  $K \gg 2\epsilon$  then the levels are effectively degenerate, i.e. their energy separation is small on the scale of the perturbation. For this strong perturbation the approximate eigenvalues are

$$E = J \pm K, \quad (\text{A.4})$$

as in helium (Section 3.2). The two eigenvalues have a splitting of  $2K$  and a mean energy of  $J$ . The eigenfunctions are admixtures of the original states with equal amplitudes.

(b) *Perturbation theory,  $K \ll 2\epsilon$*

When the perturbation is weak the approximate eigenvalues obtained by expanding eqn A.3 are

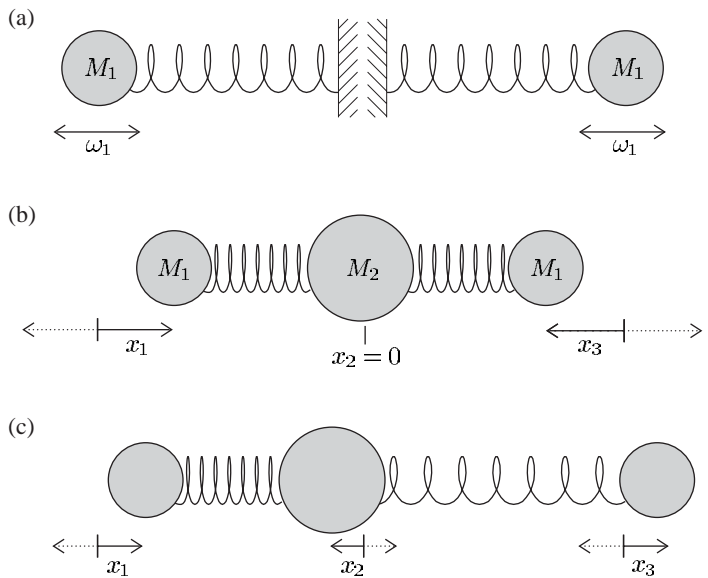
$$E = J \pm \left( \epsilon + \frac{K^2}{2\epsilon} \right). \quad (\text{A.5})$$

This is a second-order perturbation, proportional to  $K^2$ , as in eqns 6.36 and 7.92.

## A.2 Interaction of classical oscillators of similar frequencies

In this section we examine the behaviour of two classical oscillators of similar frequencies that interact with each other, e.g. the system of two masses joined by three springs shown in Fig. 3.3, or alternatively the system of three masses joined by two springs shown in Fig. A.1. The mathematics is very similar in both cases but we shall study the latter because it corresponds to a real system, namely a molecule of carbon dioxide (with  $M_1$  representing oxygen atoms and  $M_2$  being a carbon

**Fig. A.1** An illustration of degenerate perturbation theory in classical mechanics, closely related to that shown in Fig. 3.3. (a) The ‘unperturbed’ system corresponds to two harmonic oscillators, each of which has a mass  $M_1$  attached to one end of a spring and with the other end fixed. These independent oscillators both have the same resonant frequency  $\omega_1$ . (b) A system of three masses joined by two springs corresponds to two coupled harmonic oscillators. When  $M_2 \gg M_1$  the coupling is weak. The displacements  $x_1$ ,  $x_2$  and  $x_3$  are measured from the rest position of each mass (and are taken as being positive to the right). One eigenmode of the system corresponds to a symmetric stretch in which the central mass does not move; therefore this motion has frequency  $\omega_1$  (independent of the value of  $M_2$ ). (c) The asymmetric stretching mode has a frequency higher than  $\omega_1$ . (This system gives a simple model of molecules such as carbon dioxide; a low-frequency bending mode also arises in such molecules.)



atom). The equations of motion for this ‘ball-and-spring’ molecular model are

$$M_1\ddot{x}_1 = \kappa(x_2 - x_1), \quad (\text{A.6})$$

$$M_2\ddot{x}_2 = -\kappa(x_2 - x_1) + \kappa(x_3 - x_2), \quad (\text{A.7})$$

$$M_1\ddot{x}_3 = -\kappa(x_3 - x_2), \quad (\text{A.8})$$

where  $\kappa$  is the spring constant (of the bond between the carbon and oxygen atoms). The  $x$ -coordinates are the displacement of the masses from their equilibrium positions. Adding all three equations gives zero on the right-hand side since all the internal forces are equal and opposite and there is no acceleration of the centre of mass of the system. This constraint reduces the number of degrees of freedom to two. It is convenient to use the variables  $u = x_2 - x_1$  and  $v = x_3 - x_2$ . Substituting  $\kappa/M_1 = \omega_1^2$  and  $\kappa/M_2 = \omega_2^2$  leads to the matrix equation

$$\begin{pmatrix} \ddot{u} \\ \ddot{v} \end{pmatrix} = \begin{pmatrix} -(\omega_1^2 + \omega_2^2) & \omega_2^2 \\ \omega_2^2 & -(\omega_1^2 + \omega_2^2) \end{pmatrix} \begin{pmatrix} u \\ v \end{pmatrix}. \quad (\text{A.9})$$

A suitable trial solution is

$$\begin{pmatrix} u \\ v \end{pmatrix} = \begin{pmatrix} a \\ b \end{pmatrix} e^{-i\omega t}. \quad (\text{A.10})$$

This leads to an equation with the same form as eqn A.2 with  $\epsilon = 0$  (cf. eqn 3.14).

The determinantal equation yields

$$(\omega_1^2 - \omega^2)(\omega_1^2 + 2\omega_2^2 - \omega^2) = 0, \quad (\text{A.11})$$

giving the two eigenfrequencies  $\omega = \omega_1$  and  $\omega' = \sqrt{\omega_1^2 + 2\omega_2^2}$ . For frequency  $\omega_1$  the eigenvector is  $b = a$ , corresponding to a symmetric stretch (Fig. A.1(b)); this is the same as the initial frequency since  $M_2$  does not move in this normal mode. The other normal mode of higher frequency corresponds to an asymmetric stretch with  $b = -a$  (see Fig. A.1(c)). In these motions the centre of mass does not accelerate, as can be verified by summing eqns A.6, A.7 and A.8.

A treatment of two coupled oscillators of different frequencies is given in Lyons (1998) in the chapter on normal modes; this is the classical analogue of the non-degenerate case that was included in the general treatment in the previous section. The books by Atkins (1983, 1994) give a comprehensive description of molecules.

# B

## Appendix B: The calculation of electrostatic energies

<sup>1</sup>The notation indicates that the electrons are labelled 1 and 2, meaning that their locations are called  $\mathbf{r}_1$  and  $\mathbf{r}_2$ . At the same time, the electron charges are (probably) differently distributed in space (because the electrons' wavefunctions have different quantum numbers), so  $\rho_1$  and  $\rho_2$  are different functions of their arguments.

<sup>2</sup>We have called the integral  $J$  in anticipation of working out a direct integral, but an exchange integral is equally well catered for if we use appropriate formulae for  $\rho_1(\mathbf{r}_1)$  and  $\rho_2(\mathbf{r}_2)$ .

<sup>3</sup>The integrals are written with the integrand at the end to make clear the range of integration for each variable.

This appendix describes a method of dealing with the integrals that arise in the calculation of the electrostatic interaction of two electrons, as in the helium atom and other two-electron systems. Consider two electrons<sup>1</sup> whose charge densities are  $\rho_1(\mathbf{r}_1)$  and  $\rho_2(\mathbf{r}_2)$ . Their energy of electrostatic repulsion is (cf. eqn 3.15)

$$J = \iint \rho_1(\mathbf{r}_1) \frac{e^2}{4\pi\epsilon_0 r_{12}} \rho_2(\mathbf{r}_2) d^3\mathbf{r}_1 d^3\mathbf{r}_2. \quad (\text{B.1})$$

In this expression we shall leave open the precise form of the two charge densities, so the theorem we are to set up will apply equally to direct and to exchange integrals.<sup>2</sup> Also, we shall permit the charge density  $\rho_1(\mathbf{r}_1) = \rho(r_1, \theta_1, \phi_1)$  to depend upon the angles  $\theta_1$  and  $\phi_1$ , as well as upon the radius  $r_1$ , and similarly for  $\rho_2(\mathbf{r}_2)$ ; neither charge density is assumed to be spherically symmetric.

In terms of the six spherical coordinates the integral takes the form

$$\begin{aligned} J = & \int_0^\pi d\theta_1 \sin\theta_1 \int_0^{2\pi} d\phi_1 \int_0^\pi d\theta_2 \sin\theta_2 \int_0^{2\pi} d\phi_2 \\ & \times \int_0^\infty dr_1 r_1^2 \rho_1(r_1, \theta_1, \phi_1) \int_0^\infty dr_2 r_2^2 \rho_2(r_2, \theta_2, \phi_2) \frac{e^2}{4\pi\epsilon_0 r_{12}}. \end{aligned}$$

In rearranging this expression, we process just the two radial integrals. Within them, we divide the range for  $r_2$  into a part from 0 to  $r_1$  and a part from  $r_1$  to infinity. The radial integrals become<sup>3</sup>

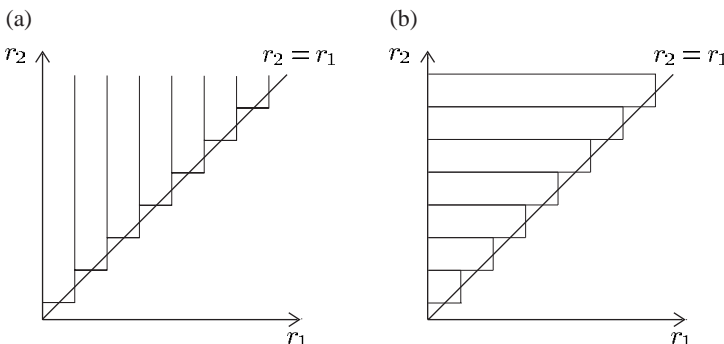
$$\begin{aligned}
& \int_0^\infty dr_1 r_1^2 \rho_1(\mathbf{r}_1) \int_0^{r_1} dr_2 r_2^2 \rho_2(\mathbf{r}_2) \frac{e^2}{4\pi\epsilon_0 r_{12}} \\
& + \int_0^\infty dr_1 r_1^2 \rho_1(\mathbf{r}_1) \int_{r_1}^\infty dr_2 r_2^2 \rho_2(\mathbf{r}_2) \frac{e^2}{4\pi\epsilon_0 r_{12}} \\
& = \int_0^\infty dr_1 r_1^2 \rho_1(\mathbf{r}_1) \int_0^{r_1} dr_2 r_2^2 \rho_2(\mathbf{r}_2) \frac{e^2}{4\pi\epsilon_0 r_{12}} \\
& \quad + \int_0^\infty dr_2 r_2^2 \rho_2(\mathbf{r}_2) \int_0^{r_2} dr_1 r_1^2 \rho_1(\mathbf{r}_1) \frac{e^2}{4\pi\epsilon_0 r_{12}} \\
& = \int_0^\infty dr_1 r_1^2 \rho_1(\mathbf{r}_1) V_{21}(\mathbf{r}_1) + \int_0^\infty dr_2 r_2^2 \rho_2(\mathbf{r}_2) V_{12}(\mathbf{r}_2). \tag{B.2}
\end{aligned}$$

Figure B.1 illustrates the rearrangement of the ranges of integration. Here  $V_{21}(\mathbf{r}_1)$  is the *partial* electrostatic potential at  $\mathbf{r}_1$  caused by the charge density  $\rho(\mathbf{r}_2)$ , partial because it is caused by only that part of  $\rho(\mathbf{r}_2)$  that lies at radii less than  $r_1$ ; and a similar definition applies to  $V_{12}(\mathbf{r}_2)$ . The entire electrostatic energy  $J$  is now obtained by integrating expression B.2 over the angles  $\theta_1$ ,  $\phi_1$ ,  $\theta_2$  and  $\phi_2$ . We obtain

$$J = \int \rho_1(\mathbf{r}_1) V_{21}(\mathbf{r}_1) d^3\mathbf{r}_1 + \int \rho_2(\mathbf{r}_2) V_{12}(\mathbf{r}_2) d^3\mathbf{r}_2. \tag{B.3}$$

Expression B.3 can be applied to any charge densities, however complicated their dependence on the angles  $\theta$  and  $\phi$ . But the significance of our result is most easily explained if we take the special case where the potentials  $V_{21}(\mathbf{r}_1)$  and  $V_{12}(\mathbf{r}_2)$  are spherically symmetric—Independent of angles—either in fact or as the result of imposing an approximation. In such a case we can think of  $V_{21}(r_1)$  as the (partial) potential resulting from a radial electric field<sup>4</sup> that is felt by electron 1 owing to the presence of electron 2; and likewise  $V_{12}(r_2)$  is the (partial) potential felt

<sup>4</sup>In the trade, the potential itself is usually referred to as a radial, or *central* field. We should point out that the functions  $V_{12}$  and  $V_{21}$  are here not necessarily the same functions of their arguments; indeed, they will generally be different unless  $\rho_1(r) = \rho_2(r)$ . Later in this book we shall discuss the central field, which is a single  $V(r)$ , acting alike on all electrons. The potentials introduced here are different from this common-to-all central field.



**Fig. B.1** Integration over the region  $r_2 > r_1 > 0$  can be carried out in two ways: (a) integration with respect to  $r_2$  from  $r_2 = r_1$  to  $\infty$ , followed by integration from  $r_1 = 0$  to  $\infty$ ; or (b) integration with respect to  $r_1$  from 0 to  $r_1 = r_2$ , followed by integration from  $r_2 = 0$  to  $\infty$ . The latter is convenient for calculating the electrostatic interaction in eqn B.2 and it leads to two contributions that are related by an interchange of the particle labels  $r_1 \leftrightarrow r_2$ . For a symmetrical configuration such as  $1s^2$  in helium these two contributions are equal and this feature reduces the amount of calculation. By definition, exchange integrals are unchanged by swapping the labels  $r_1 \leftrightarrow r_2$  and so the same comments apply to their evaluation.

by electron 2 owing to the presence of electron 1. When  $\rho(\mathbf{r}_1) = \rho(\mathbf{r}_2)$ , as in the calculation of the direct integral for the  $1s^2$  configuration (Section 3.3.1), these two parts of eqn B.3 are equal (and only one integral needs to be calculated).<sup>5</sup>

The fact that the potentials  $V_{12}$  and  $V_{21}$  are *partial* potentials deserves comment. Had we defined a  $V_{21}(\mathbf{r}_1)$  to represent the whole of the electrostatic potential from  $\rho_2(\mathbf{r}_2)$  acting on electron 1, then the interaction energy  $J$  would have been given by the single term

$$\begin{aligned} & \int_0^\pi d\theta_1 \sin \theta_1 \int_0^{2\pi} d\phi_1 \int_0^\infty dr_1 r_1^2 \rho_1(\mathbf{r}_1) V_{21}(r_1) \\ &= \int \rho_1(\mathbf{r}_1) V_{21}(\mathbf{r}_1) d^3\mathbf{r}_1, \end{aligned} \quad (\text{B.4})$$

<sup>5</sup>A similar simplification can be used in the calculation of exchange integrals, as in Exercise 3.6.

or by a similar expression with the labels 1 and 2 interchanged throughout.<sup>6</sup> Such a presentation is, of course, physically correct, but it is much less convenient mathematically than the version presented earlier; it precludes the separation of the Schrödinger equation into two equations, each describing the behaviour of one electron.

The simplified form for  $J$  given in eqn B.3 is used in the evaluation of direct and exchange integrals for helium in Chapter 3, and is generally applicable to electrostatic energies.

# Appendix C: Magnetic dipole transitions



The electric dipole transitions that lead to the emission and absorption of light by atoms are discussed in many places in this book, and the selection rules for this type of transition are summarised in Table 5.1. These rules are not obeyed in radio-frequency transitions between Zeeman sub-levels where only the magnetic quantum number changes, or in transitions between different hyperfine levels where  $F$  and  $M_F$  can change—these transitions in radio-frequency spectroscopy are magnetic dipole or M1 transitions induced by the oscillating magnetic field of the radiation<sup>1</sup>

$$\mathbf{B}_{\text{rf}} = \mathbf{B}_0 \cos \omega t. \quad (\text{C.1})$$

The transition matrix element between hyperfine levels is

$$\mu_{21} \propto \langle 2 | \boldsymbol{\mu} \cdot \mathbf{B}_{\text{rf}} | 1 \rangle, \quad (\text{C.2})$$

where  $\boldsymbol{\mu}$  is the magnetic dipole operator in eqn 5.9. This gives transitions for which  $\Delta l = \Delta L = \Delta S = 0$ .

The selection rules for magnetic dipole transitions between hyperfine states are:

$$\begin{aligned} \Delta F &= 0, \pm 1 \quad (\text{but not } 0 \rightarrow 0), \\ \Delta M_F &= 0, \pm 1. \end{aligned}$$

These are as expected from angular momentum conservation and a dipole operator that can change angular momentum by one unit (as discussed for electric dipole transitions in Section 2.3.5).

The spontaneous decay rate for radio-frequency transitions is proportional to

$$A_{21} \propto \omega^3 |\mu_{21}|^2, \quad (\text{C.3})$$

where  $\omega$  is the angular frequency, which is small relative to optical transitions. The matrix element  $\mu_{12}$  is also much smaller than that for E1 transitions:

$$\frac{|\langle 2 | \boldsymbol{\mu} \cdot \mathbf{B} | 1 \rangle|^2}{|\langle 3 | \mathbf{e} \cdot \mathbf{E} | 1 \rangle|^2} \sim \left( \frac{\mu_B/c}{ea_0/Z} \right)^2 \sim (Z\alpha)^2, \quad (\text{C.4})$$

where the factor  $c$  arises because the ratio of the magnetic to the electric field,  $|\mathbf{B}| / |\mathbf{E}| = 1/c$  in an electromagnetic wave; the atomic size scales as  $1/Z$ , see Section 1.9. Therefore spontaneous emission is negligible in radio-frequency and microwave spectroscopy. In outer space, however,

<sup>1</sup>An important exception is the Lamb shift transition, where two levels of opposite parity have a very small energy separation (see Section 2.3.4). This is an electric dipole or E1 transition.

the gas density is low and there are vast clouds of atomic hydrogen; even weak emission at a wavelength of 21 cm gives enough microwave radiation to be picked up by radio telescopes.

The selection rules for magnetic dipole radiation transitions are given in the table below, together with the electric dipole transitions for comparison.

| Electric dipole transitions                             | Magnetic dipole transitions                             |
|---|---|
| $\Delta J = 0, \pm 1$<br>(but not $J = 0$ to $J' = 0$ ) | $\Delta J = 0, \pm 1$<br>(but not $J = 0$ to $J' = 0$ ) |
| $\Delta M_J = 0, \pm 1$                                 | $\Delta M_J = 0, \pm 1$                                 |
| Parity change   | No parity change  |
| $\Delta l = \pm 1$                                      | $\Delta l = 0$  |
| Any $\Delta n$  | $\Delta n = 0$  |
| $\Delta L = 0, \pm 1$                                   | $\Delta L = 0$  |
| $\Delta S = 0$  | $\Delta S = 0$  |

In certain circumstances magnetic dipole transitions can give rise to visible transitions in atoms, and there are also electric quadrupole (E2) transitions arising from the breakdown of the dipole approximation. These forbidden transitions, i.e. forbidden for electric dipole transitions, are detailed in Corney (2000).

# Appendix D: The line shape in saturated absorption spectroscopy

D

The description of saturated absorption spectroscopy in Section 8.3 explained qualitatively how this technique gives a Doppler-free signal. This appendix gives a more quantitative treatment based on modifying eqn 8.11 to account for the change in populations produced by the light. We shall use  $N_1(v)$  to denote the number density of atoms in level 1 with velocities  $v$  to  $v + dv$  (along the direction of light) and  $N_2(v)$  to denote those in level 2 within the same velocity class. At low intensities most atoms remain in the ground state, so  $N_1(v) \simeq Nf(v)$  and  $N_2(v) \simeq 0$ . Higher intensity radiation excites atoms close to the resonant velocity (given in eqn 8.12) into the upper level, as shown in Fig. 8.4. Within each narrow range of velocities  $v$  to  $v + dv$  the radiation affects the atoms in the *same* way, so we can use eqn 7.82 for homogeneous broadening to write the difference in population densities (for atoms in a given velocity class) as

$$N_1(v) - N_2(v) = Nf(v) \times \frac{1}{1 + (I/I_{\text{sat}})L(\omega - \omega_0 + kv)}. \quad (\text{D.1})$$

This includes the Doppler shift  $+kv$  for a laser beam propagating in the opposite direction to atoms with positive velocities, e.g. the pump beam in Fig. 8.4. The Lorentzian function  $L(\omega - \omega_0 + kv)$  is defined so that  $L(0) = 1$ , namely

$$L(x) = \frac{\Gamma^2/4}{x^2 + \Gamma^2/4}. \quad (\text{D.2})$$

For low intensities  $I \ll I_{\text{sat}}$ , we can make the approximation

$$N_1(v) - N_2(v) \simeq Nf(v) \left\{ 1 - \frac{I}{I_{\text{sat}}} L(\omega - \omega_0 + kv) \right\}. \quad (\text{D.3})$$

The expression inside the curly brackets equals unity except near  $v = -(\omega - \omega_0)/k$  and gives a mathematical representation of the ‘hole burnt’ in the Maxwellian velocity distribution  $Nf(v)$  by the pump beam (as illustrated in Figs 8.3 and 8.4). In this low-intensity approximation the hole has a width of  $\Delta v = \Gamma/k$ . Atoms in each velocity class absorb light with a cross-section given by eqn 7.76, with a frequency detuning that takes into account the Doppler shift. The absorption of a weak probe

beam travelling along the  $z$ -direction through a gas with a strong pump beam in the opposite direction is given by the integral in eqn 8.17:

$$\begin{aligned}\kappa(\omega, I) &= \int \{N_1(v) - N_2(v)\} \sigma(\omega - kv) dv \\ &= \int \frac{Nf(v)}{1 + \frac{I}{I_{\text{sat}}} \frac{\Gamma^2/4}{(\omega - \omega_0 + kv)^2 + \Gamma^2/4}} \times \frac{\sigma_0 \Gamma^2/4}{(\omega - \omega_0 - kv)^2 + \Gamma^2/4} dv.\end{aligned}\quad (\text{D.4})$$

Note the opposite sign of the Doppler shift for the probe ( $-kv$ ) and pump ( $+kv$ ) beams. (Both beams have angular frequency  $\omega$  in the laboratory frame.) For low intensities,  $I/I_{\text{sat}} \ll 1$ , the same approximation as in going from eqn D.1 to D.3 gives

$$\kappa(\omega, I) = N\sigma_0 \int f(v) L(\omega - \omega_0 - kv) \left\{ 1 - \frac{I}{I_{\text{sat}}} L(\omega - \omega_0 + kv) \right\} dv. \quad (\text{D.5})$$

As  $I \rightarrow 0$ , this reduces to eqn 8.11 for Doppler broadening without saturation, i.e. the convolution of  $f(v)$  and  $L(\omega - \omega_0 - kv)$ . The intensity-dependent part contains the integral

$$\begin{aligned}&\int_{-\infty}^{\infty} f(v) L(\omega - \omega_0 - kv) L(\omega - \omega_0 + kv) dv \\ &= f(v=0) \int_{-\infty}^{\infty} \frac{\Gamma^2/4}{x^2 + \Gamma^2/4} \times \frac{\Gamma^2/4}{\{2(\omega - \omega_0) - x\}^2 + \Gamma^2/4} \frac{dx}{k}.\end{aligned}\quad (\text{D.6})$$

The product of the two Lorentzian functions is small, except where both  $\omega - \omega_0 + kv = 0$  and  $\omega - \omega_0 - kv = 0$ . Solving these two equations we find that the integrand only has a significant value when  $kv = 0$  and  $\omega - \omega_0 = 0$ . The Gaussian function does not vary significantly from  $f(v=0)$  over this region so it has been taken outside the integral. The change of variables to  $x = \omega - \omega_0 + kv$  shows clearly that the integral is the convolution of two Lorentzian functions (that represent the hole burnt in the population density and the line shape for absorption of the probe beam). The convolution of two Lorentzian functions of widths  $\Gamma$  and  $\Gamma'$  gives another of width  $\Gamma + \Gamma'$  (Exercise 8.8). The convolution of two Lorentzian functions with the same width  $\Gamma = \Gamma'$  in eqn D.6 gives a Lorentzian function of width  $\Gamma + \Gamma' = 2\Gamma$  with the variable  $2(\omega - \omega_0)$ ; this is proportional to  $g_H(\omega)$ , as defined in eqn 7.77 (see Exercise 8.8). Thus a pump beam of intensity  $I$  causes the probe beam to have an absorption coefficient of

$$\kappa(\omega) = N \times 3 \frac{\pi^2 c^2}{\omega_0^2} A_{21} g_D(\omega) \left\{ 1 - \frac{I}{I_{\text{sat}}} \frac{\pi \Gamma}{4} g_H(\omega) \right\}. \quad (\text{D.7})$$

The function in the curly brackets represents the reduced absorption at the centre of the Doppler-broadened line—it gives the peak in the probe beam intensity transmitted through the gas when  $\omega = \omega_0$ , as shown in

Fig. 8.4(b). This saturated-absorption signal comes from the velocity class of atoms with  $v = 0$ .

We assumed that  $I \ll I_{\text{sat}}$  to obtain eqn D.3, but usually in experiments the pump beam has an intensity close to saturation to give a strong signal. The simple rate equation treatment becomes inaccurate around  $I_{\text{sat}}$  and a more sophisticated approach is required based on the optical Bloch equations, as described in Letokhov and Chebotaev (1977). Also, optical pumping out of the state that interacts with the radiation into other Zeeman sub-levels, or hyperfine levels, can be the dominant way of depleting the lower-level population  $N_1(v)$ . However, the line shape remains symmetrical about  $\omega_0$ , so saturation spectroscopy gives an accurate measurement of the atomic resonance frequency.

# E

# Appendix E: Raman and two-photon transitions

|                                   |            |
|-----------------------------------|------------|
| <b>E.1 Raman transitions</b>      | <b>310</b> |
| <b>E.2 Two-photon transitions</b> | <b>313</b> |

<sup>1</sup>More rigorous treatments can be found in quantum mechanics texts.

## E.1 Raman transitions

This appendix gives an explanation of Raman (and two-photon transitions) by adapting the treatment of single-photon transitions given in Chapter 7—this approach gives much more physical insight than simply quoting the theoretical formulae from second-order time-dependent perturbation theory.<sup>1</sup> A Raman transition involves two laser beams with frequencies  $\omega_{L1}$  and  $\omega_{L2}$ , and the atom interacts with an electric field that has two frequency components:

$$\mathbf{E} = \mathbf{E}_{L1} \cos(\omega_{L1}t) + \mathbf{E}_{L2} \cos(\omega_{L2}t). \quad (\text{E.1})$$

A Raman transition between two atomic levels, labelled 1 and 2, involves a third atomic level, as shown in Fig. 9.20. This third level is labelled  $i$  for intermediate, but it is very important to appreciate that atoms are not really excited to level  $i$ . The treatment presented here emphasises that Raman transitions are fundamentally different from a process comprised of two single-photon transitions ( $1 \rightarrow i$  followed by  $i \rightarrow 2$ ). As in Section 9.8, we take the frequencies of the levels to be related by  $\omega_i \gg \omega_2 > \omega_1$ .

Firstly, we consider the perturbation produced by the light at  $\omega_{L1}$  for the transition between levels 1 and  $i$ . This is the same situation as for a two-level atom interacting with an oscillating electric field that was described in Chapter 7, but here the upper level is labelled  $i$  instead of having the label 2 (and we write  $\omega_{L1}$  rather than  $\omega$ ). For a weak perturbation, the lower state  $|1\rangle$  has amplitude  $c_1(0) = 1$  and the amplitude of  $|i\rangle$ , from eqn 7.14, is

$$c_i(t) = \frac{\Omega_{i1}}{2} \left[ \frac{1 - \exp\{i(\omega_i - \omega_1 - \omega_{L1})t\}}{\omega_i - \omega_1 - \omega_{L1}} \right]. \quad (\text{E.2})$$

<sup>2</sup>We assume that the Rabi frequency is real, i.e.  $\Omega_{i1}^* = \Omega_{i1}$ .

Here the Rabi frequency for the transition  $\Omega_{i1}$  is defined in terms of  $\mathbf{E}_{L1}$  as in eqn 7.12.<sup>2</sup> We define the difference between the laser frequency  $\omega_{L1}$  and the frequency of the transition between levels 1 and  $i$  as

$$\Delta = \omega_1 + \omega_{L1} - \omega_i. \quad (\text{E.3})$$

From eqn 7.76 the wavefunction of the atom is

$$\Psi_n(\mathbf{r}, t) = e^{-i\omega_1 t} |1\rangle - \frac{\Omega_{i1}}{2\Delta} e^{-i\omega_i t} |i\rangle + \frac{\Omega_{i1}}{2\Delta} e^{-i(\omega_1 + \omega_{L1})t} |i\rangle. \quad (\text{E.4})$$

The perturbation produces the admixture of two terms into the initial state  $|1\rangle$  that both have the same small amplitude  $\Omega_{i1}/|2\Delta| \ll 1$ . We will find that the term with angular frequency  $\omega_i$  represents real excitation to  $|i\rangle$ . The term with angular frequency  $\omega_1 + \omega_{L1}$  corresponds to a virtual level, i.e. in the mathematics this term acts as if there is a level at an energy  $\hbar\omega_{L1}$  above the ground state that has the symmetry properties of  $|i\rangle$ , but in reality there is no such level.

To determine the effect of the field oscillating at  $\omega_{L2}$  on the perturbed atom, we take eqn 7.10, which states that for a single-photon transition  $i\dot{c}_2 = \Omega \cos(\omega t) e^{i\omega_0 t} c_1$ , and make the replacements  $\omega \rightarrow \omega_{L2}$ ,  $\omega_0 \rightarrow \omega_2 - \omega_i$  and  $\Omega \rightarrow \Omega_{2i}$  to obtain<sup>3</sup>

$$i\dot{c}_2(t) = \Omega_{2i} \cos(\omega_{L2}t) e^{i(\omega_2 - \omega_i)t} c_i(t). \quad (\text{E.5})$$

Insertion of the expression for  $c_i(t)$  from eqn E.2 yields

$$\begin{aligned} i\dot{c}_2(t) &= -\Omega_{2i} \cos(\omega_{L2}t) e^{-i(\omega_i - \omega_2)t} \times \frac{\Omega_{i1}}{2\Delta} \left[ 1 - e^{i(\omega_i - \omega_1 - \omega_{L1})t} \right] \\ &= -\frac{\Omega_{2i}\Omega_{i1}}{4\Delta} [e^{i\omega_{L2}t} + e^{-i\omega_{L2}t}] \cdot \left[ e^{-i(\omega_i - \omega_2)t} - e^{i\{(\omega_2 - \omega_1) - \omega_{L1}\}t} \right]. \end{aligned} \quad (\text{E.6})$$

Integration and the rotating-wave approximation lead to

$$\begin{aligned} c_2(t) &= \frac{\Omega_{2i}\Omega_{i1}}{4\Delta} \left[ \frac{1 - e^{-i(\omega_i - \omega_2 - \omega_{L2})t}}{\omega_i - \omega_2 - \omega_{L2}} + \frac{1 - e^{i\{(\omega_2 - \omega_1) - (\omega_{L1} - \omega_{L2})\}t}}{(\omega_2 - \omega_1) - (\omega_{L1} - \omega_{L2})} \right] \\ &= \frac{\Omega_{2i}\Omega_{i1}}{4\Delta(\Delta + \delta)} [1 - e^{-i(\Delta + \delta)t}] - \frac{\Omega_{2i}\Omega_{i1}}{4\Delta\delta} [1 - e^{-i\delta t}], \end{aligned} \quad (\text{E.7})$$

where

$$\delta = (\omega_{L1} - \omega_{L2}) - (\omega_2 - \omega_1) \quad (\text{E.8})$$

is the frequency detuning from the Raman resonance condition that the difference in the laser frequencies matches the energy difference between levels 1 and 2, over  $\hbar$  (see Fig. 9.20).<sup>4</sup> Equation E.7 looks complicated but its two parts have a straightforward physical interpretation—we can find the conditions for which each part is important by examining their denominators. Raman transitions are important when  $\delta \simeq 0$  and  $\Delta$  is large ( $|\delta| \ll |\Delta|$ ) so that the second part of eqn E.7 dominates (and the individual single-photon transitions are far from resonance). Defining an effective Rabi frequency as

$$\Omega_{\text{eff}} = \frac{\Omega_{2i}\Omega_{i1}}{2\Delta} = \frac{\langle 2 | \mathbf{e}\mathbf{r} \cdot \mathbf{E}_{L2} | i \rangle \langle i | \mathbf{e}\mathbf{r} \cdot \mathbf{E}_{L1} | 1 \rangle}{\hbar^2 (\omega_i - \omega_1 - \omega_{L1})}, \quad (\text{E.9})$$

we can write eqn E.7 as

$$c_2(t) = \frac{\Omega_{\text{eff}}}{2} \frac{1 - e^{-i(\Delta + \delta)t}}{\Delta + \delta} - \frac{\Omega_{\text{eff}}}{2} \frac{1 - e^{-i\delta t}}{\delta}. \quad (\text{E.10})$$

The first term can be neglected when  $|\delta| \ll |\Delta|$  to yield

$$|c_2(t)|^2 = \frac{1}{4} \Omega_{\text{eff}}^2 t^2 \operatorname{sinc}^2\left(\frac{\delta t}{2}\right). \quad (\text{E.11})$$

<sup>3</sup>The possibility that radiation at angular frequency  $\omega_{L1}$  could drive this transition between  $i$  and 2 is considered later for two-photon transitions.

<sup>4</sup>Notice that this condition does not depend on  $\omega_i$ . The Raman transition can be viewed as a coupling between  $|1\rangle$  and  $|2\rangle$  via a virtual level, whose origin can be traced back to the term (with a small amplitude) at frequency  $\omega_1 + \omega_{L1}$  in eqn E.4. However, although a virtual level gives a useful physical picture it is entirely fictitious—during a Raman transition there is negligible population in the excited state and hence negligible spontaneous emission.

This is the same as eqn 7.15 for one-photon transitions, but  $\Omega_{\text{eff}}$  has replaced  $\Omega$ . This presentation of Raman transitions has assumed a weak perturbation and we have found results analogous to those for the weak excitation of a single-photon transition (Section 7.1); a more comprehensive treatment of the Raman coupling between  $|1\rangle$  and  $|2\rangle$  with effective Rabi frequency  $\Omega_{\text{eff}}$ , analogous to that in Section 7.3, shows that Raman transitions give rise to Rabi oscillations, e.g. a  $\pi$ -pulse transfers all the population from 1 to 2, or the reverse. Raman transitions are coherent in the same way as radio-frequency, or microwave, transitions directly between the two-levels, e.g. a Raman pulse can put the atomic wavefunction into a coherent superposition state  $A|1\rangle + B|2\rangle$ .<sup>5</sup>

<sup>5</sup>Raman transitions can impart momentum to the atoms and this makes them extremely useful for manipulating atoms and ions (see Section 9.8).

<sup>6</sup>Similarly, the quantity  $\Delta + \delta = \omega_i - \omega_2 - \omega_{L2}$  (in eqn E.7) is small when  $\omega_{L2}$  matches the frequency of the transition between  $|i\rangle$  and  $|2\rangle$ . For this condition the single-photon transition between levels  $i$  and 2 is the dominant process. The single-photon processes can be traced back to the small amplitude with time dependence  $\exp(i\omega_i t)$  in eqn E.4.

<sup>7</sup>The generalisation to the case where  $\Omega_{i1} \neq \Omega_{2i}$  is straightforward.

**Example E.1** The duration of a  $\pi$ -pulse (that contains both frequencies  $\omega_{L1}$  and  $\omega_{L2}$ ) is given by

$$\Omega_{\text{eff}} t_\pi = \pi. \quad (\text{E.12})$$

For simplicity, we shall assume that both Raman beams have similar intensities so that  $\Omega_{i1} \simeq \Omega_{2i} \simeq \Omega$  and hence  $\Omega_{\text{eff}} \simeq \Omega^2/\Delta$  (neglecting small factors).<sup>7</sup> From eqn 9.3 we find that the rate of scattering of photons on the transition  $|1\rangle$  to  $|i\rangle$  is approximately  $\Gamma\Omega^2/\Delta^2$ , since for a Raman transition  $\Delta$  is large ( $\Delta \gg \Gamma$ ). Thus the number of spontaneously-emitted photons during the Raman pulse is

$$R_{\text{scatt}} t_\pi \simeq \frac{\Gamma\Omega^2}{\Delta^2} \frac{\pi\Delta}{\Omega^2} \simeq \frac{\pi\Gamma}{\Delta}. \quad (\text{E.13})$$

<sup>8</sup>The hyperfine splitting is  $\omega_2 - \omega_1 = 2\pi \times 1.7 \text{ GHz}$  but we do not need to know this for this calculation.

This shows that spontaneous emission is negligible when  $\Delta \gg \Gamma$ . As a specific example, consider the Raman transition between the two hyperfine levels in the 3s ground configuration of sodium<sup>8</sup> driven by two laser beams with frequencies such that  $\Delta = 2\pi \times 3 \text{ GHz}$ . The 3p  ${}^2\text{P}_{1/2}$  level acts as the intermediate level and has  $\Gamma = 2\pi \times 10^7 \text{ s}^{-1}$ . Thus  $R_{\text{scatt}} t_\pi \simeq 0.01$ —this means that the atoms can be subjected to many  $\pi$ -pulses before there is a spontaneous emission event that destroys the coherence (e.g. in an interferometer as described in Section 11.7). Admittedly, this calculation is crude but it does indicate the relative importance of the coherent Raman transitions and excitation of the intermediate level by single-photon processes. (It exemplifies the order-of-magnitude estimate that should precede calculations.) The same ap-

proximations give the duration of a  $\pi$ -pulse as

$$t_\pi = \frac{\pi}{\Omega_{\text{eff}}} \simeq \frac{\pi\Delta}{\Omega^2} \simeq \frac{2\pi\Delta}{\Gamma^2} \frac{I_{\text{sat}}}{I}, \quad (\text{E.14})$$

where eqn 7.86 has been used to relate  $\Omega^2$  to intensity. Thus in a Raman experiment carried out with two laser beams, each of intensity  $3I_{\text{sat}}$ , and the above values of  $\Delta$  and  $\Gamma$  for sodium, the pulse has a duration of  $t_\pi = 10\ \mu\text{s}$ .

## E.2 Two-photon transitions

The intuitive description of Raman transitions as two successive applications of the first-order time-dependent perturbation theory result for a single-photon transition can also be applied to two-photon transitions between levels 1 and 2 via  $i$ , where  $\omega_2 > \omega_i > \omega_1$ . The two-photon rate between levels 1 and 2 is

$$R_{12} = \left| \sum_i \left\{ \frac{\langle 2 | \mathbf{e}\mathbf{r} \cdot \mathbf{E}_{L2} | i \rangle \langle i | \mathbf{e}\mathbf{r} \cdot \mathbf{E}_{L1} | 1 \rangle}{\hbar^2 (\omega_i - \omega_1 - \omega_{L1})} + \frac{\langle 2 | \mathbf{e}\mathbf{r} \cdot \mathbf{E}_{L1} | i \rangle \langle i | \mathbf{e}\mathbf{r} \cdot \mathbf{E}_{L2} | 1 \rangle}{\hbar^2 (\omega_i - \omega_1 - \omega_{L2})} \right\} \right|^2 \times g(\omega_{L1} + \omega_{L2}). \quad (\text{E.15})$$

This has the form of the modulus squared of a sum of amplitudes multiplied by the line shape function  $g(\omega_{L1} + \omega_{L2})$ . There are two contributing amplitudes from (a) the process where the atom interacts with the beam whose electric field is  $\mathbf{E}_{L1}$  and then with the beam whose field is  $\mathbf{E}_{L2}$ , and (b) the process where the atom absorbs photons from the two laser beams in the opposite order.<sup>9</sup> The energy increases by  $\hbar(\omega_{L1} + \omega_{L2})$  independent of the order in which the atom absorbs the photons, and the amplitude in the excited state is the sum of the amplitudes for these two possibilities. In Doppler-free two-photon spectroscopy (Section 8.4) the two counter-propagating laser beams have the same frequency  $\omega_{L1} = \omega_{L2} = \omega$ , and we shall also assume that they have the same magnitude of electric field (as would be the case for the apparatus shown in Fig. 8.8). This leads to an excitation rate given by

$$R_{12} \simeq \left| 2 \sum_i \frac{\Omega_{2i}\Omega_{i1}}{\omega_i - \omega_1 - \omega} \right|^2 \cdot \frac{\tilde{\Gamma}/(2\pi)}{(\omega_{12} - 2\omega)^2 + \tilde{\Gamma}^2/4}, \quad (\text{E.16})$$

with  $\Omega_{i1}$  and  $\Omega_{2i}$  as defined in the previous section. The transition has a homogeneous width  $\tilde{\Gamma}$  greater than, or equal to, the natural width of the upper level  $\tilde{\Gamma} \geq \Gamma$ ; this Lorentzian line shape function has a similar form to that in eqn 7.77, with a maximum at the two-photon resonance frequency  $\omega_{12} = \omega_2 - \omega_1$  (as in Section 8.4). The constraint that the two photons have the same frequency means that the frequency detuning from the intermediate level  $\Delta = \omega_i - (\omega_1 + \omega)$  is generally much larger than in Raman transitions, e.g. for the 1s–2s transition in

<sup>9</sup>Only one of these paths is near resonance for Raman transitions because  $\omega_{L1} - \omega_{L2} \neq \omega_{L2} - \omega_{L1}$ .

hydrogen the nearest level than can provide an intermediate state is 2p, which is almost degenerate with the 2s level (see Fig. 8.4); thus  $\omega_i \simeq \omega_2$  and  $\Delta \simeq \omega = 2\pi \times 10^{15} \text{ s}^{-1}$  (or  $4 \times 10^5$  times larger than the frequency detuning used in the example of a Raman transition in the previous section). There are two important consequences of this large frequency detuning: (a) in real atoms there are many levels with comparable frequency detuning and taking these other paths ( $1 \rightarrow i \rightarrow 2$ ) into account leads to the summation over  $i$  in eqn E.16; and (b) the rate of two-photon transitions is small even for high intensities (cf. allowed single-photon transitions).<sup>10</sup>

<sup>10</sup>A rough estimate of the two-photon rate can be made in a similar way to the calculations for Raman transitions in the previous section (Demtröder 1996).

# Appendix F: The statistical mechanics of Bose–Einstein condensation



This appendix does not attempt to reproduce the standard treatment of a Bose–Einstein condensate found in statistical mechanics texts, but aims to give a complementary viewpoint, that emphasises the link between photons and atoms, and also to describe BEC in a harmonic potential.

|  |     |
|--|-----|
| F.1 The statistical mechanics of photons | 315 |
| F.2 Bose–Einstein condensation           | 316 |

## F.1 The statistical mechanics of photons

The Planck formula for the energy density of radiation per unit bandwidth  $\rho(\omega)$ , used in the Einstein treatment of radiation (see eqn 1.29), can be written as a product of three factors:

$$\rho(\omega) d\omega = \hbar\omega \times f_{\text{ph}}(\omega) \times D_{\text{ph}}(\omega) d\omega. \quad (\text{F.1})$$

Here  $\hbar\omega$  is the photon energy, the function  $f_{\text{ph}}(\omega) = 1/(e^{\beta\hbar\omega} - 1)$ , with  $\beta = 1/k_B T$ , determines the number of photons per energy level and  $D_{\text{ph}}(\omega)$  is the density of states per unit bandwidth.<sup>1</sup> Although the distribution  $f_{\text{ph}}$  becomes very large as  $\omega \rightarrow 0$  (infra-red divergence), the integration over the frequency distribution (using the substitution  $x = \beta\hbar\omega$ ) yields a finite result for the total energy of the radiation in the volume  $V$ :

$$E = V \int_0^\infty \rho(\omega) d\omega \propto VT^4. \quad (\text{F.2})$$

This result follows from dimensional considerations, without the evaluation of the definite integral.<sup>2</sup> This integral for  $E$  is a particular case of the general expression in statistical mechanics for the energy of the system which is obtained by summing the energy over all occupied levels:

$$E = \sum_i f(\varepsilon_i) \varepsilon_i. \quad (\text{F.3})$$

Here  $f(\varepsilon_i)$  gives the distribution over the levels of energy  $\varepsilon_i$ . The integral in eqn F.2, for the particular case of photons, gives a close approximation

<sup>1</sup>The number of states in phase-space with wavevectors between  $k$  and  $k + dk$  equals the volume of a spherical shell of thickness  $dk$  times the density of the states in  $k$ -space,  $4\pi k^2 dk \times V/(2\pi)^3$ . For photons we need an extra factor of 2, because of the different possible polarizations, and the substitution  $k = \omega/c$ .

<sup>2</sup>The energy density  $E/V$  has the same  $T^4$  dependence as the Stefan–Boltzmann law for the power per unit area radiated by a black body (as expected, since  $c E/V$  corresponds to power divided by area).

to this summation when the system occupies many levels to give an almost continuous distribution. The density of states in the integral represents a summation over the number of levels within each frequency (or energy) interval  $d\omega$  ( $\equiv d\varepsilon/\hbar$ ).

## F.2 Bose–Einstein condensation

The crucial difference between photons and particles in statistical mechanics is that photons simply disappear as the temperature tends to zero, as we can see from eqn F.2. In contrast, for a system of particles, such as a gas of atoms or molecules in a box, the number remains constant. This introduces a second constraint on the distribution function, namely that the sum of the populations in all the energy levels equals the total number  $\mathcal{N}$ . Note that the symbol ‘ $\mathcal{N}$ ’ is used here because ‘ $N$ ’ was used in Chapter 7 to represent the number density (the convention usually adopted in laser physics). Here, number density is denoted by ‘ $n$ ’, as is usual in statistical mechanics. Hence

$$\mathcal{N} = \sum_i f(\varepsilon_i). \quad (\text{F.4})$$

This equation for conservation of number, and eqn F.3 for the total energy, apply to any system of particles. We shall consider particles with integer spin that follow the Bose–Einstein distribution function

$$f_{\text{BE}}(\varepsilon) = \frac{1}{e^{\beta(\varepsilon - \mu)} - 1}. \quad (\text{F.5})$$

This function has two parameters  $\beta$  and  $\mu$  that can be determined by the two constraints. For the particular case of bosons at low temperatures, the chemical potential  $\mu$  has little consequence *except* for atoms in the lowest energy state, so that for the higher-lying levels  $f_{\text{BE}}(\varepsilon)$  closely resembles the distribution of photons! We can justify this assertion by considering the properties of a system with a significant population  $\mathcal{N}_0$  in the ground state.<sup>3</sup> The number of atoms in the lowest level with energy  $\varepsilon_0$  is given by

$$\mathcal{N}_0 = \frac{1}{e^{\beta(\varepsilon_0 - \mu)} - 1}. \quad (\text{F.6})$$

Hence

$$\frac{\varepsilon_0 - \mu}{k_B T} = \ln \left( 1 + \frac{1}{\mathcal{N}_0} \right) \simeq \frac{1}{\mathcal{N}_0}. \quad (\text{F.7})$$

Einstein originally considered gases with a large total number of atoms,  $\mathcal{N} \sim 10^{23}$ , so, even when  $\mathcal{N}_0$  is only a small fraction of  $\mathcal{N}$ , the difference  $\varepsilon_0 - \mu$  is negligible in comparison to the thermal energy  $k_B T$ . (This thermodynamic, or large number, approximation works even for samples of  $10^6$  magnetically-trapped atoms.<sup>4</sup>) The equation shows that the chemical potential is lower than  $\varepsilon_0$ , the lowest energy level in the system.<sup>5</sup> For the first excited level we find that

$$\varepsilon_1 - \mu = (\varepsilon_1 - \varepsilon_0) + (\varepsilon_0 - \mu) \simeq \hbar\omega + \frac{k_B T}{\mathcal{N}_0} \simeq \hbar\omega.$$

<sup>3</sup>This may appear to be a circular argument since the large occupation of the lowest level is the signature of the Bose–Einstein condensation that we want to investigate! This section shows that this is a consistent solution of the equations for bosons, and the validity of this treatment can be appreciated more readily after deriving the equations.

<sup>4</sup>We assume a thermal energy  $k_B T$  much greater than the spacing between the energy levels. Otherwise, particles sit in the ground state simply because of the Boltzmann factor  $\exp\{-\beta(\varepsilon_1 - \varepsilon_0)\} \ll 1$ , where  $\varepsilon_1$  is the energy of the first excited level (Section 12.9).

<sup>5</sup>Otherwise there would be an energy for which  $\varepsilon - \mu = 0$ ; this would make the denominator in eqn F.5 equal to zero so that  $f(\varepsilon) \rightarrow \infty$ .

Hence, *except for the ground-state population*,  $\mu$  can be neglected and  $f_{\text{BE}}$  becomes the same as the distribution for photons:

$$f(\varepsilon) \simeq \frac{1}{e^{\beta\varepsilon} - 1}. \quad (\text{F.8})$$

From what has been said above you may wonder how neglecting the chemical potential can be consistent with conservation of particle number in eqn F.4. This equation can be expressed as an integral of  $f(\varepsilon)$  times the density of states *for particles*,  $D(\varepsilon)$ ,

$$\mathcal{N} = \mathcal{N}_0 + \int_0^\infty f(\varepsilon) D(\varepsilon) d\varepsilon. \quad (\text{F.9})$$

The number in the ground state,  $\mathcal{N}_0$ , has to be put in explicitly because the integral does not properly count these atoms. Effectively, we have replaced  $\mu$  as a parameter by  $\mathcal{N}_0$  (these are related by eqn F.7). The two terms in eqn F.9 give the number of particles in the two parts, or subsystems, that make up the whole. From this perspective we regard the  $\mathcal{N} - \mathcal{N}_0$  particles in the excited states ( $\varepsilon > \varepsilon_0$ ) as a sub-system that exchanges particles with the condensate (atoms in the ground state). Thus atoms in the excited states behave as if there is no number conservation:  $\mathcal{N} - \mathcal{N}_0 \rightarrow 0$  when  $T \rightarrow 0$ , as for photons.

The integral in eqn F.9 contains the distribution function from eqn F.8 times the density of states for particles given by

$$D(\varepsilon) = AV\varepsilon^{1/2} d\varepsilon, \quad (\text{F.10})$$

where  $A$  is a constant.<sup>6</sup> With the substitution  $x = \beta\varepsilon$ , eqn F.9 becomes

$$\mathcal{N}_0 = \mathcal{N} - AV(k_B T)^{3/2} \zeta, \quad (\text{F.11})$$

where  $\zeta$  represents the value of the integral given in statistical mechanics texts as

$$\zeta = \int_0^\infty \frac{x^{1/2}}{e^x - 1} dx = 2.6 \times \frac{\sqrt{\pi}}{2}. \quad (\text{F.12})$$

The ground-state occupation goes to zero,  $\mathcal{N}_0 = 0$ , at the critical temperature  $T_C$  given by

$$\frac{\mathcal{N}}{V} = A(k_B T_C)^{3/2} \zeta. \quad (\text{F.13})$$

With  $A = 2\pi(2M)^{3/2}/h^3$  and eqn F.12 for  $\zeta$ , this gives eqn 10.14. The discussion here supposes that there is a large population in the lowest level (the Bose–Einstein condensate) and determines the temperature at which  $\mathcal{N}_0$  goes to zero. (A different perspective adopted in many treatments is to consider what happens as atoms are cooled down towards  $T_C$ .) Dividing eqn F.11 by F.13 gives the fraction of particles in the ground state for a Bose gas in a box as

$$\frac{\mathcal{N}_0}{\mathcal{N}} = 1 - \left( \frac{T}{T_C} \right)^{3/2}. \quad (\text{F.14})$$

<sup>6</sup>  $D(\omega)$  differs fundamentally from  $D_{\text{ph}}(\omega)$  in eqn F.1 because a particle's energy is proportional to the square of its wavevector,  $\varepsilon \propto k^2$ , i.e.  $\varepsilon = p^2/2M$  with momentum  $p = \hbar k$ .

Note that the strength of the interaction between the atoms does not appear in this treatment—the value of  $T_C$  does not depend on the scattering length. This shows that *BEC arises from quantum statistics*. In real experiments there must be interactions so that atoms have a finite collision cross-section, otherwise there would not be any mechanism for establishing thermal equilibrium and evaporative cooling would not be possible. (A non-interacting Bose gas has some curious properties.)

### F.2.1 Bose–Einstein condensation in a harmonic trap

The volume of the trapped atomic cloud depends on temperature as  $V \propto T^{3/2}$  (from eqn 10.16); hence we find that for a trapped atom the equation equivalent to eqn F.11 is

$$\mathcal{N} - \mathcal{N}_0 \propto T^3. \quad (\text{F.15})$$

This dependence on the cube of  $T$  arises because the density of states for particles in a harmonic trap is different to that given in eqn F.10 for a gas in a box of fixed volume (i.e. an infinite square-well potential). This affects the way that the states fill up and hence the conditions for BEC. An argument analogous to that leading to eqn F.14 gives the fraction in the ground state as

$$\frac{\mathcal{N}_0}{\mathcal{N}} = 1 - \left( \frac{T}{T_C} \right)^3. \quad (\text{F.16})$$

This is a stronger dependence on  $T/T_C$  than in a homogeneous gas. At  $T = 0.99 T_C$  this equation predicts a condensate fraction of  $\mathcal{N}_0/\mathcal{N} = 0.03$ , so that even just below  $T_C$  a cloud of  $\mathcal{N} \sim 10^6$  trapped atoms gives  $1/\mathcal{N}_0 \ll 1$ , and this partly justifies the assumptions made after eqn F.7. Typically, experiments are carried out at around  $T/T_C \sim 0.5$ , or below, where only a fraction  $(0.5)^3 = 0.125$  of the atoms remain in the thermal cloud. This gives a sufficiently pure condensate for most purposes and further evaporative cooling would cut deeply into the condensate and reduce  $\mathcal{N}_0$ .<sup>7</sup>

<sup>7</sup> A large condensate has a chemical potential that is considerably greater than the energy of the harmonic oscillator ground state; however, this turns out not to seriously affect results such as eqn F.16.

# References

- Acheson, D. (1997). *From calculus to chaos—an introduction to dynamics*. Oxford University Press.
- Allen, L. and Eberly, J. H. (1975). *Optical resonance and two-level atoms*. New York: Wiley.
- Amoretti, M., Amsler, C., Bonomi, G., Bouchta, A., Bowe, P., Carraro, C., Cesar, C. L., Charlton, M., *et al.*; The ATHENA Collaboration (2002). Production and detection of cold antihydrogen atoms. *Nature*, **419**, 456.
- Anderson, M. H., Ensher, J. R., Matthews, M. R., Wieman, C. E. and Cornell, E. A. (1995). Observation of Bose–Einstein condensation in a dilute atomic vapor. *Science*, **269**, 198.
- Andrews, M. R., Townsend, C. G., Miesner, H.-J., Durfee, D. S., Kurn, D. M. and Ketterle, W. (1997). Observation of interference between two Bose condensates. *Science*, **275**, 637.
- Annett, J. F. (2004). *Superconductivity, superfluids and condensates*. Oxford University Press.
- Arndt, M., Nairz, O., Vos-Andreae, J., Keller, C., van der Zouw, G. and Zeilinger, A. (1999). Wave–particle duality of C-60 molecules. *Nature*, **401**, 680.
- Ashkin, A. (1997). Optical trapping and manipulation of neutral particles using lasers. *Proc. Natl. Acad. Sci. USA*, **94**, 4853.
- Ashkin, A., Dziedzic, J. M., Bjorkholm, J. E. and Chu, S. (1986). Observation of a single-beam gradient force optical trap for dielectric particles. *Optics Lett.*, **11**, 288.
- Atkins, P. W. (1983). *Molecular quantum mechanics*, 2nd edn. Oxford University Press.
- Atkins, P. W. (1994). *Physical chemistry*, 5th edn. Oxford University Press.
- Baird, P. E. G., Blundell, S. A., Burrows, G., Foot, C. J., Meisel, G., Stacey, D. N. and Woodgate, G. K. (1983). Laser spectroscopy of the tin isotopes. *J. Phys. B*, **16**, 2485.
- Bardou, F., Bouchaud, J.-P., Aspect, A. and Cohen-Tannoudji, C. (1991). *Levy statistics and laser cooling: how rare events bring atoms to rest*. Cambridge University Press.
- Barnett, S. M. and Radmore, P. M. (1997). *Methods in theoretical quantum optics*. Oxford University Press.
- Basdevant, J.-L. and Dalibard, J. (2000). *The quantum mechanics solver*. Berlin: Springer.

- Berkeland, D. J., Miller, J. D., Bergquist, J. C., Itano, W. M. and Wineland, D. J. (1998). Laser-cooled mercury ion trap frequency standard. *Phys. Rev. Lett.*, **80**, 2089.
- Berman, P. R. (ed) (1997). *Atom interferometry*. San Diego: Academic Press.
- Bethe, H. A. and Jackiw, R. (1986). *Intermediate quantum mechanics*, 3rd edn. Menlo Park, CA: Benjamin/Cummings.
- Bethe, H. A. and Salpeter, E. E. (1957). *Quantum mechanics of one- and two-electron atoms*. Berlin: Springer.
- Bethe, H. A. and Salpeter, E. E. (1977). *Quantum mechanics of one- and two-electron atoms*. New York: Plenum.
- Bleaney, B. I. and Bleaney, B. (1976). *Electricity and magnetism*, 3rd edn. Oxford University Press.
- Blundell, S. (2001). *Magnetism in condensed matter*. Oxford University Press.
- Blythe, P. J., Webster, S. A., Margolis, H. S., Lea, S. N., Huang, G., Choi, S.-K., Rowley, W. R. C., Gill, P. and Windeler, R. S. (2003). Subkilohertz absolute-frequency measurement of the 467-nm electric-octupole transition in  $^{171}\text{Yb}^+$ . *Phys. Rev. A*, **67**, 020501.
- Boshier, M. G., Baird, P. E. G., Foot, C. J., Hinds, E. A., Plimmer, M. A., Stacey, D. N., Swan, J. B., Tate, D. A., Warrington, D. M. and Woodgate, G. K. (1989). Laser spectroscopy of the 1s–2s transition in hydrogen and deuterium: determination of the 1s Lamb shift and the Rydberg constant. *Phys. Rev. A*, **40**, 6169.
- Bransden, B. H. and Joachain, C. J. (2003). *Physics of atoms and molecules*, 2nd edn. London: Longman.
- Brink, D. M. and Satchler, G. R. (1993). *Angular momentum*, 3rd edn. Oxford: Clarendon Press.
- Brooker, G. A. (2003). *Optics*. Oxford University Press.
- Budker, D., Kimball, D. F. and DeMille, D. P. (2003). *Atomic physics: an exploration through problems and solutions*. Oxford University Press.
- Butcher, L. S., Stacey, D. N., Foot, C. J. and Burnett, K. (1999). Ultracold collisions for Bose–Einstein condensation. *Phil. Trans. R. Soc. Lond., Ser. A*, **357**, 1421.
- Carnal, O. and Mlynek, J. (1991). Young’s double-slit experiment with atoms: a simple atom interferometer. *Phys. Rev. Lett.*, **66**, 2689.
- Chapman, M. S., Ekstrom, C. R., Hammond, T. D., Schmiedmayer, J., Wehinger, S. and Pritchard, D. E. (1995). Optics and interferometry with  $\text{Na}_2$  molecules. *Phys. Rev. Lett.*, **74**, 4783.
- Chu, S., Hollberg, L., Bjorkholm, J. E., Cable, A. and Ashkin, A. (1985). 3-dimensional viscous confinement and cooling of atoms by resonance radiation pressure. *Phys. Rev. Lett.*, **55**, 48.
- Chu, S., Bjorkholm, J. E., Ashkin, A. and Cable, A. (1986). Experimental-observation of optically trapped atoms. *Phys. Rev. Lett.*, **57**, 314.

- Cohen-Tannoudji, C., Diu, B. and Laloë, F. (1977). *Quantum mechanics*. New York: Wiley.
- Cohen-Tannoudji, C., Dupont-Roc, J. and Grynberg, G. (1992). *Atom-photon interactions: basic processes and applications*. New York: Wiley.
- Condon, E. U. and Odabasi, H. (1980). *Atomic structure*. Cambridge University Press.
- Corney, A. (2000). *Atomic and laser spectroscopy*. Oxford University Press.
- Cowan, R. D. (1981). *The theory of atomic structure and spectra*. Berkeley: University of California Press.
- Cummins, H. K. and Jones, J. A. (2000). Nuclear magnetic resonance: a quantum technology for computation and spectroscopy. *Contemporary Phys.*, **41**, 383.
- Dalibard, J. and Cohen-Tannoudji, C. (1985). Dressed-atom approach to atomic motion in laser-light—the dipole force revisited. *J. Optical Soc. Amer. B*, **2**, 1707.
- Dalibard, J. and Cohen-Tannoudji, C. (1989). Laser cooling below the Doppler limit by polarization gradients: simple theoretical models. *J. Optical Soc. Amer. B*, **6**, 2023.
- Davis, C. C. (1996). *Lasers and electro-optics*. Cambridge University Press.
- Dehmelt, H. (1990). Less is more: experiments with an individual atomic particle at rest in free space. *Amer. J. Phys.*, **58**, 17.
- Demtröder, W. (1996). *Laser spectroscopy*, 2nd edn. Berlin: Springer.
- Dieckmann, K., Spreeuw, R. J. C., Weidemüller, M. and Walraven, J. T. M. (1998). Two-dimensional magneto-optical trap as a source of slow atoms. *Phys. Rev. A*, **58**, 3891.
- Diedrich, F., Bergquist, J. C., Itano, W. M. and Wineland, D. J. (1989). Laser cooling to the zero-point energy of motion. *Phys. Rev. Lett.*, **62**, 403.
- Dirac, P. A. M. (1981). *The principles of quantum mechanics*, 4th edn. Oxford University Press.
- Einstein, A. (1917). Zur Quantentheorie der Strahlung. *Physikalische Zeitschrift*, **18**, 121.
- Eisberg, R. and Resnick, R. (1985). *Quantum physics of atoms, molecules, solids, nuclei, and particles*, 2nd edn. New York: Wiley.
- Feynman, R. P., Leighton, R. B. and Sands, M. (1963–1965). *The Feynman lectures on physics*. Reading, MA: Addison-Wesley.
- Foot, C. J., Couillaud, B., Beausoleil, R. G. and Hänsch, T. W. (1985). Continuous-wave two-photon spectroscopy of the 1S–2S transition in hydrogen. *Phys. Rev. Lett.*, **54**, 1913.
- Fox, M. (2001). *Optical properties of solids*. Oxford University Press.
- French, A. P. and Taylor, E. F. (1978). *An introduction to quantum physics*. London: Chapman and Hall.

- Gallagher, T. F. (1994). *Rydberg atoms*. Cambridge monographs on atomic, molecular, and chemical physics. Cambridge University Press.
- Gerstenkorn, S., Luc, P. and Verges, J. (1993). *Atlas du spectre d'absorption de la molécule d'iode: 7220 cm<sup>-1</sup>–11 200 cm<sup>-1</sup>*. Laboratoire Aimé Cotton: CNRS, Orsay, France.
- Ghosh, P. K. (1995). *Ion traps*. Oxford University Press.
- Godun, R., D'Arcy, M. B., Summy, G. S. and Burnett, K. (2001). Prospects for atom interferometry. *Contemporary Phys.*, **42**, 77.
- Grant, I. S. and Phillips, W. R. (2001). *The elements of physics*. Oxford University Press.
- Greenhow, R. C. (1990). *Introductory quantum mechanics*. Bristol: Institute of Physics Publishing.
- Griffiths, D. J. (1995). *Introduction to quantum mechanics*. Englewood Cliffs, NJ: Prentice Hall.
- Griffiths, D. J. (1999). *Introduction to electrodynamics*. Englewood Cliffs, NJ: Prentice Hall.
- Grisenti, R. E., Schöllkopf, W., Toennies, J. P., Hegerfeldt, G. C. and Köhler, T. (1999). Determination of atom–surface van der Waals potentials from transmission-grating diffraction intensities. *Phys. Rev. Lett.*, **83**, 1755.
- Haar, R. R. and Curtis, L. J. (1987). The Thomas precession gives  $g_e - 1$ , not  $g_e/2$ . *Amer. J. Phys.*, **55**, 1044.
- Hartree, D. R. (1957). *The calculation of atomic structures*. New York: Wiley.
- Hechenblaikner, G. (2002). *Mode coupling and superfluidity of a Bose-condensed gas*. D. Phil., University of Oxford.
- Heilbron, J. L. (1974). *H. G. J. Moseley: the life and letters of an English physicist, 1887–1915*. Berkeley: University of California Press.
- Holzwarth, R., Udem, Th., Hänsch, T. W., Knight, J. C., Wadsworth, W. J. and Russell, P. St. J. (2000). Optical frequency synthesizer for precision spectroscopy. *Phys. Rev. Lett.*, **85**, 2264.
- Itano, W. M., Bergquist, J. C., Bollinger, J. J. and Wineland, D. J. (1995). Cooling methods in ion traps. *Physica Scripta*, **T59**, 106.
- Jennings, D. A., Petersen, F. R. and Evenson, K. M. (1979). Direct frequency measurement of the 260 THz (1.15 μm)  $^{20}\text{Ne}$  laser: and beyond. In *Laser Spectroscopy IV* (eds. H. Walter and K. W. Rothe). Springer series in optical sciences, vol. 21. Berlin: Springer.
- Kinoshita, T. (1995). New value of the  $\alpha^3$  electron anomalous magnetic moment. *Phys. Rev. Lett.*, **75**, 4728.
- Kinoshita, T. and Nio, M. (2003). Revised  $\alpha^4$  term of lepton  $g2$  from the Feynman diagrams containing an internal light-by-light scattering subdiagram. *Phys. Rev. Lett.*, **90**, 021803.
- Kittel, C. (2004). *Introduction to solid state physics*, 8th edn. New York: Wiley.

- Kronfeldt, H. D. and Weber, D. J. (1991). Doppler-free two-photon spectroscopy in Eu: fine structure, hyperfine structures, and isotope shifts of odd levels between 34 400 and 36 700 cm<sup>-1</sup>. *Phys. Rev. A*, **43**, 4837.
- Kuhn, H. G. (1969). *Atomic spectra*, 2nd edn. London: Longmans.
- Lang, M. J. and Bloch, S. M. (2003). Resource letter: laser-based optical tweezers. *Amer. J. Phys.*, **71**, 201.
- Letokhov, V. S. and Chebotaev, V. P. (1977). *Nonlinear laser spectroscopy*. Berlin: Springer.
- Lewis, E. L. (1977). Hyperfine structure in the triplet states of cadmium. *Amer. J. Phys.*, **45**, 38.
- Loudon, R. (2000). *Quantum optics*, 3rd edn. Oxford University Press.
- Lyons, L. (1998). *All you wanted to know about mathematics but were afraid to ask*. Vol. 2. Cambridge University Press.
- Mandl, F. (1992). *Quantum mechanics*. New York: Wiley.
- Maragò, O., Hechenblaikner, G., Hodby, E. and Foot, C. (2001). Temperature dependence of damping and frequency shifts of the scissors mode of a trapped Bose–Einstein condensate. *Phys. Rev. Lett.*, **86**, 3938.
- Margolis, H. S., Huang, G., Barwood, G. P., Lea, S. N., Klein, H. A., Rowley, W. R. C. and Gill, P. (2003). Absolute frequency measurement of the 674-nm <sup>88</sup>Sr<sup>+</sup> clock transition using a femtosecond optical frequency comb. *Phys. Rev. A*, **67**, 032501.
- Mathews, J. and Walker, R. L. (1964). *Mathematical methods of physics*. New York: Benjamin.
- McIntyre, D. H., Beausoleil, R. G., Foot, C. J., Hildum, E. A., Couillaud, B. and Hänsch, T. W. (1989). Continuous-wave measurement of the hydrogen 1s–2s transition frequency. *Phys. Rev. A*, **39**, 4591.
- Meschede, D. (2004). *Optics, light and lasers: an introduction to the modern aspects of laser physics, optics and photonics*. New York: Wiley-VCH.
- Metcalf, H. J. and van der Straten, P. (1999). *Laser cooling and trapping*. Berlin: Springer.
- Morse, P. M. and Feshbach, H. (1953). *Methods of theoretical physics*. International series in pure and applied physics. New York: McGraw-Hill.
- Munoz, G. (2001). Spin–orbit interaction and the Thomas precession: a comment on the lab frame point of view. *Amer. J. Phys.*, **69**, 554.
- Nairz, O., Arndt, M. and Zeilinger, A. (2003). Quantum interference experiments with large molecules. *Amer. J. Phys.*, **71**, 319.
- Nasse, M. and Foot, C. J. (2001). Influence of background pressure on the stability region of a Paul trap. *Euro. J. Phys.*, **22**, 563.
- Nielsen, M. A. and Chuang, I. L. (2000). *Quantum computation and quantum information*. Cambridge University Press.
- Pais, A. (1982). ‘Subtle is the Lord’—the science and life of Albert Einstein. Oxford University Press.

- Pais, A. (1986). *Inward bound*. Oxford University Press.
- Pathra, R. K. (1971). *Statistical mechanics*. Monographs in natural philosophy, vol. 45. Oxford: Pergamon.
- Pethick, C. J. and Smith, H. (2001). *Bose-Einstein condensation in dilute gases*. Cambridge University Press.
- Phillips, W. D., Prodan, J. V. and Metcalf, H. J. (1985). Laser cooling and electromagnetic trapping of neutral atoms. *J. Optical Soc. Amer. B*, **2**, 1751.
- Pitaevskii, L. P. and Stringari, S. (2003). *Bose-Einstein condensation*. Oxford University Press.
- Rae, A. I. M. (1992). *Quantum mechanics*, 3rd edn. Bristol: Institute of Physics.
- Ramsey, N. F. (1956). *Molecular beams*. Oxford University Press.
- Rioux, F. (1991). Direct numerical integration of the radial equation. *Amer. J. Phys.*, **59**, 474.
- Roberts, M., Taylor, P., Barwood, G. P., Gill, P., Klein, H. A. and Rowley, W. R. C. (1997). Observation of an electric-octupole transition in a single ion. *Phys. Rev. Lett.*, **78**, 1876.
- Sakurai, J. J. (1967). *Advanced quantum mechanics*. Reading, MA: Addison-Wesley.
- Sandars, P. G. H. and Woodgate, G. K. (1960). Hyperfine structure in the ground state of the stable isotopes of europium. *Proc. R. Soc. Lond., Ser. A*, **257**, 269.
- Schöllkopf, W. and Toennies, J. P. (1994). Nondestructive mass selection of small van-der-Waals clusters. *Science*, **266**, 1345.
- Segrè, E. (1980). *From X-rays to quarks: modern physicists and their discoveries*. San Francisco: Freeman.
- Series, G. W. (1988). *The spectrum of atomic hydrogen*. Singapore: World Scientific.
- Slater, J. C. (1960). *Quantum theory of atomic structure*. Vol. II. New York: McGraw-Hill.
- Sobelman, I. I. (1996). *Atomic spectra and radiative transitions*, 2nd edn. Berlin: Springer.
- Softley, T. P. (1994). *Atomic spectra*. Oxford chemistry primers. Oxford University Press.
- Steane, A. (1991). *Laser cooling of atoms*. D. Phil., University of Oxford.
- Steane, A. (1997). The ion trap quantum information processor. *Appl. Phys. B*, **64**, 623.
- Steane, A. (1998). Quantum computing. *Rep. Prog. Phys.*, **61**, 117.
- Stolze, J. and Suter, D. (2004). *Quantum computing: a short course from theory to experiment*. New York: Wiley.
- Thorne, A. P., Litzén, U. and Johansson, S. (1999). *Spectrophysics: principles and applications*. Berlin: Springer.
- Udem, Th., Diddams, S. A., Vogel, K. R., Oates, C. W., Curtis, E. A., Lee, W. D., Itano, W. M., Drullinger, R. E., Bergquist, J. C. and Hollberg, L. (2001). Absolute frequency measurements of the  $\text{Hg}^+$

- and Ca optical clock transitions with a femtosecond laser. *Phys. Rev. Lett.*, **86**, 4996.
- Udem, Th., Holzwarth, R. and H\"ansch, T. W. (2002). Optical frequency metrology. *Nature*, **416**, 233.
- Van Dyck, Jr, R. S., Schwinberg, P. B. and Dehmelt, H. G. (1986). Electron magnetic moment from geonium spectra: early experiments and background concepts. *Phys. Rev. D*, **34**, 722.
- Vannier, J. and Audouin, C. (1989). *The quantum physics of atomic frequency standards*. Bristol: Adam Hilger.
- Wieman, C. E., Pritchard, D. E. and Wineland, D. J. (1999). Atom cooling, trapping, and quantum manipulation. *Rev. Mod. Phys.*, **71**, S253.
- Wineland, D. J. and Itano, W. M. (1979). Laser cooling of atoms. *Phys. Rev. A*, **20**, 1521.
- Wineland, D. J., Bergquist, J. C., Bollinger, J. J. and Itano, W. M. (1995). Quantum effects in measurements on trapped ions. *Physica Scripta*, **T59**, 286.
- Woodgate, G. K. (1980). *Elementary atomic structure*. Oxford University Press.
- Wuerker, R. F., Shelton, H. and Langmuir, R. V. (1959). Electrodynamic containment of charged particles. *J. Appl. Phys.*, **30**, 342.

# Index

absolute laser calibration 169–71  
absorption, optical absorption  
  cross-section 138–41  
a.c. Stark effect (light shift) 144–5  
  in two-photon spectroscopy 167  
alkaline earths 80  
  intermediate coupling 86–9  
   $jj$ -coupling scheme 84–6  
   $LS$ -coupling scheme 81–2  
    fine structure 83–4  
  transitions 90  
  Zeeman effect 90–2  
alkali atoms  
  central-field approximation 64–8  
  electronic configurations 60–1  
  fine structure 73–5  
  fine-structure transitions 74–5  
  quantum defects 63–4  
  Schrödinger equation 68–71  
  spin–orbit interaction 71–3  
allowed orbits, determination of 4  
allowed transitions, *see* selection rules  
angular momentum  
  in one-electron systems 38–40, 71–3  
  orbital, operator for 23  
  spin 36  
  vector model 38–40,  
  Wigner–Eckart theorem (projection  
    theorem) 83–4  
angular momentum coupling schemes  
   $IJ$ -coupling scheme 99, 102  
  intermediate coupling 86–9  
   $jj$ -coupling scheme 84–6, 88, 94  
   $LS$ -coupling scheme 81–4, 86, 88, 94  
angular momentum quantisation,  
  Stern–Gerlach experiment 114–15  
angular solution, Schrödinger equation 23–6  
anomalous  $g$ -value of electron, 40–1,  
  274–5  
anomalous Zeeman effect, *see* Zeeman  
  effect  
anti-bunching of photons 146  
antimatter trapping 279  
antisymmetric wavefunctions 48–52  
atom interferometry 246–7, 257  
  diffraction gratings 249–51  
  diffraction of atoms by light 253–5  
  Raman interferometry 255–7

double-slit experiment 249  
measurement of rotation 251–3  
three-grating interferometer 251–2,  
  257  
atom lasers 242  
atomic clocks 118–19  
  caesium fountain frequency  
    standards 212–13  
atomic fountains 211–13  
  Ramsey fringes 134  
atomic number and X-ray spectra 7–11  
atomic units 18–19  
atomic-beam slowing 179–82  
  chirp cooling 184–5  
  Zeeman slowing 182–4  
atomic-beam technique 114–18  
axial confinement in ion traps 265  
axial confinement in magnetic traps  
  221–4  
Balmer series 2, 3  
Balmer- $\alpha$  line 41–2  
  spectroscopy 159–63  
barium ion, laser cooling 267  
Beer’s law 138–9  
Becquerel 14  
Biot–Savart law 101  
Bloch equations, optical 137, 146  
Bloch sphere 131–2  
  in description of qubit  
    transformations 283–4  
Bloch vector 128–32  
Bohr magneton 18  
Bohr radius 4, 18  
Bohr theory 3–5  
Boltzmann factor 13  
Bose–Einstein condensates 234–8  
  atom lasers 242  
  division of 241  
  observation of 239  
  properties 239  
    coherence 240–1  
    healing length 240  
    speed of sound 239–40  
Bose–Einstein condensation (BEC)  
  226–8  
  in trapped atomic vapours 228  
    statistical mechanics 316–18  
bosons 226–7  
  *see also* Bose–Einstein condensation

broadening mechanisms 153  
  collision broadening (pressure  
    broadening) 154–5, 165  
  in Doppler-free spectroscopy 167  
natural broadening 11, 134–7, 141–2,  
  156, 165–7, 269–70  
power broadening 143, 157, 177  
  *see also* homoge-  
    neous/inhomogeneous  
    broadening  
  transit-time broadening 154  
  *see also* Doppler broadening  
Buckyballs ( $C_60$ ), diffraction  
  experiments 249  
buffer gas cooling in ion trapping 266–7  
‘building-up’ principle 60  
  
C<sub>60</sub> molecules (Buckyballs), diffraction  
  experiments 249  
cadmium, measurement of hyperfine  
  structure 112–14  
caesium  
  atomic clocks 118–19  
  atomic fountains 212–13  
  chirp cooling 184  
  fine structure 74  
  Ramsey fringes from atomic fountain  
    134  
calcium ions, detection in Paul trap  
  267–8  
calibration in laser spectroscopy 168  
  absolute calibration 169–71  
  of relative frequency 168–9  
  optical frequency combs 171–4  
  reference standards 170  
capture velocity, magneto-optical trap  
  193–4  
cathode rays 14  
central-field approximation 64–8  
charged particles, trapping of 272  
  *see also* ion trapping  
chirp cooling 184–5  
circular orbits, Bohr’s theory 3–5  
classical oscillator 13–18, 134–7,  
  197–202  
Clebsch–Gordan coefficients 73  
closed shells 60–1  
coherence in Bose condensates 239–41  
coherences of density matrix 129

- cold atoms, need for in atomic fountains 212
- collimation, effect on Doppler broadening 153–4
- collision broadening (pressure broadening) 154–5, 165
- collisions, scattering theory 229–34
- commutation relations 81, 111
- compensation coils in Ioffe–Pritchard trap 224
- complex terms 88
- configuration 60, 93
- ground state of elements, inside front cover
  - mixing 93–4
- controlled-NOT (CNOT) gate 287–9
- cooling, *see* evaporative cooling; laser cooling
- core polarization 67
- correspondence principle 20–1, 68
- Coulomb force 3
- coupling schemes, *see* angular momentum coupling schemes
- coupling, use of word 84
- critical temperature and density in BEC 237
- cross-over resonances in saturated absorption spectroscopy 159–60
- crossed-beam Doppler-free laser spectroscopy 153–5
- d-series 34
- damping
- in optical molasses technique 186–7
  - of classical dipole 135–6
- Darwin term 39–40
- de Broglie wavelength 227
- of matter waves 246
  - relationship to allowed orbits 6
- decay, radiative 11
- decoherence in quantum computing 292
- degeneracy 12, 47
- degenerate perturbation theory 16, 48–9
- mathematics of 298–9
- density matrices 129
- density, critical in BEC 237
- determinantal function, *see* Slater determinant
- deuterium
- HD molecule 57
  - use in spectroscopy 159
- diffraction gratings for atoms 249–51
- dipole force (gradient force) 194–7
- theory of 197–200
- dipole moment of atom 129
- dipole-force traps 199–200
- optical lattice 201–2
- trapping of sodium atoms 200–1
- Dirac equation, 39–40
- direct integral in excited states of helium 54–5
- distinguishability
- of particles 51
  - of qubits 285
- Doppler-free laser spectroscopy 151
- calibration 169–70
  - crossed-beam method 153–5
  - measurement of hyperfine structure 114
  - saturated absorption spectroscopy 155
  - broadening mechanisms 167
  - cross-over resonances 159–60
  - line shape 307–9
  - of atomic hydrogen 159–63
  - principle 156–9
  - two-photon spectroscopy 314–5
- Doppler broadening 113–14, 151–3
- Doppler cooling
- of ions 267–8
  - see also* laser cooling
- Doppler cooling limit 188–90
- Doppler effect, second-order 167
- Doppler shift 151
- double-slit experiment
- with helium atoms 249
  - Young's 246–8
- 'dressed atom' 144
- dye lasers 168
- Earnshaw's theorem 260
- effective atomic number ( $Z_{\text{eff}}$ ) 66, 73
- effective principal quantum number ( $n^*$ ) 62–4, 74
- Ehrenfest's theorem 197
- eigenfunctions and eigenstates 23–6, 28, 48, 51, 73, 81, 84, 102
- Einstein  $A$  coefficients 11–13
- Einstein  $B$  coefficients 11–13, 126–7
- electric dipole transitions 29
- see also* selection rules
- electric fields
- behaviour of ions in a.c. field 262
  - Earnshaw's theorem 260
  - force on ions 259–60
- electron beam ion trap (EBIT) 275–7
- electron orbits
- Bohr's theory 3–5
  - relativistic effects 5–7
- electron shells 7–10
- electronic configuration, *see* configuration
- electrons
- discovery of 14
  - magnetic moment 97–8, 274–5
  - spin 35–6
- spin–orbit interaction 36–8
- wave properties 246
- electrostatic energies, calculation of 302–4
- electrostatic repulsion between electrons 64–5
- elliptical orbits, Sommerfeld's theory 6–7
- emission, induced 11–13, 126, 140
- spontaneous 11–13
- encryption, implications of quantum computing 290
- energy, units of 18
- entanglement 284–6
- equivalent electrons 80–1
- étalon, Fabry–Perot 17, 153, 168–9
- euroium, hyperfine structure 104–5
- evanescent wave 201–2
- evaporative cooling 218, 224–6
- exchange degeneracy 46–51, 57
- exchange integral, in excited states of helium 55–6
- excitation probability function 125
- f*-value 149–50
- Fabry–Perot étalon 17
- resolving power 153
  - use in laser calibration 168–9
- factorisation, value of quantum computing 290
- femtosecond lasers 172–3
- Fermi contact interaction 99
- Fermi's golden rule 29, 123
- fine structure 34
- comparison with hyperfine structure 102–4
  - in *LS*-coupling scheme 83–4
  - Lamb shift 40–1
  - of alkalis 73–5
  - of hydrogen atom 38–40
  - spin of the electron 35–6
  - spin–orbit interaction 36–8
  - transition between levels 41–2
- fine-structure constant ( $\alpha$ ) 6
- flop-in arrangement 117
- flop-out arrangement 116
- forbidden transitions, *see* selection rules
- Fourier transform 118–19, 134
- Franck–Condon principle 277
- Fraunhofer diffraction 133
- frequency chains 170–1
- frequency combs 171–4
- frozen core approximation 67
- g*-factors, Landé 90
- see also* magnetic moments
- gases
- Doppler broadening 152–3
  - velocities of atoms 152

- Gauss' theorem 260  
golden rule (Fermi) 29, 123  
gradient force, *see* dipole force  
Gross–Pitaevskii equation 234–5  
ground states, *see* configuration
- Hadamard transformation 284  
hard spheres modelling of atoms 229–31  
harmonic potential of trapped atoms 235  
Hartree method 70–1  
hartree, atomic unit of energy 18  
Hartree–Fock method 70–1  
HD molecule 57  
healing length 240  
helium  
diffraction experiments 249  
double-slit experiment 249  
energy levels 87, 89  
entanglement 284, 286  
excited states 46–51  
evaluation of integrals 54–6  
spin eigenstates 51–2  
transitions 52–3  
ground state 45–6  
evaluation of integrals 53–6  
superfluid 227  
Zeeman effect 92  
helium–neon laser, as frequency standard 170  
hole burning 157  
homogeneous broadening mechanisms 153, 165  
homonuclear diatomic molecules 57  
Hund's rules 81–2  
hydrogen atom  
1s–2s transition 165–8  
allowed transitions 33–4  
Doppler-free laser spectroscopy 159–63  
fine structure 38–40  
Lamb shift 40–1  
transition between levels 41–2  
gross structure 5, 27  
hyperfine structure 99–100, 104  
Schrödinger equation 22–9  
spectrum of 2–3  
transitions 29–34  
two-photon spectroscopy 165–8  
Zeeman effect on hyperfine structure 109–10, 112–13  
hydrogen maser 100–1, 119  
hyperfine structure 97  
comparison with fine structure 102–4  
isotope shift 105–8  
for  $l \neq 0$  101–2  
for s-electrons 97–100  
measurement 112–14  
atomic-beam technique 114–18
- of europium 104–5  
of hydrogen atom 99–100, 104  
Zeeman effect 109–10, 112–13  
Zeeman effect 108–9  
intermediate fields 111  
strong fields 110–12  
weak fields 109–10, 112
- identical particles 51–2, 56–7, 316–18  
modification of scattering theory 233  
IJ-coupling scheme 99, 102  
impact parameter 230–1  
inert gases 60–1  
diffraction experiments 249  
inhomogeneous broadening  
mechanisms 153, 157  
*see also* Doppler broadening  
integrals, evaluation in helium 53–6  
intensity ratios  
in fine structure 74–5  
in Zeeman effect 17, 91  
interaction, use of word 84  
intercombination lines 90  
interference fringes  
in Young's double-slit experiment 248  
of Bose condensates 240–1  
Ramsey fringes 132–4  
in atomic fountains 212–13  
intermediate coupling 86–9  
interval rule 84, 87–9  
for hyperfine structure 101–2  
inverted pendulum 264  
iodine, as reference in laser spectroscopy 169–70  
Ioffe–Pritchard magnetic trap 221–4  
evaporative cooling 225  
ion trapping  
buffer gas cooling 266–7  
Earnshaw's theorem 260  
electron beam ion trap (EBIT) 275–7  
forces on ions 259  
Paul trap 261–6, 271–2  
Penning trap 271  
quantum jumps 269–70  
sideband cooling 277–9  
ionization energies  
of helium 46  
of inert gases and alkalis 61  
ions  
behaviour in a.c. field 262  
force in an electric field 259–60  
laser cooling 267–8, 277, 279  
for quantum computing 282  
mass spectroscopy 274  
isotope shift 5  
mass effects 105–6  
volume shift 106–8
- jj*-coupling scheme 84–6, 88, 94
- ladder operators 23–4  
Lamb shift 40–1, 168, 275  
Landé formula 73, 102  
Landé *g*-factor 90  
Larmor frequency 14  
laser bandwidth in two-photon spectroscopy 165–7  
laser cooling 213  
atomic beam slowing 182–5  
development of process 178–9  
magneto-optical trap 190–4  
of ions 267–8, 277, 279  
optical molasses technique 185–7  
Doppler cooling limit 188–90  
Raman cooling 210–11  
random recoil 188–9  
scattering force 179–82  
Sisyphus cooling technique 203–7  
limit 207–8  
laser light, modification of Beer's law 139  
laser spectroscopy  
calibration 168  
absolute 169–71  
of relative frequency 168–9  
optical frequency combs 171–4  
reference standards 170  
*see also* Doppler-free laser spectroscopy
- lasers 12  
CO<sub>2</sub> 125  
slowing of atoms 179–82  
level 39, 93  
lifetime, radiative ( $\tau$ ) 11  
light shift (Stark effect) 144–5  
in two-photon spectroscopy 167  
light, diffraction of atoms 253–5  
limitations  
Doppler cooling 188–90  
evaporative cooling 226  
Sisyphus cooling (recoil limit) 207–8  
linear Paul trap 262–6, 271–2  
logic gates in quantum computing 287–9, 291  
Lorentz force 14  
lowering operator 24  
LS-coupling scheme 81–2, 88, 94  
conditions 86  
fine structure 83–4  
selection rules 90  
Lyman series (p-series) 2–3, 34
- Mach–Zehnder interferometer 251–2, 256
- magnesium  
energy levels 86–7  
transitions 90
- magnetic dipole transitions 305  
magnetic fields  
electrons,  $l \neq 0$  101

- in spin-orbit interaction 36–8  
 Zeeman effect 13–18
- magnetic flux density 98  
 magnetic force evaluation 219  
 magnetic moments  
   electron 40–1, 274–5  
   nuclear 97, 109–10, 112–13  
   proton 100
- magnetic quadrupole 220–1  
 magnetic quantum number 23–4, 31–2  
 magnetic resonance technique in  
   atomic beam 116–18
- magnetic traps  
   comparison with magneto-optical  
     traps 194  
   confinement in axial direction 221–4  
   confinement in radial direction 220–1  
   evaporative cooling 224–6  
   comparison with ion trap 259  
   principle 218–20
- magneto-optical trap (MOT) 190–4  
   use with magnetic trap 223
- magnetrons 273
- masers, hydrogen 100–1, 119
- mass, effect in isotope shift 105–6  
   reduced 5,
- mass spectroscopy of ions 274
- Mathieu equation 264
- matter-wave experiments 246–7, 257  
   diffraction gratings 249–51  
   double-slit experiment 249  
   measurement of rotation 251–3  
   three-grating interferometer 251–2,  
     257
- matter waves 242  
   de Broglie relation 246  
   diffraction by light 253–5  
   Raman interferometry 255–7  
   mean oscillation frequency 236
- mercury  
   anomalous Zeeman effect 92  
   energy levels 87–8  
   transitions 90
- mercury ion clock 266
- metastable states 53
- micromotion 265
- microscopy, optical tweezers 196–7
- mirror symmetry (parity) 33
- molecular potentials 229, 231
- monochromatic radiation, interaction  
   with 127–32, 138
- Moseley, and atomic number 7–11
- motion-induced orientation 207
- moving molasses technique 212
- muonic atom 122
- nano-fabrication of gratings 246, 249
- neutrons, de Broglie wavelengths 246
- normal mass shift 106
- normal Zeeman effect, *see* Zeeman  
   effect
- nuclear magnetic moments 97  
 nuclear magnetic resonance (NMR),  
   quantum computing  
   experiments 287–9, 291
- nuclear magneton 97
- nuclear radius 106–8
- nuclear spin 97
- optical absorption by moving atoms  
   155–6
- optical absorption cross-section  
   138–41, 147  
   for pure radiative broadening 141–2  
   power broadening 143  
   saturation intensity 142–3
- optical Bloch equations 137, 146
- optical frequency combs 171–4
- optical lattice 201–2
- optical molasses technique 178, 185–7  
   Doppler cooling limit 188–90  
   in magneto-optical trap 190–4  
   use with dipole trapping 200–1
- optical pumping 140, 204–5, 207
- optical spectroscopy  
   effect of Doppler broadening 153  
   measurement of hyperfine structure  
     113–14, 161  
   measurement of Zeeman splitting  
     17–19
- optical tweezers 196–7
- orbital angular momentum quantum  
   number 24
- oscillating electric field, perturbation  
   by 124–5
- oscillator strength 149–50
- oscillators, interaction of 299–301
- $\pi$ -pulse duration 312–13  
 $\pi$ -pulses and  $\pi/2$ -pulses 128  
 $\pi$ -transitions 31
- p-series 34
- p-wave scattering 231
- parallelism in quantum computing  
   289–90
- parity 32–4
- partial electrostatic potential 303–4
- Paschen–Back effect 91, 93–4
- Paul trap 261–2, 271–2  
   use in quantum computing 282
- Pauli exclusion principle 46, 60
- pendulum, inverted 264
- Penning trap 271–3  
   magnetic moment of electron 274–5  
   mass spectroscopy of ions 274
- periodic table 60–1
- perturbation by oscillating electric field  
   124–5
- perturbation theory  
   interaction of classical oscillators of  
     similar frequencies 299–301
- mathematics of 298–9
- photo-ionization 145
- photoelectric effect 145–6
- photons  
   anti-bunching 146  
   statistical mechanics 315–16
- pinch coils 222–4
- Planck distribution law 13
- polarizability 197
- polarization 15–16, 29–31, 91, 127,  
   140–1  
   gradient 204–7
- positron, magnetic moment 275
- power broadening 143
- precession 37
- pressure broadening, *see* collision  
   broadening
- principal quantum number 5
- probability density 9, 62, 99
- probe beam, saturated absorption  
   spectroscopy 157–9
- projection theorem, *see* Wigner–Eckart  
   theorem
- pulsed lasers 172
- pump beam, saturated absorption  
   spectroscopy 157–9
- quadrupole interaction 102
- quadrupole magnetic fields 220–1  
   in linear Paul trap 263
- quantisation 145–6
- quantum computing 282, 291, 293–4  
   decoherence 292  
   logic gates 287–9  
   parallelism 289–90  
   qubits 283–6
- quantum defect 62–4, 68
- quantum electrodynamics (QED) 40  
   in bound systems 274–7
- quantum error correction (QEC) 292–3
- quantum harmonic oscillator, ground  
   state 235
- quantum jumps in ions 269–70
- quantum number, dependence of  
   energy on 61
- quantum scattering 229–34
- quasi-electrostatic traps (QUEST) 125
- qubits 283–4, 291  
   distinguishability 285  
   entanglement 284–6
- Rabi frequency 124  
   at saturation 143
- Rabi oscillations 128
- Rabi, Isador 119
- radial confinement in magnetic traps  
   220–1
- radial solution, Schrödinger equation  
   26–9
- radiation  
   black body 13, 316

excitation probability function 125  
 interaction of atoms with 123–4,  
     146–7  
     a.c. Stark effect 144–5  
     Einstein  $B$  coefficients 126–7  
     monochromatic radiation 127–32  
     optical absorption cross-section  
         138–41  
             power broadening 143  
             saturation intensity 142–3  
     optical Bloch equations 137  
     perturbation by oscillating electric  
         field 124–5  
     radiative damping 134–7, 146–7  
     Ramsey fringes 132–4  
     rotating-wave approximation 125  
     semiclassical treatment 145–6  
     quantisation 146  
 radiation emission, Einstein  $A$  and  $B$   
     coefficients 11–13  
 radiation force 179  
 radiation pressure 179  
 radiative damping 134, 146–7  
     of classical dipole 135–6  
 radiative decay 11  
 raising operator 24  
 Raman cooling 210–11  
 Raman interferometry 255–7  
 Raman scattering 164  
 Raman transitions 310–13  
     velocity selection 208–10  
 Ramsey fringes 132–4  
     in atomic fountains 212–13  
 random recoil in laser cooling 188–9  
 random telegraph signal 269  
 rate equations 12, 146–7  
 recoil limit 208  
     wavelength of atoms and photons  
         231  
 recoil velocity 180–1  
 red frequency detuning 185, 267  
 reduced mass 232–3  
 reflection 33  
     of atoms by evanescent wave 201–2  
     resultant force 194–5  
 refraction, resultant force 194–5  
 refractive index 195–6  
 relative frequency, laser calibration  
     168–9  
 relativistic effects 5–7, 36  
 residual electrostatic interaction 80  
 restoring force 14  
 Ritz combination principle 2  
 Röntgen 14  
 rotating-wave approximation 125  
 rotation  
     measurement in atom interferometry  
         251–3  
     parity 33  
 rubidium, chirp cooling 184

runaway evaporation 225  
 Russell–Saunders coupling, *see*  
     *LS*-coupling scheme  
 Rydberg atoms 11  
 Rydberg constant 2, 5  
 $\sigma$ -transitions 31  
 s-electrons  
     hyperfine structure 97–100  
     radial functions 28  
 s-series 34  
 s-wave 231  
 s–p transition, absorption of light 141  
 saddle, rotating 262  
 Sagnac interferometer 251  
 saturated absorption spectroscopy 155  
     cross-over resonances 159–60  
     line shape 307–9  
     of atomic hydrogen 159–63  
     principle 156–9  
 saturation intensity 142–3  
 scattering amplitude 130  
 scattering force 179–82  
     theory of 199  
 scattering length 231–3  
     for sodium 236  
 Schrödinger equation 22–3  
     angular part 23–6  
     for alkalis 68–71  
     for helium 45–8  
     inclusion of interaction between  
         atoms 234  
     numerical solution 69  
     radial part 26–9  
     time-dependent 123–4  
 Schrödinger’s cat 249, 251  
 screening  
     alkali atoms 64–8, 74–5, 81–2  
     helium atom 55  
     hyperfine structure 102–4  
     X-rays 9  
 second, definition of 118  
 second-order Doppler effect in  
     two-photon spectroscopy  
         167  
 selection rules 30–2, 42, 90  
     for  $F$  116–18, 305  
     for  $j$  42  
     for  $J$  90  
     for  $l$  32  
     for  $L$  90  
     for  $M_F$  116–18, 305  
     for  $M_I$  288  
     for  $M_J$  90–1  
     for  $m_l$  30–2  
     for  $M_L$  96  
     for  $M_S$  96  
     for  $S$  52  
     parity 32–4  
     summary 90, 305  
*see also* transitions  
 self-consistent solutions 70–1  
 semiclassical theory 145–6  
 semiconductor diode lasers 168  
 shape of Bose–Einstein condensates  
     237, 239  
 shell structure of electrons 7–10  
     and periodic table 60–1  
 shell, definition 61  
 ‘shooting’ method, *see* Schrödinger  
     equation, numerical solution  
 sideband cooling 277–9  
 silicon, *LS*-coupling scheme 81–2  
 Sisyphus cooling technique 178, 203–7  
     limit 207–8  
 Slater determinant 71  
 slowly-varying envelope approximation  
     135  
 sodium  
     chirp cooling 184  
     collimation, effect on Doppler  
         broadening 153–4  
     de Broglie wavelength 246  
     diffraction patterns 249–50  
     dipole trapping 200–1  
     fine structure 74  
     fine-structure transitions 74–5  
     interaction with polarized beam  
         140–1  
     probability density of electrons 61–2  
     properties of a BEC condensate 236  
     recoil limit 208  
     slowing 181  
 solid-state lasers, use in dipole  
     trapping 200  
 Sommerfeld 34  
     theory of electron orbits 6  
 sound, speed of 239  
 specific mass shift 106  
 spectroscopy  
     history 1–2  
     use of optical pumping 207  
     *see also* Doppler-free laser  
     spectroscopy; optical  
         spectroscopy  
 spherical harmonics  
     expansion of  $1/r_{12}$  55  
     table 25  
 spin eigenstates, helium 51–2  
 spin of electrons 35–6  
     in helium 46  
 spin–orbit interaction 36–8, 101  
     in alkalis 71–3  
      $jj$ -coupling scheme 84–6  
     *LS*-coupling scheme 83–4  
 spin–spin interactions 89  
 standing waves in atom interferometry  
     253–5  
 Stark effect 144–5  
 statistical mechanics

- Bose–Einstein condensation 316–18  
of photons 315–16
- Stern–Gerlach experiment 35, 114–15
- stopping distance 181–2
- sub-Doppler cooling 190, 203–4  
motion-induced orientation 207  
*see also* Sisyphus cooling technique
- sub-recoil cooling  
Raman cooling 210–11
- velocity-selective coherent population trapping 211  
*see also* evaporative cooling
- sub-shell, definition 61
- superconducting magnetic traps 219
- superfluidity 239–40  
healing length 240
- symmetric wavefunctions 48–52
- sympathetic cooling 266–7
- synchrotrons 10–11
- tellurium, use in laser calibration 169–70
- temperature  
critical in BEC 237  
determination in ions 269  
meaning of 208
- terms, in *LS*-coupling scheme 81
- Thomas precession factor 37, 101
- Thomas–Fermi regime 235–7
- Thompson, J. J. 14
- three-grating interferometer 251–2  
comparison with Raman interferometer 257
- time dilation 167
- time-dependent perturbation theory (TDPT) 29, 123
- tin, Doppler-free laser spectroscopy 114
- transformations, parity 33
- transit-time broadening 154
- transit time in two-photon spectroscopy 165
- transitions  
in alkaline earths 90  
in alkalis 74–5  
in helium 52–3  
in hydrogen atom 29–30  
parity 32–4  
selection rules 30–2
- trapped atoms, harmonic potential 235
- trapping  
effect on transition frequency measurement 211–12  
*see also* ion trapping; magnetic traps; magneto-optical trap
- triangle rule 42
- tunable lasers 168
- two-level atom 123–4
- two-photon spectroscopy 163–8
- two-photon transition 313–14
- units, inside back cover  
atomic 18–19
- uranium, ionization of 276
- vacuum fluctuations 40
- vector model 37, 83–4, 90
- vector operator 83–4, 90
- velocity selection by Raman transitions 208–10
- velocity-selective coherent population trapping 211
- vibrational energy levels 277–9
- volume shift between isotopes 106–8
- wave–particle duality 246
- wavefunctions  
angular 25–6  
radial 27–9  
symmetric and antisymmetric 48–52
- wavenumbers 2
- Wigner–Eckart theorem 83
- X-ray spectra 7–11
- X-rays, discovery of 14
- Young’s double-slit experiment 133–4, 246–8
- ytterbium ion transitions 270
- Zeeman effect 13–16  
and hyperfine structure 108–9  
intermediate fields 111  
of hydrogen 109–10, 112–13  
strong fields 110–12  
weak fields 109–10, 112
- anomalous 35  
experimental observation 17–18  
in alkalis 75  
in *LS*-coupling scheme 90–2  
normal 13–16, 35, 91  
Zeeman slowing 182–4  
Zeeman sub-levels 93